This is to certify that the

dissertation entitled

APPLICATION OF E-PULSE AND CEPSTRAL ANALYSIS
TO TARGET DETECTION AND DISCRIMINATION

presented by

Glen Stuart Wallinga

has been accepted towards fulfillment
of the requirements for

Ph.D. degree in Electrical Eng.

Edward J Rothwell
Major professor

Date June 17, 1997

APPLICATION OF E-PULSE AND CEPSTRAL ANALYSIS TO RADAR TARGET DETECTION AND DISCRIMINATION

By

Glen Stuart Wallinga

A DISSERTATION

Submitted to
Michigan State University
in partial fulfillment of the requirements
for the degree of

DOCTOR OF PHILOSOPHY

Department of Electrical Engineering

1997

ABSTRACT

APPLICATION OF E-PULSE AND CEPSTRAL ANALYSIS TO RADAR TARGET DETECTION AND DISCRIMINATION

By

Glen Stuart Wallinga

This thesis addresses several topics related to the use of ultra-wideband radar for target detection and discrimination. A new method to determine the scattered field from an infinite length, perfectly-conducting, periodic sea-surface has been formulated. This method is based on a periodic surface-current representation. The motivation for doing this work is to create a computationally efficient method for determining the scattered field from periodic surfaces.

An enhanced detection algorithm for radar-target detection in a sea-clutter environment has been formulated using the E-pulse method. The theory behind this new method is discussed, several static test cases presented, and a dynamic test case presented showing the functionality of the detection algorithm for a target moving over an evolving sea-surface. The effect of different target types on the detection algorithm has been tested. Also, the effect of multipath on the detection algorithm has been investigated. Finally, the new method has been compared to a simple detection algorithm based on clutter reduction using coherent signal processing.

A target discrimination scheme using only the magnitude of its spectral response has been devised based upon real cepstral analysis. Basic cepstral analysis techniques and the minimum-phase condition are discussed. A discrimination scheme based upon

the E-p
time-do
represen
reconstr
associa
parame
measure

the E-pulse method was used. A library of E-pulse waveforms was generated from the time-domain scattered return of each anticipated target type. The time-domain representation of an unknown target was generated using the minimum-phase reconstruction method. The target discrimination algorithm was used to identify an associated geometry in the target library file. Test cases included: a) thin-wire scattering geometries using a theoretical scattering program, and b) actual anechoic chamber measurements of small-scale aircraft and missiles.

ACKNOWLEDGMENTS

Many people deserve acknowledgement for their participation in helping me complete this work. My foremost appreciation must go to my advisor Dr. E.J. Rothwell. Thank you for your time, patience, and guidance over the past several years. I could have never completed this thesis without your help. A special thanks to Dr. K.M Chen who generously invited me to work in an outstanding lab during my studies. I am also indebted to Dr. D.P. Nyquist for his guidance and teaching. To Dr. Byron Drachman, thank you for participating on my guidance committee and for your assistance.

I also wish to thank Dr. William Peake, whose enthusiasm for electromagnetics motivated me to pursue this area of study.

Many people in this lab have helped me during my study here. I am especially grateful to Adam Norman for his generous help and guidance. Also, a special thank you to Mike Havrilla and David Infante for their company and advice.

TABLE OF CONTENTS

LIST OF TABLES

LIST OF FIGURES

Chapter 1

Introduction

Detecting the presence of small targets in a nonstationary clutter background is a fundamental problem in radar detection and tracking scenarios. The detection of both low altitude and low cross section antiship missiles is of prime concern to the navy, and early detection becomes critical to a ship's survival by successfully tracking and engaging the missile. A radar detection system that provides clutter suppression and fine range resolution offers a significant advantage over systems which lack these capabilities.

Interest in ultra-wideband (UWB) radar systems arises in their potential use for target identification and for low altitude, low radar cross section target detection over water [1]. Compared with conventional continuous wave (CW) radars, UWB radars are characterized by very large relative bandwidth and fine range resolution [1]-[2]. Another major advantage offered by UWB radar technology is its clutter suppression capability, therefore making it useful for detecting low-flying missiles and aircraft in sea clutter environments [1]-[3].

Within the electromagnetics laboratory (EM Lab) at Michigan State University (MSU), a great deal of effort has been devoted to problems in the area of target detection and discrimination using UWB radar returns. One proposed discrimination scheme, called the "Extinction-pulse" or "E-pulse" technique, has been applied to a large number of problems. Early development in this area can be found in the work of Baum [4] and Rothwell [5]. Several other authors have contributed to further research in this area [6] -

[8]. A major portion of this thesis wil

schemes using the E-pulse method.

This thesis will cover a wide ran

target detection and discrimination. In th

of previous work done by previous MS

determine the scattered field from an infi

PEC) sea-surface has been formulated

current representation. The motivation f

efficient method for determining the

important in that the scattered return

computed and later used for testing dif

An enhanced algorithm for radar

been formulated using the E-pulse

formulation, electromagnetic scattering

serves as a review and a starting point fo

Chapter 4 develops a new app

environment. This approach, rooted in

some of the difficulties encountered whe

theory for detection enhancement, some

required to solve the detection proble

computational time is E-pulse construc

involves a global minimization schem

[8]. A major portion of this thesis will be devoted to new detection and identification schemes using the E-pulse method.

This thesis will cover a wide range of topics involving the use of UWB radar for target detection and discrimination. In this respect, the present work will be an extension of previous work done by previous MSU researchers. In chapter 2, a new method to determine the scattered field from an infinite-length, periodic, perfectly electric conducting (PEC) sea-surface has been formulated. This method is based on a periodic surface current representation. The motivation for doing this work is to create a computationally efficient method for determining the scattered field for periodic surfaces. This is important in that the scattered return from a sea-like surface can be theoretically computed and later used for testing different detection algorithms.

An enhanced algorithm for radar target detection in a sea clutter environment has been formulated using the E-pulse scheme. Chapter 3 discusses basic E-pulse formulation, electromagnetic scattering calculations, and target detection. This chapter serves as a review and a starting point for the work on the enhanced detection algorithm.

Chapter 4 develops a new approach used to detect targets in a sea clutter environment. This approach, rooted in the basic E-pulse detection scheme, overcomes some of the difficulties encountered when using the E-pulse method. After discussing the theory for detection enhancement, some time will be devoted to the numerical methods required to solve the detection problem. One particular area requiring considerable computational time is E-pulse construction. The construction of an optimal E-pulse involves a global minimization scheme. A convenient approach is to use a genetic algorithm. Implementation of the genet

To verify the new enhanced dete
First, a stationary sea-surface will be te
be examined. In the latter case, the sea
computed as a function of time. The
surface interaction will also be investigat
to a coherent processing clutter reductio

One area that is common to a
processing in one form or another. Mos
data in the frequency domain and trans
which may require some careful plannin
with discrete data sets. This is especial
a high signal to noise ratio obtained fro
most frequency data contain both magnit
can be obtained with a minimum of effo
other hand, under certain conditions the
it still may be possible to obtain a t
discrimination scheme using the E-puls
topic, and several chapters in this thesi
using the method of cepstral analysis.

An overview of cepstral analys
method an attempt will be made to reco

algorithm. Implementation of the genetic algorithm will be discussed in detail.

To verify the new enhanced detection technique, several approaches will be taken. First, a stationary sea-surface will be tested. Next, a simulated dynamic sea surface will be examined. In the latter case, the scattered field from a changing sea surface will be computed as a function of time. The effect on target detection from target and sea surface interaction will also be investigated. Finally, this new technique will be compared to a coherent processing clutter reduction algorithm.

One area that is common to all aspects of this research is the use of signal processing in one form or another. Most analyses will numerically generate a set of radar data in the frequency domain and transform this information to the time domain. This effort may require some careful planning in order to avoid problems normally associated with discrete data sets. This is especially true when requiring a transient response with a high signal to noise ratio obtained from data measured in the frequency domain. Since most frequency data contain both magnitude and phase information, the transient response can be obtained with a minimum of effort by using an inverse Fourier transform. On the other hand, under certain conditions the phase information might be absent. In this case it still may be possible to obtain a transient response that can be used in a target discrimination scheme using the E-pulse method. A great deal of time is spent on this topic, and several chapters in this thesis will be devoted to UWB signal reconstruction using the method of cepstral analysis.

An overview of cepstral analysis will be presented in chapter 5. Using this method an attempt will be made to reconstruct a radar target transient response from the

magnitude of its frequency-domain spe
important topics of minimum phase cond
energy relation will provide some phy
minimum phase condition. Minimum p
time components of a target's transient
presented illustrating the use of cepstr
early and late-time signal in both the fre
the minimum phase reconstruction algo

The motivation behind cepstr
discrimination. Chapter 6 will present a
the E-pulse method [9] and the ideas p
a library of E-pulse waveforms asso
constructed. The E-pulse waveform w
been constructed using both the frequen
time-domain representation of an unkn
reconstruction method. The target disc
associated geometry in a target library
geometries using a theoretical scatter
measurements of small-scale aircraft an

Due to the extensive use of scatt
been devoted to this topic. Topics cover
and windowing functions. Measureme

magnitude of its frequency-domain spectrum. Theoretical discussion will include the important topics of minimum phase conditions and minimum phase energy relations. The energy relation will provide some physical insight into signal characteristics and the minimum phase condition. Minimum phase reconstructed signals for the early and late-time components of a target's transient signal will be discussed. Many examples will be presented illustrating the use of cepstral reconstruction. Finally, the separation of the early and late-time signal in both the frequency and time domain will be discussed using the minimum phase reconstruction algorithm.

The motivation behind cepstral reconstruction is the application to target discrimination. Chapter 6 will present a simple automated discrimination algorithm using the E-pulse method [9] and the ideas presented in chapter 5. In this detection scheme, a library of E-pulse waveforms associated with different target geometries will be constructed. The E-pulse waveform will be generated from time-domain data that has been constructed using both the frequency-domain magnitude and phase information. The time-domain representation of an unknown target will be generated using the cepstral reconstruction method. The target discrimination algorithm will attempt to identify an associated geometry in a target library file. Test cases include: a) thin-wire scattering geometries using a theoretical scattering program, and b) actual anechoic chamber measurements of small-scale aircraft and missiles.

Due to the extensive use of scattering measurements, a section in the appendix has been devoted to this topic. Topics covered will include measurement systems, procedures, and windowing functions. Measurement systems will examine the physical setup and description of measurements made in

procedure section will review the ste

Finally, the most common windowing f

description of measurements made in the anechoic chamber at the EM Lab. The procedure section will review the steps necessary to obtain reliable measurements. Finally, the most common windowing functions used in this thesis will be discussed.

C

Scattering from a Periodic
F

2.1 Introduction

A great deal of effort has

electromagnetic scattering from ocean

frequently encountered is the physical

memory required and the computer pro

great deal of research has been devoted

these models. This research has inclu

measurements in an anechoic chamber

surface roughness in one dimension. Fo

that various as a function of x but

Theoretical study of scattering from the

electric field integral equation using

computationally expensive for a gener

surface. However, this leads to problem

can be simplified by putting some cons

For periodic infinite surfaces, t

efficient way. Norman has done extens

chapter is to propose another method

calculated for an infinite periodic surf

Chapter 2

Scattering from a Periodic Surface Using a Periodic Current Function

2.1 Introduction

A great deal of effort has been devoted to the numerical solution of electromagnetic scattering from ocean-like surfaces [10]-[11]. One of the problems frequently encountered is the physical constraints imposed by the amount of computer memory required and the computer processing speed available. In the MSU EM Lab, a great deal of research has been devoted to the study of scattering from various sea surface wave models. This research has included both theoretical scattering and experimental measurements in an anechoic chamber. All the wave models used are constrained to surface roughness in one dimension. For example, a simple sinusoid surface has a height z that various as a function of x but the wave height is invariant in the y direction. Theoretical study of scattering from these surfaces involves the numerical solution of an electric field integral equation using the method of moments. Most often this is computationally expensive for a general surface and forces the use of a finite extent surface. However, this leads to problems associated with edge effects. Often the problem can be simplified by putting some constraints on the surface.

For periodic infinite surfaces, the scattered fields can be determined in a more efficient way. Norman has done extensive research in this area [12]. The purpose of this chapter is to propose another method whereby the current and scattered fields can be calculated for an infinite periodic surface. The approach described in this chapter is similar to a periodic-surface moment m

This chapter is divided in the f

theory will be covered. Several sectio

computer scattering examples will be co

will provide both comparisons to other

types of surfaces. Since researchers in

fields from rather small surfaces (typic

time is devoted to larger surfaces using

included focusing on the advantages an

2.2 Theory

2.2.1 Scattered field - simple expan

Figure 2.1 shows a plane wave, I

periodic surface of wavelength D. The

crests of the surface and the angle betw

given by ϕ. A surface current $\vec{K}(x)$

Furthermore, due to the periodic nature

modeled with the following expression

$$K(x) = \sum_{n}$$

where

$$K_0(x) = \begin{cases} K \\ 0 \end{cases}$$

$$\beta_n = n\,k\,\mathrm{c}$$

similar to a periodic-surface moment method described by Chen and West [13].

This chapter is divided in the following manner. First, a detailed discussion of theory will be covered. Several sections will be devoted to this. Next, some simple computer scattering examples will be computed using this new method. These examples will provide both comparisons to other methods, and illustrate scattering from various types of surfaces. Since researchers in the EM lab have typically calculated scattered fields from rather small surfaces (typical wavelength of surface is about 4 inches), some time is devoted to larger surfaces using the new method. A final discussion will also be included focusing on the advantages and shortcomings of this new method.

2.2 Theory

2.2.1 Scattered field - simple expansion

Figure 2.1 shows a plane wave, having propagation constant k, impinging on a 2-d periodic surface of wavelength D. The polarization of the electric field is parallel to the crests of the surface and the angle between the horizon and the propagation vector $\vec{k}$ is given by ϕ_o. A surface current $\vec{K}(x) = \hat{z}\,K(x)$ will be induced by the electric field. Furthermore, due to the periodic nature of the surface, a periodic surface current can be modeled with the following expression

$$K(x) = \sum_{n=-\infty}^{\infty} K_0(x-nD)\, e^{j\beta_n D} \tag{2.1}$$

where

$$K_0(x) = \begin{cases} K(x), & -\dfrac{D}{2} \le x \le \dfrac{D}{2} \\ 0 & elsewhere \end{cases} \tag{2.2}$$

$$\beta_n = n\,k\cos\phi_0 \tag{2.3}$$

The scattered field from the induced cu

$$E_z^s(x,y) = -\frac{k\eta}{4}\int_{-\infty}^{\infty} K(x')\, H_0^{(2)}$$

where $H_0^{(2)}$ represent a Hankel functi

differential line element length are gi

intrinsic impedance of the medium. Usi

making the substitution $u = x' - nD$ yie

$$E_z^s(x,y) = -\frac{k\eta}{4}\int_{-D/2}^{D/2} \sum_{n=-\infty}^{\infty} K(u) \, e^{\dots} H_0^{(2)}$$

The periodic nature of the scattering

periodicity yields two useful relations

$$f(u$$

$$L(u$$

Using the above relations, the scattered

for the periodic surface

$$E_z^s(x,y) = -\frac{k\eta}{4}$$

where

$$K(x,x') = \sum_{-\infty}^{\infty} e^{j\beta_n d} H_0^{(2)}$$

To numerically compute the ke

can be accelerated. One way of doing

method like terms from the series are

relation that can be more easily comput

The scattered field from the induced current is given by [14]

$$E_z^s(x,y) = -\frac{k\eta}{4}\int_{-\infty}^{\infty} K(x')\, H_0^{(2)}\!\left(k\sqrt{(x-x')^2 + (f(x)-f(x'))^2}\,\right) L(x')\,dx' \qquad \textbf{(2.4)}$$

where $H_0^{(2)}$ represent a Hankel function of the second kind. The surface height and differential line element length are given by f(x) and L(x)dx respectively. η is the intrinsic impedance of the medium. Using the periodic surface current given by (2.1) and making the substitution u = x'- nD yields the following form for the scattered field

$$E_z^s(x,y) = -\frac{k\eta}{4}\int_{-D/2}^{D/2} \sum_{n=-\infty}^{\infty} K_0(u)\,e^{j\beta_n D} H_0^{(2)}\!\left(k\sqrt{(x-u-nD)^2 + (f(x)-f(u+nD))^2}\,\right) L(u+nD)\,du \qquad \textbf{(2.5)}$$

The periodic nature of the scattering surface can be used to simplify (2.5). The periodicity yields two useful relations

$$\begin{aligned} f(u+nD) &= f(u) \\ L(u+nD) &= L(u) \end{aligned} \qquad \textbf{(2.6)}$$

Using the above relations, the scattered field can be written in terms of a kernel K(x,x') for the periodic surface

$$E_z^s(x,y) = -\frac{k\eta}{4}\int_{-\frac{D}{2}}^{\frac{D}{2}} K_0(x')K(x,x')L(x')\,dx' \qquad \textbf{(2.7)}$$

where

$$K(x,x') = \sum_{-\infty}^{\infty} e^{j\beta_n d} H_0^{(2)}\!\left(k\sqrt{(x-x'-nD)^2 + (f(x)-f(x'))^2}\,\right) \qquad \textbf{(2.8)}$$

To numerically compute the kernel the convergence of the series given by (2.8) can be accelerated. One way of doing this is given by Kummer's method [15]. In this method like terms from the series are added and subtracted in hopes of yielding a new relation that can be more easily computed. If (2.8) is expanded and like terms are added and subtracted the following relation is

$$K(x,x') = H_0^{(2)}\left(k_1 \sqrt{(x-x')^2 + (f(x) \ldots}\right.$$

$$- \sum_{n=1}^{\infty} e^{-j(nD)k\sin\phi_i} H_0^{(2)}\left(k_1 (r \ldots\right.$$

$$- \quad e^{-j(nD)k\sin\phi_i} H_0^{(2)}\left(k_1 (r \ldots\right.$$

$$- \quad \sum_{n=1}^{\infty} A_n(x,x') \quad - \ldots$$

Next, the forms for A_n and A_n' must

converge the terms given by A_n and

function for large arguments. The Ha

its arguments involving the following

$$s' = nD \sqrt{1 - \frac{(x \ldots}{\ldots}}$$

which for large values of n can simply

$$s' \ldots$$

Furthermore, for large arguments the H

$$H_0^{(2)}(\ldots$$

Next, the Hankel function argument inv

for the exponential term in (2.12). The

If the terms within the braces of (2.

obtained

and subtracted the following relation is formed

$$
\begin{aligned}
K(x,x') = {} & H_0^{(2)}\left(k\sqrt{(x-x')^2+(f(x)-f(x'))^2}\right) \\
& + \sum_{n=1}^{\infty}\left\{ e^{jnkD\cos\phi_0} H_0^{(2)}\left(k\sqrt{(nD-(x-x'))^2+(f(x)-f(x'))^2}\right) - A_n^-(x,x') \right. \\
& + \left. e^{-jnkD\cos\phi_0} H_0^{(2)}\left(k\sqrt{(nD+(x-x'))^2+(f(x)-f(x'))^2}\right) - A_n^+(x,x') \right\} \\
& + \sum_{n=1}^{\infty} A_n^-(x,x') + \sum_{n=1}^{\infty} A_n^+(x,x')
\end{aligned}
\tag{2.9}
$$

Next, the forms for A_n^- and A_n^+ must be determined. If the series given by (2.9) is to converge the terms given by A_n^- and A_n^+ should approach the value of the Hankel function for large arguments. The Hankel function enclosed within the braces of (2.9) has arguments involving the following term

$$
s^{\pm} = nD\sqrt{1 + \frac{(x-x')^2 + (f-f')^2}{(nD)^2} \pm 2\frac{(x-x')}{nD}}
\tag{2.10}
$$

which for large values of n can simply be written as

$$
s^{\pm} = nD \pm (x - x')
\tag{2.11}
$$

Furthermore, for large arguments the Hankel function can be written as

$$
H_0^{(2)}(z) = \sqrt{\frac{2j}{\pi}}\,\frac{e^{-jz}}{\sqrt{z}}
\tag{2.12}
$$

Next, the Hankel function argument involving the term given in (2.11) can be substituted for the exponential term in (2.12). The denominator argument can be replaced by knD. If the terms within the braces of (2.9) are compared then the following relation is obtained

$$A_n^\pm(x,x') = \sqrt{\frac{2j}{\pi}}$$

Some simplifying yields

$$A_n^\pm = \sqrt{\ }$$

where

$$Z_0^\pm =$$

With the form of A_- chosen, the last tw

$$S^\pm(x,x$$

and substituting (2.14) into the above r

$$S^\pm(x,x') = \sqrt{\frac{2j}{\pi k}}$$

A change of index in the summation g

$$S^\pm(x,x') = \sqrt{\ }$$

This sum can be written in terms of th

$$\Phi(z,s,v$$

Comparing (2.18) and (2.19) allows th

$$S^\pm(x,x') = \sqrt{\frac{2j}{\pi k}}$$

The Lerch transcendent, given by an i

integral as [16]

$$A_n^{\pm}(x,x') = \sqrt{\frac{2j}{\pi}}\, e^{\mp jnkD\cos\phi_0}\, \frac{e^{-jknD}}{\sqrt{knD}}\, e^{\mp jk(x-x')} \tag{2.13}$$

Some simplifying yields

$$A_n^{\pm} = \sqrt{\frac{2j}{\pi kD}}\, e^{\mp jk(x-x')}\, \frac{(Z_0^{\pm})^n}{\sqrt{n}} \tag{2.14}$$

where

$$Z_0^{\pm} = e^{-jkD(1\, \pm\, \cos\phi_0)} \tag{2.15}$$

With the form of A_n chosen, the last two sums in (2.9) can be evaluated. Letting

$$S^{\pm}(x,x') = \sum_{n=1}^{\infty} A_n^{\pm}(x,x') \tag{2.16}$$

and substituting (2.14) into the above relation yields

$$S^{\pm}(x,x') = \sqrt{\frac{2j}{\pi kD}}\, e^{\mp jk(x-x')}\, Z_0^{\pm} \sum_{n=1}^{\infty} \frac{(Z_0^{\pm})^{n-1}}{\sqrt{n}} \tag{2.17}$$

A change of index in the summation gives

$$S^{\pm}(x,x') = \sqrt{\frac{2j}{\pi kD}}\, e^{\mp jk(x-x')}\, Z_0^{\pm} \sum_{n=0}^{\infty} \frac{(Z_0^{\pm})^{n}}{\sqrt{n+1}} \tag{2.18}$$

This sum can be written in terms of the "Lerch transcendent", which is given by [16]

$$\Phi(z,s,v) = \sum_{n=0}^{\infty} (v+n)^{-s}\, z^n \tag{2.19}$$

Comparing (2.18) and (2.19) allows the sum to be expressed as

$$S^{\pm}(x,x') = \sqrt{\frac{2j}{\pi kD}}\, e^{\mp jk(x-x')}\, Z_0^{\pm}\, \Phi(Z_0^{\pm}, \tfrac{1}{2}, 1) \tag{2.20}$$

The Lerch transcendent, given by an infinite summation, can be written in terms of an integral as [16]

$$\Phi(z, \tfrac{1}{2},$$

Due to the singularity of the integrand

numerically. To evaluate this integral

following relation

$$\Phi(z, \tfrac{1}{2}, 1) = \frac{1}{\sqrt{\pi}} \int_0^{\infty} \frac{1}{e^{t} - z}$$

The second integral in (2.22) is given

to

$$\Phi(z, \tfrac{1}{2}, 1) = \frac{1}{1 - z}$$

The advantage of the above relation is

since the integral argument is proporti

2.2.2 Scattered field - higher orde

The convergence rate of (2.9) i

rate of convergence higher order term

asymptotic form of the Hankel functio

developed simple relations given by

higher order terms necessary to increa

for $A_n^{\pm}$ in the preceding sections conta

goal of this section is to show a devel

$$\Phi(z,\tfrac{1}{2},1) = \frac{1}{\sqrt{\pi}} \int_0^{\infty} \frac{t^{-\frac{1}{2}}}{e^t - z} dt \tag{2.21}$$

Due to the singularity of the integrand for t = 0, the above integral is difficult to solve numerically. To evaluate this integral, like terms are added and subtracted to form the following relation

$$\Phi(z,\tfrac{1}{2},1) = \frac{1}{\sqrt{\pi}} \int_0^{\infty} \left[\frac{1}{e^t - z} - \frac{e^{-t}}{1-z} \right] t^{-\frac{1}{2}} dt + \frac{1}{\sqrt{\pi}} \frac{1}{1-z} \int_0^{\infty} \frac{e^{-t}}{\sqrt{t}} dt \tag{2.22}$$

The second integral in (2.22) is given by $\sqrt{\pi}$ [16]. Therefore, (2.22) can be simplified to

$$\Phi(z,\tfrac{1}{2},1) = \frac{1}{1-z} + \frac{1}{\sqrt{\pi}} \frac{z}{1-z} \int_0^{\infty} \frac{e^{-t} - 1}{\sqrt{t}} \frac{dt}{e^t - z} \tag{2.23}$$

The advantage of the above relation is that the integral in this form converges much better since the integral argument is proportional to the square root of t for small arguments.

2.2.2 Scattered field - higher order expansion

The convergence rate of (2.9) is determined by the forms of $A_n^{\pm}$. To increase the rate of convergence higher order terms in both the Hankel function argument and the asymptotic form of the Hankel function itself must be considered. The preceding section developed simple relations given by (2.11) and (2.12). This section will develop the higher order terms necessary to increase the rate of convergence. The terms developed for $A_n^{\pm}$ in the preceding sections contains a summation index n dependence of $n^{-1/2}$. The goal of this section is to show a development that has an index dependence for terms up to n^{-2}. Although the development is le

the rate of convergence for the series i

The argument to the Hankel fu

$$s =$$

where

$$u = \frac{(x - x\ )^2}{(}$$

Expanding the square root in (2.24) to

$$s = nD(1 + \frac{1}{2}u -$$

Substituting for u and keeping terms o

$$s = nD + (x - x\ ) + \frac{(f - f\ )^2}{2nD} +$$

The asymptotic form for the Hankel f

$$H_0^2(z) = \sqrt{\frac{2j}{\pi}}\frac{1}{\sqrt{z}}e^{-jz}\ 1 + \frac{j}{8z}$$

with z = ks , (2.28) becomes

$$H_0^2(s) = \sqrt{\frac{2j}{\pi k}}e^{-jks}\ \frac{1}{s^{1/2}} + \frac{j}{8k}\frac{1}{s^{3/2}}$$

To evaluate the above relation, approp

the terms involving inverse powers o

exponential term can be approximatec

to $n^{-7/2}$. Although the development is lengthy, the extra terms derived will greatly increase the rate of convergence for the series in (2.9).

The argument to the Hankel function given in (2.9) is proportional to

$$s = nD\sqrt{1 + u} \tag{2.24}$$

where

$$u = \frac{(x - x')^2 + (f - f')^2}{(nD)^2} \pm \frac{2(x - x')}{nD} \tag{2.25}$$

Expanding the square root in (2.24) to include higher order terms gives

$$s = nD\left(1 + \frac{1}{2}u - \frac{1}{8}u^2 + \frac{1}{16}u^3 - \frac{5}{128}u^4 + \ldots\right) \tag{2.26}$$

Substituting for u and keeping terms only up to $(nD)^{-3}$ yields

$$s \approx nD \pm (x - x') + \frac{(f - f')^2}{2nD} \mp \frac{(x - x')(f - f')^2}{2(nD)^2} + \frac{1}{2}\frac{(x - x')^2(f - f')^2}{(nD)^3} - \frac{1}{8}\frac{(f - f')^4}{(nD)^3} \tag{2.27}$$

The asymptotic form for the Hankel function is given by [17]

$$H_0^2(z) = \sqrt{\frac{2j}{\pi}\frac{1}{\sqrt{z}}}\, e^{-jz}\left[1 + \frac{j}{8z} - \frac{9}{128z^2} - j\frac{225}{3072}\frac{1}{z^3} + \frac{11025}{98304}\frac{1}{z^4} + \ldots\right] \tag{2.28}$$

with z = ks , (2.28) becomes

$$H_0^2(s) = \sqrt{\frac{2j}{\pi k}}\, e^{-jks}\left[\frac{1}{s^{1/2}} + \frac{j}{8k}\frac{1}{s^{3/2}} - \frac{9}{128k^2}\frac{1}{s^{5/2}} - j\frac{225}{3072}\frac{1}{k^3}\frac{1}{s^{7/2}} + \frac{11025}{98304}\frac{1}{k^4}\frac{1}{s^{9/2}} + \ldots\right] \tag{2.29}$$

To evaluate the above relation, appropriate terms must be found for the exponential and the terms involving inverse powers of s. Using the relation given for s in (2.27) the exponential term can be approximated as

$$e^{-jks} = e \ldots$$

where

$$\alpha = \frac{(f-f\,)^2}{2nD} \doteq \frac{(x-x\,)(f-\ldots}{2(nD)^2 \ldots}$$

A simple expansion of the exponential ...

$$e^{-jk\alpha} = 1 - \ldots$$

Since α contains terms up to $(nD)^{-3}$, ...

should be used. To see this, a substit...

terms up to $(nD)^{-3}$ whereas a term ...

Hence, in order to expand the compl...

terms should be included in the evaluat...

expansion can be written as

$$e^{-jks} = e^{-jknD} e^{-jk \ldots} \Big\{ 1 \ldots$$

$$+ \frac{\ldots}{(n \ldots}$$

$$+ \frac{\ldots}{(n \ldots}$$

To attack the problem of finding rela...

(2.24) can be expanded to give

$$\frac{1}{s} = \ldots$$

Thus

$$\frac{1}{s^{1/2}} = \frac{1}{(nD)^{1/2}}(1 + u)^{-1/4} = \ldots$$

$$e^{-jks} \approx e^{-jknD} e^{\mp jk(x-x')} e^{-jk\alpha} \tag{2.30}$$

where

$$\alpha = \frac{(f-f')^2}{2nD} \mp \frac{(x-x')(f-f')^2}{2(nD)^2} + \frac{1}{2}\frac{(x-x')^2(f-f')^2}{(nD)^3} - \frac{1}{8}\frac{(f-f')^4}{(nD)^3} \tag{2.31}$$

A simple expansion of the exponential term containing the inverse powers of n yields

$$e^{-jk\alpha} \approx 1 - jk\alpha - \frac{k^2}{2}\alpha^2 + j\frac{k^3}{6}\alpha^3 \tag{2.32}$$

Since α contains terms up to $(nD)^{-3}$, no higher order terms than those shown in (2.32) should be used. To see this, a substitution for α into the second term of (2.32) yields terms up to $(nD)^{-3}$ whereas a term proportional to α^4 will yield terms with $(nD)^{-4}$. Hence, in order to expand the complex exponential to include additional terms, more terms should be included in the evaluation of α. With terms up to $(nD)^{-3}$, the exponential expansion can be written as

$$\begin{aligned} e^{-jks} \approx e^{-jknD} e^{\mp jk(x-x')} \Big\{ 1 &- \frac{1}{nD}\left(\tfrac{1}{2}jk(f-f')^2 \right) \\ &+ \frac{1}{(nD)^2}\left(\pm\tfrac{1}{2}jk(x-x')(f-f')^2 - \tfrac{1}{8}k^2(f-f')^4 \right) \\ &+ \frac{1}{(nD)^3}\Big(-\tfrac{1}{2}jk(x-x')^2(f-f')^2 + \tfrac{1}{8}jk(f-f')^4 \\ &\qquad \pm\tfrac{1}{4}k^2(x-x')(f-f')^4 + \tfrac{1}{48}jk^3(f-f')^6 \Big) \Big\} \end{aligned} \tag{2.33}$$

To attack the problem of finding relations for the inverse powers of s, the inverse of (2.24) can be expanded to give

$$\frac{1}{s} = \frac{1}{nD}(1 + u)^{-1/2} \tag{2.34}$$

Thus

$$\frac{1}{s^{1/2}} = \frac{1}{(nD)^{1/2}}(1 + u)^{-1/4} = \frac{1}{(nD)^{1/2}}\left(1 - \frac{1}{4}u + \frac{5}{32}u^2 - \frac{15}{128}u^3 + \ldots\right)$$

$$\frac{1}{s^{3/2}} = \frac{1}{(nD)^{3/2}}(1 + u)^{-3/4} =$$

$$\frac{1}{s^{5/2}} = \frac{1}{(nD)^{5/2}}(1 + u)^{-5/4} =$$

$$\frac{1}{s^{7/2}} = \frac{1}{(nD)^{7/2}}(1 + u)^{-7/4} =$$

To keep only terms up to $(nD)^{-2}$ only

need to be used. A quick review of (

proportional to nD and $(nD)^2$, and e

and n^2. The Hankel function in (2.29)

term with the inverse power terms.

exponential (i.e. the unity term) by th

order to have the n^{-2} requirement. Al

Therefore, the power terms can be rev

$$\frac{1}{s^{1/2}} \approx \frac{1}{(nD)^{1/2}}($$

$$\frac{1}{s^{3/2}} \approx \frac{1}{(nD)^{3/2}}($$

$$\frac{1}{s^{5/2}} \approx \frac{1}{(nD)^{5/2}}($$

$$\frac{1}{s^{7/2}} \approx \frac{1}{(nD)^{7/2}}$$

Multiplication of the complex expon

additional terms not needed in the fin

$$\frac{1}{s^{3/2}} = \frac{1}{(nD)^{3/2}}(1 + u)^{-3/4} = \frac{1}{(nD)^{3/2}}(1 - \frac{3}{4}u + \frac{21}{32}u^2 - \frac{77}{128}u^3 + ...)$$

$$\frac{1}{s^{5/2}} = \frac{1}{(nD)^{5/2}}(1 + u)^{-5/4} = \frac{1}{(nD)^{5/2}}(1 - \frac{5}{4}u + \frac{45}{32}u^2 - \frac{195}{128}u^3 + ...) \qquad \textbf{(2.35)}$$

$$\frac{1}{s^{7/2}} = \frac{1}{(nD)^{7/2}}(1 + u)^{-7/4} = \frac{1}{(nD)^{7/2}}(1 - \frac{7}{4}u + \frac{77}{32}u^2 - \frac{385}{128}u^3 + ...)$$

To keep only terms up to $(nD)^{-7/2}$ only a limited number of terms in the above relations need to be used. A quick review of (2.25) and (2.33) shows that u has terms inversely proportional to nD and $(nD)^2$, and e^{-jks} has terms inversely proportional to unity, n, n^2, and n^3. The Hankel function in (2.29) is formed by multiplying the complex exponential term with the inverse power terms. By multiplying the first term in the complex exponential (i.e. the unity term) by the $s^{-1/2}$ term the highest power of u must be u^3 in order to have the $n^{-7/2}$ requirement. Also the highest power of u for $s^{-3/2}$ term must be u^2. Therefore, the power terms can be rewritten as

$$\begin{aligned}
\frac{1}{s^{1/2}} &\approx \frac{1}{(nD)^{1/2}}(1 - \frac{1}{4}u + \frac{5}{32}u^2 - \frac{15}{128}u^3) \\
\frac{1}{s^{3/2}} &\approx \frac{1}{(nD)^{3/2}}(1 - \frac{3}{4}u + \frac{21}{32}u^2) \\
\frac{1}{s^{5/2}} &\approx \frac{1}{(nD)^{5/2}}(1 - \frac{5}{4}u) \\
\frac{1}{s^{7/2}} &\approx \frac{1}{(nD)^{7/2}}
\end{aligned} \qquad \textbf{(2.36)}$$

Multiplication of the complex exponential term and the power terms will introduce additional terms not needed in the final expression. In this case, terms such as $(nD)^{-9/2}$, (nD)... will of course be dropped

At this point a relation exists f

(2.33), and the power terms (2.36). Ne

only terms up to n are retained. A

$$H_0^{2}(x,x') = \sqrt{\frac{2j}{\pi kD}}\, e^{\dots} e^{\dots}$$

where

$$\xi_{12} = 1$$

$$\xi_{32} = \dots(x-x') \quad jk(f \; f)$$

$$\xi_{52} = 6(x-x')^2 - 3(f \; f)^2$$

$$-\frac{9}{8k^2} \quad 2k^2(f$$

$$\xi_{72} = \frac{45}{k^2}(x-x') - j\frac{60}{k}($$

$$-\, 60kj(f-f')^4 - 120$$

$$-\, 96k^2(x-x')(f \; f')$$

With the above result the asymptotic f

by (2.9). Using the relation for Z_n gi

$$A_n^{\prime} = \sqrt{\frac{2j}{\pi kD}}\, e^{-jk(x \; x')}(Z_0^{\prime})^n\{$$

$(nD)^{-11/2}$, ... will of course be dropped.

At this point a relation exists for the Hankel function (2.29), the exponential term (2.33), and the power terms (2.36). Next, (2.33) and (2.36) are substituted into (2.29) and only terms up to $n^{-7/2}$ are retained. Avoiding the pages of algebra, the final result is

$$H_0^{(2)}(x,x')^{\pm} \approx \sqrt{\frac{2j}{\pi kD}} e^{-jknD} e^{\mp jk(x-x')} \Big\{ \frac{1}{n^{1/2}}\xi_{1/2} + \frac{1}{2D}\xi_{3/2}\frac{1}{n^{3/2}} + \frac{1}{16D^2}\xi_{5/2}\frac{1}{n^{5/2}} + \frac{1}{256D^3}\xi_{7/2}\frac{1}{n^{7/2}} \Big\} \tag{2.37}$$

where

$$\begin{aligned}
\xi_{1/2} &= 1 \\
\xi_{3/2} &= \mp(x-x') - jk(f-f')^2 + \frac{j}{4k} \\
\xi_{5/2} &= 6(x-x')^2 - 3(f-f')^2 \mp \frac{3j}{k}(x-x') \pm 12jk(x-x')(f-f')^2 \\
&\quad - \frac{9}{8k^2} - 2k^2(f-f')^4 \\
\xi_{7/2} &= \pm\frac{45}{k^2}(x-x') + j\frac{60}{k}(x-x')^2 \mp 80(x-x')^3 - \frac{15j}{k}(f-f')^2 \\
&\quad + 60kj(f-f')^4 \pm 120(x-x')(f-f')^2 - 304jk(x-x')^2(f-f')^2 \\
&\quad \pm 96k^2(x-x')(f-f')^4 - j\frac{225}{12k^3} + j\frac{16}{3}k^3(f-f')^6
\end{aligned} \tag{2.38}$$

With the above result the asymptotic forms for $A_n^{\pm}$ can be derived using the relation given by (2.9). Using the relation for Z_0 given by (2.15), the higher order forms for $A_n^{\pm}$ are

$$A_n^{\pm} = \sqrt{\frac{2j}{\pi kD}} e^{\mp jk(x-x')}(Z_0^{\pm})^n \Big\{ \frac{1}{n^{1/2}}\xi_{1/2} + \frac{1}{2D}\xi_{3/2}\frac{1}{n^{3/2}} + \frac{1}{16D^2}\xi_{5/2}\frac{1}{n^{5/2}} + \frac{1}{256D^3}\xi_{7/2}\frac{1}{n^{7/2}} \Big\} \tag{2.39}$$

The evaluation of (2.16) using the exp

$$S(x,x')^{*} = \sqrt{\frac{2j}{\pi kD}}\, e^{\pm jk(x-x')} Z_0^{*} \left\{ \xi_{12} \Phi \right.$$

$$+ \frac{}{16}$$

where the integral forms for the Lerch

$$\Phi(z, 3/2,$$

$$\Phi(z, 5/2, 1$$

$$\Phi(z, 7/2, 1$$

2.2.3 Electric Field Integral Equat

The scattered field written in t

by (2.7). To determine the surface c

applied at the surface of the perfectly

$$E_z^s(x,y) + E_z^i(x,y$$

where $E_z^i(x,y)$ represents the inciden

$$\int_{-D/2}^{D/2} K_o(x')\, K(x,x'$$

The surface current $K_o(x')$ can be exp

$$K_o(x')$$

The evaluation of (2.16) using the expanded form for A_n is given by

$$S(x,x')^{\pm} = \sqrt{\frac{2j}{\pi kD}}\, e^{\mp jk(x-x')} Z_0^{\pm} \left\{ \xi_{1/2}\,\Phi(Z_0^{\pm},1/2,1) + \frac{1}{2D}\xi_{3/2}\,\Phi(Z_0^{\pm},3/2,1) + \frac{1}{16D^2}\xi_{7/2}\,\Phi(Z_0^{\pm},5/2,1) + \frac{1}{256D^3}\xi_{7/2}\,\Phi(Z_0^{\pm},7/2,1) \right\} \tag{2.40}$$

where the integral forms for the Lerch transcendent are

$$\Phi(z,3/2,1) = \frac{2}{\sqrt{\pi}} \int_0^{\infty} \frac{t^{1/2}}{e^t - z} dt \tag{2.41}$$

$$\Phi(z,5/2,1) = \frac{4}{3\sqrt{\pi}} \int_0^{\infty} \frac{t^{3/2}}{e^t - z} dt \tag{2.42}$$

$$\Phi(z,7/2,1) = \frac{8}{15\sqrt{\pi}} \int_0^{\infty} \frac{t^{5/2}}{e^t - z} dt \tag{2.43}$$

2.2.3 Electric Field Integral Equation (EFIE) solution

The scattered field written in terms of the kernel for the period surface is given by (2.7). To determine the surface current the following boundary condition must be applied at the surface of the perfectly conducting surface

$$E_z^s(x,y) + E_z^i(x,y) = 0 \qquad x,y \in surface \tag{2.44}$$

where $E_z^i(x,y)$ represents the incident electric field. Combining (2.44) with (2.7) yields

$$\int_{-D/2}^{D/2} K_o(x')\, K(x,x')\, L(x')\, dx' = \frac{4}{k\eta}\, E_z^i(x, f(x)) \tag{2.45}$$

The surface current $K_o(x')$ can be expanded as a finite series of terms taking the form

$$K_o(x') = \sum_{n=1}^{N} a_n\, K_n(x') \tag{2.46}$$

where $K_n(x')$ represents the current ba

discrete points x_m in the interval from

now be written as

$$\sum_{n=1}^{N} a_n \int_{-D/2}^{D/2} K_n(x')\, K(x_m, x')\, L$$

The above equation can be written in

$$\sum_{n=1}^{N} a_n A_{mn} =$$

where

$$A_{mn} = \int_{-D/2}^{D/2} K$$

$$b_m = -$$

If the interval between -D 2 and D 2 i

x_n, a pulse basis function can be defin

$$K_n(x') = \begin{cases} 1 \\ 0 \end{cases}$$

With the pulse-basis function defined

$$A_{mn} = \int_{x_n -}^{x_n +}$$

The self-term (m = n) can be approxim

is a straight line with width w_m given

$$w_m = \sqrt{\Delta^2 + [}$$

where $K_n(x')$ represents the current basis function. Next, point-matching is applied at N discrete points x_m in the interval from -D/2 to D/2. The integral equation in (2.45) can now be written as

$$\sum_{n=1}^{N} a_n \int_{-D/2}^{D/2} K_n(x')\, K(x_m,x')\, L(x')\, dx' = \frac{4}{k\eta} E_z^i(x_m, f(x_m)) \qquad m = 1,\ldots,N \tag{2.47}$$

The above equation can be written in matrix form as

$$\sum_{n=1}^{N} a_n A_{mn} = b_m \qquad m = 1, \ldots, N \tag{2.48}$$

where

$$A_{mn} = \int_{-D/2}^{D/2} K_n(x')\, K(x_m,x')\, L(x')\, dx' \tag{2.49}$$

$$b_m = \frac{4}{k\eta} E_z^i\,(x_m, f(x_m)) \tag{2.50}$$

If the interval between -D/2 and D/2 is divided into N segments of length Δ and center x_n, a pulse basis function can be defined as

$$K_n(x') = \begin{cases} 1 & x_n - \dfrac{\Delta}{2} \le x \le x_n + \dfrac{\Delta}{2} \\ 0 & \textit{elsewhere} \end{cases} \tag{2.51}$$

With the pulse-basis function defined in (2.51) the matrix term given by (2.49) becomes

$$A_{mn} = \int_{x_n - \frac{\Delta}{2}}^{x_n + \frac{\Delta}{2}} K(x_m,x')\, L(x')\, dx' \tag{2.52}$$

The self-term (m = n) can be approximated by assuming that the segment between points is a straight line with width w_m given by

$$w_m = \sqrt{\Delta^2 + [\, f(x_m - \tfrac{\Delta}{2}) - f(x_m + \tfrac{\Delta}{2})\,]^2} \tag{2.53}$$

The kernel can be written in terms of

$$A_{mm} =$$

The Hankel function can be evalua

arguments as [18]

$$H_o^{(2)}(u) = 1 - j$$

where $\gamma = 1.781$. Evaluation of the in

$$A_{mm} = w_m \; 1$$

For non-diagonal elements, the expre

rectangular rule integration as

$$A_{mn} =$$

where the expression for the kernel

section.

2.2.4 Electric Field Scattering Solu

A solution to the matrix equat

coefficients a_n. These values can be u

First, consider the scattered field due

infinitely periodic structure. For this

$$E_z^s(\bar{\rho}) = -\frac{k\eta}{4}\int_{-D/2}^{D/2} K$$

where the field and source points are

The kernel can be written in terms of the Hankel function. Hence, (2.52) becomes

$$A_{mm} = \int_{-w_m/2}^{w_m/2} H_o^{(2)}(k\,|x'|)\,dx' \tag{2.54}$$

The Hankel function can be evaluated using the asymptotic expression for small arguments as [18]

$$H_o^{(2)}(u) \approx 1 - j\frac{2}{\pi}\ln\left(\frac{\gamma u}{2}\right) \qquad \textit{for} \quad u \ll 1 \tag{2.55}$$

where $\gamma = 1.781$. Evaluation of the integral in (2.54) becomes

$$A_{mm} = w_m\left[1 - j\frac{2}{\pi}\left(\ln\left(\frac{k\gamma}{4}w_m\right) - 1\right)\right] \tag{2.56}$$

For non-diagonal elements, the expression given by (2.52) can be approximated using rectangular rule integration as

$$A_{mn} = K(x_m,x_n)\,L(x_n)\,\Delta \tag{2.57}$$

where the expression for the kernel must be determined as discussed in the previous section.

2.2.4 Electric Field Scattering Solution in the Far Field

A solution to the matrix equation (2.48) yields values for the unknown current coefficients a_n. These values can be used to obtain an expression for the scattered field. First, consider the scattered field due to the surface current from a single period of the infinitely periodic structure. For this case the scattered field is given by

$$E_z^s(\vec{\rho}) = -\frac{k\eta}{4}\int_{-D/2}^{D/2} K_o(x')\,H_o^{(2)}(k\,|\vec{\rho} - \vec{\rho}\,'|)\,L(x')\,dx' \tag{2.58}$$

where the field and source points are

$$\vec{\rho} = \rho$$

$$\vec{\rho}\,' = x$$

In the above relation ρ and α represent

The Hankel function argument can be

and (2.60) as

$$k\,|\vec{\rho} - \vec{\rho}\,'| = k\rho\,[1 - \frac{2}{\rho}(x$$

For the far-field $\rho >> \rho'$, and (2.61) ca

expanding. The simplification becom

$$k\,|\vec{\rho} - \vec{\rho}\,'| \approx k\,(\rho$$

Next, for large arguments the Hank

relation

$$H_o^{(2)}$$

Substituting (2.62) into (2.63) and

argument yields

$$H_o^{(2)}(k\,|\vec{\rho} - \vec{\rho}\,'|) \approx$$

Substituting the relations given by (2.

is

$$E_z^s(\vec{\rho}) \approx -\eta\sqrt{\frac{jk}{8\pi}}\,\frac{e^{-jk\rho}}{\sqrt{\rho}}\,\sum_n$$

The relation given by (2.65) provides

$$\vec{\rho} = \rho\cos\alpha\,\hat{x} + \rho\sin\alpha\,\hat{y} \tag{2.59}$$

$$\vec{\rho}' = x'\hat{x} + f(x')\,\hat{y} \tag{2.60}$$

In the above relation ρ and α represent the distance and scattering angle to the field point. The Hankel function argument can be written in terms of the parameters given in (2.59) and (2.60) as

$$k|\vec{\rho} - \vec{\rho}'| = k\rho\left(1 - \frac{2}{\rho}(x'\cos\alpha + f(x')\sin\alpha) + \frac{x^2 + f(x')^2}{\rho^2}\right)^{\frac{1}{2}} \tag{2.61}$$

For the far-field $\rho \gg \rho'$, and (2.61) can be simplified by dropping the quadratic term and expanding. The simplification becomes

$$k|\vec{\rho} - \vec{\rho}'| \approx k\left(\rho - (x'\cos\alpha + f(x')\sin\alpha)\right) \tag{2.62}$$

Next, for large arguments the Hankel function can be expanded with the following relation

$$H_o^{(2)}(u) \approx \sqrt{\frac{2j}{\pi u}}\, e^{-ju} \tag{2.63}$$

Substituting (2.62) into (2.63) and using only the ρ dependence for the amplitude argument yields

$$H_o^{(2)}(k|\vec{\rho} - \vec{\rho}'|) \approx \sqrt{\frac{2j}{k\pi}}\,\frac{e^{-jk\rho}}{\sqrt{\rho}}\, e^{+jk(x'\cos\alpha + f(x')\sin\alpha)} \tag{2.64}$$

Substituting the relations given by (2.46), (2.51), and (2.64), the scattered field in (2.58) is

$$E_z^s(\vec{\rho}) \approx -\eta\sqrt{\frac{jk}{8\pi}}\,\frac{e^{-jk\rho}}{\sqrt{\rho}}\sum_{n=1}^{N} a_n \int_{x_n - \frac{\Delta}{2}}^{x_n + \frac{\Delta}{2}} e^{jk(x'\cos\alpha + f(x')\sin\alpha)}\, L(x')\,dx' \tag{2.65}$$

The relation given by (2.65) provides an expression for the scattered field from a single period of the infinitely periodic sur

additional periods of the surface. In t

scattering period and M periods are or

total field can be written as

$$E_z^s(\vec{\rho}) \approx -\eta \sqrt{\frac{jk}{8\pi}} \frac{e^{-jk\rho}}{\sqrt{\rho}}$$

$$\sum_{n=1}^{N} a_n \int_{x_n}^{x_n}$$

Some simplification of the above rela

$$E_z^s(\vec{\rho}) \approx -\eta \sqrt{\frac{jk}{8\pi}} \frac{e^{-jk\rho}}{\sqrt{\rho}}$$

$$\left\{ \sum_{n=1}^{N} a \right.$$

The first summation term given by t

contribution which can be put in a mo

$$\sum_{l=-M}^{M} e^{jkD(\cos\alpha + \cos\phi_o)l} = e$$

The summation on the right hand side

$$\sum_{l=0}^{k}$$

With (2.69) the array factor in (2.68)

period of the infinitely periodic surface. Next, consider the contribution from 2M additional periods of the surface. In this case M periods appear to the left of the central scattering period and M periods are on the right. With the surface period given by D, the total field can be written as

$$E_z^s(\vec{\rho}) \approx -\eta\sqrt{\frac{jk}{8\pi}}\,\frac{e^{-jk\rho}}{\sqrt{\rho}}\sum_{l=-M}^{l=M}\Bigg\{ e^{jlkD\cos\phi_o} \sum_{n=1}^{N} a_n \int_{x_n-\frac{\Delta}{2}}^{x_n+\frac{\Delta}{2}} e^{jk[\,(x'+lD)\cos\alpha\,+\,f(x')\sin\alpha\,]}\,L(x')\,dx'\Bigg\} \tag{2.66}$$

Some simplification of the above relation yields the following expression

$$E_z^s(\vec{\rho}) \approx -\eta\sqrt{\frac{jk}{8\pi}}\,\frac{e^{-jk\rho}}{\sqrt{\rho}}\sum_{l=-M}^{l=M} e^{jlkD(\cos\alpha\,+\,\cos\phi_o)} \Bigg\{\sum_{n=1}^{N} a_n \int_{x_n-\frac{\Delta}{2}}^{x_n+\frac{\Delta}{2}} e^{jk[\,x'\cos\alpha\,+\,f(x')\sin\alpha\,]}\,L(x')\,dx'\Bigg\} \tag{2.67}$$

The first summation term given by the preceding form simply yields an array factor contribution which can be put in a more useful form

$$\sum_{l=-M}^{M} e^{jkD(\cos\alpha\,+\,\cos\phi_o)l} = e^{-jkMD(\cos\alpha\,+\,\cos\phi_o)}\sum_{l=0}^{2M} e^{jkD(\cos\alpha\,+\,\cos\phi_0)l} \tag{2.68}$$

The summation on the right hand side of (2.68) is just a geometric series of the form

$$\sum_{l=0}^{k} r^{l} = \frac{1 - r^{k+1}}{1 - r} \tag{2.69}$$

With (2.69) the array factor in (2.68) becomes

$$\sum_{l=-M}^{M} e^{jkD(\cos\alpha - \cos\phi_o)l} = e^{-j}$$

Simplifying (2.70) yields

$$\sum_{l=-M}^{M} e^{jkD(\cos\alpha - \cos\phi_o)l}$$

Thus, the scattered field is given by

$$E_z^s(\bar{\rho}) \approx -\eta\sqrt{\frac{jk}{8\pi}}\,\frac{e^{-jk\rho}}{\sqrt{\rho}}$$

$$\left\{\sum_{n=1}^{N} c\right.$$

2.3 Discussion

2.3.1 Comparison with other meth

In the previous sections, the
scattering from a conducting periodic
purpose of those sections was to devel
hence would allow the determination
the validity of the developed theory
previously developed by A. Norman [
treatment for the scattering of plane

$$\sum_{l=-M}^{M} e^{jkD(\cos\alpha\ +\ \cos\phi_o)l} = e^{-jkMD(\cos\alpha\ +\ \cos\phi_o)} \frac{1 - e^{jkD(2M+1)(\cos\alpha + \cos\phi_o)}}{1 - e^{jkD(\cos\alpha + \cos\phi_o)}} \tag{2.70}$$

Simplifying (2.70) yields

$$\sum_{l=-M}^{M} e^{jkD(\cos\alpha\ +\ \cos\phi_o)l} = \frac{\sin\left[\frac{kD}{2}(2M+1)\left(\cos\alpha + \cos\phi_o\right)\right]}{\sin\left[\frac{kD}{2}\left(\cos\alpha + \cos\phi_o\right)\right]} \tag{2.71}$$

Thus, the scattered field is given by

$$E_z^s(\vec{\rho}) \approx -\eta\sqrt{\frac{jk}{8\pi}}\,\frac{e^{-jk\rho}}{\sqrt{\rho}}\,\frac{\sin\left[\frac{kD}{2}(2M+1)\left(\cos\phi_o + \cos\alpha\right)\right]}{\sin\left[\frac{kD}{2}\left(\cos\phi_o + \cos\alpha\right)\right]} \left\{ \sum_{n=1}^{N} a_n \int_{x_n - \frac{\Delta}{2}}^{x_n + \frac{\Delta}{2}} e^{jk[\,x'\cos\alpha\ +\ f(x')\sin\alpha\,]}\, L(x')\, dx' \right\} \tag{2.72}$$

2.3 Discussion

2.3.1 Comparison with other methods

In the previous sections, the theoretical aspects of TE incident plane wave scattering from a conducting periodic surface was considered for the infinite case. The purpose of those sections was to develop a method which is computationally efficient and hence would allow the determination of the scattered fields from larger surfaces. To test the validity of the developed theory several comparisons will be made with a model previously developed by A. Norman [12]. Norman has developed a rigorous and general treatment for the scattering of plane waves from a perfectly electric conducting (PEC) periodic surface. An integral-operato

to as the electric field integral equatio

induced on the PEC surface are calcul

function (PGF) kernel. With the surf

the scattered fields once again makin

The goal of using Norman's

periodic structure at different frequenc

by the new model several experimen

various periodic surfaces. The calcula

has been done extensively in the pa

intensive task requiring the calculatio

windowing the data, and then perform

Fourier transform) to determine the tr

require these steps but the calculatio

should require far less computer pro

finite surface a comparison between th

of light on the usefulness of the peri

Norman has used a geomet

Figure 2.2. As can be seen, this g

Figure 2.1. Major difference include

placement with respect to the origi

definition (forcing the author to make

periodic surface. An integral-operator-based analysis has been employed and is referred to as the electric field integral equation method of moments (EFIE-MOM). The currents induced on the PEC surface are calculated as solutions to an EFIE with a periodic Green's function (PGF) kernel. With the surface currents known, it is then possible to determine the scattered fields once again making use of the PGF.

The goal of using Norman's model was to compare the surface current over a periodic structure at different frequencies. In addition to analyzing the currents generated by the new model several experiments were done to calculate the scattered fields from various periodic surfaces. The calculation of scattered fields from a finite periodic surface has been done extensively in the past. Solutions to these fields is a computationally intensive task requiring the calculation of the scattered field at every frequency point, windowing the data, and then performing an inverse discrete Fourier transform (via a fast Fourier transform) to determine the transient scattered field. The new method would also require these steps but the calculation of the current and field at each frequency point should require far less computer processing time. Although one case is based upon a finite surface a comparison between the transient scattered fields should shed a great deal of light on the usefulness of the periodic current model.

Norman has used a geometry model from a sinusoidal surface defined in Figure 2.2. As can be seen, this geometry is slightly different from that shown in Figure 2.1. Major difference include the angle of incidence and the sinusoidal surface placement with respect to the origin. The results of this study will use Norman's definition (forcing the author to make small changes in his program). Several frequency

points were chosen for the current c
field with frequency points at 2.95, 5.
at 85 degrees (near grazing). The i
crests (TE polarization). The surface
height of .0127 meters. The induc
conducting surface are shown in Figu
imaginary parts of the calculated cu
As can be seen in each of these figure
currents calculated using the new met
Since Norman's method has been ext
validates the new method.

The spectral domain scattere
calculated for several periodic surfac
zone approximation using two differe
based upon the solution of an EFIE
model using the periodic current gene
the periodic current only over a finit
In this respect we can see that the pe
of this type of model is to multiply t
factor.

The spectral domain scattered
(L = .09 meters, h = .0254 meters) g

points were chosen for the current comparison. The author selected to use an incident field with frequency points at 2.95, 5.00, and 9.00 GHz., while the angle of incidence was at 85 degrees (near grazing). The incident field polarization was parallel to the wave crests (TE polarization). The surface has a period length (L) of .1016 meters and wave height of .0127 meters. The induced surface currents on one period of the infinite conducting surface are shown in Figure 2.3 -Figure 2.5. Each figure shows the real and imaginary parts of the calculated current as a function of normalized surface position. As can be seen in each of these figures, there is excellent agreement between the surface currents calculated using the new method and those calculated by Norman's EFIE-MOM. Since Norman's method has been extensively researched and used , the good comparison validates the new method.

The spectral domain scattered fields and their associated transient fields were calculated for several periodic surfaces. The scattered field was calculated with the far zone approximation using two different methods: (1) a 2-d finite length scattering model based upon the solution of an EFIE using the method of moments, and (2) a scattering model using the periodic current generated from an infinite surface. The latter model uses the periodic current only over a finite number of periods to generate the scattered field. In this respect we can see that the periodic current model is a hybrid model. The effect of this type of model is to multiply the scattered field from a single period by an array factor.

The spectral domain scattered fields from a 9-period conducting sinusoidal surface (L = .09 meters, h = .0254 meters) generated by a TE plane wave with incidence and scattering angle of 30 degrees from t

the far zone as a function of frequen

step size. The spectral amplitude of

length and infinite period current m

Figure 2.7.

To find the transient scattered

by a short pulse, the spectral results

cosine taper function (see Appendix

cosine taper window corresponding t

in Figure 2.8. A short pulse is synth

this window. The synthesized inciden

The time-domain scattered fi

methods are shown in Figure 2.10.

response for both cases agree quite we

and trailing edge of the surface. Th

current model is an exact solution wit

model is not an exact solution.

A second scattering surface, k

The period of this surface is 17.78 c

profile to fourth order [19] can be ex

kx

$y = -\beta \cos(\theta)$

scattering angle of 30 degrees from the horizon (see Figure 2.1) have been calculated in the far zone as a function of frequency over the bandwidth .8 - 12.98 GHz at .01 GHz step size. The spectral amplitude of the backscattered field is computed using the finite length and infinite period current models. The results are shown in Figure 2.6 and Figure 2.7.

To find the transient scattered field from the conducting sinusoidal surface created by a short pulse, the spectral results of the scattered field are windowed using a 1/8 cosine taper function (see Appendix A) and then inverse Fourier transformed. The 1/8 cosine taper window corresponding to the spectral band from .8 to 12.98 GHz is shown in Figure 2.8. A short pulse is synthesized by applying an inverse Fourier transform to this window. The synthesized incident pulse is shown in Figure 2.9.

The time-domain scattered fields created by the short pulse for both scattering methods are shown in Figure 2.10. It is observed in this figure that the backscattered response for both cases agree quite well. Exceptions to this agreement occur at the leading and trailing edge of the surface. This is to be expected since the finite (non-periodic) current model is an exact solution with edge discontinuities, whereas the periodic current model is not an exact solution.

A second scattering surface, known as a Stoke's surface, is shown in Figure 2.11. The period of this surface is 17.78 cm and wave height is 4.96 cm. A Stoke's wave profile to fourth order [19] can be expressed mathematically by

$$kx = \beta k \sin(\theta) + \theta \tag{2.73}$$

$$y = -\beta\cos(\theta) + \frac{2}{3}k^3(\beta - \frac{3}{8}\beta^3)\cos(2kx) \tag{2.74}$$

where y is the vertical displacement

θ is the parameter of the parametric c

simple cycloid can be generated by c

(2.74) and setting k = β = 1. The wav

(2.73) and (2.74) for the simple cyclo

given height and wavelength.

The frequency-domain scatter

Figure 2.12. The scattered field wa

scattering angles of 30 degrees. The

GHz step size. The solution method

no periodicity in the current). Figure

period Stoke's wave illuminated unc

generated by windowing the magnitu

taper waveform and then applying an

transient fields using both the period

larger view of the scattering between

in the scattering solution techniques

solutions, except at the front and bac

2.3.2 Large surface

The spectral domain scatter

sinusoidal surface generated by a TE

where y is the vertical displacement of the surface and x is the horizontal displacement. θ is the parameter of the parametric curve, while k and β are wave shaping variables. A simple cycloid can be generated by dropping the second term on the right hand side of (2.74) and setting $k = \beta = 1$. The wave profile shown in Figure 2.11 was generated using (2.73) and (2.74) for the simple cycloid case and then scaling in the x-y direction for the given height and wavelength.

The frequency-domain scattered field for the 11 period Stoke's wave is shown in Figure 2.12. The scattered field was generated using a TE wave having incident and scattering angles of 30 degrees. The frequency range was from .8 to 12.86 GHz at .01 GHz step size. The solution method used an EFIE using only a finite length surface (i.e. no periodicity in the current). Figure 2.13 shows the periodic current solution for a 11 period Stoke's wave illuminated under the same conditions. The transient fields were generated by windowing the magnitude of the frequency-domain data with a 1/8 cosine taper waveform and then applying an inverse Fourier transform. Figure 2.14 shows the transient fields using both the periodic and non-periodic solutions. The inset shows a larger view of the scattering between the crests. As can be seen, even with a difference in the scattering solution techniques there is remarkable agreement between the two solutions, except at the front and back of the wave.

2.3.2 Large surface

The spectral domain scattered field from 11 periods of a large conducting sinusoidal surface generated by a TE plane wave with an incidence and scattering angle of 30 degrees is calculated using the

of the surface are 1.0 and .25 m resp

with a frequency step size of .005 G

field is shown in Figure 2.15.

To find the time-domain scatt

is Fourier transformed after being w

Fourier transforming a uniform spect

been weighted with a 1 8 cosine tap

cosine taper widow and the synthe

scattered field created by the short p

to the data in Figure 2.15 and then t

shown in Figure 2.18. The fre

resemblance to those generated fro

Figure 2.7. Similarly the transient sc

to the transient scattered field from t

2.4 Computational Consideratio

The amount of computational

current model algorithm. As indicate

Stoke's wave was generated using a

data was generated over a 20 hou

of 30 degrees is calculated using the periodic current model. The wavelength and height of the surface are 1.0 and .25 m respectively. The frequency band is from .5 to 3.0 GHz with a frequency step size of .005 GHz. The spectral amplitude of the total scattered field is shown in Figure 2.15.

To find the time-domain scattered fields due to a short pulse, the frequency data is Fourier transformed after being windowed. A short pulse is synthesized by inverse Fourier transforming a uniform spectral response over a bandwidth .5 - 3.0 GHz that has been weighted with a 1/8 cosine taper window. Figure 2.16 and Figure 2.17 show the cosine taper widow and the synthesized short pulse respectively. The time-domain scattered field created by the short pulse can be obtained by applying the same window to the data in Figure 2.15 and then taking the inverse transform. The transient field is shown in Figure 2.18. The frequency-domain scattered field shows remarkable resemblance to those generated from a smaller sinusoidal surface in Figure 2.6 and Figure 2.7. Similarly the transient scattered field shown in Figure 2.18 can be compared to the transient scattered field from the smaller sinusoidal surface in Figure 2.10.

2.4 Computational Considerations

The amount of computational effort can be greatly reduced using the new periodic current model algorithm. As indicated in Figure 2.12 the scattered field from a 11 period Stoke's wave was generated using an EFIE computational solution. The scattered field data was generated over a 20 hour period using a Pentium 100 computer with 8 megabytes of memory. In contrast, th

generated in approximately 1 hour us

speed indicates the usefulness of this

One area of interest is the n

given by (2.39). Table 2.1 shows t

number of approximation terms. Th

computed for the Stoke's surface

computational speed improves as m

going from 3 to 4 terms is not highly

by adding more terms, but it must be

processing time. At some point the p

improve the speed of the overall com

amount of processing time required

For 1 and 2 term approximations, th

solution. The addition of the third te

terms are significant.

2.4 Conclusions

In this chapter a new radar sca

new method was compared to severa

technique. Several cases were run

method agreed quite well with previo

megabytes of memory. In contrast, the scattered field data represented in Figure 2.13 was generated in approximately 1 hour using the same computer. This significant increase in speed indicates the usefulness of this algorithm.

One area of interest is the number of terms to be used for the approximations given by (2.39). Table 2.1 shows the matrix fill time associated with using different number of approximation terms. The data corresponds to a subset of frequency points computed for the Stoke's surface as shown in Figure 2.13. In most cases the computational speed improves as more terms are added, although the improvement in going from 3 to 4 terms is not highly significant. Some improvements may be expected by adding more terms, but it must be kept in mind that more terms will also require more processing time. At some point the processing time to compute those extra terms will not improve the speed of the overall computation. One significant feature of Table 2.1 is the amount of processing time required to compute the matrix fill for the 10.0 GHz point. For 1 and 2 term approximations, there was some difficulty in obtaining a converging solution. The addition of the third term overcame this problem. In this respect the extra terms are significant.

2.4 Conclusions

In this chapter a new radar scattering method has been developed and tested. This new method was compared to several established methods in order to validate this new technique. Several cases were run and findings indicated that the results of the new method agreed quite well with previous methods. The utility of this new method is that the scattering problem from an infini

The results obtained can then be used

algorithms.

the scattering problem from an infinite surface can be solved in a more efficient manner. The results obtained can then be used in conjunction with testing different target-detection algorithms.

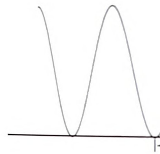

Figure 2.1 Scattering geometry fo

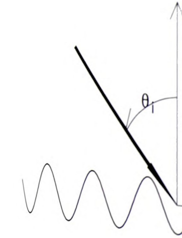

Figure 2.2 Infinite, conducting si

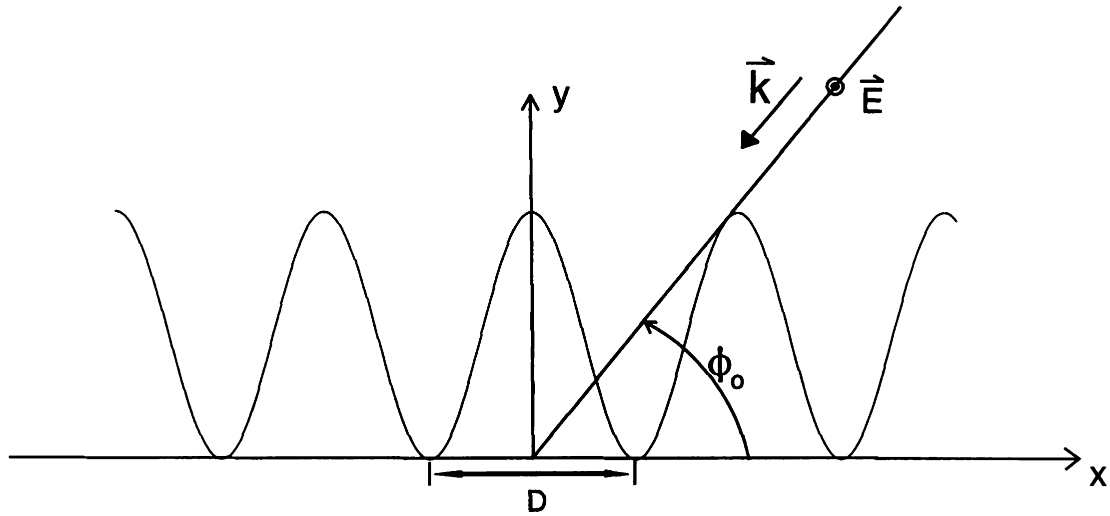

Figure 2.1 Scattering geometry for periodic surfaces.

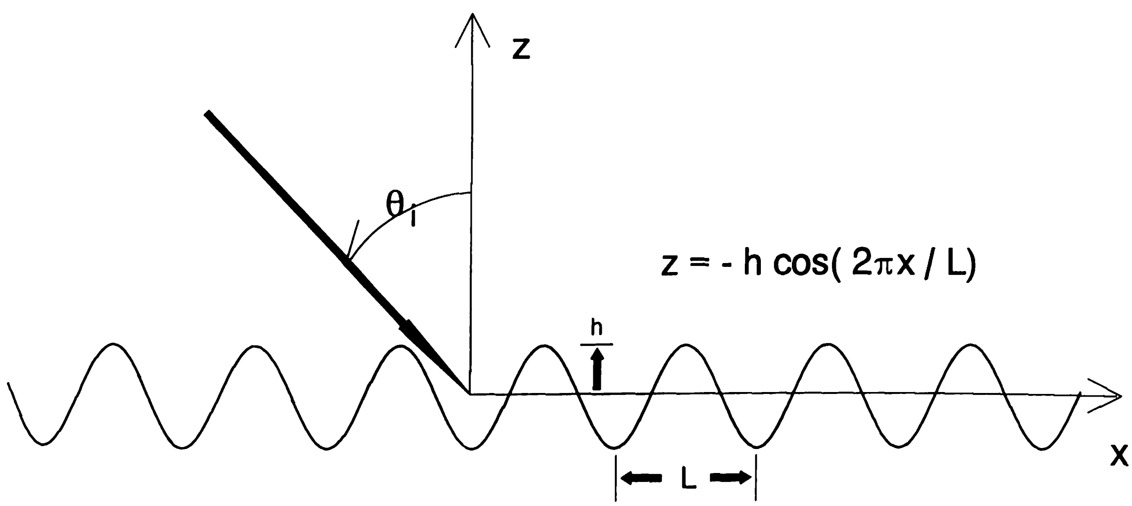

Figure 2.2 Infinite, conducting sinusoidal surface scattering geometry.

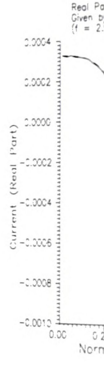

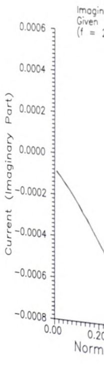

Figure 2.3 Induced surface curre
surface for TE excitat
85° from vertical axis

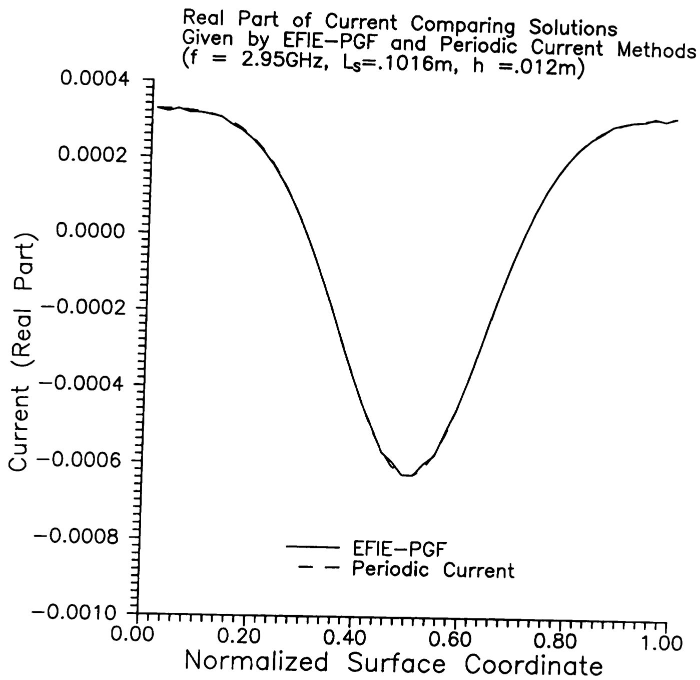

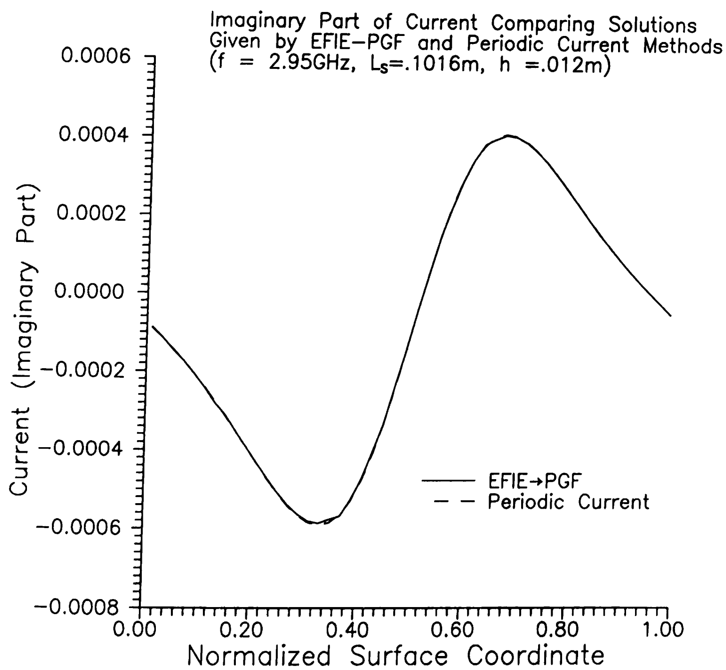

Figure 2.3 Induced surface current on one period of infinite, conducting sinusoidal surface for TE excitation at 2.95 GHz. Angle of incidence and scattering 85° from vertical axis.

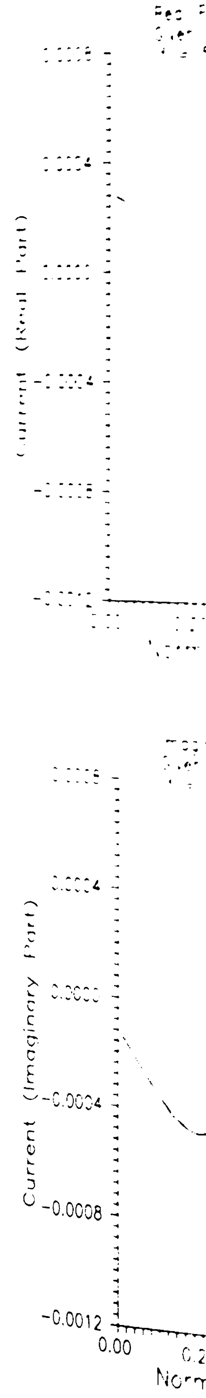

Figure 2.4 Induced surface curre
surface for TE excitat
from vertical.

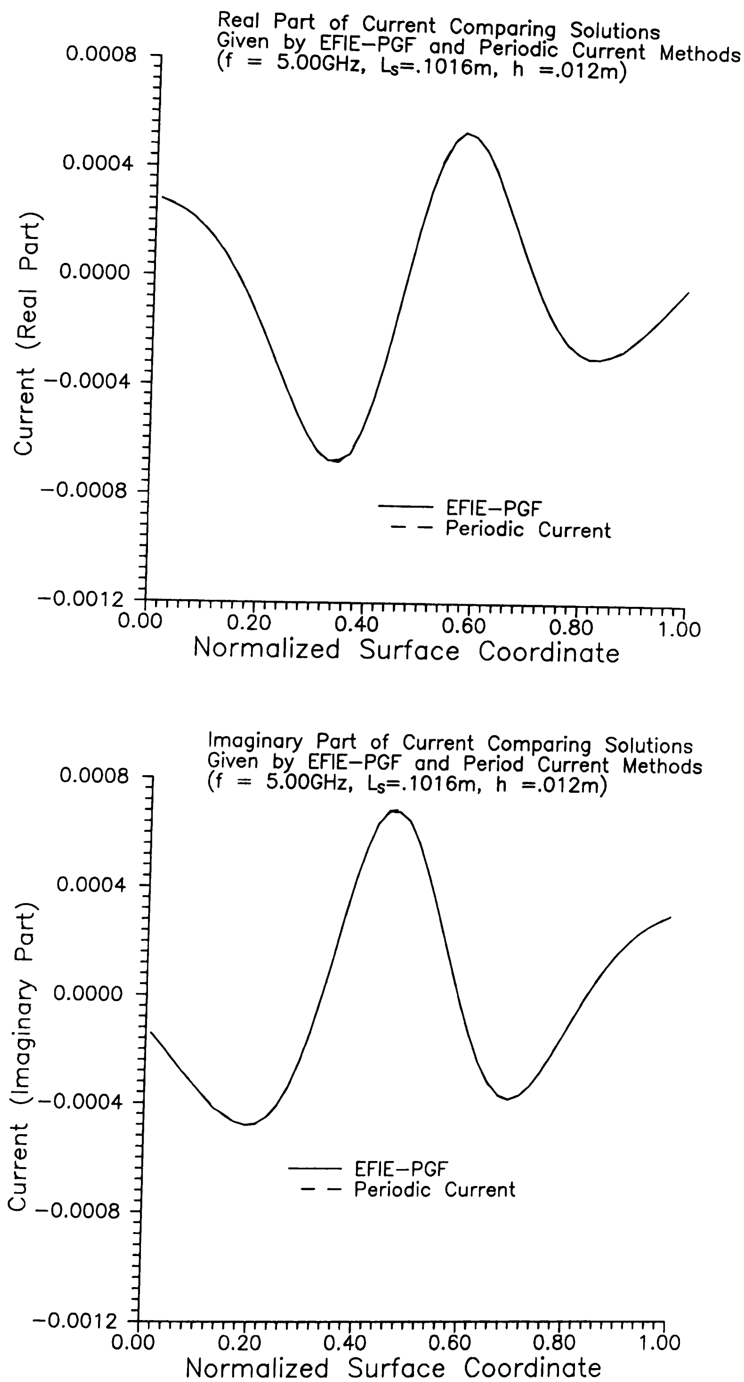

Figure 2.4 Induced surface current on one period of infinite, conducting sinusoidal surface for TE excitation at 5 GHz. Angle of incidence and scattering 85° from vertical.

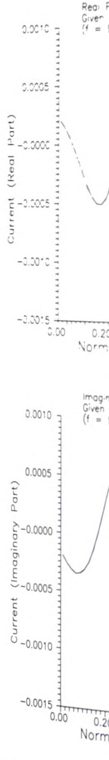

Figure 2.5 Induced surface curre
surface for TE excitati
vertical.

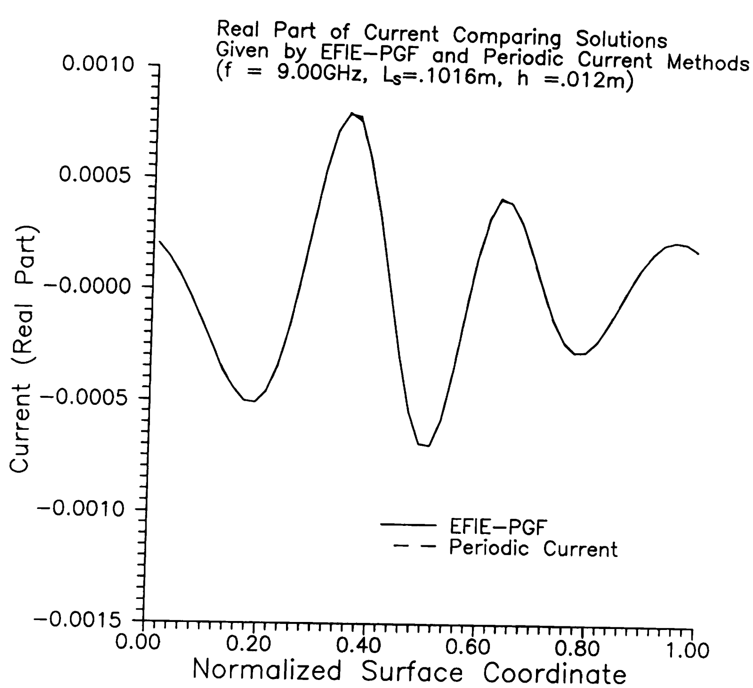

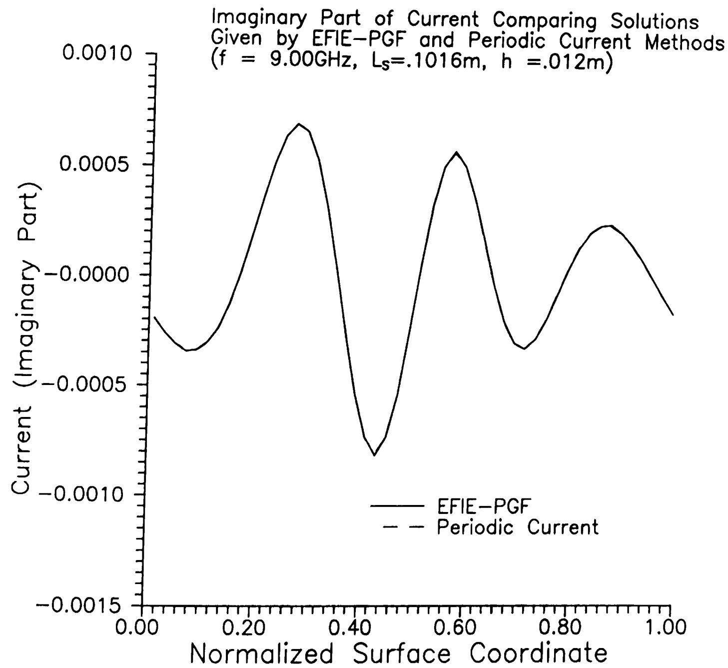

Figure 2.5 Induced surface current on one period of infinite, conducting sinusoidal surface for TE excitation at 9 GHz. Incident and scattering angles 85° from vertical.

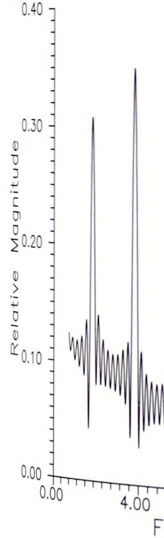

Figure 2.6 Magnitude of backsca
as a function of freq
model used. (L = .09

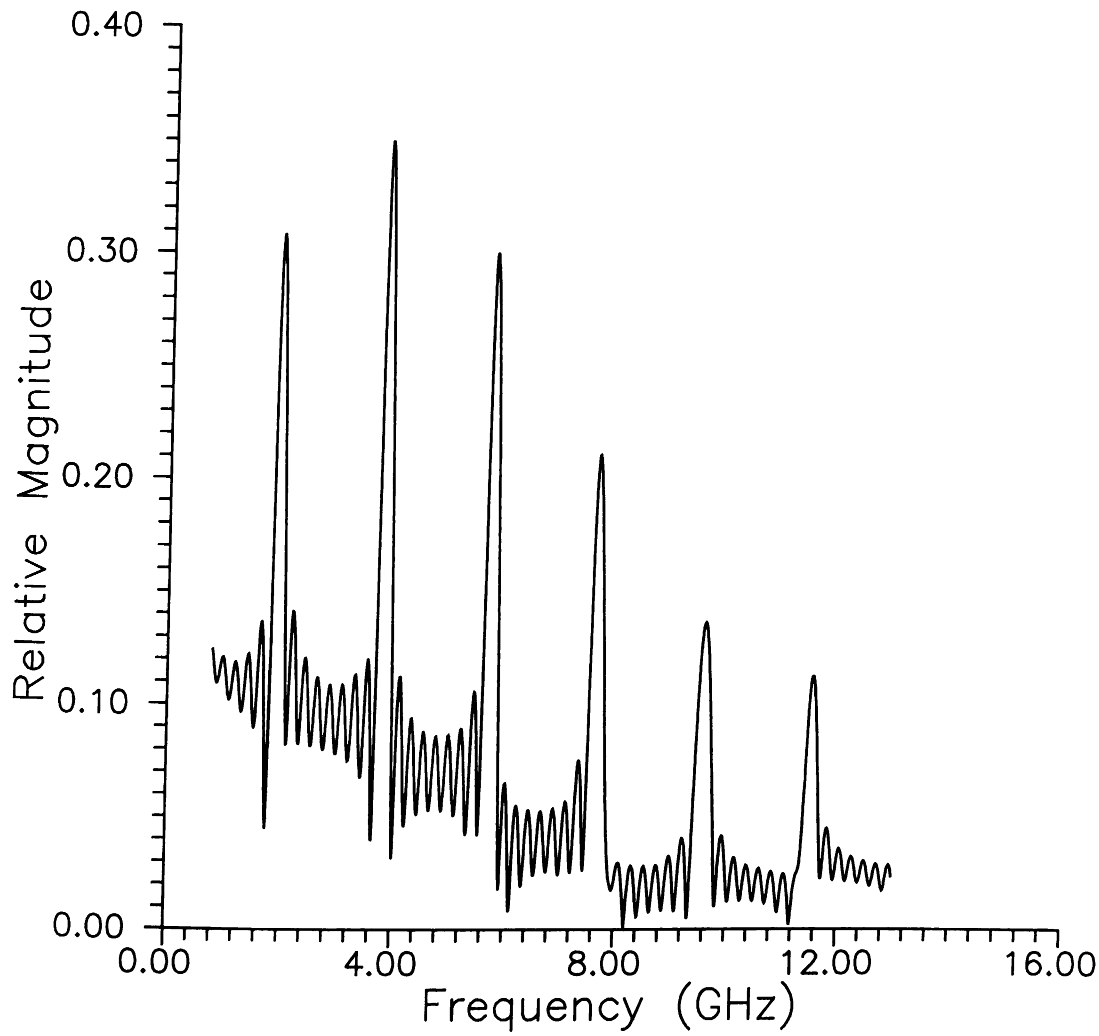

Figure 2.6 Magnitude of backscattered electric field from 9-period sinusoidal surface as a function of frequency for TE excitation. Finite length scattering model used. (L = .09m, h = .0254m, ϕ_o = 30°)

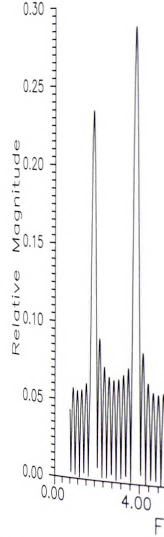

Figure 2.7 Magnitude of bacscat
as a function of freque
(L = .09m, h = .025

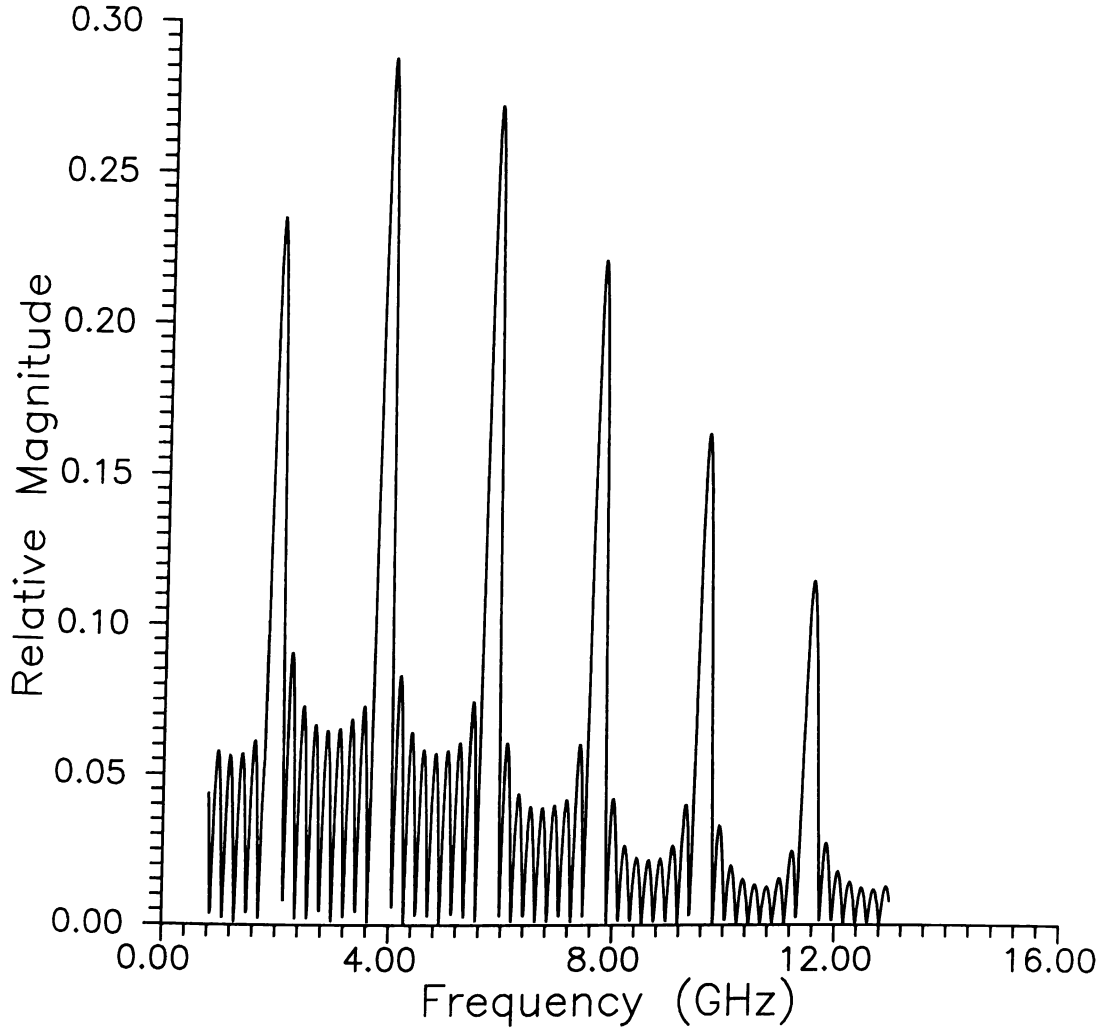

Figure 2.7 Magnitude of bacscattered electric field from 9 period sinusoidal surface as a function of frequency for TE excitation. Periodic current model used. (L = .09m, h = .0254, ϕ_o = 30°)

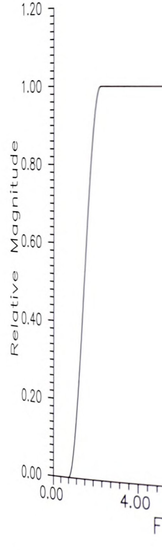

Figure 2.8 1/8 cosine taper wind

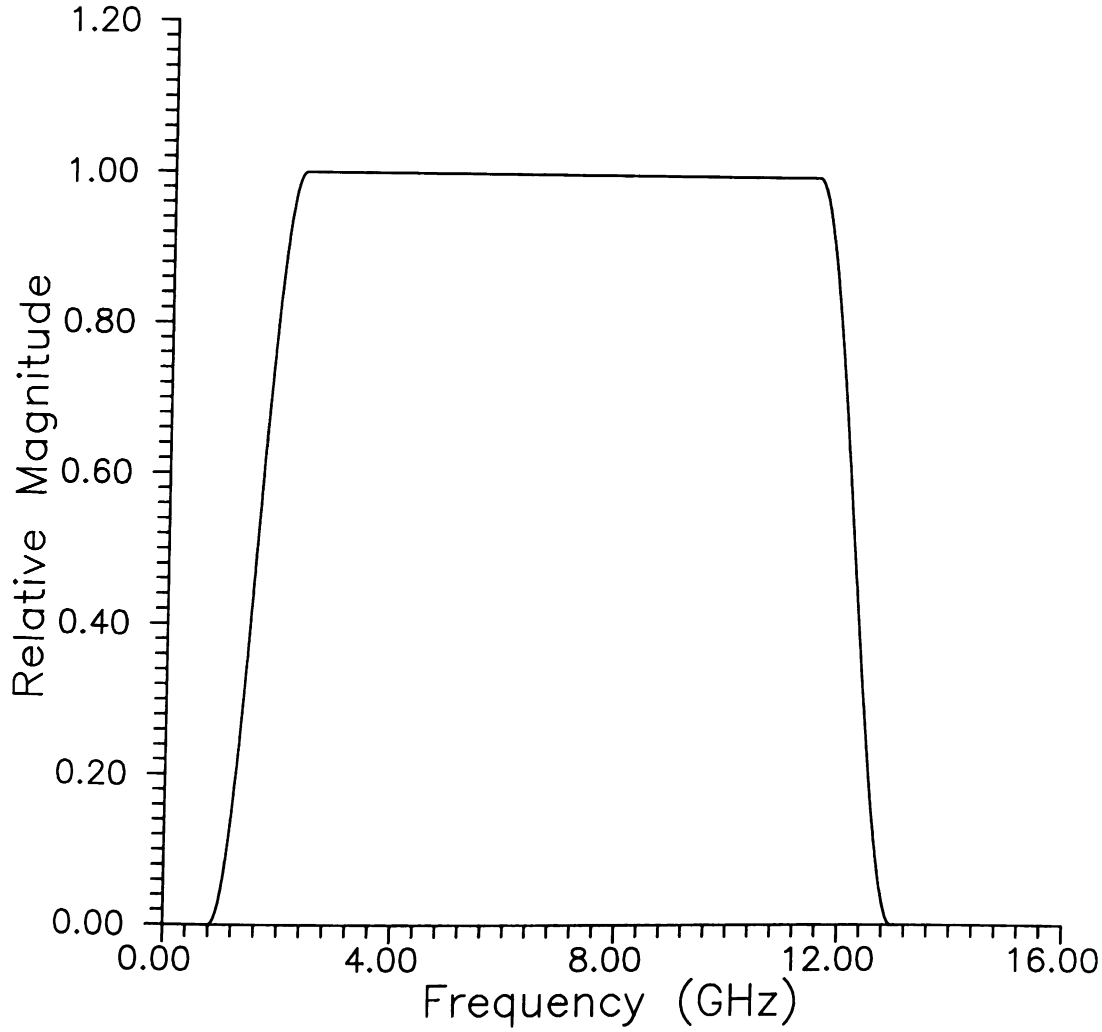

Figure 2.8 1/8 cosine taper window for the frequency band .8 - 12.98 GHz.

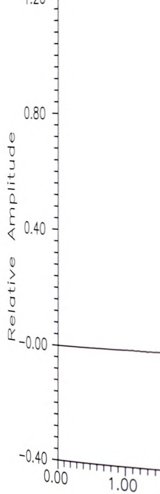

Figure 2.9 Short input pulse, sym
tapered, uniform spe
GHz.

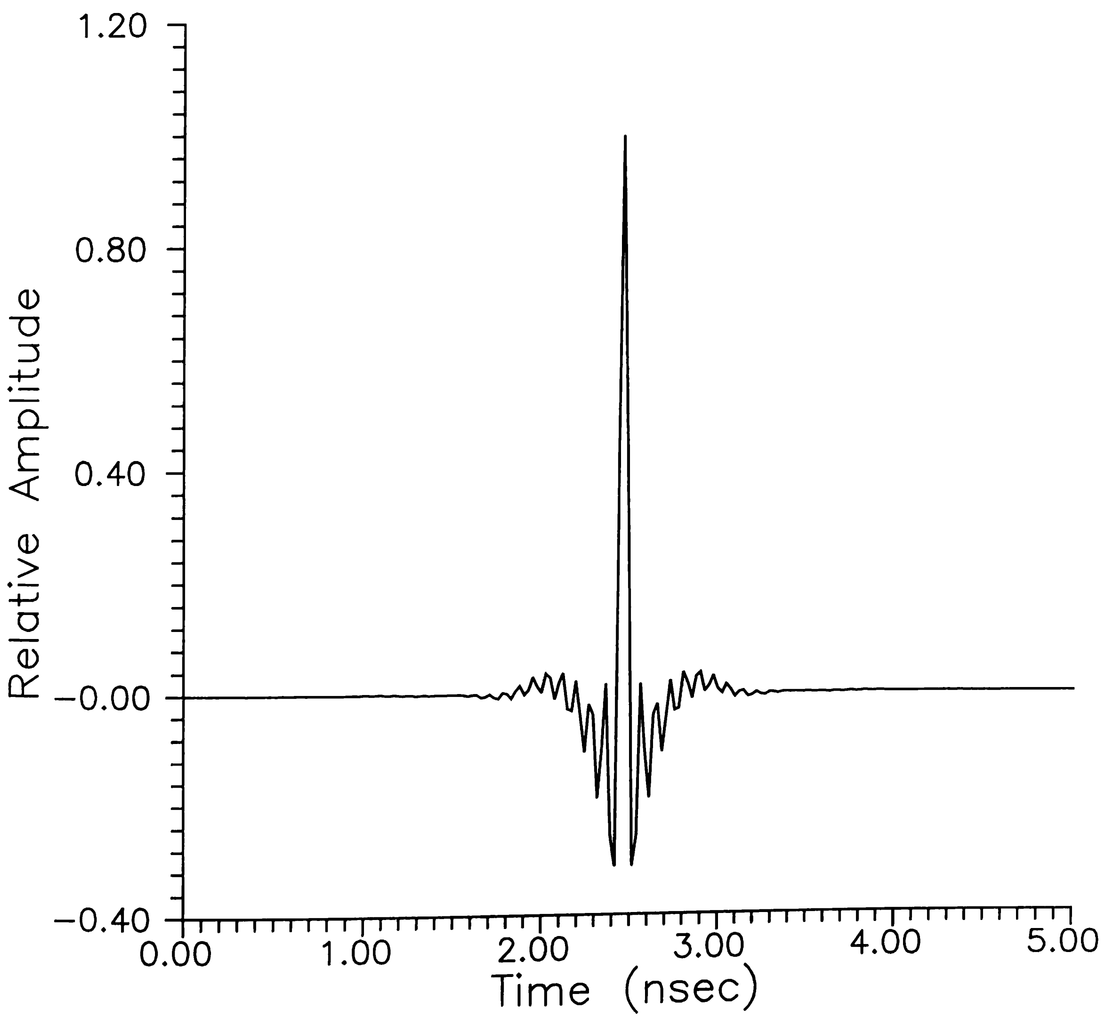

Figure 2.9 Short input pulse, synthesized by inverse fourier transforming a 1/8 cosine tapered, uniform spectral response in the frequency band of .8 - 12.98 GHz.

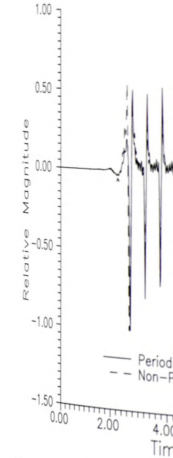

Figure 2.10 Periodic and non-peri
a short pulse from a
and scattering angles

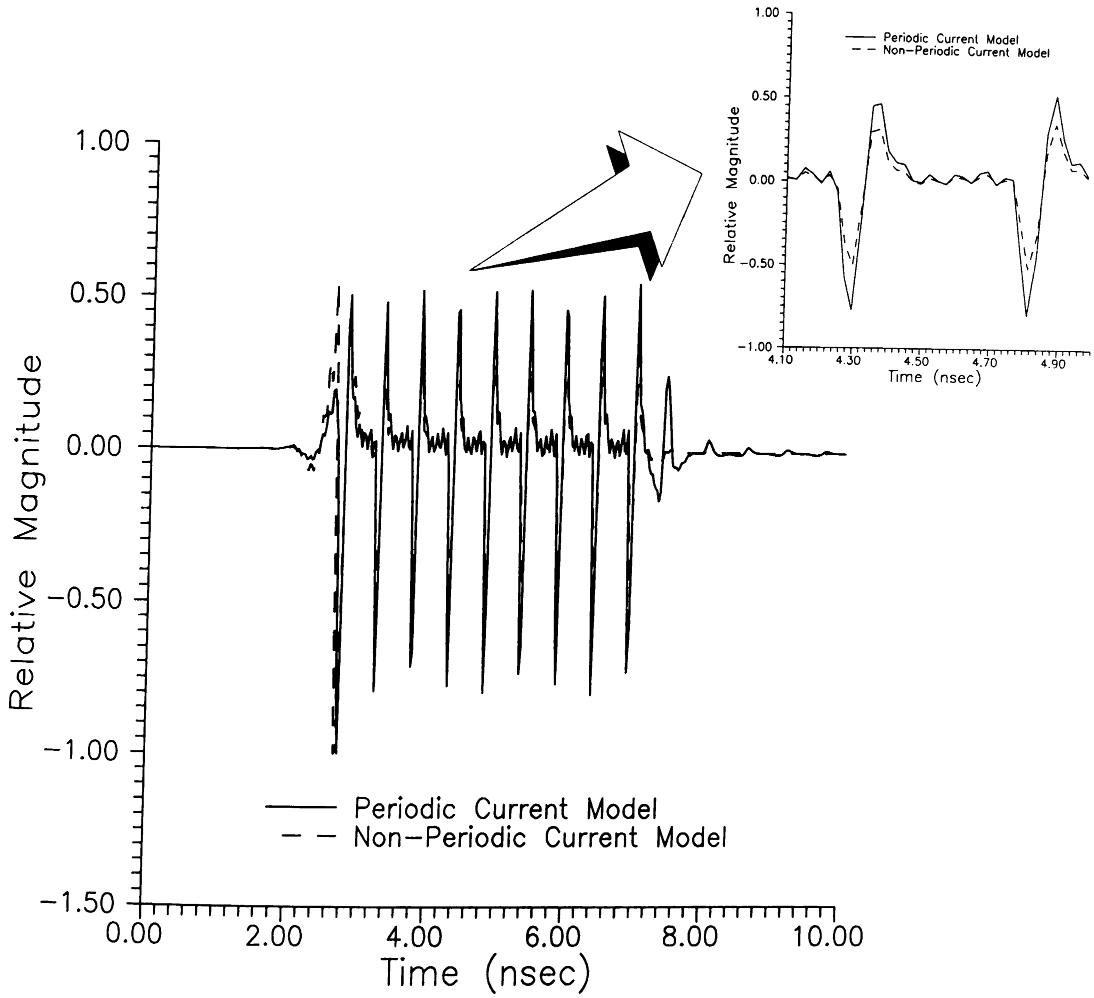

Figure 2.10 Periodic and non-periodic transient backscattered electric fields created by a short pulse from a finite sinusoidal surface for TE excitation. Incident and scattering angles are 30 degrees. (L = .09m, h = .0254m)

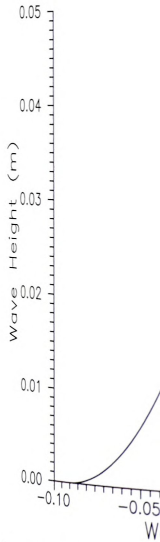

Figure 2.11 Stokes wave represe

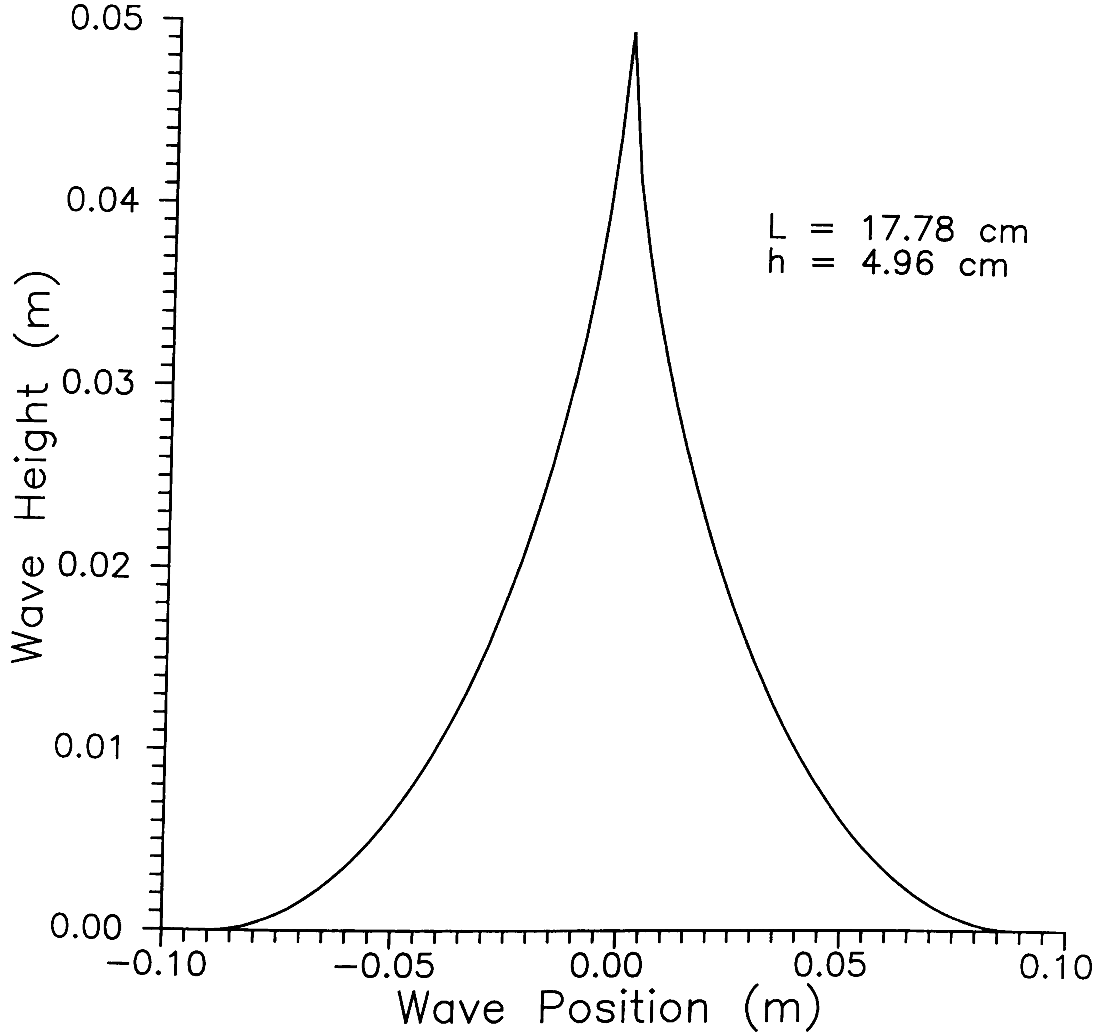

Figure 2.11 Stokes wave representation showing only one period.

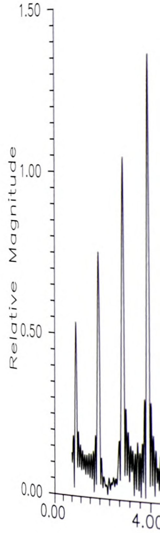

Figure 2.12 Magnitude of backsc
function of frequenc
used. (L = .1778m, l

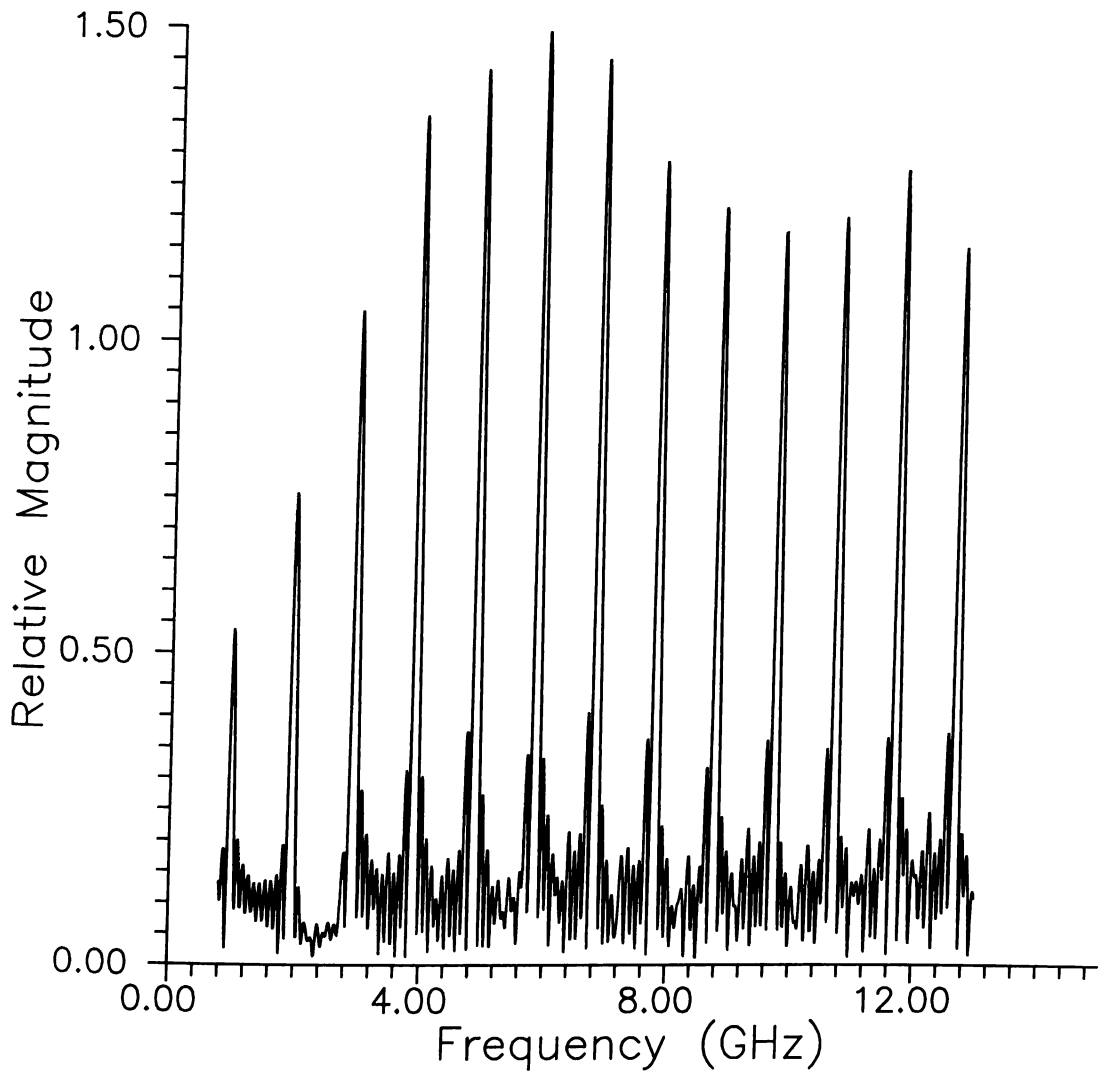

Figure 2.12 Magnitude of backscattered electric field for 11 period Stoke's surface as function of frequency for TE excitation. Finite length scattering model used. (L = .1778m, h = .0496m, ϕ_o = 30°)

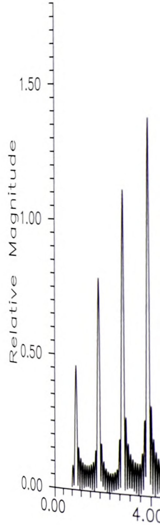

Figure 2.13 Magnitude of backsc
a function of freque
model used. (L =

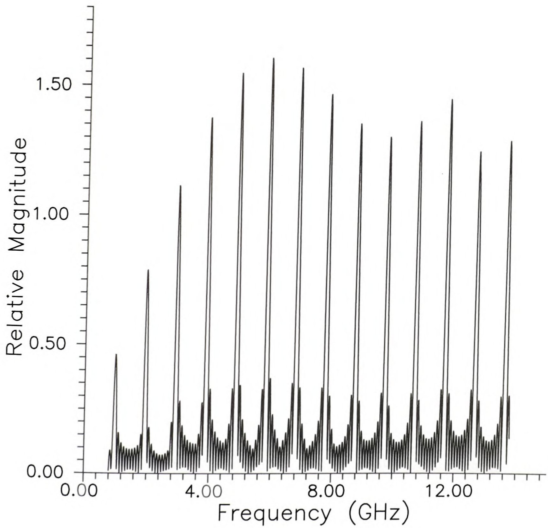

Figure 2.13 Magnitude of backscattered electric field for 11 period Stoke's surface as a function of frequency for TE excitation. Periodic current scattering model used. (L = .1778m, h = .0496m, ϕ_o = 30°)

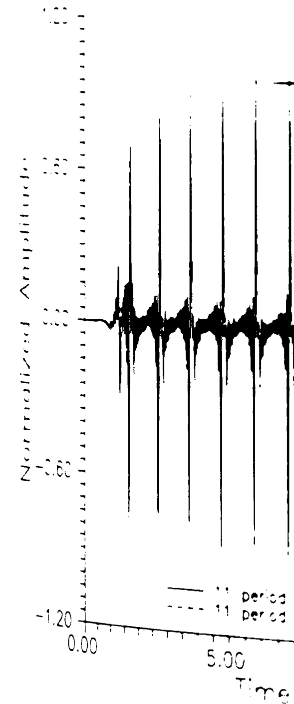

Figure 2.14 Periodic and non-per
pulse from a finite S
(L = .1778m, h = .

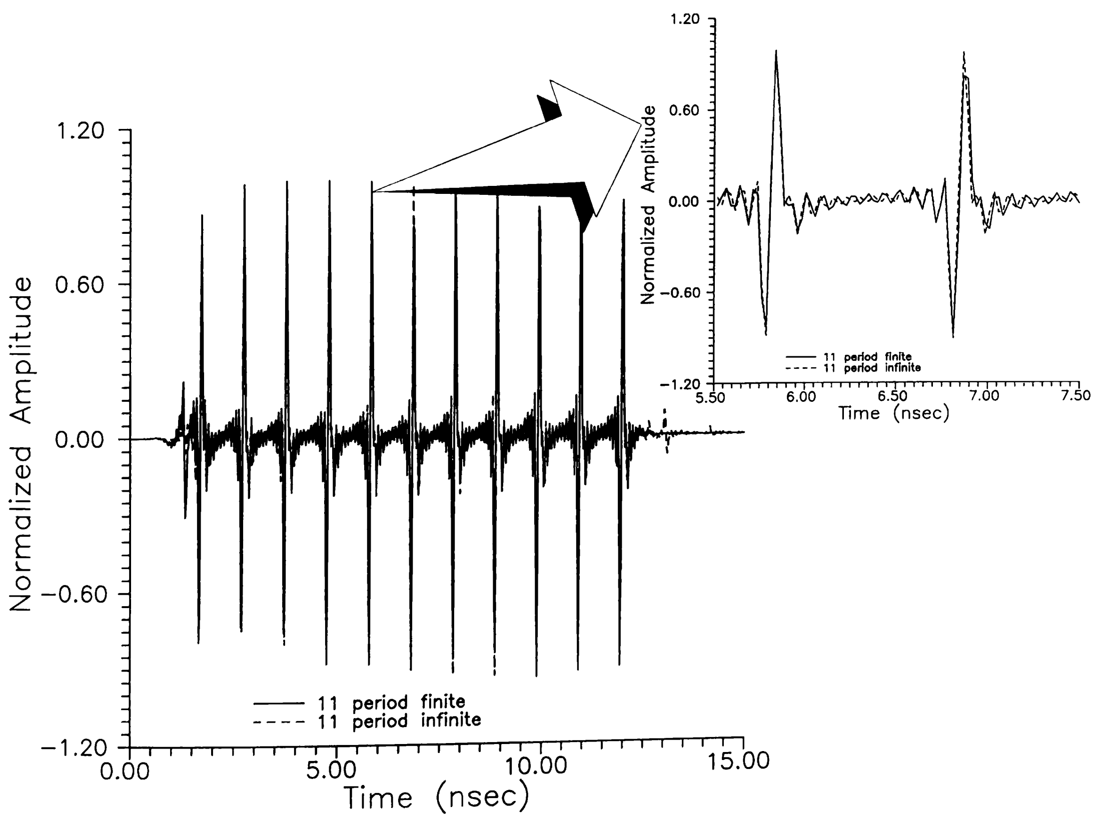

Figure 2.14 Periodic and non-periodic transient backscattered fields created by a short pulse from a finite Stoke's surface for TE excitation.
(L = .1778m, h = .0254m, ϕ_o = 30°)

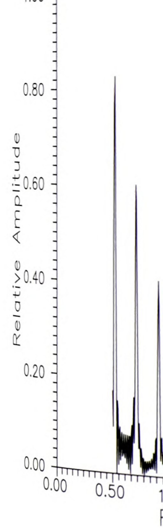

Figure 2.15 Magnitude of backsc
sinusoidal surface fo
current model used.

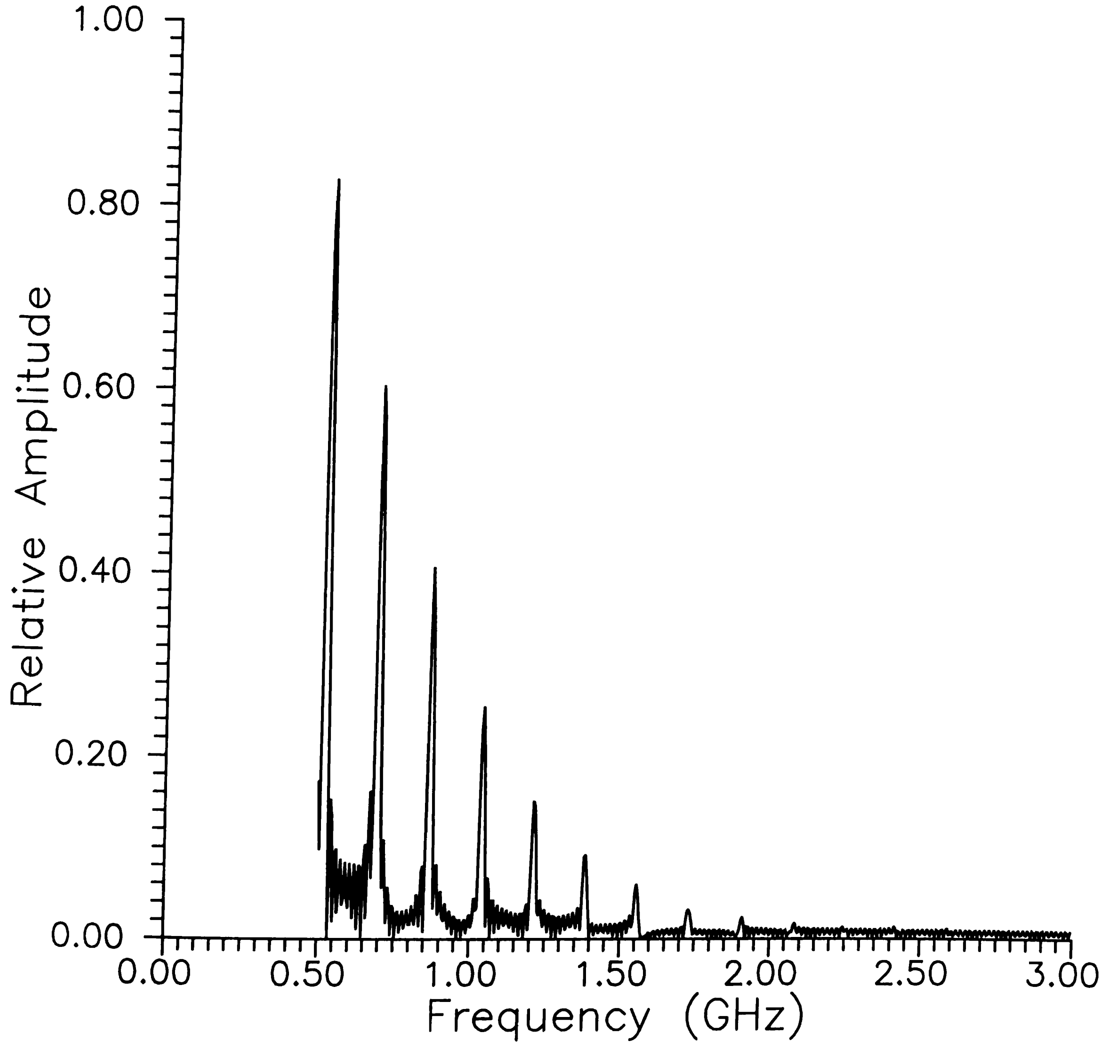

Figure 2.15 Magnitude of backscattered electric field from 11 periods of a conducting sinusoidal surface for TE excitation in the frequency domain. Periodic current model used. (L = 1.0m, h = .25m, ϕ_o = 30°)

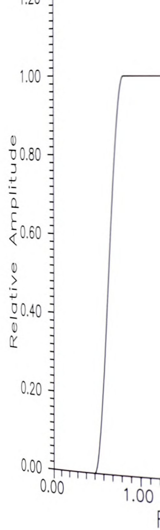

Figure 2.16 1/8 cosine taper win

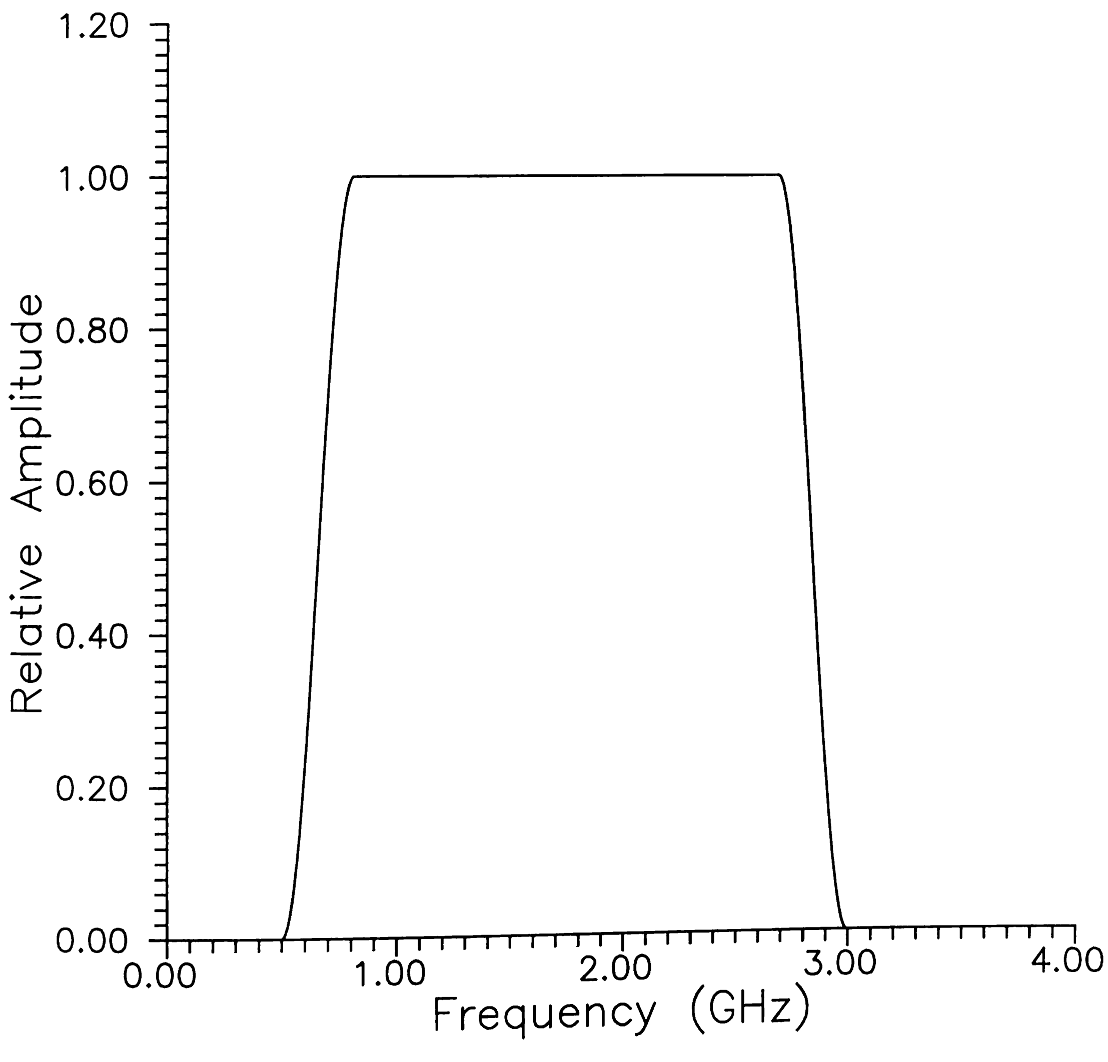

Figure 2.16 1/8 cosine taper window from .5 - 3.0 GHz.

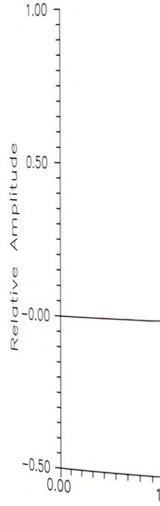

Figure 2.17 Synthesized pulse co

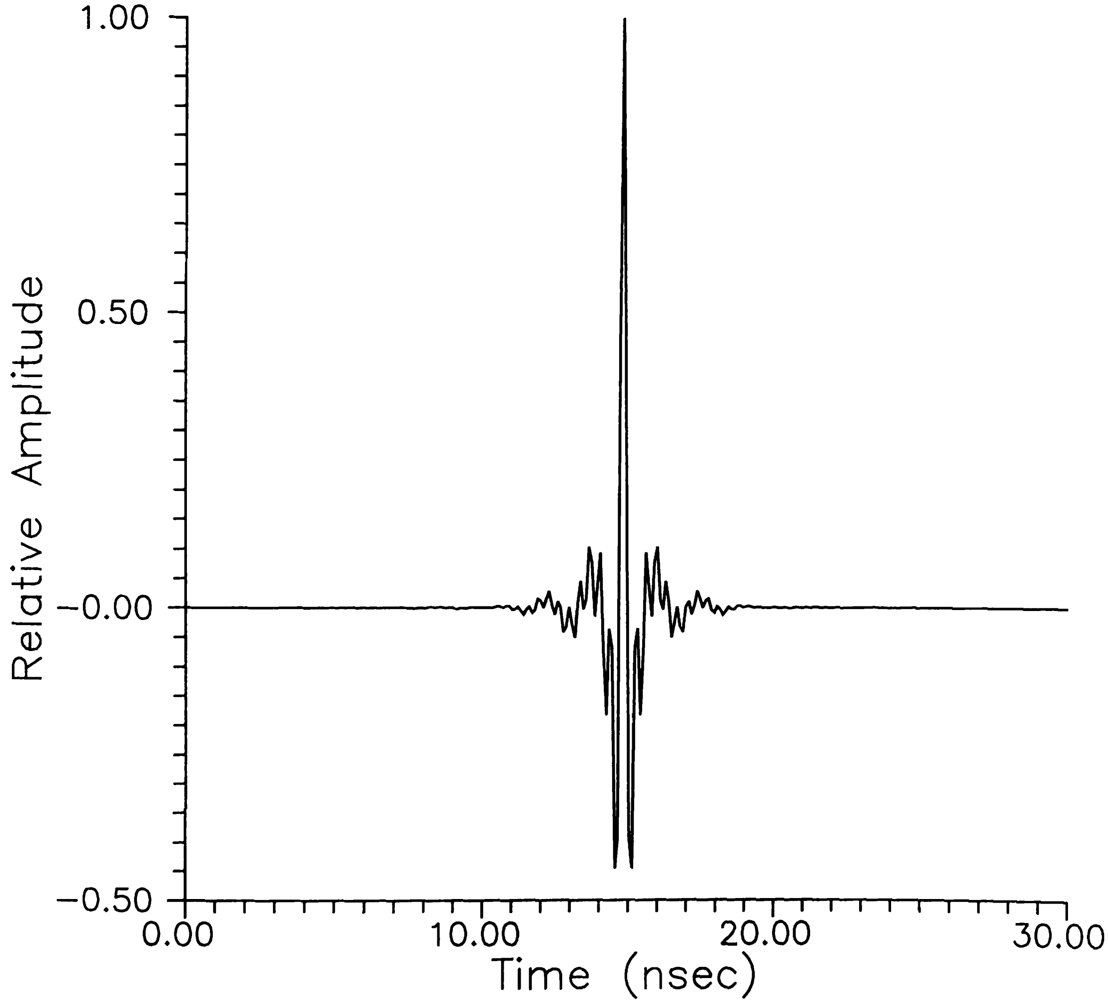

Figure 2.17 Synthesized pulse constructed from 1/8 cosine taper.

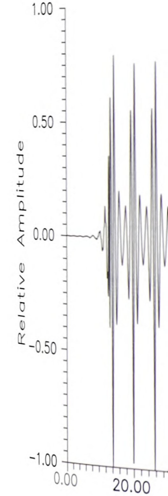

Figure 2.18 Transient backscatte
conducting sinusoida
= 45°)

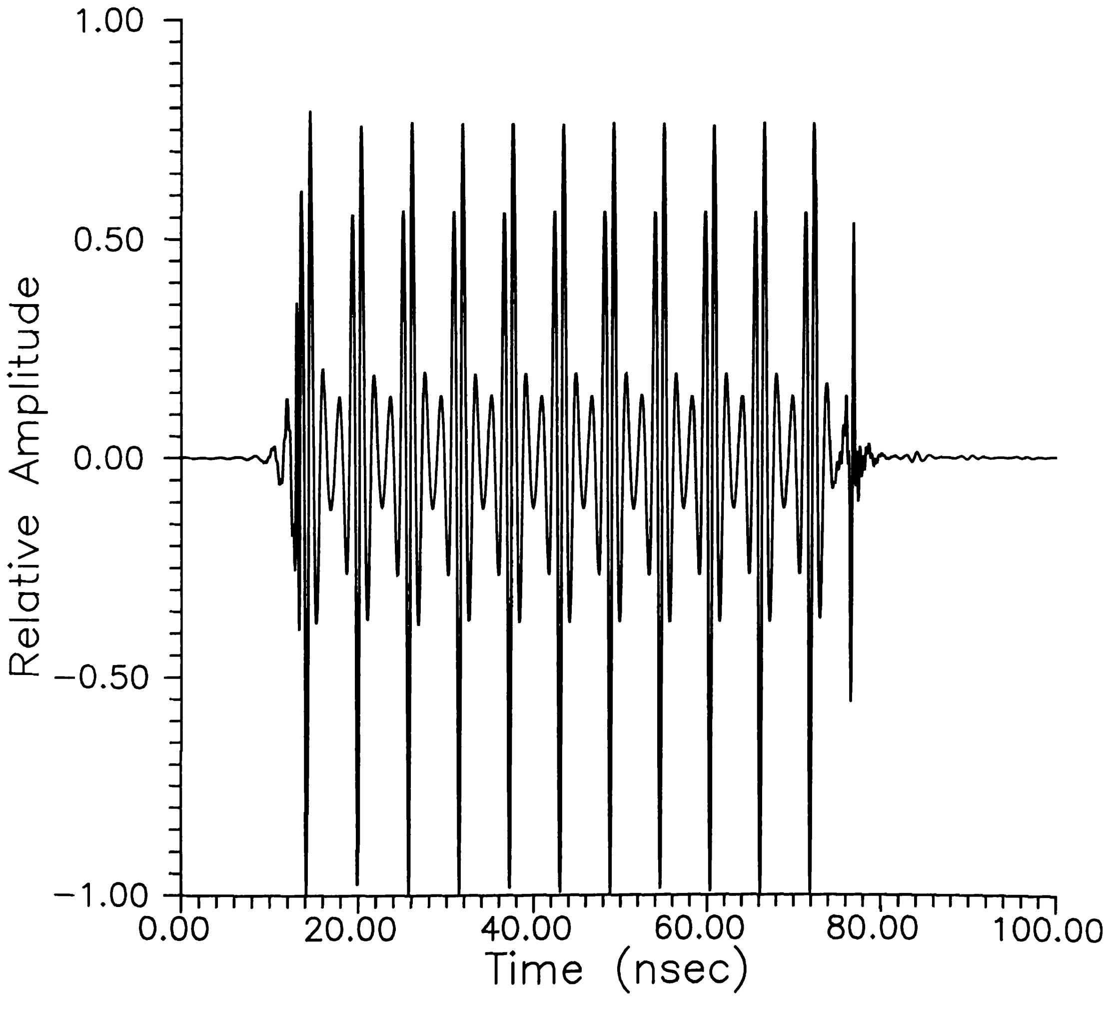

Figure 2.18 Transient backscattered electric field from incident pulse for 11 period conducting sinusoidal surface for TE excitation. (L = 1.0m, h = .25m, ϕ_o = 45°)

Table 2.1 Matrix fill time comp

	Fill Ti
Freq. (GHz)	1
1.0	10.65
2.0	9.78
3.0	9.43
4.0	9.83
5.0	10.49
6.0	10.22
7.0	10.38
8.0	10.55
9.0	10.88
10.0	71.67
11.0	11.64
12.0	11.97

Table 2.1 Matrix fill time comparison for Stoke's scattering problem.

	Fill Time (secs) for Different Number of Terms			
Freq. (GHz)	1	2	3	4
1.0	10.65	3.57	2.03	1.76
2.0	9.78	3.13	1.05	1.26
3.0	9.43	3.02	1.70	1.32
4.0	9.83	3.02	1.70	1.36
5.0	10.49	3.02	1.75	1.43
6.0	10.22	3.13	1.82	1.43
7.0	10.38	3.18	1.85	1.43
8.0	10.55	3.35	1.87	1.48
9.0	10.88	3.40	1.92	1.48
10.0	71.67	33.89	1.93	1.48
11.0	11.64	3.40	1.92	1.53
12.0	11.97	3.68	1.98	1.59

Review of Target De

3.1 Introduction

Considerable effort by resea

discrimination of radar targets u

[4],[9],[20]-[22]. This chapter v

implemented at MSU. Particular at

in a sea clutter environment using

conjunction with the E-pulse tech

illustrate and validate the E-pulse c

lay the foundation for the material

will be used for a new target detect

in conjunction with cepstral analys

of the numerical methods to determ

conducting, 2-dimensional, finite-le

Section 3.2 of this chapter

method for radar target detection

examples for a band-limited signal

section will present the theoretical

current on, and scattered field, fr

length. Difficulties such as compu

Chapter 3

Review of Target Detection and Scattering Techniques

3.1 Introduction

Considerable effort by researchers at MSU has been devoted to the detection and discrimination of radar targets using the extinction pulse (E-pulse) technique [3]-[4],[9],[20]-[22]. This chapter will review the E-pulse discrimination scheme as implemented at MSU. Particular attention will be placed on the detection of radar targets in a sea clutter environment using a stepped-frequency ultra-wideband (UWB) radar in conjunction with the E-pulse technique. Several new examples will be presented to illustrate and validate the E-pulse detection technique. The purpose of this review is to lay the foundation for the material in chapters 4 and 6. In chapter 4 the E-pulse method will be used for a new target detection algorithm. Chapter 6 will use the E-pulse method in conjunction with cepstral analysis for target identification. In section 3.4 a review of the numerical methods to determine the electromagnetic scattered fields for perfectly-conducting, 2-dimensional, finite-length surfaces will also be reviewed.

Section 3.2 of this chapter reviews the theoretical foundation of the E-pulse method for radar target detection in a sea clutter environment. In section 3.3 several examples for a band-limited signal will be used to illustrate this technique. The final section will present the theoretical methods that will be used for calculating the induced current on, and scattered field, from a perfectly conducting sea-like surface of finite length. Difficulties such as computer memory limitations and computational speed will be discussed.

3.2 Review of Target Detectio

Detection of objects locate

considerable detail at MSU. Detect

the clutter signal from the ocean s

Interest in UWB radar for targe

background clutter and enhance the

a high-resolution, time-domain rad

thus allowing the clutter signal to

using a UWB system, the period

increasing the probability of target

For a surface profile that i

scattered field response from the

measurement is made at time τ and

then the scattered field will be av

signal from the surface profile in

damped sinusoids [4]

$$r(t) = \sum_{n=1}^{N} a_n e^{\sigma_n}$$

where a_n and ϕ_n represent the

$s_n = \sigma_n + j\omega_n$ represents the com

approximately periodic nature of t

be discussed.

3.2 Review of Target Detection Using the E-pulse Method

Detection of objects located above a disturbed sea surface has been studied in considerable detail at MSU. Detection, using conventional radar, becomes difficult when the clutter signal from the ocean surface becomes large compared to the target return. Interest in UWB radar for target detection arises from the ability to reduce the background clutter and enhance the overall resolution capabilities of the radar [23]. With a high-resolution, time-domain radar, the dominant scattering events can be separated, thus allowing the clutter signal to be reduced and the target signal to be extracted. By using a UWB system, the periodic nature of the sea clutter return can be reduced, increasing the probability of target detection.

For a surface profile that is approximately periodic in nature the time-domain scattered field response from the surface is also approximately periodic. If a radar measurement is made at time τ and the two-way transit time across the range bin is T_R then the scattered field will be available in the time range $\tau < t < \tau + T_R$. The clutter signal from the surface profile in this time range bin can be modeled as a sum of N damped sinusoids [4]

$$r(t) = \sum_{n=1}^{N} a_n e^{\sigma_n t} \cos(\omega_n t + \phi_n) \qquad \tau < t < \tau + T_R \tag{3.1}$$

where a_n and ϕ_n represent the amplitude and phase of the nth scattering mode, $s_n = \sigma_n + j\omega_n$ represents the complex frequency of the nth mode. By using the approximately periodic nature of this waveform, a clutter reducing transmit waveform

(CRTW) [3] can be created which

will reduce the background clutter

A CRTW e(t) is a wavefor

sea surface clutter return r(t), resul

$$c(t) = e(t) * r(t) = \int_{\tau}^{\tau + T_R}$$

Application of the Laplace transfor

the CRTW

$$C($$

where E(s) and R(s) are the Lapl

condition for creating the CRTW [

$$E(s = s_n) = E($$

where s_n^* is the complex conjugate

Numerical construction of t

e(t) in a set of K basis functions as

$$e$$

where $\{g_k(t)\}$ is an appropriate set

(3.5) into the convolution integral

weighting function $\{W_m\}$ gives

(CRTW) [3] can be created which, when either transmitted or used in post-processing, will reduce the background clutter yet preserve the target signal.

A CRTW e(t) is a waveform of finite duration T_E that, when convolved with the sea surface clutter return r(t), results in a null response given by

$$c(t) = e(t) * r(t) = \int_{\tau}^{\tau + T_R} r(t') e(t-t') dt' = 0 \qquad \tau + T_E < t < \tau + T_R \tag{3.2}$$

Application of the Laplace transform to (3.2) leads to the following condition for creating the CRTW

$$C(s) = E(s) R(s) = 0 \tag{3.3}$$

where E(s) and R(s) are the Laplace spectra of e(t) and r(t) respectively. Hence a condition for creating the CRTW [24] is

$$E(s = s_n) = E(s = s_n^*) = 0 \qquad n = 1,2,\ldots N \tag{3.4}$$

where s_n^* is the complex conjugate of s_n.

Numerical construction of the CRTW is performed by expanding the waveform e(t) in a set of K basis functions as [20]

$$e(t) = \sum_{k=1}^{K} \alpha_k g_k(t) \tag{3.5}$$

where $\{g_k(t)\}$ is an appropriate set of basis functions. Substituting the expansion from (3.5) into the convolution integral of (3.2) and taking inner products with a set of weighting function $\{W_m\}$ gives

$$\sum_{k=1}^{K} \alpha_k \int_{t'=0}^{T_E} \int_{\tau - T_E}^{\tau - T_R} g_k(t') r(t$$

Using (3.6), a solution for α_k for alm

be found by choosing M = 2N an

inhomogeneous matrix equation wit

matrix to be singular. Furthermo

simplified by using rectangular puls

Different values for T_E resu

choice of T_E can have a significant

resonant frequencies [4]. A suitable

error per point between the original

situation, the following must be mi

$$\epsilon = \| r(t)$$

where

$$\hat{r}(t) =$$

The extracted frequencies $\hat{s}_n = \hat{\sigma}_n$

amplitudes in (3.6) and then using t

equation of the form

$$\sum_{k=1}^{K} \alpha_k \int_{t'=0}^{T_E} \int_{\tau+T_E}^{\tau+T_R} g_k(t')\, r(t-t')\, W_m(t)\, dt\, dt' = 0 \qquad m = 1,2,\ldots,M \tag{3.6}$$

Using (3.6), a solution for α_k for almost any choice of T_E ("forced" E-pulse solution) can be found by choosing M = 2N and K = 2N+1. For this condition (3.6) becomes an inhomogeneous matrix equation with solution for any choice of T_E that does not cause the matrix to be singular. Furthermore, the evaluation of the integral in (3.6) can be simplified by using rectangular pulse basis functions and weighting impulse functions.

Different values for T_E result in significantly different CRTW waveforms. The choice of T_E can have a significant effect on the constructed E-pulse and the extracted resonant frequencies [4]. A suitable choice of T_E is one that yields the minimum squared error per point between the original data r(t) and a reconstructed waveform $\hat{r}(t)$. In this situation, the following must be minimized over the sample interval

$$\epsilon = \| r(t) - \hat{r}(t) \| = \sum_i [r(t_i) - \hat{r}(t_i)]^2 \tag{3.7}$$

where

$$\hat{r}(t) = \sum_{n=1}^{N} \hat{a}_n e^{\hat{\sigma}_n t} \cos(\hat{\omega}_n t + \hat{\phi}_n) \tag{3.8}$$

The extracted frequencies $\hat{s}_n = \hat{\sigma}_n + j\hat{\omega}_n$ can be found by solving for the E-pulse basis amplitudes in (3.6) and then using the relation given by (3.4). This leads to a polynomial equation of the form

$$\sum_{k=1}^{2N+1} \alpha_k Z^k = 0 \tag{3.9}$$

where $Z = e^{-s\Delta}$ and Δ is the bas

Once the natural frequenc

applied to (3.7) and (3.8) to yiel

waveform. Different values of T_E

of T_E can be varied to construct th

process, the E-pulse amplitudes,

obtained.

3.3 E-pulse Target Detection

The use of the CRTW tec

a sea surface clutter environme

implementation [22]. The followi

for the case of band-limited signa

The theoretical pulse resp

surface models with surface profil

for an incident wave whose electri

polarization). The incident and sc

the horizon. The moment method

in the frequency range 0 to 14 GH

band limiting the scattered field sp

see Appendix A) shown in Figure

the band 9-14 GHz, with a 3 d

where $Z = e^{-s\Delta}$ and Δ is the basis function width.

Once the natural frequencies are determined, a least-squares fitting routine is applied to (3.7) and (3.8) to yield the amplitude and phase terms for the reconstructed waveform. Different values of T_E will of course lead to values of ε that differ. The value of T_E can be varied to construct the waveform that yields the smallest value of ε. In this process, the E-pulse amplitudes, frequencies, and best fit reconstructed waveform are obtained.

3.3 E-pulse Target Detection Using Band-limited Signals

The use of the CRTW technique to detect the presence of a target embedded in a sea surface clutter environment has previously been reported using a baseband implementation [22]. The following examples will illustrate the validity of the technique for the case of band-limited signals.

The theoretical pulse responses of two finite-length, perfectly-conducting, sea surface models with surface profiles shown in Figure 3.1 were computed (see section 3.4) for an incident wave whose electric field was polarized parallel to the surface crests (TE-polarization). The incident and scattering angles were both 12.5 degrees with respect to the horizon. The moment method was used to compute the frequency-domain response in the frequency range 0 to 14 GHz. A stepped, ultra-wideband signal was simulated by band limiting the scattered field spectra with a GMC window (f_c = 11 GHz, T = .5 nsec, see Appendix A) shown in Figure 3.3. This window limited the frequency response to the band 9-14 GHz, with a 3 dB bandwidth of 1.2 GHz (about 11% of the center frequency of 11 GHz). The time

Figure 3.4. is obtained by applying

frequency spectrum. The band

surface are shown in Figure 3.5.

allow comparison with measuren

match the dimensions of actual se

After the time-domain si

response of a five inch long missi

to produce a prechosen target-to-

target signal strength to maximum

leading edge of the finite length

missile and clutter signals for the

to discern the presence of any targ

least-squares minimization fitting

surface are shown in Figure 3.7.

combinations are shown in Figure

after application of the CRTW co

discerned from the clutter backgro

3.4 Review of Theoretical Conducting Sea Surfaces

This section reviews elec

conducting surfaces. The numeric

frequency of 11 GHz). The time-domain representation of the incident pulse, shown in Figure 3.4, is obtained by applying an inverse fast Fourier transform (IFFT) to the tapered frequency spectrum. The band limited spectra for the sinusoid and double sinusoid surface are shown in Figure 3.5. Also, the size of the sea surface models was chosen to allow comparison with measurements taken within an anechoic chamber, and do not match the dimensions of actual sea surfaces.

After the time-domain signals for the surfaces were computed, the measured response of a five inch long missile target was added. The missile amplitude was scaled to produce a prechosen target-to-clutter ratio (TCR) defined as the ratio of maximum target signal strength to maximum clutter signal strength (excluding the response from the leading edge of the finite length surface). Figure 3.6 shows the superposition of the missile and clutter signals for the two surfaces. From this figure it is obviously difficult to discern the presence of any target from the band-limited background clutter. Using the least-squares minimization fitting routine (section 3.2), the CRTWs created for each surface are shown in Figure 3.7. The convolution of the CRTWs with the clutter/target combinations are shown in Figure 3.8. The presence of the target is clearly enhanced after application of the CRTW convolution. For each surface, the missile can easily be discerned from the clutter background.

3.4 Review of Theoretical Scattering Methods for Finite-Length, Perfectly-Conducting Sea Surfaces

This section reviews electromagnetic scattering from finite-length, perfectly-conducting surfaces. The numerical solution of an electric field integral equation using the method of moments will be fo

surface roughness in one dimensi

Figure 3.9 shows a plane v

polarization of the electric field i

and the angle between the x-axis

varying electric field E_z^i impres

current $K_z(x)$ on the conducting

electric field E_z^s given by [14]

$$E_z^s(\bar{\rho}) = -\frac{k\eta}{4}$$

where $H_0^{(2)}$ represents a Hankel fu

and source points respectively, ar

The propagation constant and im

respectively. The differential line

integration for the surface are L_1

terms of their coordinates as

$$\vec{\rho}$$

$$\vec{\rho}'$$

where ρ represents the distance

scattering angle measured from th

the differential line element lengt

the method of moments will be formulated for the case of scattering from surfaces having surface roughness in one dimension.

Figure 3.9 shows a plane wave impinging on a perfectly conducting surface. The polarization of the electric field is parallel to the crests of the surface (TE-polarization) and the angle between the x-axis and the propagation vector is given by ϕ_o. The time-varying electric field E_z^i impressed upon the surface generates a z-directed induced current $K_z(x)$ on the conducting surface. These currents in turn generate a scattered electric field E_z^s given by [14]

$$E_z^s(\vec{\rho}) = -\frac{k\eta}{4}\int_{L_1}^{L_2} K_z(x')\, H_o^{(2)}(k\,|\vec{\rho} - \vec{\rho}'|)\, L(x')\, dx' \tag{3.10}$$

where $H_0^{(2)}$ represents a Hankel function of the second kind, ρ and $\vec{\rho}'$ represent the field and source points respectively, and K(x) represents the induced surface current density. The propagation constant and impedance of the medium are symbolized by k and η respectively. The differential line element length is given by L(x)dx and the limits of integration for the surface are L_1 and L_2. The field and source points can be written in terms of their coordinates as

$$\vec{\rho} = \rho\cos\alpha\,\hat{x} + \rho\sin\alpha\,\hat{y} \tag{3.11}$$

$$\vec{\rho}' = x'\hat{x} + f(x')\,\hat{y} \tag{3.12}$$

where ρ represents the distance from the origin to the field point, α represents the scattering angle measured from the x-axis, and f(x) represents the surface height. Finally, the differential line element length can be written as

$L(x'$

To determine the surface

applied at the surface of the perf

$E_z^s(x,y) - E$

Combining (3.14) with (3.10) yie

$$\int_{L_1}^{L_2} K_z(x')\, H_o^{(2)}(k$$

The surface current density can b

K

where $K_n(x')$ represents the curre

N discrete points x_m in the interv

now be written as

$$\sum_{n=1}^{N} a_n \int_{L_1}^{L_2} K_n(x')\, H$$

$=$

The above equation can be writte

$$\sum_{n=1}^{N} a_n A$$

where

$$A_{mn} = \int_{L_1}^{L_2} K_n(x')\, H_o^{(2)}($$

$$L(x')dx' = \sqrt{1 + f'(x)^2}\; dx' \tag{3.13}$$

To determine the surface current, the following boundary condition must be applied at the surface of the perfectly conducting surface

$$E_z^s(x,y) + E_z^i(x,y) = 0 \qquad x,y \in surface \tag{3.14}$$

Combining (3.14) with (3.10) yields the following integral equation

$$\begin{aligned} &\int_{L_1}^{L_2} K_z(x')\, H_o^{(2)}\!\left(k\sqrt{(x-x')^2 + (f(x)-f(x'))^2}\right) L(x')\,dx' \\ &\qquad = \frac{4}{k\eta}\, E_z^i(x, f(x)) \qquad L_1 \le x \le L_2 \end{aligned} \tag{3.15}$$

The surface current density can be expanded as a finite series of terms taking the form

$$K_z(x') = \sum_{n=1}^{N} a_n\, K_n(x') \tag{3.16}$$

where $K_n(x')$ represents the current basis functions. Next, point-matching is applied at N discrete points x_m in the interval from L_1 to L_2. The integral equation in (3.15) can now be written as

$$\begin{aligned} &\sum_{n=1}^{N} a_n \int_{L_1}^{L_2} K_n(x')\, H_o^{(2)}\!\left(k\sqrt{(x_m-x')^2 + (f(x_m)-f(x'))^2}\right) L(x')\,dx' \\ &\qquad = \frac{4}{k\eta}\, E_z^i(x_m, f(x_m)) \qquad m = 1,\ldots,N \end{aligned} \tag{3.17}$$

The above equation can be written in matrix form as

$$\sum_{n=1}^{N} a_n\, A_{mn} = b_m \qquad m = 1, \ldots, N \tag{3.18}$$

where

$$A_{mn} = \int_{L_1}^{L_2} K_n(x')\, H_o^{(2)}\!\left(k\sqrt{(x_m-x')^2 + (f(x_m)-f(x'))^2}\right) L(x')\,dx' \tag{3.19}$$

$$b_m$$

If the interval between L_1 and L_2

a pulse basis function can be def

$$K_n(x') = \{$$

With the pulse-basis function def

$$A_{mn} = \int_{x_n - \frac{\Delta}{2}}^{x_n - \frac{\Delta}{2}} H_o^{(2)}(k$$

The self-term (m = n) can be appr

is a straight line having width w_m

$$w_m = \sqrt{\Delta}$$

The relation in (3.22) for the self

$$A_{mm}$$

For small arguments the hankel f

$$H_o^{(2)}(u) \approx 1$$

where $\gamma = 1.781$. Evaluation of

yields

$$A_{mm} = w$$

For non-diagonal elements, the ex

$$b_m = \frac{4}{k\eta} E_z^i \,(x_m, f(x_m)) \tag{3.20}$$

If the interval between L_1 and L_2 is divided into N segments of length Δ and center x_n, a pulse basis function can be defined as

$$K_n(x') = \begin{cases} 1 & x_n - \dfrac{\Delta}{2} \le x \le x_n + \dfrac{\Delta}{2} \\ 0 & elsewhere \end{cases} \tag{3.21}$$

With the pulse-basis function defined in (3.21) the matrix term given by (3.19) becomes

$$A_{mn} = \int_{x_n - \frac{\Delta}{2}}^{x_n + \frac{\Delta}{2}} H_o^{(2)}\left(k\sqrt{(x_m - x')^2 + (f(x_m) - f(x'))^2}\,\right) L(x')\, dx' \tag{3.22}$$

The self-term (m = n) can be approximated by assuming that the segment between points is a straight line having width w_m given by

$$w_m = \sqrt{\Delta^2 + [\, f(x_m - \tfrac{\Delta}{2}) - f(x_m + \tfrac{\Delta}{2})\,]^2} \tag{3.23}$$

The relation in (3.22) for the self term becomes

$$A_{mm} = \int_{-w_m/2}^{w_m/2} H_o^{(2)}(k\,|x'|)\, dx' \tag{3.24}$$

For small arguments the hankel function becomes [18]

$$H_o^{(2)}(u) \approx 1 - j\frac{2}{\pi} \ln(\frac{\gamma u}{2}) \qquad for \quad u \ll 1 \tag{3.25}$$

where $\gamma = 1.781$. Evaluation of the integral in (3.24) with the relation given by (3.25) yields

$$A_{mm} = w_m \left[1 - j\frac{2}{\pi} (\, \ln(\frac{k\gamma}{4} w_m) - 1) \right] \tag{3.26}$$

For non-diagonal elements, the expression given by (3.22) can be approximated by simple rectangular rule integration as

$$A_{mn} = H_o^{(2)}\left(k\sqrt{(\right.$$

Evaluation of the matrix e

basis function amplitudes given b

the pulse basis function amplitu

evaluated using (3.16) and (3.10

field approximation should be co

can be expanded as

$$k\,|\vec{\rho} - \vec{\rho}\,'| \approx$$

For large arguments the Hankel f

Substituting (3.28) into (3.29) a

argument yields

$$H_o^{(2)}(k\,|\vec{\rho} - \vec{\rho}\,'|)$$

Substituting the relations given b

(3.10) becomes

$$E_z^s(\vec{\rho}) \approx -\eta\sqrt{\frac{jk}{8\pi}}\;\frac{e^{-}}{\sqrt{}}$$

rectangular rule integration as

$$A_{mn} = H_o^{(2)}\left(k\sqrt{(x_m - x_n)^2 + (f(x_m) - f(x_n))^2}\right) L(x_n)\,\Delta \tag{3.27}$$

Evaluation of the matrix elements in (3.26) and (3.27) is needed to solve the pulse basis function amplitudes given by the solution of the matrix equation in (3.18). Once the pulse basis function amplitudes are determined, the scattered electric field can be evaluated using (3.16) and (3.10). However, to simplify the evaluation of (3.10) a far field approximation should be considered. In this case, the Hankel function argument can be expanded as

$$k\,|\vec{\rho} - \vec{\rho}\,'| \approx k\left(\rho - (x'\cos\alpha + f(x')\sin\alpha)\right) \tag{3.28}$$

For large arguments the Hankel function can be expanded with the following relation

$$H_o^{(2)}(u) \approx \sqrt{\frac{2j}{\pi u}}\, e^{-ju} \tag{3.29}$$

Substituting (3.28) into (3.29) and using only the ρ dependence for the amplitude argument yields

$$H_o^{(2)}(k\,|\vec{\rho} - \vec{\rho}\,'|) \approx \sqrt{\frac{2j}{k\pi}}\, \frac{e^{-jk\rho}}{\sqrt{\rho}}\, e^{+jk(x'\cos\alpha + f(x')\sin\alpha)} \tag{3.30}$$

Substituting the relations given by (3.16),(3.21), and (3.30) the scattered field given by (3.10) becomes

$$E_z^s(\vec{\rho}) \approx -\eta\sqrt{\frac{jk}{8\pi}}\, \frac{e^{-jk\rho}}{\sqrt{\rho}} \sum_{n=1}^{N} a_n \int_{x_n - \frac{\Delta}{2}}^{x_n + \frac{\Delta}{2}} e^{jk(x'\cos\alpha + f(x')\sin\alpha)}\, L(x')\, dx' \tag{3.31}$$

which for rectangular rule integr

$$E_z^s(\vec{\rho}) \approx -\eta \sqrt{\frac{jk}{8\pi}}$$

The determination of the

system of equations in many un

solution of large linear systems

computers. A typical linear syste

requires at least 2 Mbytes of real

complex arithmetic and 4 Mbyte

Doubling the number of equation

leading to memory resource prob

to use some sort of virtual memor

very attractive due to the large

memory and that found on the ha

problem using the spatial decomp

If the process of calculat

necessary to store the entire matr

into a number of subsections o

scattering object separated from i

adjacent subzones carry tange

electromagnetic field boundary c

one side of the interface must be

which for rectangular rule integration becomes

$$E_z^s(\vec{\rho}) \approx -\eta \sqrt{\frac{jk}{8\pi}} \frac{e^{-jk\rho}}{\sqrt{\rho}} \sum_{n=1}^{N} a_n e^{jk(x_n \cos\alpha + f(x_n)\sin\alpha)} L(x_n)\,\Delta \qquad \textbf{(3.32)}$$

The determination of the surface current involves finding a solution to a large system of equations in many unknowns. A typical problem often encountered in the solution of large linear systems is the memory constraint imposed by most desktop computers. A typical linear system composed of 512 equations in 512 unknown variables requires at least 2 Mbytes of real memory to store the matrix values for single precision complex arithmetic and 4 Mbytes of memory for double precision complex arithmetic. Doubling the number of equations and unknowns requires four times as much memory, leading to memory resource problems for small systems. One solution to the problem is to use some sort of virtual memory management scheme. However, this alternative is not very attractive due to the large amount of time required to swap data between real memory and that found on the hard disk. Another approach, taken here, is to solve the problem using the spatial decomposition technique (SDT) [25].

If the process of calculating the matrix elements is fairly fast, it may not be necessary to store the entire matrix. In the SDT method the scattering object is divided into a number of subsections or subzones. Each subzone is considered a distinct scattering object separated from its nearest neighbor by a virtual surface. Furthermore, adjacent subzones carry tangential electric and magnetic virtual currents. The electromagnetic field boundary conditions requires that the tangential virtual currents on one side of the interface must be equal to, but opposite from the other side. An integral equation solution, using the m

approximate solution to the prob

the subzones, and then the solu

some stopping criteria is satisfie

Consider again the electr

into (3.14). A compact represen

aid of the operator $\mathfrak{L}_1^{JJ}$ [25] as

where

$$\mathfrak{L}_1^{JJ} = \int_C$$

and C represents the contour of i

the surface is divided into N sub

be written as [25]

$$E_z^i(\vec{\rho}) - \sum_{n=}^{N}$$

where

$$\mathfrak{L}_{1n}^{JJ} = \int_{C_n}$$

Here, $K_{zn}(x')$ represents the sur

the contour of integration over th

left-hand side of (3.35) the total e

excitation and the additional te

equation solution, using the method of moments, is applied to each subzone. An approximate solution to the problem is determined by sequentially scanning through all the subzones, and then the solution is refined through successive approximations until some stopping criteria is satisfied.

Consider again the electric field integral equation formed by substituting (3.10) into (3.14). A compact representation of this integral equation can be written with the aid of the operator $\mathfrak{L}_1^{JJ}$ [25] as

$$\mathfrak{L}_1^{JJ}\,[K_z(x')] = E_z^i(\vec{\rho}) \tag{3.33}$$

where

$$\mathfrak{L}_1^{JJ} = \int_C \frac{k\eta}{4} H_0^{(2)}(k(\vec{\rho}-\vec{\rho}\,'))L(x')\,dx' \tag{3.34}$$

and C represents the contour of integration over the limits of the conducting surface. If the surface is divided into N subzones, the electric field integral for the ith subzone can be written as [25]

$$E_z^i(\vec{\rho}) - \sum_{n=1}^{N} \mathfrak{L}_{1n}^{JJ}\,[K_{zn}(x')] = \mathfrak{L}_{1i}^{JJ}\,[K_{zi}(x')] \tag{3.35}$$

where

$$\mathfrak{L}_{1n}^{JJ} = \int_{C_n} \frac{k\eta}{4} H_0^{(2)}(k(\vec{\rho}-\vec{\rho}\,'))L(x')\,dx' \tag{3.36}$$

Here, $K_{zn}(x')$ represents the surface current density over the nth subzone, C_n represents the contour of integration over the nth subzone, and $\vec{\rho}$ is located on subzone i. On the left-hand side of (3.35) the total excitation on spatial subzone i is given by the plane-wave excitation and the additional terms due to the other subzones. To implement the algorithm, the value of i starts at

method of moments. The algori

subsection is calculated. This pr

current for each subsection on the

has been completed an approxim

Successive sweeps across the su

stopping criteria is satisfied.

The advantage of the SD

can be solved on a computer sys

an electrically large scattering su

matrix is of size N_p x N_p. Howev

into N subsections of N_L points,

x N_L. Hence, the memory limit

surface into enough subsections.

To illustrate the use of t

sinusoid surface was computed.

wave and scattered field calcula

polarization of the incident field w

The surface geometry consists of

peak wave height of .0254 mete

sections to determine the numbe

current. All computations were

algorithm, the value of i starts at 1 and the current only on subzone 1 is calculated by the method of moments. The algorithm then shifts to subzone 2 where the current on this subsection is calculated. This process sequentially steps through each subzone until the current for each subsection on the entire surface has been calculated. Once the full sweep has been completed an approximate solution for the surface current has been obtained. Successive sweeps across the surface lead to a convergent iterative process until some stopping criteria is satisfied.

The advantage of the SDT method is that the current on electrically large objects can be solved on a computer system with a modest memory capacity. For example, if an electrically large scattering surface is broken into N_p discrete points, then the system matrix is of size N_p x N_p. However, by using the SDT method the surface can be broken into N subsections of N_L points, where $N_L = N_p/N$. Now the system matrix is of size N_L x N_L. Hence, the memory limitation problem can be managed nicely by breaking the surface into enough subsections.

To illustrate the use of the above technique the scattered field from a simple sinusoid surface was computed. The surface consists of 255 segments with the incident wave and scattered field calculated at 30 degrees with respect to the horizon. The polarization of the incident field was parallel to the crests of the surface (TE polarization). The surface geometry consists of 11 periods, a period length of .1016 m, and a peak to peak wave height of .0254 meters. The surface was divided into a different number of sections to determine the number of iterations and computational time to solve for the current. All computations were performed on a Pentium-100 system (24 Mbytes). The

iteration stopping criteria for all
shows the computational results
example illustrate the effectivene
five segments does not lead to lo
the calculations. However, divi
longer computation times. This
divided into 15 segments.

A second example consis
running the same test. Table 3
frequencies. The results in this t
number of surface segments used
surface segments but not enough

3.5 Conclusions

This chapter reviewed tw
thesis. First, the E-pulse techni
illustrating the application of the
environment. Next, the numeri
scattering from a finite-length, pe
The use of the spatial decompo
cases were described. The spa
computer systems with a limited

iteration stopping criteria for all work was set at a relative tolerance of 10^{-4}. Table 3.1 shows the computational results for three different frequencies. The results of this example illustrate the effectiveness of this technique. Dividing the surface into three or five segments does not lead to longer computation time and requires less memory to do the calculations. However, dividing the surface into too many segments can lead to longer computation times. This can be seen for the case where the surface has been divided into 15 segments.

A second example consists of dividing the same surface into 500 segments and running the same test. Table 3.2 shows the computational results for three different frequencies. The results in this table suggest that this technique is very effective for the number of surface segments used. The computation time varies for different numbers of surface segments but not enough to suggest any large increases in computation time.

3.5 Conclusions

This chapter reviewed two important topics which will be used throughout this thesis. First, the E-pulse technique was presented. Several examples were presented illustrating the application of the E-pulse method to the detection of target in a sea-clutter environment. Next, the numerical solution to the electric field integral equation for scattering from a finite-length, perfectly-conducting, 2-dimensional surface was reviewed. The use of the spatial decomposition technique was presented and several sample test cases were described. The spatial decomposition technique is extremely useful for computer systems with a limited amount of memory.

Table 3.1 Spatial decompos
from 255 segment

N_s/N_p	num.
f = 3.	
1/255	
3/85	1
5/51	1
15/17	3
f = 3.	
1/255	
3/85	1
5/51	1
15/17	2
f = 3.	
1/255	
3/85	1
5/51	1
15/17	3

* double precision complex arit

Table 3.1 Spatial decomposition iterative scheme efficiency results for scattering from 255 segment sinusoid surface

N_s/N_p	num. of iters.	comp. time (sec)	matrix storage (kbytes)*
f = 3.0 GHz			
1/255	1	15	1016
3/85	12	21	112
5/51	12	15	41
15/17	35	36	5
f = 3.1 GHz			
1/255	1	15	1016
3/85	11	19	112
5/51	13	17	41
15/17	29	31	5
f = 3.2 GHz			
1/255	1	15	1016
3/85	11	19	112
5/51	14	19	41
15/17	34	35	5

* double precision complex arithmetic (16 byte arithmetic)

Table 3.2 Spatial decompos
from 500 segment

N_s/N_p	num. (
f = 3.	
1/500	
2/250	
4/125	1
5/100	1
10/50	2
f = 3.	
1/500	
2/250	
4/125	1
5/100	1
10/50	2
f = 3.	
1/500	
2/250	
4/125	1
5/100	1
10/50	2

* double precision complex arit

Table 3.2 Spatial decomposition iterative scheme efficiency results for scattering from 500 segment sinusoid surface

N_s/N_p	num. of iters.	comp. time (sec)	matrix storage (kbytes)*
f = 3.0 GHz			
1/500	1	107	3906
2/250	5	81	977
4/125	15	103	244
5/100	16	94	156
10/50	23	104	39
f = 3.1 GHz			
1/500	1	108	3906
2/250	4	65	977
4/125	16	110	244
5/100	15	88	156
10/50	24	108	39
f = 3.2 GHz			
1/500	1	107	3906
2/250	5	80	977
4/125	15	103	244
5/100	15	88	156
10/50	24	109	39

* double precision complex arithmetic (16 byte arithmetic)

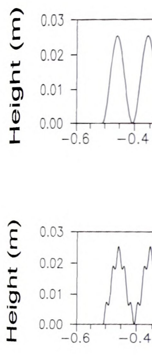

Figure 3.1 Simple sinusoid a

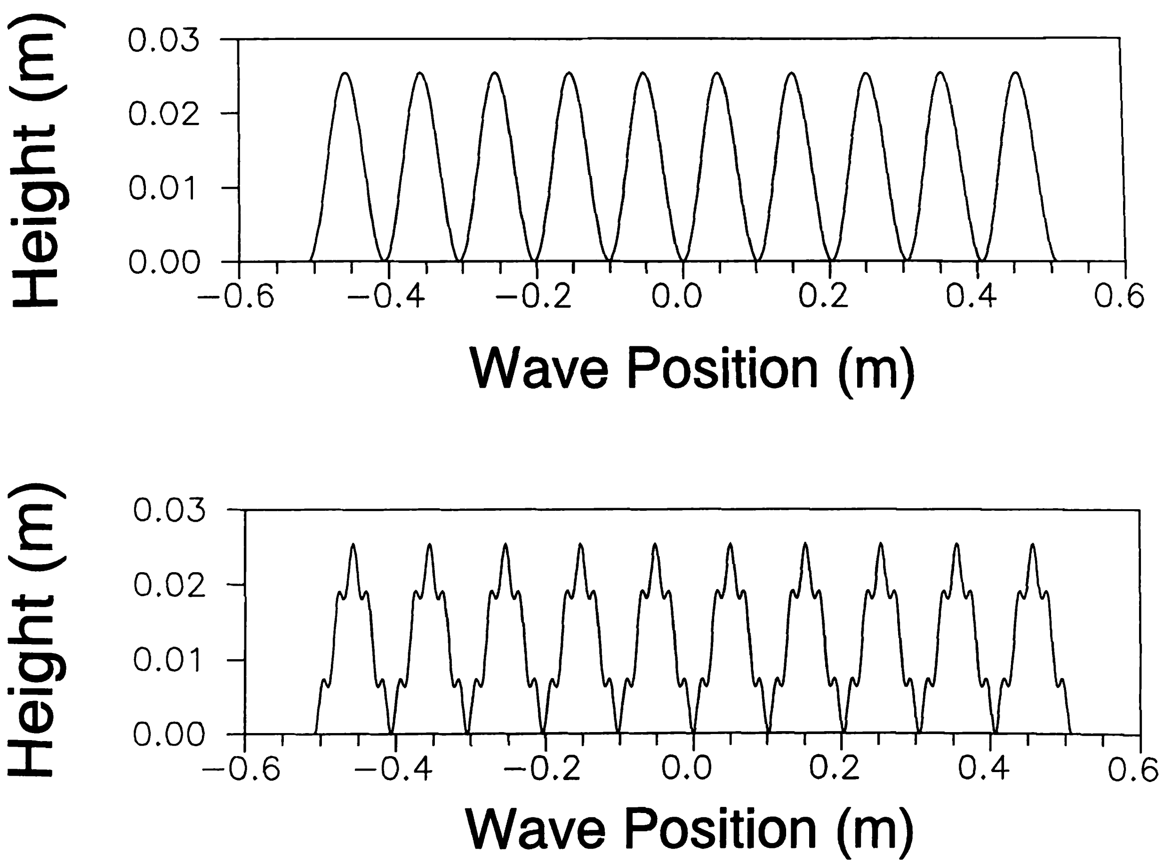

Figure 3.1 Simple sinusoid and double sinusoid surface geometry.

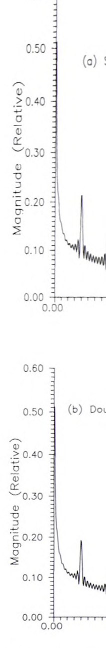

Figure 3.2 Calculated scatter
sinusoid surface.

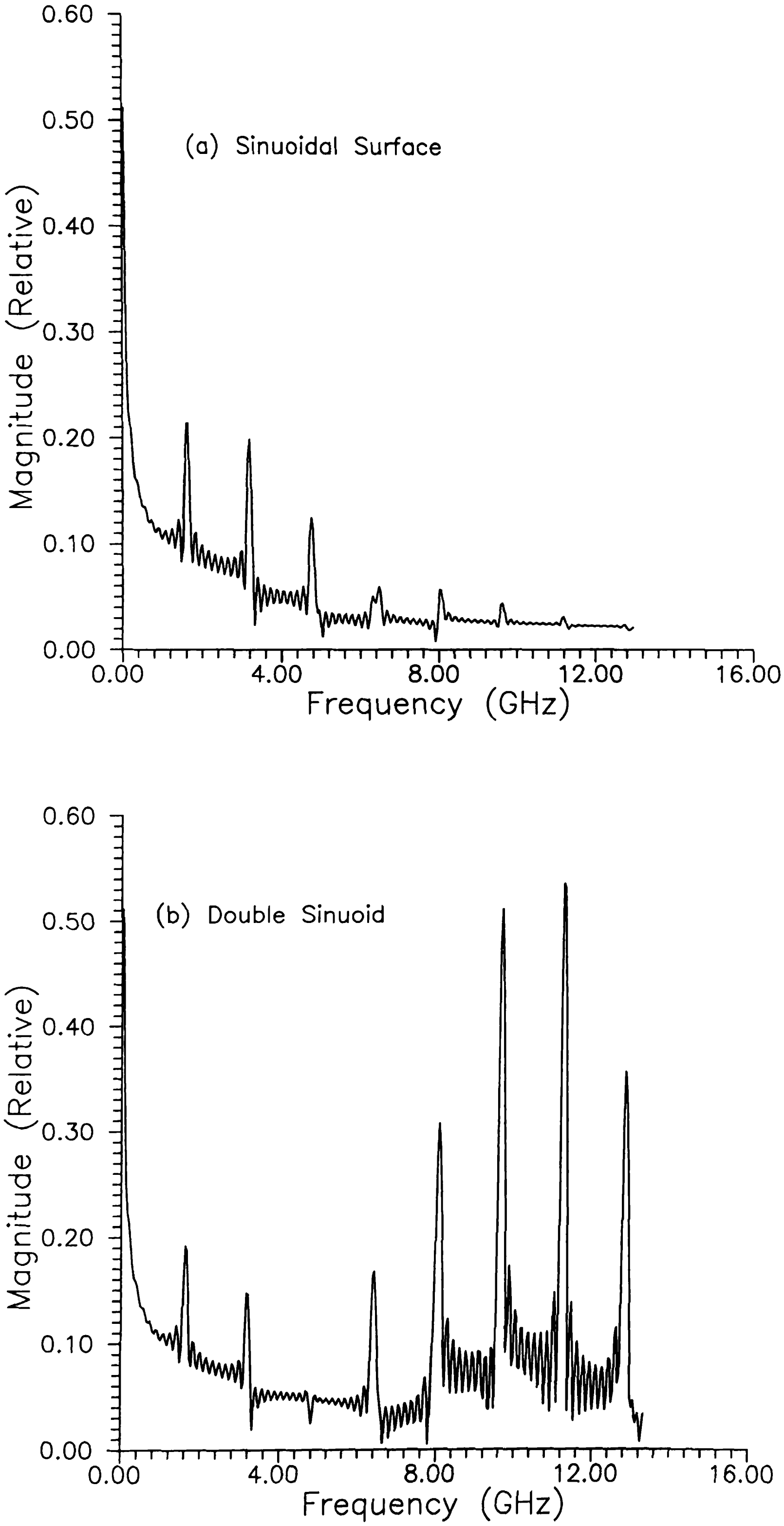

Figure 3.2 Calculated scattered field from (a) single sinusoid surface and (b) double sinusoid surface.

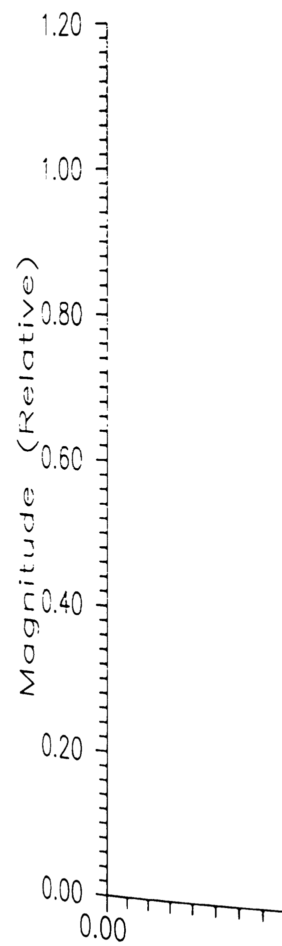

Figure 3.3 Spectral domain

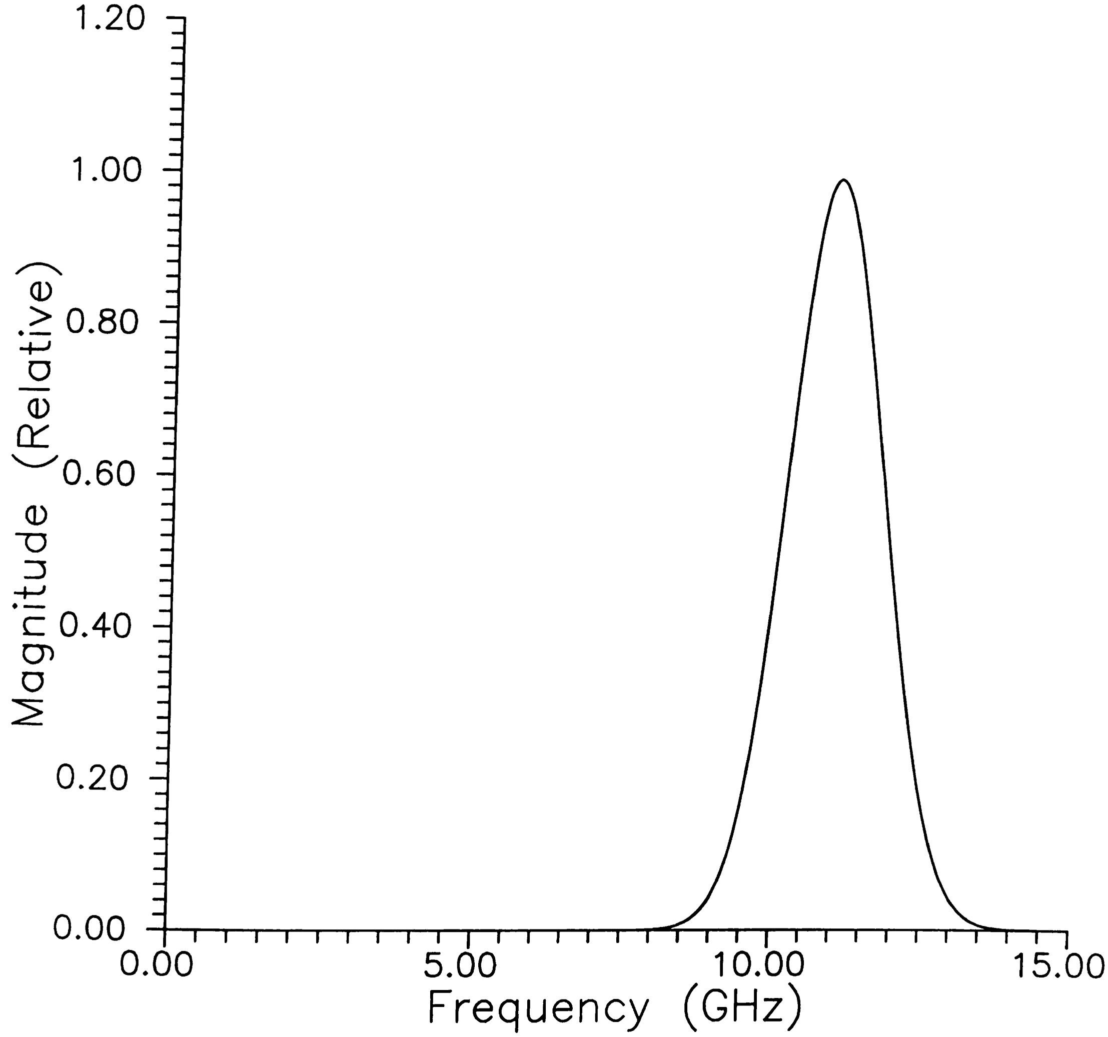

Figure 3.3 Spectral domain of incident waveform.

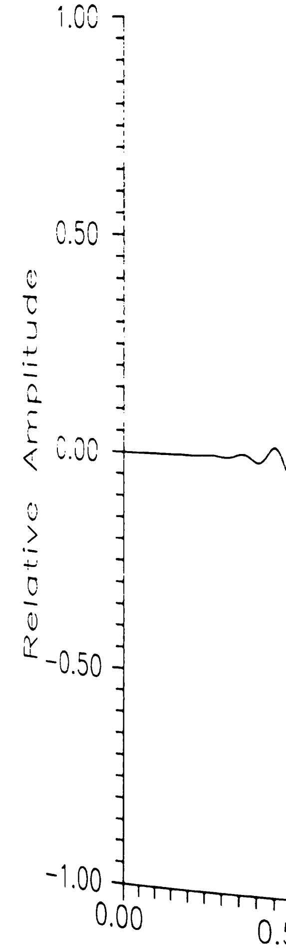

Figure 3.4 Time domain repr

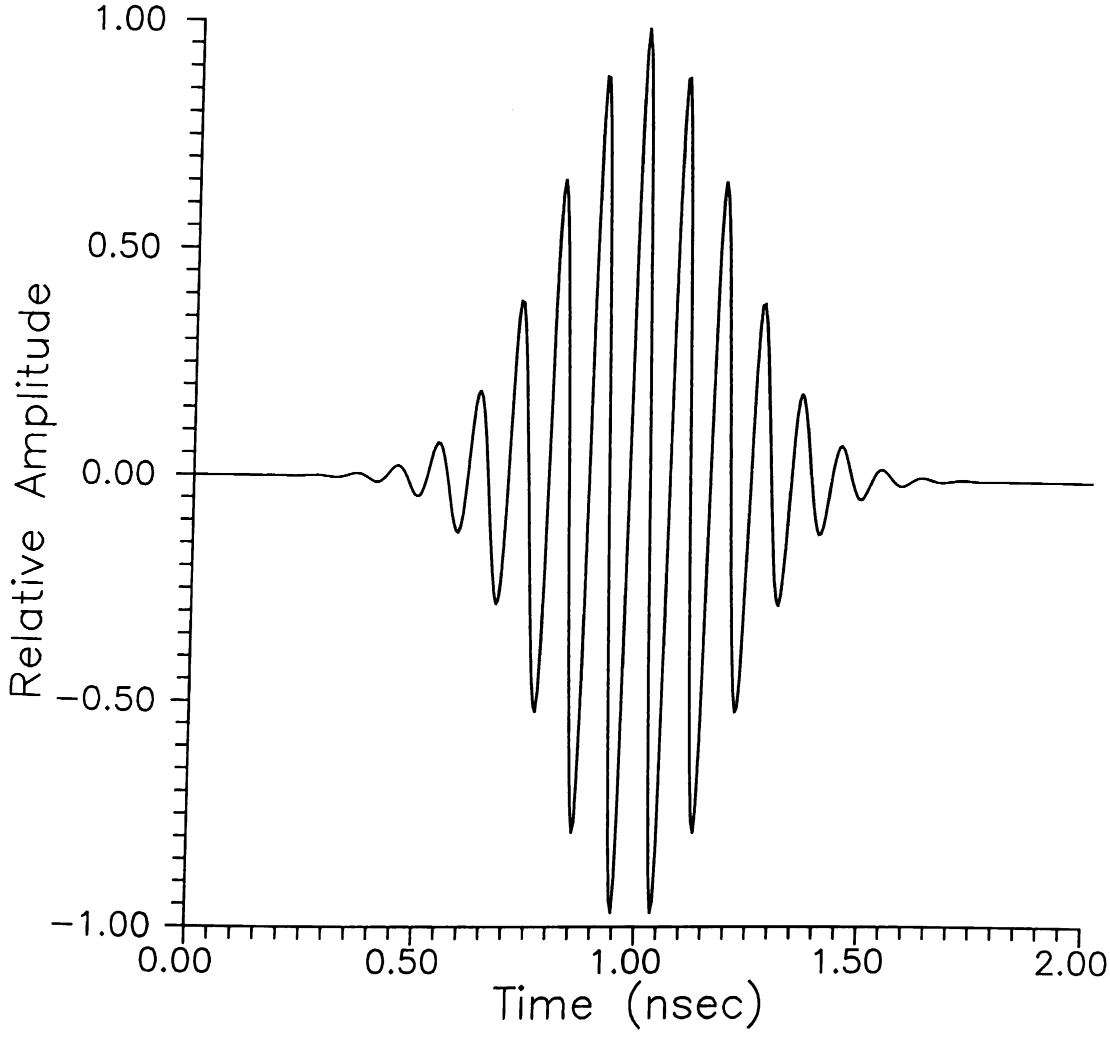

Figure 3.4 Time domain representation of incident pulse.

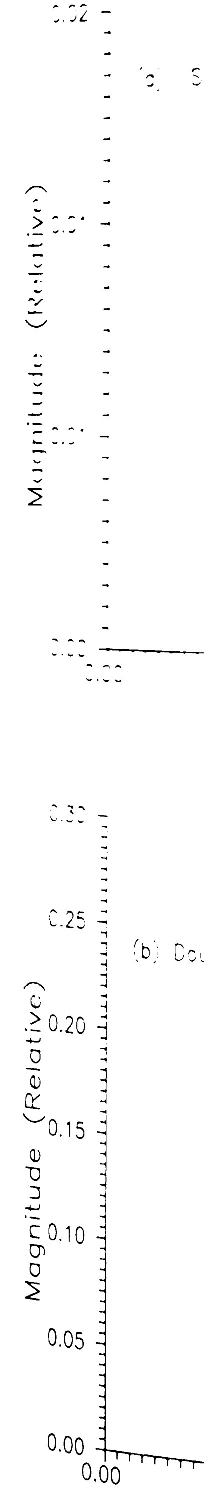

Figure 3.5 Band-limited resp
sinusoid surface.

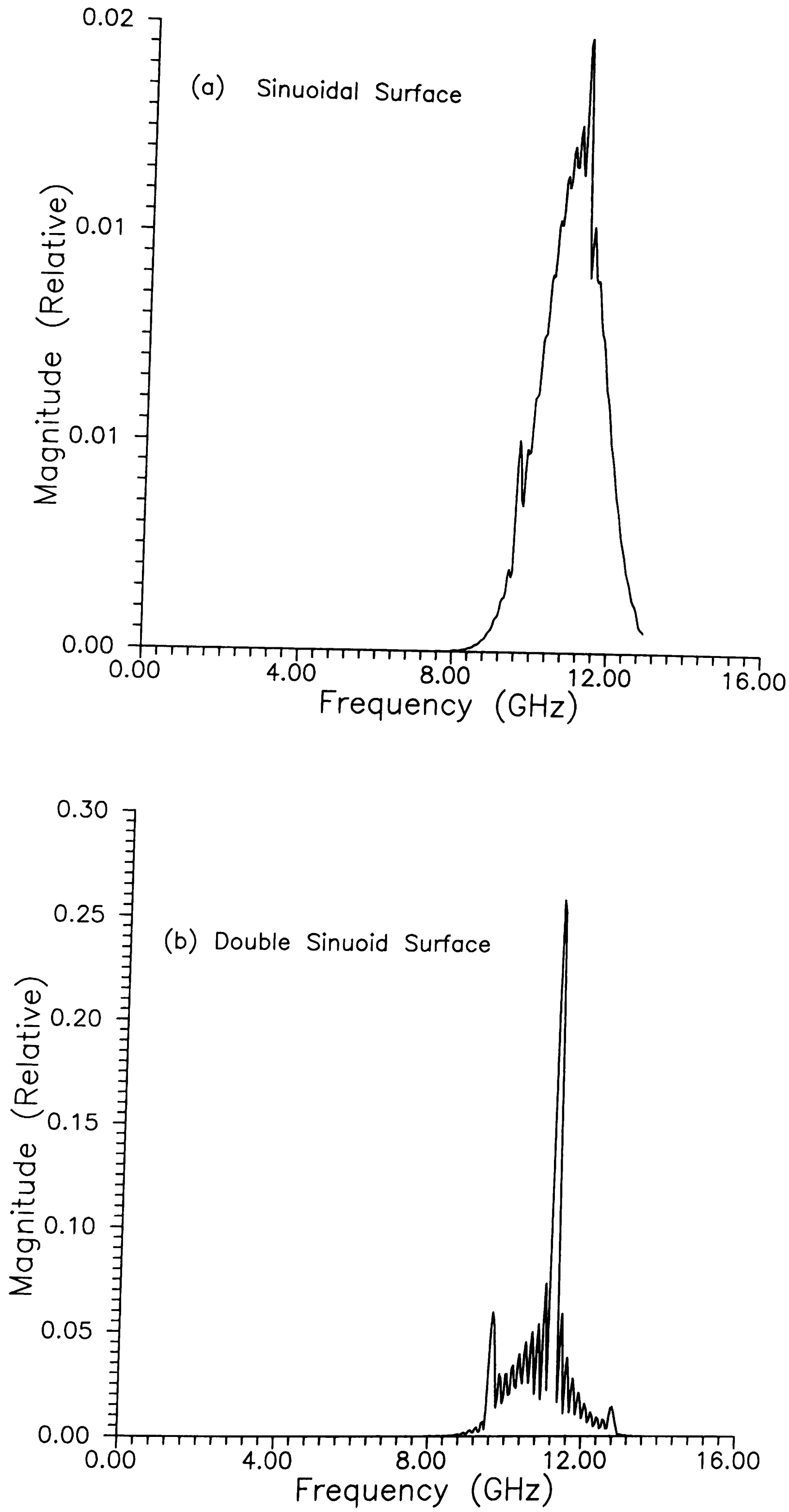

Figure 3.5 Band-limited response for (a) single sinusoid surface and (b) double sinusoid surface.

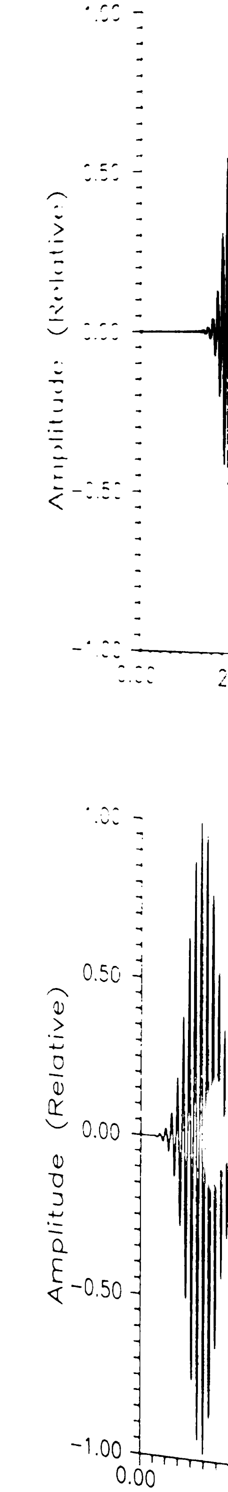

Figure 3.6 Transient respons
double sinusoid s

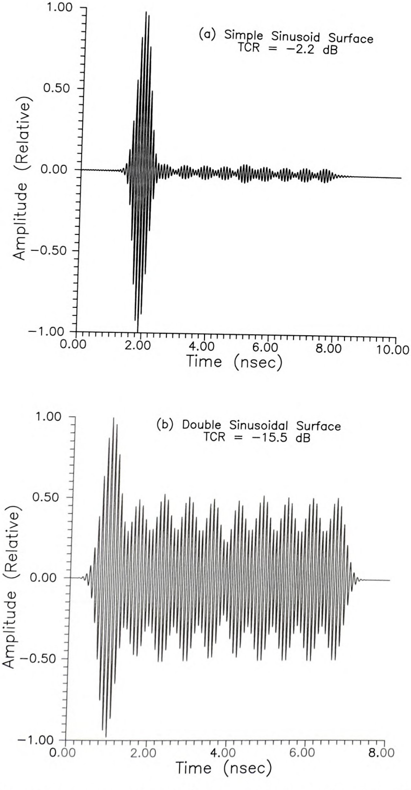

Figure 3.6 Transient response for missile above (a) single sinusoid surface and (b) double sinusoid surface.

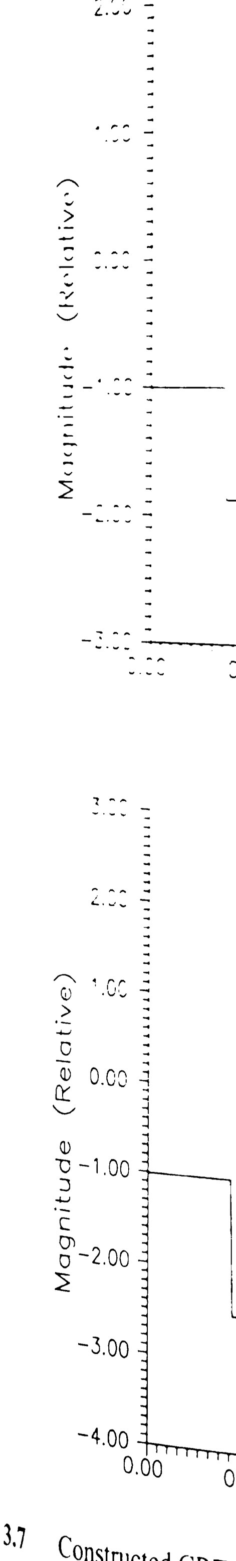

Figure 3.7 Constructed CRTV
surface.

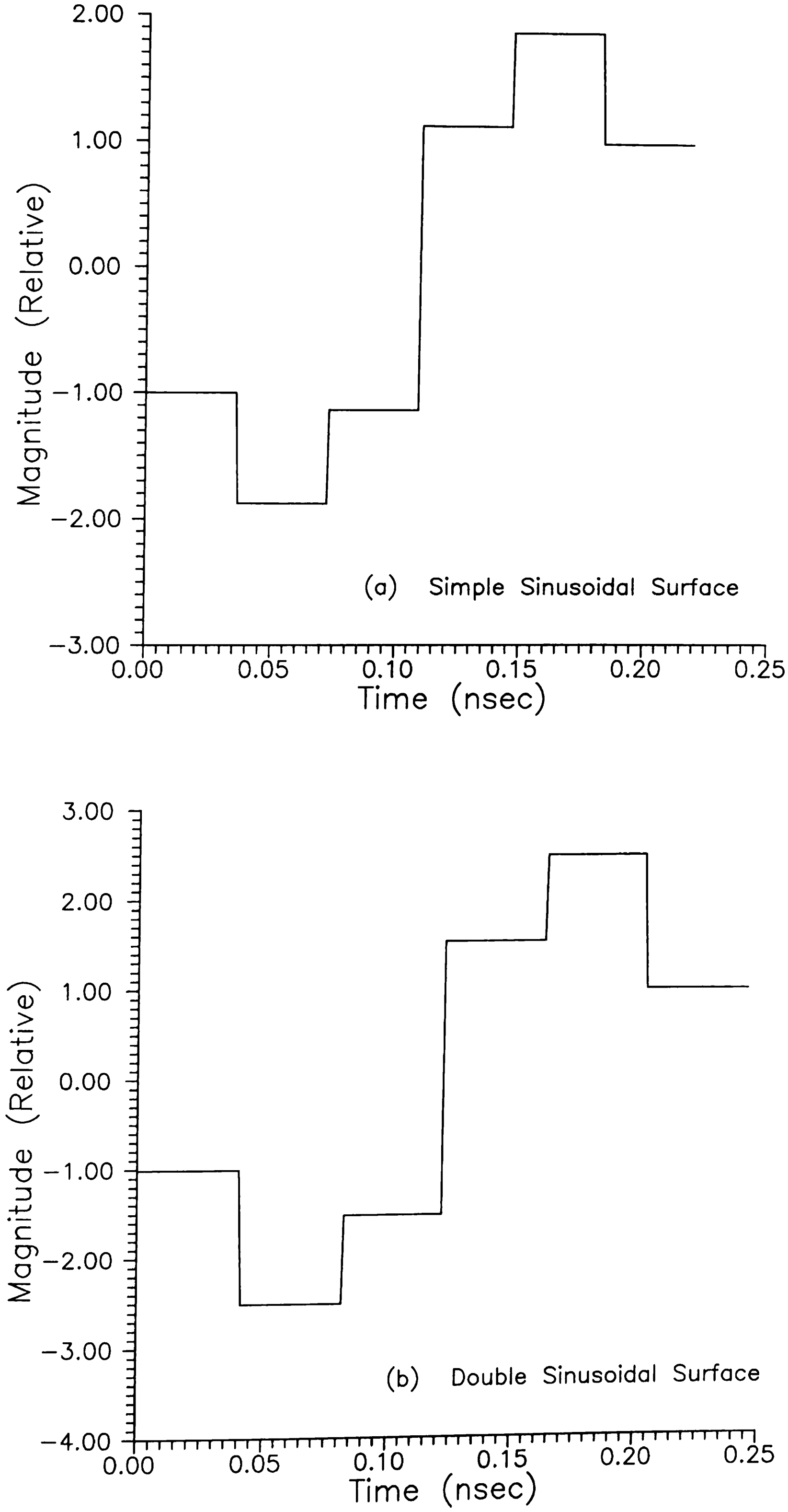

Figure 3.7 Constructed CRTWs for (a) single sinusoid surface and (b) double sinusoid surface.

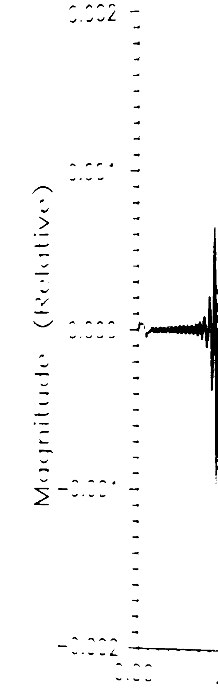

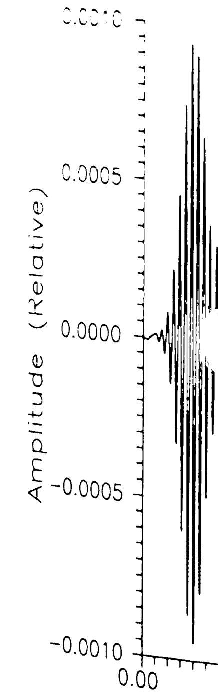

Figure 3.8 Convolution of C
single sinusoid su

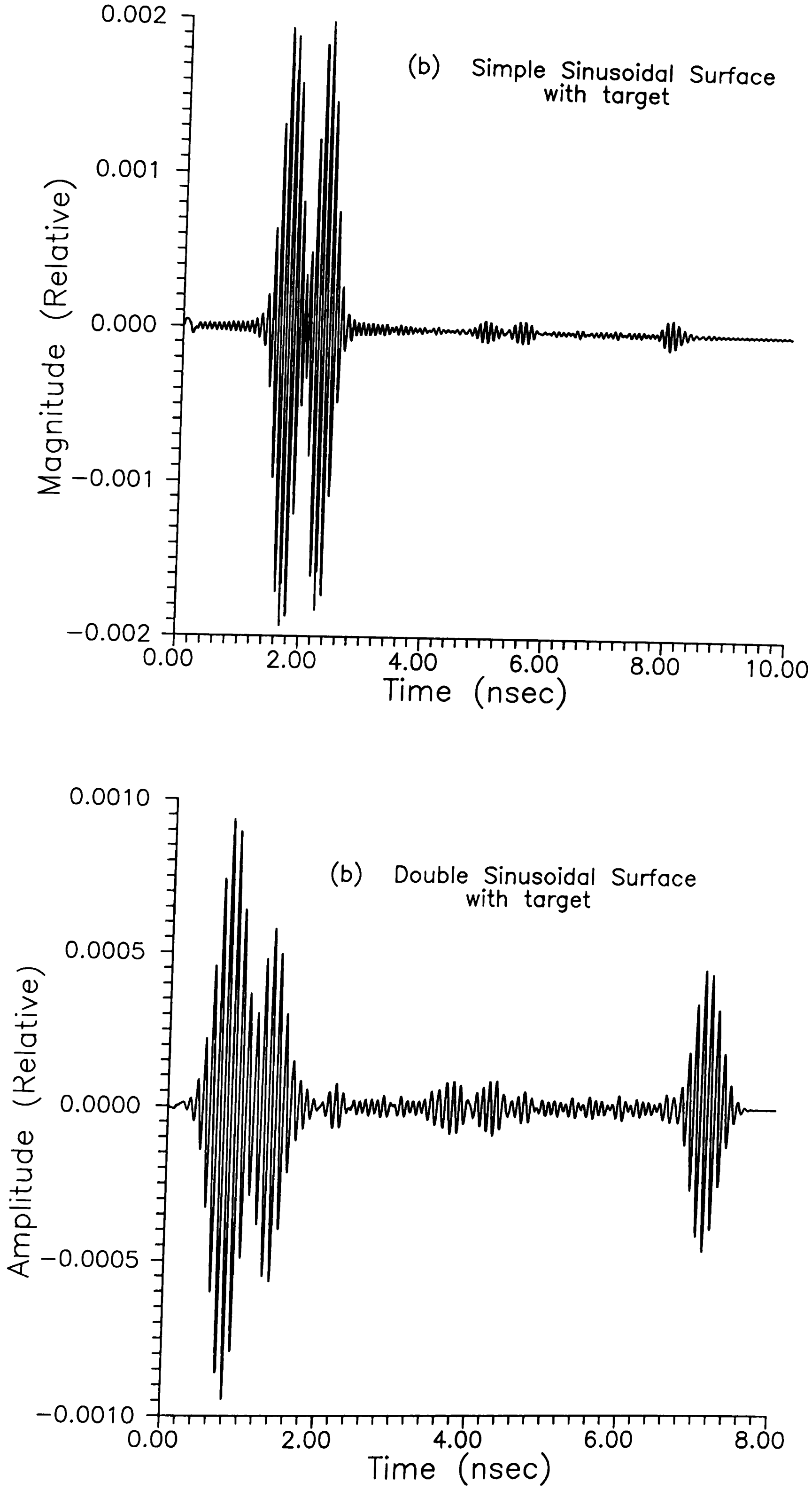

Figure 3.8 Convolution of CRTW with missile response immersed in clutter for (a) single sinusoid surface and (b) double sinusoid surface.

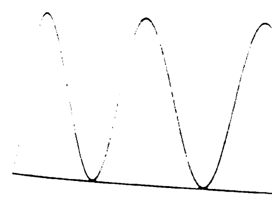

Figure 3.9 TE scatter field g

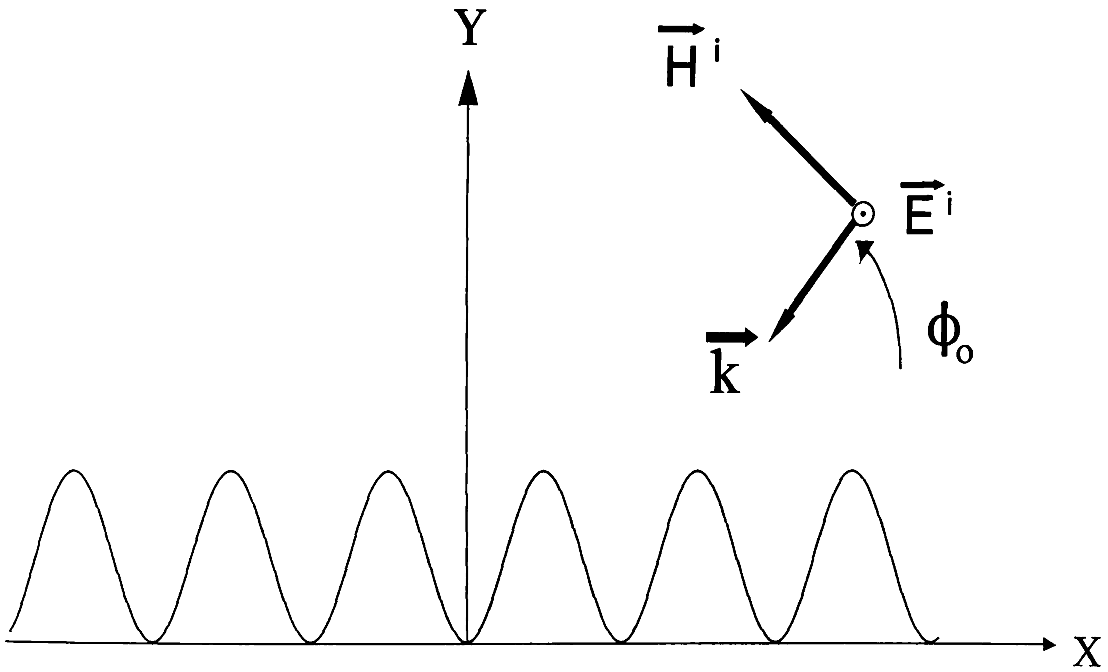

Figure 3.9 TE scatter field geometry.

Enhanced Target I

4.1 Introduction

A basic problem faced b

skimming missile immersed in b

wideband (UWB) radar systems

use of an UWB system become

is small compared to the b

(characteristic of UWB radar)

transmit waveform (CRTW) ca

enhance the target response [22

A new technique, based

allows detection of low signal t

difficulties in using the classica

eradicate merely the sea-clutte

attenuated, resulting in a poor

problem is not to eradicate the

energy ratio.

The content of this cha

presents the theory and algorithm

technique. The basic ideas behi

Chapter 4

Enhanced Target Detection in a Sea Clutter Environment

4.1 Introduction

A basic problem faced by on-board ship radar systems is the detection of a sea-skimming missile immersed in background clutter from the sea-surface. Interest in ultra-wideband (UWB) radar systems arise from their potential use for target detection. The use of an UWB system becomes more important when the signal returned by the target is small compared to the background clutter. Using the increased bandwidth (characteristic of UWB radar) and the periodic nature of sea swell, a clutter reducing transmit waveform (CRTW) can be created which will eradicate the clutter return and enhance the target response [22].

A new technique, based upon E-pulse concepts [24], has been devised which allows detection of low signal targets in a sea-clutter environment. One of the inherent difficulties in using the classical E-pulse method is that when an attempt is made to eradicate merely the sea-clutter return, both the sea-clutter and target response are attenuated, resulting in a poor target to clutter ratio (TCR). A new approach to the problem is not to eradicate the clutter altogether but to maximize the target to clutter energy ratio.

The content of this chapter will be divided into several sections. Section 2 presents the theory and algorithm development for target detection using the new CRTW technique. The basic ideas behind the CRTW development will be presented as well as qualitative arguments supportin

diagram summarizing the basic

The new CRTW technic

the drawbacks of this techniqu

function of many parameters an

optimization routine. Sectior

optimization problem.

Several examples will b

technique in sections 4 and 5.

a highly conducting sea-surface

from a small missile model. A

surface target return data set. T

show that this new technique w

changing sea-surface is extreme

considers a more realistic mo

simulation of an evolving se

numerically calculated. Using a

initial sea-surface. A simulatio

the evolving sea-surface was c

simulation show the effects of a

need for periodic updates to an

Target detection using t

qualitative arguments supporting the usefulness of this new technique. Finally, a block diagram summarizing the basic algorithm for target detection will be presented.

The new CRTW technique will be shown to be quite effective. However, one of the drawbacks of this technique is in the construction of the CRTW. The CRTW is a function of many parameters and therefore an optimal solution requires the use of a global optimization routine. Section 3 will discuss a genetic algorithm solution to the optimization problem.

Several examples will be presented showing the usefulness of this new CRTW technique in sections 4 and 5. The first example uses the measured clutter return from a highly conducting sea-surface model, in conjunction with the measured scattered return from a small missile model. A CRTW is constructed and applied to a combined sea-surface/target return data set. This first example, presented in section 4, is designed to show that this new technique works for a simple static situation. Since the effect of a changing sea-surface is extremely important, a second example presented in section 5 considers a more realistic model that can evolve over time. In this case, a time-simulation of an evolving sea-surface was created and the scattered fields were numerically calculated. Using a measured missile model, a CRTW was calculated for the initial sea-surface. A simulation was then performed in which a missile traveling over the evolving sea-surface was detected using the CRTW technique. Results of that simulation show the effects of an evolving sea-surface on the CRTW technique and the need for periodic updates to an initial CRTW.

Target detection using the new CRTW technique involves the computation of

convolution energy ratios. The
window size. At certain point
as a target enters the radar syst
the integral over which the con
determine the effect of window
step of the CRTW algorithm.

CRTW construction is b
is optimized for a specific targe
CRTW be effective in detectin
7 will address this topic.

The effect of multipath
detection problem will be discu

Finally, section 9 will
processing clutter reduction tec

4.2 Theory

Consider a UWB radar
where a target is anticipated. I
finite portion of the sea-surface
time range $\tau < t < \tau + W$, where
pulse concepts, can be constru
modeled as a series of complex

convolution energy ratios. The convolution energy ratio is a function of time and time-window size. At certain points in time, the energy ratio will take on maximum values as a target enters the radar system's range bin. The window size defines the domain of the integral over which the convolution energy is calculated. The goal of section 6 is to determine the effect of window size on the convolution energy ratio during the detection step of the CRTW algorithm.

CRTW construction is based on an anticipated or expected target; i.e., the CRTW is optimized for a specific target. This, however, raises an important question: will the CRTW be effective in detecting other targets of similar size or configuration? Section 7 will address this topic.

The effect of multipath and target/sea-surface electromagnetic coupling on the detection problem will be discussed in section 8.

Finally, section 9 will compare the new CRTW technique to the coherent processing clutter reduction technique as discussed by Iverson [26].

4.2 Theory

Consider a UWB radar system illuminating a finite portion of the sea surface where a target is anticipated. If the two-way transit time of the radar signal across the finite portion of the sea-surface is W, then the transient scattered field is available in the time range $\tau < t < \tau+W$, where τ is the time of measurement. A CRTW, based on E-pulse concepts, can be constructed if the clutter return from the sea-surface can be modeled as a series of complex exponentials

$$c(t) =$$

where A_n and Q_n are comp

Furthermore, the CRTW e(t), li

when convolved with the sea-c

$$r(t) = e(t) * c(t) =$$

Hence, only a small signal wil

sea-clutter.

One of the problems a

signal embedded in the clutter r

to-clutter ratio is not really im

such that the following energy

$$\epsilon(t,\tau,t') = \frac{\int_{t-\Delta/2}^{t+\Delta/2} \{e(x)}{\int_{t-\Delta/2}^{t+\Delta/2}}$$

In this case, the energy ratio is

is the time response of an antic

target response within the time

supporting the use of (4.3) can

$$c(t) = \sum_{n=-N}^{N} A_n e^{Q_n t} \qquad \tau < t < \tau + W \tag{4.1}$$

where A_n and Q_n are complex parameters appearing in complex-conjugate pairs. Furthermore, the CRTW e(t), like the E-pulse, is a waveform of finite duration T_E which when convolved with the sea-clutter signal yields the null result

$$r(t) = e(t) * c(t) = \int_{\tau}^{\tau+W} c(t')e(t-t')dt' = 0 \qquad \tau + T_E < t < \tau + W \tag{4.2}$$

Hence, only a small signal will be returned if the CRTW is radiated in the presence of sea-clutter.

One of the problems arising in the construction of the CRTW is that a target signal embedded in the clutter return is also reduced, often to such a point that the target-to-clutter ratio is not really improved. An alternative to (4.2) is to construct a CRTW such that the following energy ratio is maximized

$$\epsilon(t,\tau,t') = \frac{\int_{t-\Delta/2}^{t+\Delta/2} \{e(x)*[c(\tau+x)+T(t'+x)]\}^2 dx}{\int_{t-\Delta/2}^{t+\Delta/2} \{e(x)*c(\tau+x)\}^2 dx} \qquad T_E + \frac{\Delta}{2} < t < W - \frac{\Delta}{2} \tag{4.3}$$

In this case, the energy ratio is computed in a window of length Δ centered at time t. T is the time response of an anticipated target and t' is a parameter which time shifts the target response within the time range bin of the clutter signal. A qualitative argument supporting the use of (4.3) can be made by observing that the term in the denominator should be quite small as give

terms: the convolution of the

CRTW with the time-shifted tar

CRTW/clutter convolution to b

The net result is that the energ

To envision the detectio

at some initial time τ_0 a measur

A pre-recorded response T(t) o

clutter waveform. Next, a CR

in (4.3). In this case the ener

represents the position of the e

Careful observation of (4.3) al

window width Δ. The optimal

maximum energy and optimal t

that $t_m = t_m'$.

Once e(t) has been det

surface return at some later tim

$$\bar{\epsilon}(t) = \frac{\int_{t-\Delta/2}^{t+\Delta/2} \{e(\ldots}{\int_{t-\Delta/2}^{t+\Delta/2} \{e(\ldots}$$

is computed. If no target has

essentially stationary, the ener

should be quite small as give by (4.2). On the other hand, the numerator contains two terms: the convolution of the CRTW with the clutter return and the convolution of the CRTW with the time-shifted target response. Once again, consider the term involving the CRTW/clutter convolution to be small, but hopefully the second convolution will not be. The net result is that the energy ratio may be significant for the correct choice of e(t).

To envision the detection process, the ensuing procedure must be followed. First, at some initial time τ_0 a measurement is made of the sea-clutter waveform $c_0(t) = c(\tau_0+t)$. A pre-recorded response T(t) of the anticipated target is then added to the measured sea-clutter waveform. Next, a CRTW is constructed to maximize the energy ratio $\varepsilon(t,\tau_0,t')$ in (4.3). In this case the energy ratio is a function of the parameters t and t' where t represents the position of the energy window and t' corresponds to the target time shift. Careful observation of (4.3) also shows that the energy ratio is a function of the time window width Δ. The optimal positions of t_m and t_m' represent the window position for maximum energy and optimal target position for detection. In most cases it is expected that $t_m = t_m'$.

Once e(t) has been determined, detection can progress by measuring the sea-surface return at some later time $\tau > \tau_0$. At this time an energy ratio given by

$$\bar{\epsilon}(t) = \frac{\int_{t-\Delta/2}^{t+\Delta/2} \{e(x) * c(\tau + x)\}^2 dx}{\int_{t-\Delta/2}^{t+\Delta/2} \{e(x) * c(\tau_0 + x)\}^2 dx} \qquad T_E + \frac{\Delta}{2} < t < W - \frac{\Delta}{2} \tag{4.4}$$

is computed. If no target has entered the observation bin and the sea surface remains essentially stationary, the energy ratio will be unity for all t. Given that the denominator term in (4.4) remains small, th

when a target enters the range b

to the target position and shou

position corresponding to t_m.

It is important to consid

$> t_0$, the sea-surface will be dif

computed using (4.4) will slov

detect a target in the range bi

recompute e(t). Figure 4.1 sho

4.3 Computational Consid

The construction of a

maximizing the ratio given in (

basis functions with amplitudes

where

$$g_k(x) =$$

The energy ratio given by (4.3)

amplitudes α_k, (b) E-pulse durat

the window duration Δ and num

term in (4.4) remains small, the value of $\bar{\epsilon}(t)$ should be significantly greater than unity when a target enters the range bin. The value of $\bar{\epsilon}(t)$ should be large for t corresponding to the target position and should reach a maximum value when the target reaches the position corresponding to t_m.

It is important to consider the effect of an evolving sea-surface on $\bar{\epsilon}(t)$. For $\tau > \tau_0$, the sea-surface will be different than that used to compute e(t) and the energy ratio computed using (4.4) will slowly change. As $\bar{\epsilon}(t)$ rises above unity, the ability to detect a target in the range bin will degrade. It is therefore necessary to periodically recompute e(t). Figure 4.1 shows a flowchart for the detection process.

4.3 Computational Considerations

The construction of a CRTW for the new target detection scheme involves maximizing the ratio given in (4.3). The CRTW, modeled as a sum of N rectangular basis functions with amplitudes α_k, can be expressed as

$$e(x) = \sum_{k=1}^{N} \alpha_k g_k(x) \tag{4.5}$$

where

$$g_k(x) = \begin{cases} 1, & \frac{T_E}{N}(k-1) < x < \frac{T_E}{N} \\ 0, & elsewhere \end{cases} \tag{4.6}$$

The energy ratio given by (4.3) is dependent on the following: (a) E-pulse basis function amplitudes α_k, (b) E-pulse duration T_E, and (c) target response time shift t'. In addition, the window duration Δ and number of rectangular basis functions N will effect the value of ε calculated in (4.3). How

respect to these variables, but

The process of numer

problem and choosing an appro

First, the amount of compute

important. Second, but probab

a global maximum. This, how

is a function of many variable

evident that it may be quite d

possible alternative is to design

by applying a global search ro

gradient search algorithm to de

algorithm has extreme difficult

often gets trapped in local mini

sort of initial solution guess to

"seed" or initial guess for the g

A global optimization sch

(4.3). One scheme often used i

problems based on the ideas of

population of N individuals kn

population can be represented by

L bits. In analogy to genetics, e

of ε calculated in (4.3). However, the author did not choose to optimize (4.3) with respect to these variables, but regarded them as fixed during the optimization process.

The process of numerically optimizing (4.3) is a computationally expensive problem and choosing an appropriate solution technique requires several considerations. First, the amount of computer time required to find the solution can be extremely important. Second, but probably more important, is the convergence of the solution to a global maximum. This, however, can be computationally slow for an expression that is a function of many variables and contains many local extreme values. It is quite evident that it may be quite difficult to get both speed and global optimization. A possible alternative is to design some hybrid method whereby the problem may be solved by applying a global search routine to target a global maximum and then applying a gradient search algorithm to determine a better solution. By itself, a gradient search algorithm has extreme difficulty finding a "best" solution since this type of algorithm often gets trapped in local minima. In addition, these types of algorithms require some sort of initial solution guess to get started. A hybrid method can be used to produce a "seed" or initial guess for the gradient search routine.

A global optimization scheme should be used to find those values which maximize (4.3). One scheme often used is the genetic algorithm (GA)[27]. This method solves problems based on the ideas of heredity and evolution of the fittest. A GA maintains a population of N individuals known as chromosomes. Each chromosome within the population can be represented by a data structure containing M bit strings each of length L bits. In analogy to genetics, each bit string is referred to as a gene. Furthermore, the bit string representation in e

parameter. A problem contai

single chromosome. Figure

structures used in this analys

potential solution to the optim

with each chromosome, a new

discards those with weak trai

process called crossover. In a

population. Each new generati

and mutation. Successive ge

hopefully after a number of g

settings.

The GA is initiated by

be done for the entire populat

Next, each chromosome is eva

done by decoding the binary g

x_j represent a design paramete

bit string of length L called g_j

$$x_j =$$

where $g_{j,l}$ is the lth bit of g

function, such as (4.3), is ev

bit string representation in each gene is an encoding of the actual problem design parameter. A problem containing M design variables can be encoded as ML bits on a single chromosome. Figure 4.2 shows the relation between different genetic data structures used in this analysis. Each chromosome from the population represents a potential solution to the optimization problem. By calculating a fitness value associated with each chromosome, a new population can be formed which selects fit individuals and discards those with weak traits. Also, traits from fit individuals can be mixed in a process called crossover. In addition, bit mutations can occur at random throughout the population. Each new generation is formed through the processes of selection, crossover, and mutation. Successive generations will tend to create more fit chromosomes and hopefully after a number of generations the genes will contain the optimized variable settings.

The GA is initiated by filling each gene with random bit information. This must be done for the entire population of N chromosomes (where N is an even number). Next, each chromosome is evaluated to give some measure of its fitness value. This is done by decoding the binary gene strings into actual design parameters. Let the variable x_j represent a design parameter defined on $[X_j^{\min}, X_j^{\max}]$. The variable x_j is coded as a bit string of length L called g_j and recovered through

$$x_j = X_j^{\min} + \frac{X_j^{\max} - X_j^{\min}}{2^L - 1} \sum_{l=1}^{L} g_{j,l}\, 2^{l-1} \tag{4.7}$$

where $g_{j,l}$ is the lth bit of gene g_j. Using the decoded gene values, a user defined function, such as (4.3), is evaluated. After all the individuals in the population are evaluated, the most fit chromo

calculating an expected alloca

where F_i represents the fitness

chromosome are copied to the

the integer part of the enclosed

are chosen at random with pro

Following the selection

traits from the population pool

of chromosomes from the chro

defined probability P_c by swapp

data chain. This point, known

Here N_c is the chromosome

probability P_m as bit string swa

mutation, the new population

repeated for a predetermined

genetic algorithm.

4.4 Stationary Surface De

To demonstrate some of

fields from two highly condu

consisting of aluminum foil ac

evaluated, the most fit chromosomes are selected. A simple selection scheme involves calculating an expected allocation value defined as

$$e_k = NF_k \Big(\sum_{k=1}^{N} F_k \Big)^{-1} \tag{4.8}$$

where F_k represents the fitness value of the kth chromosome. Next, $[e_k]$ values of the kth chromosome are copied to the new breeding population. Here, square brackets indicate the integer part of the enclosed value. The remaining elements of the breeding population are chosen at random with probability e_k - $[e_k]$.

Following the selection process, a new population is created by mixing inherited traits from the population pool. This is done by randomly selecting or mating N/2 pairs of chromosomes from the chromosome pool. The chromosome pairs are bred with user defined probability P_c by swapping bit string information at a point along the chromosome data chain. This point, known as the crossover point, is a random integer from 1 to N_c-1. Here N_c is the chromosome length. Finally, a random chosen bit is mutated with probability P_m as bit string swapping is taking place. Following selection, crossover, and mutation, the new population is ready for its next generation. The above steps are repeated for a predetermined number of times. Figure 4.3 shows a flowchart for the genetic algorithm.

4.4 Stationary Surface Demonstration

To demonstrate some of the ideas presented in the preceding section, the scattered fields from two highly conducting sea-like surfaces were measured. The surfaces, consisting of aluminum foil adhered to styrofoam [12], have the cross-sectional shape

shown in Figure 4.4. The sc
measured within an anechoic c
points. The frequency-domain
shape parameter $\tau = 8$ (see A
using an IFFT to give the clutte
to allow measurements in the a

The first surface, know
and is a simple model used to s
is discussed in some detail in
cycloid of 10 periods. Each p
.0496 m. Using an electric fi
incidence angle of 10° from the
in Figure 4.5. As can be seen
main crests of the Stoke's wav
double sinusoid and was measu
surface is characterized by
$y(x) = .025(1 - \cos 35.4x) +$
shown in Figure 4.6. Once ag
the sea-wave crests. A 10 cm
expected target. The scattere
measurement the electric field
angle of incidence was again 1

shown in Figure 4.4. The scattered fields from the two-dimensional surfaces were measured within an anechoic chamber in the band 1 to 17 GHz using 1601 frequency points. The frequency-domain data was then windowed using a cosine taper function with shape parameter $\tau = 8$ (see Appendix A) and then transformed into the time domain using an IFFT to give the clutter signal $c_0(t)$. The dimensions of the surface were chosen to allow measurements in the anechoic chamber.

The first surface, known as a Stoke's wave [19], is characterized by steep slopes and is a simple model used to simulate periodic ocean waves. The Stoke's representation is discussed in some detail in section 2.3.1. Figure 4.4 shows the case of a simple cycloid of 10 periods. Each period for this surface is .1778 m and the wave height is .0496 m. Using an electric field parallel to the wave crest (TE polarization), and an incidence angle of 10° from the horizon, the scattered field for the Stoke's wave is shown in Figure 4.5. As can be seen, the scattered field is dominated by reflections from the main crests of the Stoke's wave. The second surface, also consisting of 10 periods, is a double sinusoid and was measured under the same conditions as the Stoke's wave. This surface is characterized by two-scale roughness. The wave profile is give by $y(x) = .025(1 - \cos 35.4x) + .06 \sin 177x \quad (m)$. The scattered field for this surface is shown in Figure 4.6. Once again the scattered fields are dominated by reflection from the sea-wave crests. A 10 cm long scale-model Phoenix missile model was used as the expected target. The scattered field from this target is shown in Figure 4.7. In this measurement the electric field was perpendicular to the long axis of the missile and the angle of incidence was again 10° with respect to the long axis of the missile.

Using the target and c
Figure 4.8 were constructed
construction of the CRTW (m
algorithm. To simulate the de
20% of the clutter maximum v
response. For the Stoke's wav
two locations: t = 4.9 nsec an
response was added at location
ratio response given by (4.4) v
Figure 4.9 and Figure 4.10 for
included in these figures is th
(4.4). Figure 4.9 shows that v
reaches 22 dB and the target i
= 8 nsec has a lower value $\overline{\epsilon}$ =
the target. The energy ratio c
similar patterns. At t = 11 nsec
detection. In contrast, at t =
location for a target to be de
window have a value of $\overline{\epsilon}(t)$
signal used in the detection sc

As discussed in section
frequently reduces the target si

Using the target and clutter responses scaled to unity, the CRTWs shown in Figure 4.8 were constructed by maximizing the ratio given in (4.3). The actual construction of the CRTW (maximization of (4.3)) was implemented using a genetic algorithm. To simulate the detection response, the missile scattered field was scaled by 20% of the clutter maximum value (TCR = -14 dB) and added to the sea-clutter surface response. For the Stoke's wave the target response was added to the clutter response at two locations: t = 4.9 nsec and t= 7.8 nsec. For the double sinusoid surface the target response was added at locations t = 5.6 nsec and t = 11.0 nsec. The convolution energy ratio response given by (4.4) was computed for each surface. The results are shown in Figure 4.9 and Figure 4.10 for the Stoke's and double sinusoid waves, respectively. Also included in these figures is the summed target and clutter response given by $c(\tau+x)$ in (4.4). Figure 4.9 shows that when the target is located at t = 5 nsec the energy ratio $\bar{\epsilon}$ reaches 22 dB and the target is easily detected. On the other hand a target located at t = 8 nsec has a lower value $\bar{\epsilon}$ = 3 dB indicating that this is not the best location to detect the target. The energy ratio corresponding to the double sinusoid (Figure 4.10) shows similar patterns. At t = 11 nsec the ratio is 9 dB indicating a large jump and hence target detection. In contrast, at t = 6 nsec the value of $\bar{\epsilon}$ is much smaller and not the best location for a target to be detected. In both figures, points outside the convolution window have a value of $\bar{\epsilon}(t)$ equal to unity (0 dB). This follows since the summed signal used in the detection scenario is identical to that used to create e(t).

As discussed in section 4.2, a CRTW designed to reduce only the clutter response frequently reduces the target signal to such an extent that the target to clutter ratio in the resulting convolution response

example of the Stoke's wave gi

eliminate only the sea-clutter r

clutter only response and th

Figure 4.12 and Figure 4.13

reduction in the sea-clutter resp

in both the sea-clutter and targ

clutter and target response le

Computation of the convolution

compared to Figure 4.9, then s

using only the sea-clutter return

magnitude of the convolution er

peaks in Figure 4.14 are signifi

indicate that this CRTW has li

needed to calculated the wavef

4.5 Simulated Sea-Surface

A more realistic sea-su

evolving sea surface profile y(x

$$y(x,t) = \int_0^\infty$$

where $\Phi(\sigma)$ is a phase shift ra resulting convolution response is not improved. This effect can be seen using the example of the Stoke's wave given above. Figure 4.11 shows the CRTW constructed to eliminate only the sea-clutter return. The convolution of this waveform with the sea-clutter only response and the combined target/sea-clutter response are shown in Figure 4.12 and Figure 4.13 respectively. Figure 4.12 clearly shows a significant reduction in the sea-clutter response; however, Figure 4.13 shows a significant reduction in both the sea-clutter and target response. In this case, the reduction in both the sea-clutter and target response leads to a very poor target to clutter detection ratio. Computation of the convolution energy (4.4) is shown in Figure 4.14. If Figure 4.14 is compared to Figure 4.9, then several problems associated with constructing the CRTW using only the sea-clutter return can be seen. First, their is a significant reduction in the magnitude of the convolution energy ratio. In addition, the number of and position of the peaks in Figure 4.14 are significantly different than those in Figure 4.9. These findings indicate that this CRTW has limited usefulness even though a great deal of effort was needed to calculated the waveform.

4.5 Simulated Sea-Surface Demonstration

A more realistic sea-surface profile has been proposed by Kinsman [19]. An evolving sea surface profile y(x,t) can be computed using the stochastic model

$$y(x,t) = \int_0^\infty \cos\left[\frac{\sigma^2}{g}x - \sigma t + \Phi(\sigma)\right]\sqrt{[A(\sigma)]^2 d\sigma} \qquad \textbf{(4.9)}$$

where $\Phi(\sigma)$ is a phase shift randomly distributed between 0 and 2π. Here the Neumann spatial frequency spectrum is u

[4

where U is the wind speed in

and C = 3.05 m^2/sec^5. A typi

Figure 4.15. A numerical m

calculated the covariance func

function [19] may be written a

$H(t_j, t$

In this case, an ensemble of f

position. It is important to not

interval. This follows from the

a 20 knot wind, Figure 4.16 sh

interval T. For T = 0 the cova

H

Integrating the spectrum over a

wave field, i.e.

Comparing (4.12) and (4.13) it

spatial frequency spectrum is used

$$[A(\sigma)]^2 = C\frac{\pi}{2}\sigma^{-6}e^{-2g^2\sigma^{-2}U^{-2}} \tag{4.10}$$

where U is the wind speed in m/sec, g = 9.81 m/sec^2 is the acceleration due to gravity, and C = 3.05 m^2/sec^5. A typical spectrum generated using 20 knot winds is shown in Figure 4.15. A numerical measure of the sea-surface evolution can be obtained by calculated the covariance function at a fixed position on the surface. The covariance function [19] may be written as

$$H(t_j,t_k) = \frac{1}{2}\int_0^\infty [A(\sigma)]^2 \cos[\sigma(t_k - t_j)]\,d\sigma \tag{4.11}$$

In this case, an ensemble of functions {y(t)} is observed at times t_j and t_k at a fixed position. It is important to note that the covariance is only a function of the observation interval. This follows from the time-invariant statistics or stationarity of the process. For a 20 knot wind, Figure 4.16 shows the covariance function in terms of the observation interval T. For T = 0 the covariance can be written as

$$H(t_j,t_k=t_j) = \frac{1}{2}\int_0^\infty [A(\sigma)]^2 d\sigma \tag{4.12}$$

Integrating the spectrum over all frequencies gives a measure of the total energy in the wave field, i.e.

$$E = \int_0^\infty [A(\sigma)]^2 d\sigma \tag{4.13}$$

Comparing (4.12) and (4.13) it is seen that

$$E = \frac{1}{2}H(t_j,t_k=t_j) \tag{4.14}$$

In this case the covariance for

through (4.14). Since the ener

is directly related to the wind

in Figure 4.16 coincides with

function is an indicator of sea-

of the sea as a function of tim

the covariance value decreases

seen that after about 2 secon

returns to its original value, al

zero. With the covariance inf

scattered field must be remeas

be updated more often than on

least once or twice a second.

A typical surface profil

shown in Figure 4.17 (sea heig

profile was computed using a

to chapter 3, section 4). The

from the horizon. Due to com

a factor of 50 (from 1000m tot

using 1000 segments. A total

1.5 GHz.

To determine the effec

In this case the covariance for a step interval of 0 is directly related to the wave energy through (4.14). Since the energy can be calculated from (4.13), it is seen that the energy is directly related to the wind speed through (4.10). The point corresponding to T = 0 in Figure 4.16 coincides with twice the energy given by (4.14). Since the covariance function is an indicator of sea-surface evolution, Figure 4.16 illustrates the progression of the sea as a function of time-separation T at a given point. As shown in this figure, the covariance value decreases as a function of time separation. From this figure it is seen that after about 2 seconds the covariance has dropped to about zero and never returns to its original value, although it does slowly creep up and then returns back to zero. With the covariance information it is possible to get some idea of how often the scattered field must be remeasured. From Figure 4.16 the measurement must certainly be updated more often than once every two seconds. A better update rate would be at least once or twice a second.

A typical surface profile and scattered field generated by the Kinsman model is shown in Figure 4.17 (sea height is not to scale). The scattered field for a PEC with this profile was computed using a 2-d Green's function and moment method solution (refer to chapter 3, section 4). The polarization is TE and the incidence angle is 10 degrees from the horizon. Due to computational constraints the sea-surface was scaled down by a factor of 50 (from 1000m total length to 20 meter total length) and the field solved for using 1000 segments. A total of 200 frequency points were computed in the band .5 - 1.5 GHz.

To determine the effects of an evolving sea-surface on the CRTW detection technique, the following scen

generated using (4.9) at inter

scattered field was calculated

Phoenix missile model was s

computed from the surface pro

scaled to a TCR of -14dB and

the position of the missile wit

that the missile was flying at

evolving sea surface profile an

Using the summed resp

was computed for each time s

where it is assumed that the

simulation. At t = 0 the missi

has not changed, and therefor

dB). At t = .25 sec the surfac

this case the energy ratio is no

surface continues to evolve th

t = .75 sec the target enters th

the target. Since the baseline

been detected with a margin o

the simulation, the effect of bo

At t = 2.0 sec the sea surface h

technique, the following scenario was devised. A series of sea-wave profiles were generated using (4.9) at intervals of .25 seconds. Each surface was scaled and the scattered field was calculated numerically as described above. The response from the Phoenix missile model was scaled to match the clutter response and a CRTW was computed from the surface profile at $\tau = 0$ sec. Next, the missile response was amplitude scaled to a TCR of -14dB and added to the evolving sea surface response. In this case the position of the missile with respect to the sea surface was determined by assuming that the missile was flying at 600 knots. The left hand side of Figure 4.18 shows the evolving sea surface profile and the missile position (indicated by the small arrow).

Using the summed response and the initial clutter response, the energy ratio $\bar{\epsilon}(t)$ was computed for each time step. This is shown on the right hand side of Figure 4.18 where it is assumed that the CRTW computed at $\tau = 0$ does not change during the simulation. At t = 0 the missile has not yet entered the range bin and the clutter signal has not changed, and therefore the energy ratio computed from (4.4) must be unity (0 dB). At t = .25 sec the surface has evolved but no target has entered the range bin. In this case the energy ratio is no longer unity but has reached a value of 3 dB. As the sea surface continues to evolve the baseline energy ratio (max value) continues to rise. At t = .75 sec the target enters the range bin and $\bar{\epsilon}(t)$ reaches a max value of 20 dB near the target. Since the baseline value of $\bar{\epsilon}(t)$ is about 5 dB at t = .75 sec, a target has been detected with a margin of about 15 dB above the baseline level. Continuing with the simulation, the effect of both the moving target and evolving sea surface can be seen. At t = 2.0 sec the sea surface has evolved to the point where only a 10 dB margin exists between the baseline clutter ra

4.6 Target Detection and

The detection of any tar

involves computing convolutio

ratio involves integrating over

the time-window interval in t

convolution energy ratio. At c

the scattered return) the conv

indicating the presence of a tar

of window size on the convolu

algorithm.

The study of the windo

investigation in sections 4 and

Stoke's surface was measured

backscattered field was measu

target. A CRTW was then co

composite return was constru

measurement from the Stoke'

algorithm was then applied to

calculate the convolution energ

only on the effects of the win

between the baseline clutter ratio and the target ratio.

4.6 Target Detection and Window Size

The detection of any target using the clutter reducing transmit waveform procedure involves computing convolution energy ratios. The calculation of the convolution energy ratio involves integrating over a time-window interval. Both the placement and size of the time-window interval in the radar's system range bin will affect the value of the convolution energy ratio. At certain points in time (corresponding to different points of the scattered return) the convolution energy ratio will possibly take on large values indicating the presence of a target. The purpose of this section is to determine the effects of window size on the convolution energy ratio during the detection phase of the CRTW algorithm.

The study of the window-size effect on the convolution energy ratio parallels the investigation in sections 4 and 5. First, the backscattered field from a highly conducting Stoke's surface was measured inside the anechoic chamber at MSU. In addition, the backscattered field was measured from a small missile model to simulate an anticipated target. A CRTW was then constructed from these two measurements. A synthesized composite return was constructed by scaling the missile return and adding it to the measurement from the Stoke's sea surface model. The detection section of the CRTW algorithm was then applied to this composite signal using a variable window width to calculate the convolution energy integral. In this procedure the investigation concentrates only on the effects of the window width since the simulated sea surface does not change in the detection step. The seco

field from an evolving sea su

calculation. The first time ste

step was used to generate a c

procedure. Using a variable

detection for non-static clutter

A simple Stoke's surf

wave model is a 2-d electric c

cm. The measured return fro

using an HP network analyzer

in the measurement was from

incident radiation was paralle

inclined 10 degrees from the

The frequency-domain return

transformed into the time do

return are shown in Figure 4.

A simple Phoenix mis

anticipated target. This mod

the physical similarity to an E

surface was made on this mis

Figure 4.7. Using the norma

was constructed using (4.3).

in the detection step. The second example involves calculating the theoretically scattered field from an evolving sea surface. Two time steps were used in the scattered field calculation. The first time step was used in the construction of a CRTW. The next time step was used to generate a composite clutter/target return to be used in the detection procedure. Using a variable window size in the detection step the effect upon target detection for non-static clutter background could be studied.

A simple Stoke's surface model has been described in section 4. The Stoke's wave model is a 2-d electric conductor of wavelength 17.78 cm and wave height of 5.08 cm. The measured return from the surface was initially done in the frequency domain using an HP network analyzer and amplifier (see Appendix A). The frequency range used in the measurement was from 1-17 GHz using 1601 data points. The electric field of the incident radiation was parallel to the wave crests and the direction of propagation was inclined 10 degrees from the horizontal with 0 degrees representing grazing incidence. The frequency-domain return was then windowed (using a cosine taper waveform) and transformed into the time domain using an IFFT. The surface and transient scattered return are shown in Figure 4.4 and Figure 4.5 respectively.

A simple Phoenix missile model approximately 10 cm in length was used for the anticipated target. This model was chosen due to its availability from a model kit and the physical similarity to an Exocet-type missile. A measurement similar to the Stoke's surface was made on this missile. The time-domain return from this model is shown in Figure 4.7. Using the normalized returns from the sea surface and the target a CRTW was constructed using (4.3). This constructed CRTW is shown in Figure 4.8. The author elected to realize the CRTW

selection was the ease of use

values. It must be kept in mi

time use.

As a detection simulati

maximum value (TCR = -1

Figure 4.19 shows both the c

expanded view gives a better

return.

Next, the convolution c

for a window width Δ = .5 ns

removed from the target the co

target the energy ratio is abo

of a target. In this example t

to calculate the CRTW. To s

.8 nsec was chosen and the co

the effect of widening the en

about 6 dB at the peak (see F

A series of different v

ratio with (4.4). Figure 4.22

seen from this figure, the pea

values of the energy window

elected to realize the CRTW by using a genetic algorithm. The reason behind this selection was the ease of use since no initial guessing is required other than a range of values. It must be kept in mind that this algorithm is not an efficient method for real-time use.

As a detection simulation, the missile response was scaled to 20% of the clutter maximum value (TCR = -14 dB) and added to the clutter signal at t = 6 nsec. Figure 4.19 shows both the original clutter response and the summed response. The expanded view gives a better idea of the effect of adding the target return to the surface return.

Next, the convolution energy was calculated using (4.4). The convolution energy for a window width Δ = .5 nsec is shown in Figure 4.20. As can be seen, for positions removed from the target the convolution energy ratio is unity (0 dB). For points near the target the energy ratio is about 19 dB. This large jump in value indicates the presence of a target. In this example the energy window was chosen to be the same as that used to calculate the CRTW. To see the effect of a different energy window a value of Δ = .8 nsec was chosen and the convolution energy ratio recomputed using (4.4). In this case, the effect of widening the energy window is to lower the convolution energy ratio to about 6 dB at the peak (see Figure 4.21).

A series of different values of Δ were used to compute the convolution energy ratio with (4.4). Figure 4.22 shows a three dimensional graph of the results. As can be seen from this figure, the peak value of the convolution energy ratio decreases for larger values of the energy window. Also, the single peak spreads out for small values of the energy window (e.g. values l

From the results of the

window size should be used

analysis is the problem assoc

problem. two sea-like surfaces

Kinsman. Two surfaces. g

Figure 4.23. The first surface

surface is generated at a sub

Figure 4.23 is not drawn to s

wave height is 3.3 meters.

computed using 2-d Green's

section 4). Due to computing

50, and the frequency range w

field from the initial sea surf

(scaled appropriately), a CRT

shown Figure 4.24.

Next, the missile mod

added to the clutter return fr

Finally, target detection was

The result is shown in Figure

sea surface has raised the max

is detected with a margin of

energy window (e.g. values less than .5 nsec).

From the results of the preceding paragraphs it might be suggested that a small window size should be used. An important parameter missing from the preceding analysis is the problem associated with an evolving sea surface. To investigate this problem, two sea-like surfaces were computed from the wind driven model proposed by Kinsman. Two surfaces, generated with wind speed of 20 knots, are shown in Figure 4.23. The first surface was generated at an initial time of t = 0 sec. The second surface is generated at a subsequent time step t = 1.25 sec. Notice that the vertical in Figure 4.23 is not drawn to scale, the total length of the wave is 1000 meters, and the wave height is 3.3 meters. The scattered fields for each surface were numerically computed using 2-d Green's function and the method of moments (refer to chapter 3, section 4). Due to computing constraints the surfaces were scaled down by a factor of 50, and the frequency range was set at .5 - 1.5 GHz with 200 points. Using the scattered field from the initial sea surface and the target return from the Phoenix missile model (scaled appropriately), a CRTW was computed using (4.3). The CRTW for this case is shown Figure 4.24.

Next, the missile model response was scaled in amplitude to TCR = -14 dB and added to the clutter return from the surface (at t = 115 nsec) in the second time step. Finally, target detection was attempted by computing $\bar{\epsilon}(t)$ with a window Δ = 4 nsec. The result is shown in Figure 4.25. This figure clearly shows a target, but the evolved sea surface has raised the maximal baseline value of $\varepsilon(t)$ to about 10 dB. Thus, the target is detected with a margin of about 10 dB. Using different values for the window size, the convolution energy ratio

Figure 4.26. The significant f

lower the target values for $\bar{\epsilon}($

is also lowered. Therefore, so

to false detection. If a sma

CRTW more often.

4.7 Application of CRTV

A clutter reducing tra

return from a surface (clutter

expected target can be meas

produced will maximize the

surface return for a specific t

question raised is, can the C

This situation can be s

and the return from a stationa

return and the scattering fro

algorithm can then be used w

and the different targets.

The scattered return f

the previous sections. The

Figure 4.5 respectively. Sev

the convolution energy ratio $\overline{\epsilon}(t)$ can be recomputed. The results are shown in Figure 4.26. The significant feature in this figure is that a wide window will broaden and lower the target values for $\overline{\epsilon}(t)$. On the other hand the maximal baseline value of $\overline{\epsilon}(t)$ is also lowered. Therefore, some care should be taken for a small window size in regards to false detection. If a small window size is used it is also advisable to update the CRTW more often.

4.7 Application of CRTW Techniques to Different Target Geometries

A clutter reducing transmit waveform can be constructed using the measured return from a surface (clutter producer) and the return from an anticipated target. The expected target can be measured in the lab or calculated theoretically. The CRTW produced will maximize the ratio of target to clutter return at some point along the surface return for a specific target. Since a particular target is anticipated an important question raised is, can the CRTW be effective in detecting other targets?

This situation can be studied be measuring the return from several different targets and the return from a stationary surface. A CRTW can be constructed using the surface return and the scattering from one of the measured targets. The CRTW detection algorithm can then be used with the returns from a combination of the stationary surface and the different targets.

The scattered return from a Stoke's surface representation has been discussed in the previous sections. The surface and transient return are shown in Figure 4.4 and Figure 4.5 respectively. Several highly conductive missile models were constructed and measured in the anechoic cha

shown in Figure 4.27. The

respectively. This notation w

missile which has an appearan

generic cruise missiles of the

time-domain returns from the

The CRTW for each r

corresponding to the return f

Figure 4.31. As can be seen

missile return it was construc

A detection scheme us

effective for detecting that t

measured, the detection sche

not work as well. If target id

some advantage in having

geometries. In this case dif

surface geometry. This coul

quite different depending on

To determine the sens

target returns in the time dom

time-domain return of the St

version of the targets shown

measured in the anechoic chamber at MSU. The missile models used for this study are shown in Figure 4.27. The missiles are labeled as A, B, and C from top to bottom respectively. This notation will be used throughout this section. Missile A is a Phoenix missile which has an appearance similar to that of an Exocet. Missiles B and C represent generic cruise missiles of the same geometry but slightly different size. The normalized time-domain returns from these models are shown in Figure 4.28.

The CRTW for each missile was created using a genetic algorithm. The CRTW corresponding to the return for the surface and each target are shown in Figure 4.29 - Figure 4.31. As can be seen from these figures each CRTW is unique to the particular missile return it was constructed from.

A detection scheme using a CRTW designed for a particular target should be quite effective for detecting that target. On the other hand, if a different target return is measured, the detection scheme (using a CRTW designed for the original missile) may not work as well. If target identification is not particularly important, then there may be some advantage in having a CRTW scheme that is not sensitive to different target geometries. In this case differences may be characterized by missile size and control-surface geometry. This could be important if the return from a missile is not static but quite different depending on radar to missile geometry.

To determine the sensitivity of the CRTW technique, different combined surface-target returns in the time domain were generated. This was essentially done by taking the time-domain return of the Stoke's surface shown in Figure 4.5 and adding a time-shifted version of the targets shown in Figure 4.28. In addition to time shifting, the magnitude of the normalized scattered tar

a combined return that was ge

was located between peaks 5 a

between the return from the su

C were also added to the Stok

was stored in different files.

Applying the detection

combined target surface return

shows the convolution energy

surface. If no missile were pr

surface. Figure 4.32 clearly

detection. More significant i

CRTW was designed for mis

as Figure 4.32 except Figure

Figure 4.34 is based upon a C

plots points to the lack of s

reasons for this lack of sensit

producing surface return. F

should be close to zero, ther

scheme is somewhat insensit

identification. It is expect

detection will still work but

of the normalized scattered target return was reduced by 90 percent. Figure 4.19 shows a combined return that was generated using target A. As shown in the inset, the target was located between peaks 5 and 6. An expanded view of the inset shows the difference between the return from the surface only, and from the surface and target. Target B and C were also added to the Stoke's surface at the same position as target A, but the data was stored in different files.

Applying the detection algorithm for a CRTW designed for missile A for each combined target/surface return results in the response shown in Figure 4.32. This figure shows the convolution energy ratio expressed in dB as a function of position along the surface. If no missile were present, the response should be flat at 0 dB with a stationary surface. Figure 4.32 clearly shows a large jump in the response indicating target detection. More significant is that missiles B and C are also detected (remember, the CRTW was designed for missile A). Figure 4.33 and Figure 4.34 show similar results as Figure 4.32 except Figure 4.33 is based upon a CRTW designed for missile B and Figure 4.34 is based upon a CRTW designed for missile C. The significance of all three plots points to the lack of sensitivity to missile size or geometry. One of the main reasons for this lack of sensitivity is that the CRTW is constructed for a particular clutter producing surface return. For this matched surface return the denominator in (4.4) should be close to zero, therefore making the response quite large. Since the detection scheme is somewhat insensitive to target type, this method should not be used for target identification. It is expected that for an even smaller measured bandwidth, target detection will still work but identification is out of the question.

4.8 Multipath Effect on T

Previous sections in th

transient scattered electric fie

individual transient fields fro

amplitude between the target a

easily be controlled. One pro

electromagnetic coupling inter

however, is the absence of mu

the surface, i.e. the multipat

scattered field from the target

formed by adding the two ind

The impact which the

is investigated in this sectio

theoretical scattered field fro

different surface heights an

calculations were of the tran

the surface/target pair with th

scattered fields from a surfac

The scattered field from seve

scaled missile model located

approaches a CRTW was cal

surface. Using this CRTW,

4.8 Multipath Effect on Target Detection

Previous sections in this chapter have considered several examples where the transient scattered electric field from the target/surface pair was formed by adding the individual transient fields from the target and the surface. By scaling the relative amplitude between the target and surface return, the TCR in the composite return could easily be controlled. One problem associated with this technique is that it neglects the electromagnetic coupling interaction between the surface and the target. More important however, is the absence of multiple excitation due to reflection of the incident wave from the surface, i.e. the multipath effect. If the multipath effect is significant, then the scattered field from the target/surface pair may be quite different from the transient field formed by adding the two individual fields.

The impact which the multipath effect has on the new CRTW detection scheme is investigated in this section. Several different approaches were taken. First, the theoretical scattered field from a cylinder/Stoke's surface pair was calculated for several different surface heights and cylinder positions with respect to the surface. The calculations were of the transient fields from the target and surface separately and then the surface/target pair with the multipath effect. A second approach was to measure the scattered fields from a surface/target pair in the anechoic chamber at the MSU EM Lab. The scattered field from several different surfaces was measured with and without a small scaled missile model located at different positions with respect to the surface. In both approaches a CRTW was calculated from the separate transient fields from the target and surface. Using this CRTW, the convolution energy ratio was calculated from the return of the surface target pair. T

composite return was formed

the scattered field was forme

cases, a comparison can be r

interaction between the surfac

Figure 4.35 depicts th

located above a Stoke's surfa

field parallel to the surface cr

consists of a Stoke's wave ha

h, and individual wavelength

of diameter t and the bottom

respect to the surface is sho

center peak on the Stoke's su

measured with respect to the

A far-field approxima

a method of moments solutio

valid only for a closed surface

direction for 320 frequency p

transient field was determine

to the time domain using an

was employed with frequenc

respectively (see Appendix

of the surface/target pair. This surface/target pair return includes two cases. First, a composite return was formed by adding the separate target and surface return. Second, the scattered field was formed by including the multipath effect. By considering both cases, a comparison can be made showing the effect of multipath and electromagnetic interaction between the surface and target.

Figure 4.35 depicts the 2-dimensional scattering geometry for a cylindrical target located above a Stoke's surface. The incident plane wave is polarized with its magnetic field parallel to the surface crests (TM). The enclosed surface shown in Figure 4.35 (a), consists of a Stoke's wave having N periods (where N is an odd number), surface height h, and individual wavelength L. The sides of the enclosed surface consist of half-circles of diameter t and the bottom is a flat surface. The position of the scattering target with respect to the surface is shown in Figure 4.35 (b) with the y-axis coincident with the center peak on the Stoke's surface. The incident angle ϕ_i, shown in Figure 4.35 (a), is measured with respect to the x-axis.

A far-field approximation to the scattered field was theoretically calculated using a method of moments solution to the magnetic-field integeral equation (MFIE) which is valid only for a closed surface [18]. The calculated field was computed in the backscatter direction for 320 frequency points starting at 1.0 GHz at a step size of .025 GHz. The transient field was determined by windowing the frequency data and then transforming to the time domain using an IFFT. For all trials a Gaussian modulated cosine window was employed with frequency and shaping parameters of f_c = 5.0 GHz, and T = .25 nsec respectively (see Appendix A for window description). The surface wavelength L for each trial was set to .1016 m

of the side half-circles was se

.005 m. The value for the

reasonable value for the TCR

the scattering calculations the

each, the sides and cylinder w

scattering angle was set to ϕ.

Several scattering cal

surface for a fixed cylinder p

the position of the cylinder w

field computed.

Figure 4.36 shows the

alone and from the surface

coupling interaction. For this

and was horizontally displac

Figure 4.36, the two returns o

about 4.4 nsec). After this

return. Figure 4.37 shows t

only return. The response of

the multipath effect.

To determine the effe

the transient response of th s

each trial was set to .1016 m, the number of periods N was set to 11, and the diameter of the side half-circles was set to .0254 m. Also, the radius of the cylinder R was set to .005 m. The value for the variable R was determined by trial and error to get a reasonable value for the TCR (about -3 to -5 dB) for a surface height h of .0254 m. For the scattering calculations the top and bottom of the surface were divided into 200 points each, the sides and cylinder were divided into 16 and 32 points respectively. Finally, the scattering angle was set to $\phi_i = 20°$ for all trials.

Several scattering calculations were performed by varying the height h of the surface for a fixed cylinder position. After that, the height of the surface was fixed and the position of the cylinder was varied both as function of height y_c and range x_c, and the field computed.

Figure 4.36 shows the normalized transient scattered field from the Stoke's surface alone and from the surface/target pair with the multipath effect and electromagnetic coupling interaction. For this case, the cylinder was located .0254 m above the surface, and was horizontally displaced .0508 m to the right of the central peak. As shown in Figure 4.36, the two returns overlap exactly before the incident wave strikes the target (at about 4.4 nsec). After this event, the composite return differs from the surface-only return. Figure 4.37 shows the difference between the composite return and the surface only return. The response of the cylinder is clearly shown as well as the later effect from the multipath effect.

To determine the effects that the multipath effect has on the detection algorithm the transient response of th surface only and the cylinder only were used to construct a

CRTW. Using the calculated

energy ratio was calculated fo

shows the convolution energy

were calculated using (4.4) fo

was generated by calculating

response having no electrom

only transient response and t

a strong convolution energy

(convolution time). The origi

between the cylinder and th

follow is from the cylinder t

Another path is from the sur

point. Also, multiple scatter

crest before the scattered fi

multipath scattering events o

Figure 4.39 and Figu

Stoke's surfaces having heig

the size and position of the c

defined convolution energy

multipath effect. For the sm

energy ratio peaks at nearly

cylinder does not change but

CRTW. Using the calculated CRTW and the surface plus target response, the convolution energy ratio was calculated for the detection phase of the CRTW algorithm. Figure 4.38 shows the convolution energy ratio as a function of time. The curves shown in this figure were calculated using (4.4) for an energy window width of .25 nsec. The dashed curve was generated by calculating the convolution energy ratio for the target plus surface response having no electromagnetic interaction. This was done by adding the surface only transient response and the cylinder only transient response. Both curves indicated a strong convolution energy ratio peak of about 14 dB occurring at about 4.6 nsec (convolution time). The origin of the secondary peaks are due to the multiple reflections between the cylinder and the surface crests. One simple path the scattered field can follow is from the cylinder to the surface crest and then back to the observation point. Another path is from the surface crest to the cylinder and then back to the observation point. Also, multiple scattering events can occur between the cylinder and the surface crest before the scattered field goes back to the observation point. In each case the multipath scattering events occur after the initial scattering from the cylinder.

Figure 4.39 and Figure 4.40 show the convolution energy ratio calculations for Stoke's surfaces having heights of .0127 m and .00635 m, respectively. In both cases, the size and position of the cylinder have not changed. Both figures clearly show a well defined convolution energy ratio peak and the secondary peaks associated with the multipath effect. For the small surface height shown in Figure 4.40, the convolution energy ratio peaks at nearly 20 dB. This result can be expected since the size of the cylinder does not change but the surface height has decreased by a factor of 4 (compared to h = .0254 m). However, t

smaller peak than in Figure 4.

of 2 (as compared to h = .0

surprising since the TCR diff

3.63 dB in Figure 4.39).

Another important fac

peaks of the cylinder lie wi

overlapping peaks (i.e. surfa

ratio will be smaller. The co

the three different surface he

The effect upon the

investigated. This was done

target height y_c. Three differ

.1143 m . In each case, the

x-coordinate of the cylinder

scattered fields from the surfa

effect for a target height of

position and some of the inte

two curves in Figure 4.42.

Figure 4.36 and Figure 4.37.

are shown in Figure 4.44 and

target and interaction is clea

to h = .0254 m). However, the convolution energy ratio shown in Figure 4.39 shows a smaller peak than in Figure 4.38 even though the surface height has decreased by a factor of 2 (as compared to h = .0254 m). Although this is a bit unexpected, it is not too surprising since the TCR difference is not that great (from -5.31 dB in Figure 4.38 to -3.63 dB in Figure 4.39).

Another important factor to consider for these different cases is where the transient peaks of the cylinder lie with respect to the peaks from the scattering surface. For overlapping peaks (i.e. surface peaks overlapping target peaks) the convolution energy ratio will be smaller. The convolution energy ratio for the multipath scattered field for the three different surface heights are combined in Figure 4.41.

The effect upon the detection process of different target heights was also investigated. This was done by fixing the Stoke's surface parameters and varying the target height y_c. Three different target heights were considered: .0635 m, .0889 m, and .1143 m . In each case, the height of the Stoke's wave was set to h = .0254 m and the x-coordinate of the cylinder was fixed at x_c = .0508 m. Figure 4.42 shows the transient scattered fields from the surface alone and from the surface plus target with the multipath effect for a target height of y_c = .0889 m. The dashed curve clearly shows the target position and some of the interaction effects. Figure 4.43 shows the different between the two curves in Figure 4.42. Similar figures for a target height of .0635 m are shown in Figure 4.36 and Figure 4.37. Also, corresponding figures for a target height of .1143 m are shown in Figure 4.44 and Figure 4.45. Using the difference figures, the effect of the target and interaction is clearly seen. For an evolving surface it would be much more difficult to distinguish the ta

After creating a CRTV

transient response. the convo

target surface pairs. Figure

target heights. Once again.

Associated with the main pe

effect. The change in the co

function of the electromagn

target and surface. In Figur

figure the peak values are ve

is caused by the electromag

convolution energy value cal

The position of the ta

height of the surface and targ

the scattered return from th

surface target pair with the

set at .0254 m and .0635 m

Stoke's peak by setting x_s =

curves in Figure 4.48. For c

a target position between th

is clearly lined up with surfa

to the surface peak causes a

difficult to distinguish the target by just taking the difference between the two curves.

After creating a CRTW from the surface only transient response and cylinder only transient response, the convolution energy ratio was calculated for each of the composite target/surface pairs. Figure 4.46 shows the convolution energy ratios for the different target heights. Once again, a well defined peak indicates the presence of a target. Associated with the main peaks are the secondary peaks corresponding to the multipath effect. The change in the convolution energy value for the different target heights is a function of the electromagnetic interaction and the relative peak location between the target and surface. In Figure 4.47 the interaction effect has not been included. In this figure the peak values are very close in value. Therefore, the effect seen in Figure 4.46 is caused by the electromagnetic interaction distorting the signal enough to effect the convolution energy value calculation.

The position of the target can also be varied along the surface. In this case, the height of the surface and target are fixed and the value of x_c is varied. Figure 4.48 shows the scattered return from the Stoke's surface alone and from the combined Stoke's surface/target pair with the multipath terms. The surface height and target height were set at .0254 m and .0635 m respectively. The target was placed directly over the central Stoke's peak by setting $x_c = 0.0$ m. Figure 4.49 shows the difference between the two curves in Figure 4.48. For comparison, Figure 4.36 and Figure 4.37 were calculated for a target position between the surface peaks at .0508 m. In Figure 4.48 the target return is clearly lined up with surface peak return. In addition, the close proximity of the target to the surface peak causes a greater interaction between the surface and the target. To

see the effect upon detection
was determined for the co
Figure 4.50 shows the results
convolution energy ratio is m
the convolution energy ratio
term is neglected. Here, the
difficult to detect the target.

The scattered electric
measured in the anechoic ch
placed above these surface a
the relative geometry betw
scattering measurements. Th
field is parallel to the wave
Phoenix missile model, appr
above the crests of the surfa
chosen for the measurements
surface peak (position 1) and
(position 2). Figure 4.4 sh
Section 4.4 discusses the par

The time-domain sca
Figure 4.53. This response
the anechoic chamber at MS

see the effect upon detection, a CRTW was calculated, and the convolution energy ratio was determined for the composite return shown in Figure 4.36 and Figure 4.48. Figure 4.50 shows the results. For a target located extremely close to a surface peak the convolution energy ratio is much lower as shown by the dashed curve. Figure 4.51 shows the convolution energy ratio calculation for the case when the electromagnetic interaction term is neglected. Here, the position of the target over the peak makes it much more difficult to detect the target.

The scattered electric fields from various scaled sea-surface models have been measured in the anechoic chamber at MSU. A Phoenix missile model has also been placed above these surface and the resultant electric field measured. Figure 4.52 shows the relative geometry between the missile and sea-surface model using during the scattering measurements. The incident electric field was polarized such that the electric field is parallel to the wave crests at an incident angle of 10° from the horizon. A Phoenix missile model, approximately 10 cm in length, was position at a height of 12" above the crests of the surface. Two missile positions with respect to the peaks were chosen for the measurements. In the first case the missile was placed directly above the surface peak (position 1) and in the second case the missile was placed between the peaks (position 2). Figure 4.4 shows the surface profiles used during the measurements. Section 4.4 discusses the parameters required to generate these surfaces.

The time-domain scattered field from the Phoenix missile model is shown in Figure 4.53. This response was synthesized from a frequency domain measurement in the anechoic chamber at MSU. The frequency domain response was measured in the frequency band from 1 GHz

data was windowed and the

taper function with a shape p

the data.

The construction of a

target and the initial sea-su

Figure 4.55 show the transi

surface for an incident angl

identical to that of the Phoe

Figure 4.55, a CRTW was co

surface.

The position of the

peaks of the scattering surfa

the transient scattered return

of .09, time shifted, and add

= -23.2 dB). Next, the ma

CRTW (see Figure 4.56), wa

time shift. Figure 4.57 show

nearly a 17 to 18 dB differen

sinusoid surface the magnitu

added to the double sinusoi

values of the convolution en

frequency band from 1 GHz to 17 GHz at a step size of .01 GHz. The frequency domain data was windowed and then transformed to the time domain using an IFFT. A cosine taper function with a shape parameter of $\tau = 8$ (see Appendix A) was used to window all the data.

The construction of a CRTW requires the transient response from the anticipated target and the initial sea-surface return having no target present. Figure 4.54 and Figure 4.55 show the transient scattered return from the Stoke's and double sinusoid surface for an incident angle of 10°. The measurement process and windowing were identical to that of the Phoenix missile model. Using the data shown in Figure 4.53 - Figure 4.55, a CRTW was constructed for the Stoke's surface and for the double sinusoid surface.

The position of the target's transient return peaks with respect to the transient peaks of the scattering surface is extremely important for target detection. To see this, the transient scattered return from the Phoenix missile was amplitude scaled by a factor of .09, time shifted, and added to the transient response from the Stoke's surface (TCR = -23.2 dB). Next, the maximum convolution energy ratio, using the Stoke's wave CRTW (see Figure 4.56), was calculated for the composite return as a function of missile time shift. Figure 4.57 shows the results for these calculations. In this figure, there is nearly a 17 to 18 dB difference in the convolution energy detection ratio. For the double sinusoid surface the magnitude of the Phoenix missile was scaled by .05, time shifted, and added to the double sinusoid return (TCR = -4.75). Figure 4.59 shows the maximum values of the convolution energy ratio using the double sinusoid CRTW (see Figure 4.58) as a function of missile time

detection ratio.

In the preceding dis

were included. The measure

Figure 4.60 and Figure 4.61

includes the surface only ret

for the missile in position

electromagnetic interaction)

and each missile position.

Stoke's surface. Similarly, F

The peak convolution energy

14 dB respectively. The sec

and surface. For position 1,

surface and are shown in Fig

the double sinusoid surface

This is most prevalent in Fig

the target itself. However, i

enough to detect the target

probably not be the case.

The effect due to th

theoretically calculated scat

between the surface and the

as a function of missile time shift. In this case there is nearly a 25 dB difference in the detection ratio.

In the preceding discussion no multipath or electromagnetic interaction effects were included. The measured transient return from the surface/missile pairs is shown in Figure 4.60 and Figure 4.61 for the Stoke's and double sinusoid surface. Each figure includes the surface only return and the return from the composite surface/missile return for the missile in position 1 or position 2. With the composite return (including electromagnetic interaction) the convolution energy ratio was calculated for each surface and each missile position. Figure 4.62 shows this ratio for missile position 2 on the Stoke's surface. Similarly, Figure 4.63 shows the results for the double sinusoid surface. The peak convolution energy ratios for the Stoke's and double sinusoid surface are 10 and 14 dB respectively. The secondary peaks correspond to the coupling between the target and surface. For position 1, the convolution energy ratios were also calculated for each surface and are shown in Figure 4.64 and Figure 4.65. For both the Stoke's surface and the double sinusoid surface the convolution energy ratio has been considerably reduced. This is most prevalent in Figure 4.64 where the effects of the interaction are as great as the target itself. However, in Figure 4.65 the convolution energy ratio may still be large enough to detect the target, although for a rapidly evolving sea surface this would probably not be the case.

The effect due to the target-surface coupling have been illustrated using both theoretically calculated scattering data and measured data. Although the interaction between the surface and the target does effect target detection, the relative position of the target with respect to the su

the target scatter return did

was able to find the target.

in the presence of the mulip

4.9 Coherent Processin

A clutter suppression

clutter has been discussed b

N samples each are collected

clutter and target return. A

the cross-range average fron

$$\tilde{s}_i(k) = s_i($$

A little reflection shows wh

clutter from all the M puls

subtracted from the sample

any clutter present in the sig

improve for increasing value

clutter suppressed signal sho

achieved. The chief problen

is that the clutter environm

target with respect to the surface wave is probably more important. For all cases where the target scatter return did not coincide with a surface crest return the detection scheme was able to find the target. The detection algorithm was able to detect the target even in the presence of the mulipath effects.

4.9 Coherent Processing Clutter Reduction

A clutter suppression technique useful for moving targets on a static background clutter has been discussed by Iverson [26]. In this technique, a set of M pulse returns of N samples each are collected. The ith pulse return $s_i(k)$ is composed of both background clutter and target return. A clutter suppressed signal $\tilde{s}_i(k)$ can be formed by subtracting the cross-range average from each pulse return, i.e.

$$\tilde{s}_i(k) = s_i(k) - \frac{1}{M}\sum_{j=1}^{M} s_j(k) \qquad k = 1 \ldots N, \quad i = 1 \ldots M \tag{4.15}$$

A little reflection shows why this formula should work. For a given sample point k, the clutter from all the M pulse returns is simply averaged. This average value is then subtracted from the sample point k for each pulse return. The net effect is to suppress any clutter present in the signal. For a static background clutter, clutter suppression will improve for increasing values of M. Following the clutter suppression step, the resulting clutter suppressed signal should be aligned and added so that coherent integration can be achieved. The chief problem associated with clutter suppression in the sea environment is that the clutter environment is far from static. For a slowly evolving sea surface

Iverson's method may work

time interval. On the other

pulse returns must be sampl

An alternative form

moving window of discrete

can be written as

$$\bar{s}_{i_r}(k) = $$

where i_r is the pulse respons

the cross-range average valu

is subtracted from the pulse

changing clutter return, it i

probably fluctuate about the

important point since subtrac

the edge of the window will

of the window may be an e

then poor performance can b

change appreciably over the

To demonstrate the u

theoretically calculated fron

stochastic model given by

evolving sea surface was calc

Iverson's method may work by using a moderate number of pulse returns M in a finite time interval. On the other hand, if the sea surface is evolving at a faster rate, then the pulse returns must be sampled at a higher rate.

An alternative form for (4.15) can be used for evolving background clutter. If a moving window of discrete width L is applied to a subset of the pulse returns, then (4.15) can be written as

$$\tilde{s}_{i_r}(k) = s_{i_r}(k) - \frac{1}{L} \sum_{j=i_r-\frac{(L-1)}{2}}^{i_r+\frac{(L-1)}{2}} s_j(k) \qquad k = 1 \ldots N \tag{4.16}$$

where i_r is the pulse response index corresponding to the center of the window. In (4.16) the cross-range average value is computed over the range of the window and this value is subtracted from the pulse return corresponding to the center of the window. For a changing clutter return, it is expected that the pulse returns within the window will probably fluctuate about the pulse response at the center of the window. This is an important point since subtracting the cross-range average from a pulse return located at the edge of the window will not lead to good clutter suppression results. Also, the size of the window may be an extremely important factor. If the window size is too large, then poor performance can be expected since the sea surface (and the clutter return) can change appreciably over the window's time space.

To demonstrate the use of Iverson's modified technique, the scattered field was theoretically calculated from an evolving sea surface which was generated from a stochastic model given by Kinsman. As in section 4.5, the scattered field from the evolving sea surface was calculated over a 2.0 sec interval every .25 seconds. Figure 4.66

shows the scattered return f

figure represents time-dom

time; successive lines repr

bottom. The sensor (radar

shown on the graph. A tim

calculate the cross range av

second scene, shown in Fig

across the signal space. A

distinguish between clutter

too large for the rate of sea

To remedy the abov

a smaller time step could

Figure 4.68 shows the sc

generated in the previous s

returns were sampled over

Once again a pulse return v

calculate the cross-range av

process using the smaller ti

the background clutter. Si

algorithm is very useful if

compared to the new CRT

implement for real-time ap

shows the scattered return from the clutter/target combination. Each horizontal line in the figure represents time-domain samples from the scatter response over some interval of time; successive lines represent a series of scatter returns with the first return on the bottom. The sensor (radar) is located on the left and successive missile locations are shown on the graph. A time window using three successive measurements was used to calculate the cross range average. After application of the clutter suppression process a second scene, shown in Figure 4.67, was generated to show the movement of the target across the signal space. As can be seen from the second figure it is very difficult to distinguish between clutter and missile return. In this case the time step is most likely too large for the rate of sea surface evolution.

To remedy the above problem a second simulation was also performed to see if a smaller time step could lead to an improvement in the clutter suppression problem. Figure 4.68 shows the scatter return and missile position for the same sea-surface generated in the previous simulation using the Kinsman model. In this case 10 pulse returns were sampled over a .45 sec duration with the time interval $\Delta T = .05$ seconds. Once again a pulse return window containing three successive pulse returns was used to calculate the cross-range average. Figure 4.69 shows the results of the clutter suppression process using the smaller time step. In this case the target is clearly distinguishable from the background clutter. Since the calculation given by (4.16) is extremely simple, this algorithm is very useful if the time step between successive pulse returns is small. As compared to the new CRTW technique this method is extremely simple and easy to implement for real-time applications.

4.10 Conclusions

This chapter has pr
pulse method. The motiv
difficulties associated with t
important topics were prese
scheme was described. Nex
The author has found this al
algorithm several examples
static sea-surface demonst
dynamic sea surface was n
surface environment and th
surface/target coupling on t
generated test cases and me
energy window size on the
see if the detection schem
missile models were measu
models was used in conjun
CRTW and to test the dete
the detection algorithm is q
The final topic covered i
technique. This method w
update rate is sufficiently f

4.10 Conclusions

This chapter has presented a new target detection technique based upon the E-pulse method. The motivation for doing this chapter was to overcome some of the difficulties associated with the conventional use of the E-pulse detection method. Several important topics were presented in this chapter. First, the theory behind the new detection scheme was described. Next, the genetic algorithm was presented and described in detail. The author has found this algorithm to be robust but quite slow. To test the new CRTW algorithm several examples were presented showing the effectiveness of this method. A static sea-surface demonstration was presented showing proof of concept. Next, a dynamic sea surface was modeled in order to show the effect of a more realistic sea-surface environment and the need to regularly update the CRTW. The effect from sea-surface/target coupling on the detection algorithm was also studied. Several theoretically generated test cases and measured results were presented. The effect of the convolution energy window size on the detection phase of the CRTW algorithm was presented. To see if the detection scheme was tolerant to different target geometries several scaled missile models were measured in the anechoic chamber. The scattered return from these models was used in conjunction with the return from a sea-surface model to generate a CRTW and to test the detection phase of the CRTW algorithm. This study showed that the detection algorithm is quite tolerant to some variation in the target's scattered return. The final topic covered in this chapter is the coherent processing clutter reduction technique. This method was tested and found to work remarkably well provided the update rate is sufficiently fast. In addition, this technique can easily be applied to real-time processing with very

time processing with very little code modification.

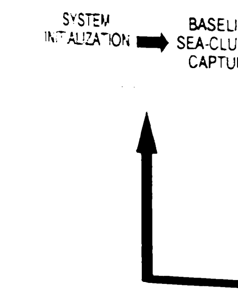

Figure 4.1 CRTW flow

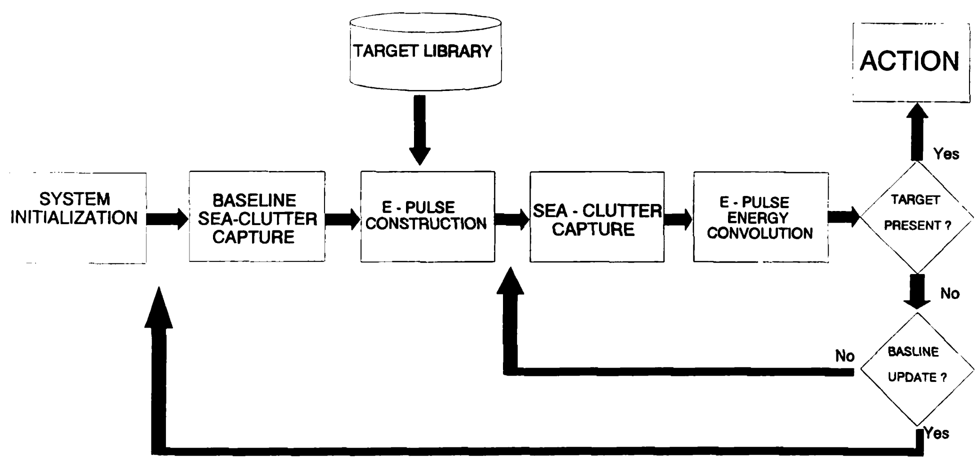

Figure 4.1 CRTW flowchart process.

Figure 4.2 Genetic algo

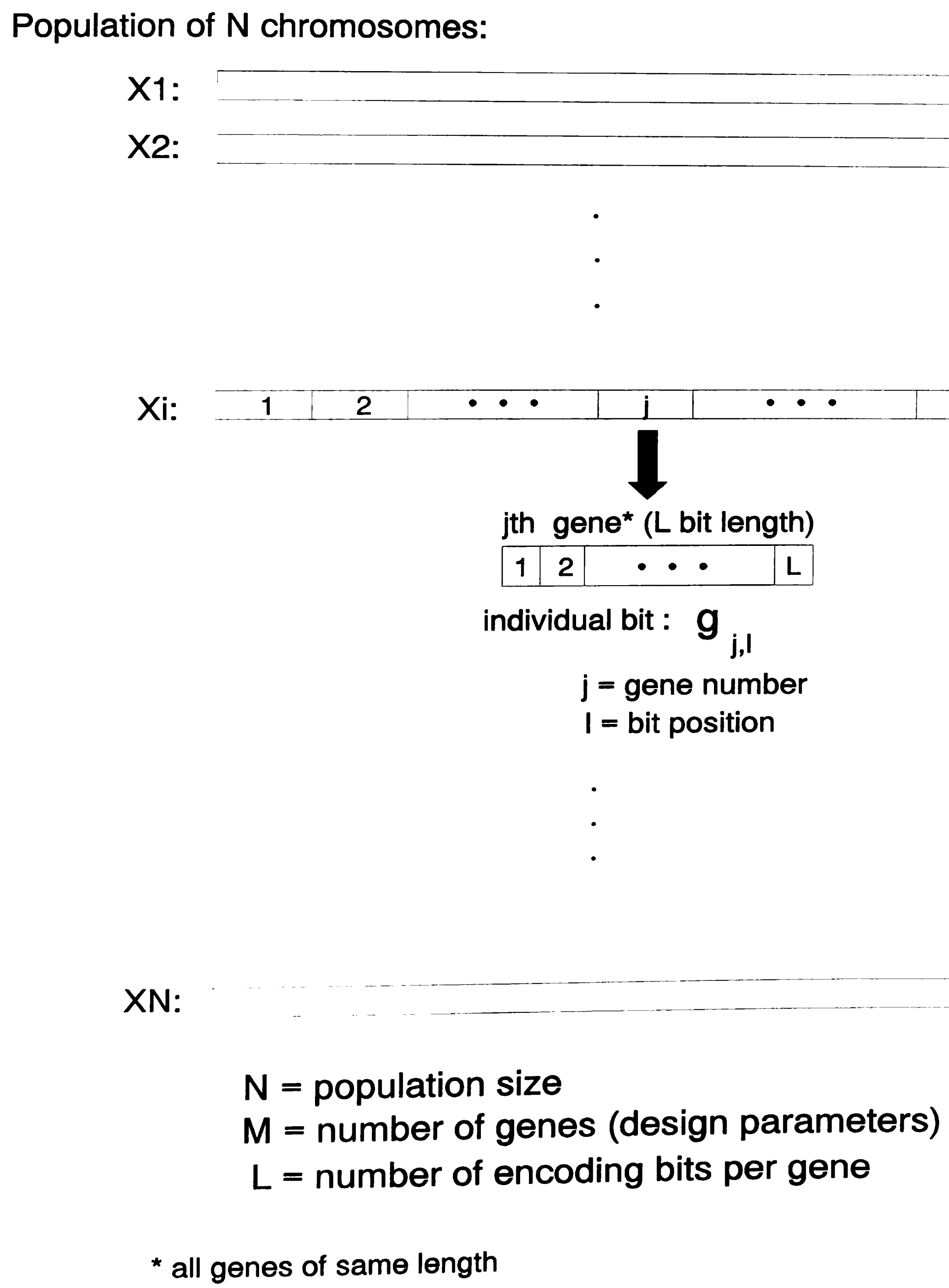

Figure 4.2 Genetic algorithm data structures.

Figure 4.3 Genetic alg

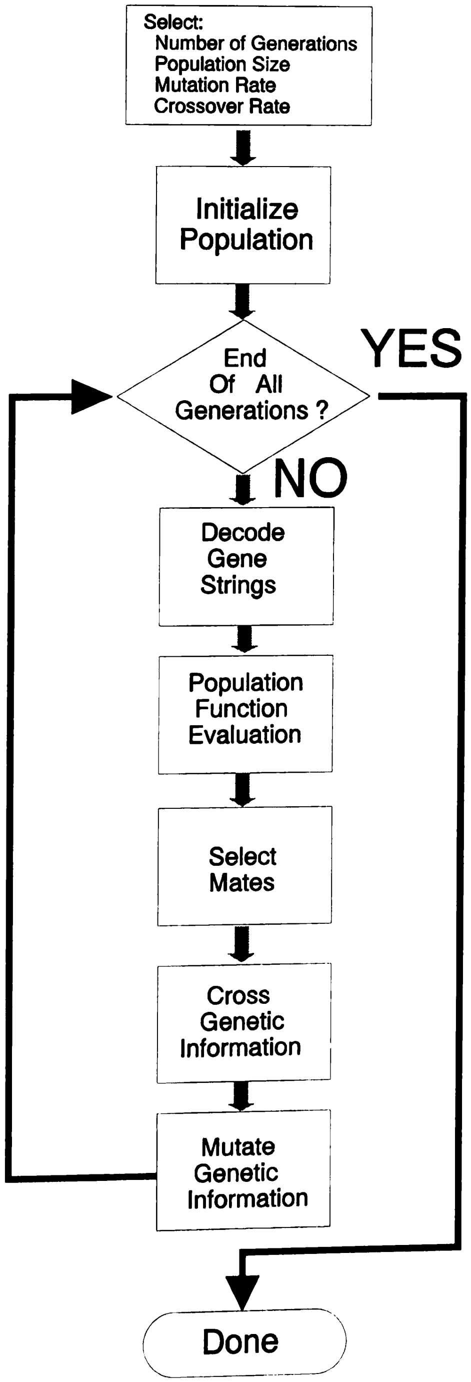

Figure 4.3 Genetic algorithm block diagram.

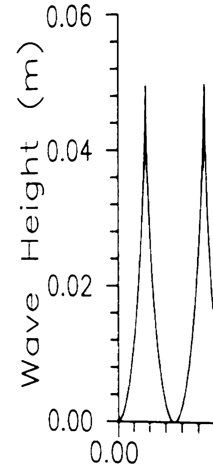

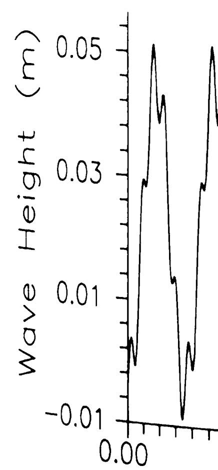

Figure 4.4 Simple PEC

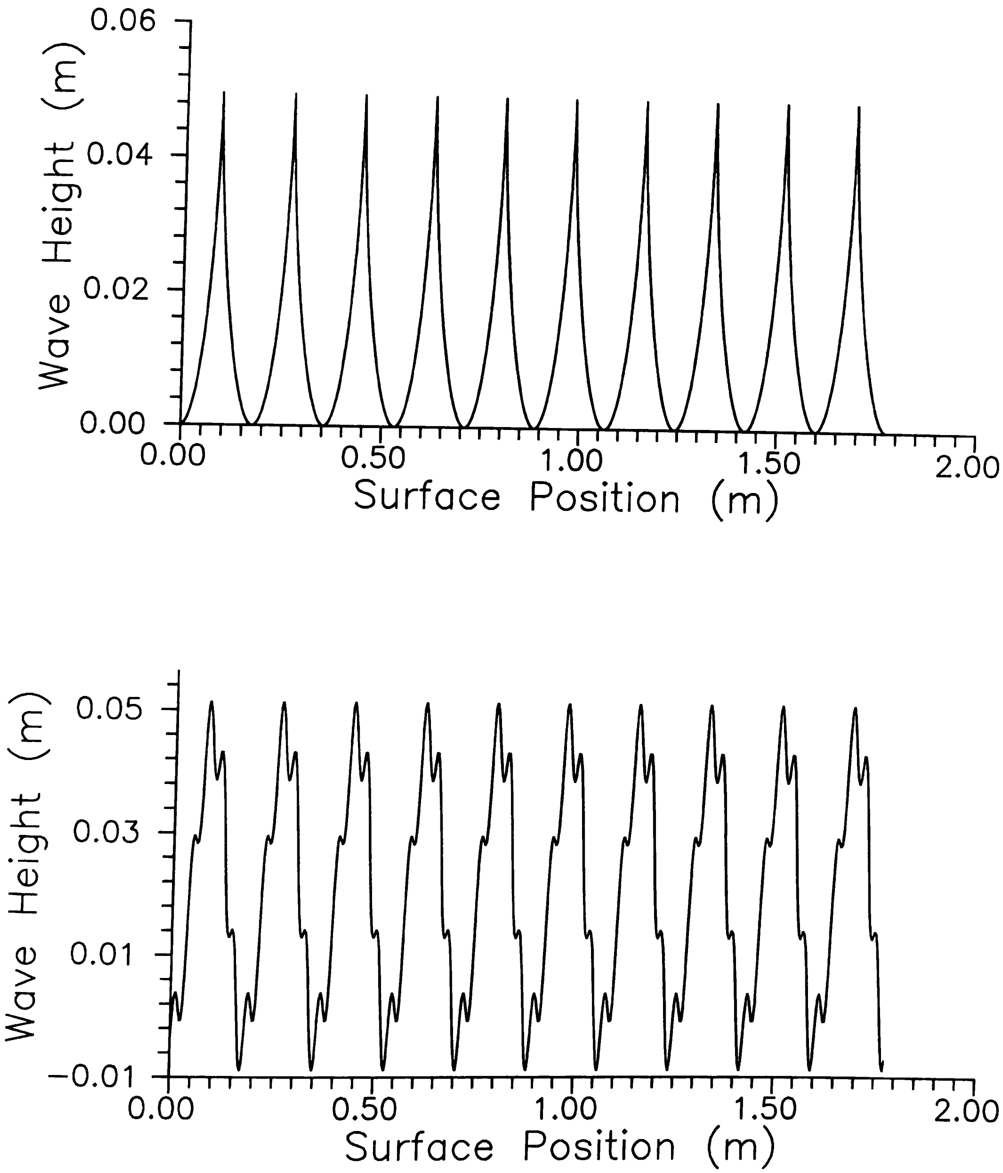

Figure 4.4 Simple PEC scaled ocean surfaces.

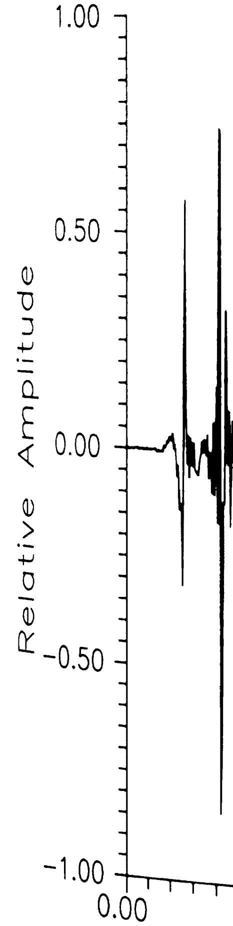

Figure 4.5 Scattered fi

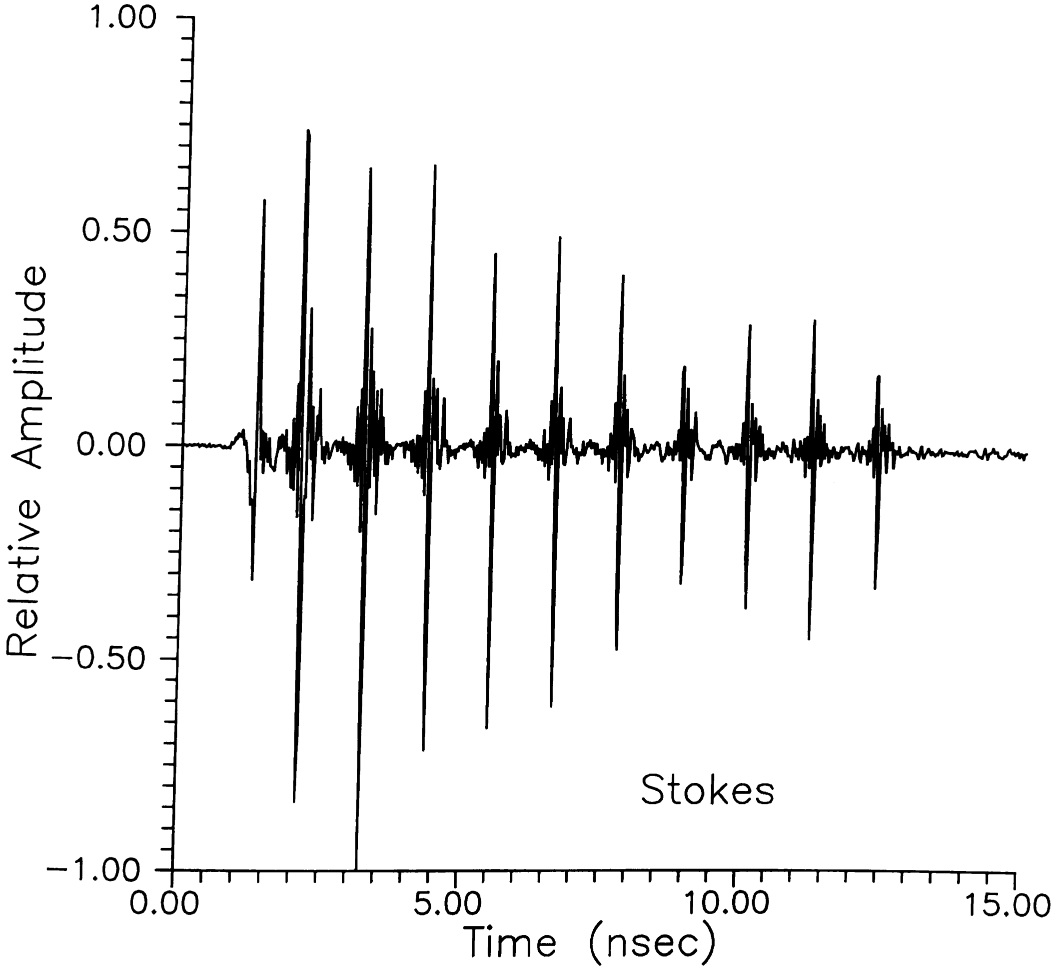

Figure 4.5 Scattered field from the PEC Stokes surface.

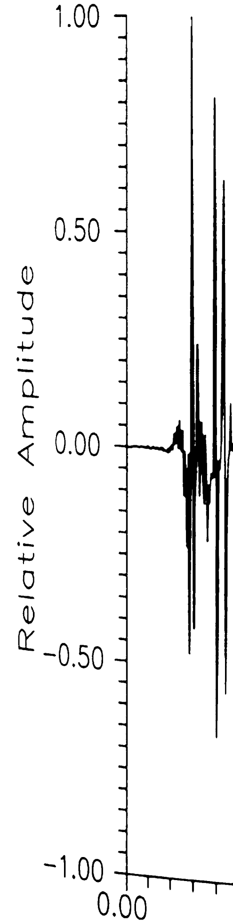

Figure 4.6 Scattered fi

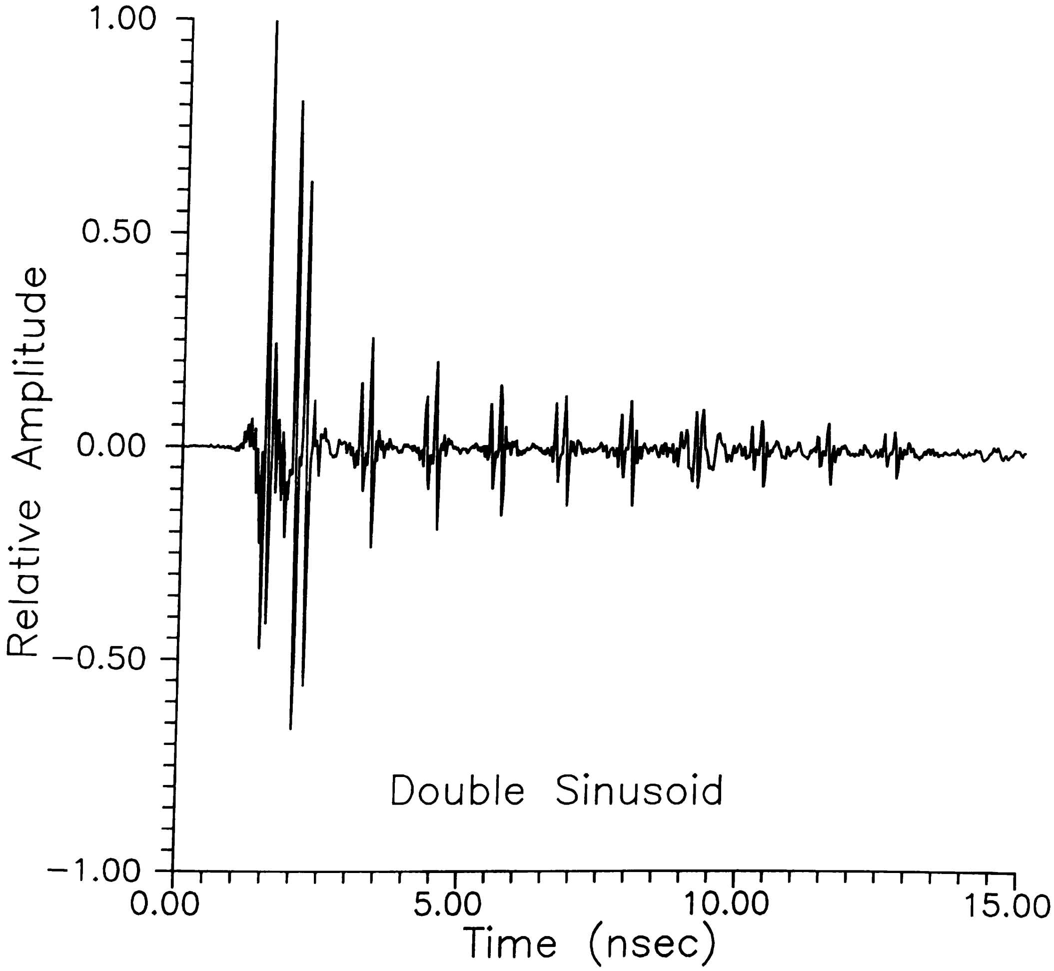

Figure 4.6 Scattered field from double sinusoid surface.

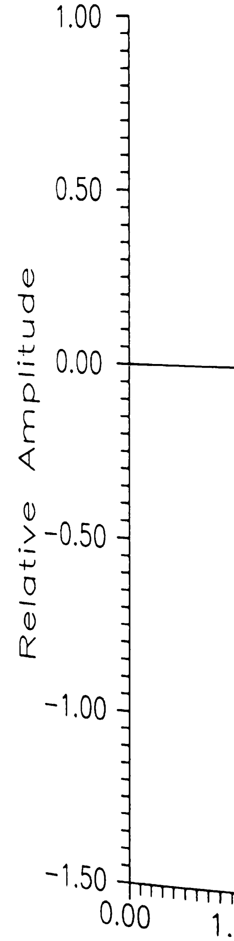

Figure 4.7 Scattered fi

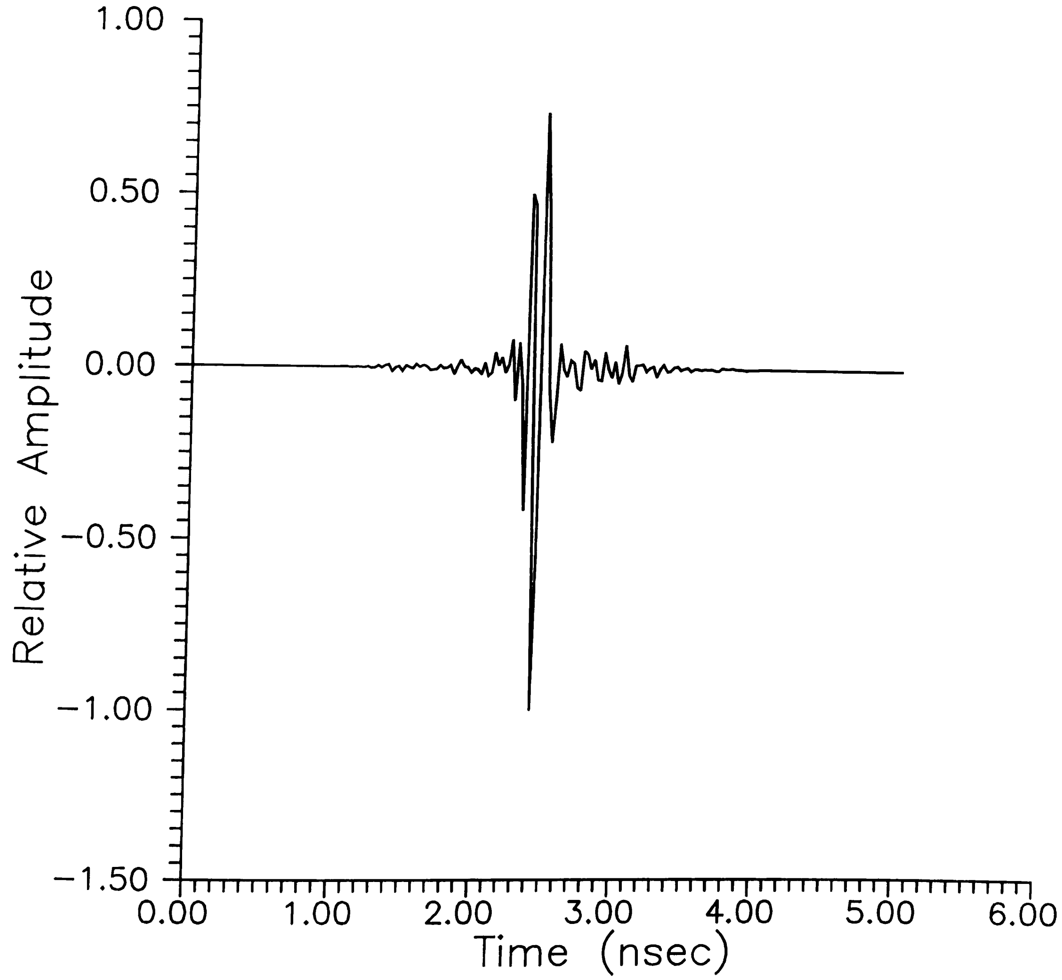

Figure 4.7 Scattered field from Phoenix missile model.

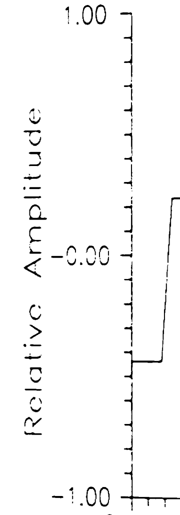

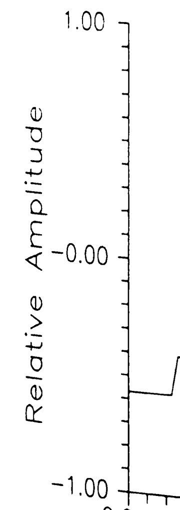

Figure 4.8 Constructed

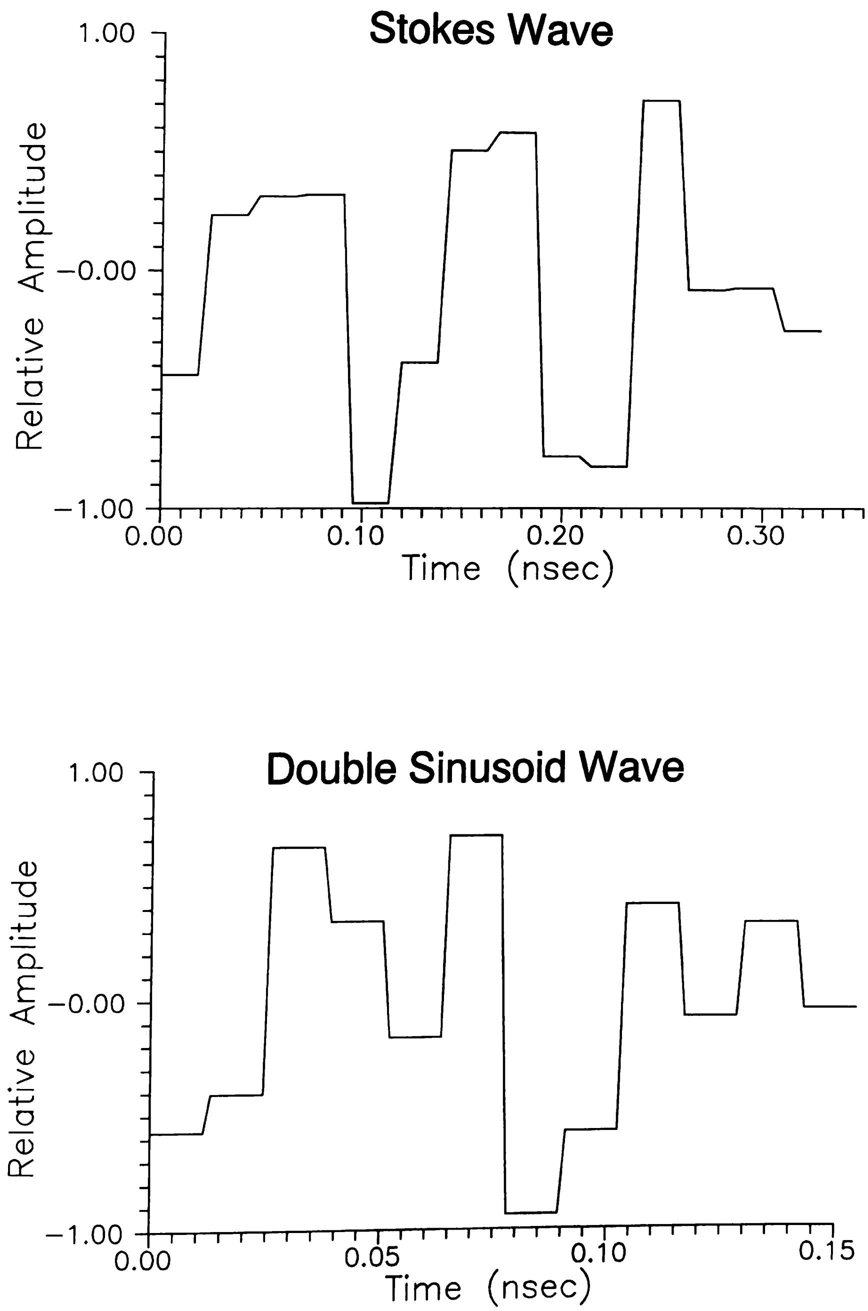

Figure 4.8 Constructed CRTWs for measured surfaces.

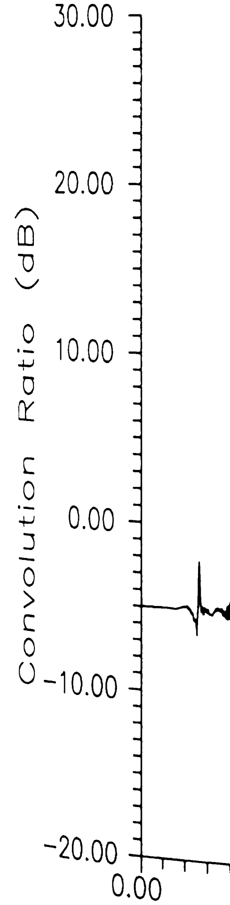

Figure 4.9 Convolution

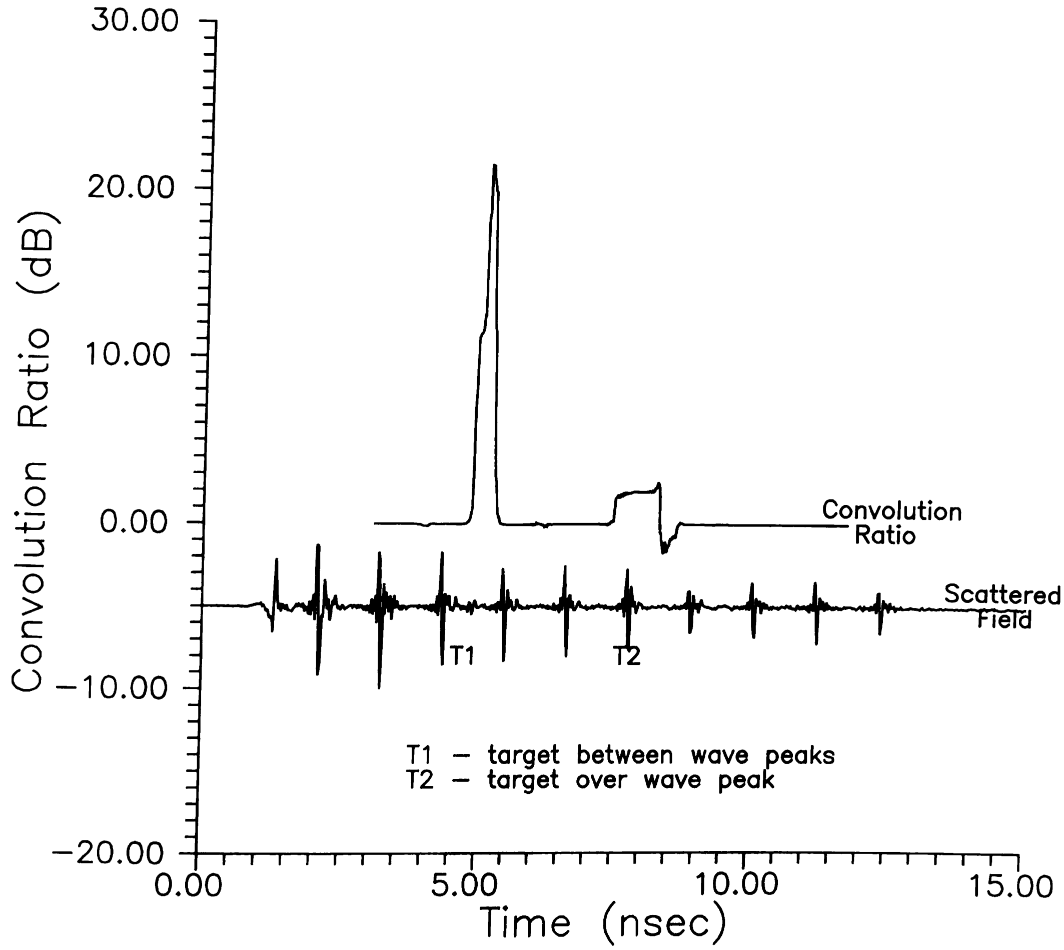

Figure 4.9 Convolution energy ratio for Stokes surface.

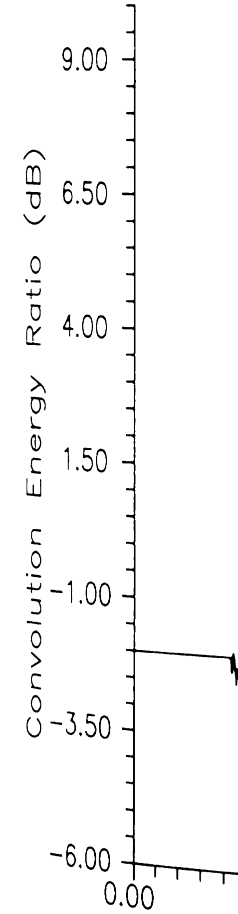

Figure 4.10 Convolution

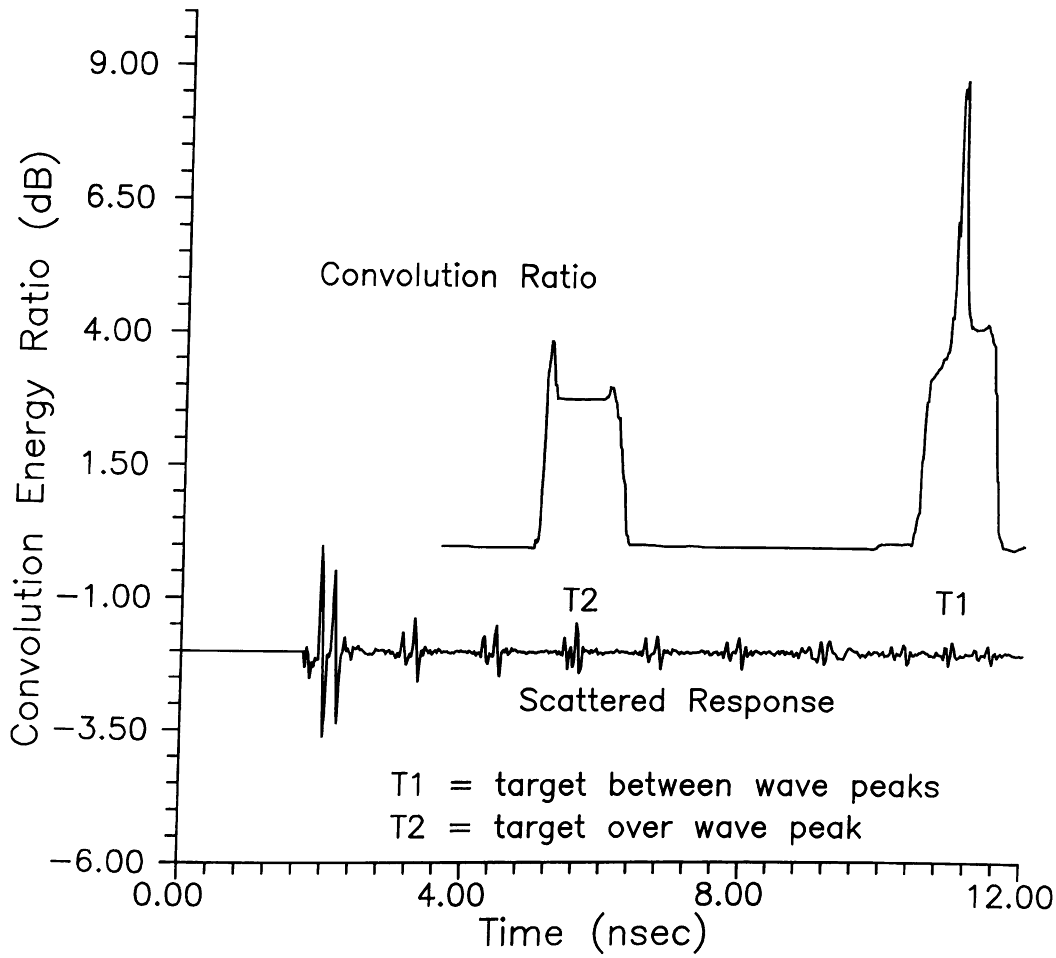

Figure 4.10 Convolution energy ratio for double sinusoid surface.

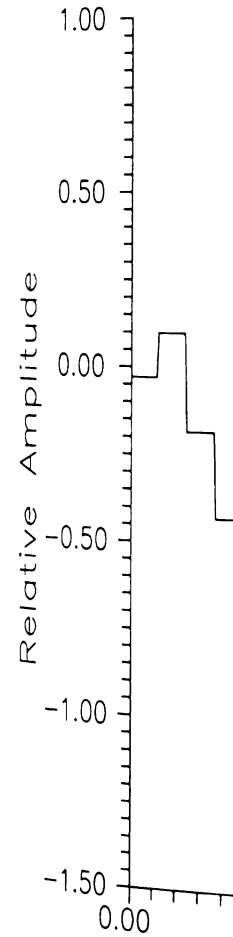

Figure 4.11 Constructed
designed to

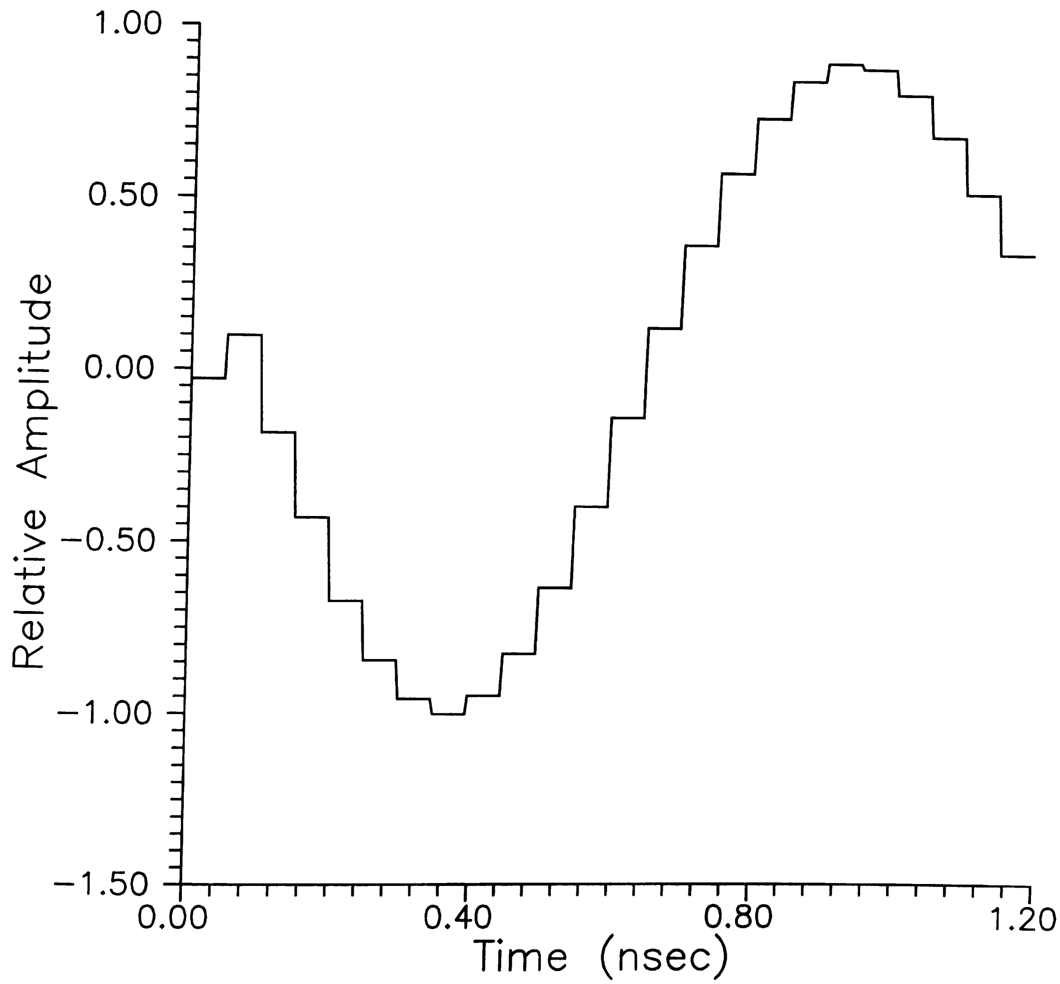

Figure 4.11 Constructed CRTW for scattered field from Stokes surface. CRTW designed to eliminate the surface clutter only.

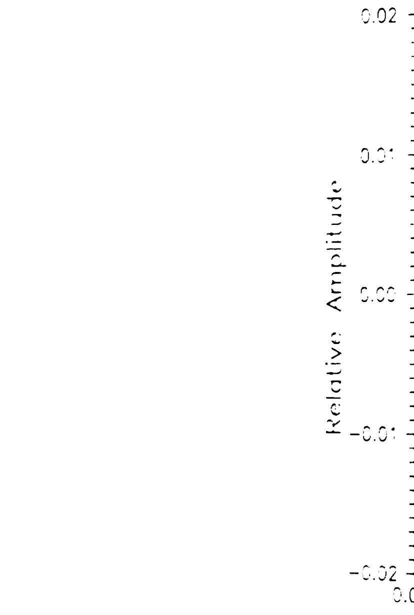

Figure 4.12 Convolution
eliminate th

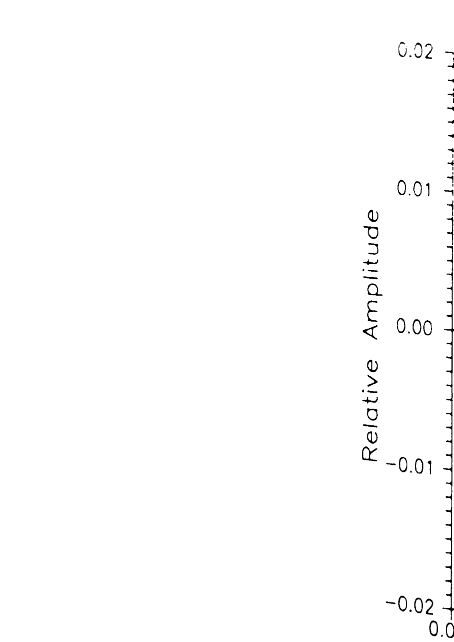

Figure 4.13 Convolution
designed to

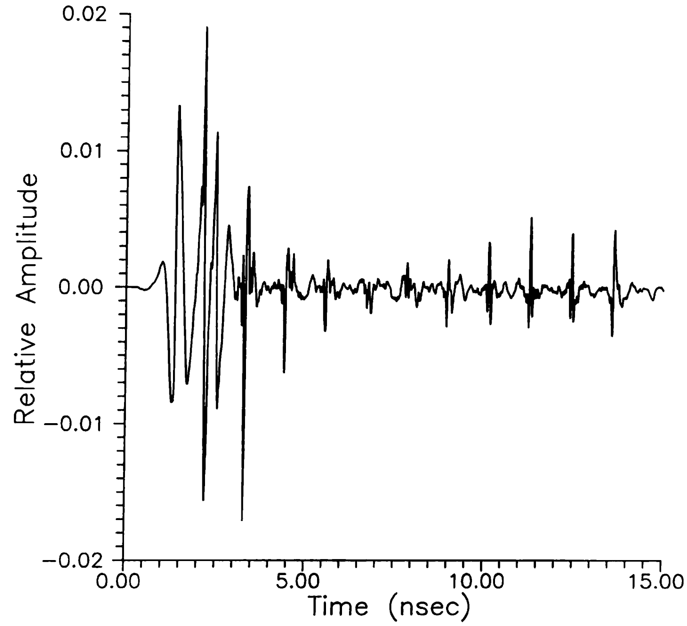

Figure 4.12 Convolution of CRTW with surface return only. CRTW designed to eliminate the surface clutter only.

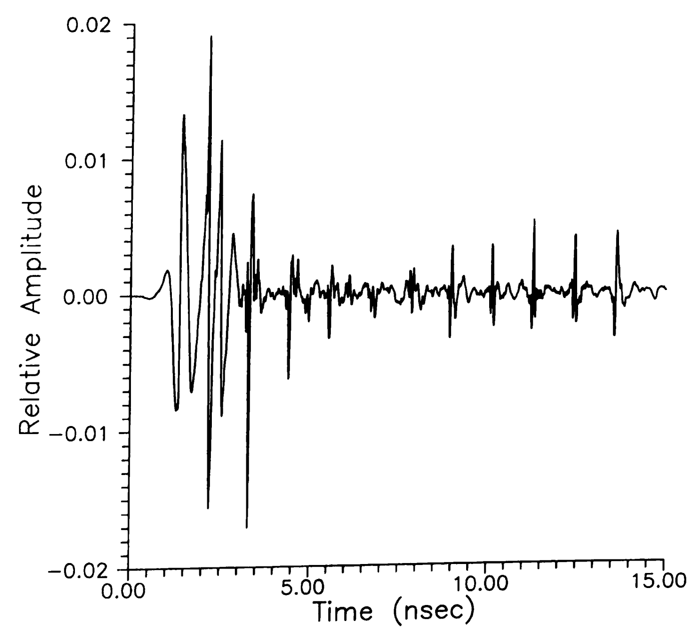

Figure 4.13 Convolution ratio of CRTW with clutter and target return. CRTW designed to eliminate the surface clutter only.

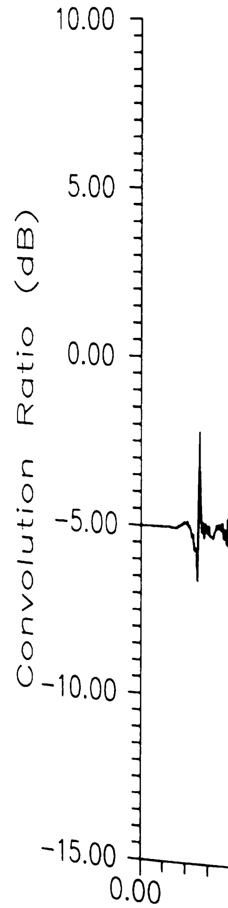

Figure 4.14 Convolution
the surface

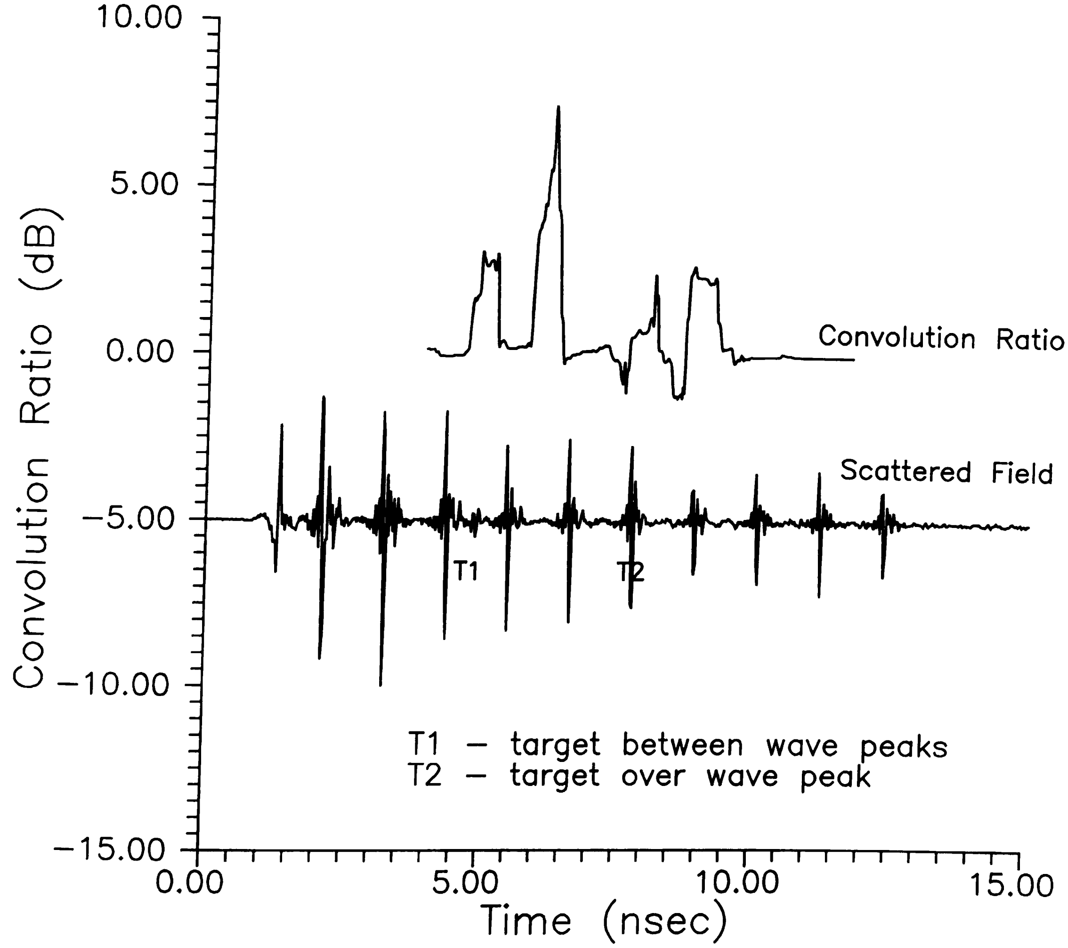

Figure 4.14 Convolution energy ratio for Stokes surface. CRTW designed to eliminate the surface clutter only.

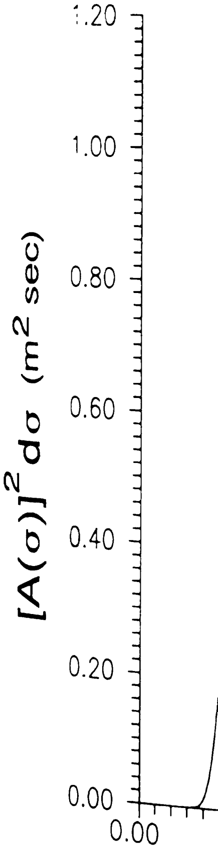

Figure 4.15 Neumann s

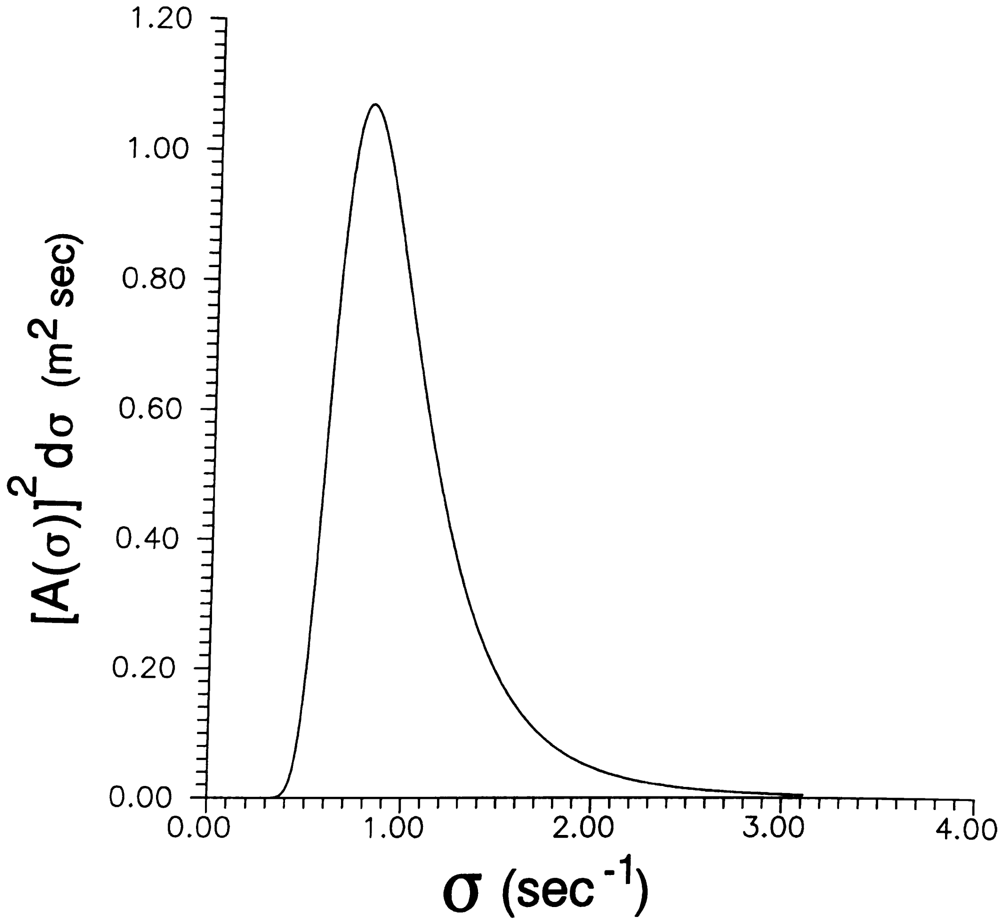

Figure 4.15 Neumann spatial frequency spectrum.

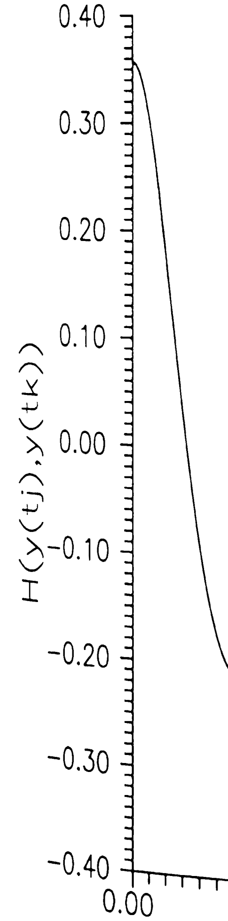

Figure 4.16 Covariance
20 knot wi

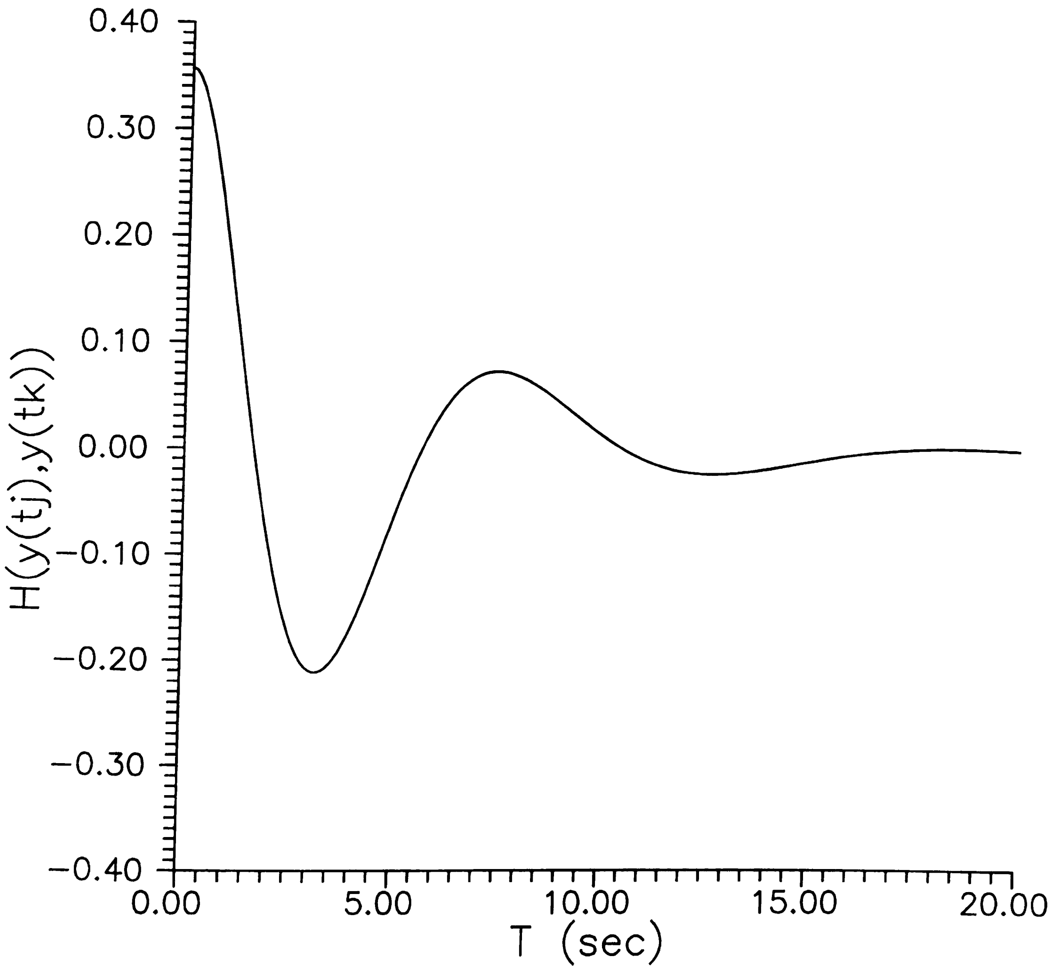

Figure 4.16 Covariance distribution generated using Neumann frequency spectrum with 20 knot winds.

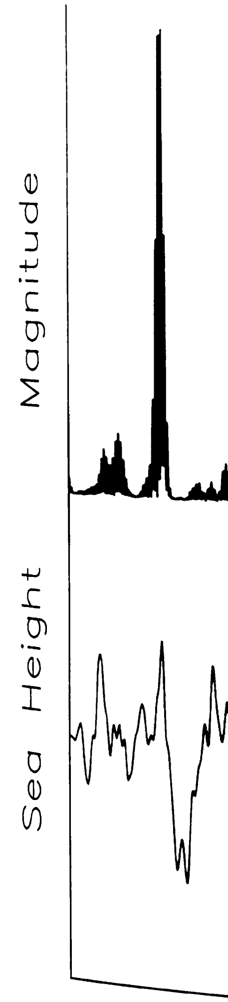

Figure 4.17 Absolute
stochastica

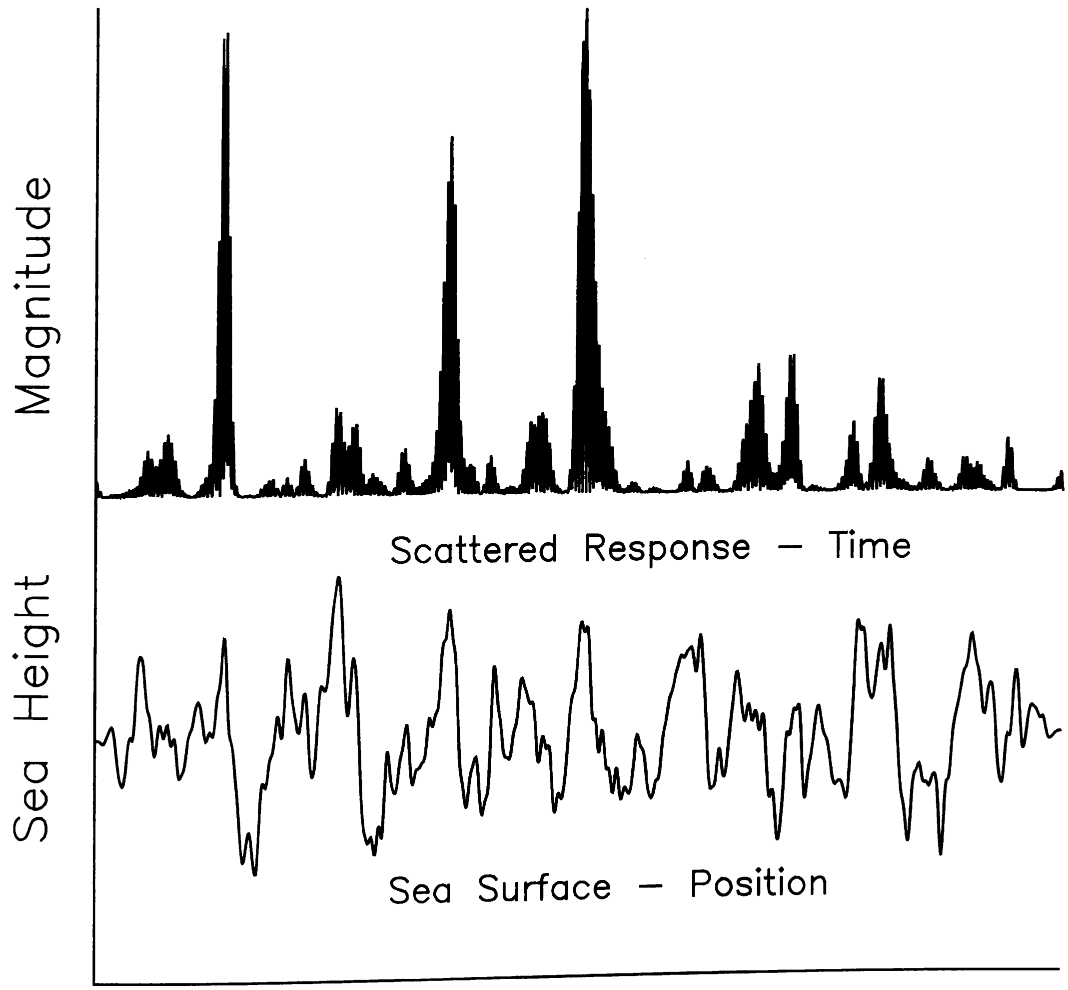

Figure 4.17 Absolute value of typical band-limited sea clutter return from stochastically-generated sea surface. Sea height is not to scale.

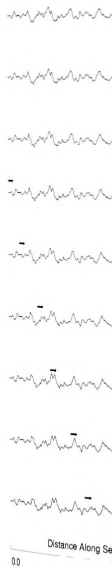

Figure 4.18 Profiles fo
energy rat
spatial pos

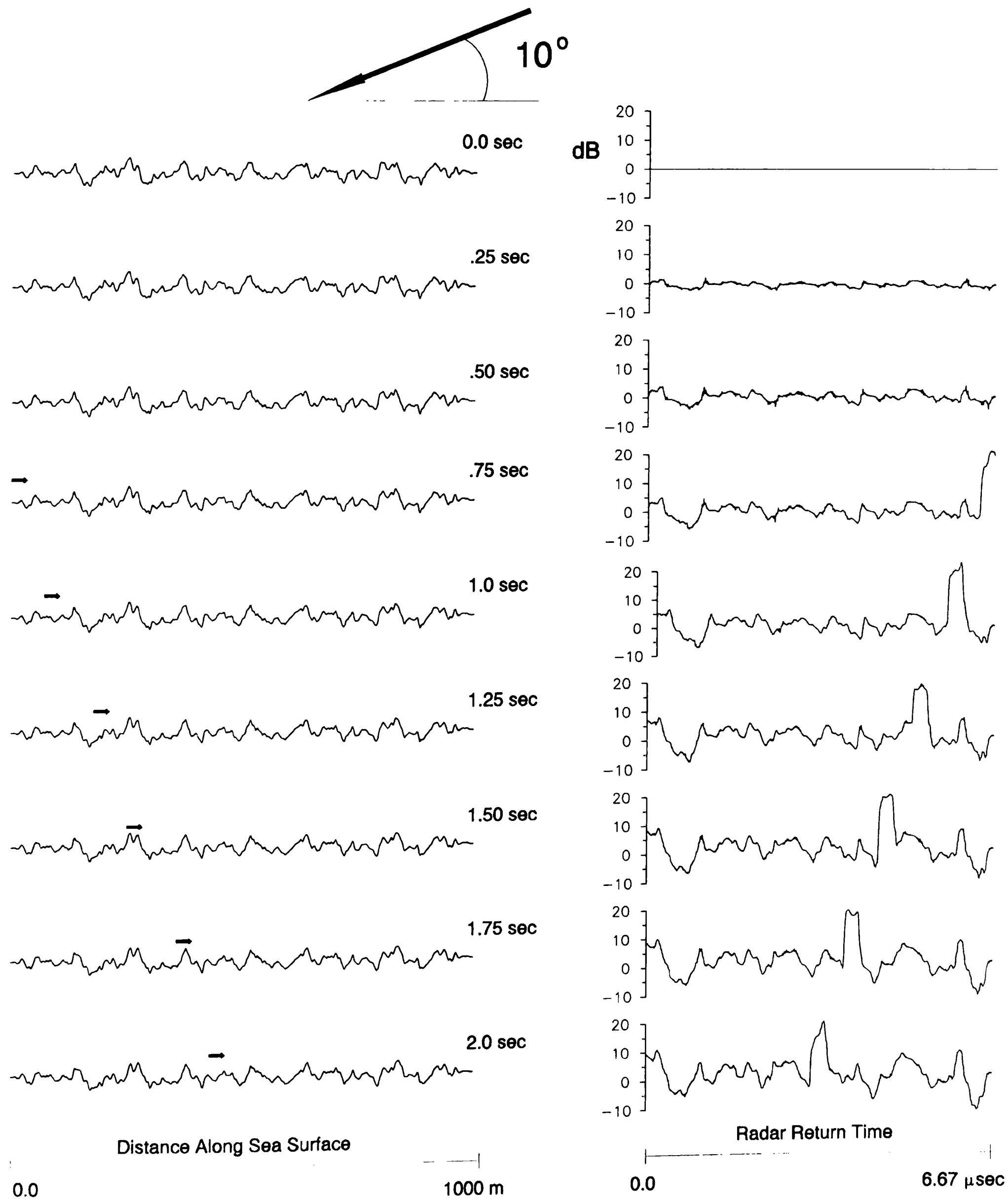

Figure 4.18 Profiles for an evolving stochastically-generated sea surface, and computed energy ratios for Phoenix missile/clutter combination. Arrow indicates spatial position of the missile.

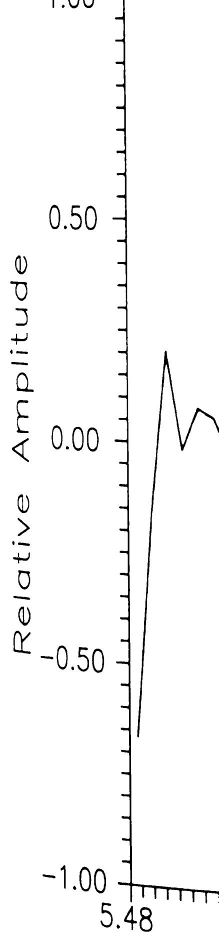

Figure 4.19 Surface res
response.

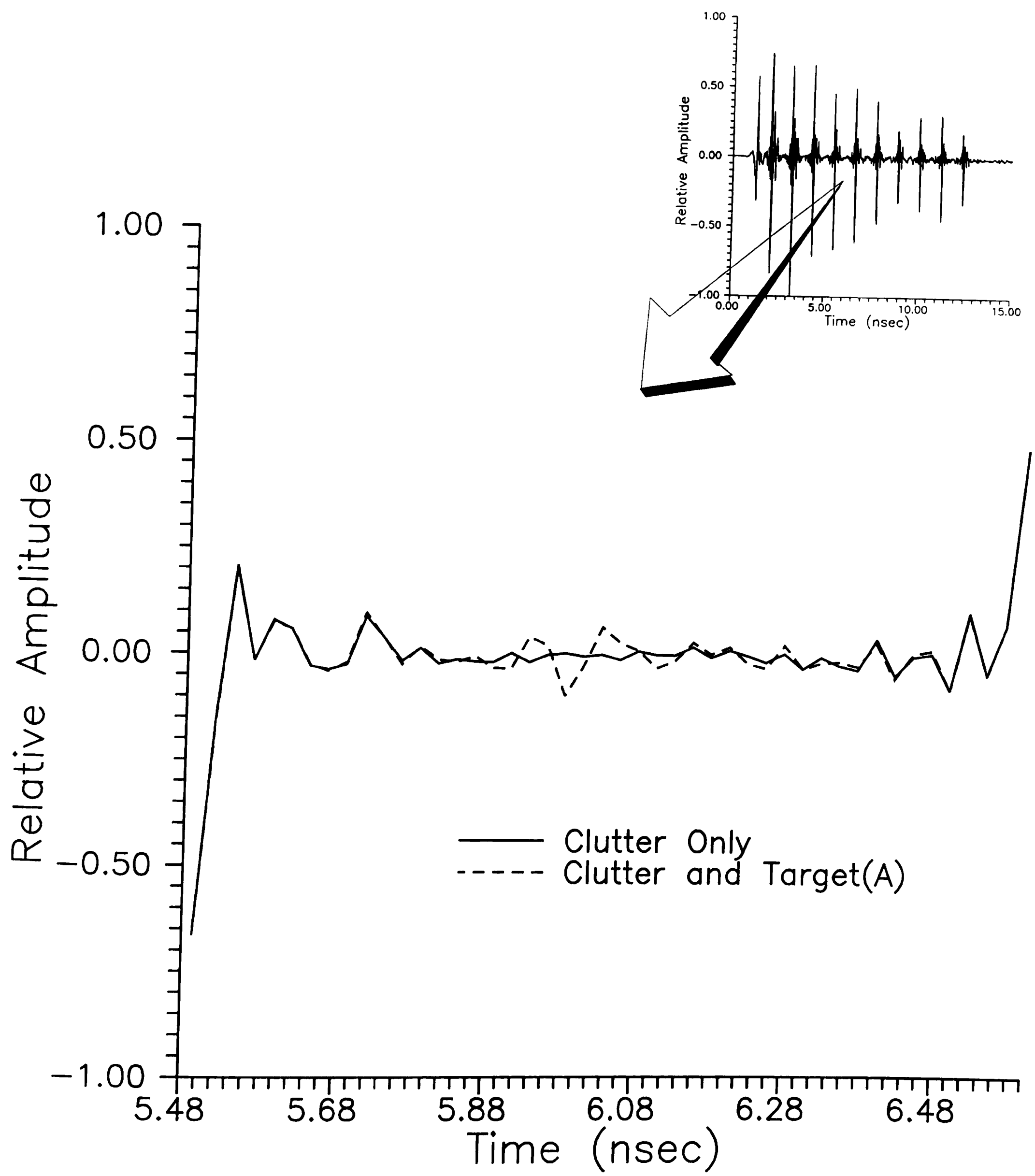

Figure 4.19 Surface response constructed by adding the missile response to the clutter response.

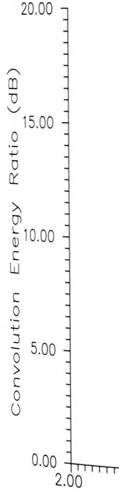

Figure 4.20 Convolutio

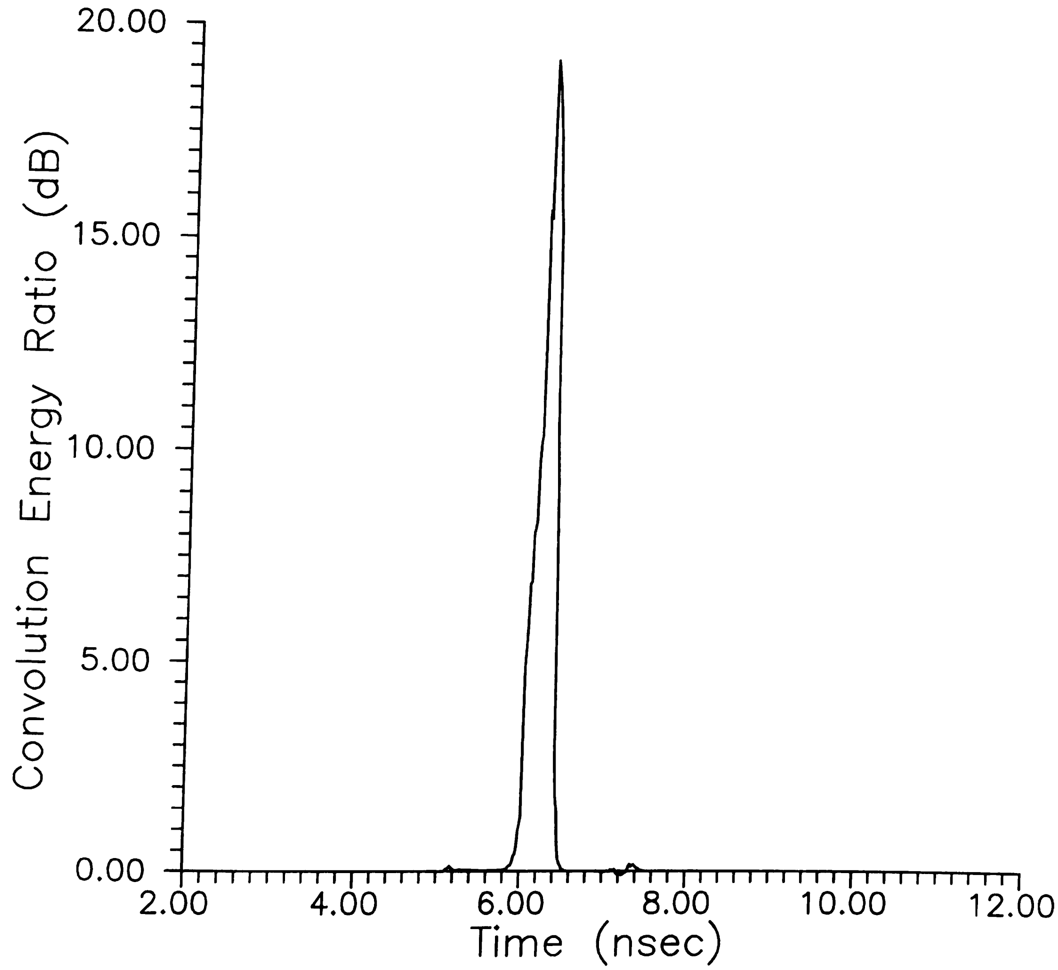

Figure 4.20 Convolution energy ratio for an energy width Δ = .5 nsec.

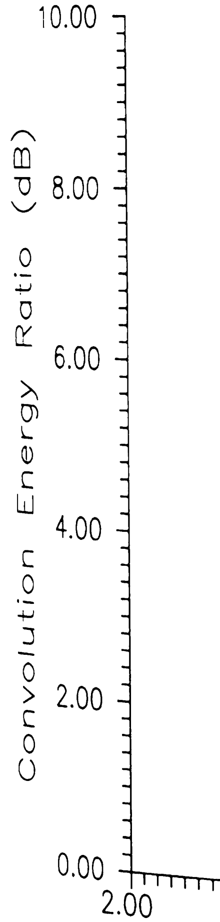

Figure 4.21 Convoluti

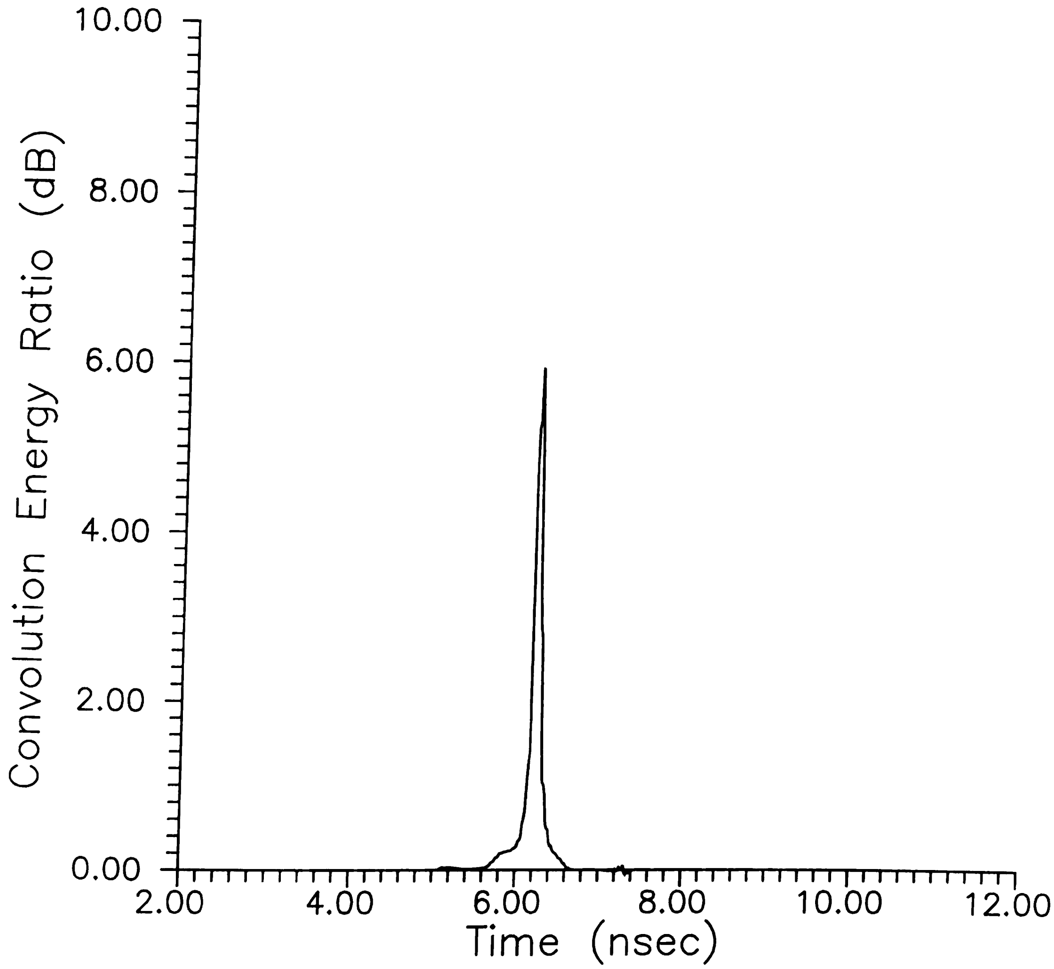

Figure 4.21 Convolution energy ratio for energy window width Δ = .8 nsec.

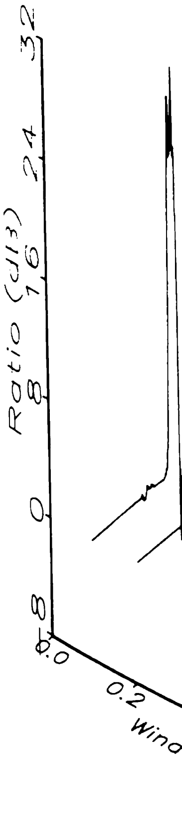

Figure 4.22 Convoluti

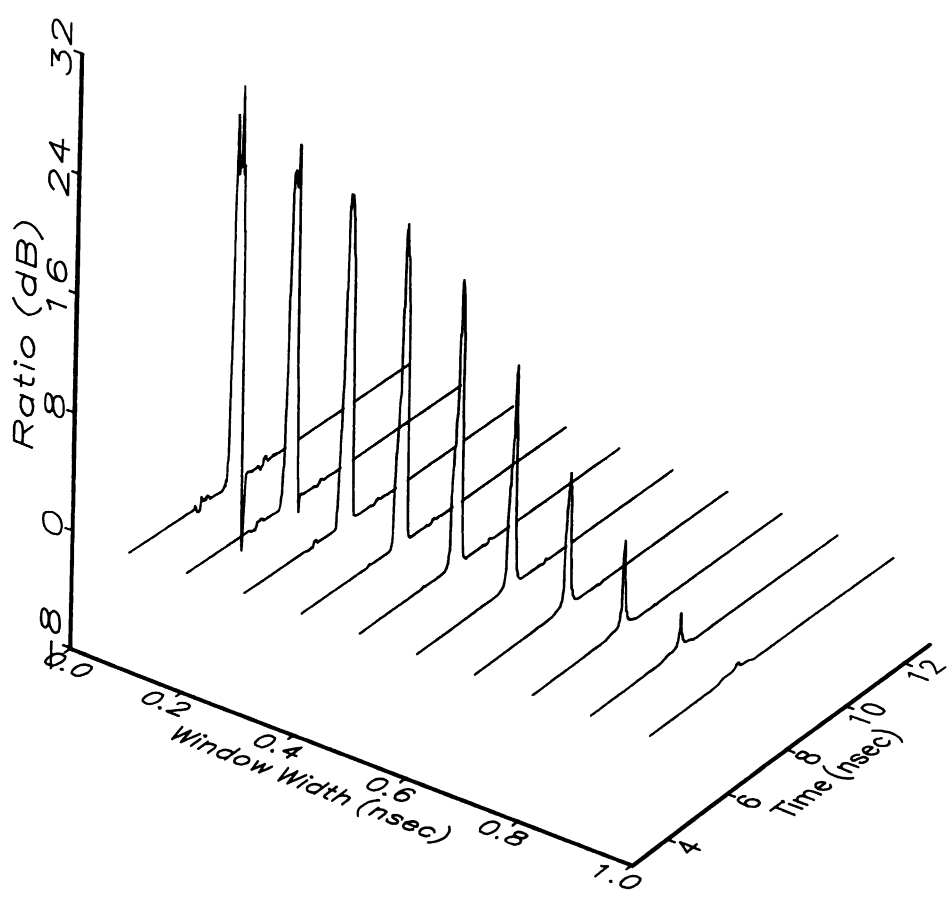

Figure 4.22 Convolution energy ratio as a function of window width and time.

Figure 4.23 Two sea su
different ti

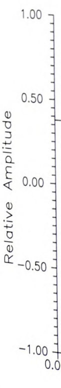

Figure 4.24 CRTW co

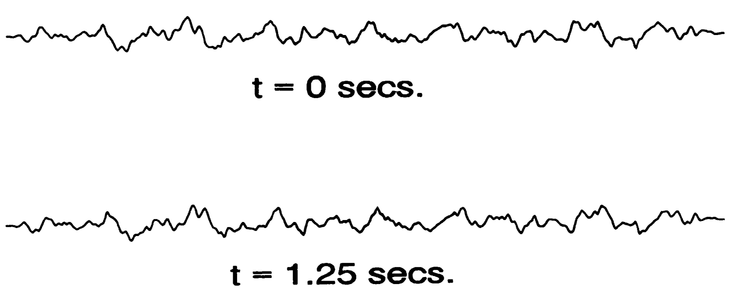

Figure 4.23 Two sea surfaces generated from the wind driven Kinsman model at two different times.

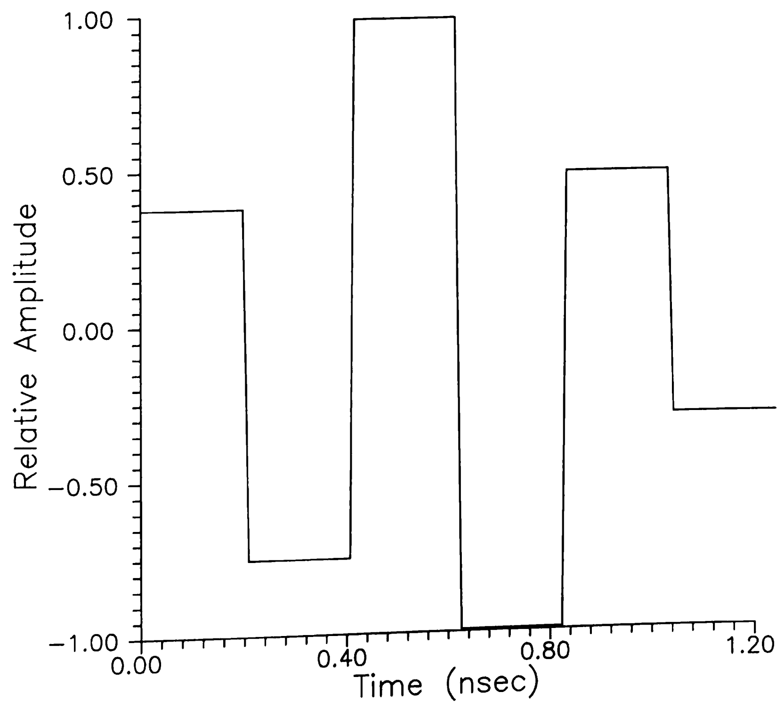

Figure 4.24 CRTW construction for initial sea surface.

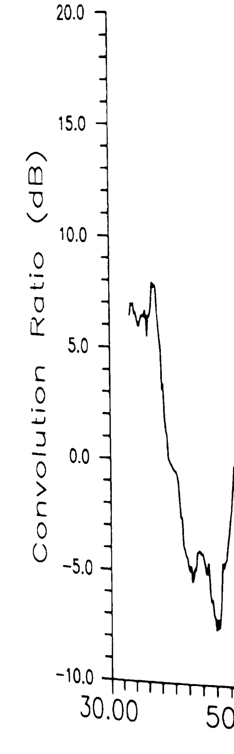

Figure 4.25 Convoluti
for a winc

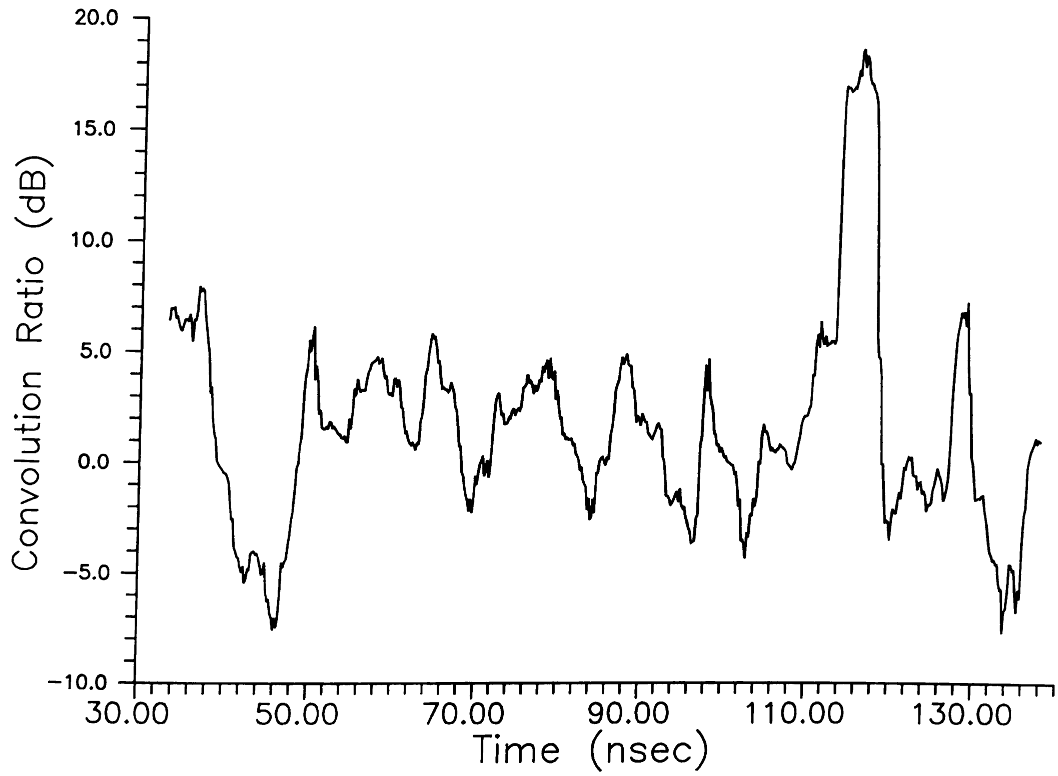

Figure 4.25 Convolution energy ratio (dB) detection diagram for a realistic sea surface for a window width of 4 nsec.

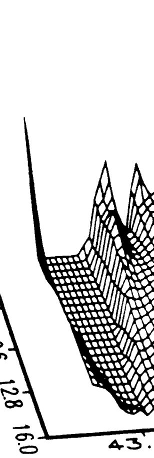

Figure 4.26 Convoluti
size and ti

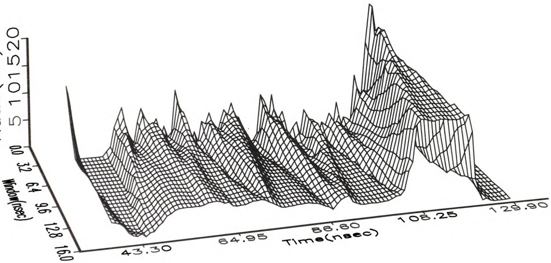

Figure 4.26 Convolution energy ratio for Kinsman sea surface as a function of window size and time.

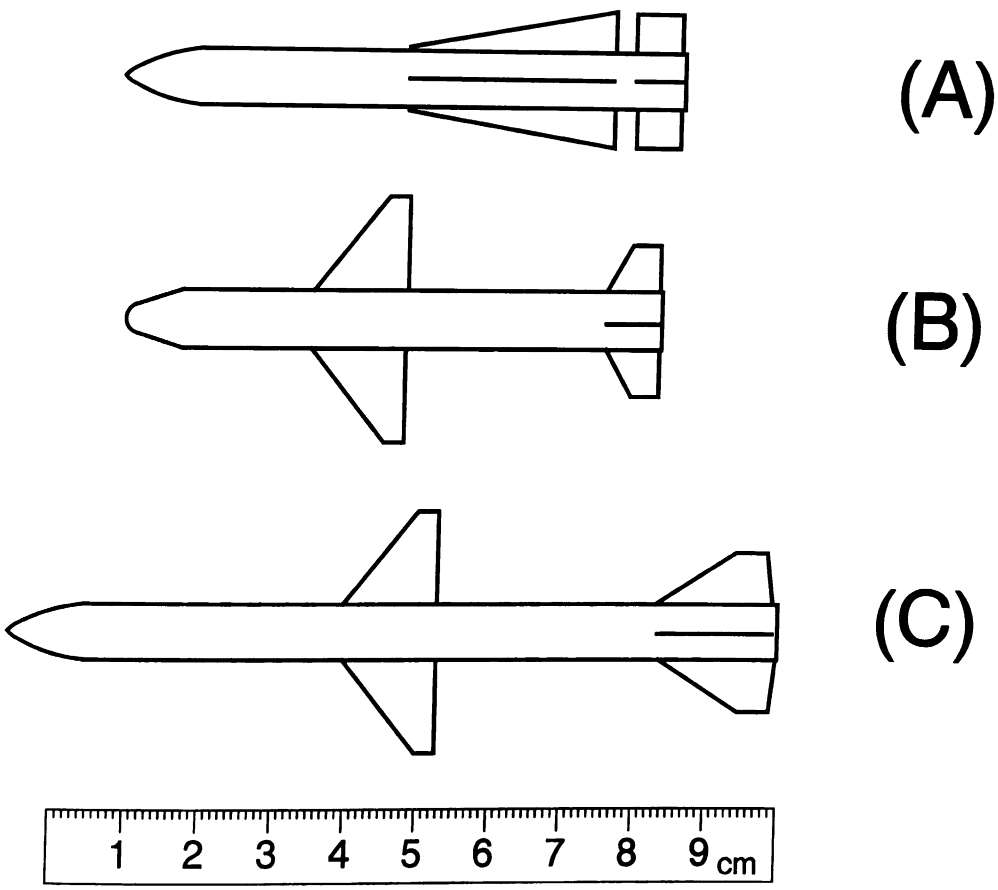

Figure 4.27 Missile models used in CRTW study.

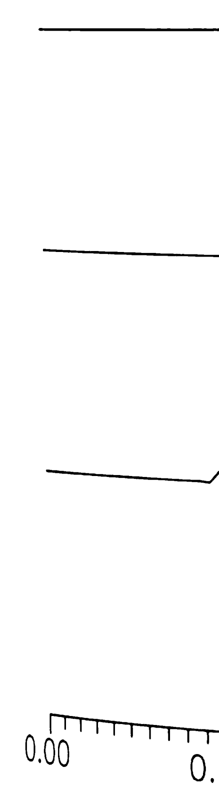

Figure 4.28 Missile sc

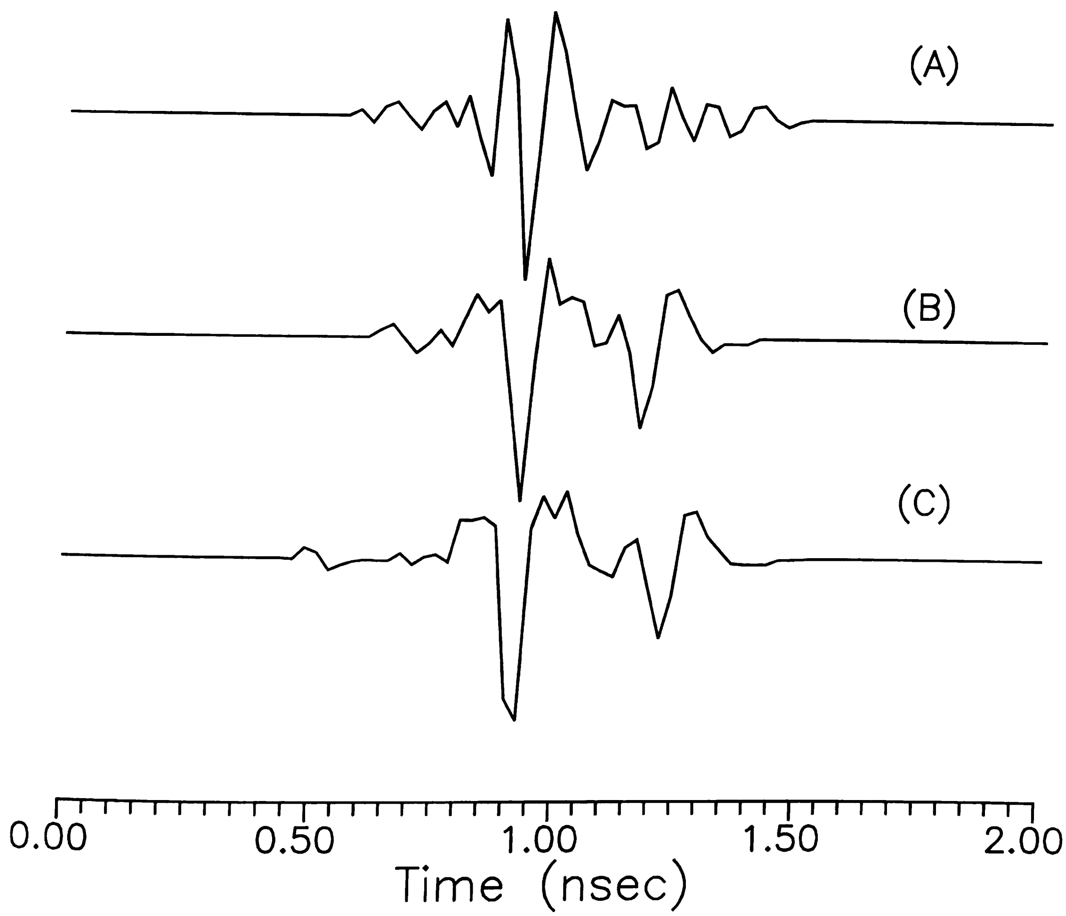

Figure 4.28 Missile scattering in the time domain.

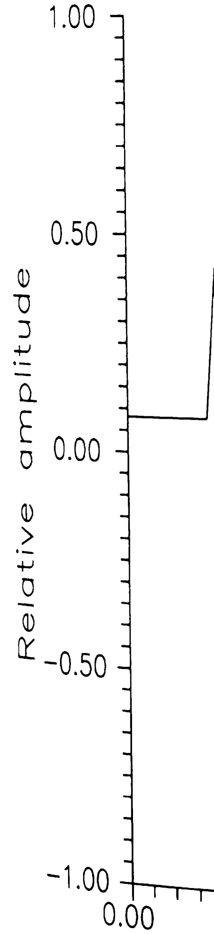

Figure 4.29 CRTW c

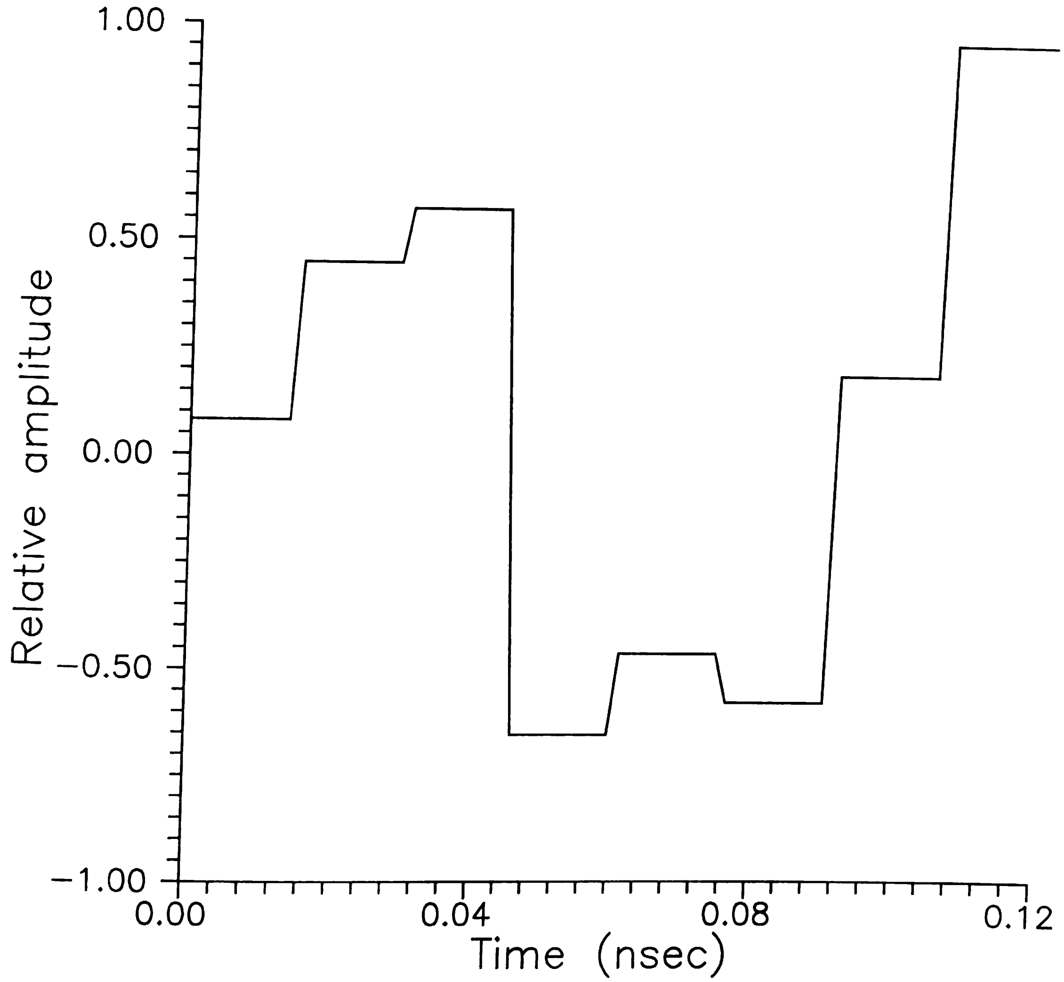

Figure 4.29 CRTW corresponding to missile type A.

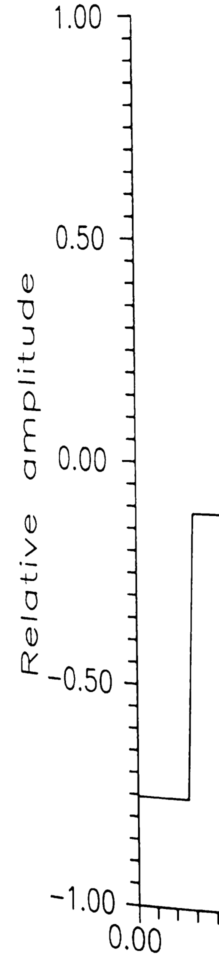

Figure 4.30 CRTW co

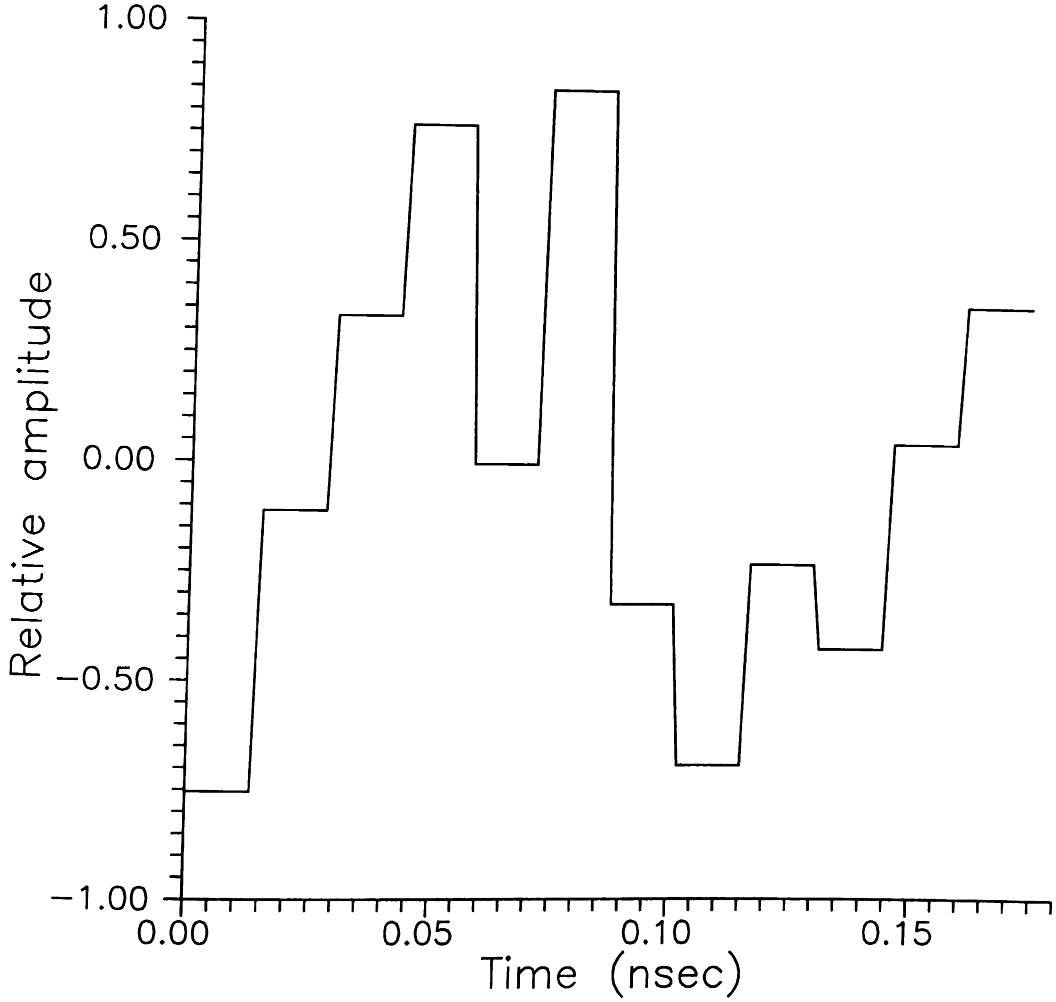

Figure 4.30 CRTW corresponding to missile type B.

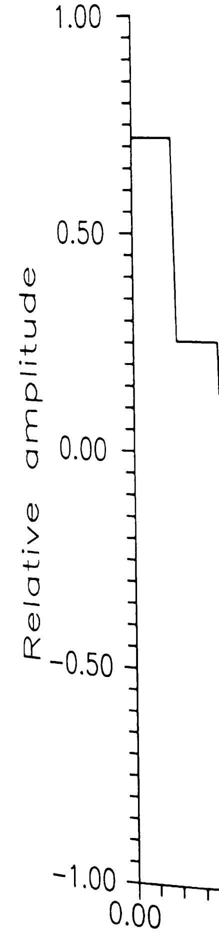

Figure 4.31 CRTW c

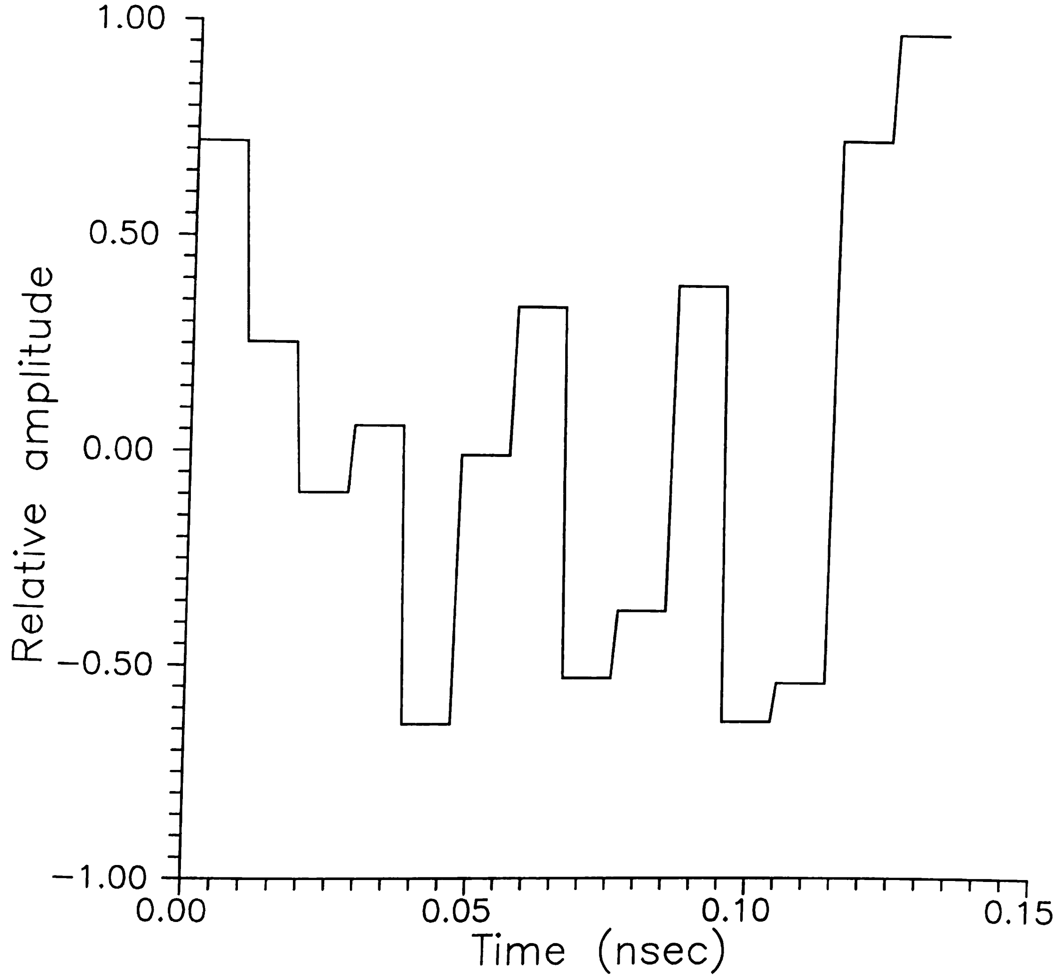

Figure 4.31 CRTW corresponding to missile type C.

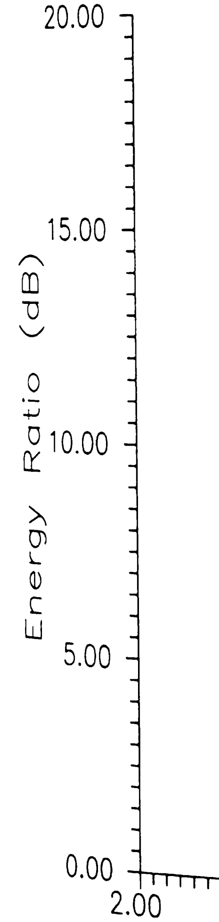

Figure 4.32 Convolut
designed

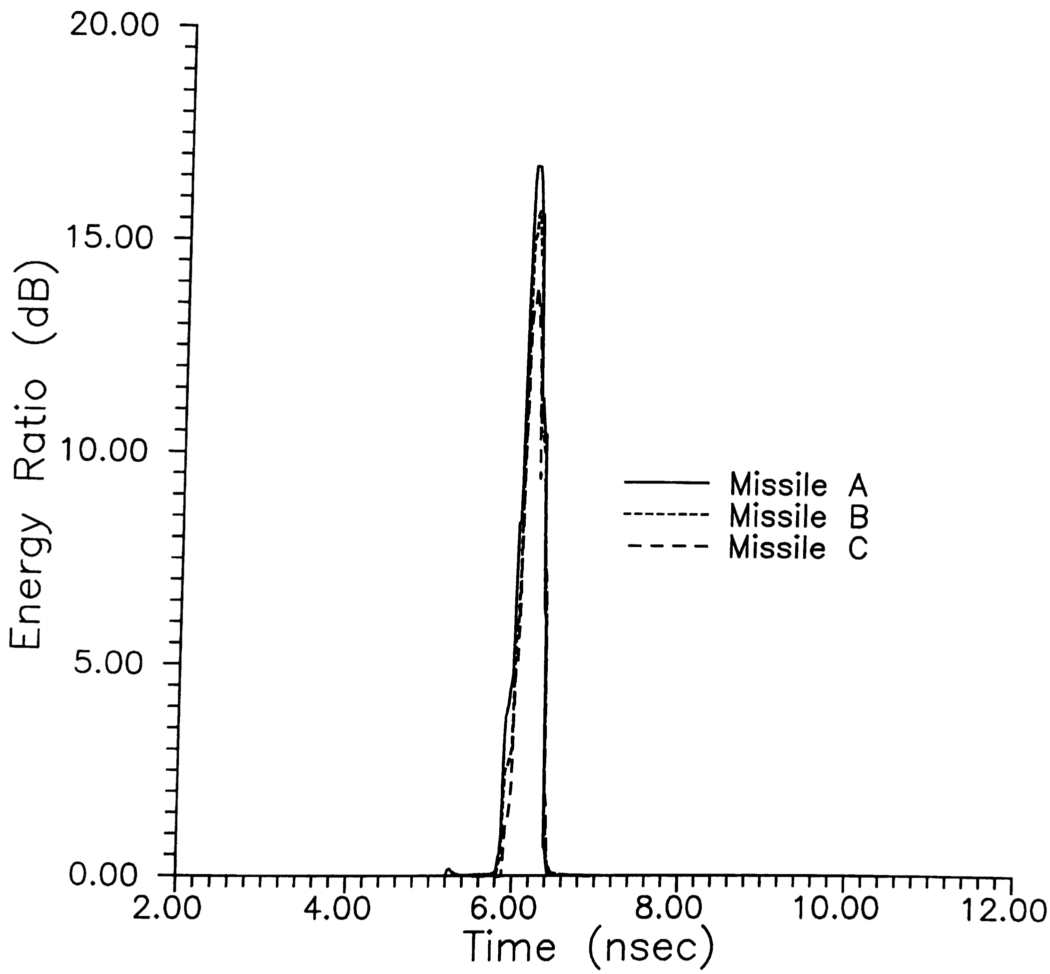

Figure 4.32 Convolution energy ratio response for each missile using a CRTW designed for missile A.

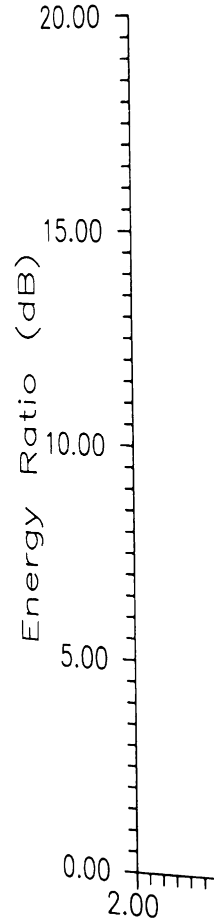

Figure 4.33 Convolut
missile ty

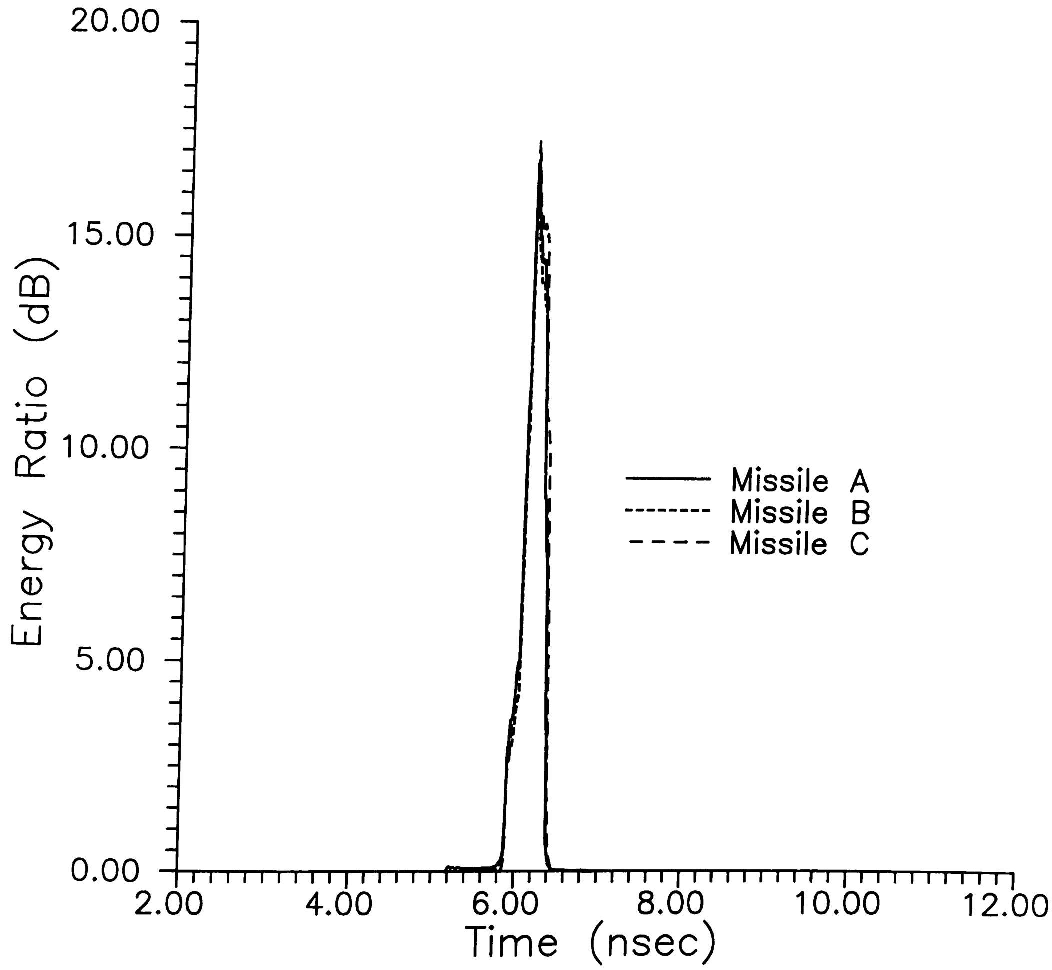

Figure 4.33 Convolution energy ratio for each missile using a CRTW designed for missile type B.

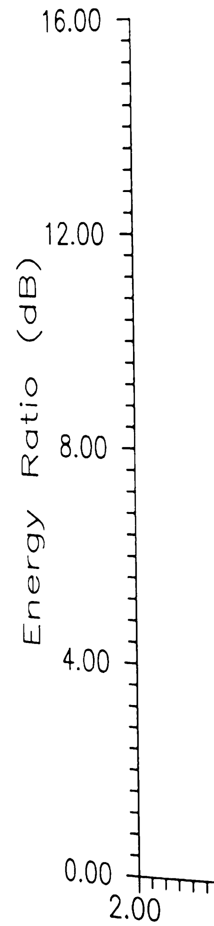

Figure 4.34 Convolut
missile t

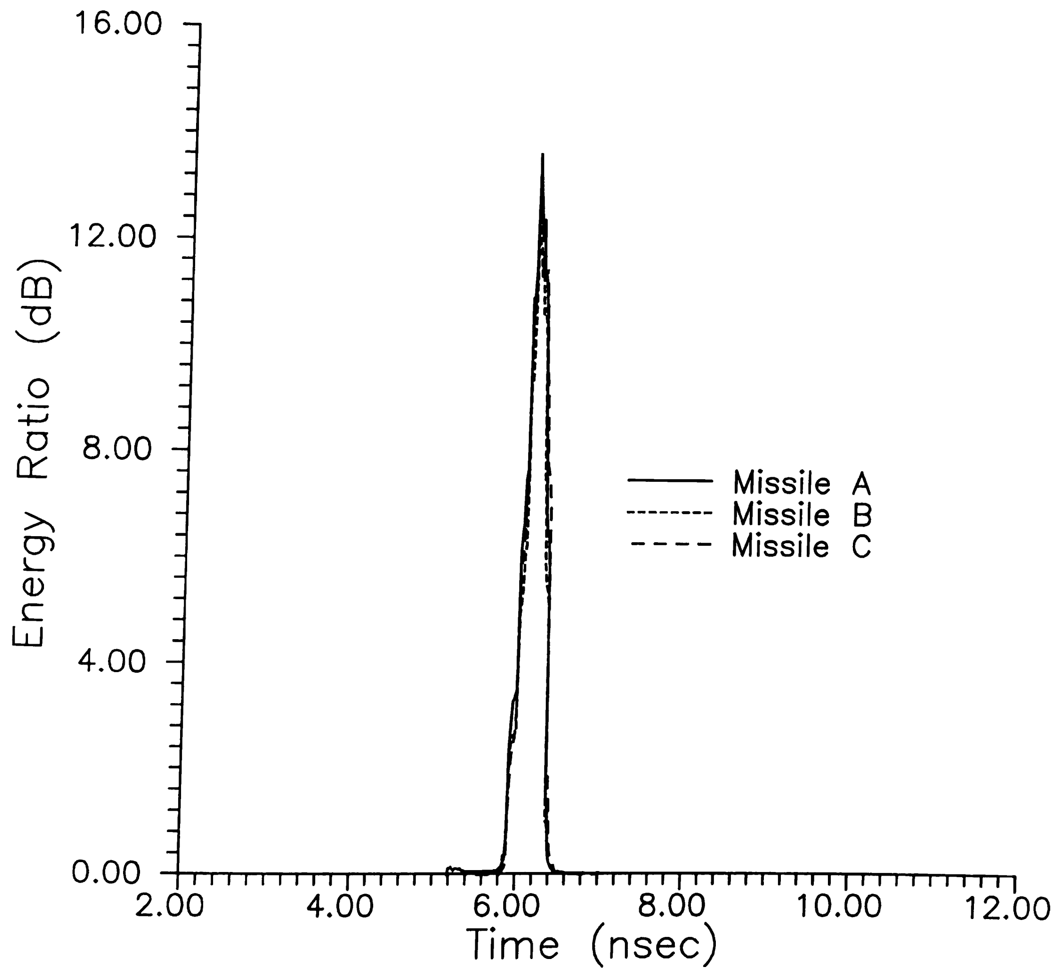

Figure 4.34 Convolution energy ratio for each missile type using a CRTW designed for missile type C.

Figure 4.35 Scatterin
(b) relati

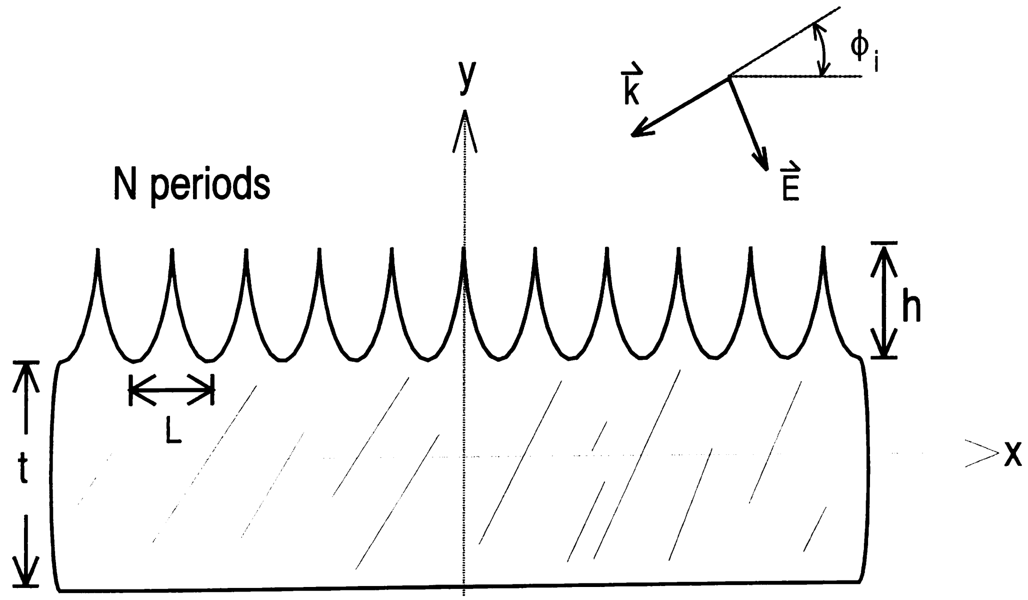

(a)

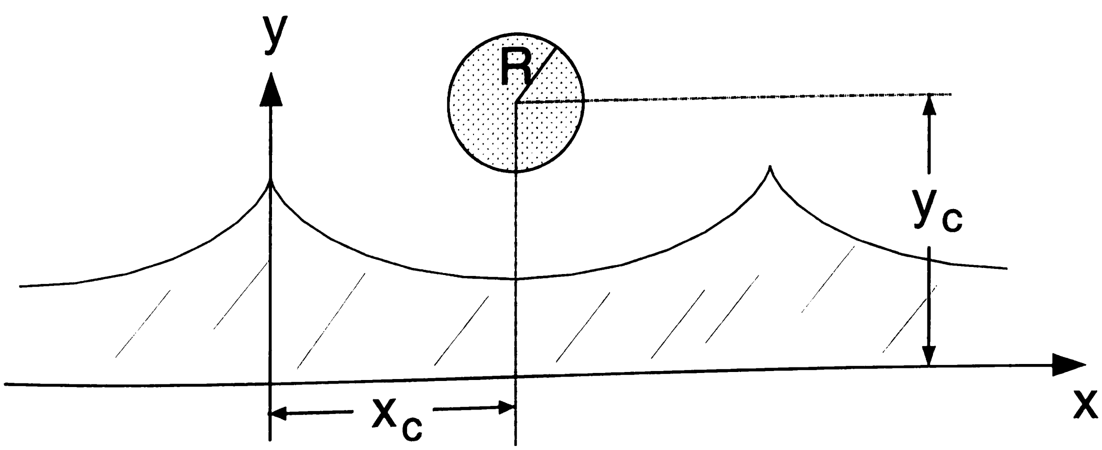

(b)

Figure 4.35 Scattering geometry for TM-polarization showing (a) Stoke's surface, and (b) relative position of cylinder with respect to Stoke's surface

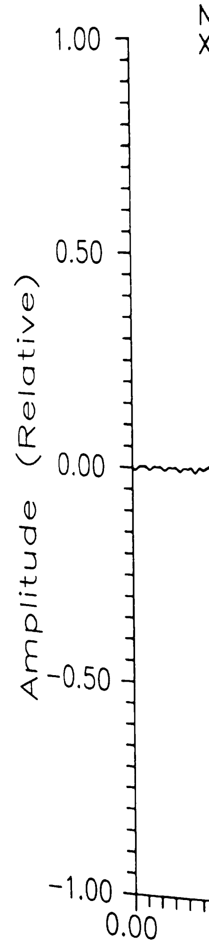

Figure 4.36 Transien
above th

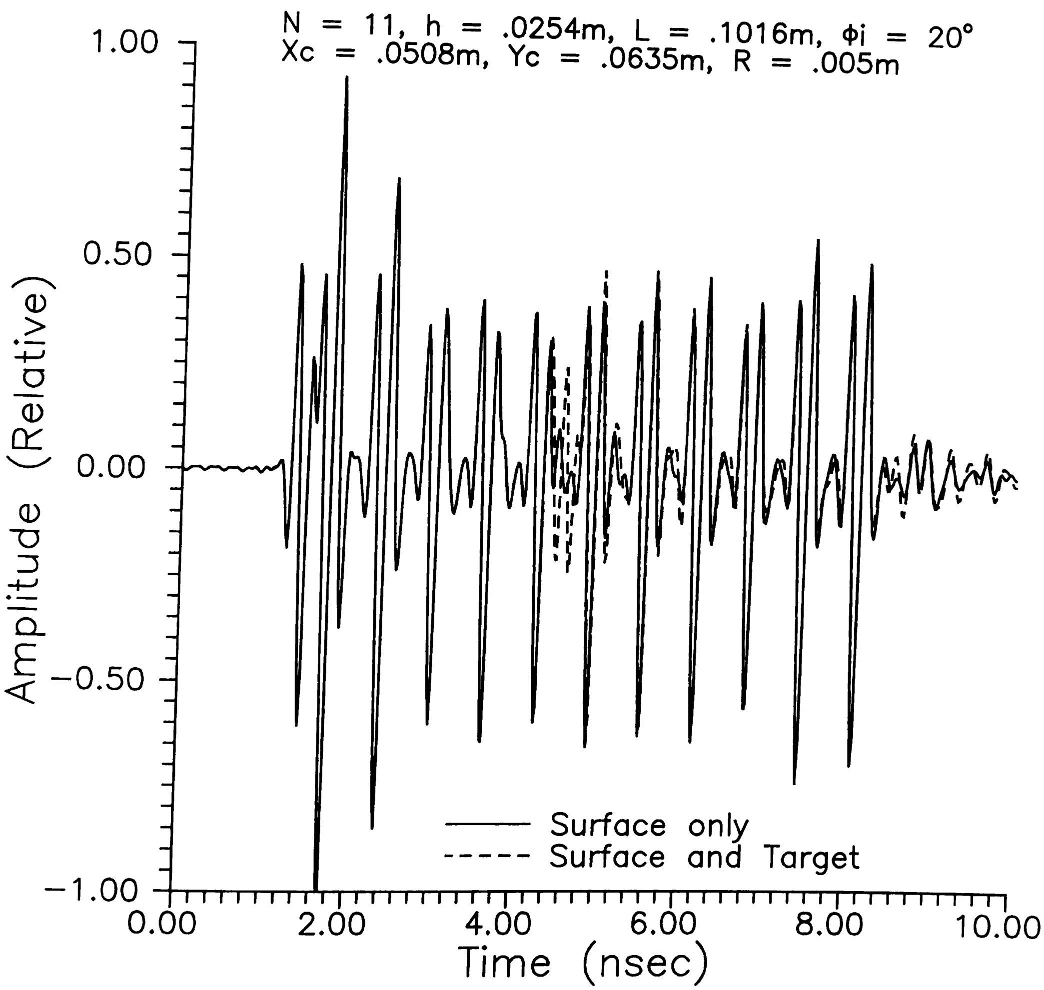

Figure 4.36 Transient scattered return from a Stoke's surface only and from a cylinder above the Stoke's surface. TCR = -5.31 dB.

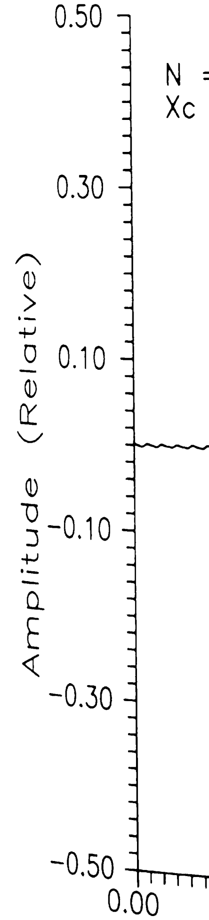

Figure 4.37 Differen
with cyl

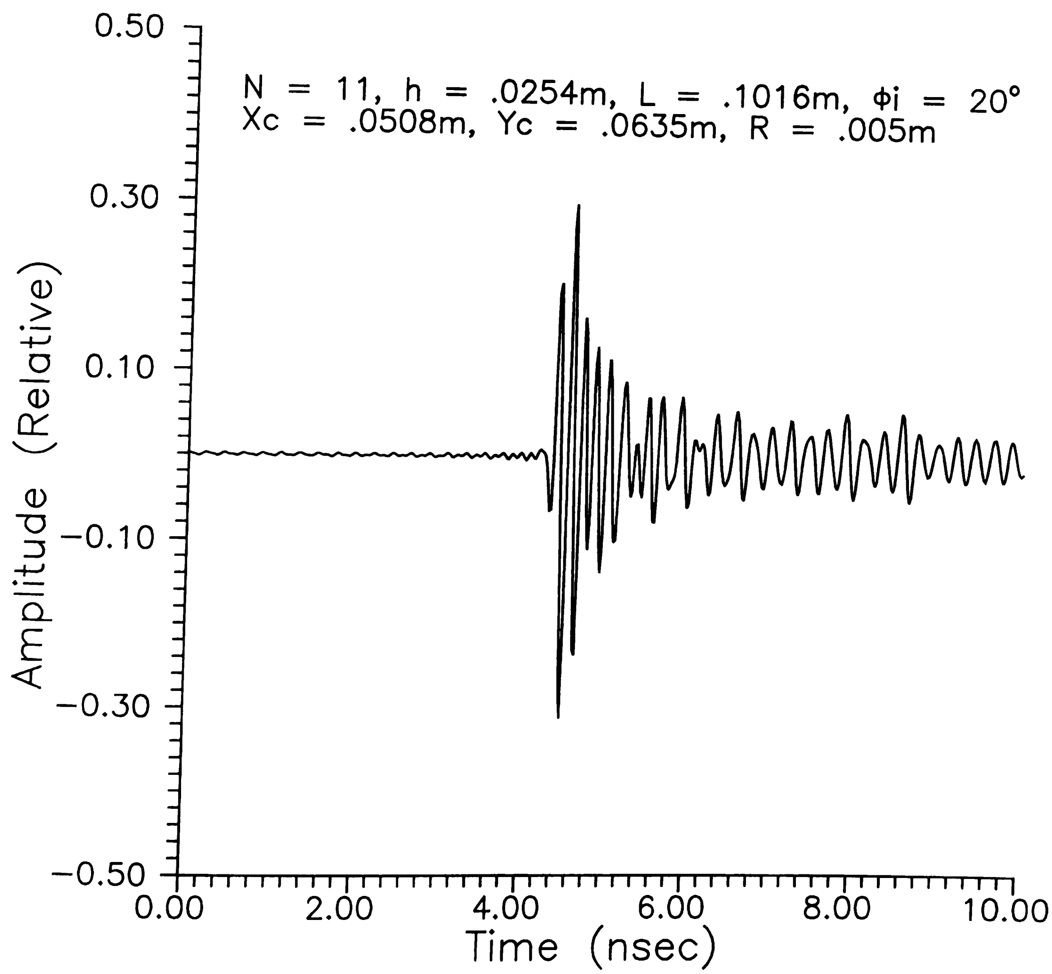

Figure 4.37 Difference between the transient scattered return from a Stoke's surface with cylinder and Stoke's surface without cylinder.

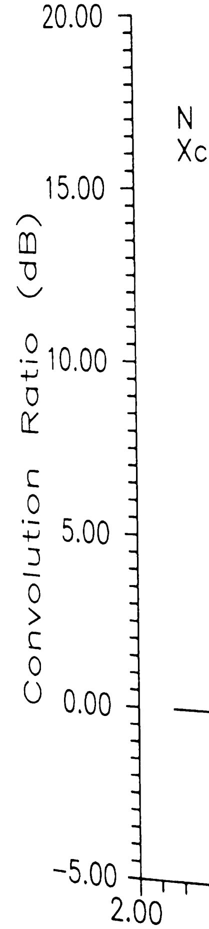

Figure 4.38 Convolu
multipat
TCR = .

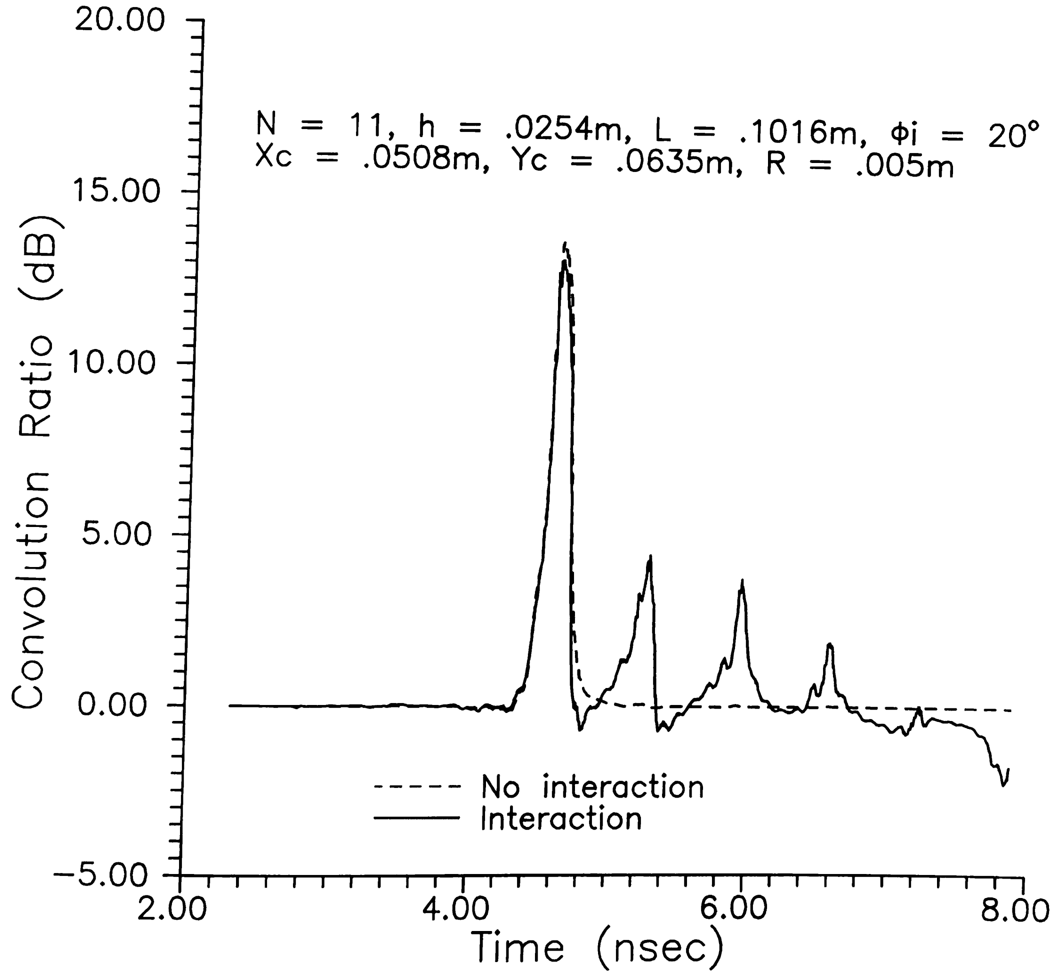

Figure 4.38 Convolution energy ratio for Stoke's surface and cylinder with no multipath effect, and Stoke's surface and cylinder with multipath effect. TCR = - 5.31 dB.

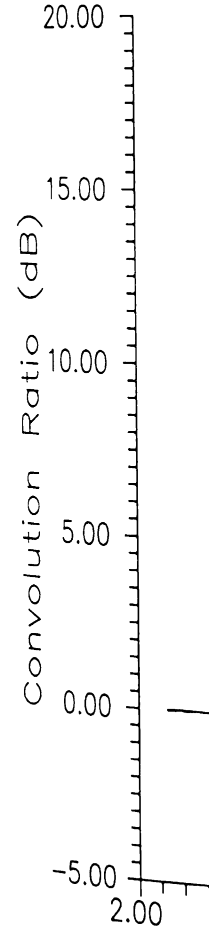

Figure 4.39 Convolu
multipat
effect.

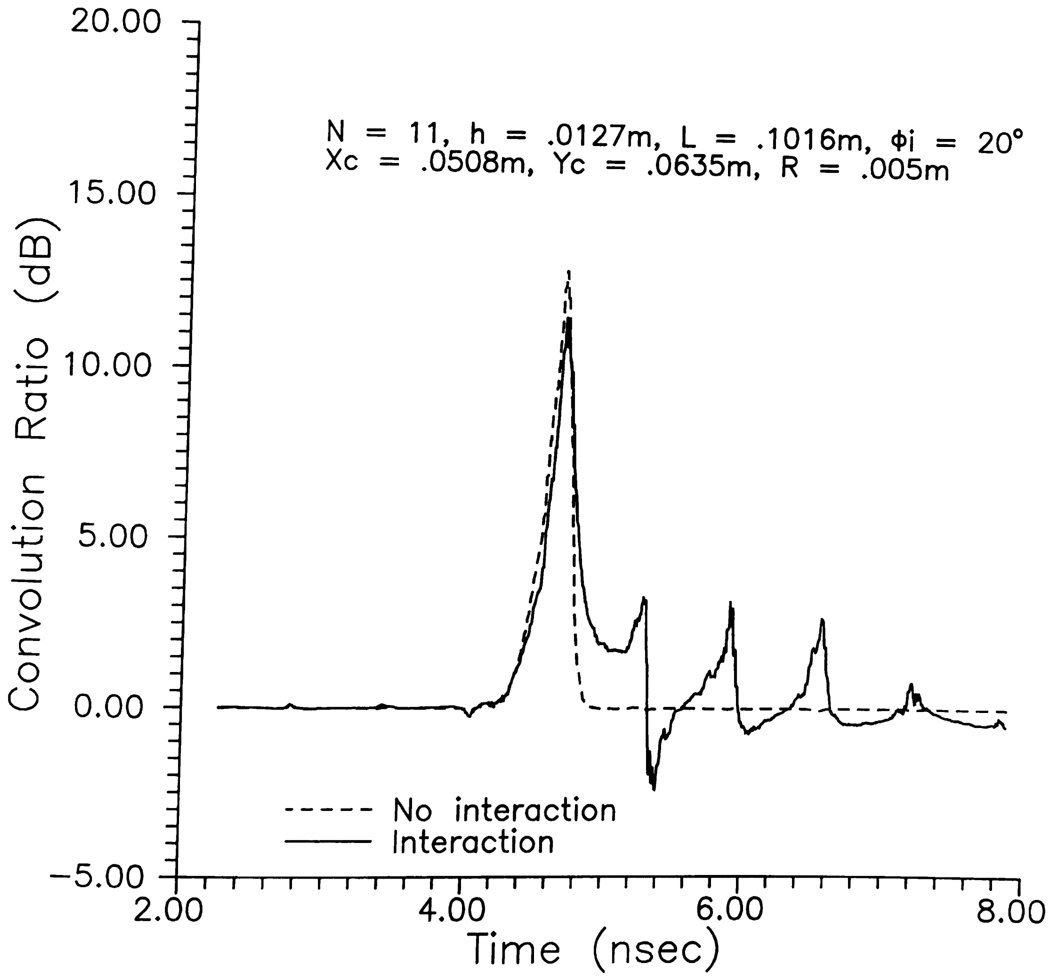

Figure 4.39 Convolution energy ratio for Stoke's surface and cylinder with no multipath effect, and Stoke's surface and cylinder with the multipath effect.

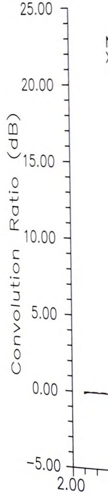

Figure 4.40 Convolu
multipat
effect.

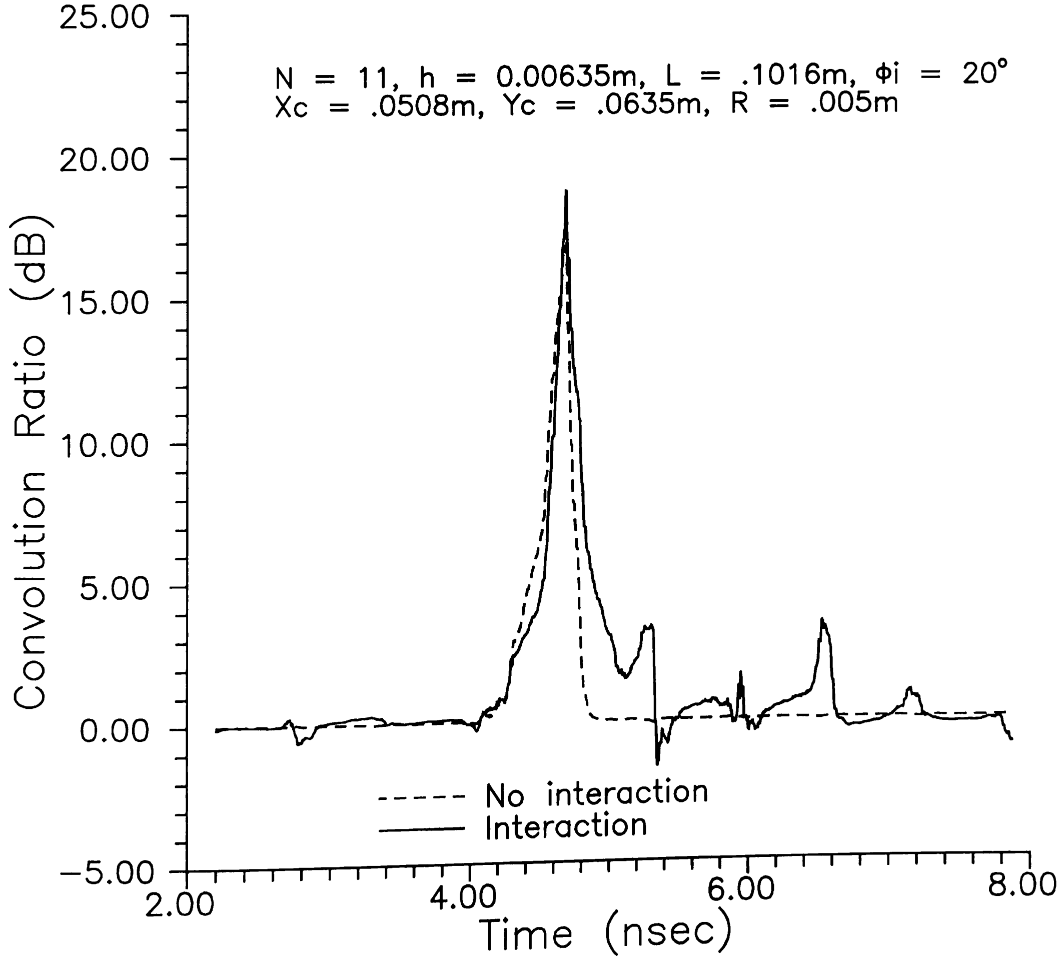

Figure 4.40 Convolution energy ratio for Stoke's surface and cylinder with no multipath effect, and Stoke's surface and cylinder with the multipath effect. TCR = -.22 dB.

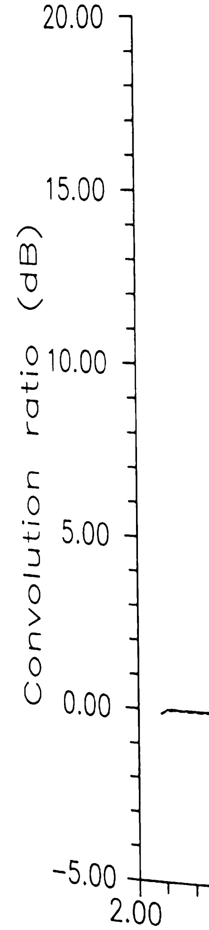

Figure 4.41 Convolu
effect a
position.

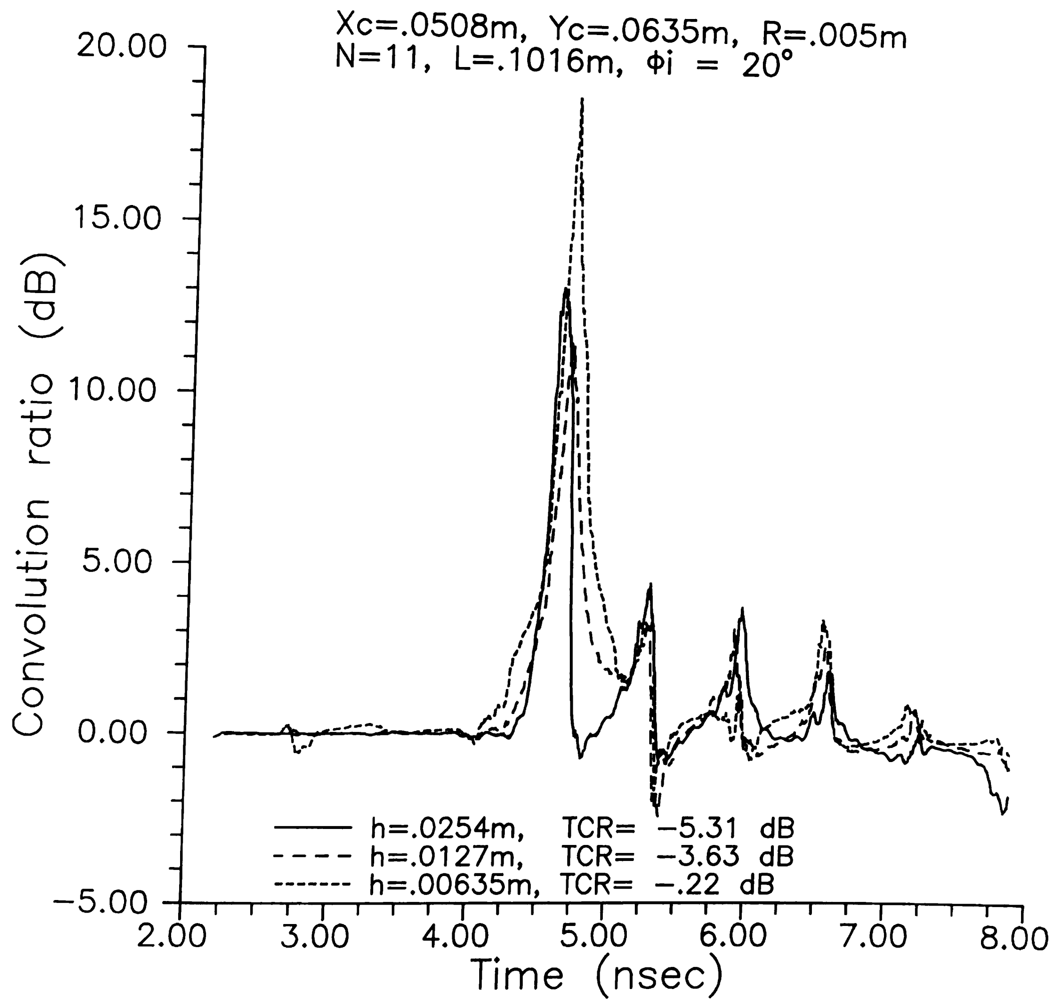

Figure 4.41 Convolution energy ratio for Stoke's surface and cylinder with multipath effect as a function of different surface heights for a fixed cylinder position.

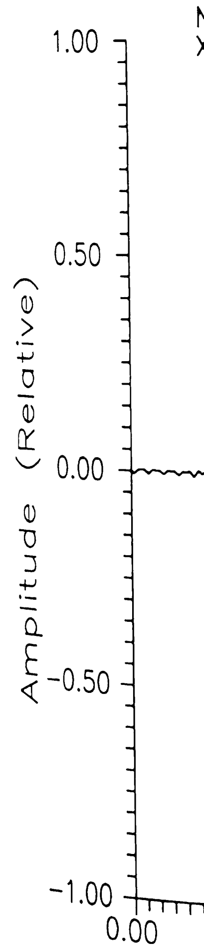

Figure 4.42 Transien
above th

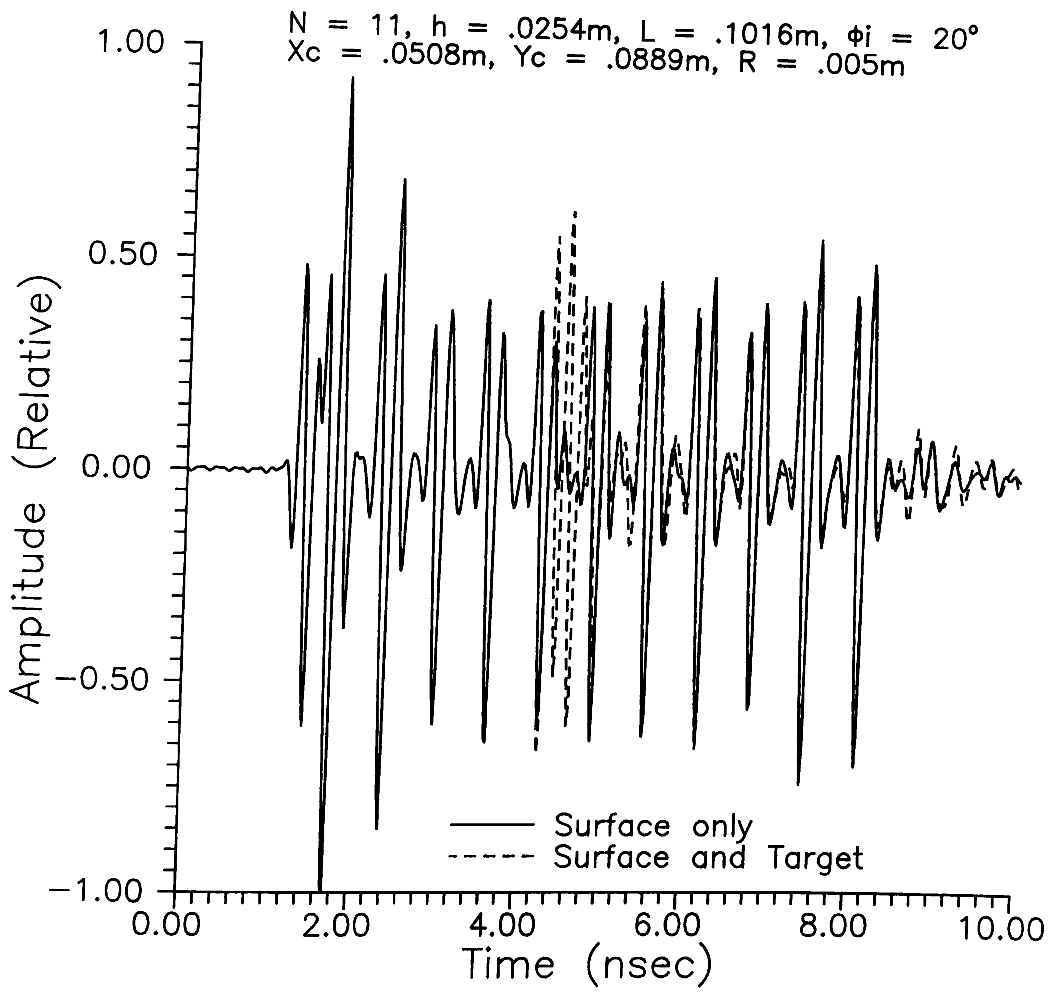

Figure 4.42 Transient scattered return from a Stoke's surface only and from a cylinder above the Stoke's surface. TCR = -5.31 dB.

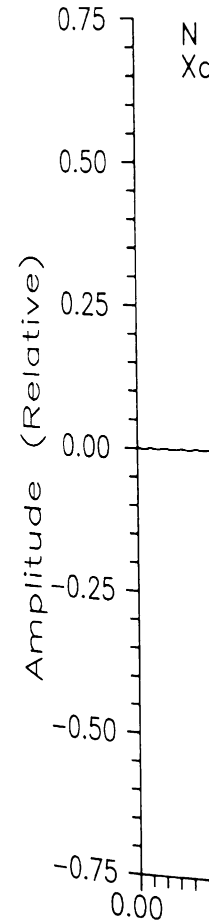

Figure 4.43 Differen
with cyl

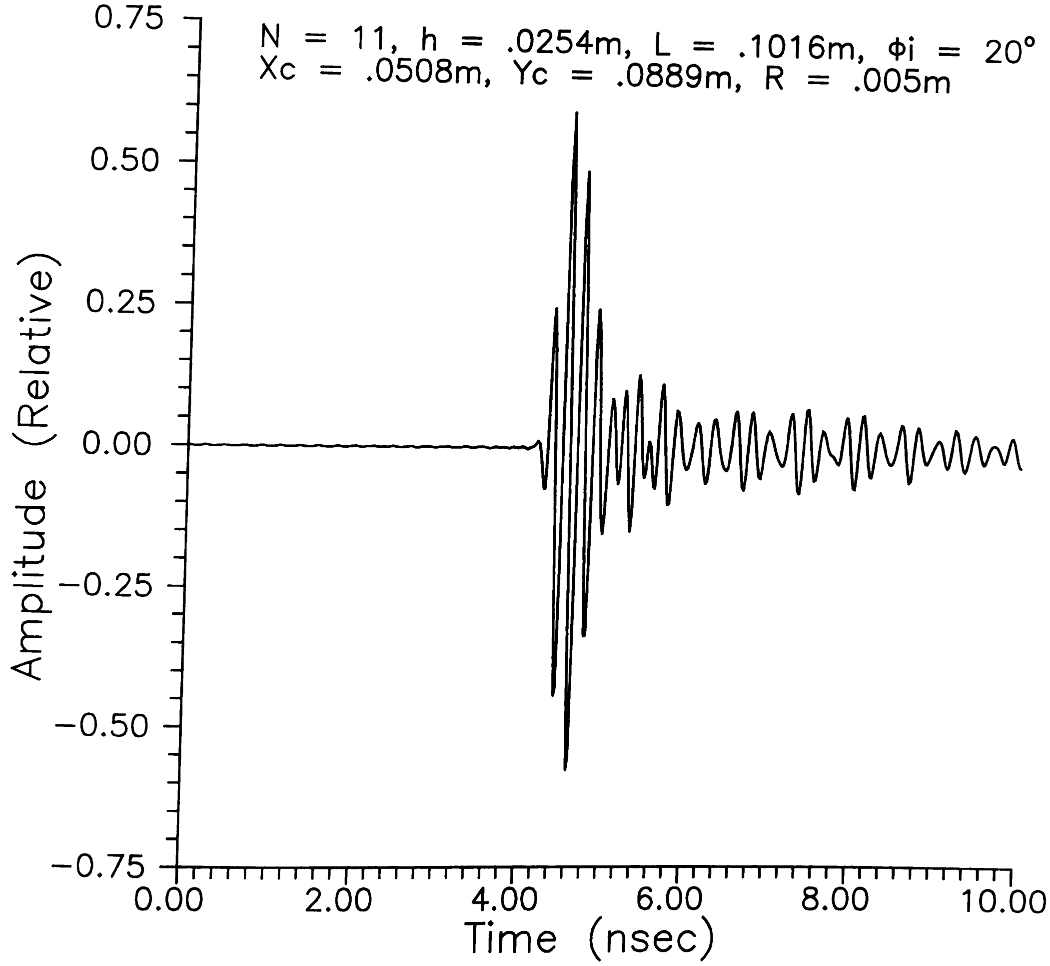

Figure 4.43 Difference between the transient scattered return from a Stoke's surface with cylinder and Stoke's surface without cylinder.

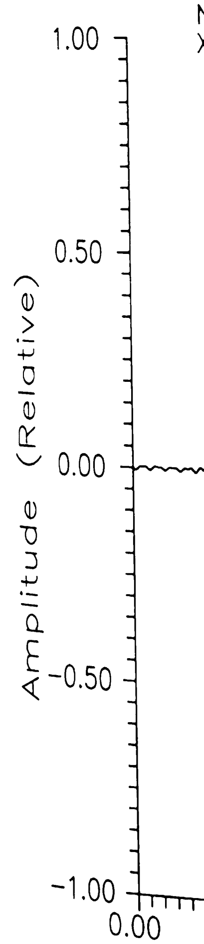

Figure 4.44 Transien
above th

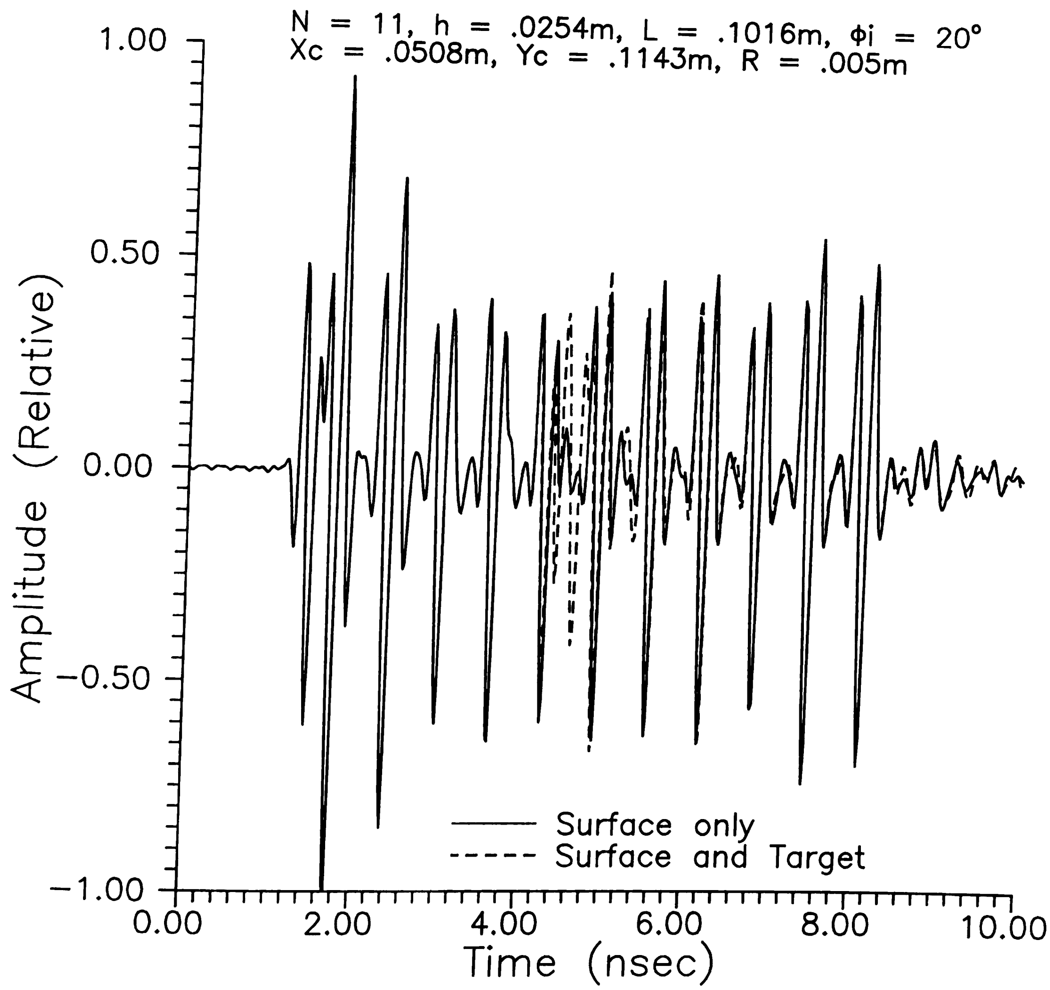

Figure 4.44 Transient scattered return from a Stoke's surface only and from a cylinder above the Stoke's surface. TCR = -5.31 dB.

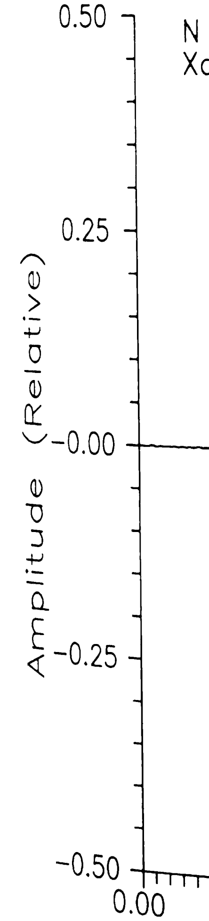

Figure 4.45 Differer
with cyl

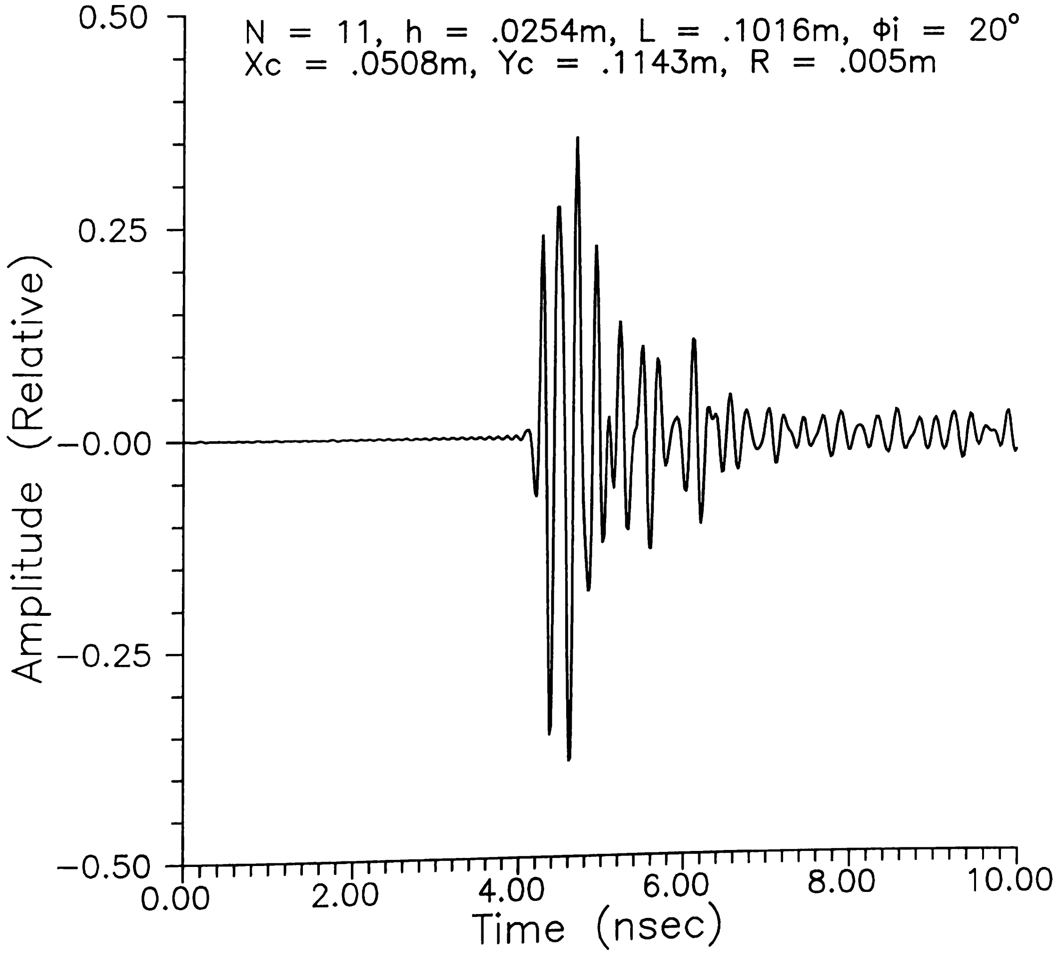

Figure 4.45 Difference between the transient scattered return from a Stoke's surface with cylinder and Stoke's surface without cylinder.

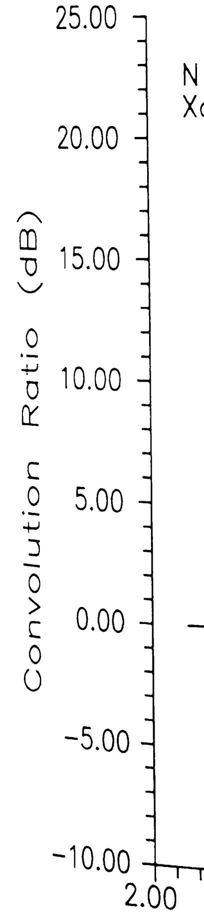

Figure 4.46 Convolu
effect a

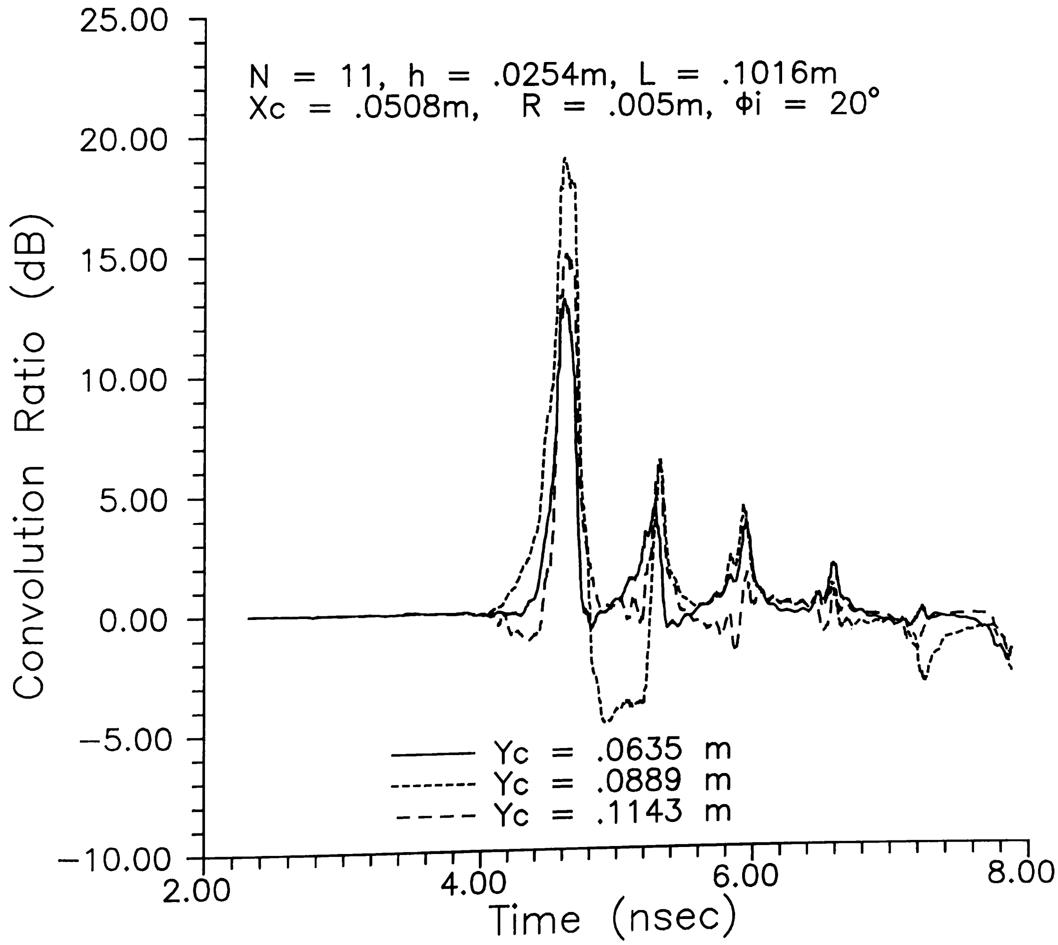

Figure 4.46 Convolution energy ratio for Stoke's surface and cylinder with multipath effect as a function of cylinder height.

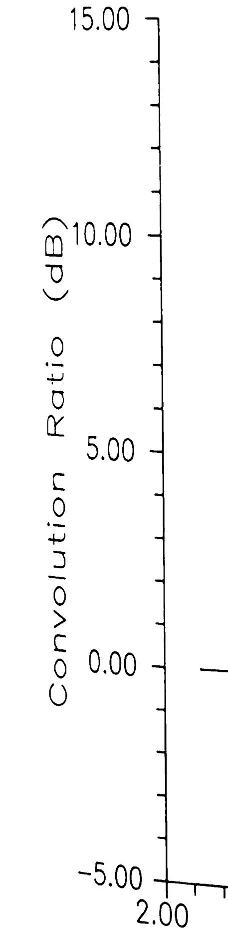

Figure 4.47 Convol
multipa

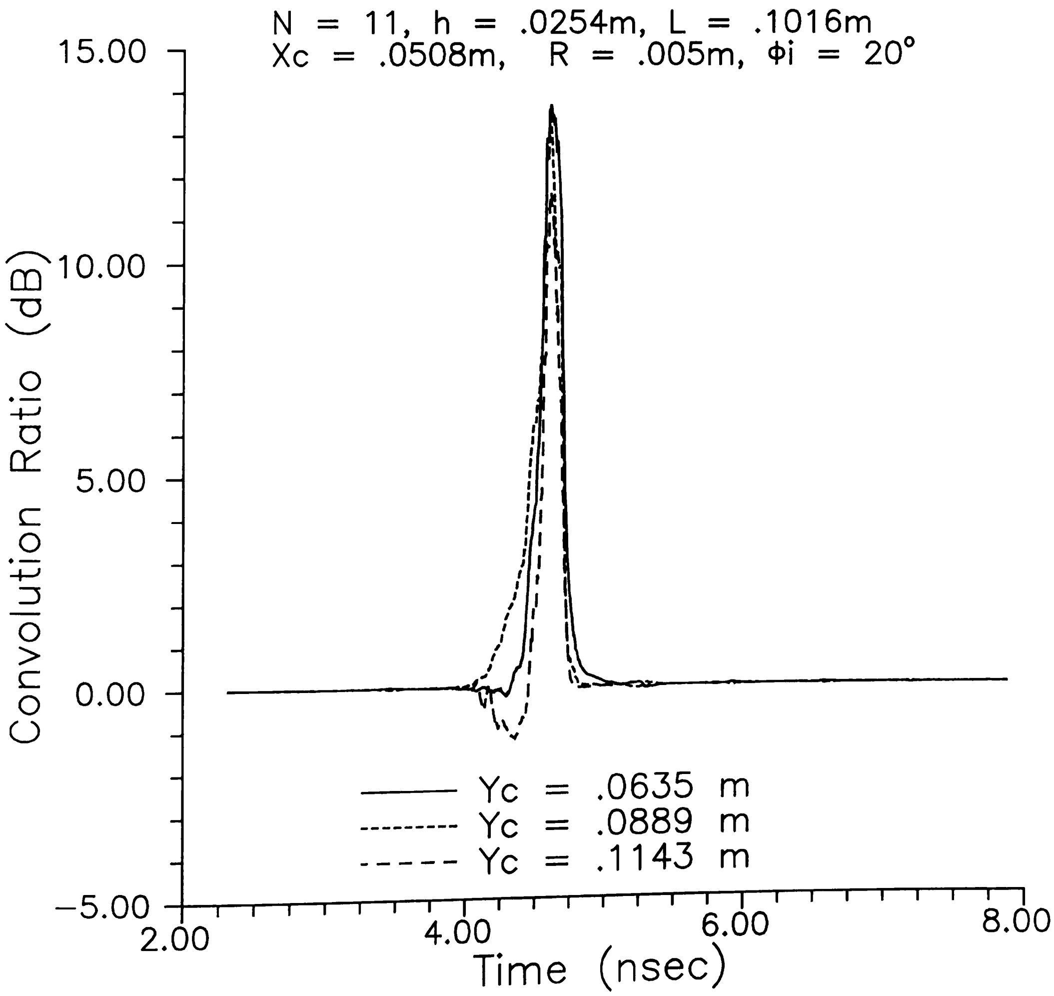

Figure 4.47 Convolution energy ratio for Stoke's surface and cylinder with no multipath effect as a function of cylinder height.

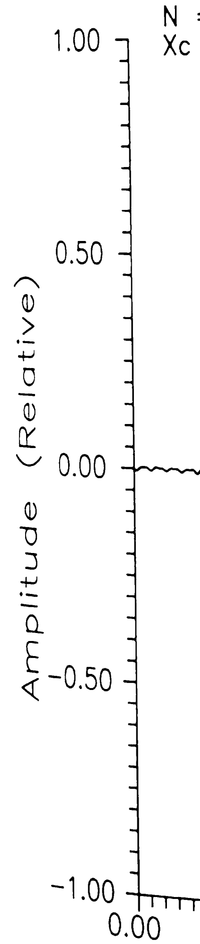

Figure 4.48 Transie
above t

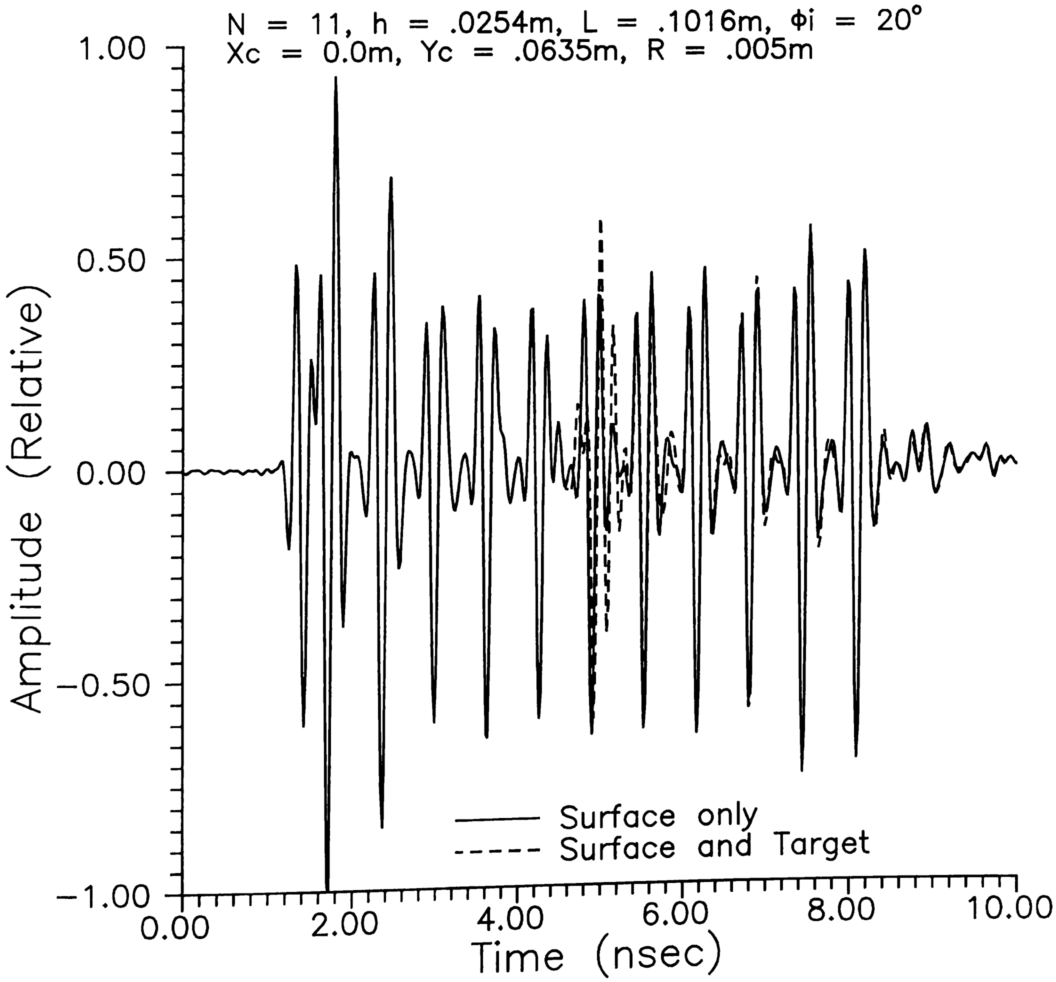

Figure 4.48 Transient scattered return from a Stoke's surface only and from a cylinder above the Stoke's surface. TCR = -5.31 dB.

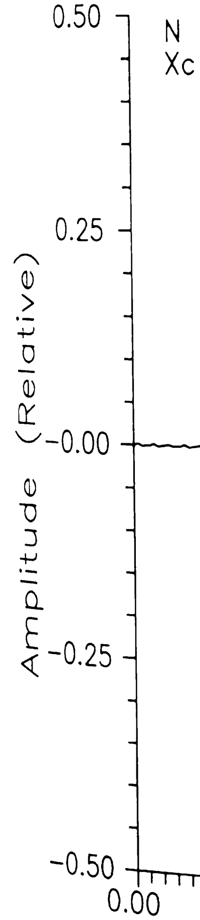

Figure 4.49 Differe
with cy

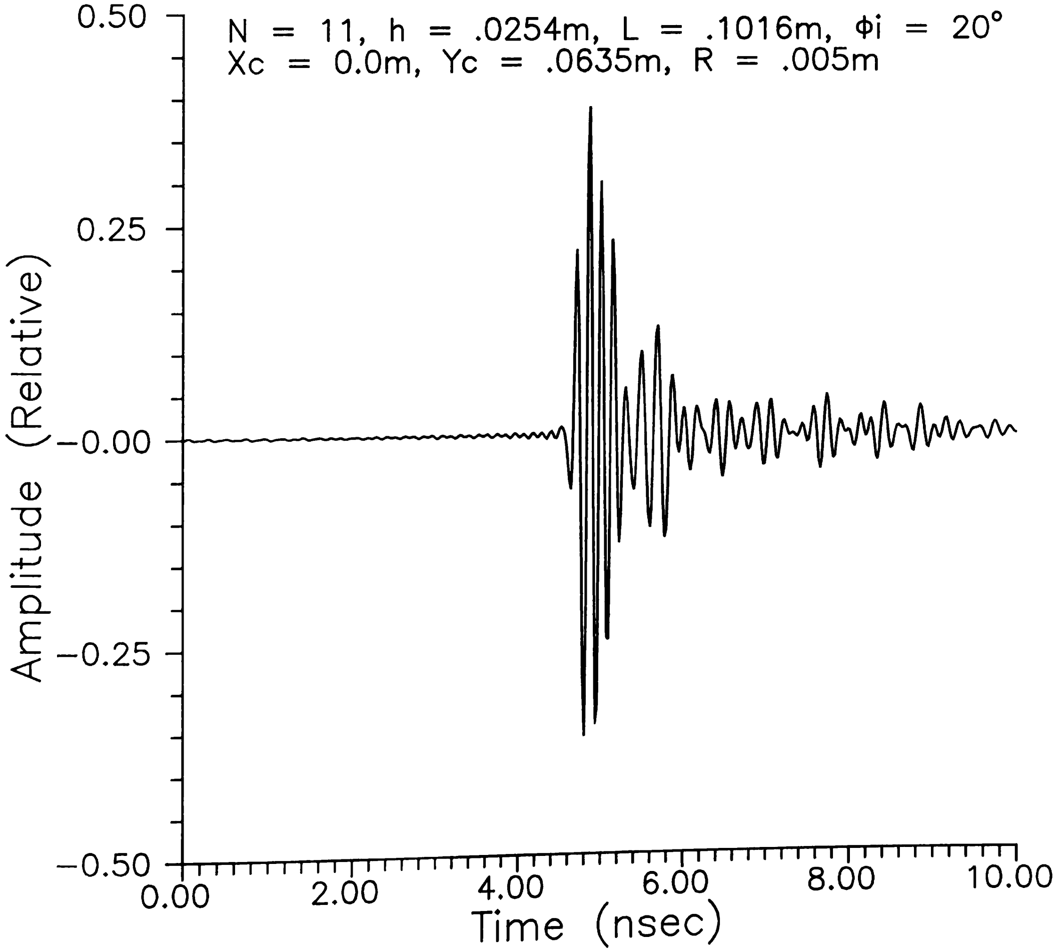

Figure 4.49 Difference between the transient scattered return from a Stoke's surface with cylinder and Stoke's surface without cylinder.

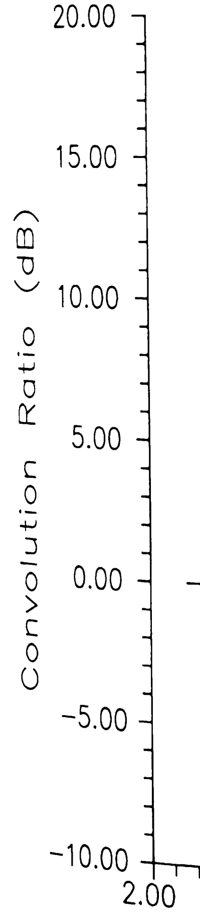

Figure 4.50 Convol
effect a

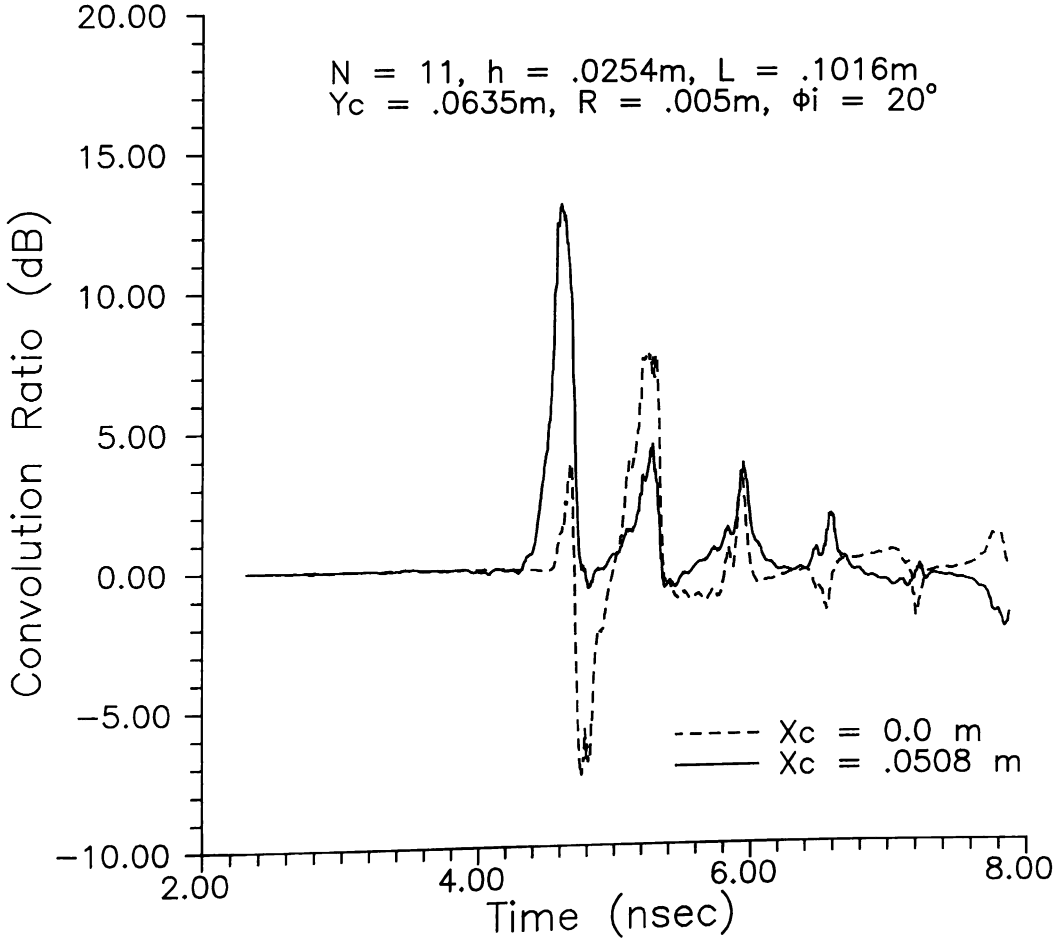

Figure 4.50 Convolution energy ratio for Stoke's surface and cylinder with multipath effect as a function of target position.

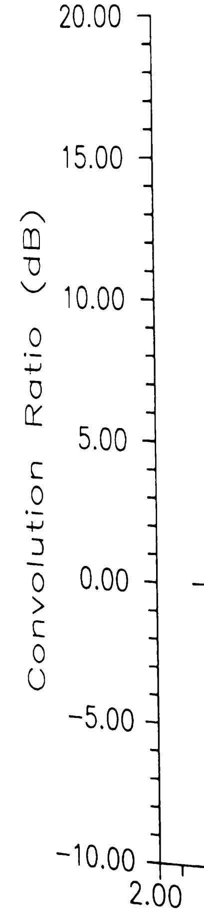

Figure 4.51 Convol
multipa

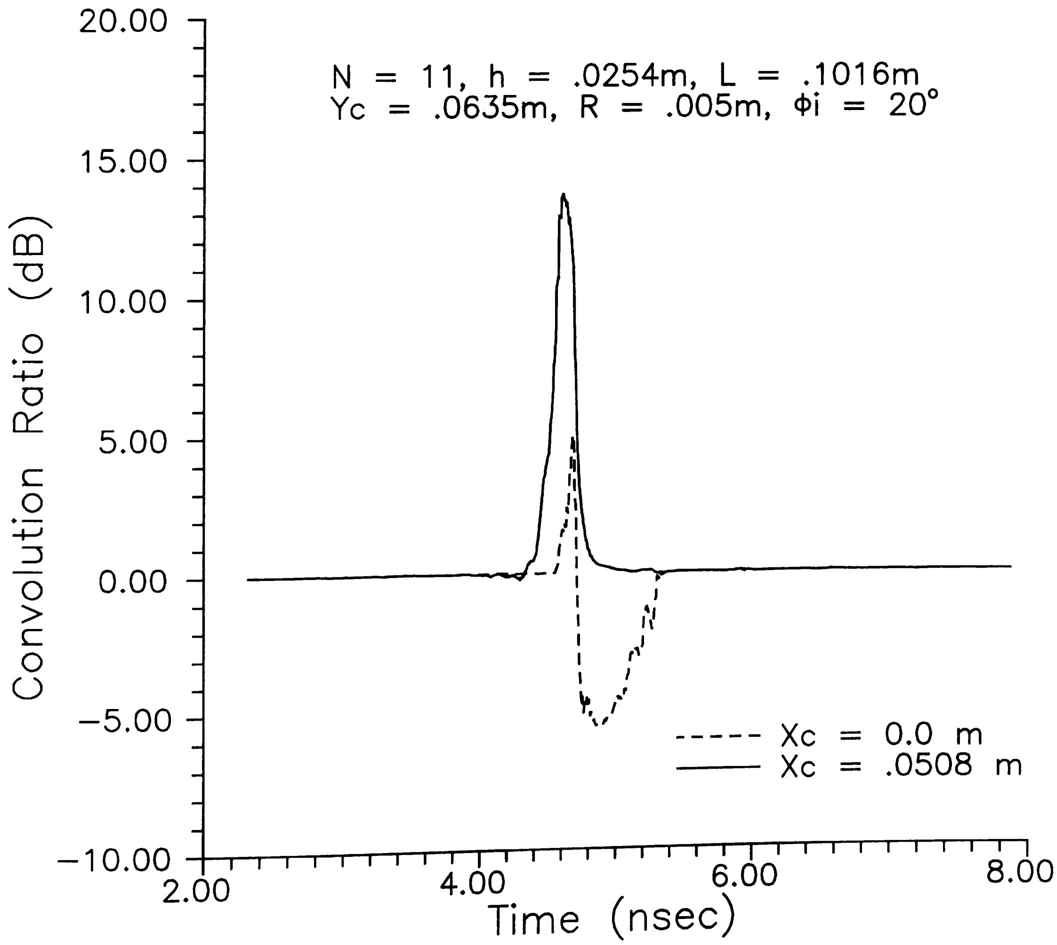

Figure 4.51 Convolution energy ratio for Stoke's surface and cylinder with no multipath effect interaction as a function of target position.

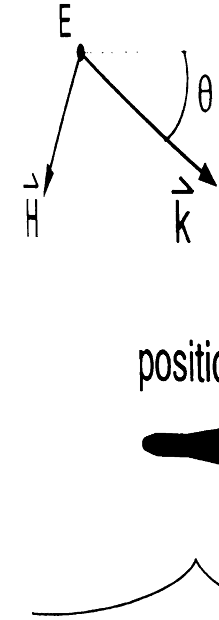

Figure 4.52 Multip

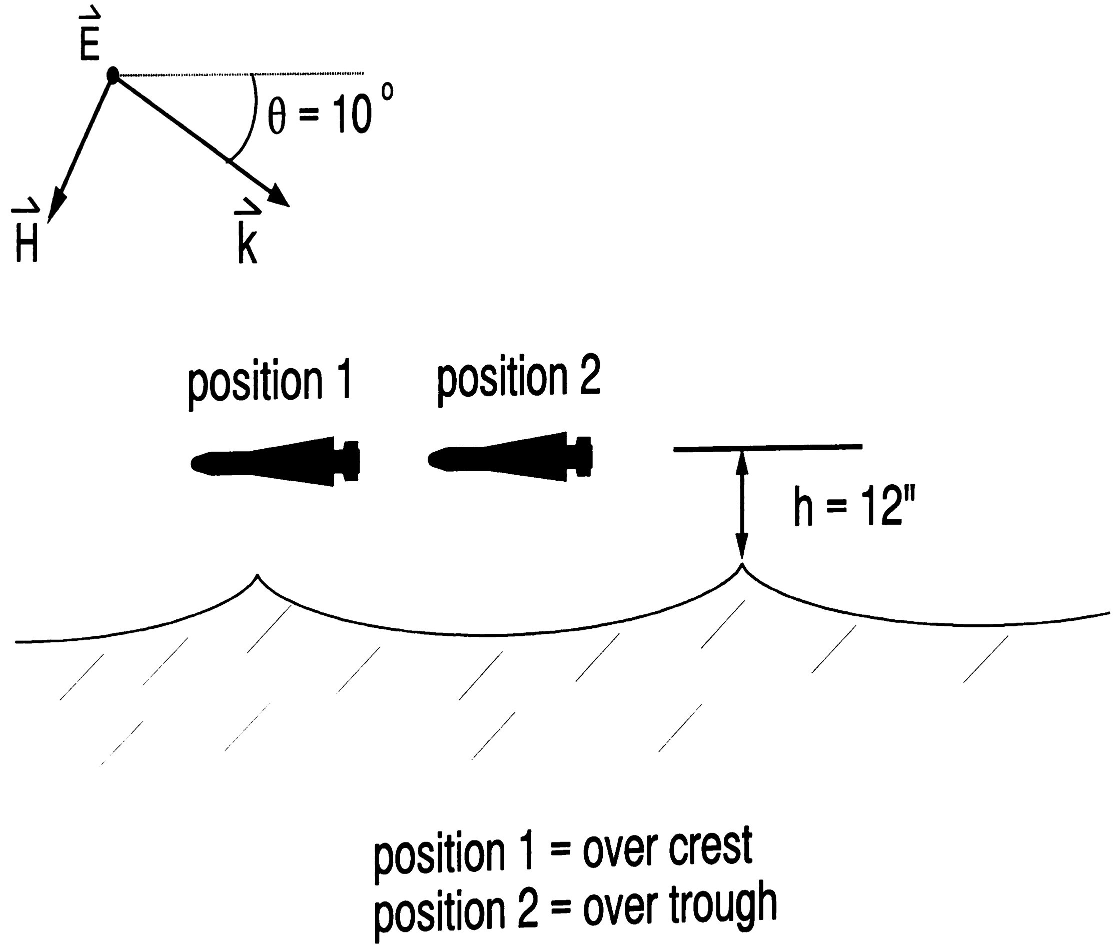

Figure 4.52 Multipath missile/sea-surface scattering geometry.

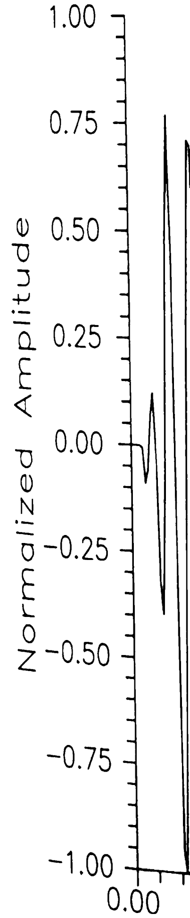

Figure 4.53 Norma
missile
degree

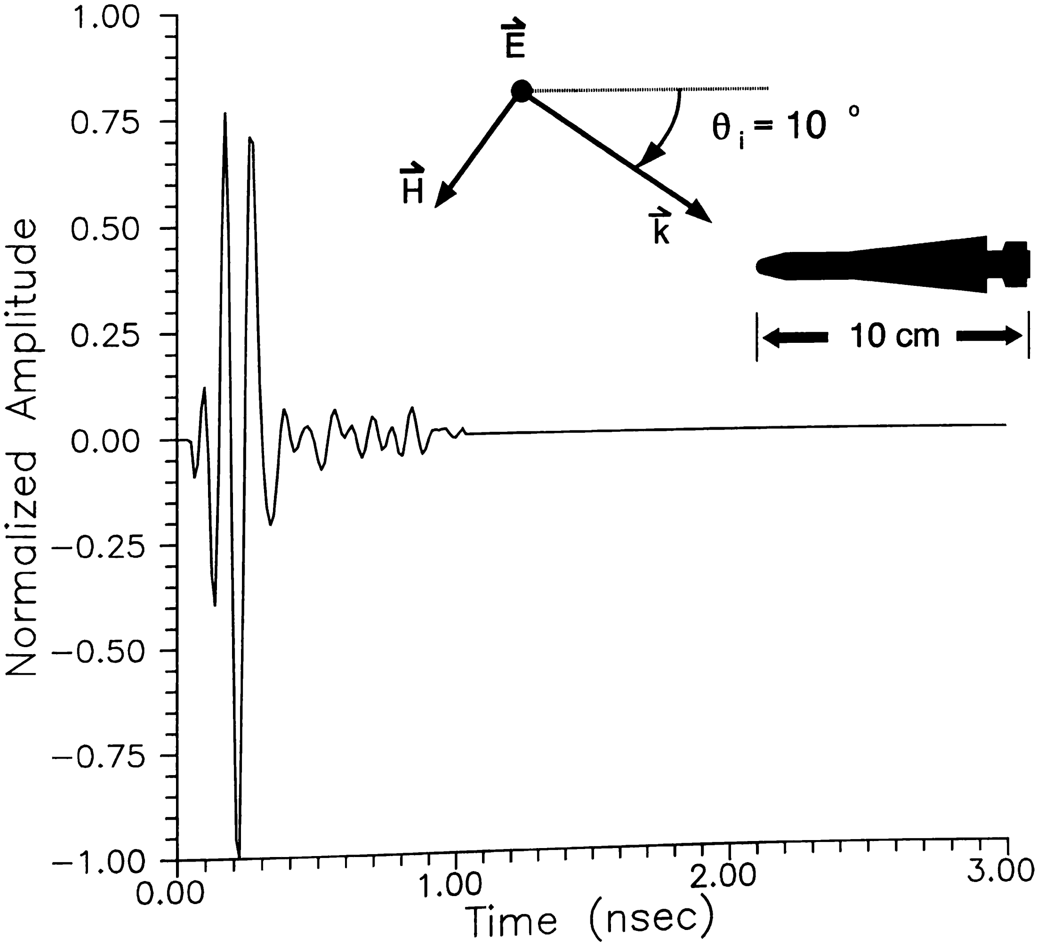

Figure 4.53 Normalized backscatter transient-response from 10 cm long phoenix missile excited by a TE incident plane wave. Incidence angle is 10 degrees from the horizontal axis.

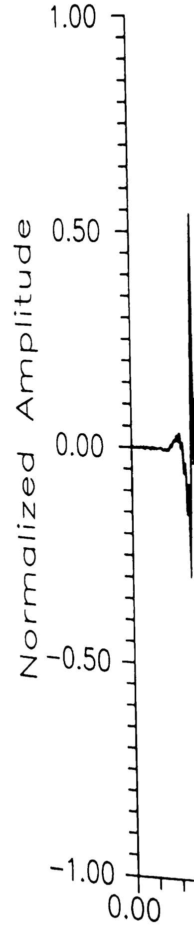

Figure 4.54 Norma
by a T
horizo

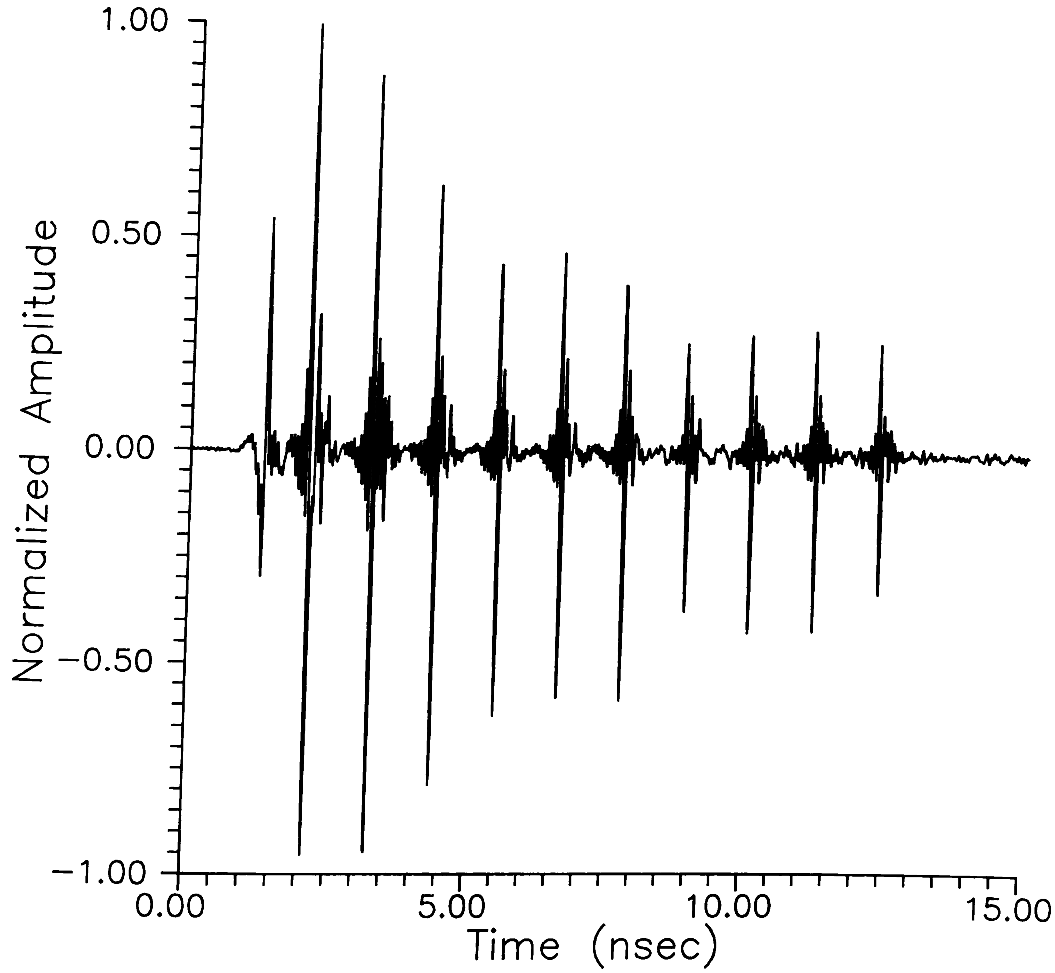

Figure 4.54 Normalized backscatter transient-response from a Stoke's surface excited by a TE incident plane wave. Incidence angle is 10 degrees from the horizontal axis.

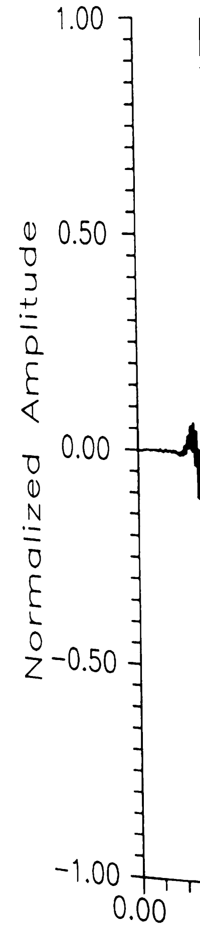

Figure 4.55 Norma
excitec
the ho

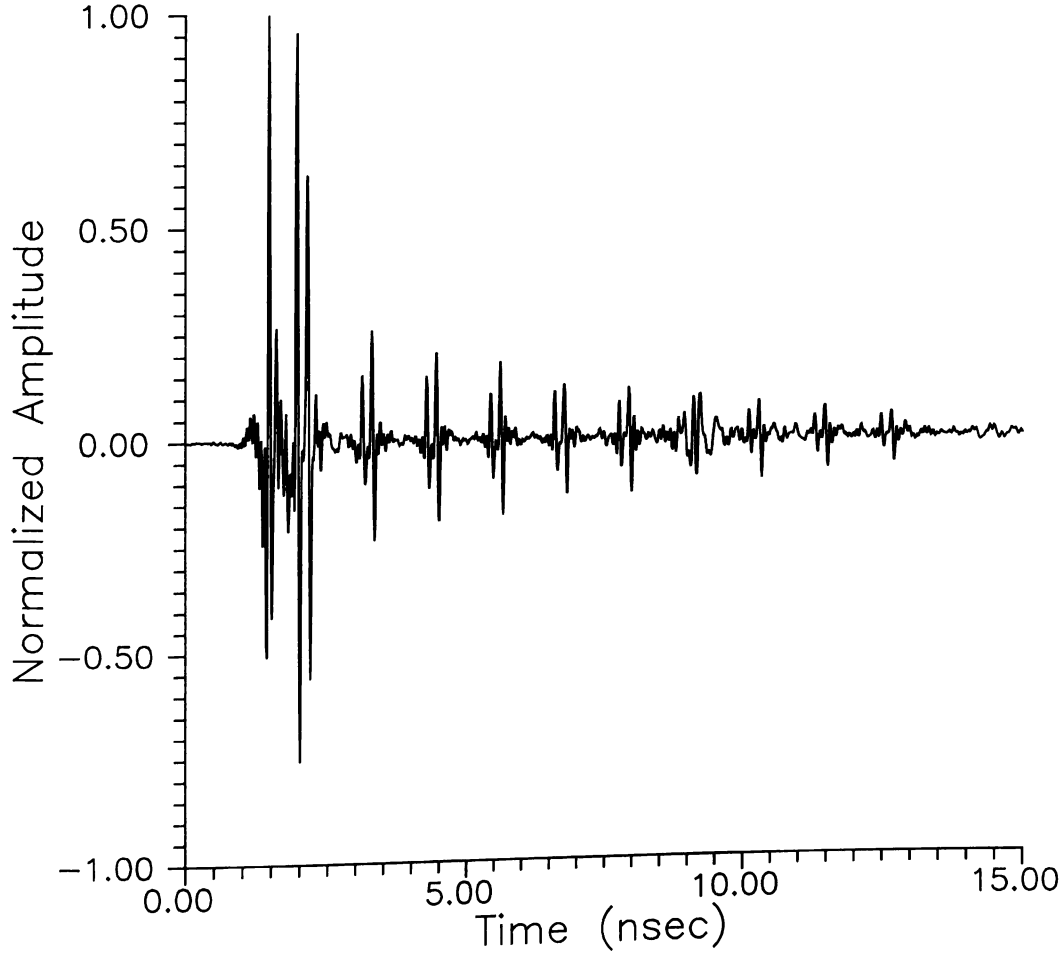

Figure 4.55 Normalized backscatter transient-response from a double-sinusoid surface excited by a TE incident plane wave. Incidence angle is 10 degrees from the horizontal axis.

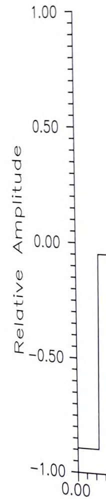

Figure 4.56 CRTW

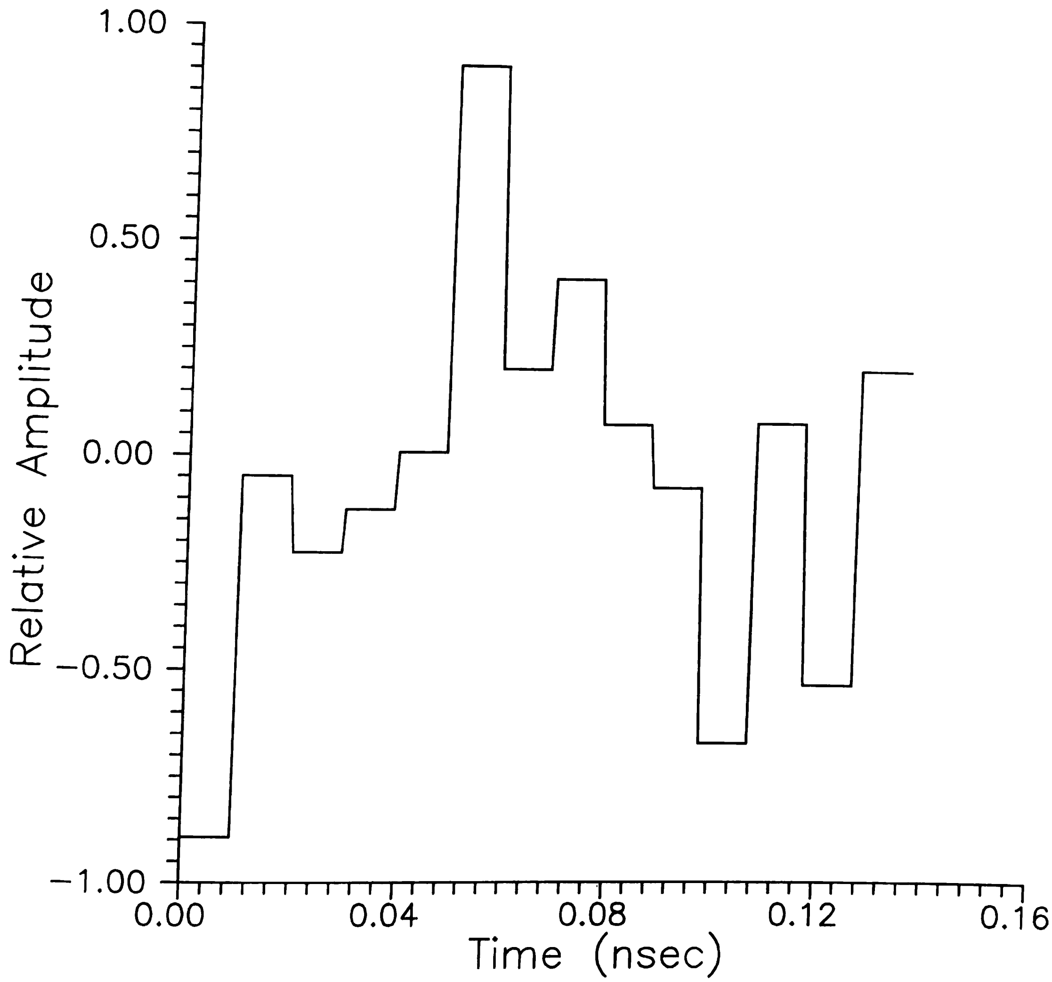

Figure 4.56 CRTW corresponding to measured Stoke's surface.

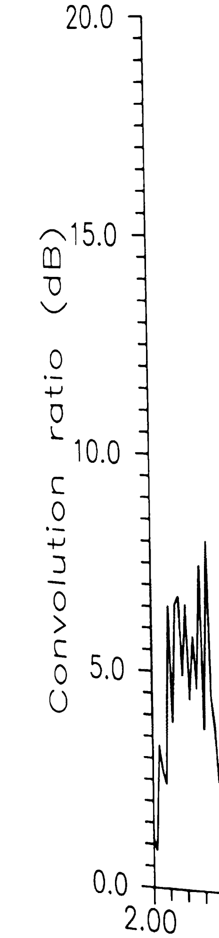

Figure 4.57 Convo
respec

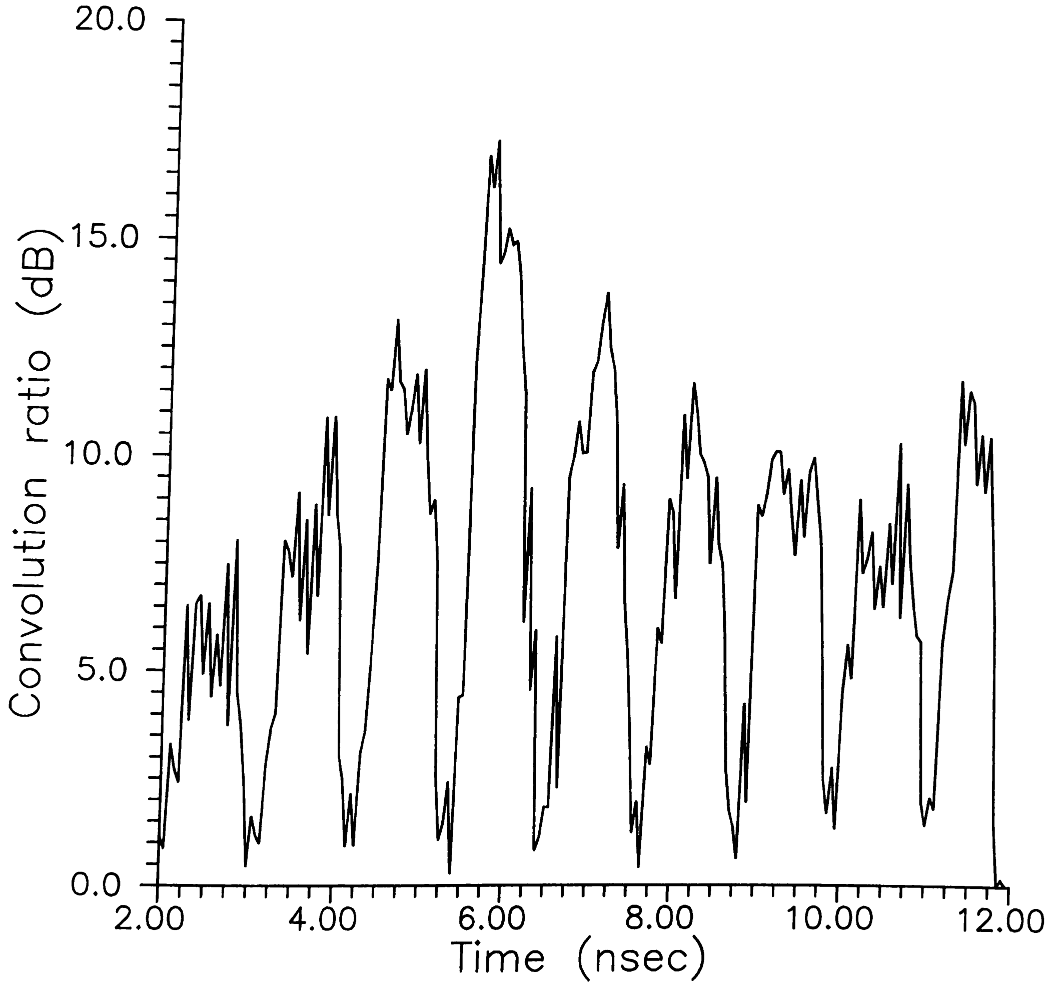

Figure 4.57 Convolution energy-ratio as a function of phoenix missile position with respect to Stoke's surface. TCR = -23.2 dB.

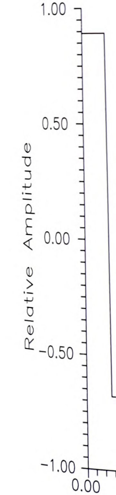

Figure 4.58 CRTW

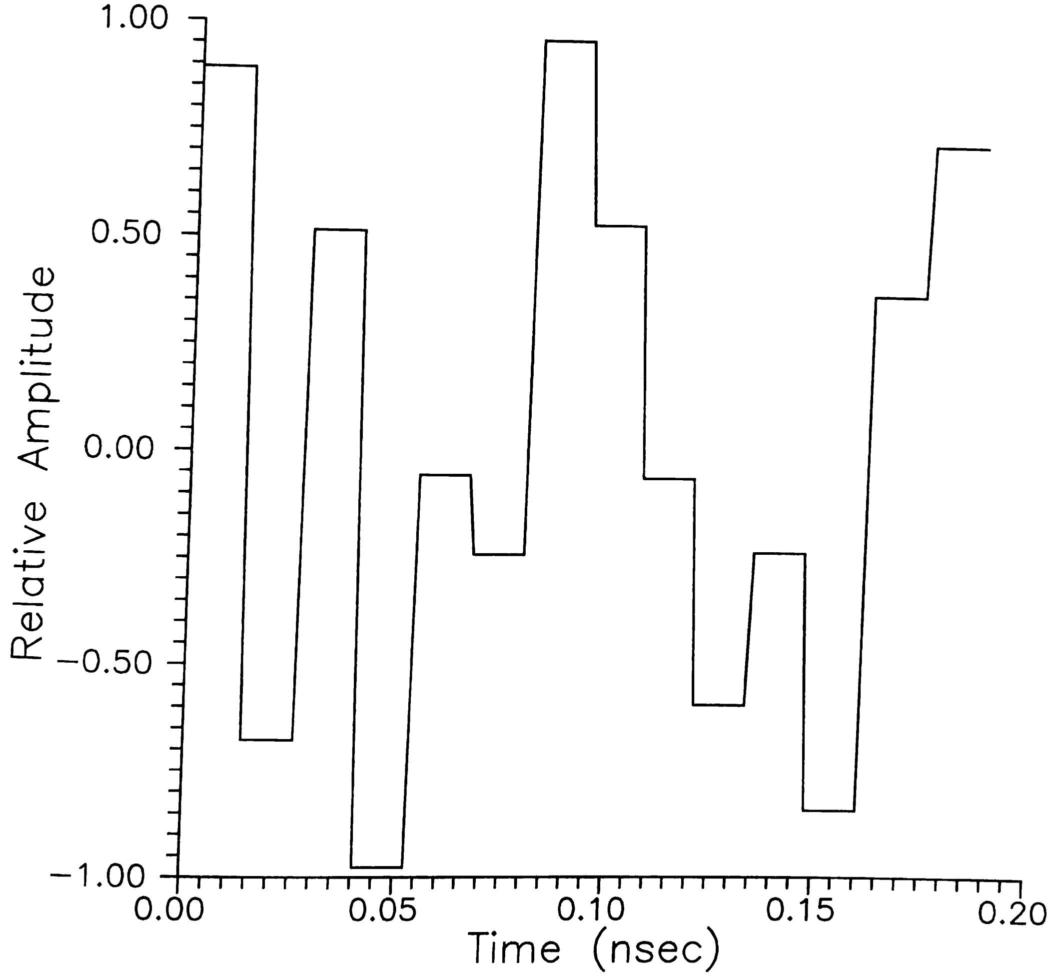

Figure 4.58 CRTW corresponding to measured double sinusoid surface.

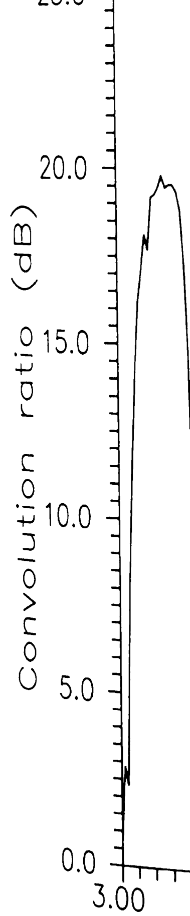

Figure 4.59 Convo
respect

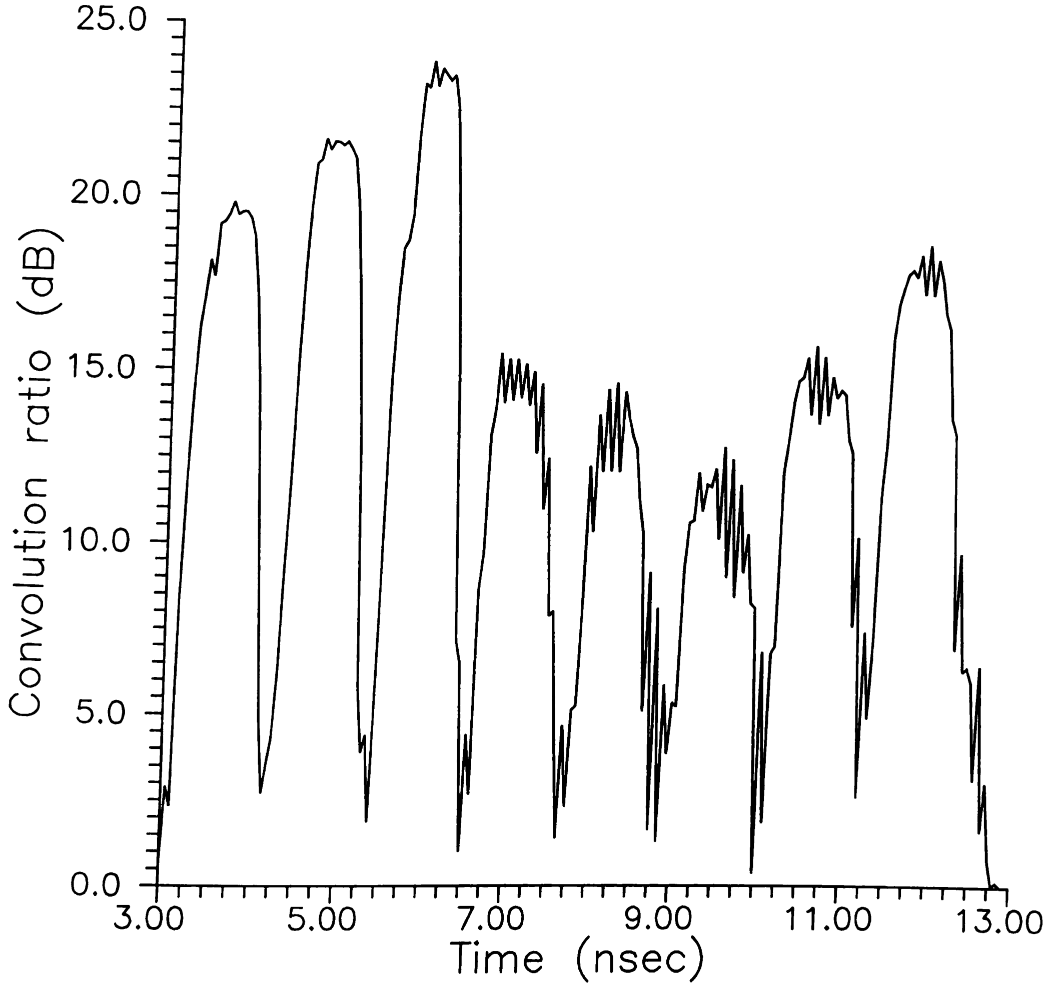

Figure 4.59 Convolution energy-ratio as a function of phoenix missile position with respect to double-sinusoid surface. TCR = -4.75 dB.

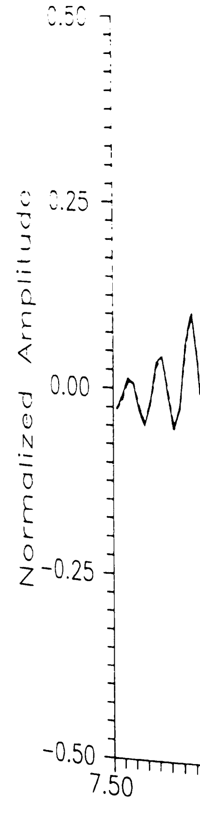

Figure 4.60 Norma
Stoke's
trough

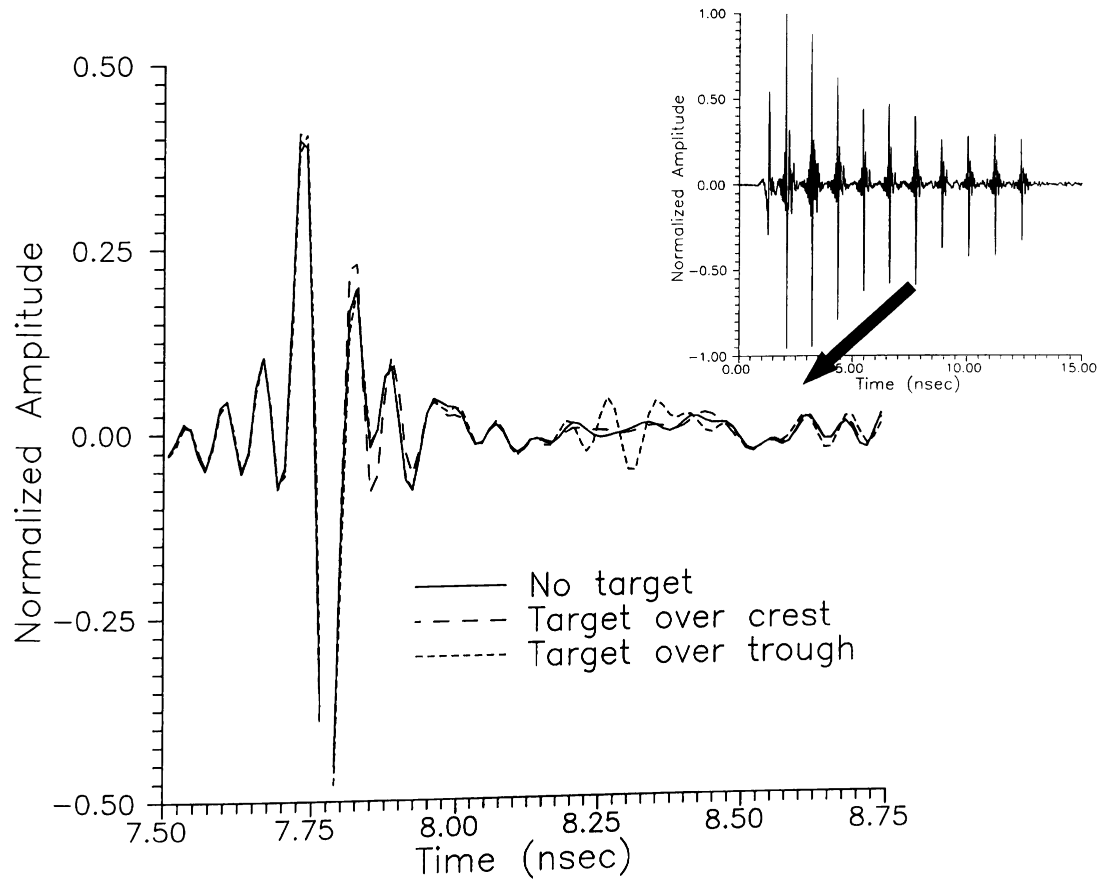

Figure 4.60 Normalized backscatter transient-response from a phoenix missile and Stoke's surface excited by a TE incident plane wave. Missile is above trough of wave and incidence angle is 10 degrees from the horizontal axis.

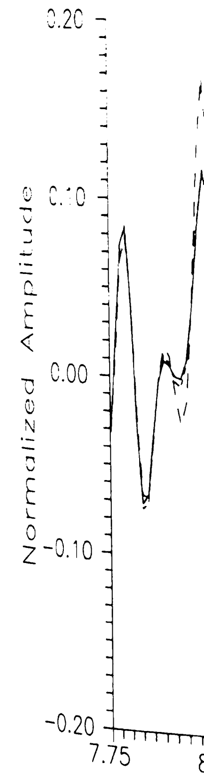

Figure 4.61 Norma
double
above
horizo

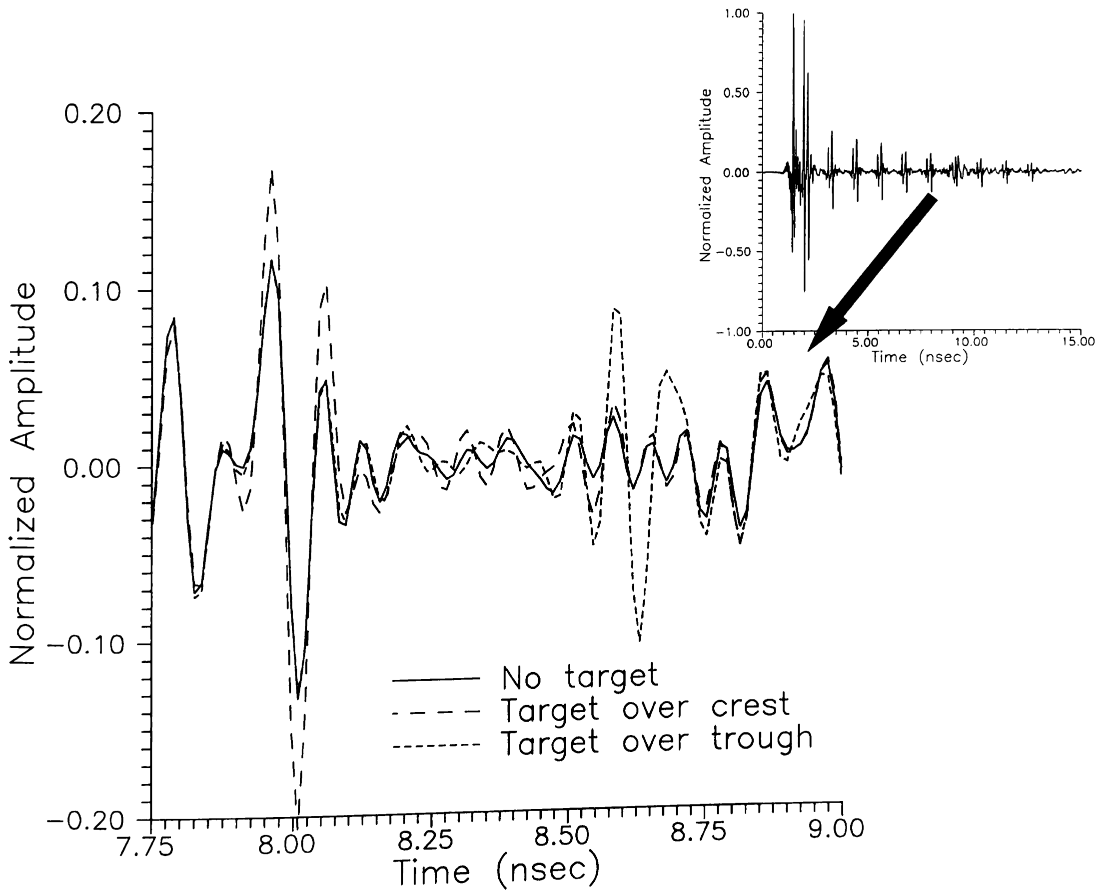

Figure 4.61 Normalized backscatter transient-response from a phoenix missile and double-sinusoid surface excited by a TE incident plane wave. Missile is above trough of wave and incidence angle is 10 degrees from the horizontal.

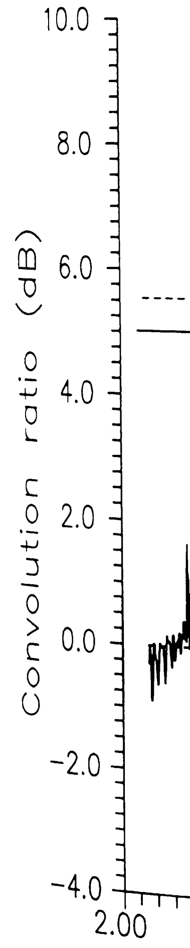

Figure 4.62 Convo
Stoke'
hybrid

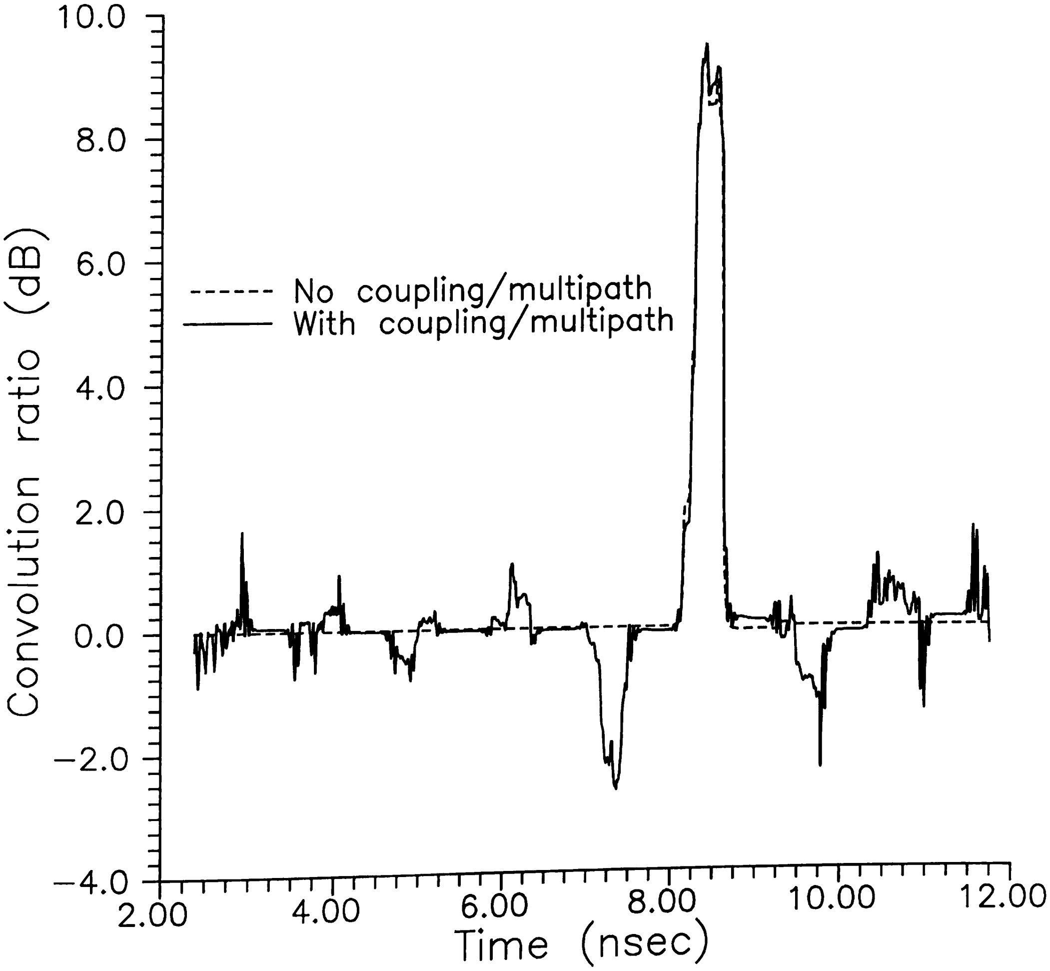

Figure 4.62 Convolution energy-ratio for phoenix missile located above a trough in Stoke's surface. Ratio was calculated from composite measured return and hybrid-composite measured return. TCR = -23.2 dB.

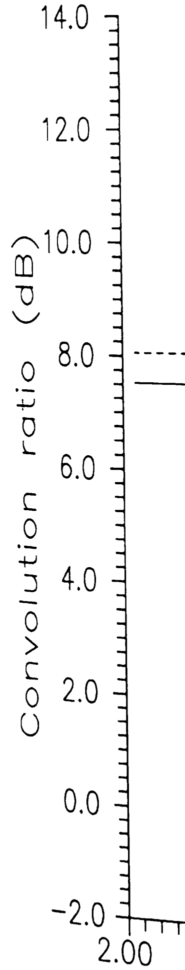

Figure 4.63 Convo
doubl
return

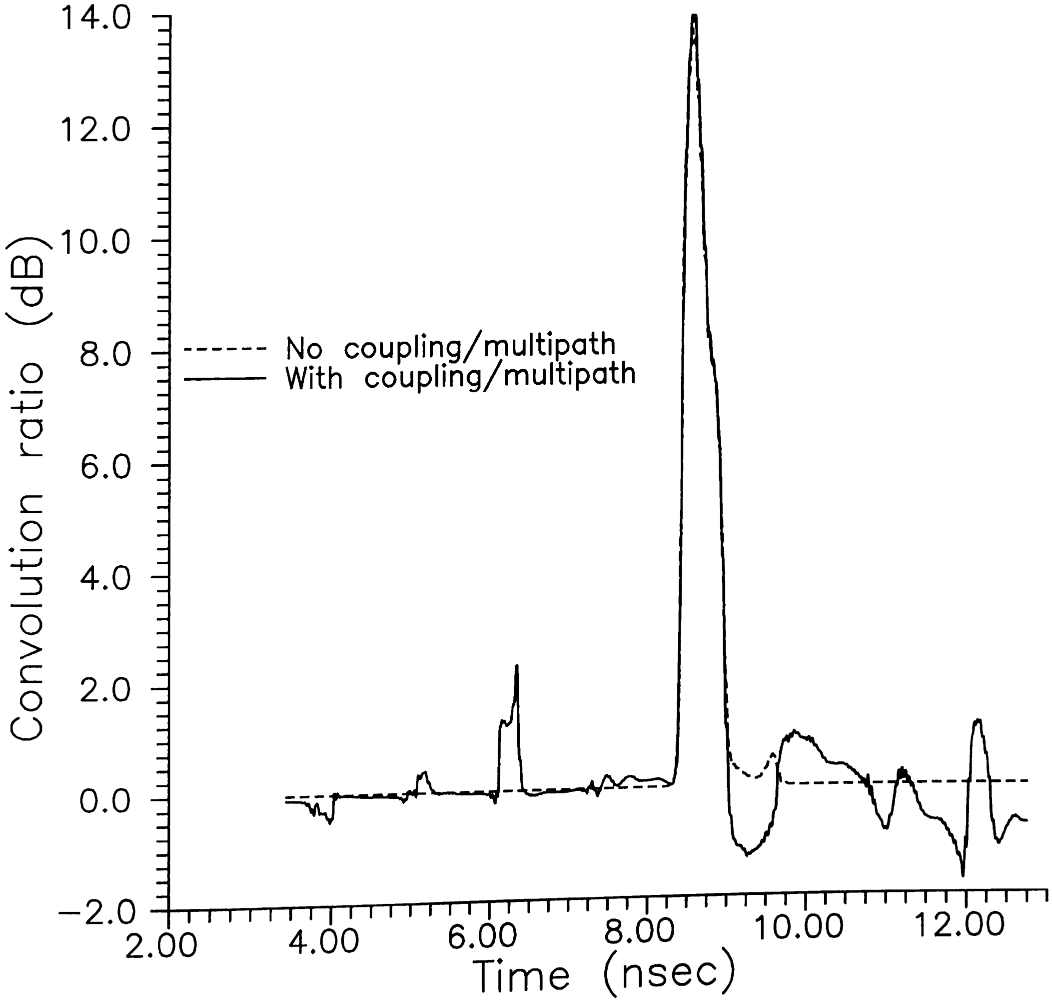

Figure 4.63 Convolution energy-ratio for phoenix missile located above a trough in double-sinusoid surface. Ratio was calculated from composite measured return and hybrid-composite measured return. TCR = -4.75 dB.

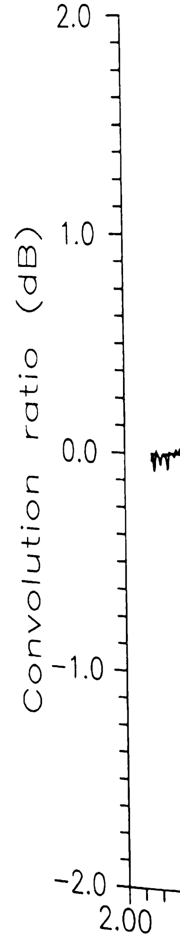

Figure 4.64 Conv
Stok
hybri

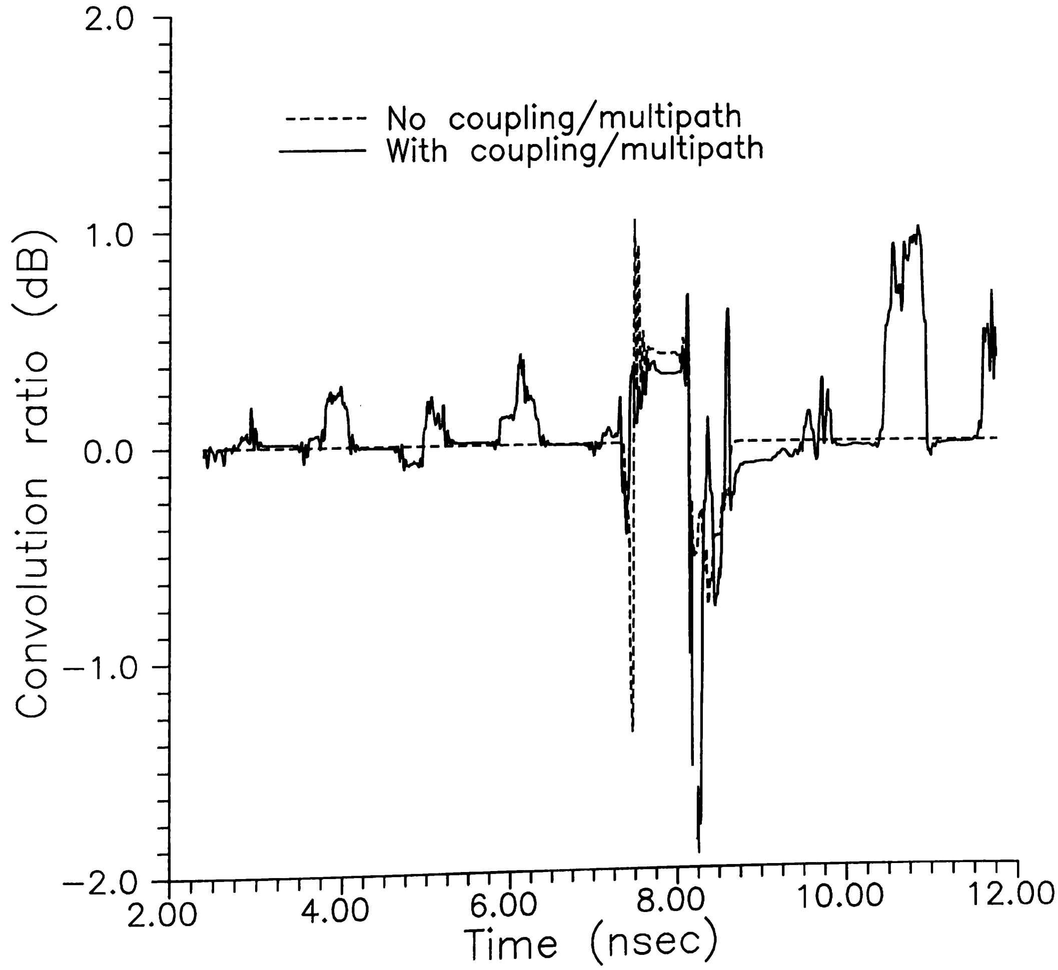

Figure 4.64 Convolution energy-ratio for phoenix missile located above a crest in Stoke's surface. Ratio was calculated from composite measured return and hybrid-composite measured return. TCR = -23.2 dB.

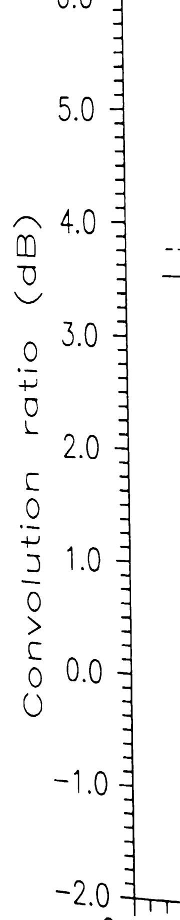

Figure 4.65 Conv
doub
retur

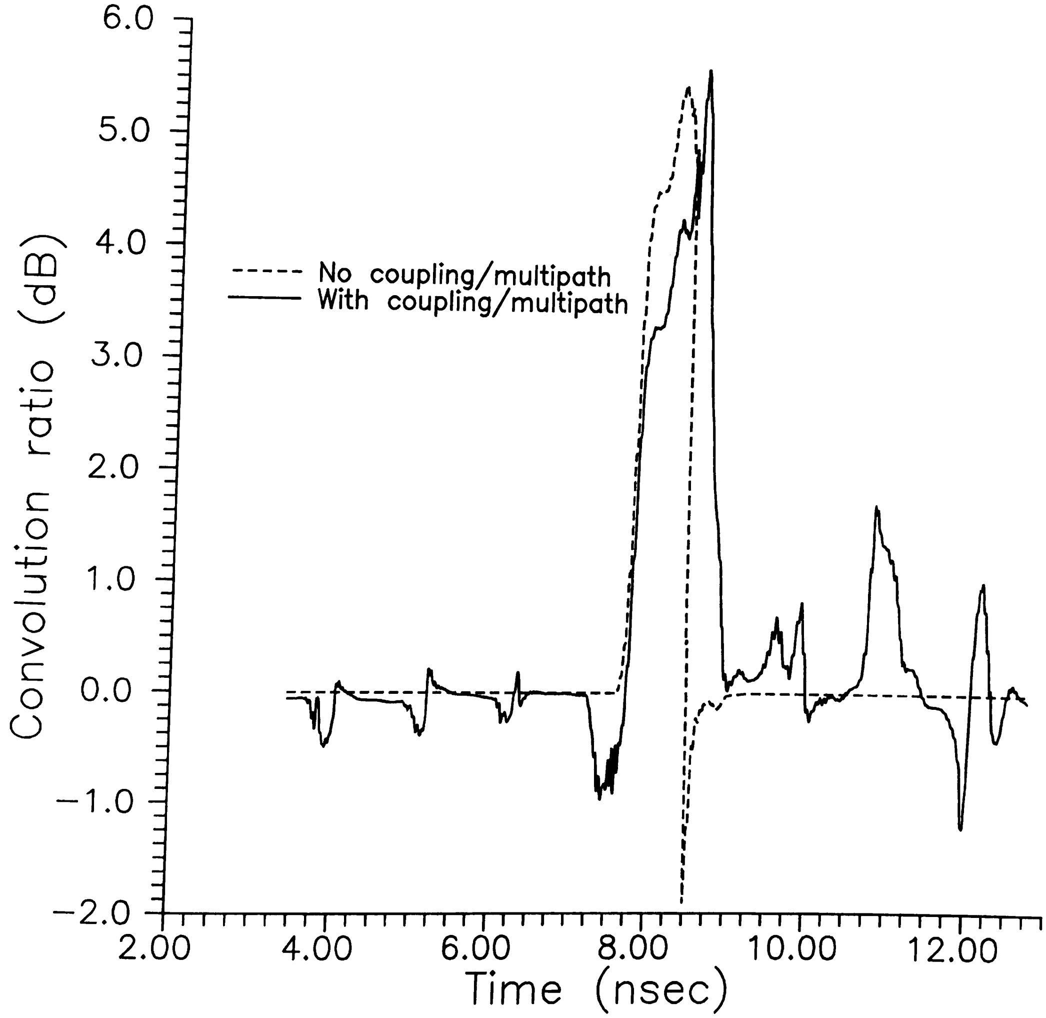

Figure 4.65 Convolution energy-ratio for phoenix missile located above a crest in double-sinusoid surface. Ratio was calculated from composite measured return and hybrid-composite measured return. TCR = -4.75 dB.

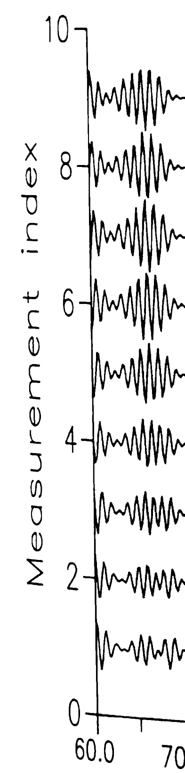

Figure 4.66 Amp
corre

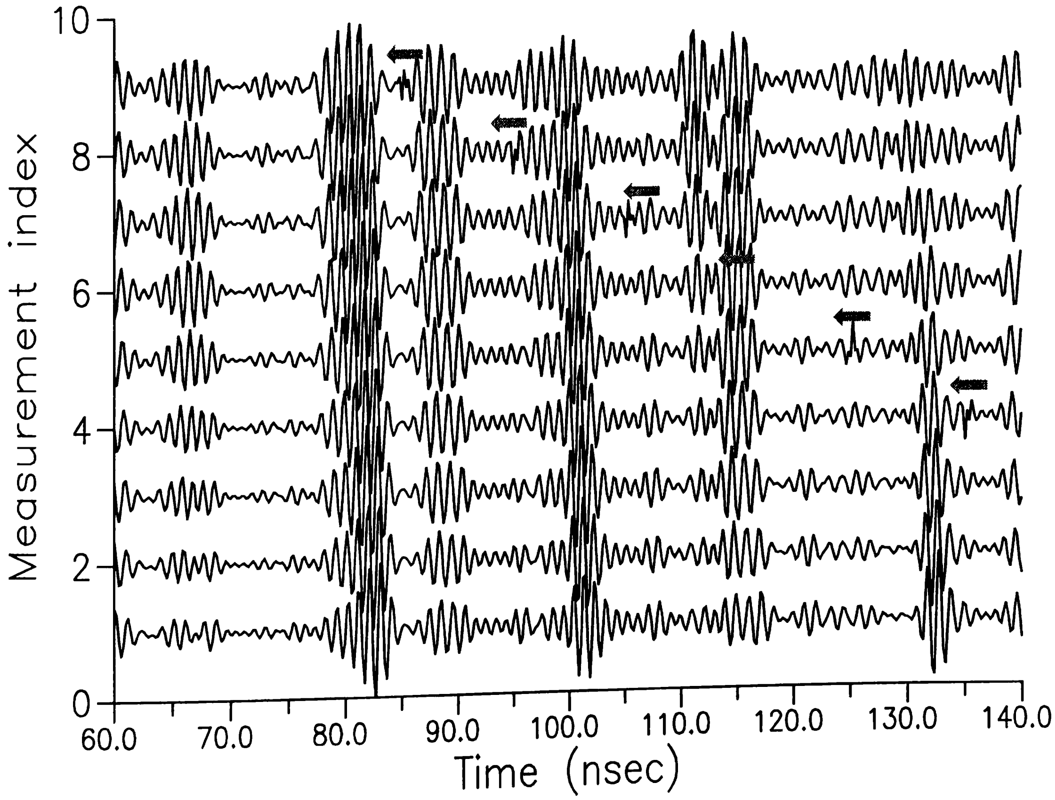

Figure 4.66 Amplitude of scattered return from an evolving sea surface. This case corresponds to a time step ΔT = .25 seconds between successive returns.

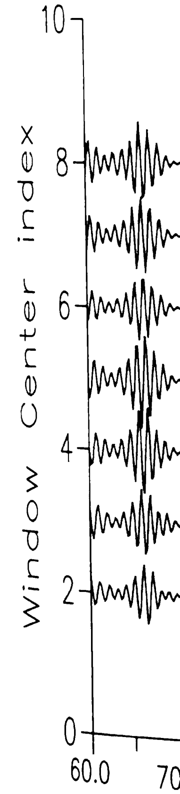

Figure 4.67 Targ
algo
over

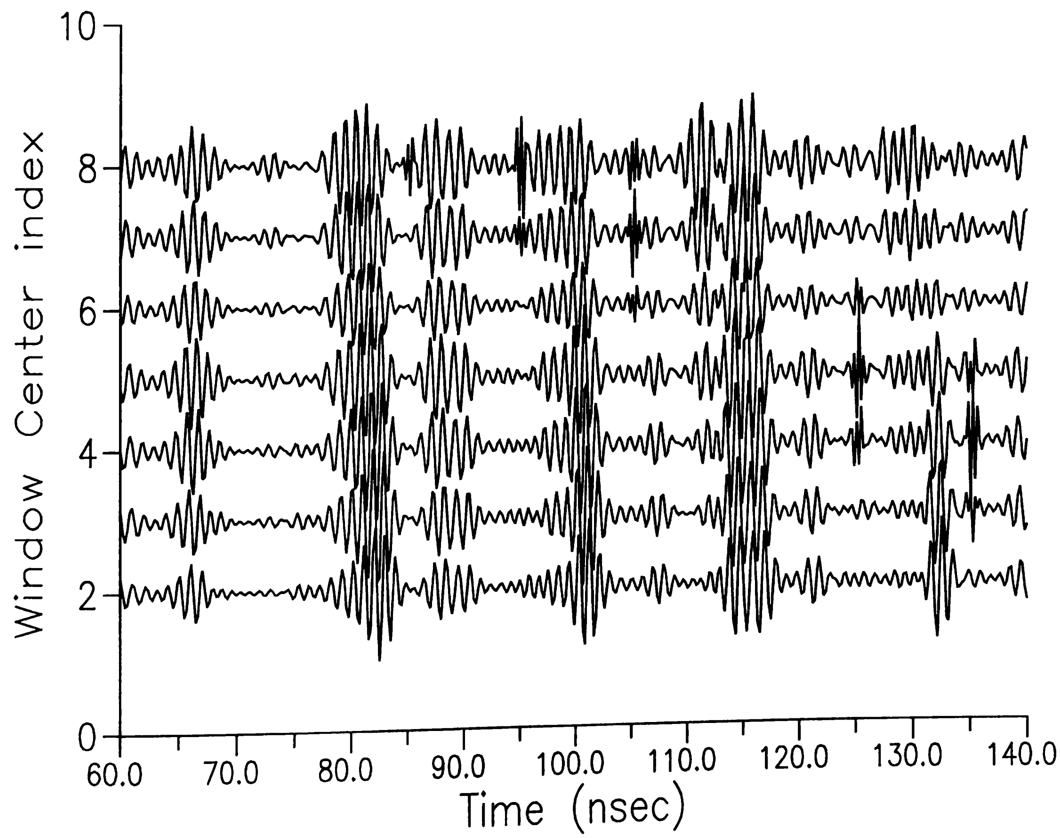

Figure 4.67 Target detection of simple missile simulation using coherent detection algorithm. Time step between pulse returns is .25 seconds, with averaging over three successive pulse returns.

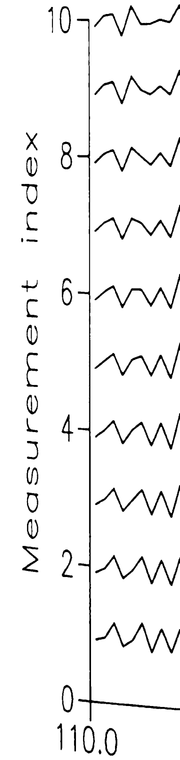

Figure 4.68 Amp
corre
returi

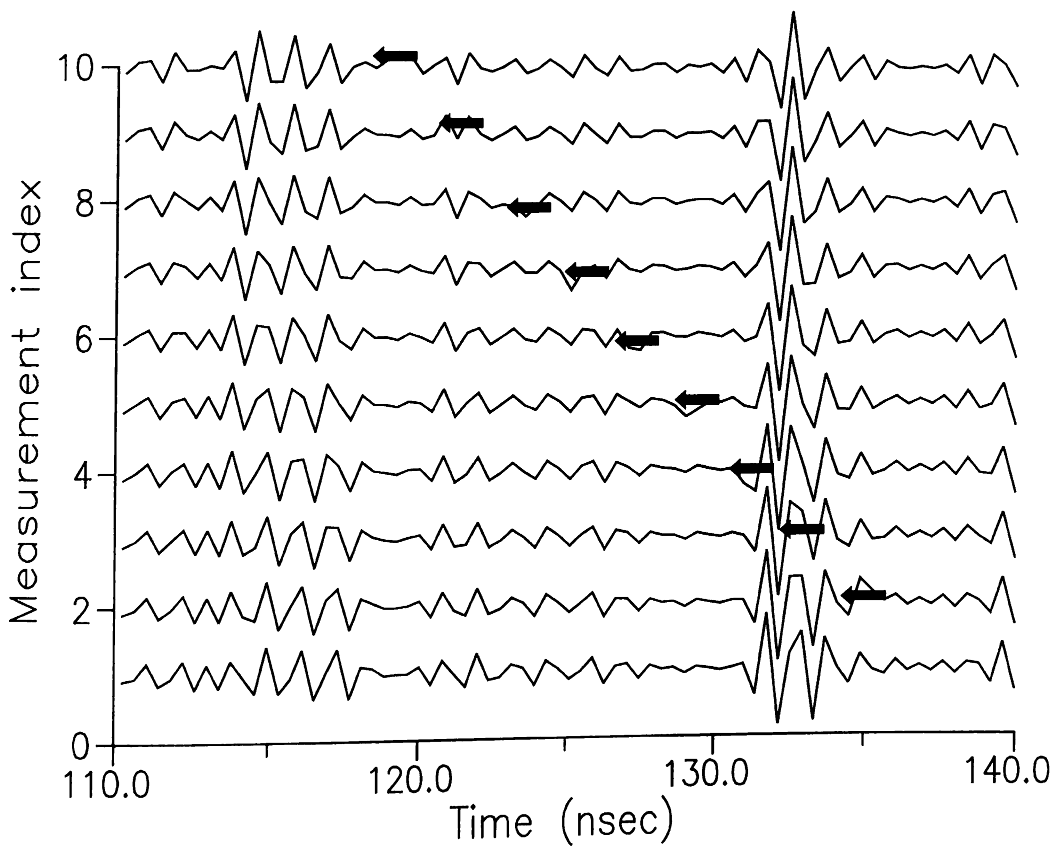

Figure 4.68 Amplitude of scattered return from an evolving sea surface. This case corresponds to a time step of $\Delta T = .05$ seconds between successive pulse returns.

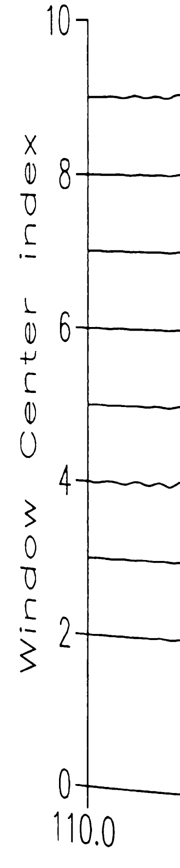

Figure 4.69 Targe
algori
over

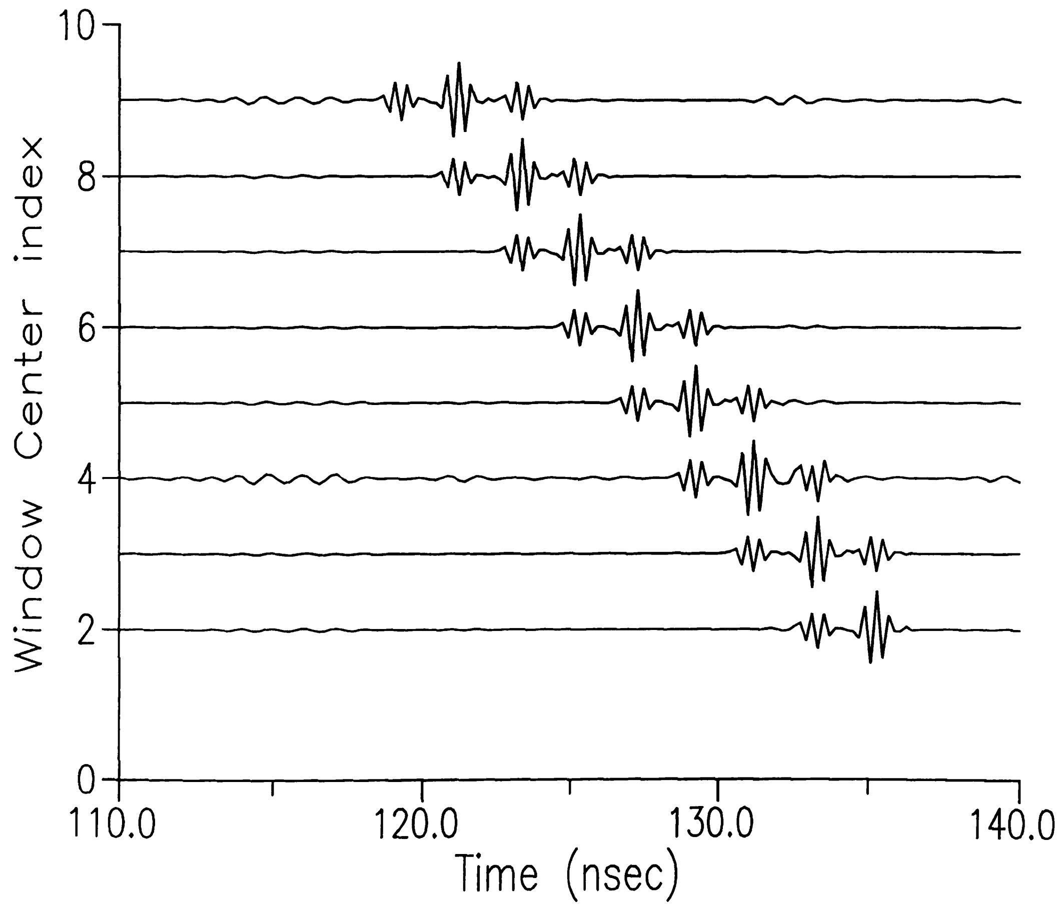

Figure 4.69 Target detection of simple missile simulation using coherent detection algorithm. Time step between pulse returns is .05 seconds, with averaging over three successive pulse returns.

Ceps

5.1 Introductio

A challengi

and/or identificatio

in the ability of rad

enhanced both the q

airborne threats is b

with that target. O

target's complex fre

transient EM field

illuminated by an

modelled as having

that the total scatte

A simple model fo

where $f_n(t)$ is the

T_n. The late-time c

Chapter 5

Cepstral Analysis and Radar Target Response

5.1 Introduction

A challenging problem encountered in radar system technology is the detection and/or identification of airborne targets in a highly cluttered environment. Advancement in the ability of radar systems to transmit and analyze signals of very short duration has enhanced both the quality and quantity of target information [1]. Recognition of potential airborne threats is based upon a system's ability to analyze specific signatures associated with that target. One technique used to identify targets is based on the uniqueness of a target's complex frequencies in the late-time transient scattered signal [4]. Consider the transient EM field scattered by a perfectly conducting, finite size radar target when illuminated by an incident EM pulse. The scattered return from the target can be modelled as having an early-time component $f_e(t)$ and a late-time component $f_l(t)$, such that the total scattered field is given by

$$f(t) = f_e(t) + f_l(t) \tag{5.1}$$

A simple model for the early-time component is [42]

$$f_e(t) = \sum_{n=1}^{N} f_n(t - T_n) \tag{5.2}$$

where $f_n(t)$ is the pulse response of the n^{th} scattering center located at temporal position T_n. The late-time component can be written as

$$f_l(t) = \sum_{m=1}^{M} a_m e^{\sigma_m t} \cos(\omega_m t + \phi_m) \qquad t > T_L \tag{5.3}$$

where $\{ s_m = \sigma_m +$

late time. The sca

However, the target

target, thereby prov

Inherent in

both magnitude and

spectral magnitude

transient signal can

under certain condi

a signal's spectrum

through a Hilbert t

frequency spectrum

more restrictive app

both the poles and

minimum phase co

through a Hilbert

response of the spe

needed if these tran

An alternat

cepstrum approach

transient signal usi

transform (FFT), t

where $\{s_m = \sigma_m + j\,\omega_m\}$ are the target natural frequencies and T_L is the beginning of late time. The scattered return from the early-time signal is aspect angle dependent. However, the target's natural frequencies are aspect angle independent and unique to the target, thereby providing a target identifier.

Inherent in the generation of these complex frequencies is the measurement of both magnitude and phase from the target scattered return. In general, a knowledge of spectral magnitude does not allow the calculation of the phase and vice-versa. Hence, the transient signal cannot be recovered with only spectral magnitude or phase. Nonetheless, under certain conditions a relationship does exist between the real and imaginary parts of a signal's spectrum. For a real, causal signal, the real and imaginary parts are related through a Hilbert transform integral [28],[29]. Typically, the magnitude of a signal's frequency spectrum is measured, rather than the real or imaginary part, and a somewhat more restrictive approach must be used. If a finite length sampled signal is causal, and both the poles and zeros of its z-transform lie inside the z-plane's unit circle (the minimum phase condition) then the phase and logarithm of the magnitude can be related through a Hilbert transform. This relation is certainly useful if only the magnitude response of the spectrum is available. On the other hand, a certain amount of caution is needed if these transforms are blindly applied to any signal.

An alternate approach for calculating the minimum phase signal is to use the cepstrum approach [28]-[29]. In this approach an attempt is made to recover the original transient signal using only the spectral magnitude. This method employs the fast Fourier transform (FFT), thus requiring considerably shorter computation time than the Hilbert integral approach.

diverse fields as sp

unique application

an ultra-wideband r

ultra-wideband rada

scattered signal.

Two questio

to the above signal

1. How must f

   What is the

2. Under wha

   $|F_l(\omega)|$ o

   $F(\omega) = \mathscr{F}$

   early and la

This chapter

many examples w

instances, cepstral

signal. Hopefully,

determine if the c

scattered return of

sections. In sectio

integral approach. The use of this technique has found specific applications in such diverse fields as speech and image processing, seismology, and acoustics [30]-[32]. A unique application of this method is to reconstruct a target's transient scattered field from an ultra-wideband radar signal. However, in order to apply this new methodology to an ultra-wideband radar signal, some fundamental questions must be answered about the scattered signal.

Two questions concerning the characteristic and application of cepstral analysis to the above signal models should be examined:

1. How must $f_n(t)$ and s_n behave so that $f_e(t)$ and $f_l(t)$ are minimum phase signals? What is the significance of these waveforms being minimum phase?
2. Under what circumstances can $f_e(t)$ and $f_l(t)$ be obtained from $|F_e(\omega)|$, $|F_l(\omega)|$ or $|F(\omega)|$? Here $F_e(\omega) = \mathscr{F}\{f_e(t)\}$, $F_l(\omega) = \mathscr{F}\{f_l(t)\}$, and $F(\omega) = \mathscr{F}\{f(t)\}$. That is, is it possible to use cepstral analysis to separate the early and late-time portions of a radar signal?

This chapter will attempt to answer these questions as rigorously as possible, and many examples will be presented for clarification. It will be shown that in many instances, cepstral analysis will work remarkably well even for a non-minimum phase signal. Hopefully, a set of guidelines or rules of thumb can be developed which will help determine if the cepstral technique can be used for reconstruction of the time-domain scattered return of a radar target. The body of this chapter will be divided into several sections. In section 2 background material is presented covering the necessary theory to understand the bas

in section three. N

discusses the use c

radar signal. The f

some further areas

identification in ch

5.2 Cepstral A

Two simple

both figures the pol

magnitude and phas

The important featu

for both sequences.

sequence for a give

using only the magn

in turn affect the p

To derive a

to see if some rela

response. A real, c

odd non-causal seq

where

understand the basic ideas of cepstral analysis. Late-time characterization is presented in section three. Next, the early-time response is discussed in section four. Section five discusses the use of cepstral analysis to separate the early and late-time portions of a radar signal. The final section summarizes the major points in this chapter, and suggests some further areas of study. The ideas presented in this chapter will be applied to target identification in chapter 6.

5.2 Cepstral Analysis - Theory

Two simple, real causal sequences are shown in Figure 5.0 and Figure 5.1. In both figures the poles and zeros associated with the z-transform are shown as well as the magnitude and phase responses obtained from the discrete time Fourier transform (DTFT). The important feature to notice is that the modulus of the Fourier transform is the same for both sequences, but the phase is not. These simple examples illustrate that the input sequence for a given magnitude response is not unique. To construct the input sequence using only the magnitude response, certain restrictions must be applied on the input which in turn affect the placement of the poles and zeros in the z-plane.

To derive a relationship between the magnitude and phase, it is quite instructive to see if some relationship exists between the real and imaginary part of the spectral response. A real, causal sequence x[n] can be written in terms of the sum of an even and odd non-causal sequence as

$$x[n] = x_e[n] + x_o[n] \tag{5.4}$$

where

A little reflection s

even part as

where the window

The real part of th

The result of the t

where $z = e^{j\omega}$.

calculated by takin

used to determine

real and imaginar

process. The rest

the system poles

for a stable causa

$$
\begin{aligned}
x_e[n] &= \tfrac{1}{2}\big[x[n] + x[-n]\big] \\
x_o[n] &= \tfrac{1}{2}\big[x[n] - x[-n]\big]
\end{aligned}
\tag{5.5}
$$

A little reflection shows that the causal sequence can be written entirely in terms of the even part as

$$x[n] = x_e[n]\cdot w[n] \tag{5.6}$$

where the window function is just

$$w[n] = \begin{cases} 2, & n>0 \\ 1, & n=0 \\ 0, & n<0 \end{cases} \tag{5.7}$$

The real part of the Fourier transform can be obtained by applying the DTFT to $x_c[n]$. The result of the transform is

$$
\begin{aligned}
X_R(e^{j\omega}) &= \sum_{n=-\infty}^{\infty} x_e[n] z^{-n} \\
&= \sum_{n=-\infty}^{\infty} x_e[n](\cos\omega n - j\sin\omega n) \\
&= \sum_{n=-\infty}^{\infty} x_e[n]\cos\omega n
\end{aligned}
\tag{5.8}
$$

where $z = e^{j\omega}$. Hence, if the real part of the spectral response is known, $x_c[n]$ can be calculated by taking the inverse Fourier transform. Once this is determined, $x_c[n]$ can be used to determine x[n] from (5.6) and (5.7). Finally, a forward DTFT will yield both the real and imaginary part of the spectrum. Figure 5.3 shows a block diagram of the process. The restrictions placed on x[n] is that it be causal and stable. In this case all the system poles must be located within the unit circle, since the region of convergence for a stable causal sequence lies outside the unit circle.

A similar a

phase of the transf

Taking the natural

Consider (5.10) to
restriction that the
in the minimum pl
with $X(e^{j\omega}) = 0$,
stable sequence th
must lie with the u
is properly windov
corresponds to the
$\hat{x}[n]$ can be ger
transform will yie
exponential can b
One final inverse
diagram of the pro
sampled sequence
is implemented w
periodicity in the

A similar argument can be used to derive a relation between the magnitude and phase of the transform. Consider the complex spectrum

$$X(e^{j\omega}) = |X(e^{j\omega})| e^{j \arg X(e^{j\omega})} \tag{5.9}$$

Taking the natural log of (5.9) yields

$$\hat{X}(e^{j\omega}) = \log|X(e^{j\omega})| + j \arg X(e^{j\omega}) \tag{5.10}$$

Consider (5.10) to be the transform of a causal stable sequence $\hat{x}[n]$ with the additional restriction that the zeros also lie within the unit circle. This additional restriction results in the minimum phase condition. Since the real part of $\hat{X}(e^{j\omega}) = \log|X(e^{j\omega})|$ diverges with $X(e^{j\omega}) = 0$, no zeros must exist within the region of convergence. For a causal, stable sequence the region of convergence lies outside the unit circle; therefore, all zeros must lie with the unit circle. $\hat{x}[n]$ can also be written in terms of an even sequence that is properly windowed as in the previous argument. In this case, the even sequence $\hat{x}_e[n]$ corresponds to the inverse transform of the log of the spectrum's modulus. Using $\hat{x}_e[n]$, $\hat{x}[n]$ can be generated by using the window function given in (5.7). A forward transform will yield the complex spectrum $\hat{X}(e^{j\omega}) = \log X(e^{j\omega})$. Finally, the complex exponential can be applied to $\log X(e^{j\omega})$ to yield the original input spectrum $X(e^{j\omega})$. One final inverse transform will yield the original sequence. Figure 5.4 shows a block diagram of the process. In this diagram, the transforms have been written in terms of a sampled sequence in the time and frequency domain; hence, the discrete Fourier transform is implemented with the FFT. As is well known, sampling in one domain will force a periodicity in the other domain with a period determined by the sampling rate. By taking the inverse FFT of

and aliased. To co

must be used

One note o

of the sampling ra

not be an exact d

frequency domain

The seque

following equation

where $|X[k]|$ is s

w[n] defined in (5

following relation

An accura

requires the minim

must lie within t

However, if the

the inverse FFT of the spectrum's modulus, the cepstrum (see below) becomes periodic and aliased. To compute $\hat{x}[n]$, a new window function defined by the following equation must be used

$$w[n] = \begin{cases} 2, & 1 \le n < N/2 \\ 1, & n = 0, N/2 \\ 0, & N/2 < n \le N-1 \end{cases} \qquad \textbf{(5.11)}$$

One note of caution is that aliasing will occur, which is a function of the number of the sampling rate in the frequency domain. In this case the final sequence $\tilde{x}[n]$ will not be an exact duplicate of the input sequence x[n]. A higher sampling rate in the frequency domain will yield a better approximation to the input sequence.

The sequence c[n] is known as the real cepstrum and can be obtained with the following equation

$$c[n] = FFT^{-1}\left(\log|X[k]|\right) \qquad \textbf{(5.12)}$$

where $|X[k]|$ is simply the magnitude of the input signal spectrum. Using the window w[n] defined in (5.11), the minimum phase sequence $\tilde{x}[n]$ can be computed using the following relation

$$\tilde{x}[n] = FFT^{-1}\left(e^{FFT(w[n]c[n])}\right) \qquad \textbf{(5.13)}$$

An accurate reconstruction of a signal using the cepstral analysis technique requires the minimum phase restriction: all poles and zeros of the signal's z-transform must lie within the unit circle. Certainly, most signals will not be minimum phase. However, if the system can be modeled as minimum phase, the cepstral analysis technique should b

the spectral respon

One impor

energy concentrati

sequence is define

By Parseval's theo

total energy conte

near the beginnin

spectral magnitud

A sequence can b

near the origin (r

technique should be able to reconstruct the original signal using only the magnitude of the spectral response.

One important property of minimum phase sequences concerns the location of energy concentration [29],[33]. The energy from m+1 samples of a finite length sequence is defined by the following relation

$$E(m) = \sum_{n=0}^{m} |x[n]|^2 \tag{5.14}$$

By Parseval's theorem, two sequences having the save spectral magnitude have the same total energy content. However, for a minimum phase signal the energy is concentrated near the beginning of the sequence. So, for signals x[n] and $x_{min}[n]$ having the same spectral magnitude, the following relation holds

$$\sum_{n=0}^{m} |x[n]|^2 \le \sum_{n=0}^{m} |x_{\min}[n]|^2 \qquad \textit{for all } m \tag{5.15}$$

A sequence can be considered minimum phase-like if most of its energy is concentrated near the origin (n = 0).

Figure 5.1 No
zer

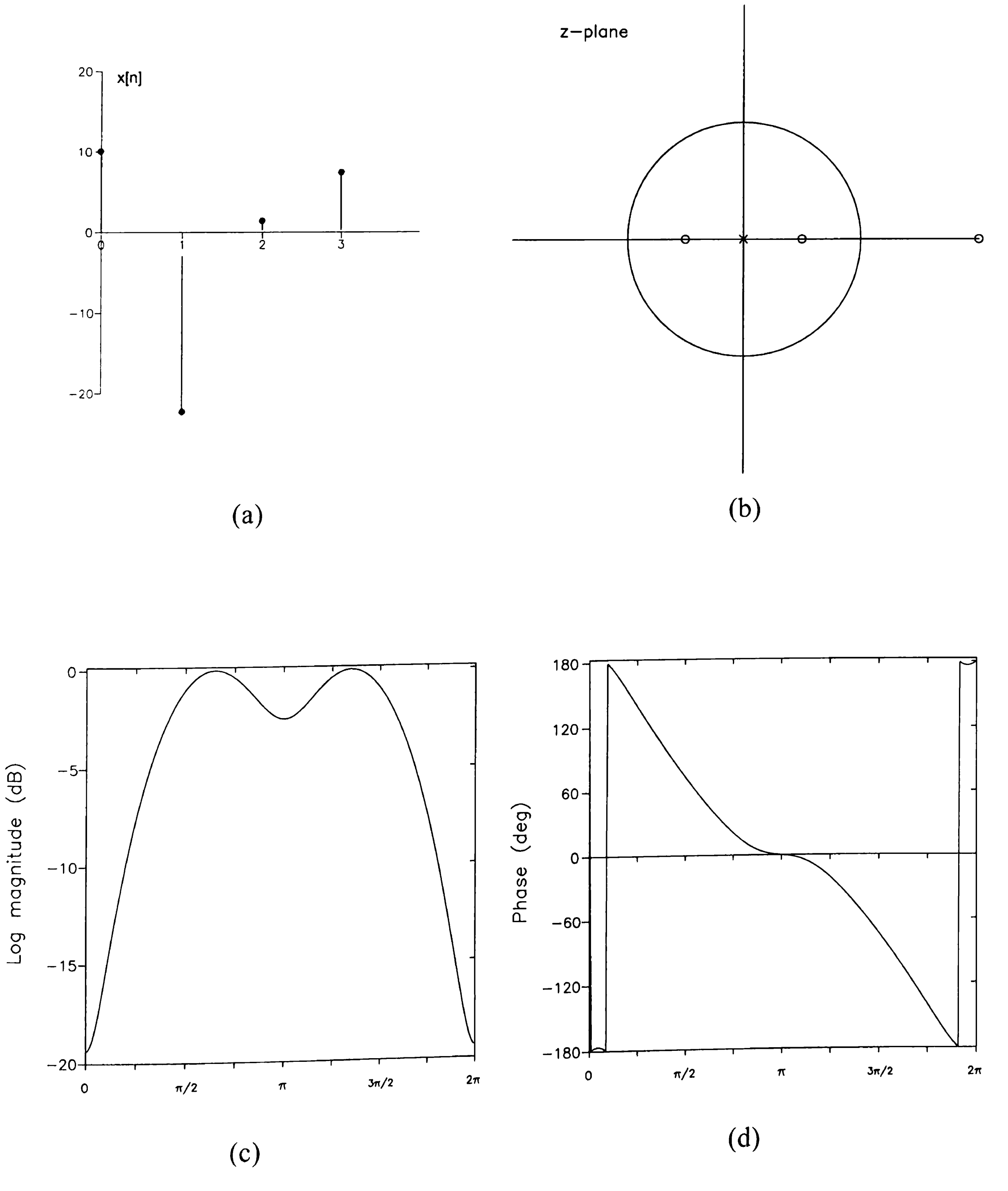

Figure 5.1 Non-minimum phase systems showing (a) input sequence; (b) z-plane pole-zero plot; (c) 20 $\log_{10} \mid X(e^{j\omega})/X_{max}(e^{j\omega}) \mid$; (d) arg [$X(e^{j\omega})$]

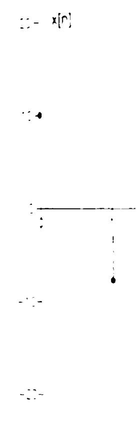

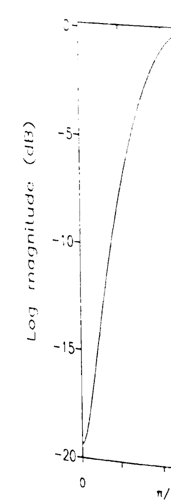

Figure 5.2 Mi
pl

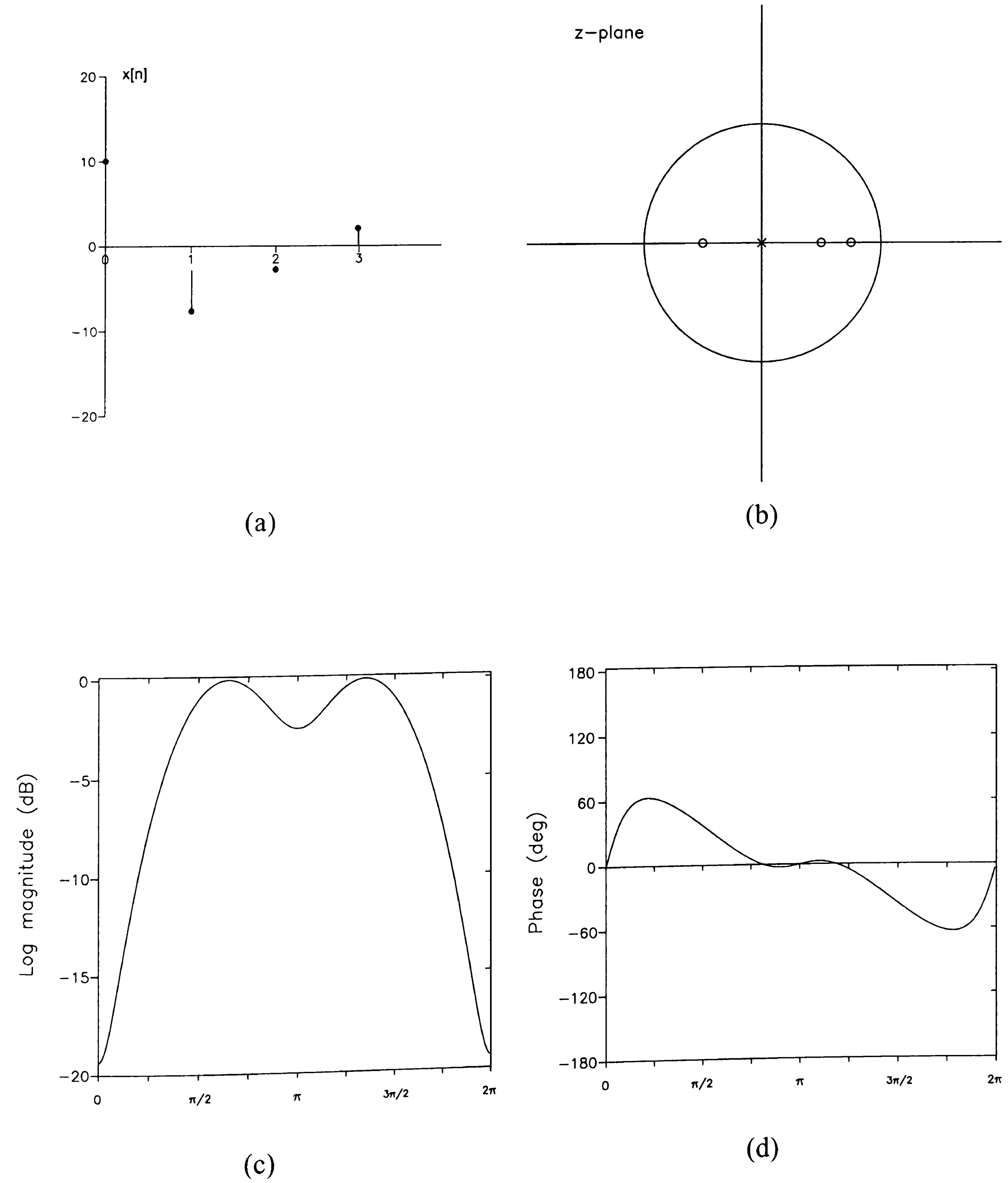

Figure 5.2 Minimum phase systems showing (a) input sequence; (b) z-plane pole-zero plot; (c) 20 $\log_{10} \mid X(e^{j\omega})/X_{max}(e^{j\omega}) \mid$; (d) arg [$X(e^{j\omega})$]

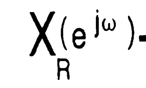

Figure 5.3 Blo
for

Figure 5.4 Bl
ma

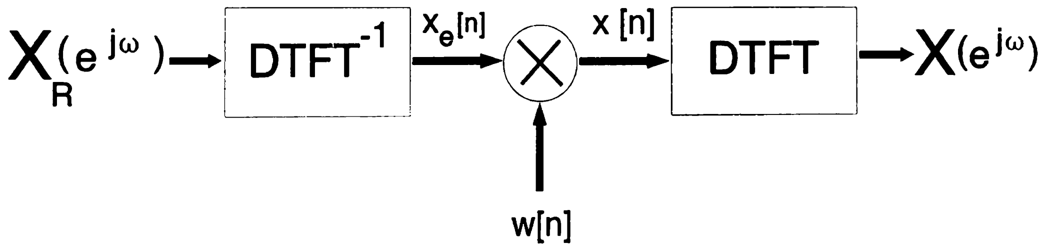

Figure 5.3 Block diagram showing conversion process from real to complex spectrum for a causal, stable input signal.

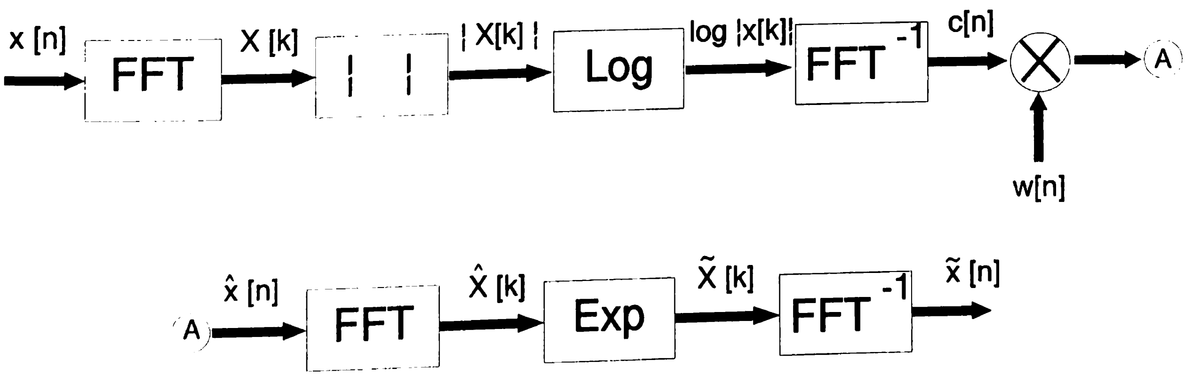

Figure 5.4 Block diagram showing construction of minimum phase signal from the magnitude of the spectral response.

5.3 Late-Time

The late-tim

as given by (5.3).

time variable t can

T as

The corresponding

where

In order for the n

aliasing), the pole

z-plane's unit circ

is just

For any finite-len

However, the zer

on the zeros are

can be written as

5.3 Late-Time Analysis

The late-time signal can be modelled using a sum of damped sinusoid components as given by (5.3). Consider a time-sampled sequence whose sampling period is T. The time variable t can then be written in terms of a sequence index n and sampling period T as

$$t = nT \tag{5.16}$$

The corresponding time-sampled sequence is then

$$f_l[n] = \sum_{m=1}^{M} c_m a_m^n \cos(\Omega_m n + \phi_m) \tag{5.17}$$

where

$$a_m = e^{\sigma_m T} \tag{5.18}$$

$$\Omega_m = \omega_m T \tag{5.19}$$

In order for the minimum phase reconstruction to match the original signal (neglecting aliasing), the poles and zeros of the sampled signal's z-transform must lie within the z-plane's unit circle. The z-transform for an N-point sampled sequence given by (5.17) is just

$$F_l(z) = \sum_{n=0}^{N-1} f_l[n] z^{-n} \tag{5.20}$$

For any finite-length sequence, the above polynomial contains N-1 poles at the origin. However, the zeros of the above polynomial are not easy to find. More properly, bounds on the zeros are difficult to establish. By expanding the z-transform polynomial (5.20) can be written as

$F_l(z) =$

For $f_l[0] \neq 0$, the

roots.

Consider t

relation

For $0 < a_m < 1$ (c

(5.22) are related

For an Nth degree

where $a_0 < a_1 < a_2$

lie within the z-pl

by (5.22) is min

sequence if the sa

To illustra

constructed with

frequency-domai

The appending o

any problems as

$$F_l(z) = \frac{1}{z^{N-1}} \left[f_l[0]\, z^{N-1} + f_l[1]\, z^{N-2} + \ldots + f_l[N-2]\, z + f_l[N-1] \right] \quad \mathbf{(5.21)}$$

For $f_l[0] \neq 0$, the above polynomial, whose coefficients are given by (5.17), has N-1 roots.

Consider the simple case of a purely damped sequence given by the following relation

$$f_l[n] = \sum_{m=1}^{M} c_m (a_m)^n \quad \mathbf{(5.22)}$$

For $0 < a_m < 1$ (corresponding to $-\infty < \sigma_m < 0$), successive values of the sequence in (5.22) are related with the following inequality

$$f_l[n+1] < f_l[n] \qquad n = 0, 1, \ldots N-2 \quad \mathbf{(5.23)}$$

For an N[th] degree polynomial of the form

$$P(z) = a_N z^N + a_{N-1} z^{N-1} + \ldots + a_1 z + a_0 \quad \mathbf{(5.24)}$$

where $a_0 < a_1 < a_2 < \ldots < a_N$, the Kakeya-Enestrom theorem [34] states that all zeros must lie within the z-plane's unit circle. Using this theorem, a simple damped sequence given by (5.22) is minimum phase and a cepstral reconstruction should match the original sequence if the sampling rate is high enough to avoid any aliasing effects.

To illustrate the above ideas, a simple 32-point ,single-mode (M=1) sequence was constructed with damping constant a_1 = .9, and amplitude coefficient c_1 = 1.0 . The frequency-domain response was formed by taking a 512-point FFT of the input signal. The appending of zeros to the input sequence in forming the frequency response limits any problems associated with aliasing. Using only the magnitude of the frequency response. a minim

original sequence

reconstructed seq

original 32-point s

zeros lie within th

origin due to the f

will show the pol

A second

Figure 5.7. In this

parameters a_1 = .7

= .5. This combi

point transform a

original sequence

reconstructed mi

since all the zeros

inside the unit ci

For the cas

extremely well

Unfortunately, th

a sum of damped

---

[1]In the follo
eigenvalues of th
[37]. All calculat

response, a minimum phase reconstructed signal was formed [35]. Figure 5.5 shows the original sequence and its cepstral (minimum phase) reconstruction. As expected, the reconstructed sequence matches the original sequence. Taking the z-transform of the original 32-point sequence and plotting the zeros[1] in the z-plane gives the result that all zeros lie within the unit circle (see Figure 5.6). Note that all the poles are located at the origin due to the finite length of the signal sequence. None of the following z-plane plots will show the pole locations.

A second example of a decaying sequence consisting of two modes is shown in Figure 5.7. In this case a 32-point sequence was formed from one mode having sequence parameters $a_1 = .7$ and $c_1 = 1.0$ and the other sequence having parameters $a_2 = .9$ and $c_2 = .5$. This combined sequence was transformed to the frequency domain using a 512-point transform and the subsequent magnitude response was used to reconstruct the original sequence. As Figure 5.7 clearly shows, the original sequence and the reconstructed minimum phase sequence match nicely. This again should be expected, since all the zeros corresponding to the z-transform of the original sequence are located inside the unit circle as shown in Figure 5.8.

For the case of a purely damped signal the cepstral reconstruction technique works extremely well if aliasing problems caused by low sampling rates are avoided. Unfortunately, the late-time model proposed consists of a sum of damped sinusoids. For a sum of damped sinusoids of arbitrary parameters it is difficult to put bounds on zero

---

[1]In the following z-plane plots, zero locations were determined by computing the eigenvalues of the companion matrix associated with the polynomial equation [34],[36]-[37]. All calculations were performed in MATLAB.

locations in the z-

sampled damped s

64-point sequence

Figure 5.9 and F

respectively. Figu

are inside the uni

sequence. Howev

point transform)

reconstruction a n

reconstruction.

As another

a damping param

slowly. Figure

reconstruction. O

sequence. The z-

indicating an orig

Both of th

condition is not

signal. One o

concentration of

sinusoid more e

phase-like appro

locations in the z-plane. In fact, it is quite easy to show with a simple example that a sampled damped sinusoid sequence may not be minimum phase. Consider a single mode, 64-point sequence with parameters given by $c_1 = 1.0$, $a_1 = .95$, $\Omega_1 = 1.0$, $\phi_1 = 80.0°$. Figure 5.9 and Figure 5.10 show the sequence and the zeros of the z-transform respectively. Figure 5.10 clearly shows a zero well outside the unit circle (the other zeros are inside the unit circle). In this case the original sequence is not a minimum phase sequence. However, if the magnitude of the frequency response is obtained (using a 512-point transform) and used to construct the minimum phase sequence using cepstral reconstruction a nice match results between the original sequence and the minimum phase reconstruction.

As another example, consider the same signal as in the previous example but with a damping parameter of $a_1 = .99$. In this example the signal sequence damps out more slowly. Figure 5.11 shows this new sequence as well as its minimum phase reconstruction. Once again, the reconstructed sequence is a good rendition of the original sequence. The z-plane zero plot (Figure 5.12) shows a single zero outside the unit circle indicating an original sequence that is not minimum phase.

Both of the previous examples show that strict observance of the minimum phase condition is not always necessary to reconstruct a sequence that matches the original signal. One of the key characteristics of the minimum phase sequence is the concentration of the signal's energy at the beginning of the sequence. For the damped sinusoid more energy is located early in the life of the signal, indicating a minimum phase-like approximation. For a non-damped sinusoid (i.e. the damping parameter > 1)

a simple example v
Consider a 64-poi
and $\phi_1 = 0.0$. Figu
zero locations resp
the original seque
maximum phase).
signal sequence, a
(after obtaining th
In this case the m
sequence. A dam
correct sequence
For radar returns
expected.

The next e
modes. The first
$\phi_1 = 0.0$. The sec
The third mode
and $\phi_3 = 0.0$.
However, the au
a 128-point sequ
generate the mag
minimum phase

a simple example will show that the cepstral reconstruction behavior does not match well. Consider a 64-point sequence using only a single mode with $c_1 = 1.0$, $a_1 = 1.2$, $\Omega_1 = 1.0$, and $\phi_1 = 0.0$. Figure 5.13 and Figure 5.14 show the original sequence and the z-transform zero locations respectively. Figure 5.14 clearly shows the non-minimum phase nature of the original sequence with all the zeros outside the unit circle (commonly denoted as maximum phase). For this sequence , the concentration of energy occurs late in the signal sequence, a feature that is clearly not minimum phase. The cepstral reconstruction (after obtaining the magnitude response with a 1024-point FFT) is shown in Figure 5.13. In this case the minimum phase sequence does not come close to matching the original sequence. A damping coefficient with values greater than unity is a real problem if the correct sequence is to be reconstructed from the magnitude of the frequency response. For radar returns in the late-time, a damping ratio greater than unity should not be expected.

The next example shows a composite damped sinusoidal signal consisting of three modes. The first mode consists of parameter values $c_1 = 1.0$, $a_1 = .987$, $\Omega_1 = .1645$, and $\phi_1 = 0.0$. The second mode has parameters $c_2 = 1.0$, $a_2 = .9935$, $\Omega_2 = .366$, and $\phi_2 = 0.0$. The third mode consists of a signal having parameters $c_3 = 1.0$, $a_3 = .978$, $\Omega_3 = .4945$, and $\phi_3 = 0.0$. The natural frequencies were obtained from actual measurements. However, the author chose the magnitude and phase coefficients. Using the above data a 128-point sequence was constructed. An FFT consisting of 2048 points was used to generate the magnitude response. Figure 5.15 shows the original sequence as well as the minimum phase reconstruction. In this case the match between the two sequences is extremely close. A

example nearly al

barely outside of t

In the prev

of non-zero phase

consider a compos

consists of parame

mode has parame

consists of a sign

Using this data a

was used to gener

as well as the mi

sequences is muc

shift between the

of the zeros for t

zeros outside the

ambiguity in the

waveform was n

target identificati

The capa

specific signature

based on the un

extremely close. A plot of the zeros for the z-transform is shown in Figure 5.16. In this example nearly all the zeros are inside the unit circle. However, due to a few zeros barely outside of the unit circle, the original sequence is not minimum phase.

In the previous example, all phase terms were set to a value of zero. The effect of non-zero phase terms can be seen by considering a similar example. Once again, consider a composite damped sinusoidal signal consisting of three modes. The first mode consists of parameter values $c_1 = 1.0$, $a_1 = .987$, $\Omega_1 = .1645$, and $\phi_1 = 30.0$. The second mode has parameters $c_2 = 1.0$, $a_2 = .9935$, $\Omega_2 = .366$, and $\phi_2 = 45.0$. The third mode consists of a signal having parameters $c_3 = 1.0$, $a_3 = .978$, $\Omega_3 = .4945$, and $\phi_3 = 90.0$. Using this data a 128-point sequence was constructed. An FFT consisting of 2048 points was used to generate the magnitude response. Figure 5.17 shows the original sequence as well as the minimum phase reconstruction. In this case the match between the two sequences is much worse than in the previous example. This plot not only shows a phase shift between the two waveforms, but also a difference in the waveform shapes. A plot of the zeros for the z-transform is shown in Figure 5.18. In this example there are more zeros outside the unit circle than in the previous case. This example illustrates the ambiguity in the phase terms for cepstral reconstruction. Even though the original waveform was not duplicated, cepstral reconstruction may still be a powerful tool for target identification.

The capability to identify a specific target depends on the ability to recover specific signatures associated with that target. One technique used to identify a target is based on the uniqueness of a target's complex (natural) frequencies in the late-time

transient scattered
minimum-phase t
sequence. Howev
match those in the
technique for targ
frequencies in a si
The extracted. na
an E-pulse least-s
two examples can
The second case
reconstruction. T
is the 3-mode. n
Table 5.1 shows t
the input signals i
closely match the
does not match th
in Table 5.1 show
very closely. T
technique will
identification alg

A late-tin
phase cepstral t

transient scattered signal. If a waveform is composed of a sum of damped sinusoids the minimum-phase technique may or may not be able to reconstruct the exact input sequence. However, if the natural frequencies contained in the reconstructed waveform match those in the original sequence then it should be possible to use the minimum-phase technique for target identification. A simple example will be used to show if the natural frequencies in a signal remain unchanged in the minimum phase reconstructed waveform. The extracted, natural frequencies for the previous two examples were calculated using an E-pulse/least-squares fitting algorithm (see chapter 3). Four cases from the previous two examples can be considered. The first case is the 3-mode, zero-phase, input signal. The second case is the 3-mode, zero-phase, composite signal obtained by cepstral reconstruction. The third case is the 3-mode, non-zero phase, input signal. The final case is the 3-mode, non-zero phase, composite signal obtained by cepstral reconstruction. Table 5.1 shows the extracted frequencies for each case. The frequencies used to generate the input signals is case 1 and 3 are also shown. In every case, the extracted frequencies closely match the original values. As shown in Figure 5.17 the reconstructed waveform does not match the original sequence for the non-zero phase case. However, the results in Table 5.1 show that the extracted frequencies for case 4 match the original frequencies very closely. This is a very nice result, indicating that the cepstral reconstruction technique will probably work very well in conjunction with the E-pulse target identification algorithm.

A late-time signal modeled using (5.3) can be reconstructed using the minimum phase cepstral technique even though the original sequence is not minimum phase.

However, the lat

minimum phase s

should be used to

frequency domain

measurements tak

cepstral algorithm

However, the late-time signal has an energy concentration nature similar to that of a minimum phase signal. It also should be kept in mind that a small sampling interval should be used to avoid aliasing. In the above examples, a small sampling interval in the frequency domain was used which lead to very good cepstral reconstruction. However, measurements taken at or near the Nyquist rate will not lead to good results using the cepstral algorithms.

Amplitude

Figure 5.5 Si
ce

Figure 5.6 Ze
ph

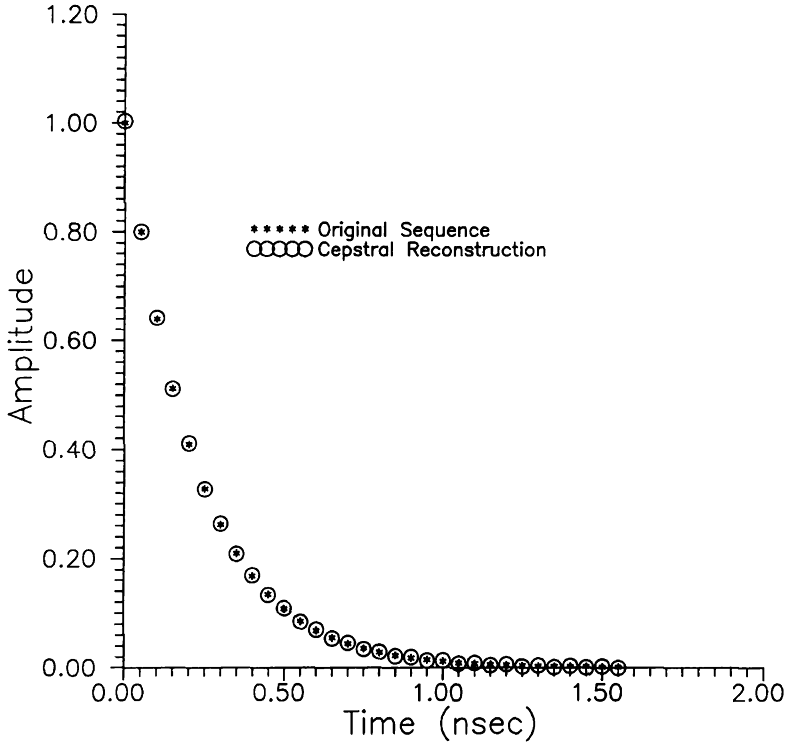

Figure 5.5 Single mode decay sequence representing a minimum-phase signal and its cepstral reconstruction.

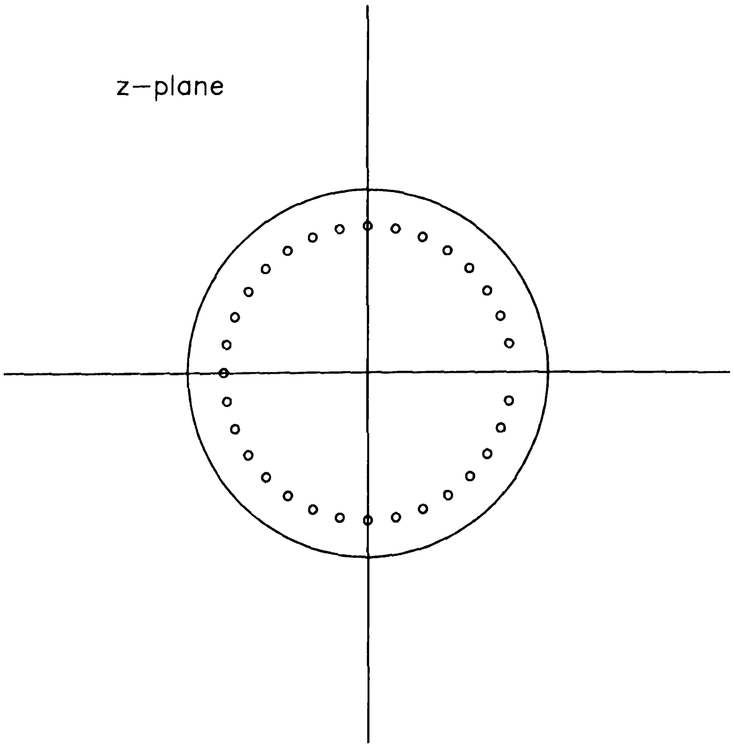

Figure 5.6 Zero locations with respect to the unit circle for a single mode minimum phase decay sequence.

Amplitude

Figure 5.7 Mu
cep

Figure 5.8 Ze
de

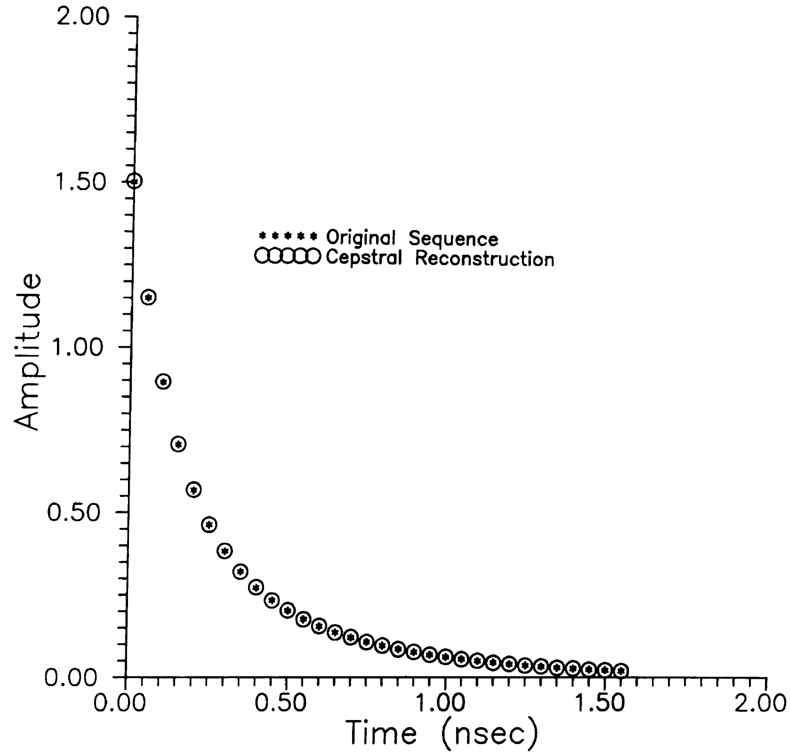

Figure 5.7 Multi-mode decay sequence representing a minimum-phase signal and its cepstral reconstruction.

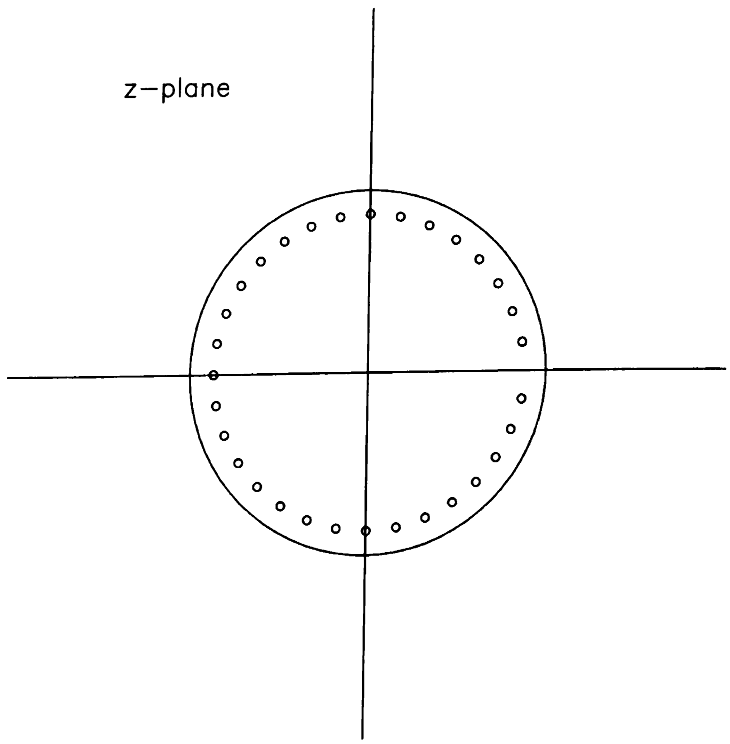

Figure 5.8 Zeros with respect to the unit circle for a multi-mode minimum phase decay sequence.

Amplitude

Figure 5.9 Si
sig

Figure 5.10 Ze
ph

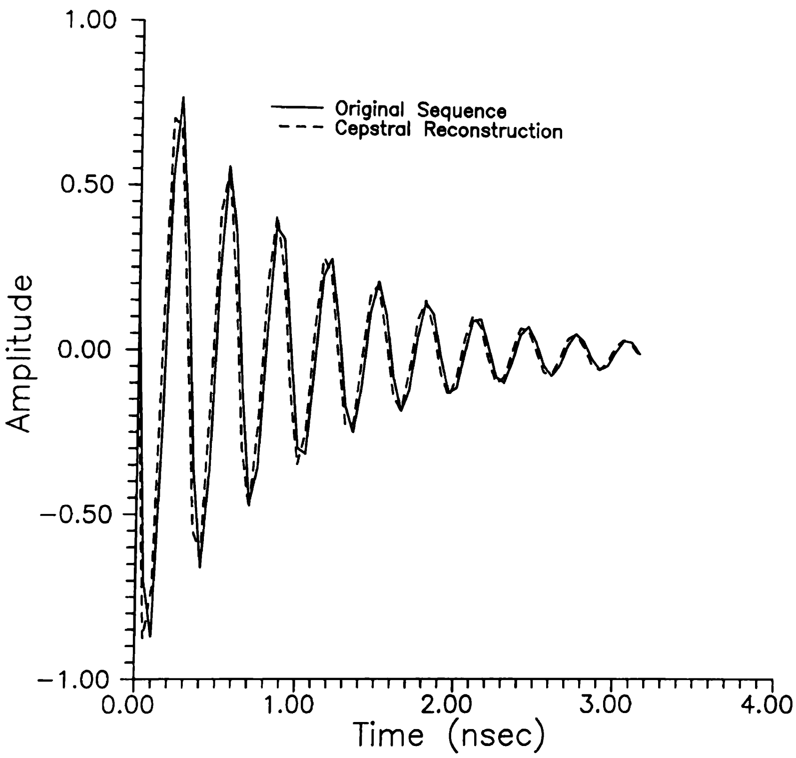

Figure 5.9 Single mode damped sinusoid signal illustrating a non-minimum phase signal and its cepstral reconstruction.

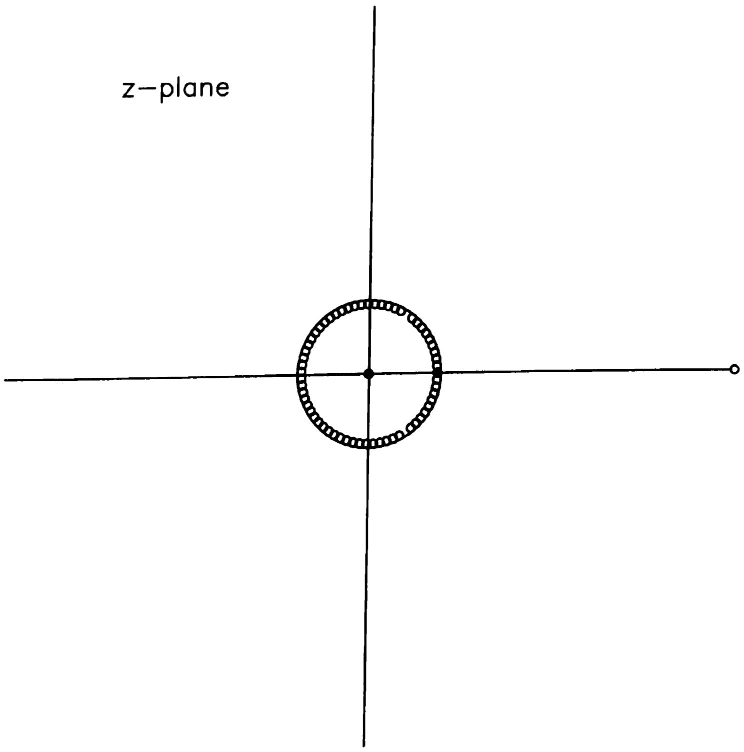

Figure 5.10 Zeros with respect to the unit circle for a damped sinusoid non-minimum phase sequence.

Amplitude

Figure 5.11 A
no

Figure 5.12 Ze
sir

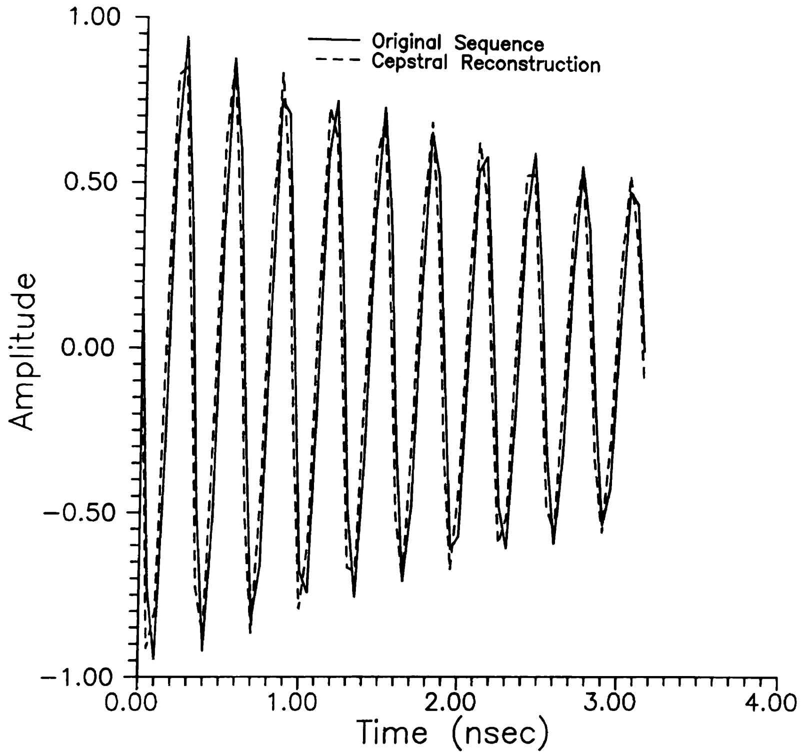

Figure 5.11 A second example of a single mode damped sinusoid signal illustrating a non-minimum phase signal and its cepstral reconstruction.

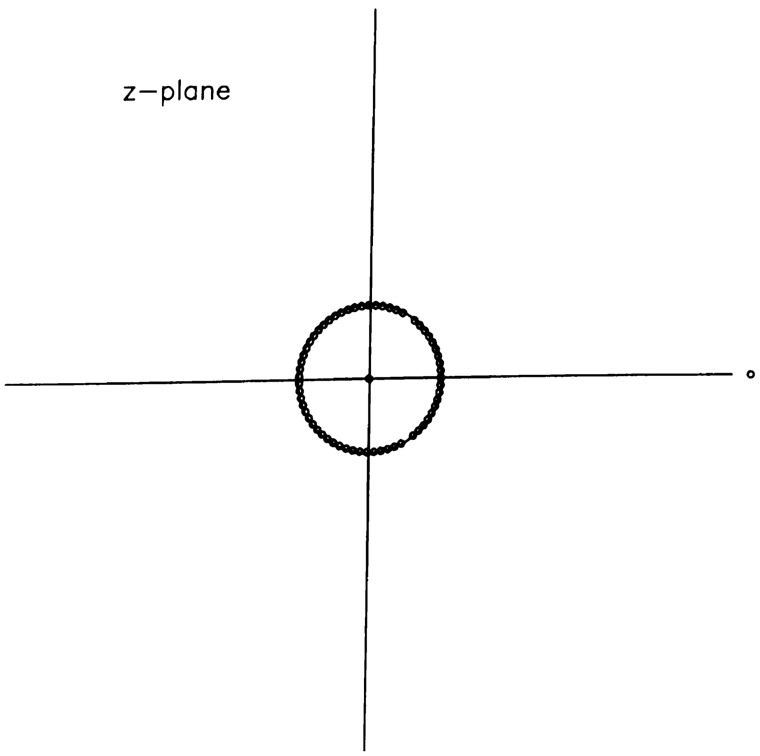

Figure 5.12 Zeros with respect to unit circle for the second example of a damped sinusoid non-minimum phase sequence.

Amplitude

Figure 5.13 Si
re

Figure 5.14 Z

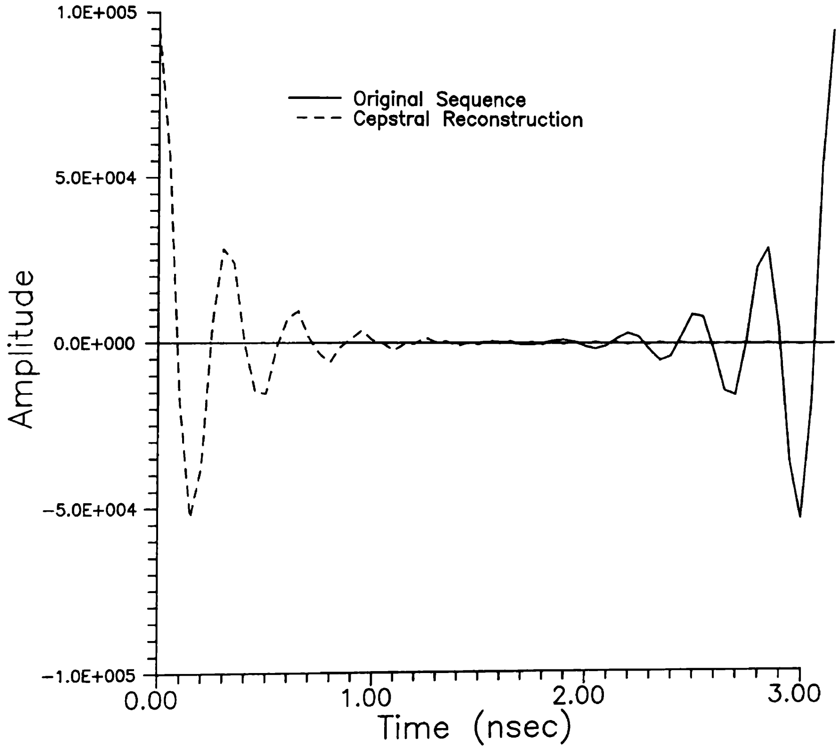

Figure 5.13 Single mode signal illustrating a maximum-phase signal and its cepstral reconstruction.

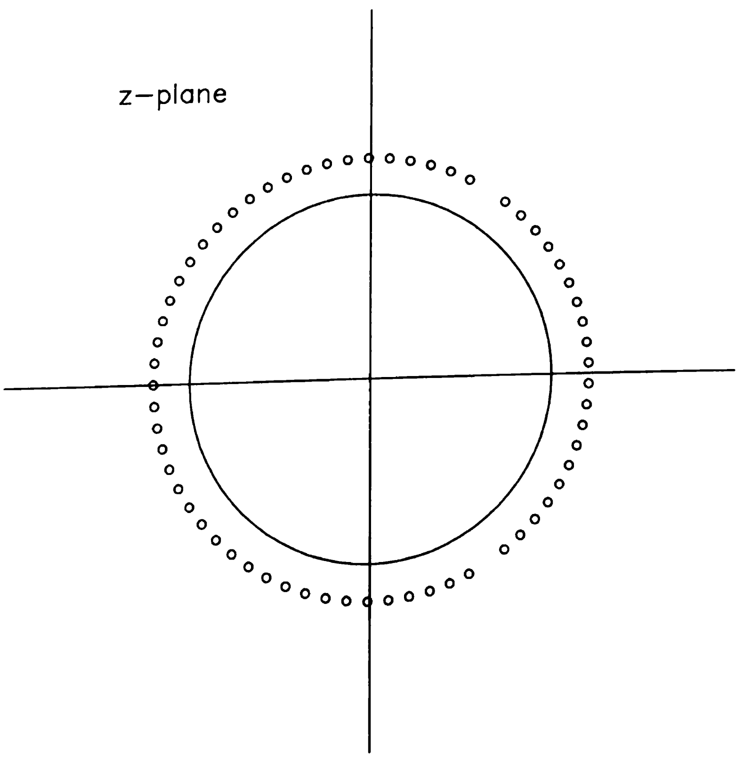

Figure 5.14 Zeros with respect to the unit circle for a maximum-phase signal.

Amplitude

Figure 5.15 C
re

Figure 5.16 Z
s

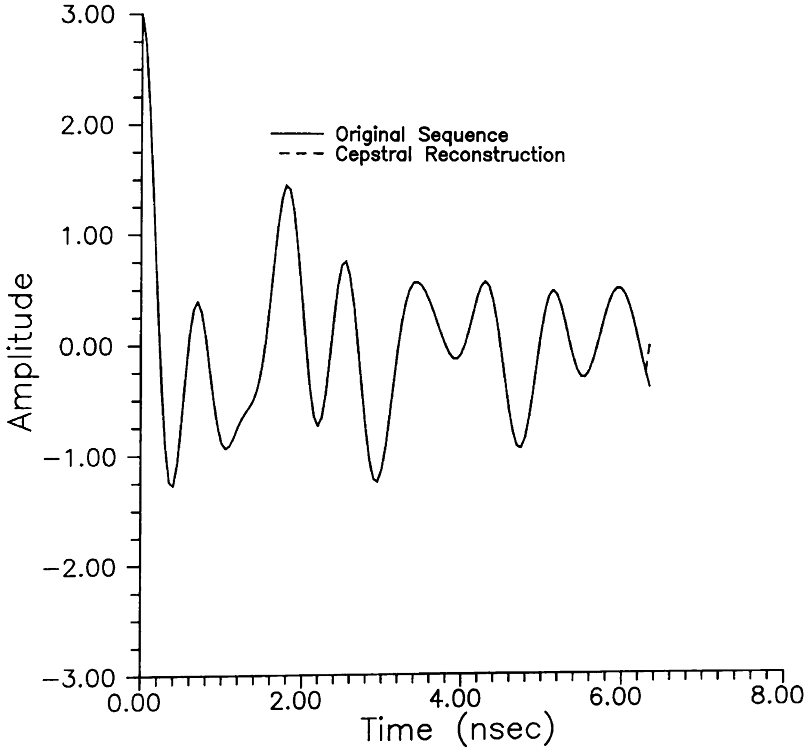

Figure 5.15 Composite 3-mode damped sinusoid signal and its minimum-phase reconstruction.

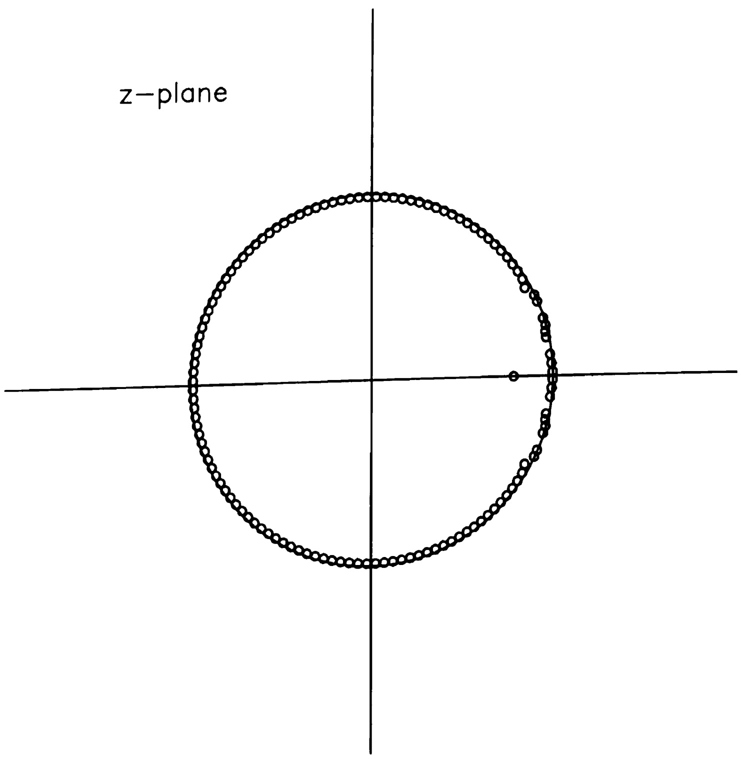

Figure 5.16 Zeros with respect to the unit circle for a composite damped sinusoid signal.

Amplitude

Figure 5.17 A
m

Figure 5.18 Ze
co

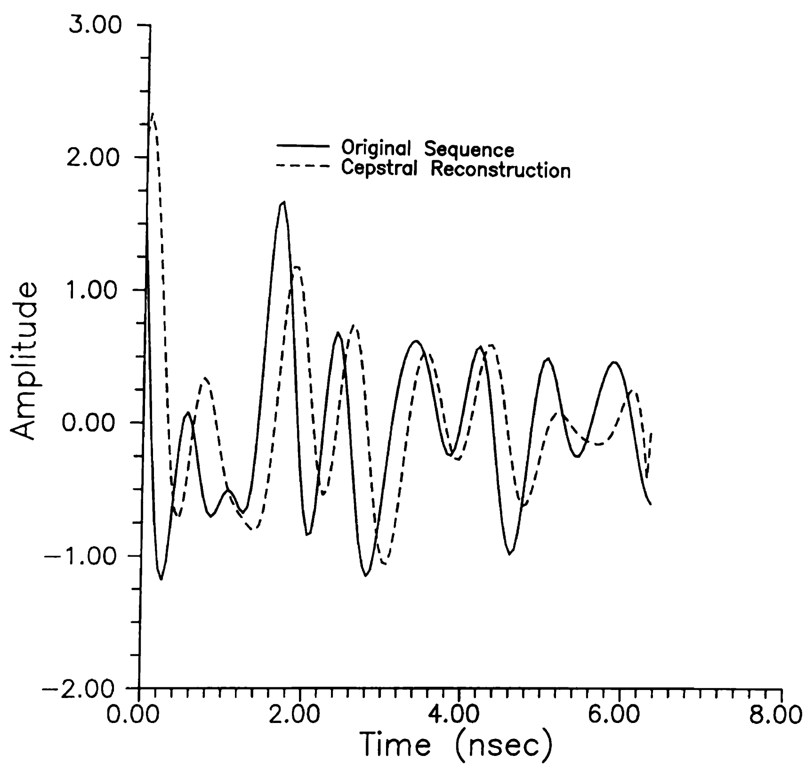

Figure 5.17 A second example of a 3-mode composite damped sinusoid signal and its minimum-phase reconstruction.

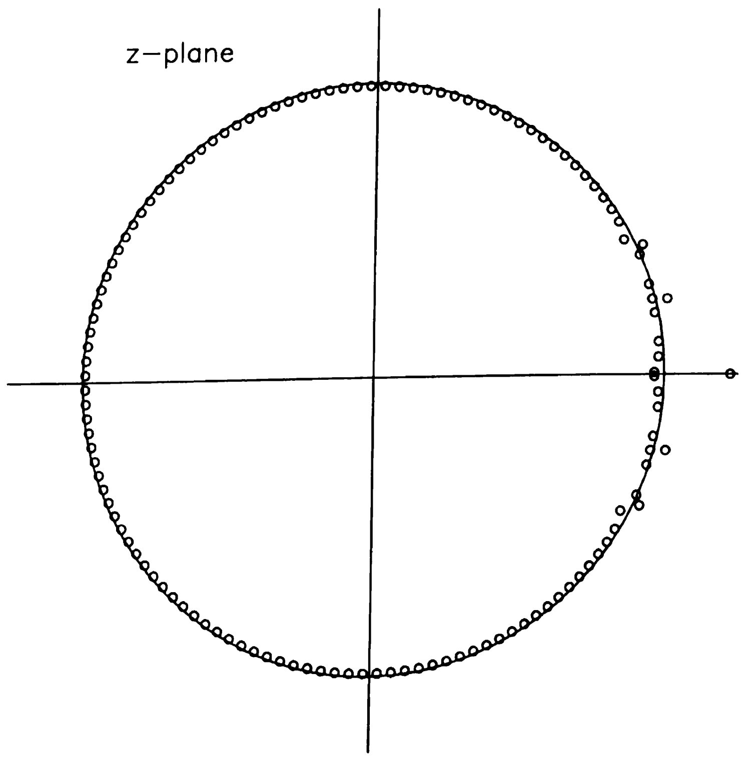

Figure 5.18 Zeros with respect to the unit circle for the second example of a 3-mode composite damped sinusoid.

Table 5.1 Na
al
ze

Case Numbe
1
2
3
4
Original Valu

Table 5.1 Natural frequencies obtained from the E-pulse/least squares extraction algorithm for composite sinusoidal input signals have zero-phase and non-zero phase components.

Case Number	Complex Frequency #1	Complex Frequency #2	Complex Frequency #3
1	.9870 + .1645 j	.9935 + .3660 j	.9780 + .4945 j
2	.9870 + .1645 j	.9935 + .3660 j	.9780 + .4945 j
3	.9870 + .1645 j	.9935 + .3660 j	.9780 + .4940 j
4	.9872 + .1660 j	.9921 + .3675 j	.9758 + .4920 j
Original Values	.9870 + .1645 j	.9935 + .3660 j	.9780 + .4945 j

5.4 Early-Ti

A simple

section. A samp

as

where n is the s

center at tempo

difficult to dete

addition, a dete

guarantee that t

forming the z-t

However, the z

correspond to th

energy concentra

to create a comp

phase.

The disc

represented as a

can be written a

where

5.4 Early-Time Analysis

A simple model for the early-time component was introduced in the introductory section. A sampled, early-time signal sequence for M scattering centers can be written as

$$f_e[n] = \sum_{i=1}^{M} f_i(n - m_i) \tag{5.25}$$

where n is the sample index and m_i represents the index corresponding to ith scattering center at temporal position T_i. Clearly, for a general pulse response it will be very difficult to determine whether (5.25) corresponds to a minimum phase sequence. In addition, a determination that each pulse response in (5.25) is minimum phase is no guarantee that the composite signal is minimum phase. This can easily be seen by forming the z-transform polynomial for each pulse response and finding the zeros. However, the zeros of the composite z-transform polynomial will not necessarily correspond to the zeros of the individual components. Since a minimum phase signal has energy concentration characteristics described in the previous two sections, it is quite easy to create a composite early-time signal having energy characteristics that are not minimum phase.

The discussion to follow assumes that the individual pulse responses can be represented as a discrete pulse of amplitude a_i over one sample interval. This response can be written as

$$f_i[n] = a_i\,\delta(n - m_i) \tag{5.26}$$

where

$$\begin{aligned} \delta(n - m_i) &= 1 \qquad n = m_i \\ &= 0 \qquad n \neq m_i \end{aligned} \tag{5.27}$$

The z-transform

which is minimu

On the o

composite respo

which is general

the first pulse i

parameters a_2 =

This polynomia

conclusion sho

match to the o

An imp

phase. Consid

and

The z-transform of (5.26) is given as

$$F_i(z) = \frac{a_i}{z^{m_i}} \qquad \textbf{(5.28)}$$

which is minimum phase.

On the other hand, if all the pulse responses are considered, the z-transform of the composite response is

$$F(z) = \sum_{i=1}^{M} \frac{a_i}{z^{m_i}} \qquad \textbf{(5.29)}$$

which is generally not minimum phase. Consider a two pulse sequence (M = 2) in which the first pulse is characterized by parameters $a_1 = 1.0$, $m_1 = 2$ and the second pulse has parameters $a_2 = 2$, and $m_2 = 3$. The z-transform of this sequence is just

$$F(z) = \frac{1}{z^3}(2 + z) \qquad \textbf{(5.30)}$$

This polynomial clearly has a root outside the unit circle at z = -2. At this point, no conclusion should be made that a cepstral reconstruction will fail to reproduce a close match to the original sequence; however, some caution should be considered.

An important question to ask is whether a sequence does exist that is minimum phase. Consider the case where

$$a_1 > a_2 > a_3 > \dots > a_M \qquad \textbf{(5.31)}$$

and

$$m_1 < m_2 < m_3 < \dots < m_{M-1} < m_M \qquad \textbf{(5.32)}$$

If the conditions
that the zeros o
sequence shown
satisfies the m
magnitude respo
of the original
matches the orig
the z-transform

The prev
using a 16-poin
zeros correspon
points in each
waveforms. O
match between
(1024-point FF
correct placeme

What ha
general, for a s
reconstruction
energy concent
be expected.
simple signals.

If the conditions in (5.31) and (5.32) are met, then the Kakeya-Enestrom theorem states that the zeros of (5.29) must all lie within the unit circle. Consider the simple 4-point sequence shown in Figure 5.19. As can be seen, this sequence is decaying and easily satisfies the minimum phase requirements. Using a 128-point FFT, the spectral magnitude response was generated and used to form the minimum-phase reconstruction of the original pulse sequence. As shown in Figure 5.19, the reconstructed sequence matches the original sequence quite well. Figure 5.20 shows the zeros corresponding to the z-transform of the original sequence; in this case all zeros lie inside the unit circle.

The previous example has all the sample pulses equally spaced. Another example using a 16-point sequence with unequally spaced pulses is shown in Figure 5.21. The zeros corresponding to the z-transform of this sequence are shown in Figure 5.22. The points in each signal have been connected to visually enhance the separation of the waveforms. Once again the input sequence in minimum phase; hence, there is a good match between the original sequence and the cepstral reconstruction shown in Figure 5.21 (1024-point FFT used to generate the frequency response). This example illustrates the correct placement of pulse locations for a minimum phase signal.

What happens when the sequence of pulses is not a decaying sequence? In general, for a sequence of pulses that does not behave in a decaying manner, a cepstral reconstruction will not yield the original sequence. However, if the original sequence has energy concentration characteristics similar to a minimum phase signal, better results can be expected. A few simple examples will illustrate the problems posed by some very simple signals.

Figure 5.

this sequence, a

expected that th

reproduce the or

reconstruction i

Figure 5.24. Th

maximum phas

reverse the inpu

reconstruction c

A final

Figure 5.25. T

aircraft with tw

propagation is p

on one wing, th

low amplitude

fuselage. It wo

good represen

reconstructed s

locations of th

example, the u

very disappoin

without phase

Figure 5.23 shows a series of five pulses embedded in a 32-point input signal. In this sequence, a much larger pulse is located late in the input waveform. Therefore, it is expected that the signal is non-minimum phase and cepstral reconstruction will fail to reproduce the original sequence. This result is indeed the case, as shown by the cepstral reconstruction in Figure 5.23 and the location of zeros outside the unit circle in Figure 5.24. The location of the zeros indicate that this signal has characteristics of a maximum phase signal [29]. In this case, the cepstral reconstruction algorithm will reverse the input waveform. This simple example illustrates just how badly the cepstral reconstruction can be for some time sequences.

A final example of a simple 32-point sequence using five pulses is shown in Figure 5.25. This sequence is very similar to the measured early-time responses of aircraft with two engines mounted on each wing (see Figure 5.44). If the direction of propagation is perpendicular to the fuselage, the first two pulses represent the two engines on one wing, the middle pulse corresponds to the return from the fuselage, and finally the low amplitude pulses represent returns from the engines that are shadowed by the fuselage. It would quite useful if the cepstral reconstruction would be able to provide a good representation of the original signal. However, as Figure 5.25 shows, the reconstructed signal does not match the original sequence. Figure 5.26 shows the zero locations of the z-transform clearly indicating a non-minimum phase signal. In this example, the use of cepstral reconstruction to reproduce the original waveform leads to very disappointing results. Clearly the input signal in this example can not be reproduced without phase information.

The anal

difficult to recon

should not be us

of the signal is c

target identificat

transient signal

beginning of ea

presence of son

The analysis presented above indicates that the early-time component is very difficult to reconstruct using only the magnitude of the spectral response. This technique should not be used for any type of imaging algorithm where correct spatial representation of the signal is critical. However, the use of the early-time response could be useful for target identification. One benefit of the cepstrum technique is that the largest point of the transient signal is usually place first (at the origin). This might be used to find the beginning of early time which has been notoriously difficult to find, especially in the presence of some noise.

Figure 5.19

Figure 5.20

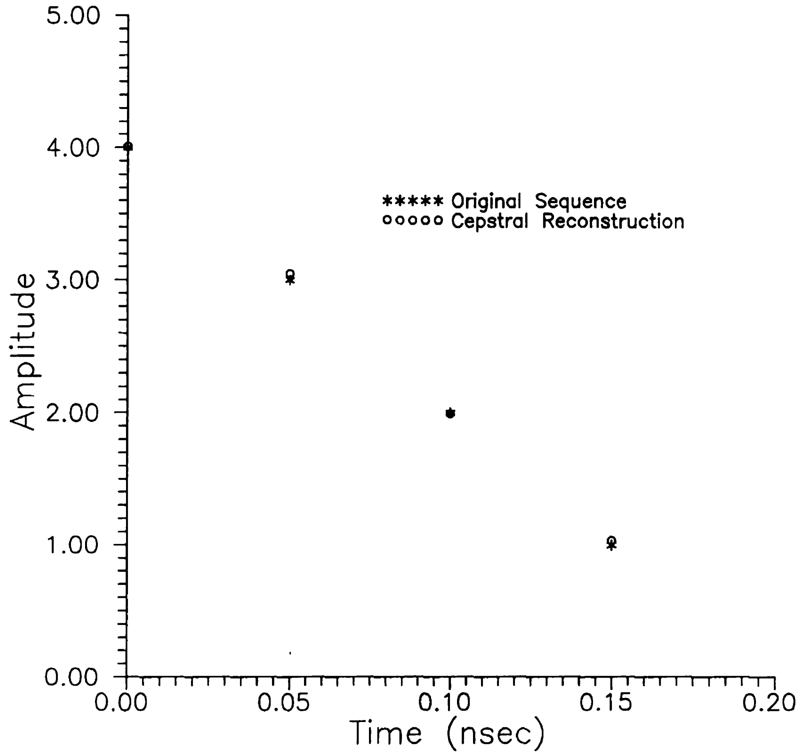

Figure 5.19 Simulated early-time and its cepstral reconstruction using a 4-point 4-pulse minimum-phase sequence.

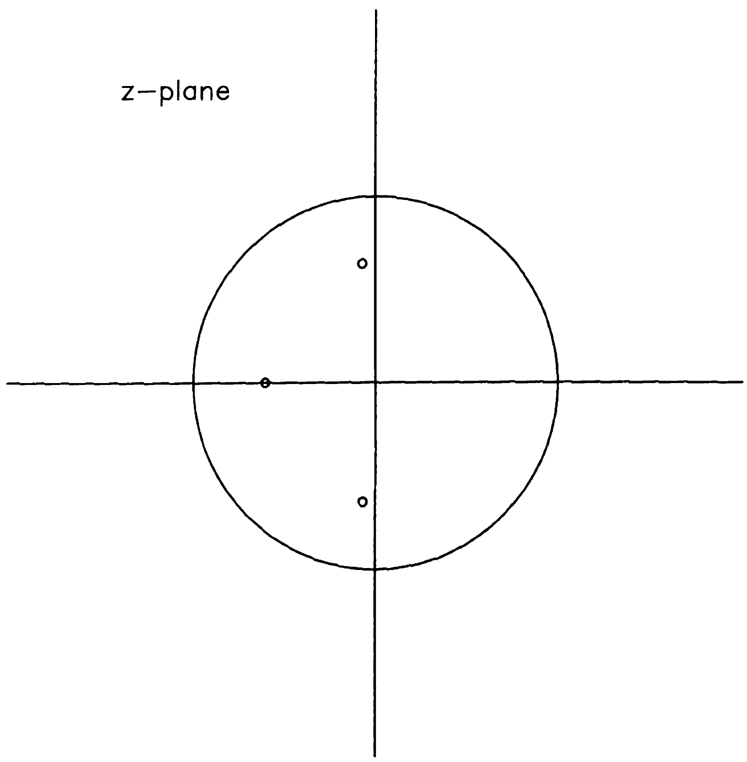

Figure 5.20 Zeros with respect to unit circle for simulated early-time 4-point 4-pulse minimum-phase sequence.

Figure 5.21

Figure 5.22

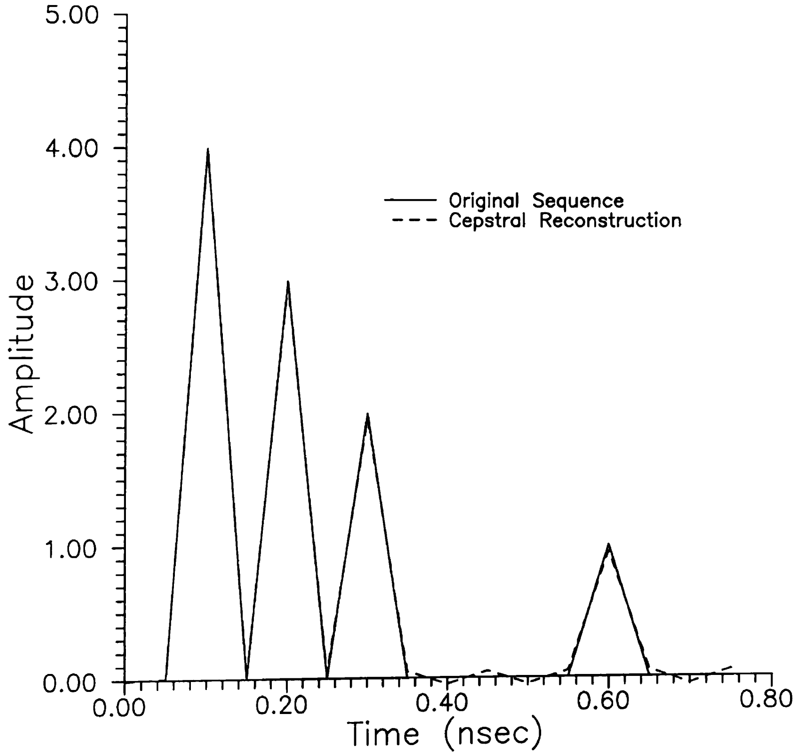

Figure 5.21 Simulated early-time and its cepstrum reconstruction using a 16-point 4-pulse minimum-phase sequence.

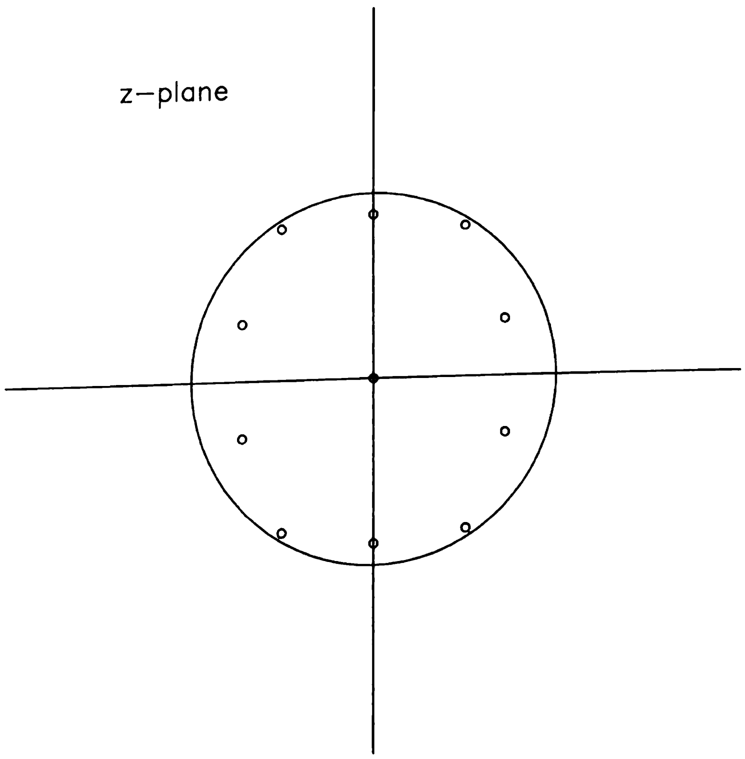

Figure 5.22 Zeros with respect to unit circle for simulated early-time 16-point 4-pulse minimum-phase sequence.

Figure 5.23

Figure 5.24

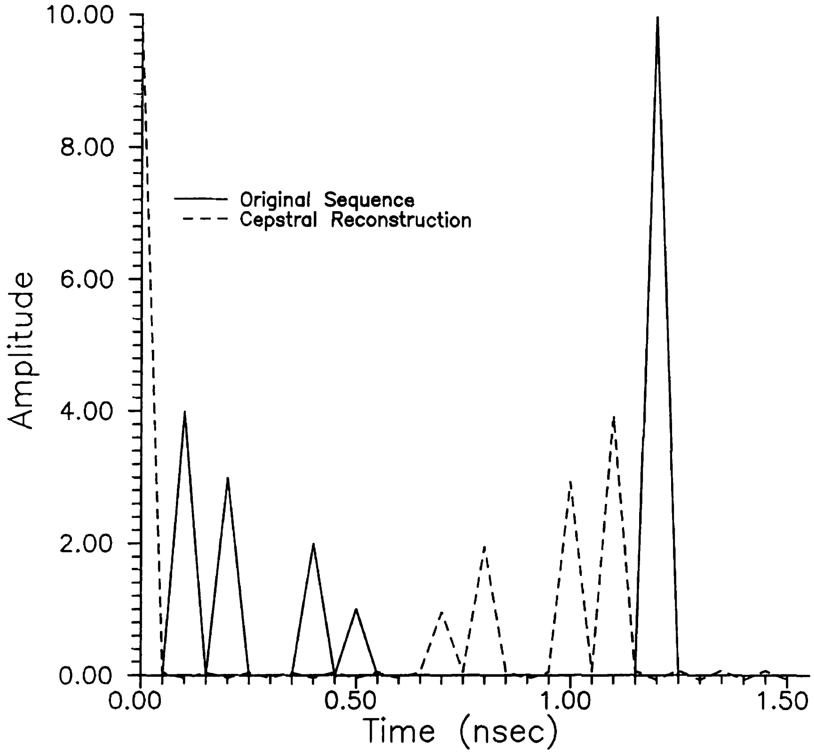

Figure 5.23 Simulated early-time and its cepstral reconstruction using a 32-point 5-pulse non minimum-phase sequence.

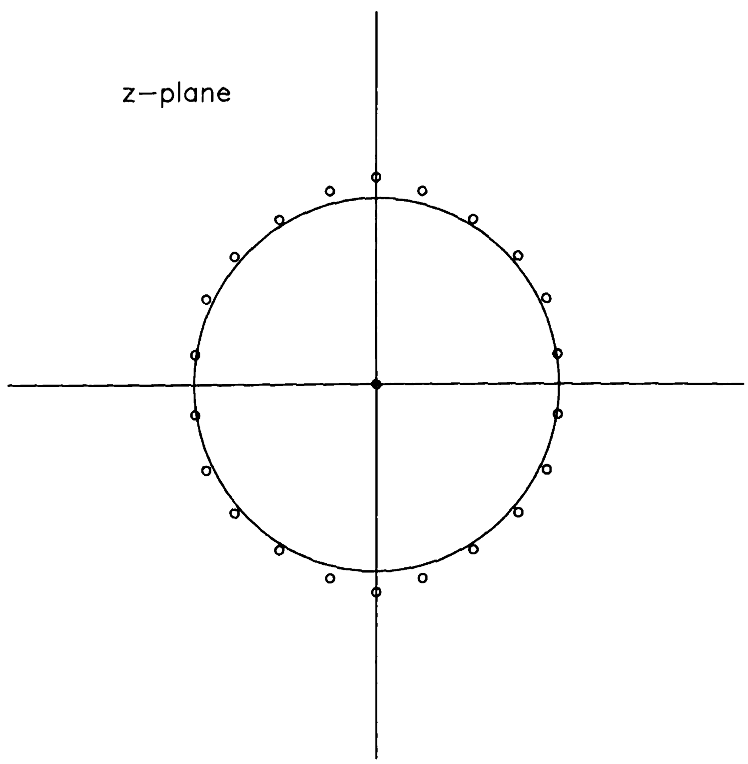

Figure 5.24 Zeros with respect to unit circle for simulated early-time 32-point 5-pulse non minimum-phase sequence.

Figure 5.25

Figure 5.26

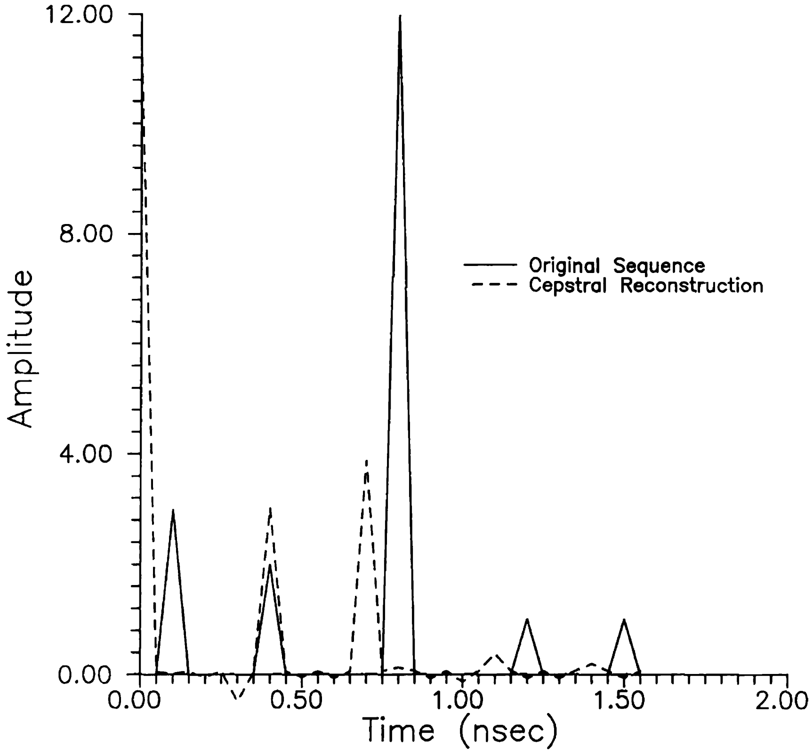

Figure 5.25 Simulated early-time and its cepstrum reconstruction using a second 32-point 5-pulse non minimum-phase sequence.

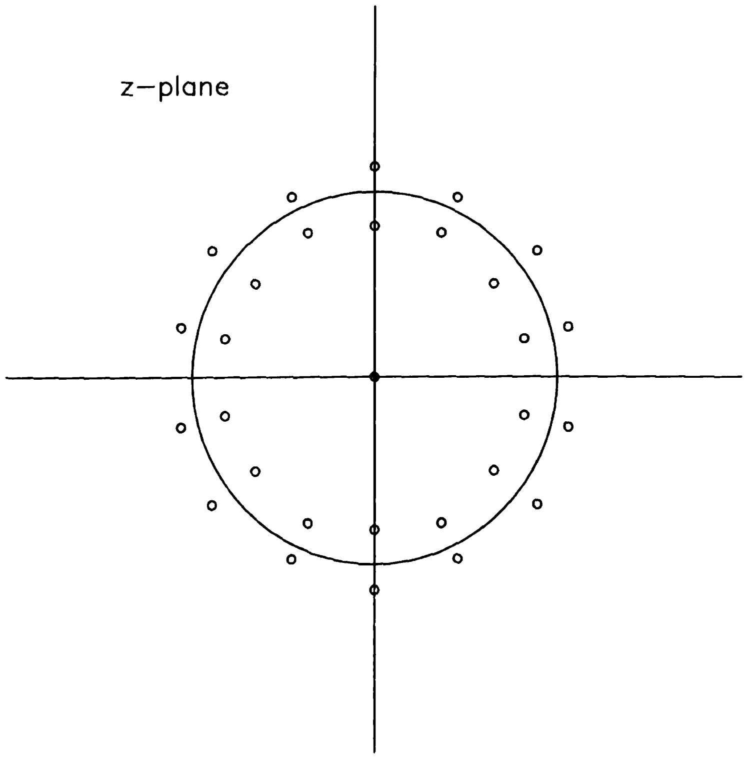

Figure 5.26 Zeros with respect to unit circle for simulated early-time second 32-point 5-pulse non minimum-phase sequence.

5.5 Separat

The pre

time cepstral re

As demonstrate

very good reali

reconstruction

component due

a poor reconst

begging to be

composite ma

More importar

phase reconstr

phase signal h

early-time con

component is

Therefore, a n

the original si

not necessarily

time compon

reconstructed

signal.

To se

5.5 Separation of Early and Late Time

The previous sections discussed some of the characteristics of early-time and late-time cepstral reconstruction if only the magnitude of the frequency response is present. As demonstrated, the minimum phase reconstruction obtained from $|F_l(\omega)|$ yields a very good realization of the late-time component. On the other hand, the minimum phase reconstruction obtained from $|F_e(\omega)|$ generally yields poor results for the early-time component due to the extremely non-minimum phase nature of the signal. In both cases a poor reconstruction will occur if aliasing is not taken into account. One question begging to be answered is the following: Will a cepstral reconstruction using the composite magnitude spectrum $|F(\omega)|$ yield a good realization of the actual signal? More importantly, will the early and late-time components separate using the minimum phase reconstruction? One way to look at this problem is to remember that a minimum phase signal has its energy concentrated earlier in the time sequence. Normally, the early-time component contains a higher concentration of energy whereas the late-time component is a decaying signal whose energy is concentrated later in the time sequence. Therefore, a minimum phase reconstruction should yield a fairly good representation of the original signal. On the other hand, reconstruction of the early-time component will not necessarily be correct. A possible rule of thumb to use is that the reconstructed early-time component will occur before the late-time component. Furthermore, the reconstructed late-time component should be a fair representation of the actual late-time signal.

To separate the early and late-time components from the composite spectral magnitude $|F($

representation u

time componen

spectral respons

late-time frequ

reconstruction

and late-time c

spectrum -- i

components. C

spectral energy

occurs even wh

The following

using the comp

frequency com

simple, multip

was a simple

Two different

fuselage (but

45 degrees w

measurement

Figure

aircraft for an

magnitude $|F(\omega)|$, two options are available. First, simply obtain the time-domain representation using a minimum phase reconstruction and then separate the early and late-time components with an appropriate window. A second option is to filter the composite spectral response $|F(\omega)|$ into a separate early-time frequency component $|F_e(\omega)|$ and late-time frequency component $|F_l(\omega)|$. Once this is done, a minimum phase reconstruction can be applied to each spectrum to yield an approximate fit to the early and late-time components. This technique will require some a-priori knowledge of the spectrum -- i.e., which part of the spectrum contributes to the early and late-time components. One of the real problems occurs when there is a great deal of overlap in the spectral energy for the early and late-time components. Of course, this problem also occurs even when using both magnitude and phase to reconstruct the transient response. The following analysis will present several examples showing cepstral reconstruction using the composite spectrum and then filtering the spectrum into early-time and late-time frequency components. The spectrum for the first two examples was created from a simple, multiple thin-wire scattering routine. For these two examples, the scattering target was a simple thin-wire aircraft made up of fuselage, wings, and tail (see Figure 5.27). Two different polarizations were used: in one case the E-field was perpendicular to the fuselage (but parallel to the tail and wings), in the second case the E-field was oriented 45 degrees with respect to the fuselage. The third example consists of a scattering measurement from a highly conducting scaled B-58 aircraft model.

Figure 5.29 shows the spectral magnitude of the scattered field from a thin-wire aircraft for an electric field polarized normal to the fuselage but parallel to the wings and tail. The figu

windowing the

parameters f_c =

domain represe

phase reconstru

good match be

A low-

capture late-tin

the filtered out

output of the

wings). Figur

both the magni

be seen, there

phase reconstr

An atte

frequency spec

spectral data a

the eliminatio

eliminated too

representation

made between

and the magni

tail. The figure contains both the raw spectral response and a spectrum formed by windowing the raw data with a Gaussian modulated cosine (GMC) window having parameters f_c = 0 GHz and T = .06 nsec (see Appendix A). Figure 5.30 shows the time-domain representation of this windowed spectrum computed using both the magnitude-phase reconstruction and the magnitude only reconstruction. In this example there is a good match between the late-time components using the minimum phase reconstruction.

A low-frequency filter was applied to the raw spectral data in an attempt to capture late-time frequency information. Figure 5.31 shows the raw frequency data and the filtered output. The filter consists of a GMC window (f_c = 0 GHz, T = .3 nsec). The output of the filter consists of one large late-time resonant mode (from the aircraft's wings). Figure 5.32 shows the time-domain representation of the filter's response using both the magnitude-phase reconstruction and the magnitude only reconstruction. As can be seen, there is a good match between the late-time components using the minimum phase reconstruction.

An attempt was made to filter out the early-time component from the composite frequency spectrum. Using a 1/8 cosine taper window function (see Appendix A) the raw spectral data and filter output are shown in Figure 5.33. The resulting filter output shows the elimination of the low frequency resonant mode. However, this filter may have eliminated too much frequency data from the high end of the spectrum. The time-domain representation of the filter output is shown in Figure 5.34. Once again a comparison is made between the time domain obtained using both magnitude and phase reconstruction and the magnitude only reconstruction. The match between the two representations is not perfect, but the

depending on t

The cor

repeated for an

In this case, a r

spectrum. Fig

spectrum comp

reconstruction

early-time sign

time componen

well with the n

presence of m

Figure

time-domain t

window with t

between the m

that some ea

selection.

The ea

are shown in

uses a 1/8 co

cepstral recon

perfect, but the main peaks in each case line up. Some improvement might be expected depending on the filter chosen, but in most cases a match is quite unlikely.

The computation of the scattering from the simple wire frame aircraft was also repeated for an electric field polarized 45 degrees with respect to the aircraft's fuselage. In this case, a new resonant mode due to the aircraft's fuselage appears in the frequency spectrum. Figure 5.35 shows the raw data frequency spectrum and the windowed spectrum computed using a GMC window (f_c = 0 GHz, T = .06 nsec). The time-domain reconstruction for the windowed spectrum is shown in Figure 5.36. As can be seen more early-time signal exists for this polarization. For the cepstral reconstruction, the early-time component as a whole is in the proper position but the components do not match well with the magnitude-phase reconstruction. In addition, the late time is affected by the presence of more early-time signal.

Figure 5.37 and Figure 5.38 shows the late-time frequency filter output and the time-domain transform outputs respectively. The low frequency filter used a GMC window with the same parameters as in the previous case. There is quite good agreement between the magnitude-phase reconstruction and the cepstral reconstruction. Also note that some early-time components exist in the time-domain signal due to the filter selection.

The early-time frequency filter response and time-domain transform representations are shown in Figure 5.39 and Figure 5.40 respectively. The early-time frequency filter uses a 1/8 cosine taper window exactly like the previous example. Once again the cepstral reconstruction does not match the original sequence obtained from both the magnitude and

all the late-tim

The fin

B-58 aircraft m

side of the air

following figu

presents some

data down to

window to the

should be take

use of the log

the values to

Figure 5.42 s

frequency resp

again a good

Figure

reconstruction

T = .4 nsec).

magnitude-ph

filter results.

a 1/8 cosine t

surprisingly g

magnitude and phase frequency components. Also the filter did not adequately remove all the late-time components.

The final example is a measured frequency response for scattering from a scaled B-58 aircraft model. For this particular case the incident electric field is incident on the side of the aircraft and polarized 45 degrees with respect to the roll-axis (see insets in following figures). The raw frequency data was measured from .5 to 5.5 GHz. This presents some problem for the cepstral reconstruction routines which require frequency data down to 0 GHz. A usable spectrum was obtained by applying a 1/8 cosine taper window to the raw frequency spectrum and zero filling the low frequency. Although, care should be taken in zero filling frequency data for cepstral reconstruction (remember the use of the logarithm function) the cepstral routines do check for this condition and set the values to a small non-zero value. Figure 5.41 shows the frequency data and Figure 5.42 shows the time-domain representation using both the magnitude-phase frequency response and the magnitude only response. The plots in Figure 5.42 show once again a good comparison for the late-time periods and a fairly good early-time match.

Figure 5.43 and Figure 5.44 show the low-pass filter and time-domain reconstruction respectively. The low-pass filter used was a GMC window (f_c = 0 GHz, T = .4 nsec). The time-domain cepstral reconstruction shows a good match with the magnitude-phase reconstruction. Finally, Figure 5.45 and Figure 5.46 show the early-time filter results. Figure 5.45 shows the filter output which was obtain by windowing with a 1/8 cosine taper window. The minimum phase reconstruction shown in Figure 5.46 is surprisingly good. Although this does not occur in general, under certain conditions the early-time scat

In each

representation

time componen

non-minimum

quite crude but

using only the

difficult to wo

of constructing

early-time scattered response is nearly minimum phase.

In each example, the late-time component using cepstral reconstruction is a good representation of the actual signal using the composite frequency response. The early-time component does not keep its temporal order under a cepstral transform due to the non-minimum phase character of the early-time signal. The filters presented above are quite crude but they do show that a late-time component can be filtered and reconstructed using only the magnitude of the spectrum. The early-time component is much more difficult to work with -- both due to the non-minimum phase character and the difficulty of constructing a good early-time frequency filter.

Figure 5.27

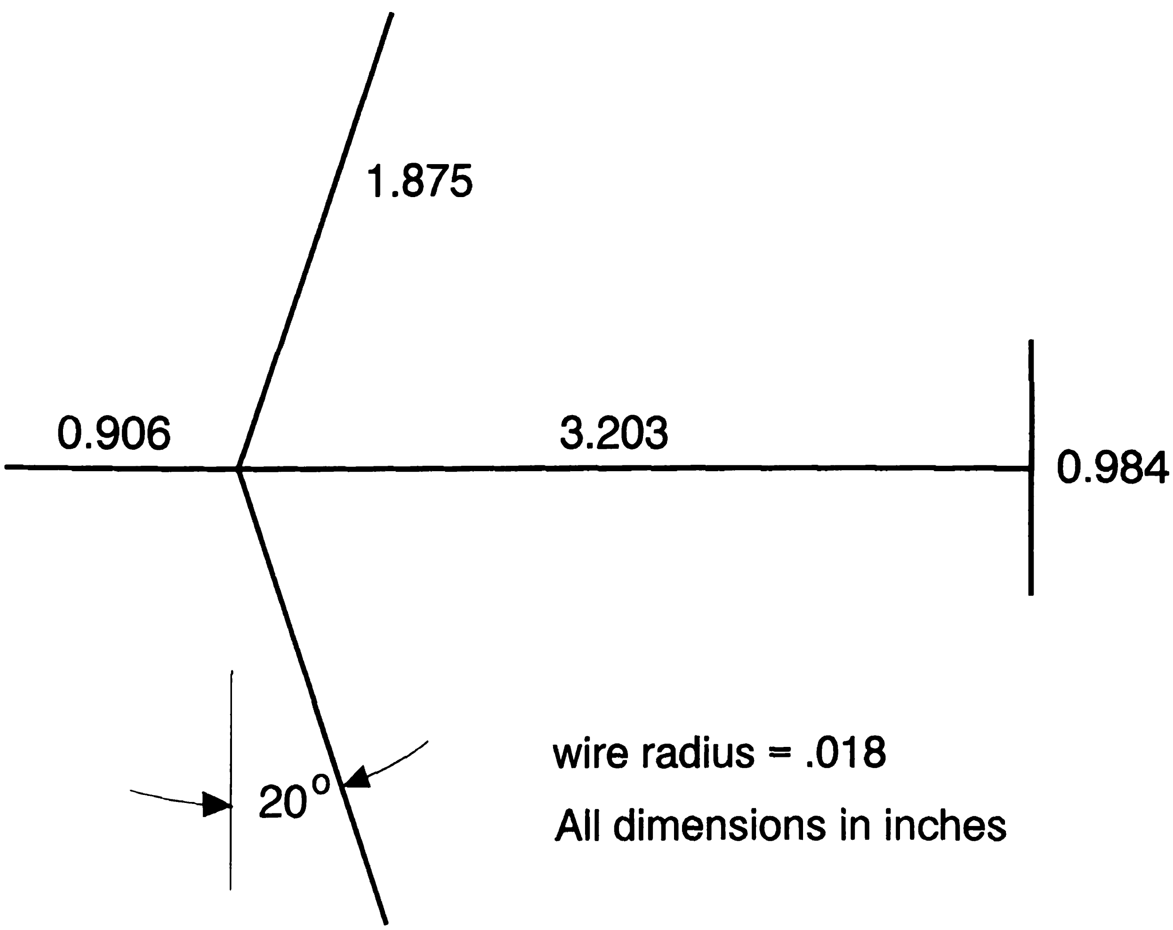

Figure 5.27 Thin wire aircraft model.

Figure 5.28

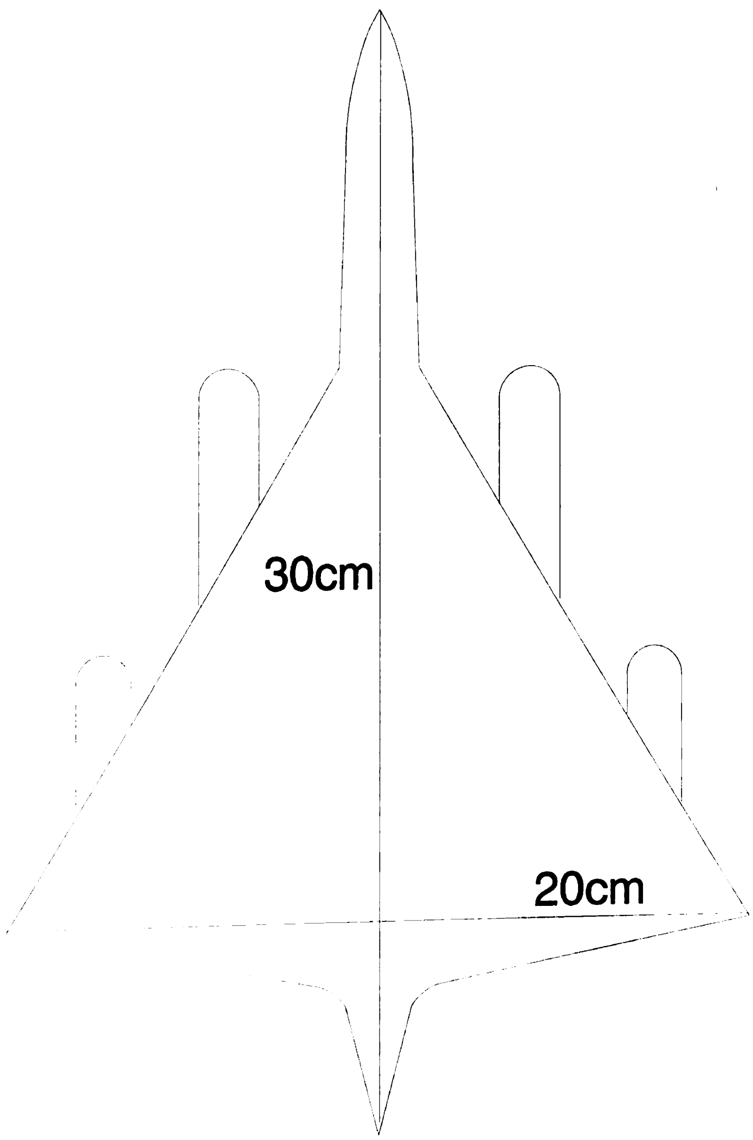

Figure 5.28 Planar view of B-58 scaled aircraft.

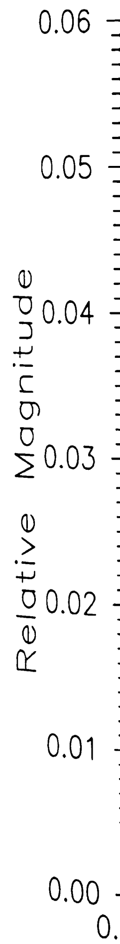

Figure 5.29

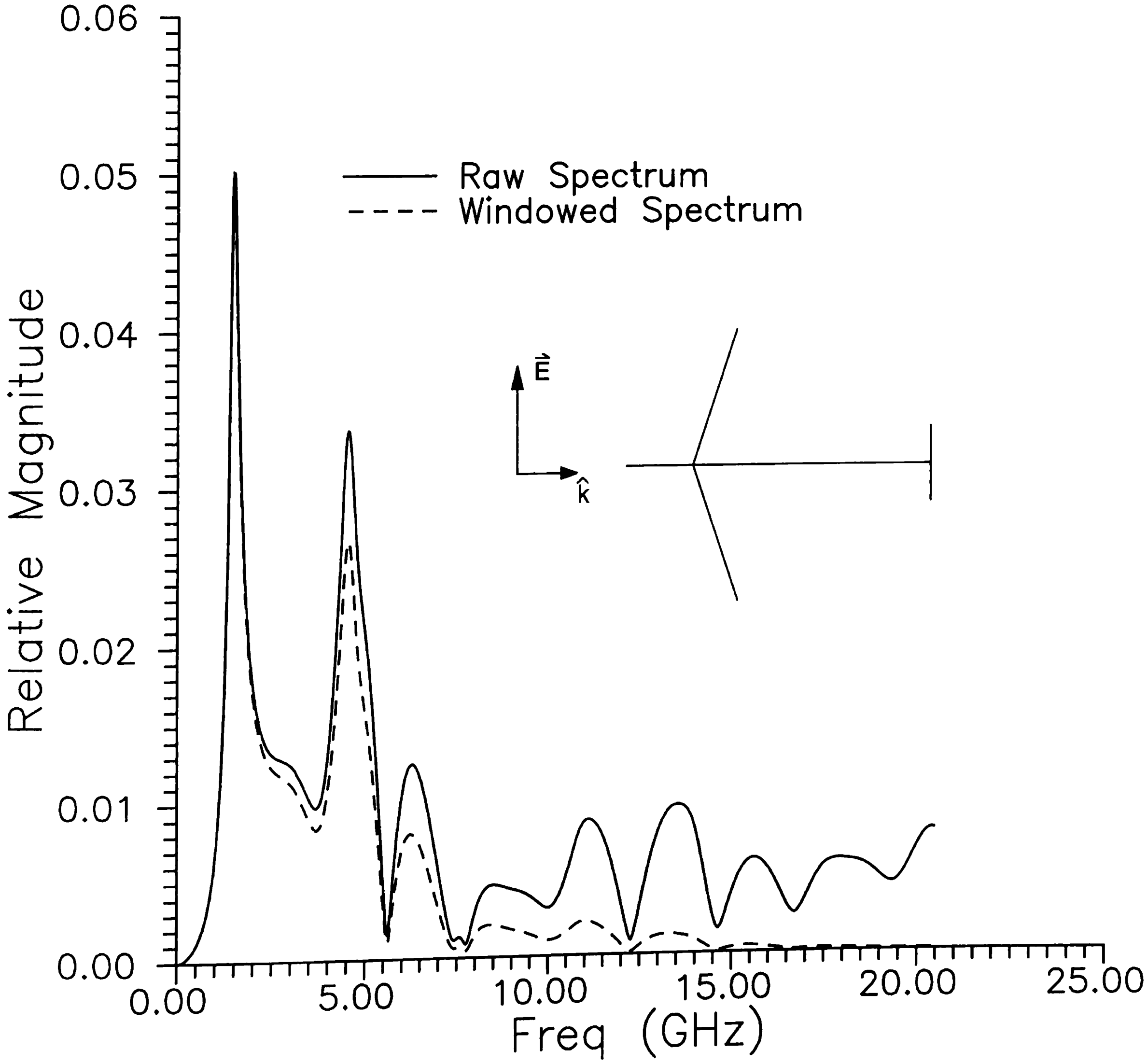

Figure 5.29 Frequency response magnitude for scattering from a simple wire aircraft. E-field polarization perpendicular to fuselage.

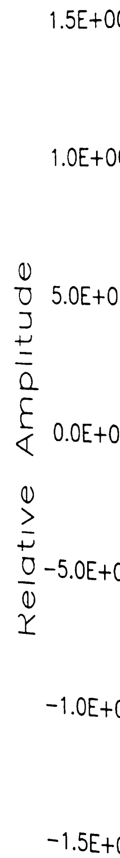

Figure 5.30

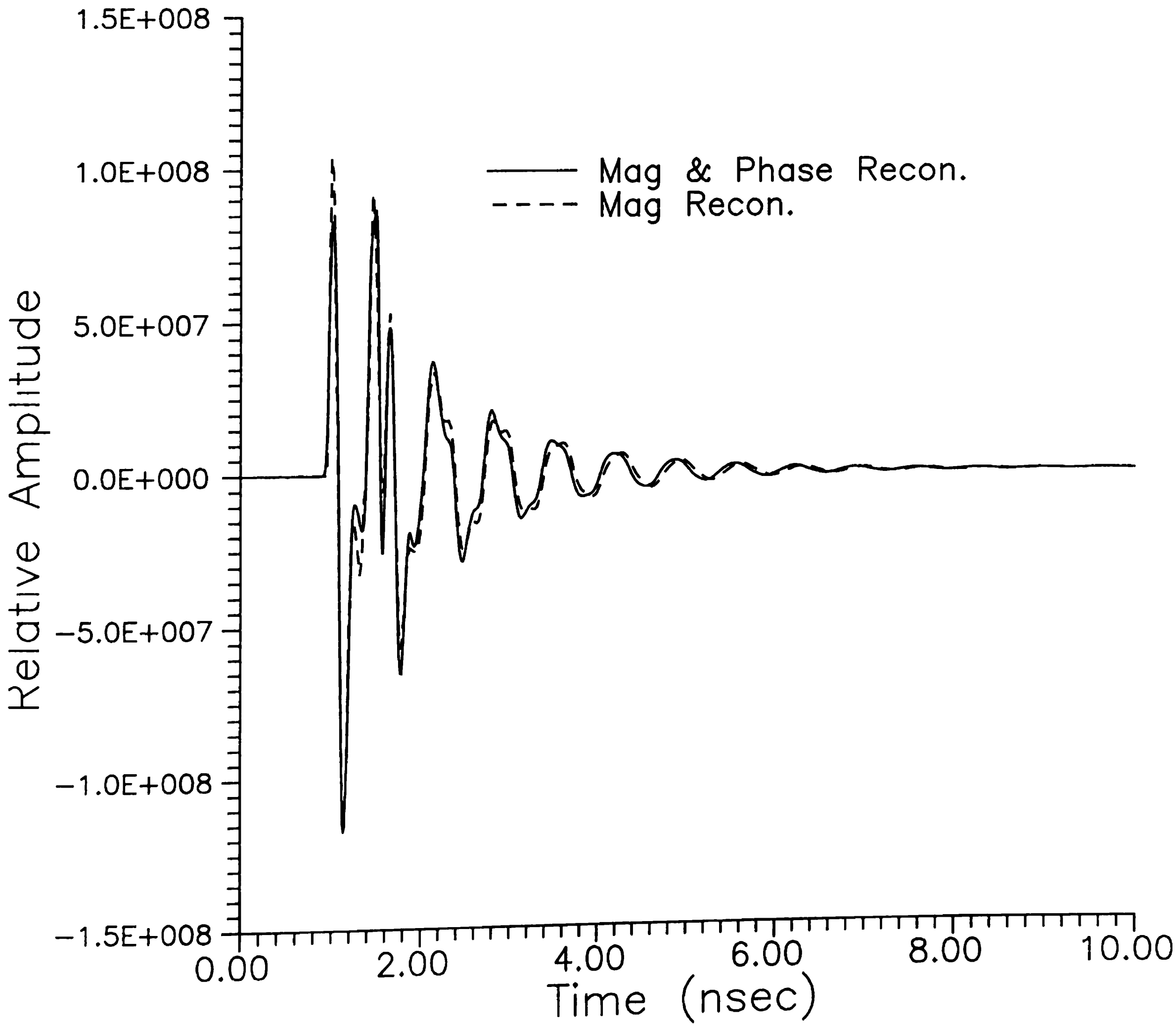

Figure 5.30 Transient scattered field for wire-frame aircraft using magnitude/phase transform and magnitude only transform.

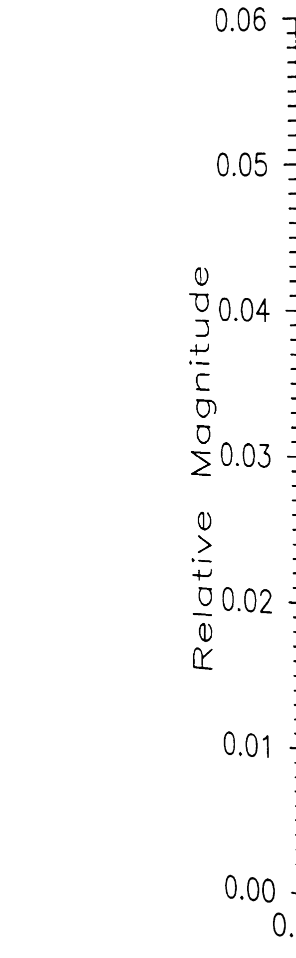

Figure 5.31

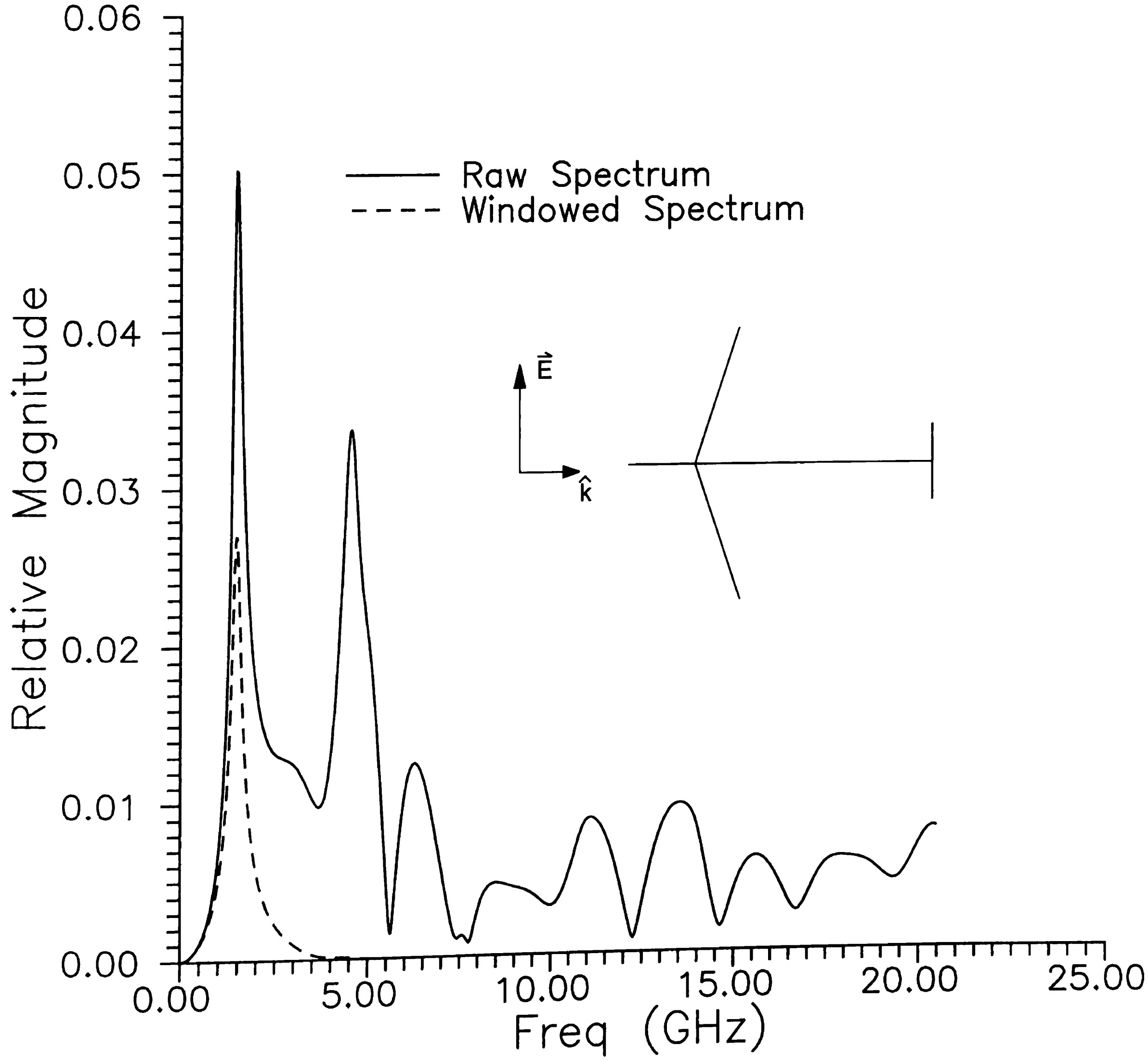

Figure 5.31 Late-time frequency filter response for scattering from a wire frame aircraft. E-field polarization perpendicular to fuselage.

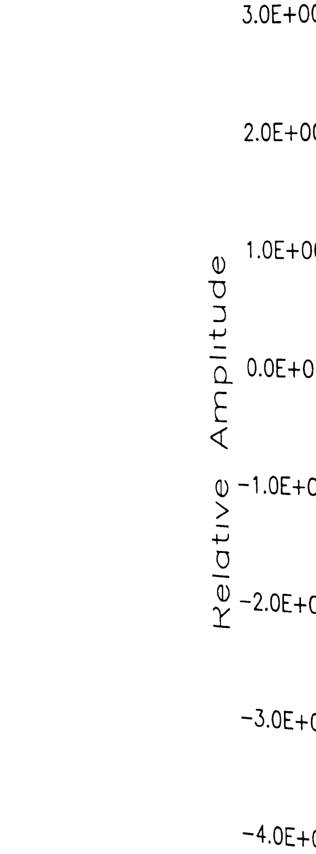

3.0E+00
2.0E+00
1.0E+00
0.0E+0
-1.0E+0
-2.0E+0
-3.0E+0
-4.0E+0
Relative Amplitude

Figure 5.32

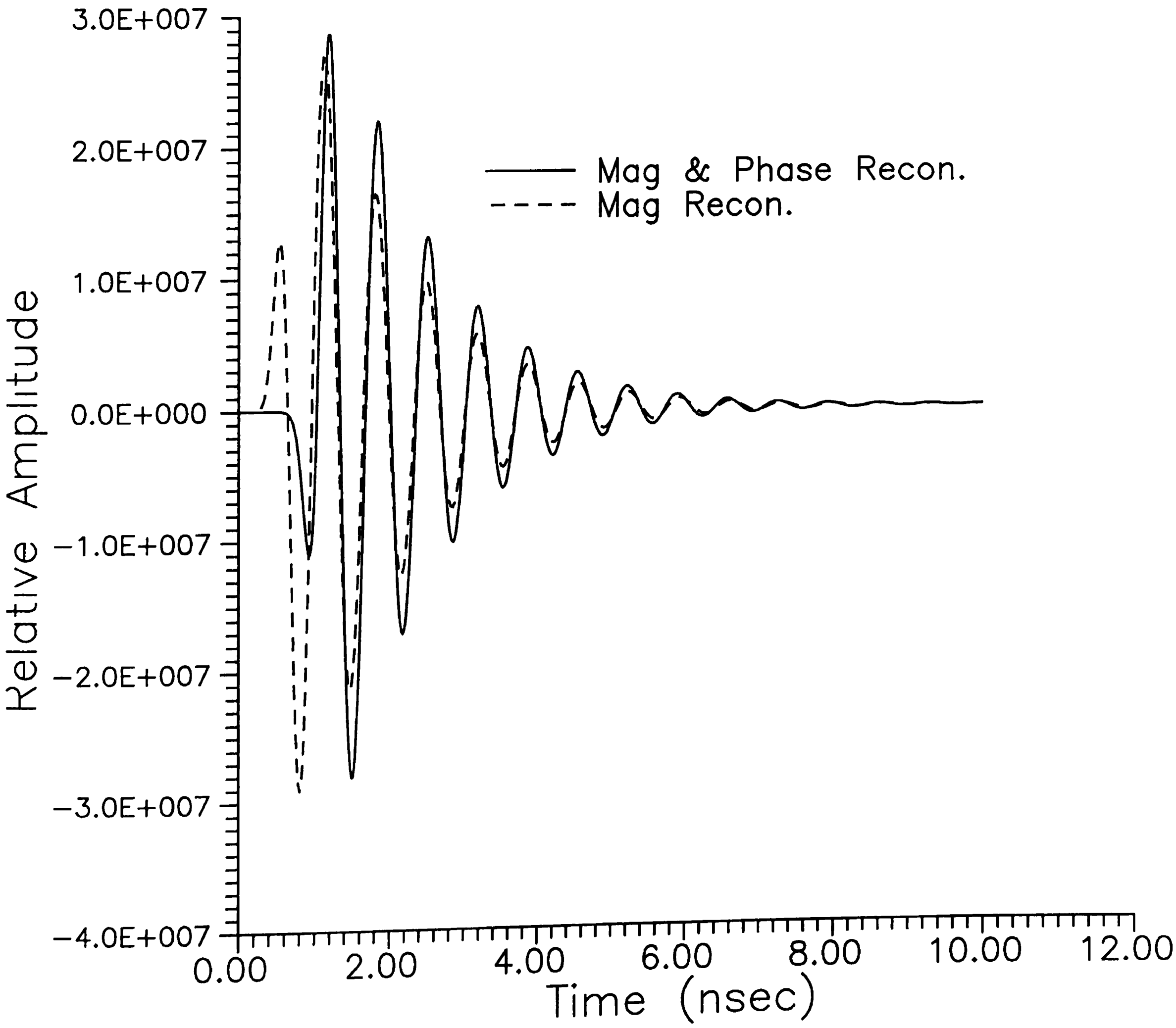

Figure 5.32 Transient scattered field for late-time response for wire-frame aircraft.

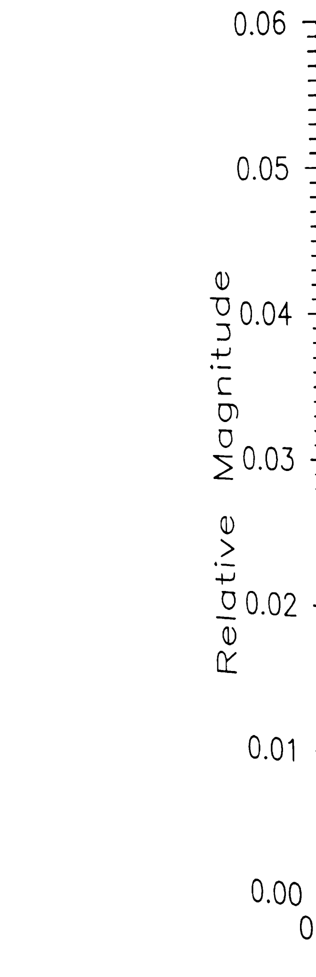

Figure 5.33

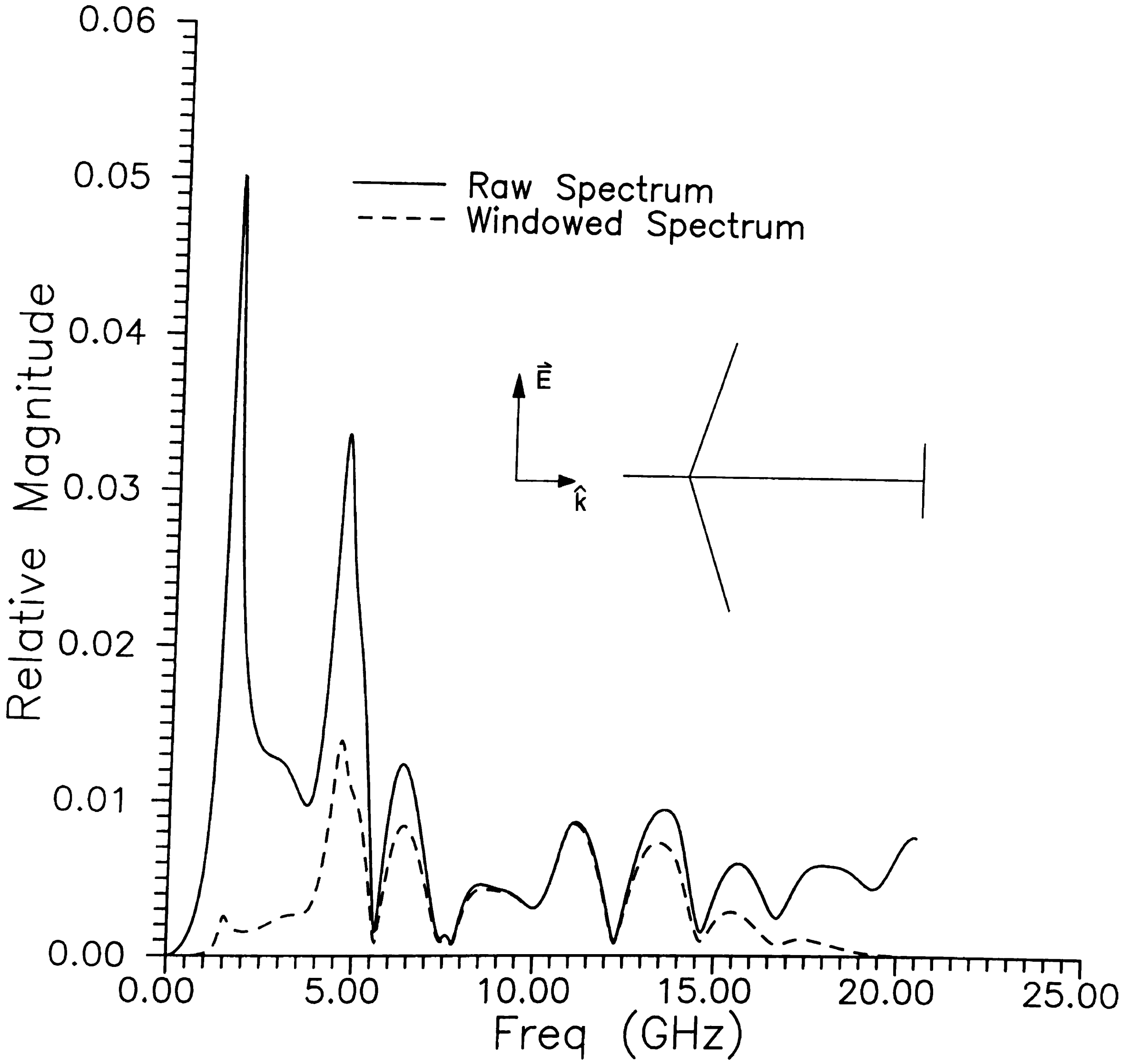

Figure 5.33 Early-time frequency filter response for scattering from a wire frame aircraft. E-field polarization perpendicular to fuselage.

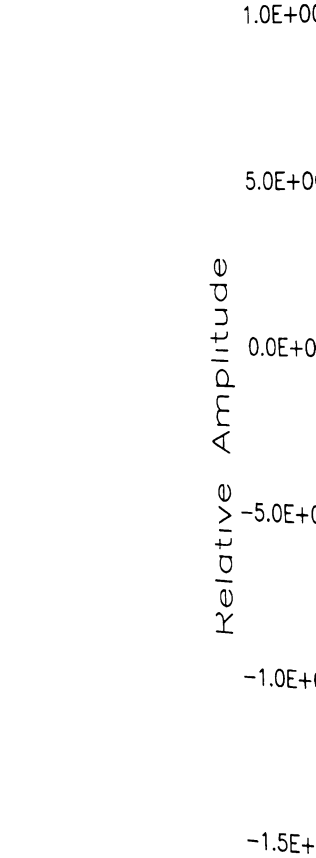

Figure 5.34

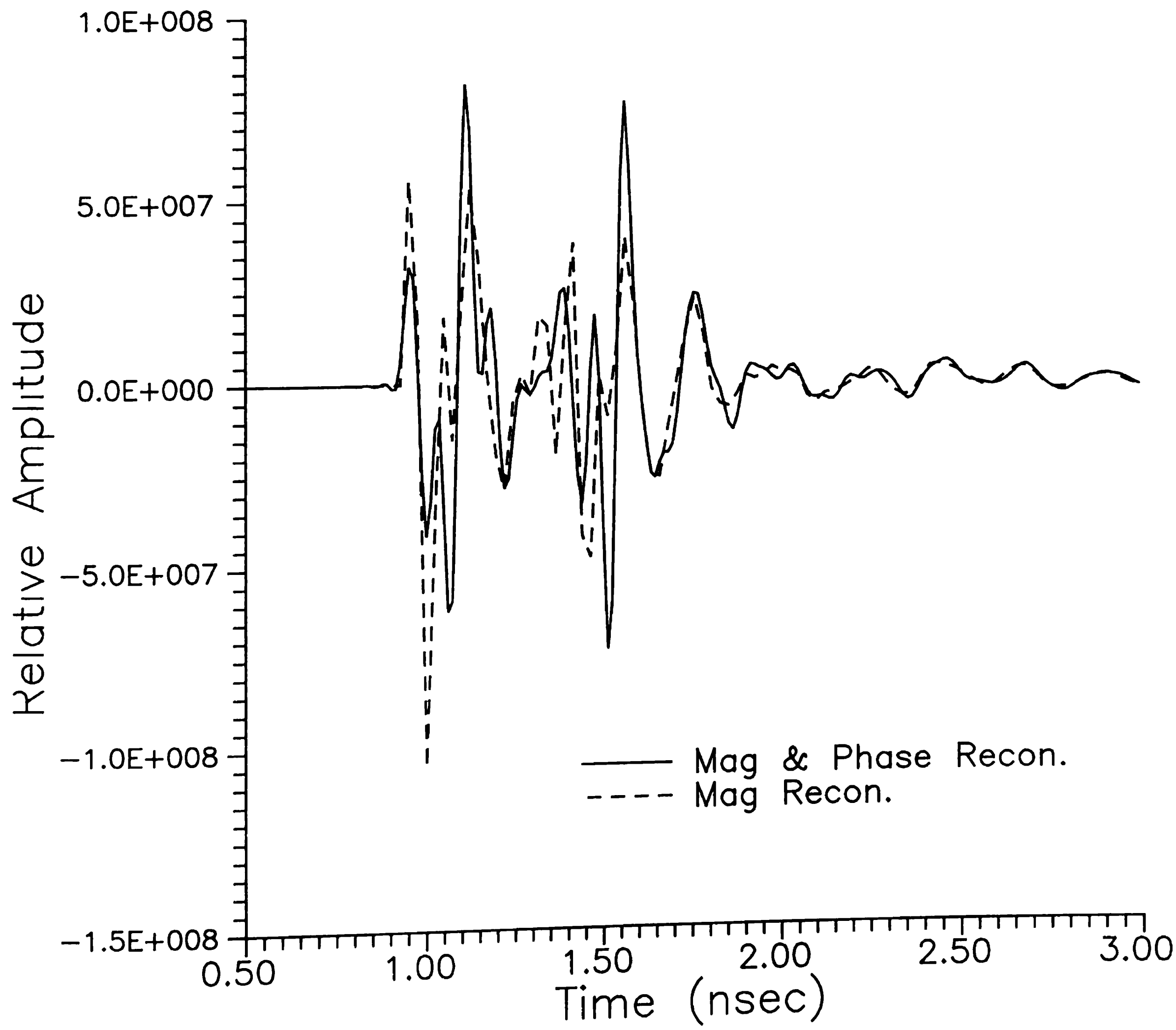

Figure 5.34 Transient scattered field using early-time frequency filtered response for a wire-frame aircraft.

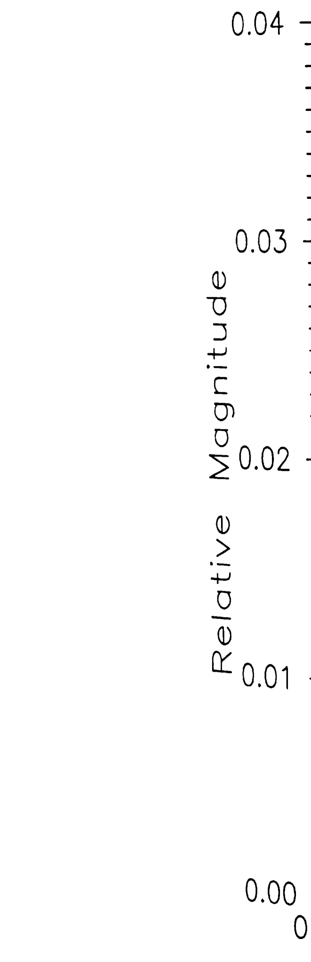

Figure 5.35

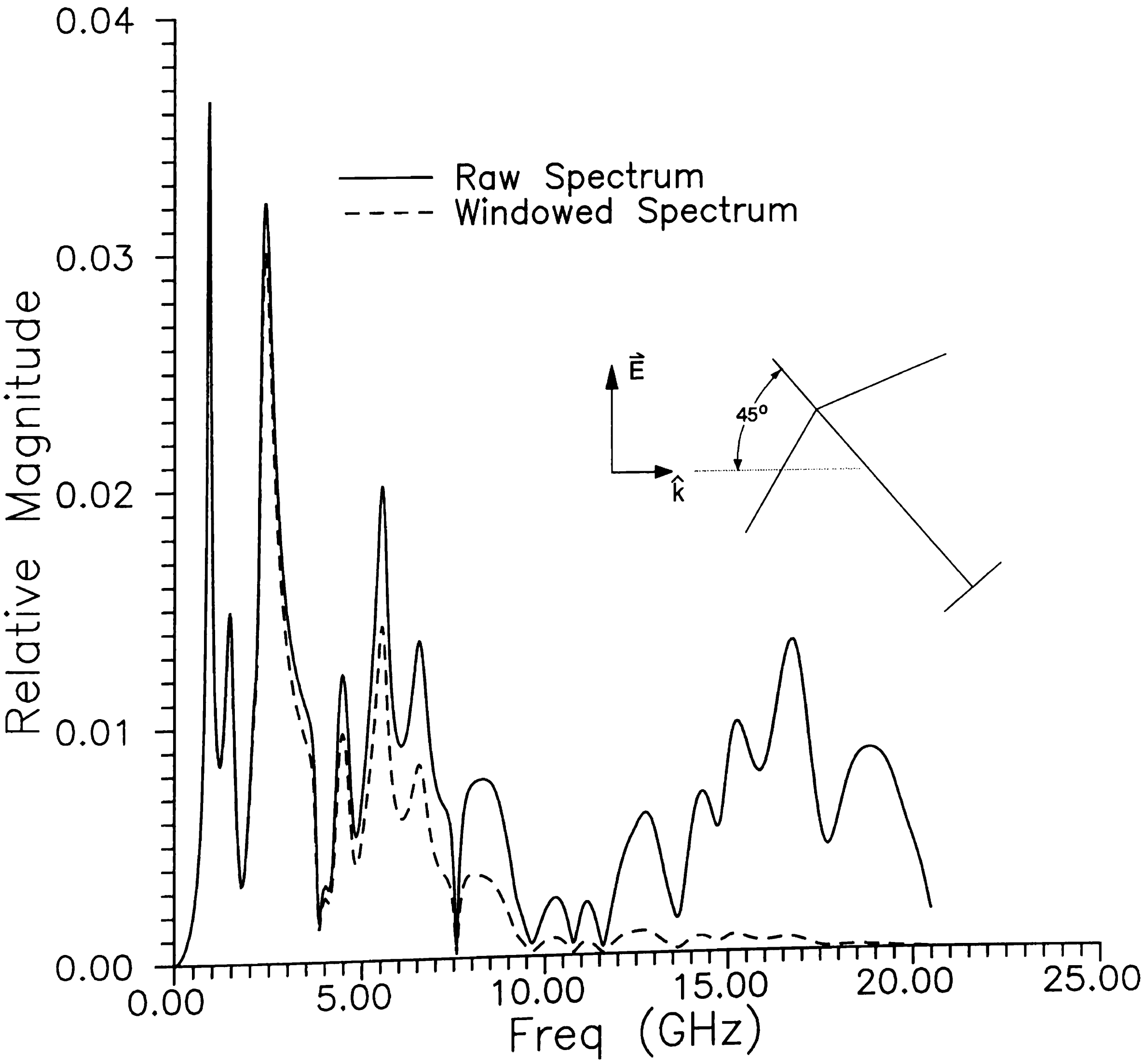

Figure 5.35 Frequency response magnitude for scattering from a wire frame aircraft. E-field polarization 45 degrees with respect to fuselage.

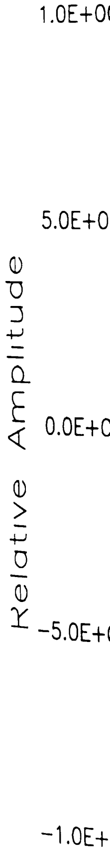

Figure 5.36

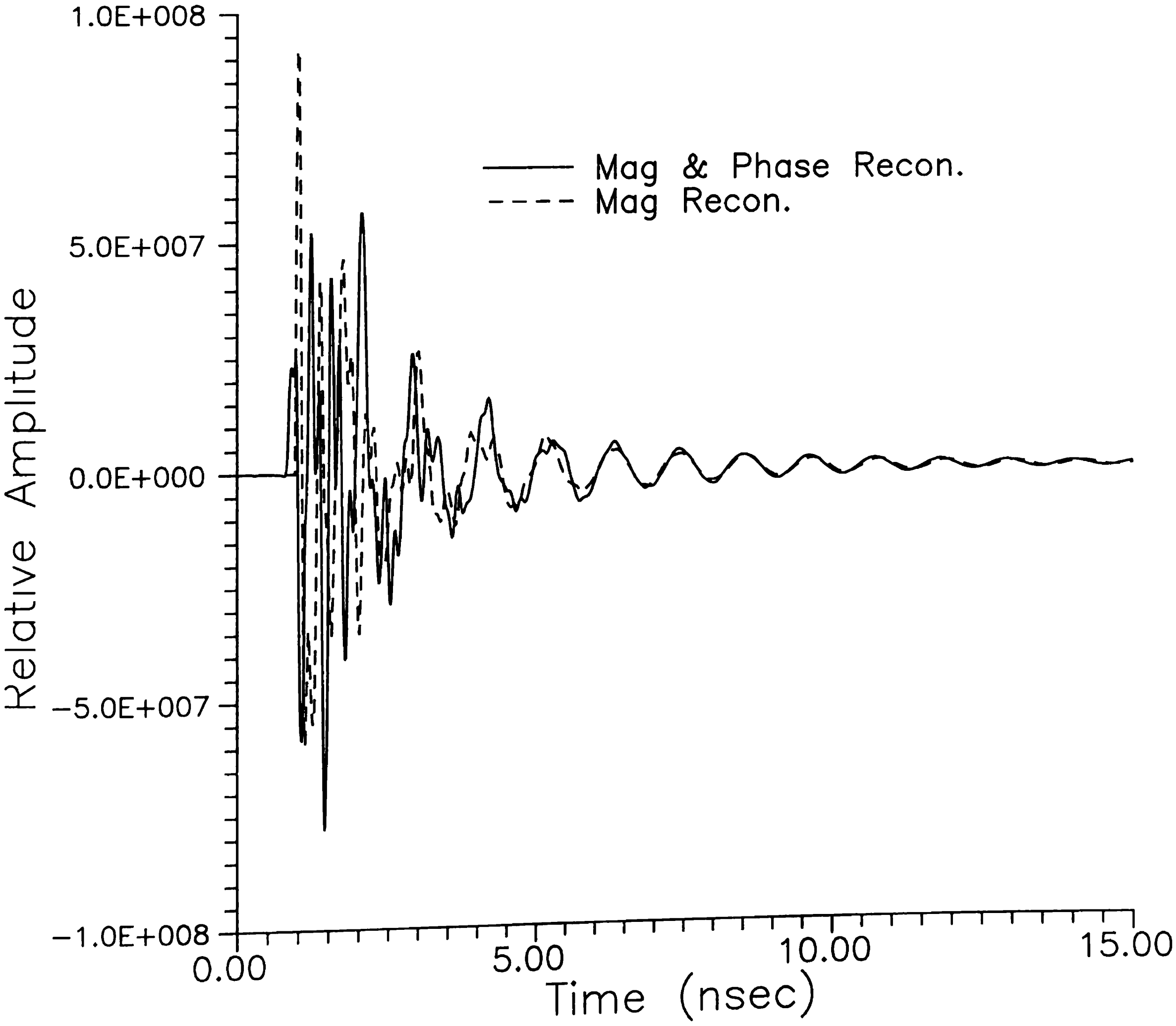

Figure 5.36 Transient scattered field from wire frame aircraft using magnitude/phase transform and magnitude only transform.

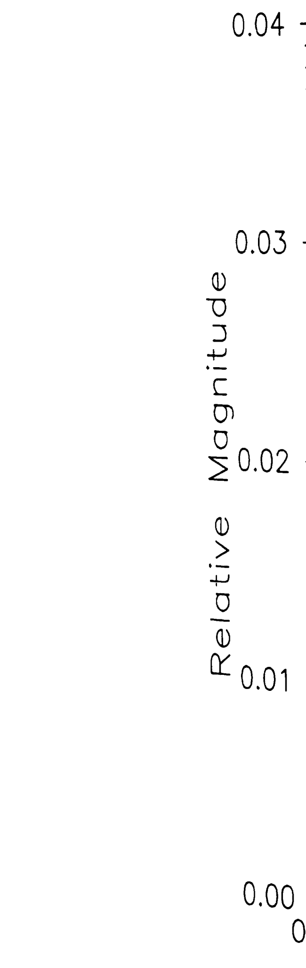

Figure 5.37

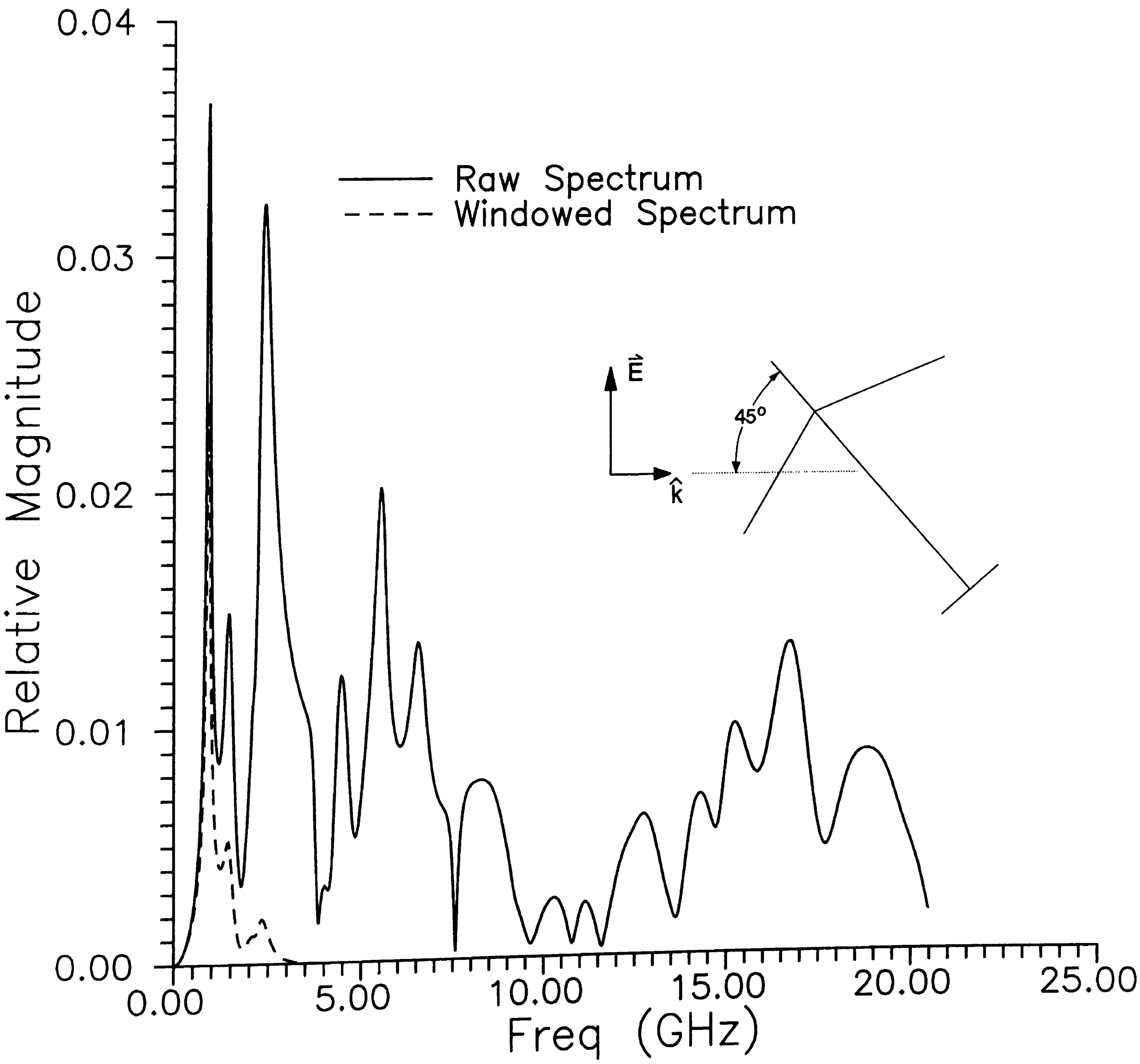

Figure 5.37 Late-time frequency filter response for scattering from a wire frame aircraft. E-field polarization 45 degrees with respect to fuselage.

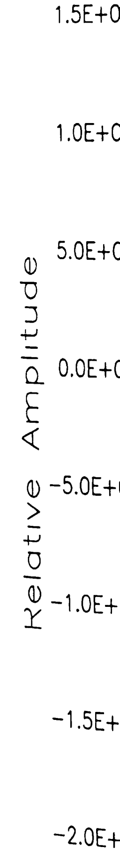

Figure 5.38

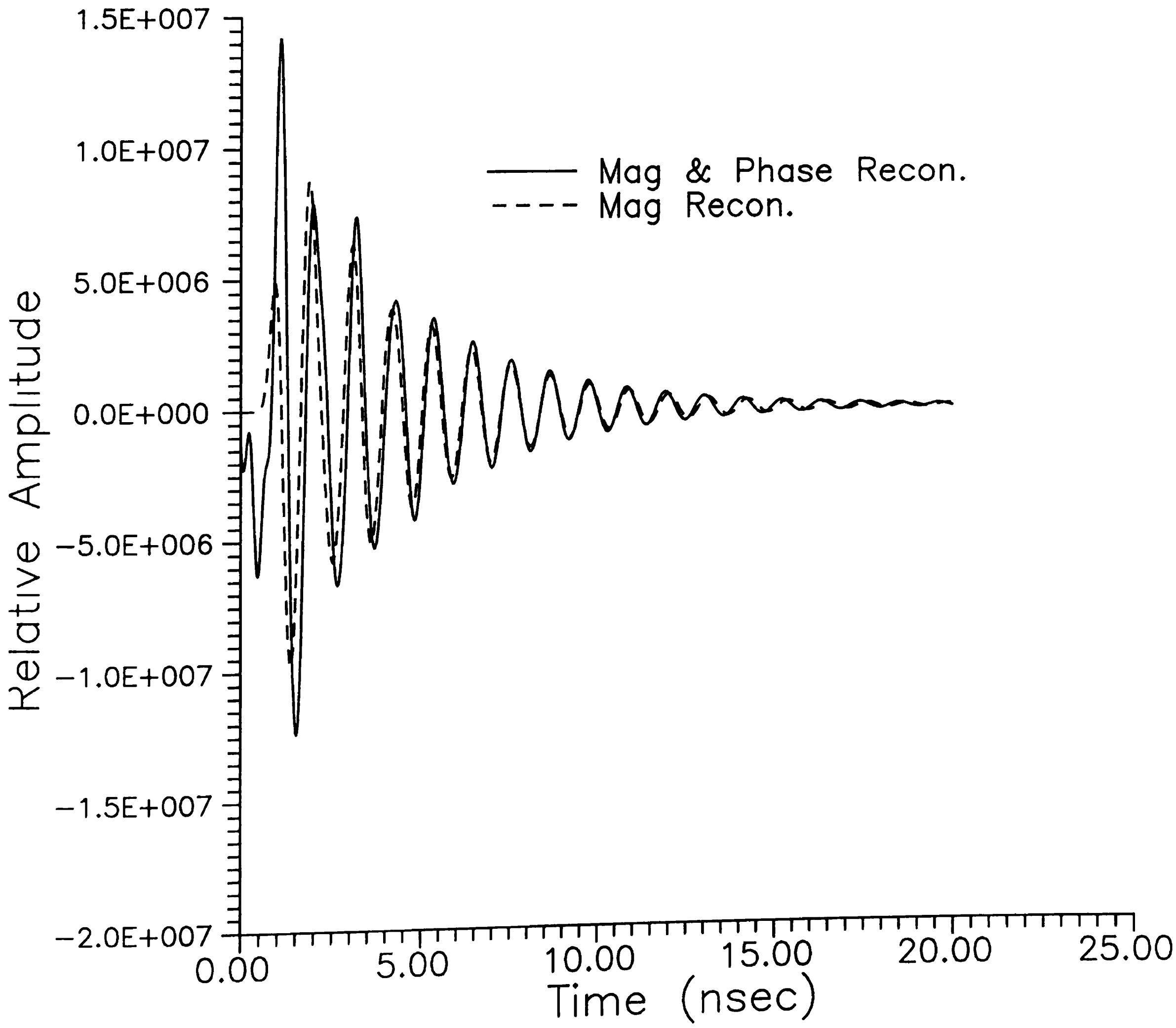

Figure 5.38 Transient scattered field for late-time response from wire frame aircraft.

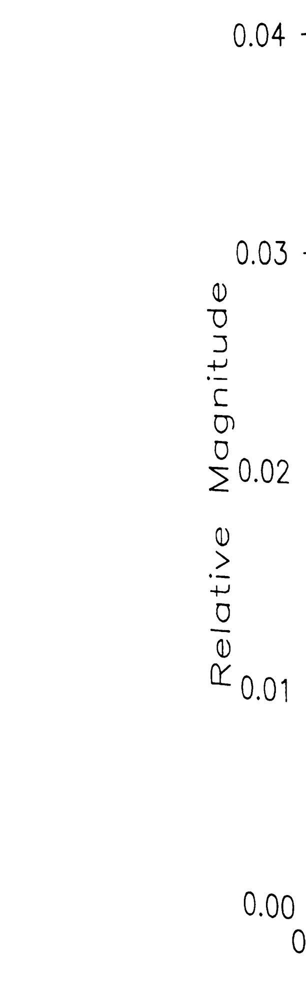

Figure 5.39

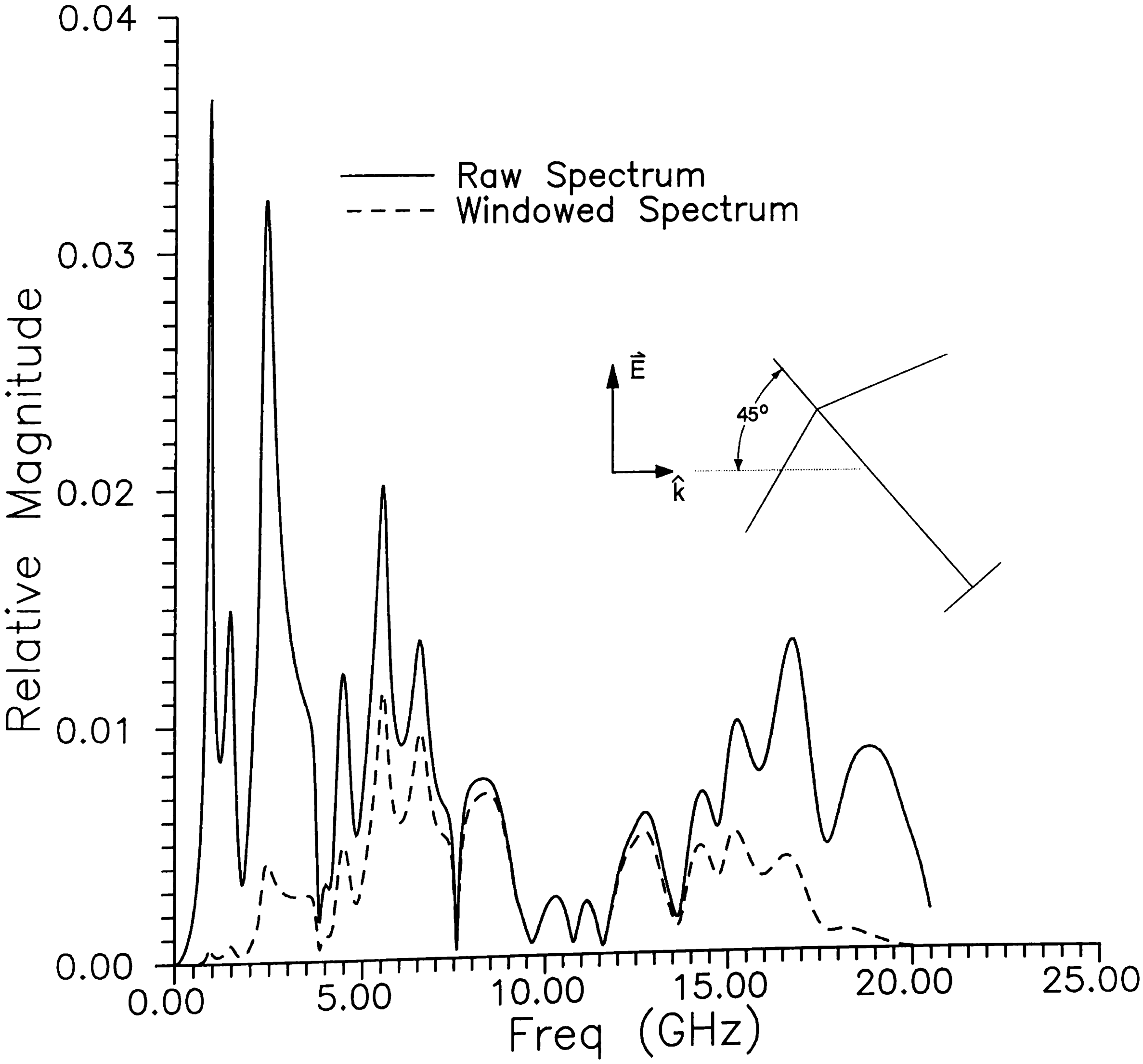

Figure 5.39 Early-time frequency filter response for scattering from a wire frame aircraft. E-field polarization 45 degrees with respect to fuselage.

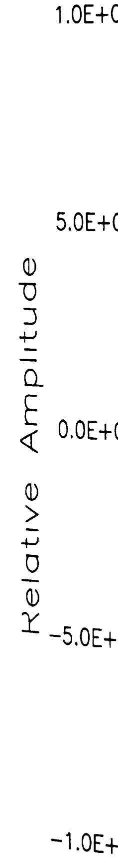

Figure 5.40

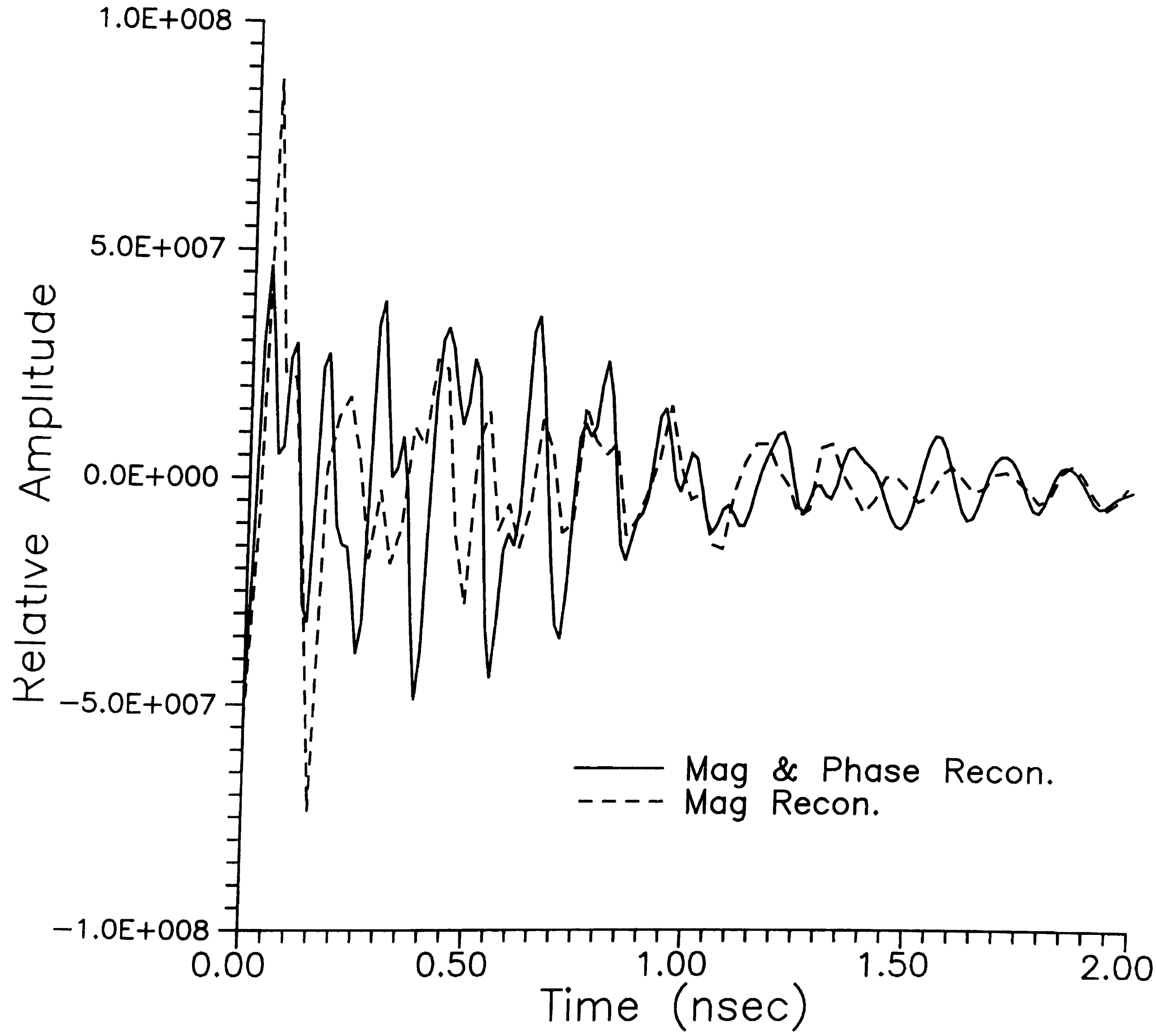

Figure 5.40 Transient scattered field using filtered early-time frequency response from wire frame aircraft.

0.02

0.02

Relative Magnitude

0.01

0.01

0.00
0

Figure 5.41

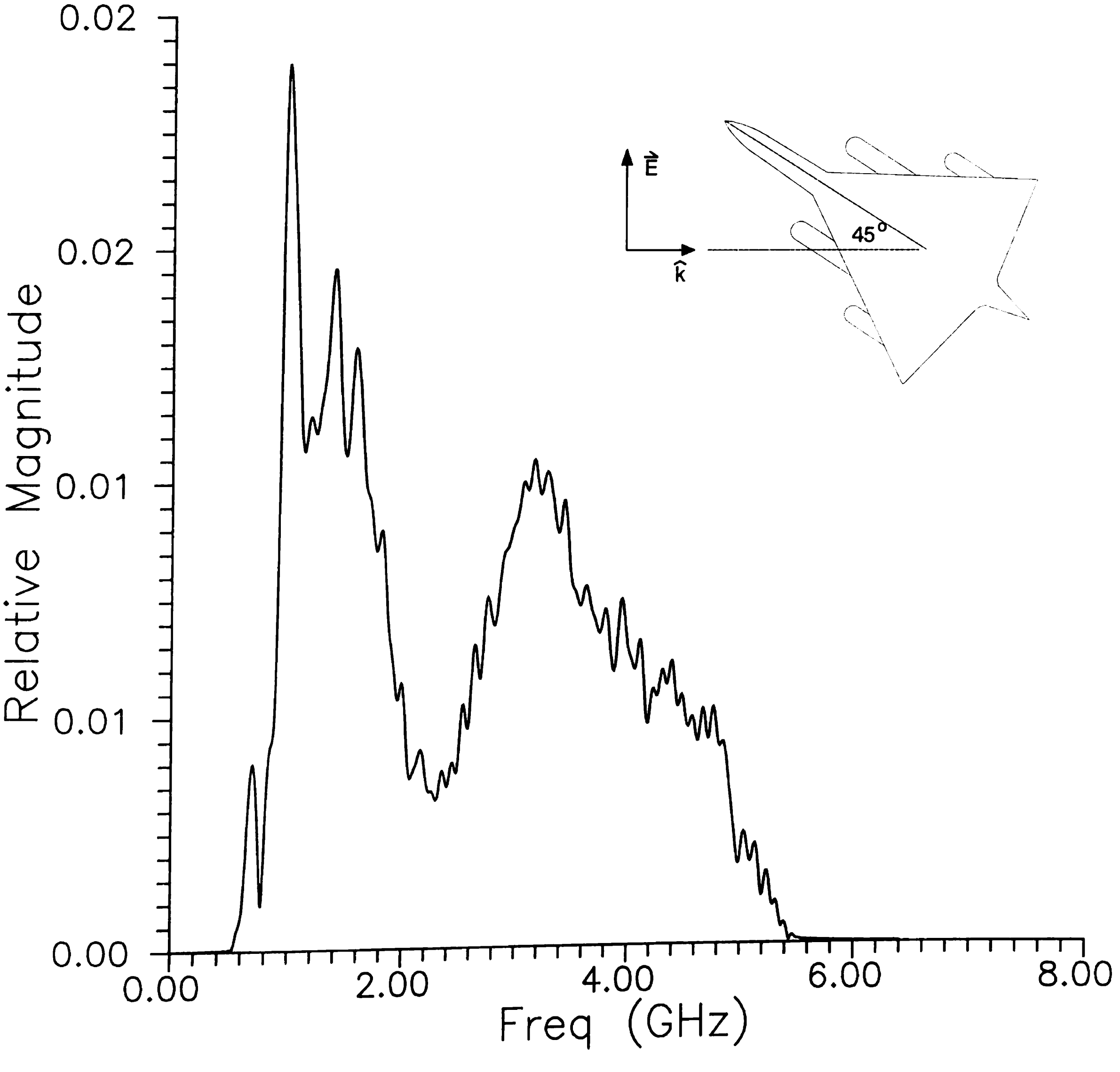

Figure 5.41 Measured frequency response magnitude for scattering from B-58 aircraft model.

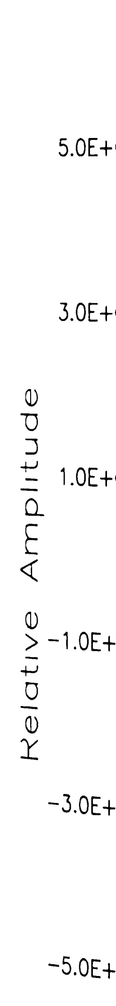

Figure 5.42

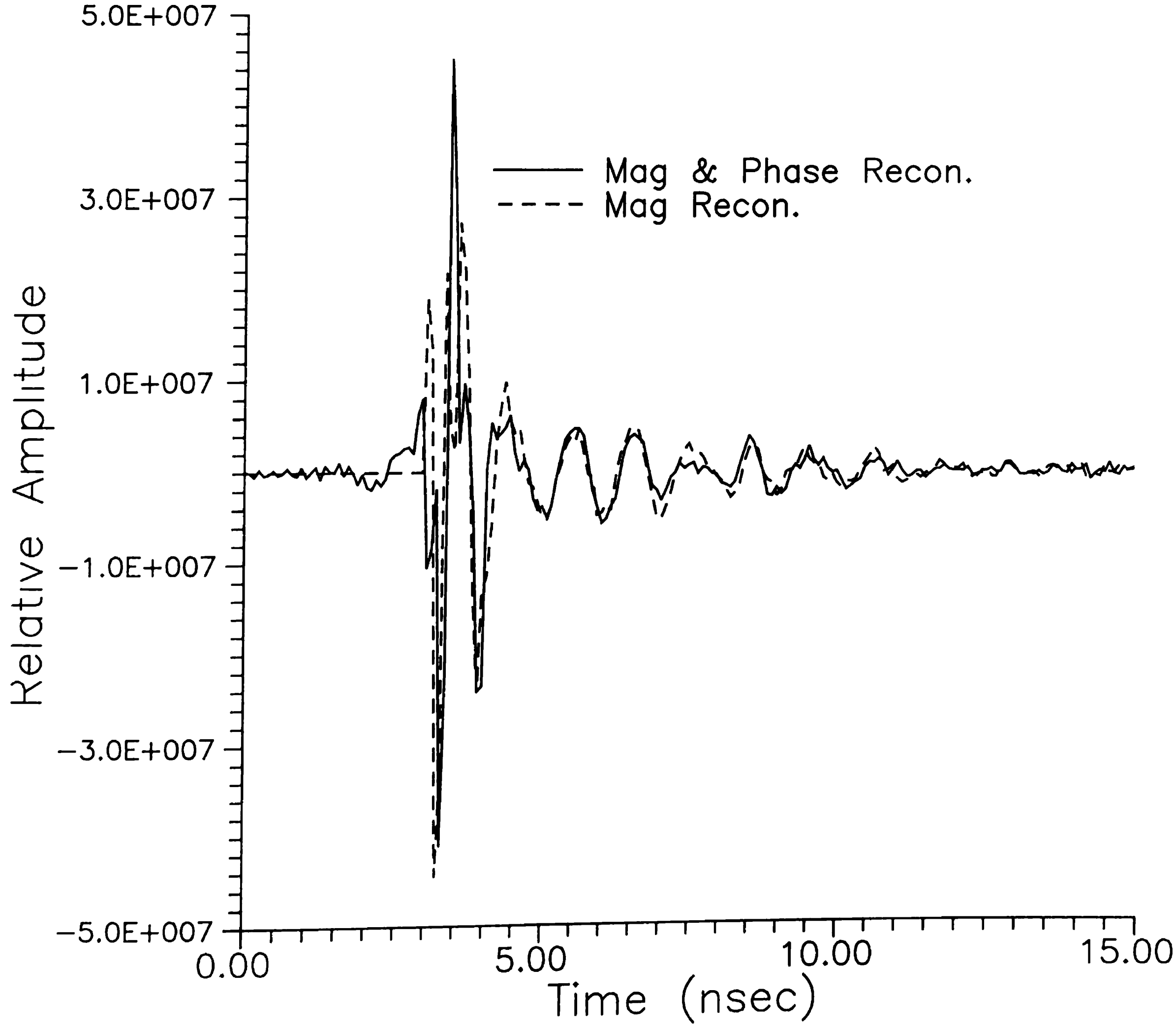

Figure 5.42 Transient scattered field from B-58 aircraft.

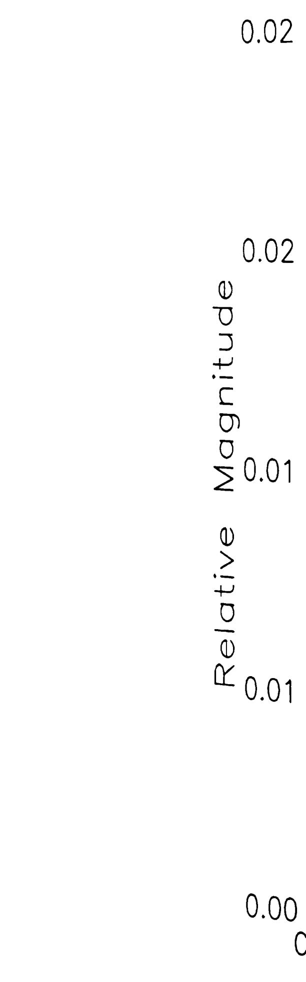

Figure 5.43

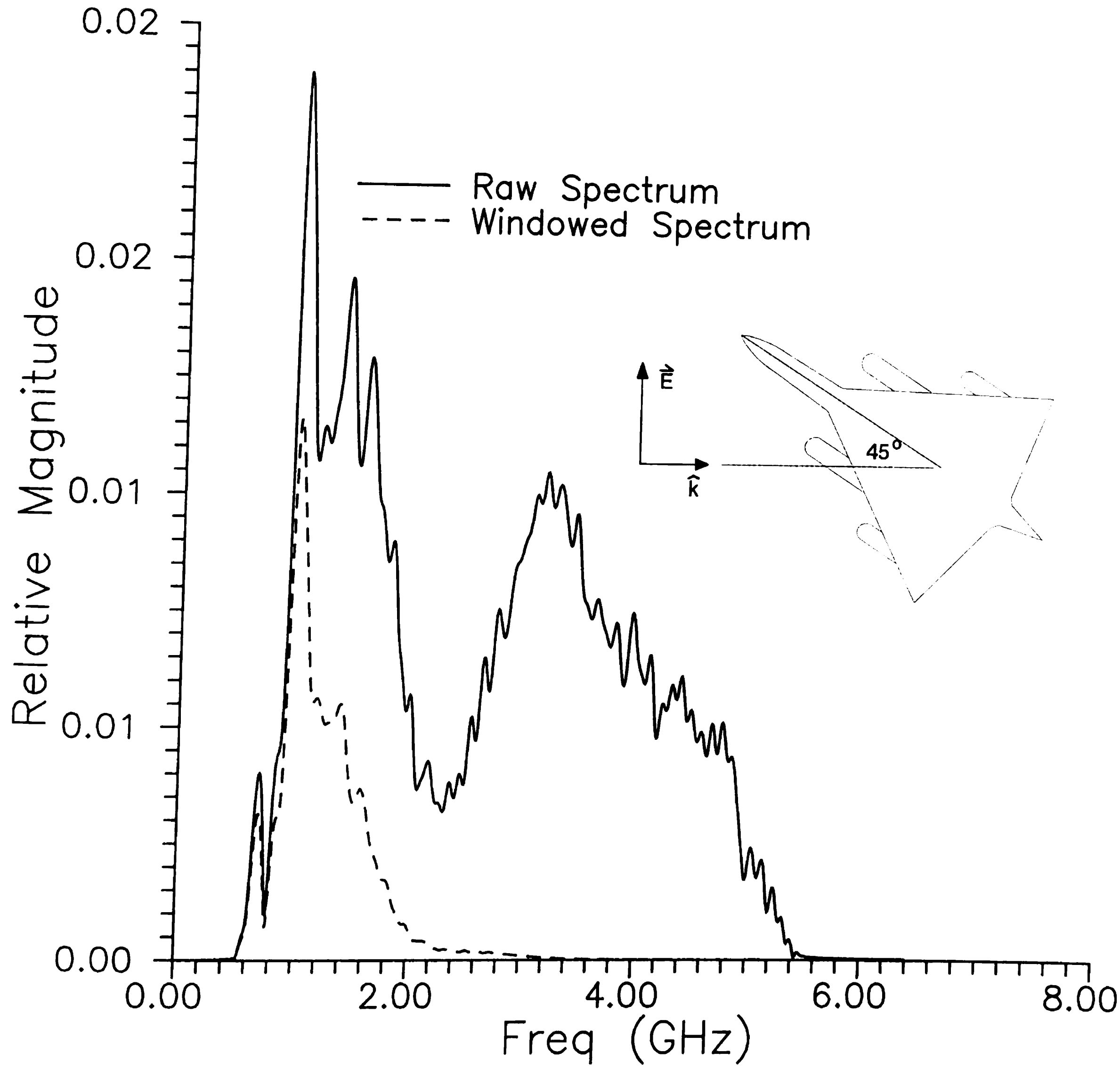

Figure 5.43 Late-time filtered frequency response for scattering from B-58 aircraft model.

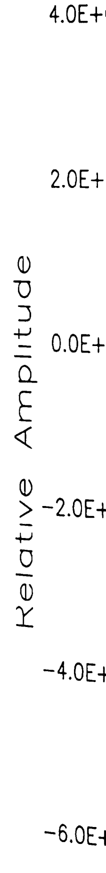

Figure 5.44

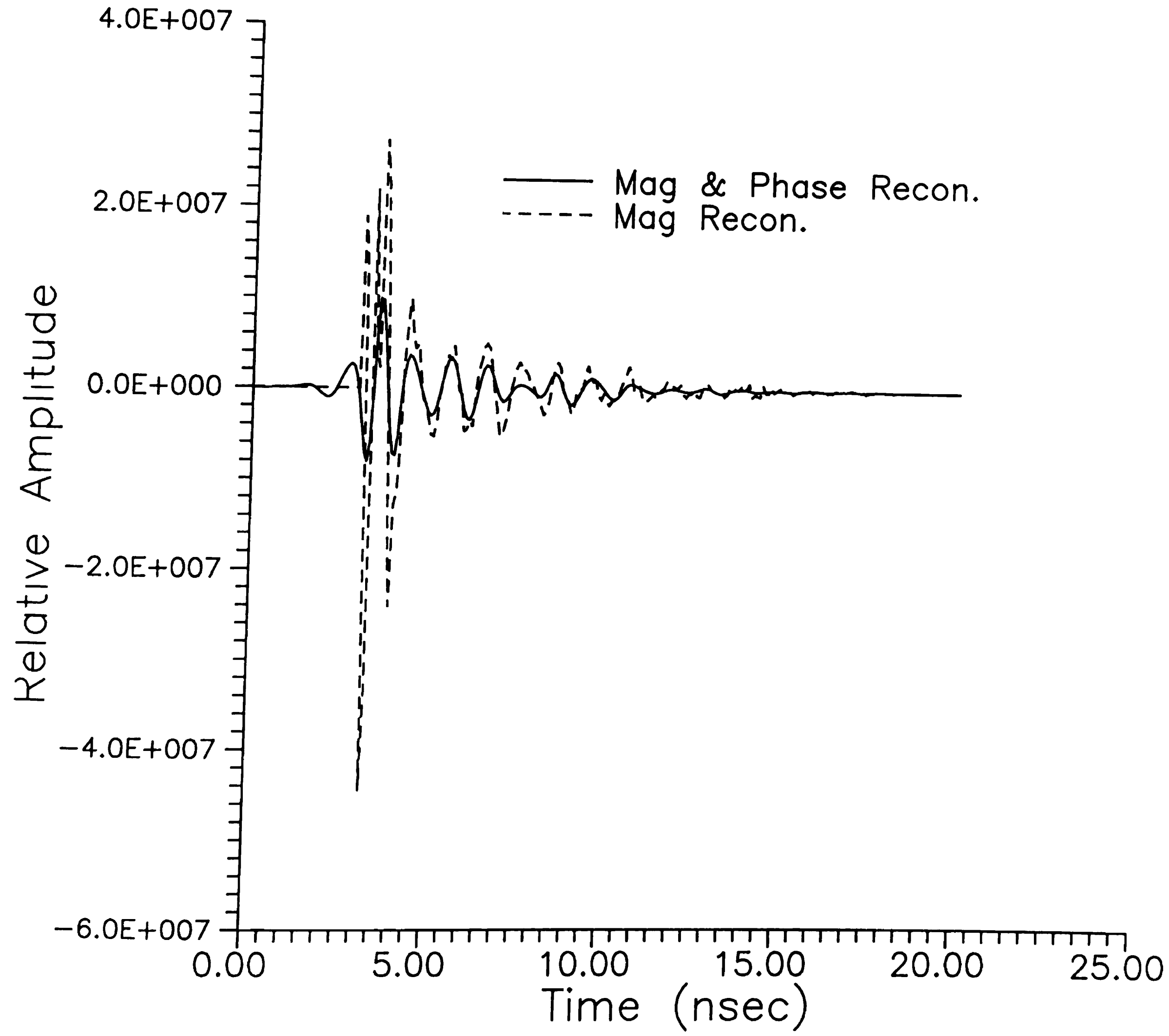

Figure 5.44 Transient scattered field for late-time response from B-58 aircraft.

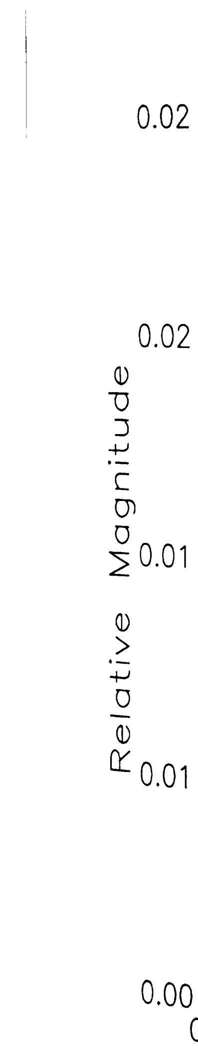

Figure 5.45

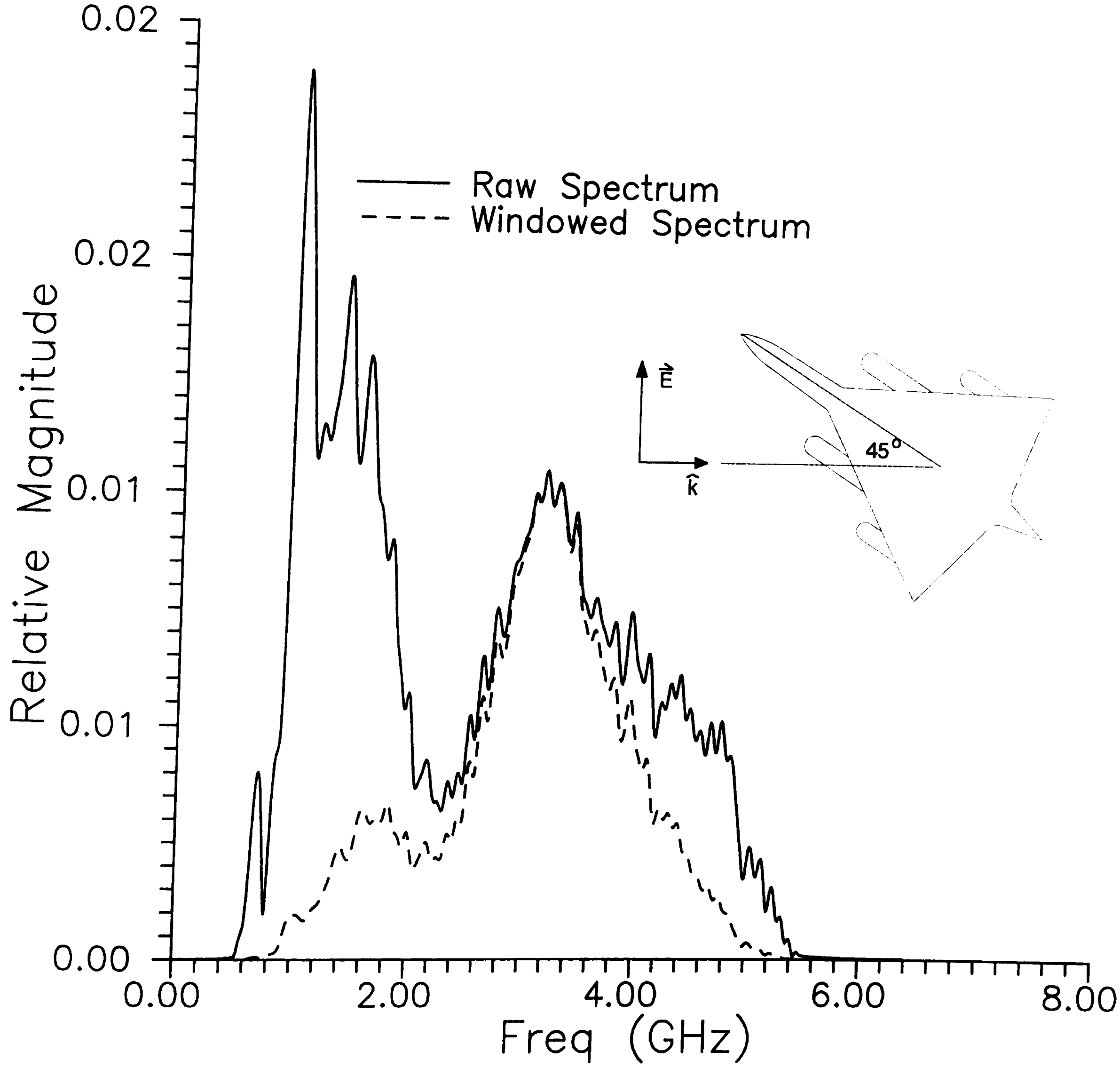

Figure 5.45 Early-time frequency filter response for scattering from B-58 aircraft.

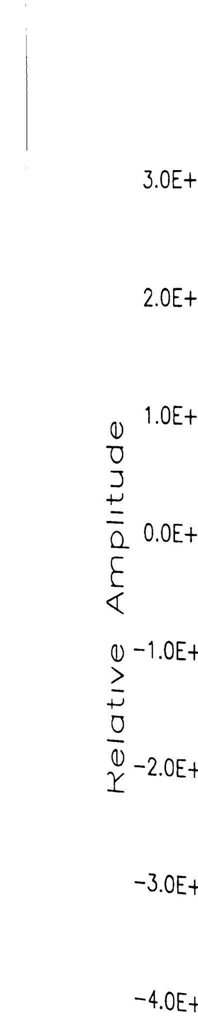

Figure 5.46

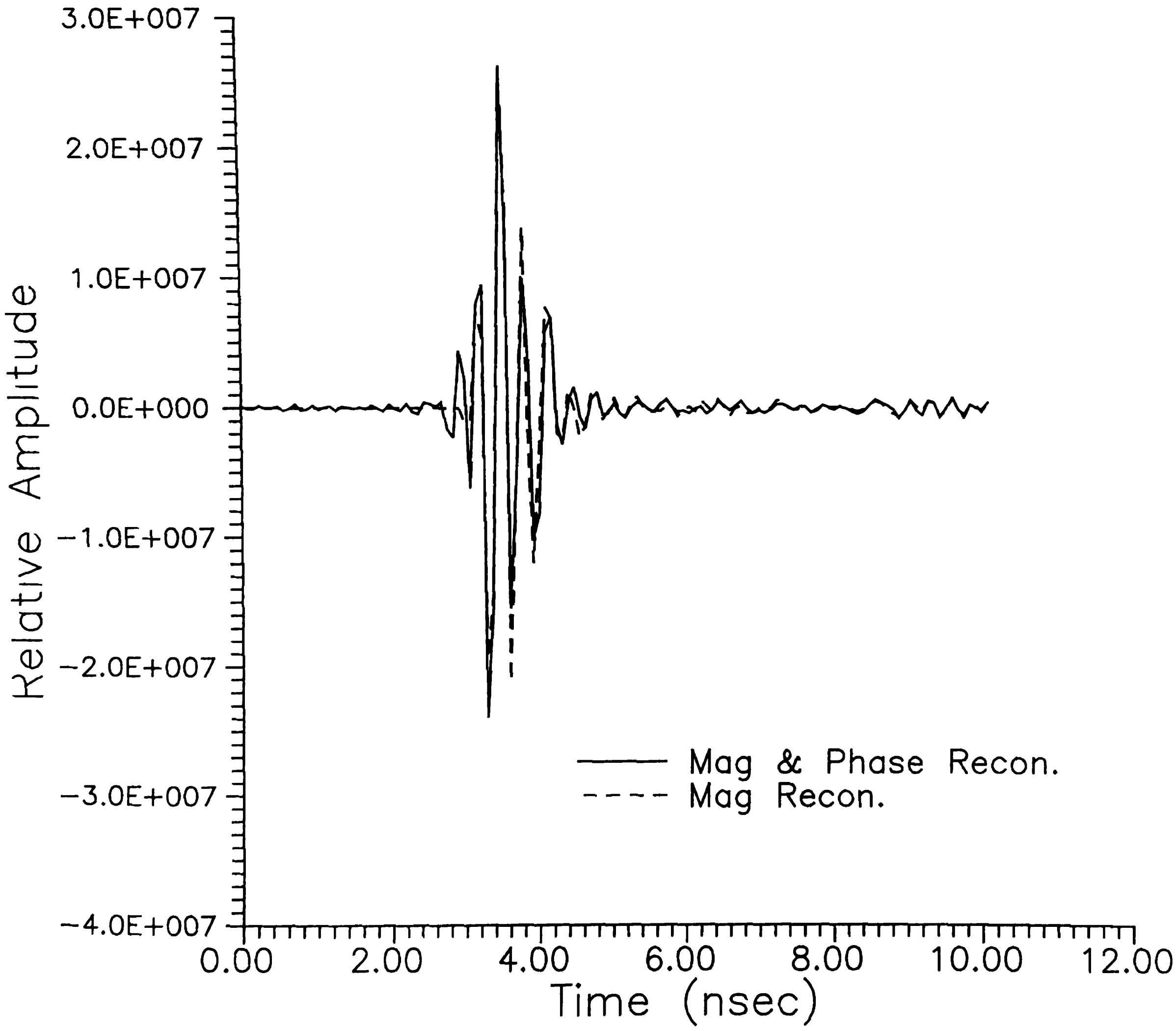

Figure 5.46 Transient scattered field using early-time filtered frequency response for scattering from B-58 aircraft.

5.6 Concl

Some

cepstral recor

1. Mi

includ

2. A

recons

respor

3. Ea

filtere

4. Th

obtair

spectr

Since

frequency sp

detection alg

should not b

possibly be

components.

features dire

5.6 Conclusions

Some important results have been demonstrated for radar target responses and cepstral reconstruction:

1. Minimum phase conditions <u>cannot</u> be guaranteed for any scattered radar signal including the late-time component.

2. Although the minimum phase condition is rarely met exactly, cepstral reconstruction can be used to obtain the late-time component of the target response.

3. Early and late time can be separated using the composite spectrum and the filtered components.

4. The early-time signal obtained by cepstral reconstruction will not match that obtained from using both the magnitude and phase components of the frequency spectrum

Since the late-time component can be obtained from only the magnitude of the frequency spectrum , this method should work in conjunction with E-pulse target detection algorithms. Early-time reconstruction performs poorly and the cepstral method should not be used in conjunction with any imaging techniques. Two future issues could possibly be worked on : First, better filtering algorithms to separate late and early-time components. Second, some consideration should be given to the analysis of the late-time features directly in the cepstral domain.

Applica

6.1 Intro

In a t

specific targ

from an anal

unknown tar

time-domain

a different a

methods of

obtained. A

or controlled

to an unkno

the time-dor

was built a

waveforms.

Chen

E-pulse disc

which, when

the annihilat

the convolut

Chapter 6

Application of Cepstral Analysis to Radar Target Discrimination Using E-Pulse Cancellation

6.1 Introduction

In a typical radar target discrimination problem, an attempt is made to identify a specific target from a set of target features or signatures. These features can be obtained from an analysis of the measured time-domain response. If the spectral waveform of the unknown target is measured, an inverse Fourier transform can be applied to obtain the time-domain representation. However, if only the modulus of the spectrum is available, a different approach must be used to reconstruct the time-domain waveform. Using the methods of cepstral analysis, an approximation to the time-domain waveform can be obtained. A set of target discriminants (signatures) obtained from scattering calculations or controlled measurements must be obtained prior to applying the discrimination scheme to an unknown target. For this study, a set of discriminant features were obtained from the time-domain waveform using the Fourier transformed spectrum. A target data base was built and later applied to the cepstrally reconstructed unknown radar-target waveforms.

Chen, *et al,* [20]-[21], [38] have developed a target identification method using the E-pulse discrimination scheme. In this method an E-pulse waveform is constructed which, when convolved with the late-time pulse response of a matched target, results in the annihilation of the natural resonant modes excited by radar illumination. However, the convolution of the same E-pulse with a target having a different resonant structure does not resu

can be cons

response.

automated ta

on a visual i

target discri

An u

to determine

domain repr

conjunction

information

be used to g

ideas of cep

there have b

response fro

cepstral theo

in this chapt

A re

probably no

However, a

detection sc

portion of t

does not result in a null convolution response. Hence, a data base of E-pulse waveforms can be constructed which, when convolved with a matched target, results in the null response. In order to effectively use the phenomena of E-pulse cancellation, an automated target discrimination scheme has been devised [9] which does not need to rely on a visual inspection of the convolved responses. The use of the ideas in the automated target discrimination scheme will be discussed and used in this chapter.

An unknown target waveform can be interrogated by E-pulse library waveforms to determine if any of the target files match the unknown target. In this scheme a time-domain representation waveform is used. A spectral response of the unknown target in conjunction with an inverse Fourier transform yields the transient response. If only information on the modulus of the spectral response is known, a different method must be used to get the time-domain waveform. The approach taken in this study is to use the ideas of cepstral analysis to reconstruct a transient response approximation. Although there have been many applications of cepstral analysis, the reconstruction of the late-time response from short pulse radars has not been investigated. A useful investigation into cepstral theory can be found in Openheim and Schaefer [29]. Much of the investigation in this chapter is based upon the work done by these authors.

A reconstructed waveform formed from a cepstral reconstruction algorithm will probably not match a waveform generated using both magnitude and phase information. However, a perfect match between the two waveforms may not be necessary for the target detection scheme to work. If the target's natural resonant modes exist within the late-time portion of the minimum-phase reconstructed signal, then the E-pulse discrimination scheme shou

late-time res

many cases.

the use of t

addition. the

even though

in mind that

for cepstral

however. si

reconstructed

The v

of E-pulse a

target discri

presented sh

The perform

derived scatt

6.2 Theo

The s

can be chara

can be mode

scheme should be able to identify the target. Chapter 5 has shown that the reconstructed late-time response, using cepstral analysis, approximates the true late-time response in many cases. Since the natural resonance modes are derived from this late-time response, the use of target discrimination using cepstral reconstruction should be effective. In addition, the reconstructed natural frequencies often match the true natural frequencies even though the reconstructed waveform does not exactly match the original signal. Keep in mind that the scattered return does not pass the minimum-phase condition necessary for cepstral reconstruction. This even applies to the late-time return. Practically, however, since the late-time return is decaying, it is minimum-phase like and the reconstructed signal works quite well.

The work which follows will be divided into several sections. First, a short review of E-pulse and cepstral analysis theory will be presented. Second, a description of a target discrimination algorithm will be discussed. Finally, numerical examples will be presented showing the performance of cepstral analysis in regards to target discrimination. The performance of the discrimination scheme is evaluated using both numerically derived scattering data and experimentally measured results from practical target models.

6.2 Theoretical Background

The scattered transient return due to a short-pulse signal incident on a radar target can be characterized by an early-time and a late-time response. The late-time response can be modeled as a sum of N damped sinusoids in the following manner

$$f(t) = \sum_{n=1}^{N} a_n e^{\sigma_n t} \cos(\omega_n t + \phi_n), \qquad t > T_l \tag{6.1}$$

where s_n =

represent the

beginning of

An E

f(t), results i

Since the na

be measured

The conditic

domain, i.e.

where E(s)

frequencies

numbers s_n a

e(t) in a s

determining

known, an

genetic algo

frequencies.

E-pulse data

E-pulse in

where $s_n = \sigma_n + j\omega_n$ is the nth aspect independent natural resonant frequency, a_n and ϕ_n represent the aspect dependent magnitude and phase, respectively, and T_l represents the beginning of the late-time period.

An E-pulse e(t) is a real waveform of finite extent T_E, that, upon convolution with f(t), results in a null late-time response

$$c(t) = e(t) * f(t) \equiv 0, \qquad t > T_L = T_l + T_E \tag{6.2}$$

Since the natural resonant frequencies are aspect independent, the target response f(t) can be measured from any aspect angle and the null late-time convolution should be obtained. The condition in (6.2) implies a particular set of zeros for the E-pulse in the frequency domain, i.e.

$$E(s) = \mathscr{L}\{e(t)\} = 0 \qquad \begin{array}{l} for\ s = s_n\ \ and\ s = s_n^* \\ n = 1,2,\ldots N \end{array} \tag{6.3}$$

where E(s) is the Laplace transform of e(t), and s_n represent all possible natural-mode frequencies of the particular target excited by an incident waveform. If the complex numbers s_n are known for a particular target, the E-pulse can be constructed by expanding e(t) in a set of basis functions (usually rectangular pulses) by applying (6.2) and determining the amplitudes of the basis functions. If the resonant frequencies are not known, an E-pulse extraction technique based on the method of least squares [39] or genetic algorithm [40] can be used to find the basis function amplitudes and the resonant frequencies. An E-pulse can be constructed for each anticipated target and added to an E-pulse data base. Next, the response of an unknown target u(t) is convolved with each E-pulse in the data base. If the zeros of a particular E-pulse match the resonant frequencies f

indicates a ta

the convolve

In or

target respon

to the time c

cepstral reco

to the trans

condition, a

discrete spe

cepstrum is

Using the v

the minimu

The evalua

must be su

If th

poles and z

All the po

frequencies found in the late time of the unknown target, a null convolution response indicates a target match. If E(s) does not contain zeros at all the natural frequencies, then the convolved waveform will be non-zero, indicating a poor match.

In order to achieve target discrimination using the E-pulse method the unknown target response u(t) must be measured. A measured spectral response can be transformed to the time domain using a Fourier transform. For a magnitude-only spectral response cepstral reconstruction (see Chapter 5, section 2) can be used to form an approximation to the transient scattered signal. Certain restrictions, known as the minimum-phase condition, are required for an exact replication of the true time-domain signal. For a discrete spectrum having $N = 2^m$ points defined by $X[k] = |X[k]|\, e^{j \arg X[k]}$, the real cepstrum is given by

$$c[n] = FFT^{-1}\left(\log |X[k]| \right) \tag{6.4}$$

Using the window function given by

$$w[n] = \begin{array}{ll} 2, & 1 \leq n < N/2 \\ 1, & n = 0, N/2 \\ 0, & N/2 < n \leq N-1 \end{array} \tag{6.5}$$

the minimum phase sequence may be computed as

$$\hat{x}[n] = FFT^{-1}\left(e^{FFT(w[n]\, c[n])} \right) \tag{6.6}$$

The evaluation of (6.4) and (6.6) can be done very quickly using the FFT. However, one must be sure to avoid complications caused by aliasing.

If the original causal stable sequence is given by x[n] is minimum phase, then the poles and zeros of its z-transform must all lie within the unit circle in the complex plane. All the poles of any finite length sequence have poles at the origin. For most finite length. samp

the sampled

decaying sec

Chapter 5, se

is not met b

sequence. I

sequence th

minimum-ph

scheme wil

minimum-ph

6.3 Targ

An E

upon which

angles. A

scattering g

all the natu

Constructio

basis functi

where $\{g_k($

length, sampled sequences the zeros do not lie with the unit circle. This even applies to the sampled values from the late-time model given by (6.1). However, for a strictly decaying sequence it is easy to show that the minimum-phase criteria is met (refer to Chapter 5, section 2). For sinusoidally decaying sequences, the minimum-phase condition is not met but the reconstructed sequence may be a good approximation to the original sequence. In this case most of the zeros lie within the unit circle. On the other hand, a sequence that is exponentially growing has all zeros outside the unit circle and a minimum-phase reconstruction is clearly wrong. The following target discrimination scheme will use a simple program that calculates the cepstral coefficients and the minimum-phase reconstructed signal.

6.3 Target Discrimination Algorithm

An E-pulse must be generated for each expected target. The expected target return upon which the E-pulse is based must be carefully measured over a set of different aspect angles. An alternative would be to calculate the scattered fields for fairly simple scattering geometries. In either case, several aspect angles are required to make sure that all the natural resonant modes are excited and included for the E-pulse construction. Construction of the E-pulse e(t) is performed by expanding the E-pulse e(t) in a set of basis functions as [20]

$$e(t) = \sum_{k=1}^{K} \alpha_k g_k(t) \tag{6.7}$$

where $\{g_k(t)\}$ is an appropriate set of basis functions. The convolution integral in (6.2) can be expar

Using the ba

with a set of

where T_W d

Usin

solution) ca

an inhomog

the matrix

impulse fur

Diff

choice of T

resonant fr

squared err

using the e

to minimiz

can be expanded as

$$c(t) = \int_0^{T_E} e(\tau) f(t-\tau) d\tau = 0 \qquad t > T_l + T_E \tag{6.8}$$

Using the basis functions in (6.7), substituting this into (6.8), and taking inner products with a set of weighting function $\{w_m\}$ gives

$$\sum_{k=1}^{K} \alpha_k \int_{\tau=0}^{T_E} \int_{T_l+T_E}^{T_W} g_k(\tau) f(t-\tau) w_m(t)\, dt\, d\tau = 0 \tag{6.9}$$

$$m = 1, 2, 3 \ldots M$$

where T_W describes the end of the measurement window.

Using (6.9), a solution for α_k for almost any choice of T_E ("forced" E-pulse solution) can be found by choosing M = 2N and K = 2N + 1. In this case (6.9) becomes an inhomogeneous matrix equation with solutions for any choice of T_E that does not cause the matrix to be singular. The use of rectangular pulse basis functions and weighting impulse functions causes the integration in (6.9) to become much simpler.

Different values for T_E result in significantly different E-pulse waveforms. The choice of T_E can have a significant effect on the constructed E-pulse and the extracted resonant frequencies [4]. One suitable choice of T_E is that which yields the minimum squared error per point between the original data f(t) and a waveform $\hat{f}(t)$ constructed using the extracted natural frequencies, amplitudes, and phases. In this case T_E is chosen to minimize the following value over the sampled interval from T_l to $T_l + T_W$

$$\epsilon = \| f(t) - \hat{f}(t) \| = \sum_i \left[f(t_i) - \hat{f}(t_i) \right]^2 \tag{6.10}$$

where

The natural

amplitudes i

functions th

where $Z = e$

determined

amplitude a

of course l

waveform h

frequencies

In th

for several

transform w

for some ta

pulse metho

For this st

realization

in the conv

where

$$\hat{f}(t) = \sum_{n=1}^{N} \hat{a}_n e^{\hat{\sigma}_n t} \cos(\hat{\omega}_n t + \hat{\phi}_n) \tag{6.11}$$

The natural frequencies $\hat{s}_n = \hat{\sigma}_n + j\hat{\omega}_n$ can be found by solving for the E-pulse basis amplitudes in (6.9) and then using the relation given by (6.3). For rectangular pulse basis functions this leads to a polynomial equation of the form

$$\sum_{k=1}^{2N+1} \alpha_k Z^k = 0 \tag{6.12}$$

where $Z = e^{-s\Delta}$ and Δ the basis function width. Once the natural frequencies are determined a least-squares fitting routine is applied to (6.10) and (6.11) to yield the amplitude and phase terms for the reconstructed waveform. Different values of T_E will of course lead to values of ε that differ. The value of T_E can be varied to yield the waveform having the smallest value of ε. In this process, the E-pulse amplitudes, natural frequencies, and best fit reconstructed waveform are obtained.

In this chapter, E-pulses are constructed from the transient response waveforms for several different targets. The waveforms were generated using an inverse Fourier transform with magnitude and phase spectral information that was theoretically calculated for some targets and measured for others. Target discrimination, performed by the E-pulse method, requires the convolution of each E-pulse with an unknown target waveform. For this study the unknown target waveform was generated from a minimum phase realization of magnitude only frequency data. A measure of the amount of signal present in the convolved late-time response c(t) is given by the E-pulse discrimination number

(EDN) [9]

where W re

is simply a

To use the

beginning a

convolution

values of co

for the mat

correct E-p

lowest valu

comparing

ratio (EDR

Hence, the

E-pulses co

6.4 Nu

Thi

two sets o

(EDN) [9]

$$EDN = \left[\int_{T_L}^{T_L+W} c^2(t)dt \right] \left[\int_0^{T_E} e^2(t)dt \right]^{-1} \tag{6.13}$$

where W represents the time window over which the signal is convolved. Equation (6.13) is simply a measure of the deviation from the expected value of zero late-time energy. To use the above quantity, the E-pulse is convolved with the unknown target waveform beginning at T_L. If a target exists in the data base matching the unknown waveform, the convolution energy should be zero, whereas the other E-pulses will produce non-zero values of convolution energy in the late time. In actual situations, the convolution energy for the matched target will not be precisely zero due to noise, problems in constructing correct E-pulse waveforms, or incorrect waveform construction. The EDN having the lowest value should then be chosen as the matched target. A quantitative measure comparing all the EDN values in the data-base is given by the E-pulse discrimination ratio (EDR)

$$EDR(dB) = 10 \log_{10} \left\{ \frac{EDN}{min\,(EDN)} \right\} \tag{6.14}$$

Hence, the E-pulse yielding the minimum EDN value has an EDR of 0 dB while other E-pulses contribute values greater than 0.

6.4 Numerical Results

This section will describe the application of the E-pulse discrimination scheme to two sets of data. The first set of scattering data was generated from a simple thin-wire scattering p

series of sc

consists of

again. E-pu

tested for t

Bac

9.5. 10.0. 1

domain me

wire appro

fixed at a r

at 256 equ

spectrum v

GHz. T =

obtain a ti

results in t

The pulse,

where τ =

maximum

each wire

scattering program. E-pulse waveforms were generated for this data set, after which a series of scattering targets were tested for identification matching. The second data set consists of scaled aircraft and missiles measured in the anechoic chamber at MSU. Once again, E-pulses were constructed for these targets and several "unknown" targets were tested for target matching.

Backscattering data was generated for simple thin wires of length l = 8.0, 8.5, 9.0, 9.5, 10.0, 10.5, 11.0, 11.5, and 12.0 cm. Scattering data was generated using a frequency-domain method-of-moments solution. Piecewise-sinusoidal basis functions and the thin wire approximation were employed with Galerkin's method. The length-to-radius was fixed at a ratio of 1000 for each wire. The complex backscattered fields were calculated at 256 equally spaced frequencies between .05 GHz and 12.8 GHz (Δf = .05 GHz). The spectrum was windowed with a Gaussian modulated cosine (GMC) function (fc = 0.0 GHz, T = .1 nsec, see Appendix A) and then inverse Fourier transformed using a FFT to obtain a time-domain waveform. The effect of windowing in the frequency-domain results in the backscatter transient response from a Gaussian pulse for the incident wave. The pulse, p(t), as a function of time can be written as

$$p(t) = e^{-\pi t^2/\tau^2} \tag{6.15}$$

where τ = .1 nsec was chosen giving a pulse width of about .2 nsec between the 4% of maximum points. Figure 6.1 shows the magnitude of the window function applied to each wire-scattering spectrum. Figure 6.2 shows a time-shifted incident pulse correspondi

For

angles: (1)

(2) 45 deg

discussed a

angle calcu

of the spe

generated u

then becar

comparisor

(using an I

wire for bı

good matc

the match

An

scheme.

subsequen

when the v

pulse acro

as

Their targ

corresponding to the inverse Fourier transform of the spectrum shown in Figure 6.1.

For each wire, the backscattering responses were computed for two incident angles: (1) broadside incidence with the E-field parallel to the long-axis of the wire, and (2) 45 degrees off of broadside with the E-field in the same plane of incidence. As discussed above, a set of E-pulses was generated for each wire (based on the two incident angle calculations) using a hybrid E-pulse/least-squares method [39] with the magnitude of the spectrum used to generate the E-pulses. A set of transient waveforms was generated using the minimum phase reconstruction algorithm. These transient waveforms then became the unknown target responses. Figure 6.3 and Figure 6.4 shows a comparison between the transient response generated using both magnitude and phase (using an IFFT) and generated from the minimum phase reconstruction for the 10.0 cm wire for broadside and 45 degrees from broadside incidence. Figure 6.3 shows a very good match between the two reconstructions in both late and early time. In Figure 6.4 the match is not quite as good.

An E-pulse data base library was generated for the radar target discrimination scheme. Table V shows the E-pulse identification and description to be used in the subsequent figures. Ilavarasan and Ross [9] determined the start of late time based upon when the wave strikes the leading edge of the target (T_b), the maximal transit time of the pulse across the target (T_{tr}), and the pulse width (T_p). The late time was then calculated as

$$T_l = T_b + T_p + 2\,T_{tr} \tag{6.16}$$

Their target data base consisted of values for T_p and T_{tr} for each target. To calculate T_b

in the prese

not conside

analyze the

responses c

Fig

broadside

generated b

As discuss

compare th

also were g

square icor

curve repre

waveform

target usin

Fig

the EDR re

Figure 6.7

incidence.

minimum

magnitude,

The

10.0 cm w

in the presence of noise, a threshold detector scheme was used. The present analysis did not consider noise, and late time was visually estimated. The purpose here was not to analyze the automation process but to determine if the minimum-phase reconstruction responses could be used in the discrimination scheme.

Figure 6.5 shows the EDR values for an unknown target generated from the broadside transient response of the 10.0 cm wire. The values in this figure were generated by convolving the unknown target response with each E-pulse in the data base. As discussed earlier, a matched target will be indicated by an EDR value of 0 dB. To compare the effect due to a target represented only by spectral magnitude, the EDR values also were generated for the Fourier transform (mag/phase) reconstruction. The curve with square icons show the EDR response for the magnitude/phase reconstruction whereas the curve represented with the triangular icons is the magnitude only reconstruction. For both waveform reconstructions the correct target is identified. As expected, the unknown target using the minimum phase reconstruction has a lower response curve.

Figure 6.6 and Figure 6.7 show similar curves for different cases. In Figure 6.6 the EDR response for the 10.0 cm wire for an incident angle of 45 degrees is shown. In Figure 6.7 the EDR response for the 9.0 cm wire is shown for broadside angle of incidence. In both cases, the correct target in the data base has been identified. Also, the minimum phase reconstructed target does not match the data base as well as the magnitude/phase reconstruction.

The resonant frequencies created from the E-pulse construction algorithm for the 10.0 cm wire are shown in Figure 6.8. Also shown are the natural resonant frequencies

extracted fr
frequencies
numeric va
natural res
noise was c
minimum p
very well.

A s
target scat
measured i
measureme
HP8720B
response o
band used
field is sli
aircraft wi
measured f
incidence c
were next s
response w
the models
following

extracted from the minimum phase reconstructed waveforms. In both cases, the resonant frequencies were derived using aspect angle calculations at 0 and 45 degrees. The numeric values along the plotted symbols indicate the late-time energy order of each natural resonant frequency. A value of 1 indicates a higher energy than 4. Since no noise was considered in this analysis, the E-pulse construction was quite accurate and the minimum phase reconstruction was also good. Therefore, the natural frequencies agree very well.

A similar target discrimination simulation was performed on data from measured target scattered-field responses. Five scaled models of similar physical size were measured in the MSU anechoic chamber. Figure 6.9 shows the scale models used in the measurements. All measurements were performed in the frequency domain using an HP8720B network analyzer. The system response was removed using the theoretical response of a 14-inch diameter calibration sphere (refer to Appendix A). The frequency band used was from .5 to 5.5 GHz at a frequency step size of .0125 GHz. The scattering field is slightly bistatic and the incident electric field is polarized in the plane of the aircraft wings or along the roll axis of the missile. Five angles of incidence were measured for each model: 0°, 30°, 45°, 60°, and 90°. An angle of 0° indicates a nose-on incidence direction whereas 90° indicates broadside. The frequency spectrum responses were next scaled to reflect actual aircraft size ratios. For this analysis the F-14 frequency response was not scaled and the other model responses were scaled to reflect changes in the models physical size. The model's physical size would need to be scaled in the following manner to reflect the correct ratios: B-58 - 1.34x, f18 - .9x, missile #1 - .27x, missile #2 -

scaling was

The

measureme

phase was i

added for

significantl

requires in

model was

Fourier tra

centered at

.268, F14 -

for the puls

for each t

windowing

pulse widt

.108, and

Fig

waveform

the nose c

correspond

loss of hi

missile #2 - .38x. It should be noted that the missiles were generic and the intent of their scaling was to create a missile smaller than the aircraft.

The low frequency band containing no data (0 GHz to the low end of the measurement) was quadratically interpolated to zero amplitude at zero frequency. The phase was interpolated using a minimization linear fit scheme. The extrapolated data was added for two reasons. First, the effect of subsequent windowing can be reduced significantly (less ripple in the time domain). Second, the minimum phase algorithm requires information down to zero frequency. Next, the transient response from each model was weighted by a GMC window and then inverse transformed using the fast Fourier transform or minimum phase reconstruction algorithm. The GMC window was centered at $f_c = 0.0$ GHz and the pulse width parameter T for each target was: B-58 - .268, F14 - .2, F18 - .18, missile #1 - .054, and missile #2 - .076 nsec. Different values for the pulse width parameter were chosen to use as much of the scattered field spectrum for each target as possible. The shape of the incident pulse formed as a result of windowing is similar to that in Figure 6.2. The selected values of T give a time-domain pulse width for each target as (see (6.15)): B-58 - .536, F14 - .4, F18 - .36, missile #1 - .108, and missile #2 - .152 nsec.

Figure 6.10 and Figure 6.11 show the windowed frequency response and transient waveform for the B58 aircraft respectively. The incident angle was measured 45° from the nose of the aircraft. The frequency response shows at least two resonant peaks corresponding to the natural resonant frequencies of the target. Figure 6.10 shows the loss of high frequency information lost due to windowing. To use higher frequency

information
or measure
Both the IF
reconstruct
between th
Fig
from the o
between th
the comple
to work.
response g
reconstruct
the missile
Usi
data base
E-pulse w
modes wo
the missile
responses
measurem
transforme
phase rec

information one can either modify the window (with subsequent time-domain problems) or measure over a wider bandwidth. The time-domain response is shown in Figure 6.11. Both the IFFT response (using magnitude and phase information) and the minimum phase reconstruction are shown for comparison. In this case there is a fairly good match between the two responses - especially in the late time.

Figure 6.12 through Figure 6.19 show the frequency and time-domain responses from the other targets. The transient responses for the F14 and F18 show a poor match between the magnitude/phase reconstruction and the cepstrum reconstruction. However, the complex frequencies may have enough similarity for the target identification scheme to work. Figure 6.17 and Figure 6.19 show excellent agreement between the transient response generated from the magnitude/phase reconstruction and the magnitude only reconstruction. This is probably due to the simple nature of the scattering geometry of the missile.

Using the time-domain transient responses generated from the IFFT, an E-pulse data base was constructed. The data base consisted of the five measured targets. Each E-pulse was constructed with five different incident angles to insure that all resonant modes would be represented. However, only the broadside measurements were used for the missile models. To determine if the discrimination scheme would work, the measured responses for the B-58, F-14, and F-18 at 45° incident angle and broadside missile measurements were used for the unknown target. The frequency-domain response was transformed to the time domain using both the full spectrum IFFT and the minimum phase reconstruction. Table VI shows the E-pulse discrimination ratio for each "unknown"

response w

is doubtful

some noise

F-14 respo

of 3.5 dB

reconstruct

the models

missiles.

aircraft. T

modes wit

resonant m

Fig

the magni

If the tim

match. As

the late-tir

In each fig

(real parts

On

E-pulse da

pulse wav

"unknown" target as a function of the E-pulse in the target data base. In each case the response was matched with the correct target. However, due to the low EDR values it is doubtful whether the procedure would work in the presence of more noise, although some noise is already in the measurement process. One can see this for the case of the F-14 response, where the F-18 was nearly identified as the correct target with a margin of 3.5 dB for the IFFT response and a margin of only 1.7 dB for the cepstral reconstruction. This probably could be expected due to the similar size and geometry for the models. The table also clearly shows that the aircraft will not be identified as the missiles. However, there is a higher chance that the missiles could be identified as aircraft. This is most likely caused by some overlap of the missile's natural resonant modes with the higher resonant modes of the aircraft. On the other hand, the low resonant modes of the aircraft will not overlap any of the mssile's natural resonant modes.

Figure 6.20 through Figure 6.24 show the natural resonant frequencies found using the magnitude/phase reconstructed response and the magnitude only transient response. If the time-domain responses matched exactly, then the resonant modes should also match. As shown in the earlier figures, the transient responses do not match exactly in the late-time period, and therefore one shouldn't expect an exact natural frequency match. In each figure, the complex frequencies are almost equal; however, the damping factors (real parts) do not match as well.

One of the difficulties in using the E-pulse discrimination scheme is creating the E-pulse data base. A great deal of time can be spent trying to generate a good set of E-pulse waveforms, but difficulties arise when using any type of measured data having some noise. One

zero - a po

using the le

reconstruct

positive da

order mode

would be a

frequency-

notably ge

the compu

the resona

become tra

However,

in every ty

6.5 Co

The

Several nu

in regards

evaluated

data from

for the th

noise. One of the most troublesome areas deals with keeping the damping factor less than zero - a positive value being non-physical. However, in creating an E-pulse waveform using the least-squares method, higher order modes may be used to obtain a better fitting reconstruction. Usually this gives a better fit, but at the cost of adding modes with positive damping factors. Clearly, positive damping factors are not correct, but if higher order modes could be added with negative damping coefficients the resulting E-pulse would be a better candidate for the discrimination data base. Several constrained natural frequency-extraction routines have been studied by researchers at the EM Lab, most notably genetic algorithms [40]-[42]. The major problem with the genetic algorithm is the computationally expensive algorithm resulting in a large amount of time to calculate the resonant frequencies. On the other hand the genetic algorithm usually does not become trapped in any type of global minimum or does not really require an initial guess. However, one must gain some experience in selecting some of the correct parameters as in every type of minimization problem.

6.5 Conclusions

The use of cepstral analysis has been applied to the target discrimination problem. Several numerical examples were presented to show the performance of cepstral analysis in regards to target identification. The performance of the discrimination scheme was evaluated using both numerically derived scattering data and experimentally measured data from scaled aircraft and missile models. Cepstral analysis worked extremely well for the theoretically generated data. In the case of the measured data there was some degradatior

with E-puls

the E-pulse

obtaining a

degradation due to the difficulty in constructing a good E-pulse. Difficulties associated with E-pulse construction will also affect any type of target discrimination scheme using the E-pulse method. This case shows the importance of the measurement process in obtaining a good data free from unwanted noise or other signal components.

Fig

Fig

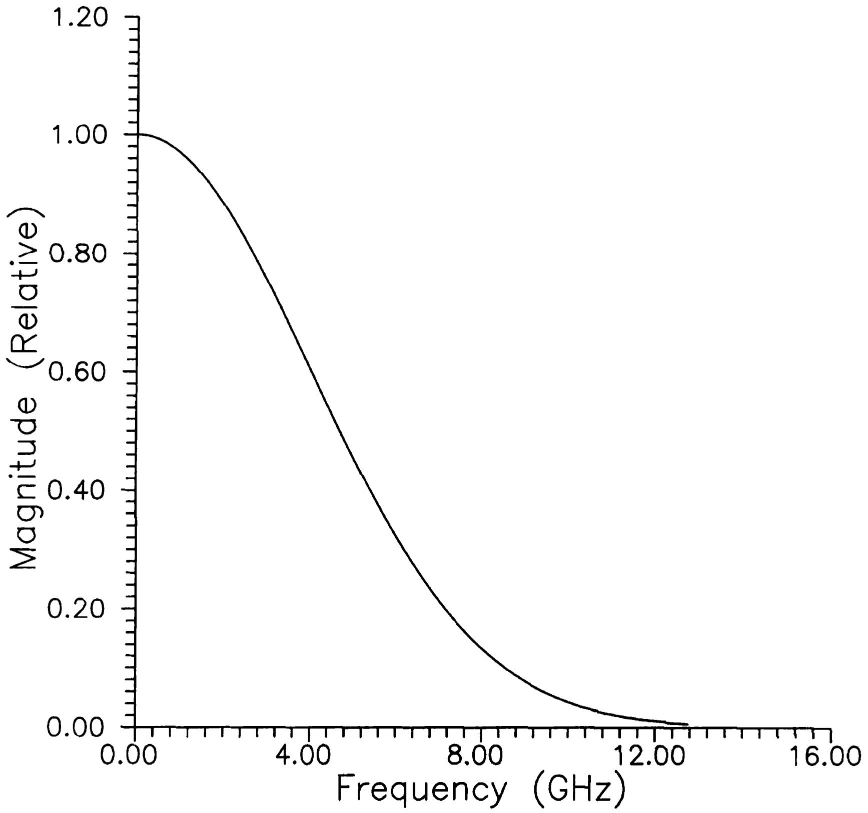

Figure 6.1 Frequency response magnitude for gaussian input pulse.

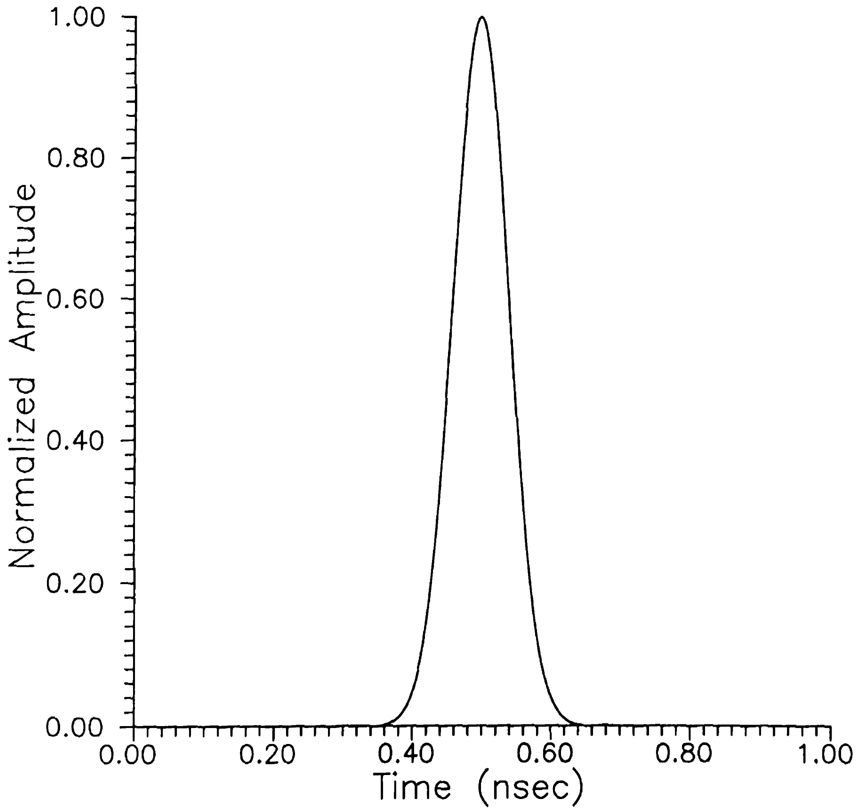

Figure 6.2 Normalized gaussian incident wave pulse.

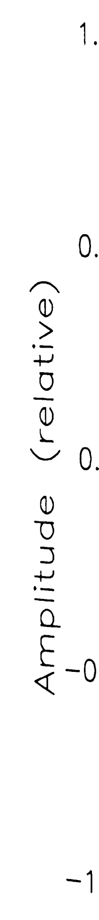

Figure 6.3

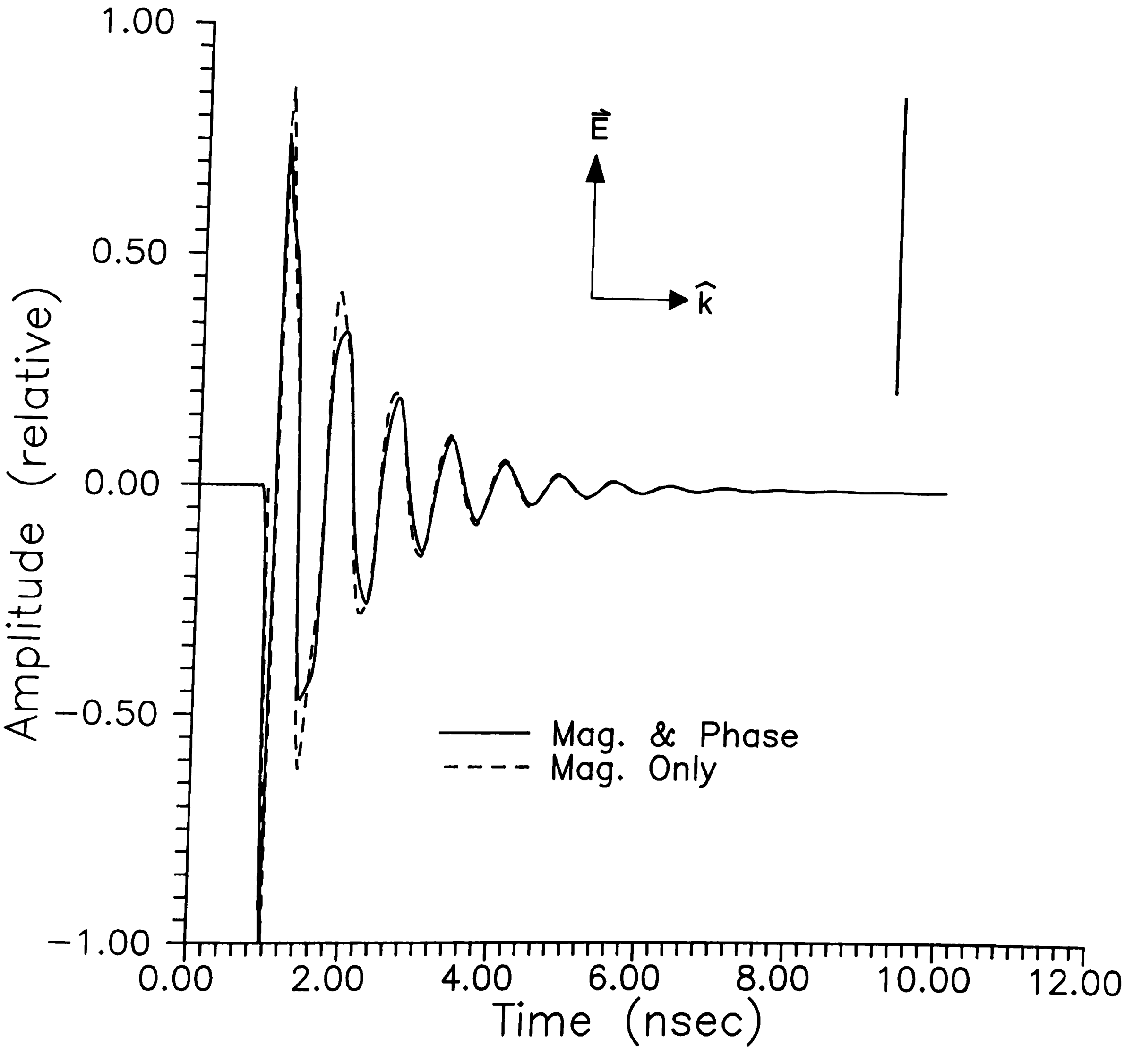

Figure 6.3 Noise-free backscattering response of a broadside 10.0 cm wire with l/a = 1000.

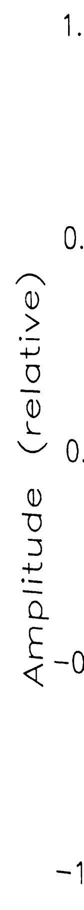

Figure 6.

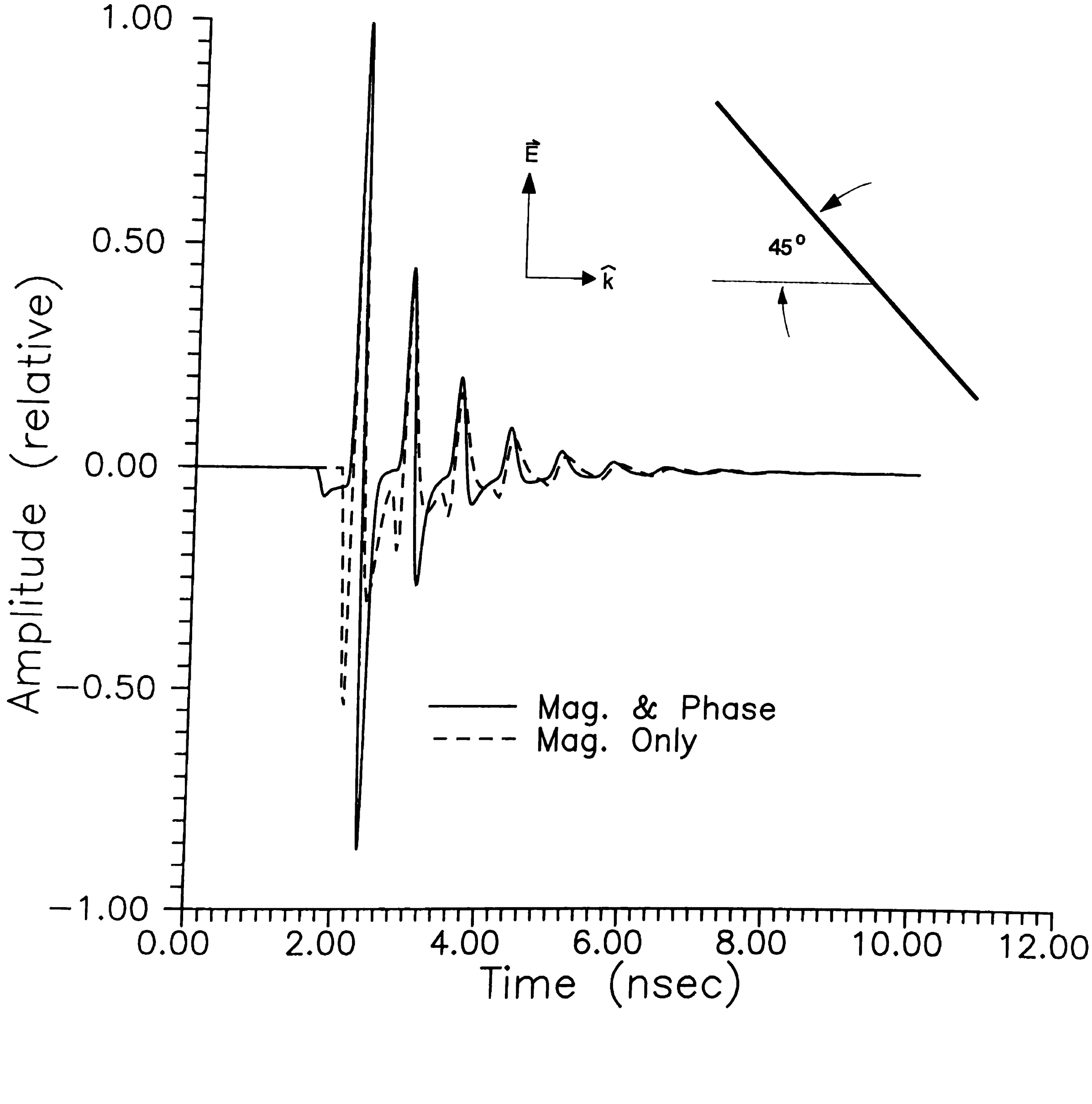

Figure 6.4 Noise-free backscattering response of a 10.0 cm wire with l/a = 1000. Incident electric field 45 degrees from axis of wire.

Table 6.1

Table 6.1 E-pulse identifiers and descriptions.

E-pulse identification	E-pulse description
A	8.0 cm wire E-pulse
B	8.5 cm wire E-pulse
C	9.0 cm wire E-pulse
D	9.5 cm wire E-pulse
E	10.0 cm wire E-pulse
F	10.5 cm wire E-pulse
G	11.0 cm wire E-pulse
H	11.5 cm wire E-pulse
I	12.0 cm wire E-pulse

Figure 6.

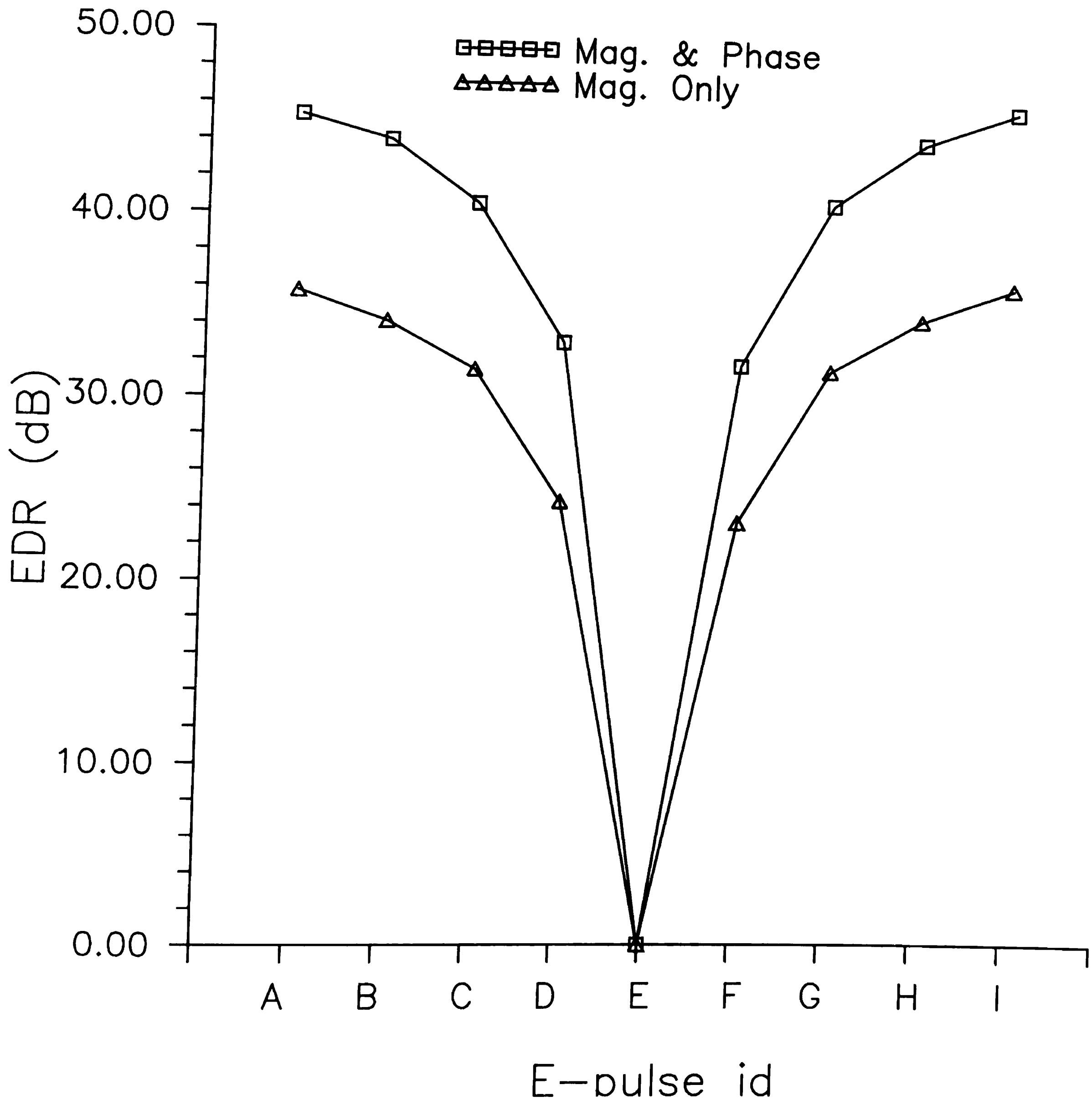

Figure 6.5 EDR values for broadside response of 10 cm wire with l/a = 1000.

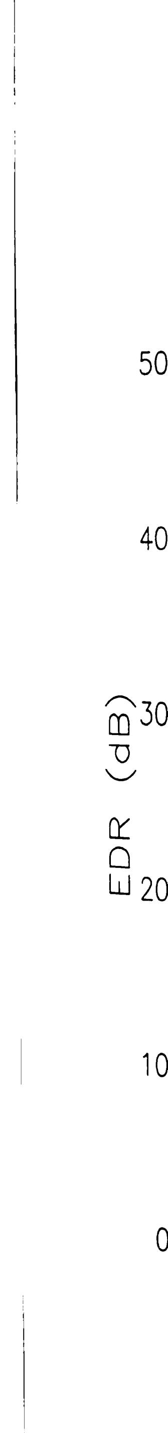

Figure 6.

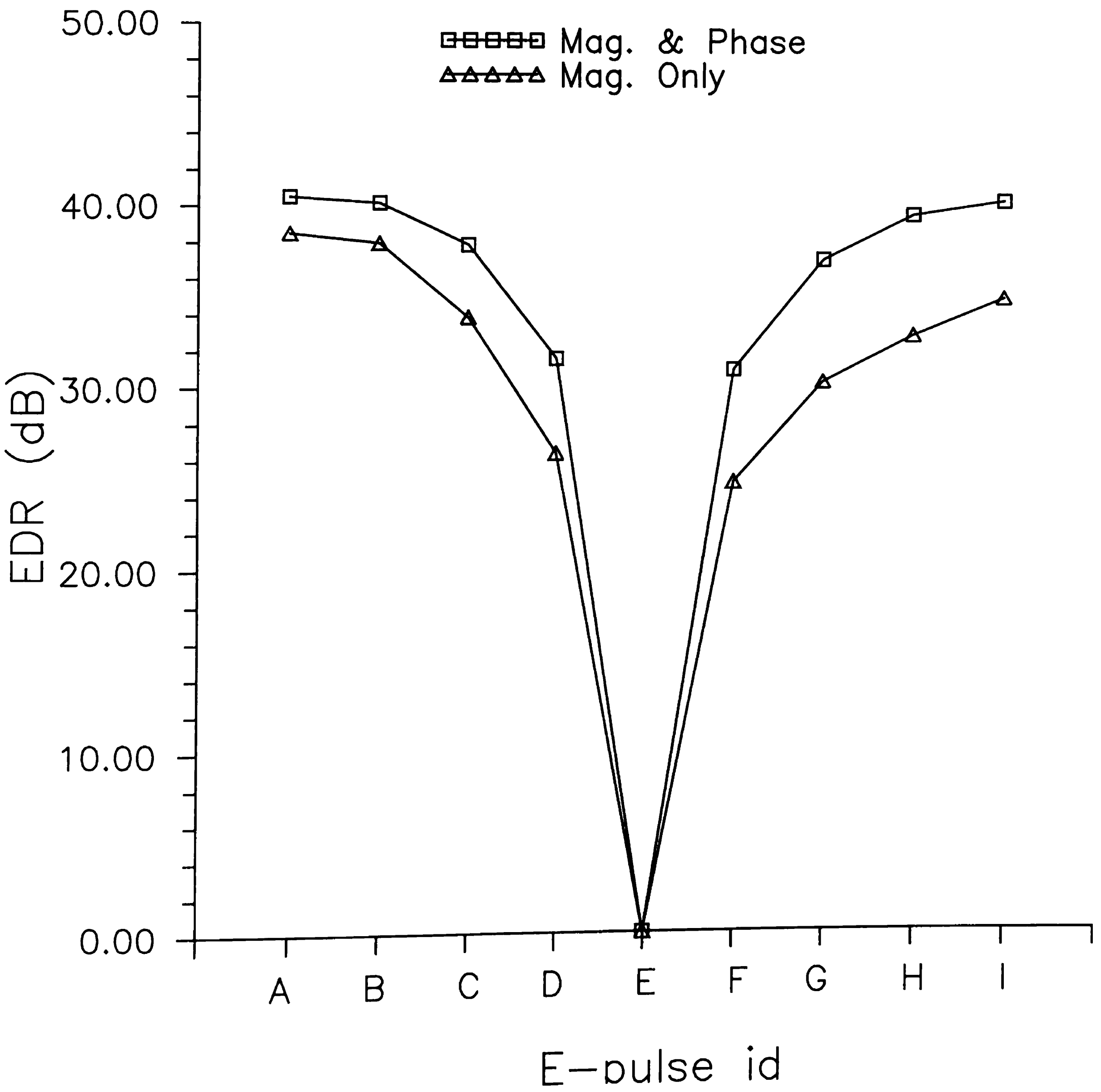

Figure 6.6 EDR values computed from response of 10 cm wire with l/a = 1000 oriented 45° from broadside.

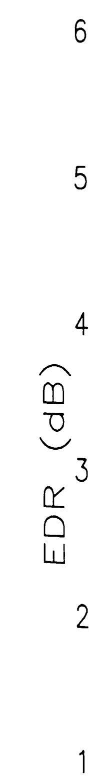

Figure

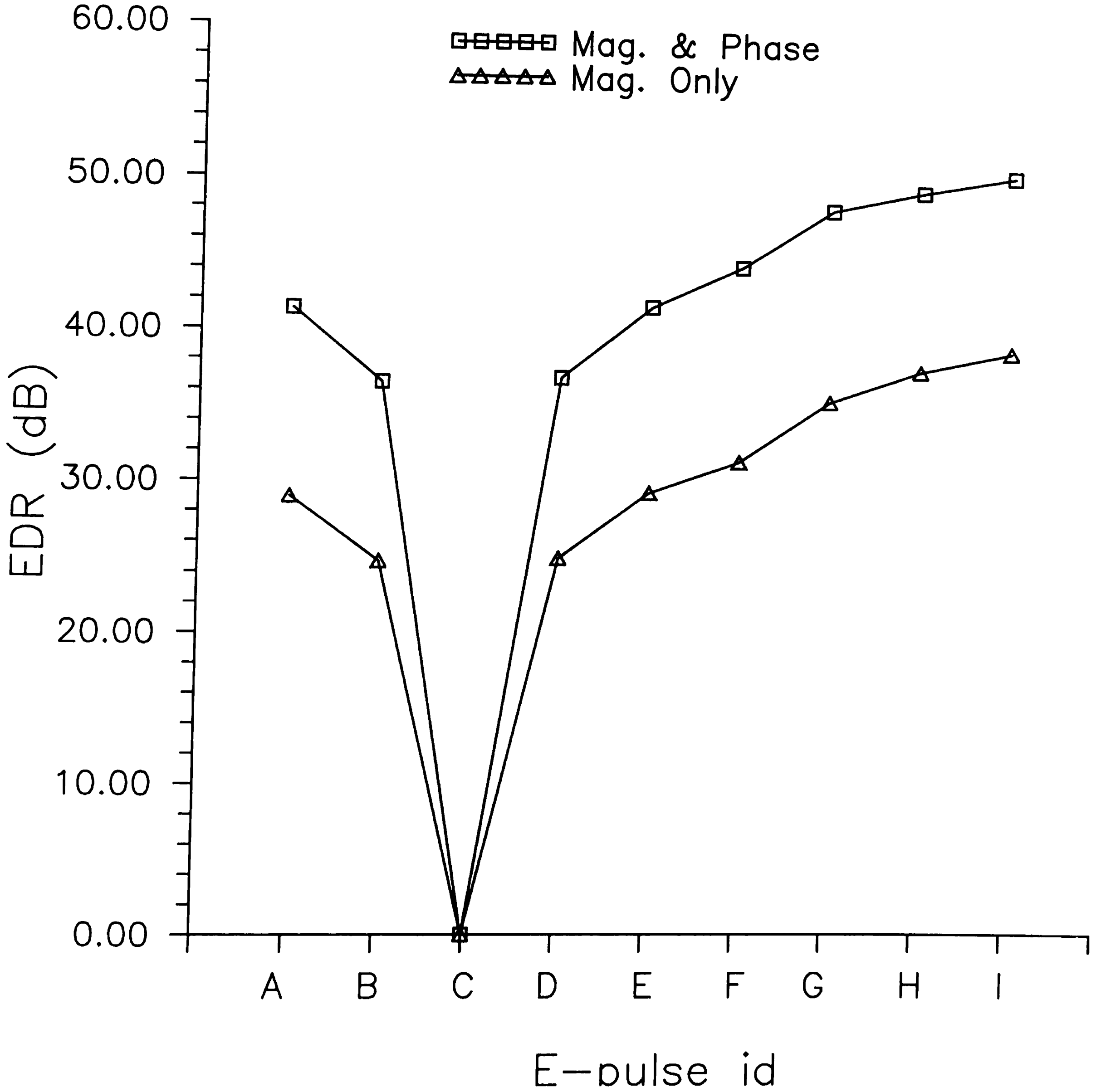

Figure 6.7 EDR values for broadside response of 9 cm wire with l/a = 1000.

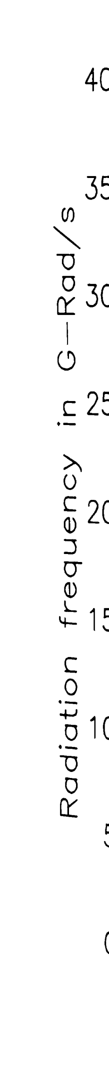

Figure

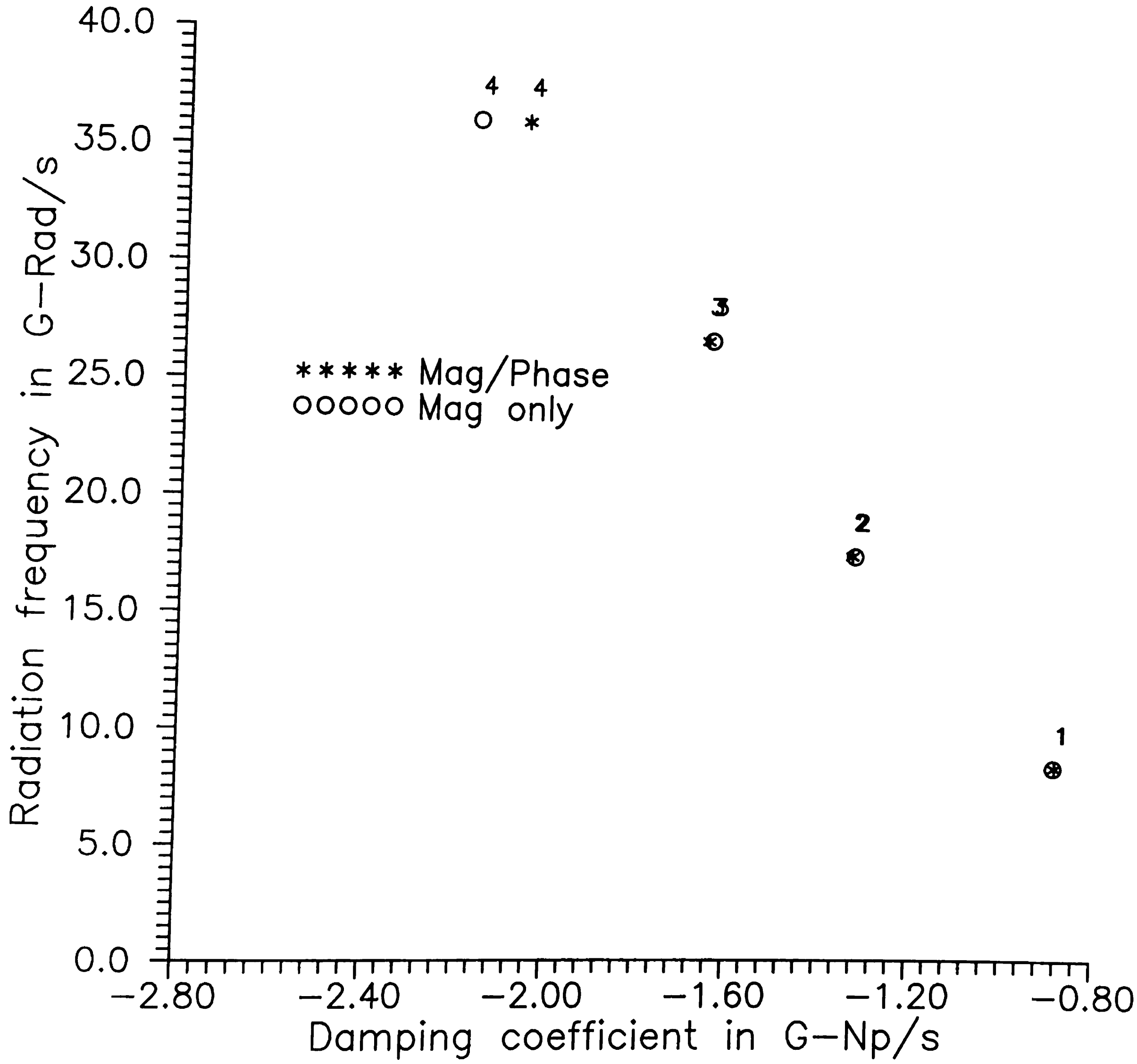

Figure 6.8 Complex frequency locations for 10.0 cm wire scattering.

Figure

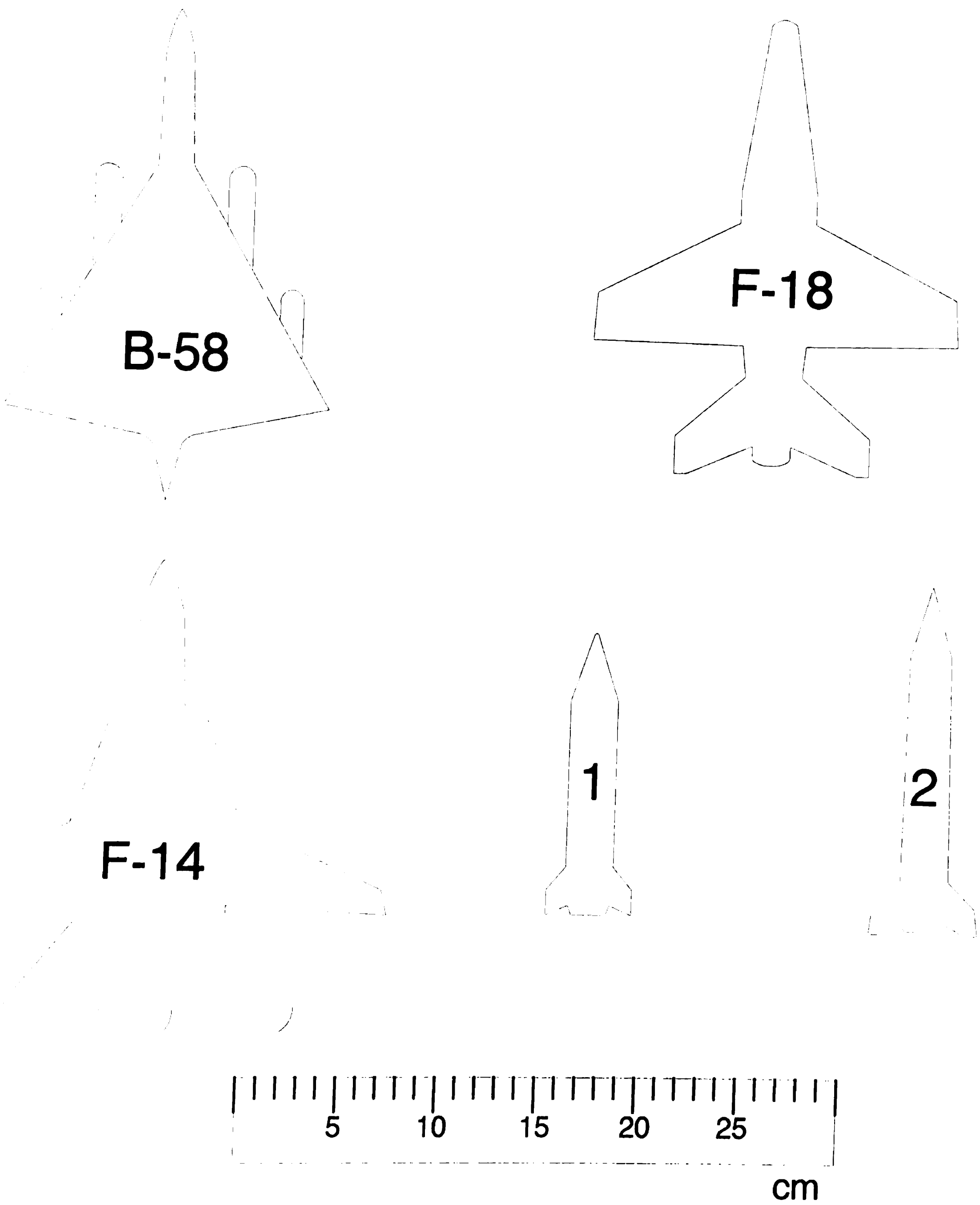

Figure 6.9 Planar view of scaled models used for target measurements.

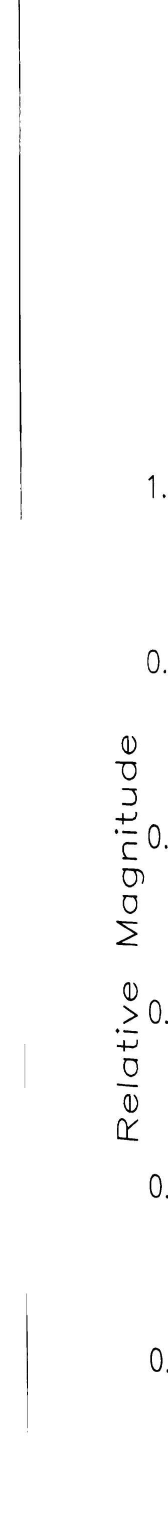

Figure (

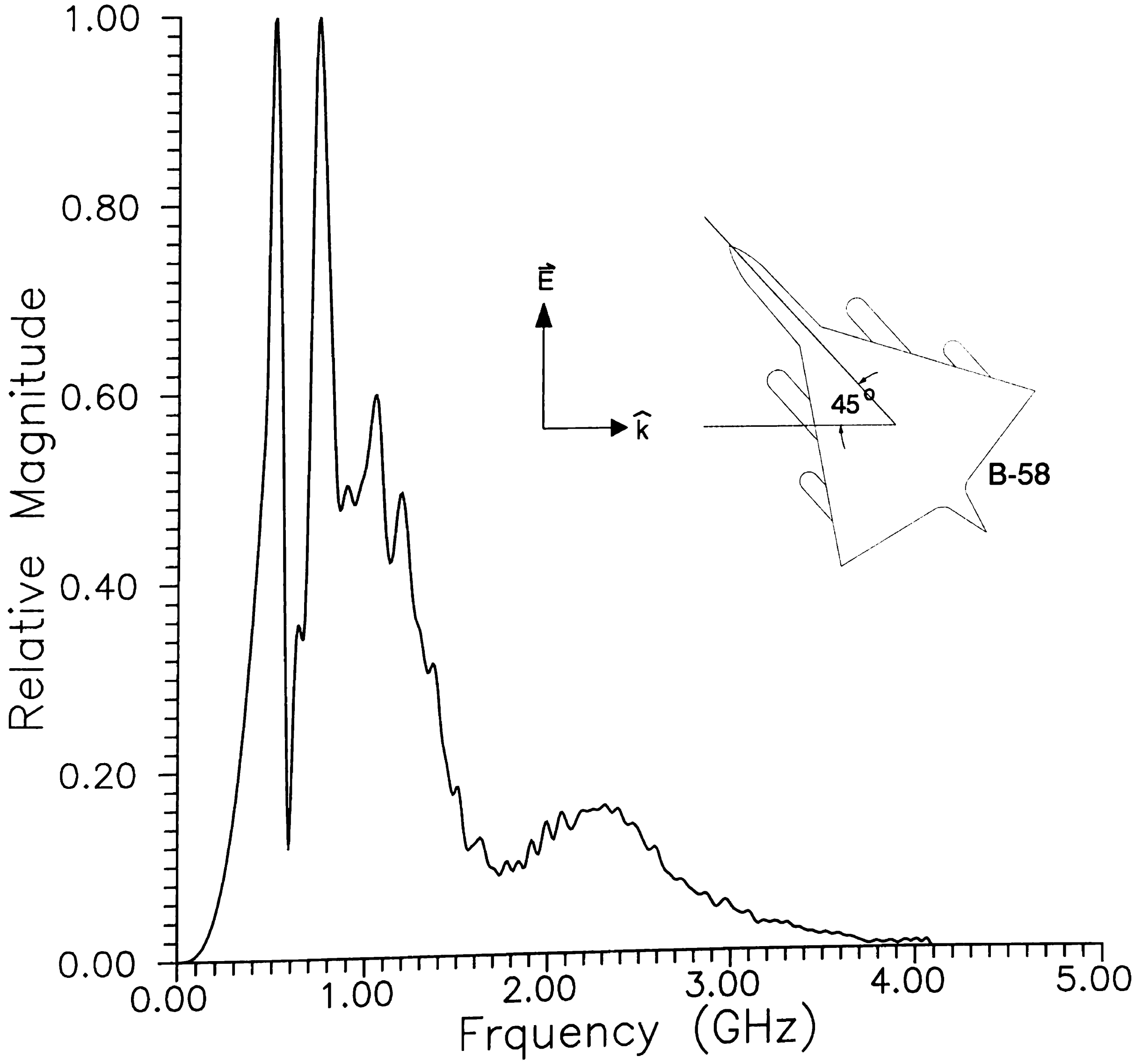

Figure 6.10 Frequency domain scattered-field response of B-58 aircraft model measured at 45 degree incident angle.

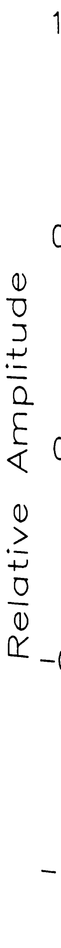

Figure 6

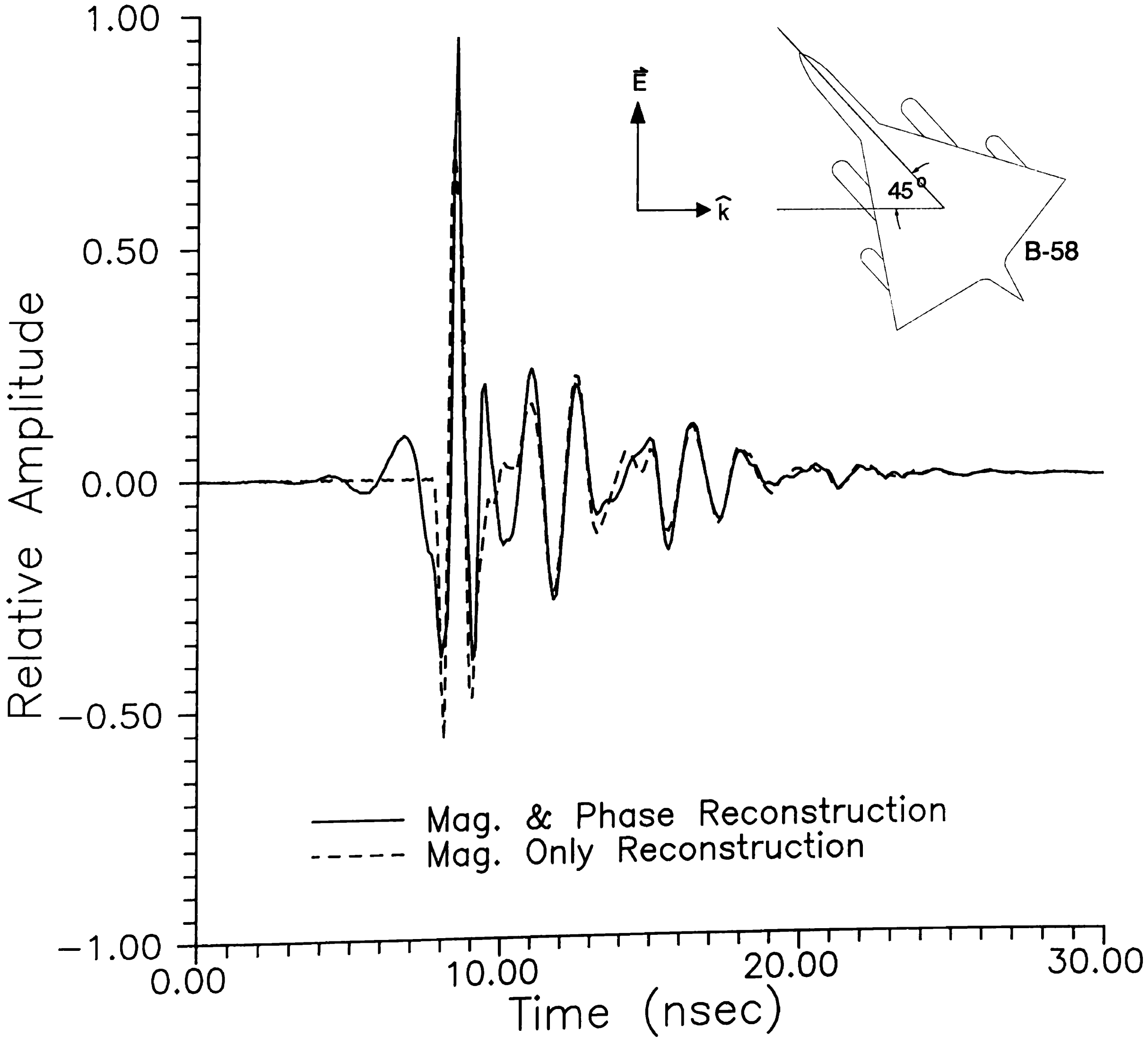

Figure 6.11 Transient response of B-58 aircraft model. Dashed line indicates the minimum-phase reconstructed response.

1.

0.

Relative Magnitude

0.

0.

0.

0.

Figure 6

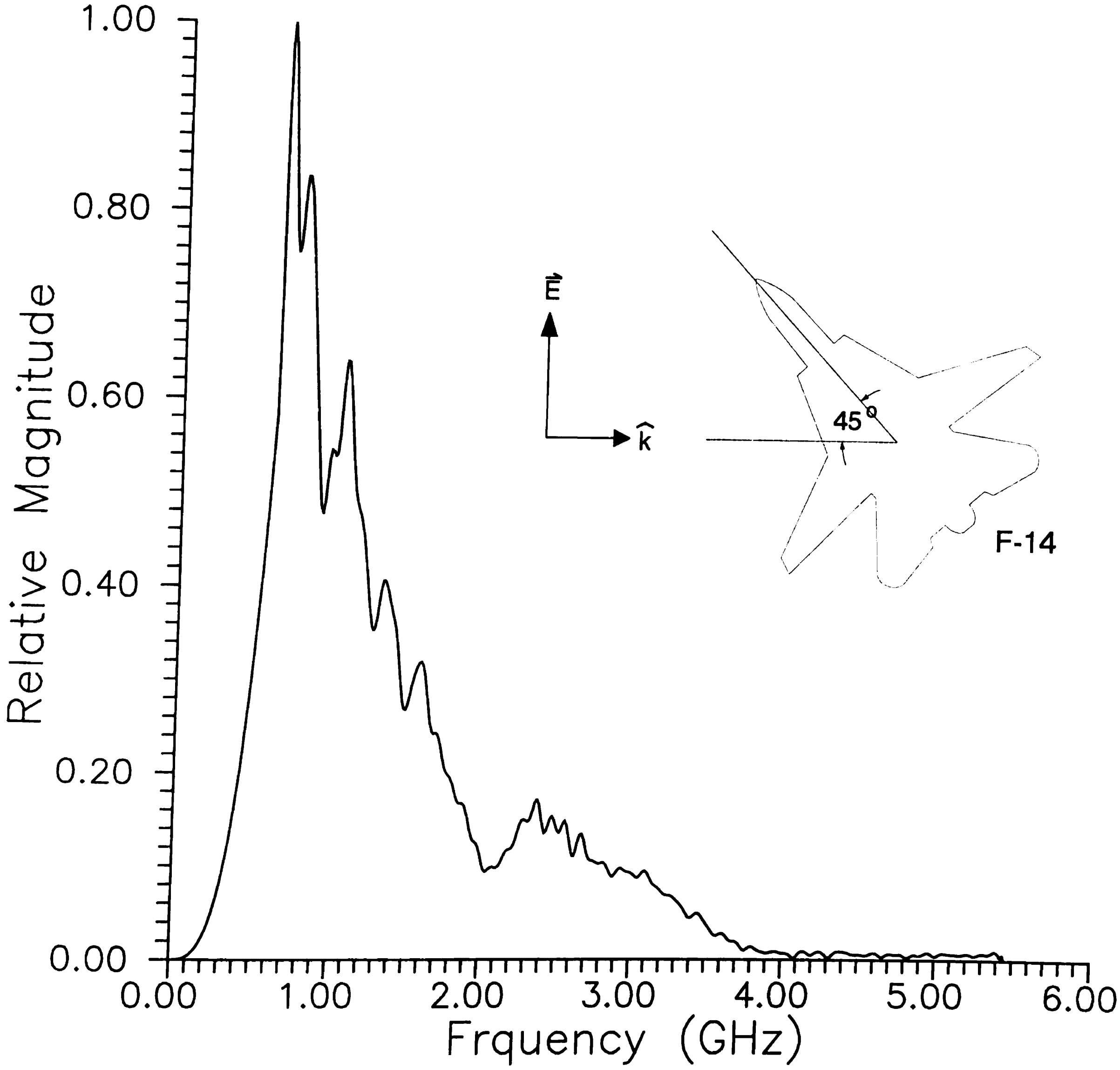

Figure 6.12 Frequency domain scattered-field response of F-14 aircraft model measured at 45 degree incidence.

Figure 6

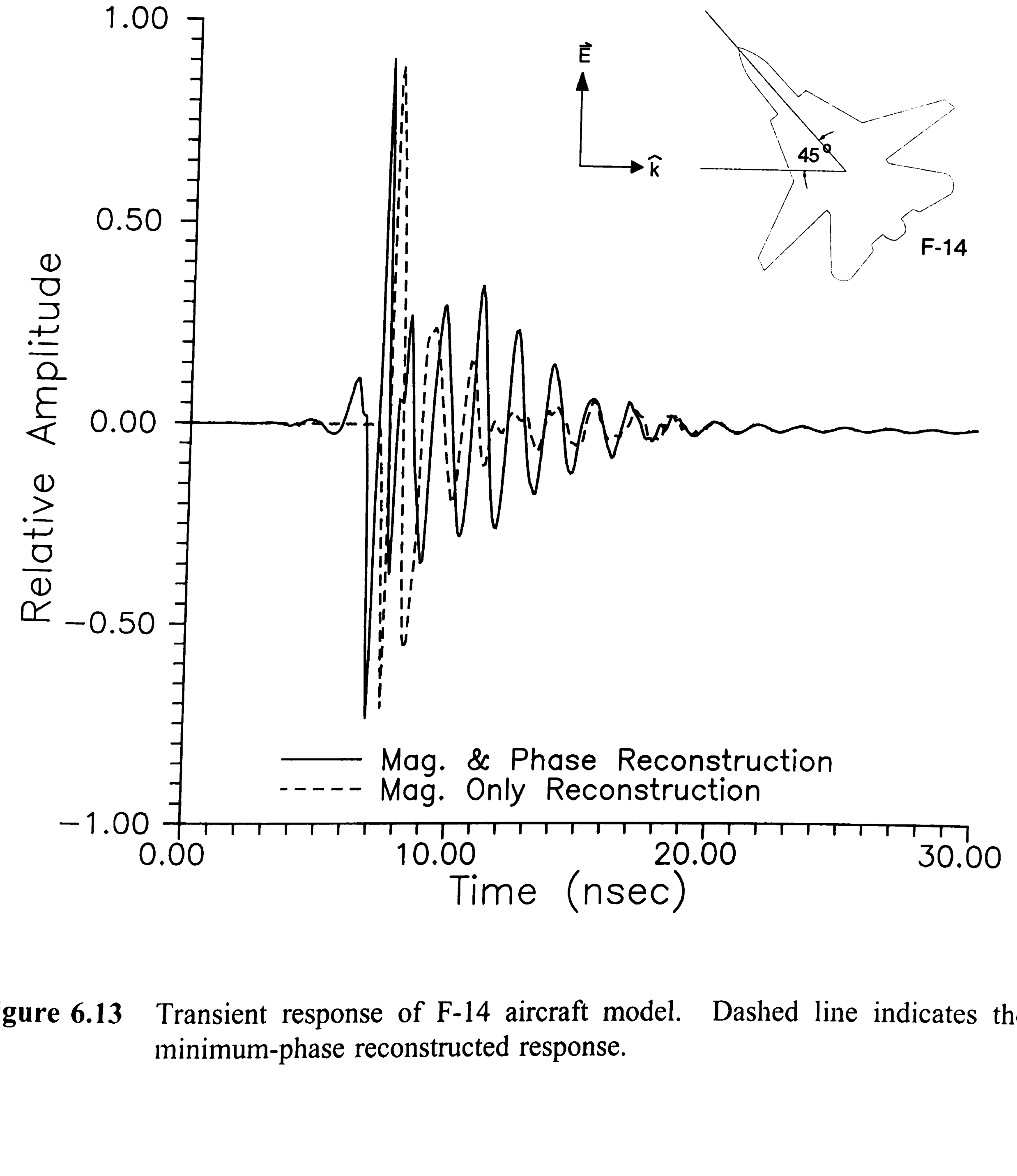

Figure 6.13 Transient response of F-14 aircraft model. Dashed line indicates the minimum-phase reconstructed response.

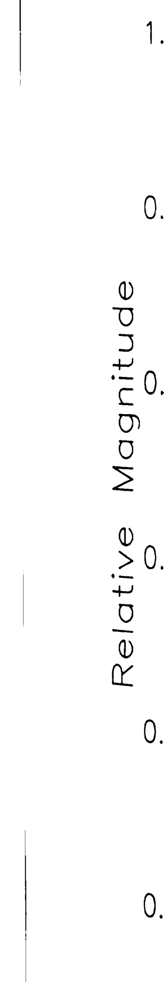

Figure 6

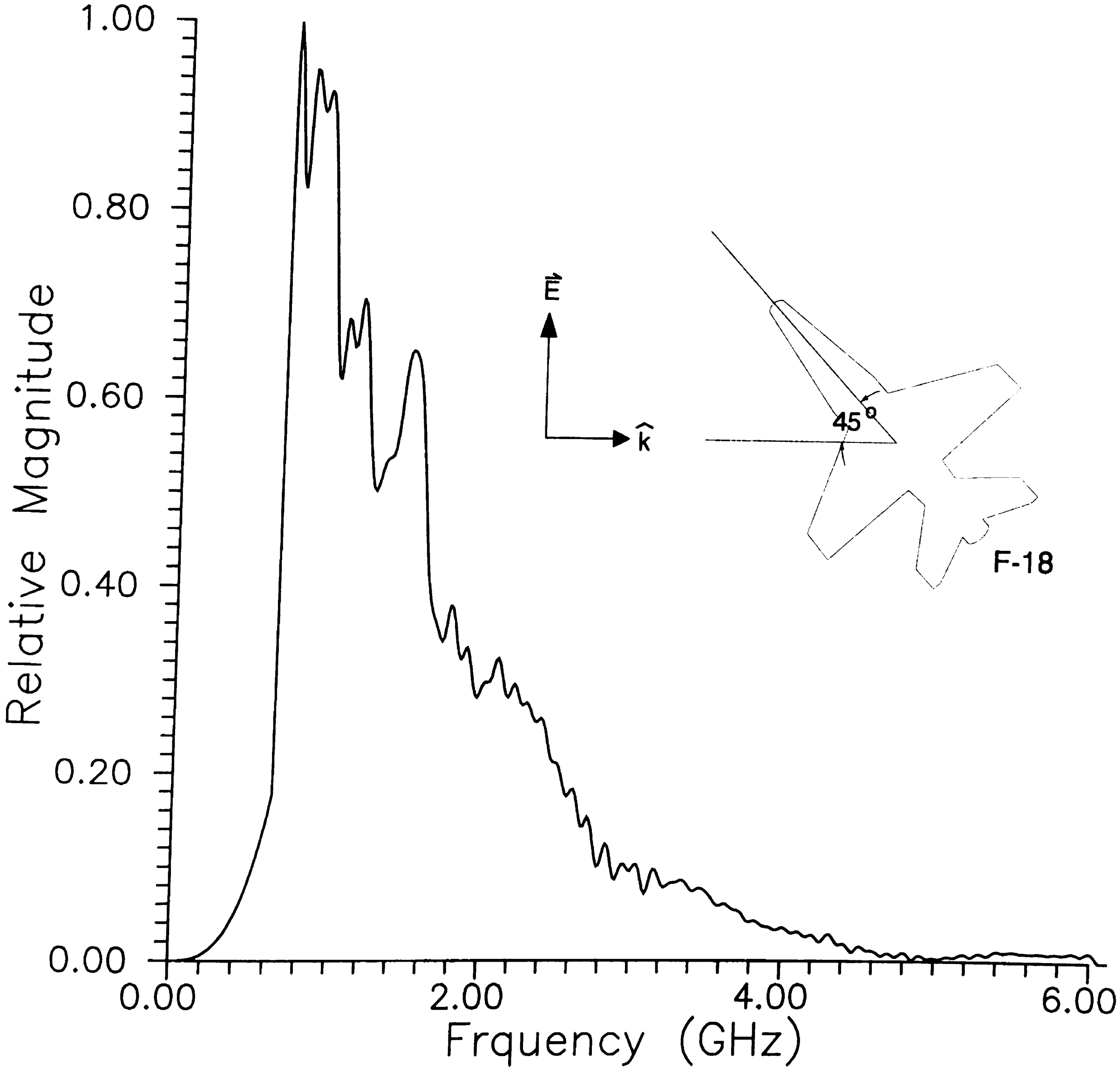

Figure 6.14 Frequency domain scattered-field response of F-18 aircraft model measured at 45 degree incident angle.

Figure 6

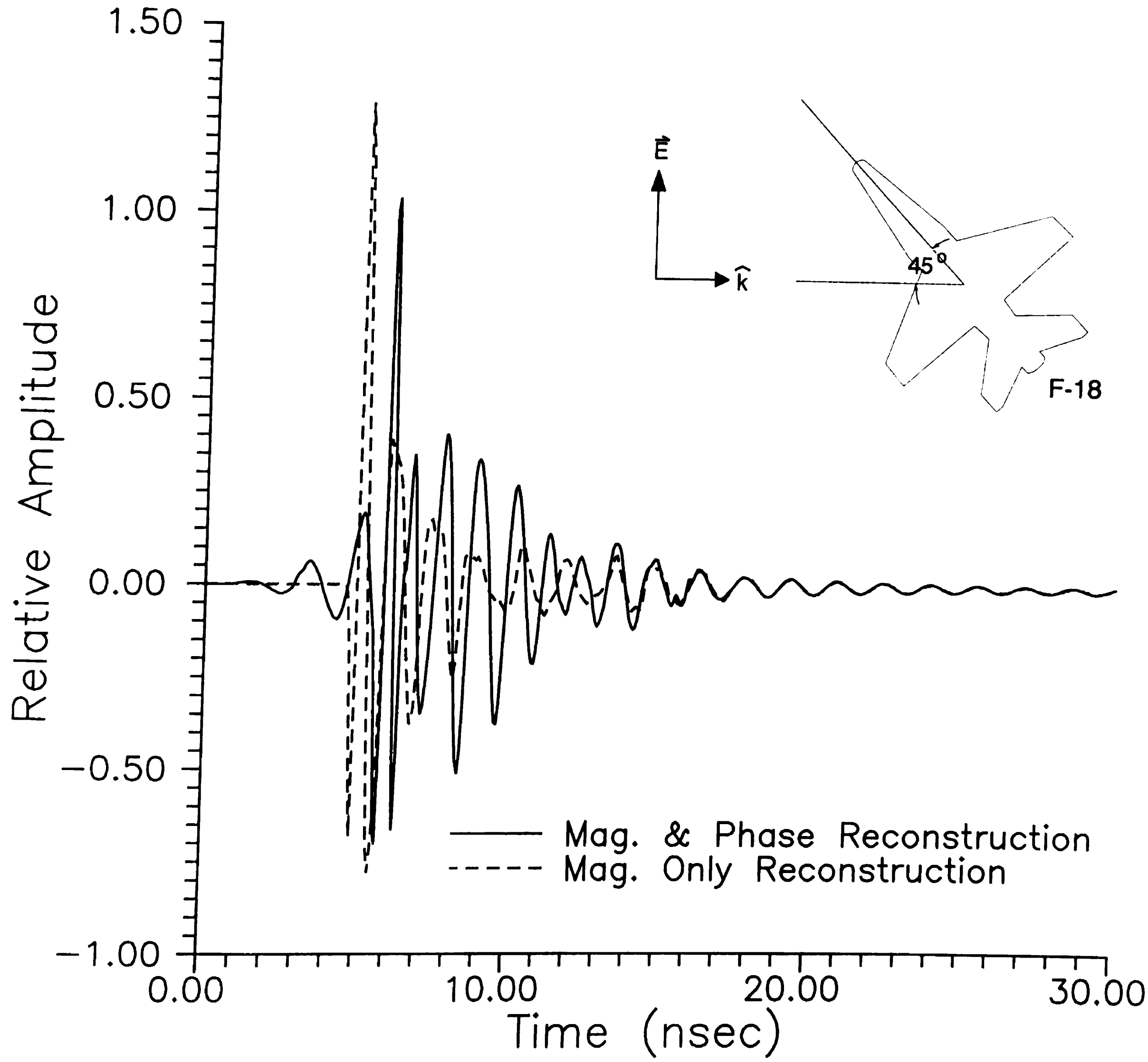

Figure 6.15 Transient response of F-18 aircraft model. Dashed line indicates the minimum phase reconstructed response.

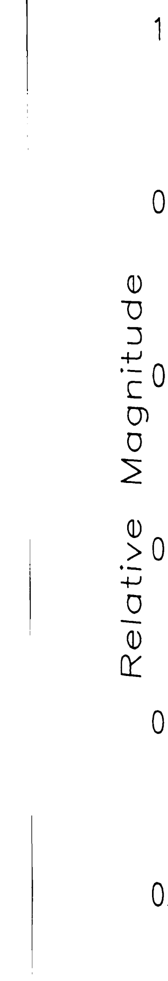

Figure (

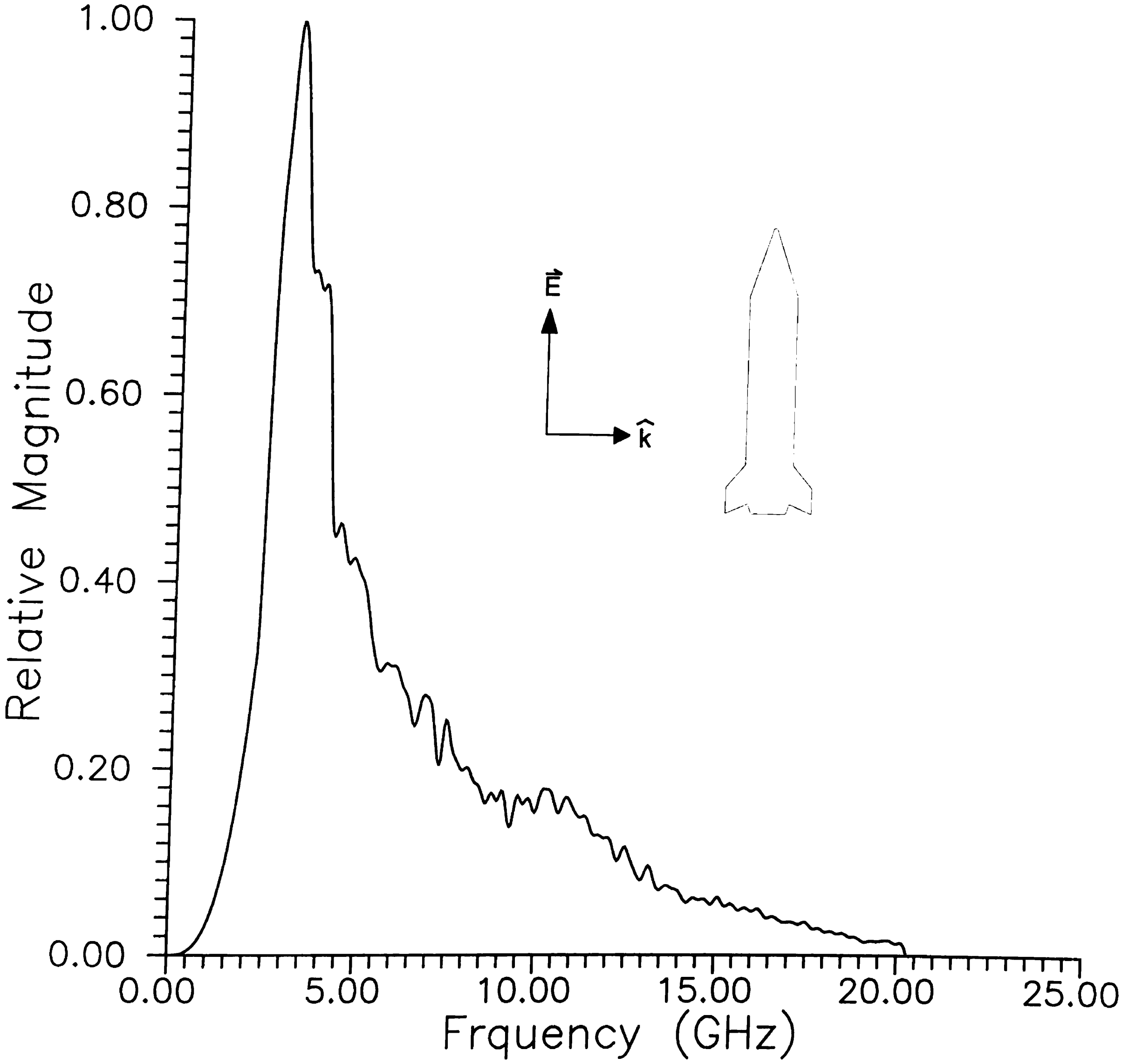

Figure 6.16 Frequency domain scattered-field response of missile #1 for a broadside measurement.

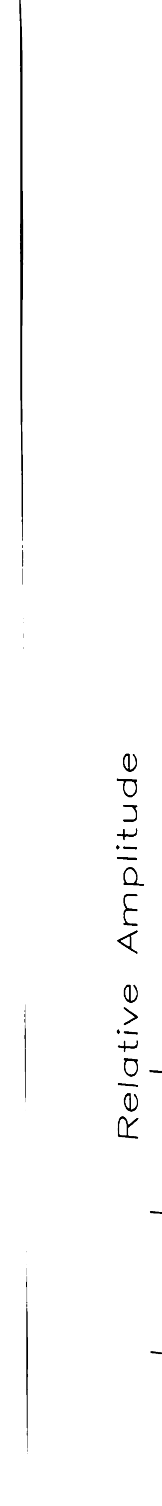

Figure

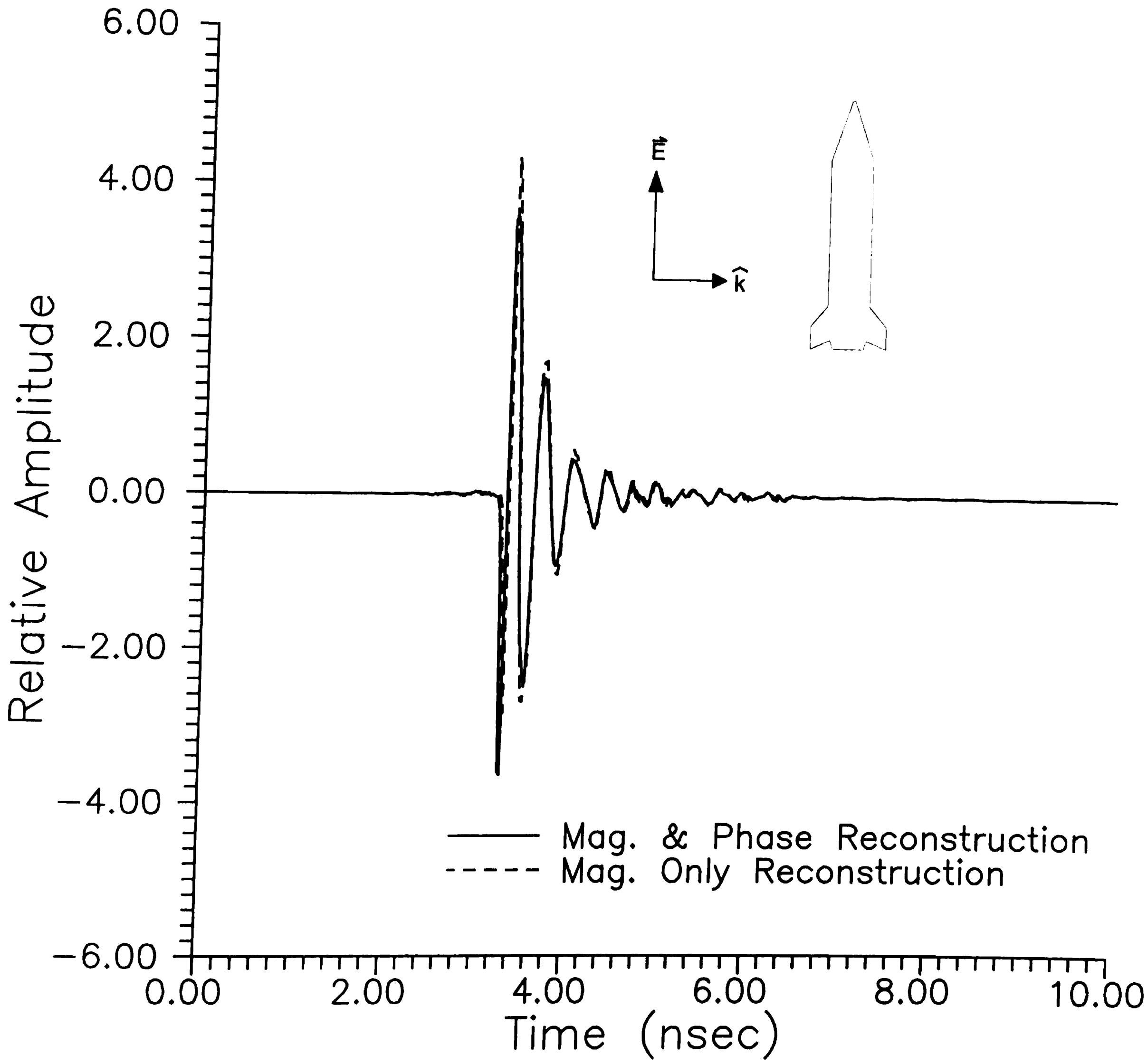

Figure 6.17 Transient response of missile #1. Dashed line indicates the minimum phase reconstructed response.

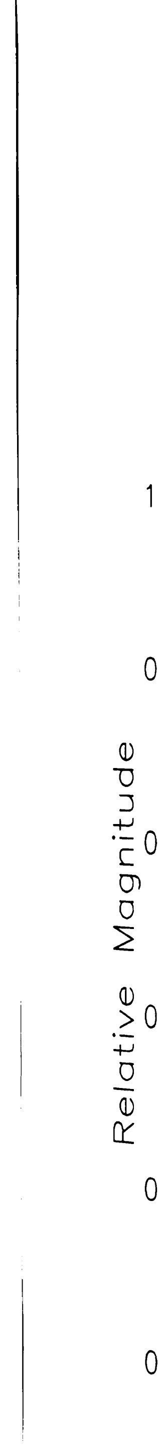

Figure

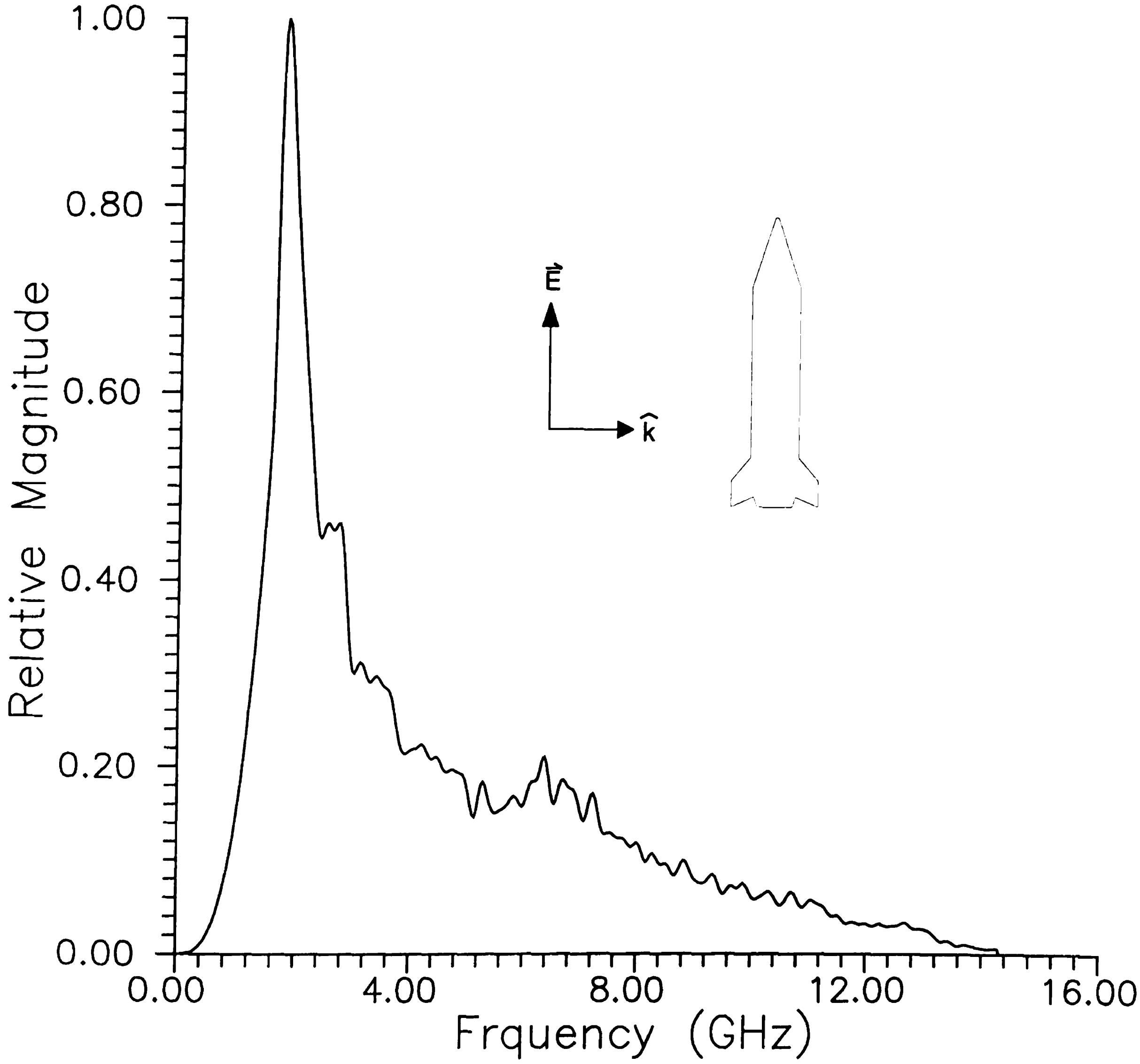

Figure 6.18 Frequency domain scattered-field response of missile #2 for a broadside measurement.

Figure

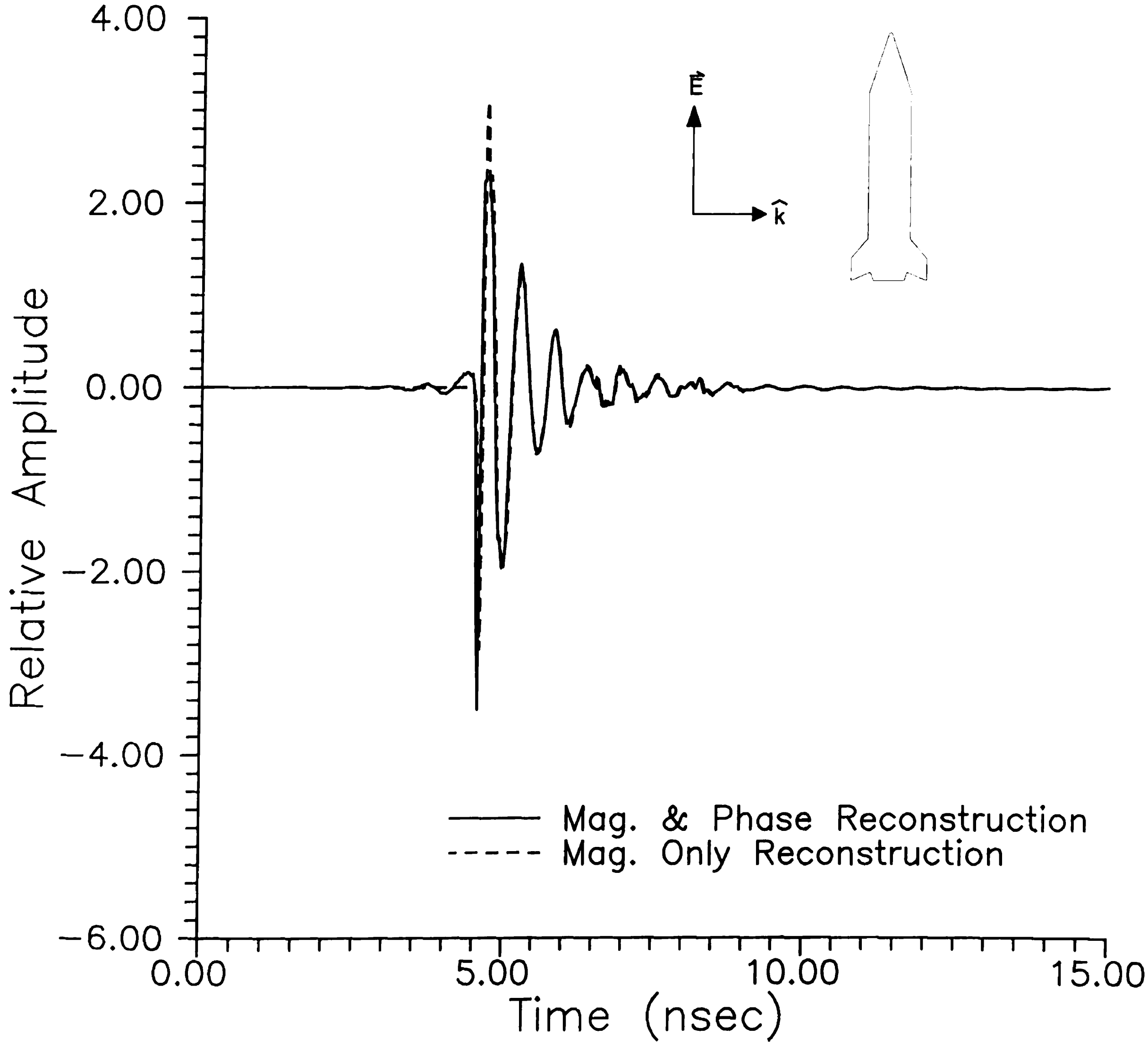

Figure 6.19 Transient response of missile #2. Dashed line indicates the minimum phase reconstructed response.

Table 6

Input

* = indi

Table 6.2 E-pulse discrimination ratio (dB) for each library E-pulse as a function of input waveform response.

Input Response	Target data base response				
	B-58	F-14	F-18	mis1	mis2
B-58	0.0	7.8	13.2	29.2	26.5
F-14	19.0	0.0	3.5	40.4	40.5
F-18	32.7	21.9	0.0	44.7	41.9
mis1	14.6	8.2	6.8	0.0	15.3
mis2	20.7	18.9	11.4	33.2	0.0
B-58*	0.0	7.8	13.0	24.1	25.7
F-14*	16.7	0.0	1.7	31.8	32.1
F-18*	21.6	12.0	0.0	36.2	35.1
mis1*	14.0	7.2	5.9	0.0	14.1
mis2*	17.7	17.3	9.5	31.3	0.0

* = indicates a minimum phase reconstruction

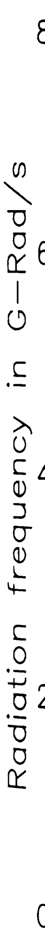

Figure

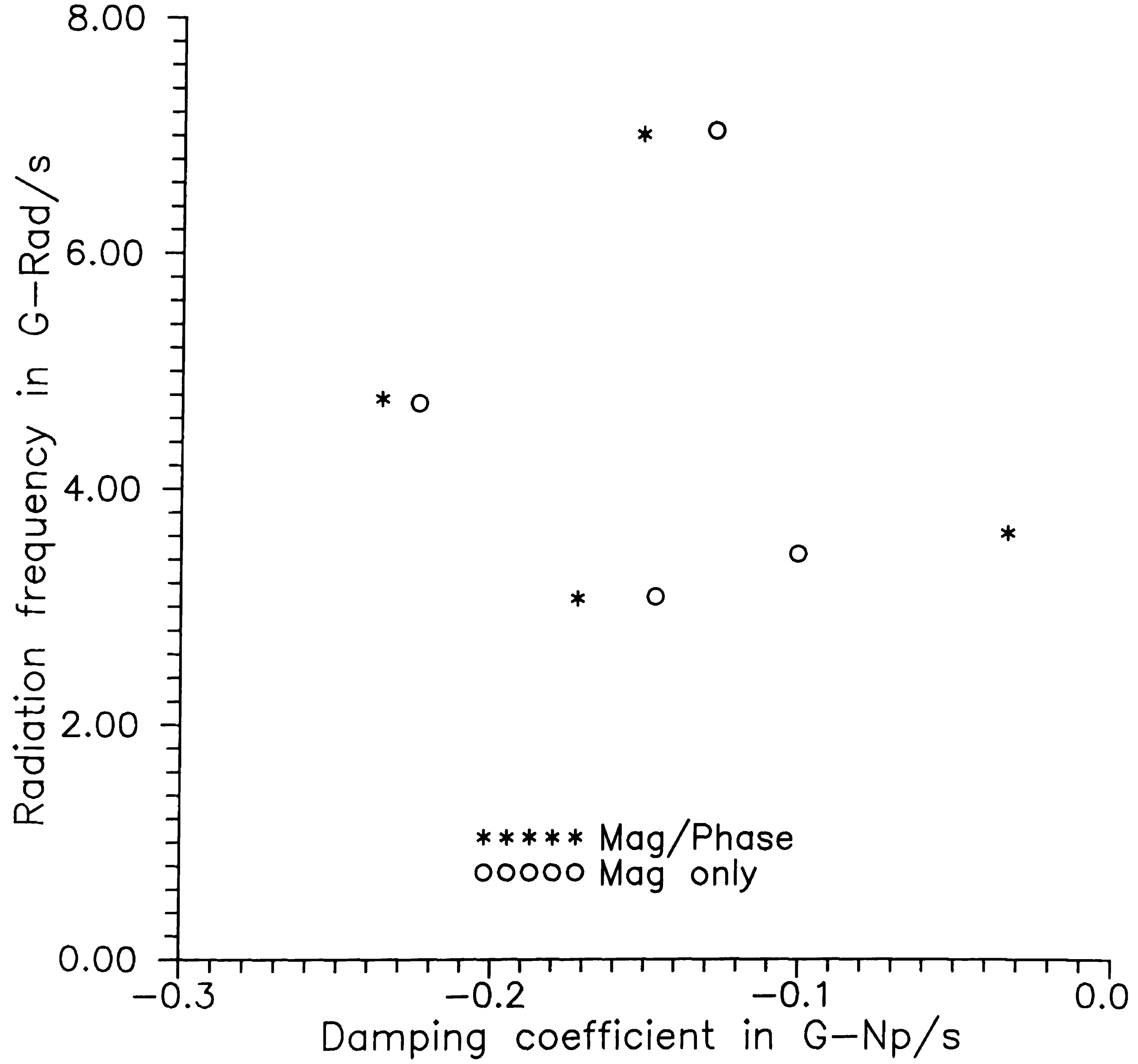

Figure 6.20 Complex frequency locations for late-time response of B-58

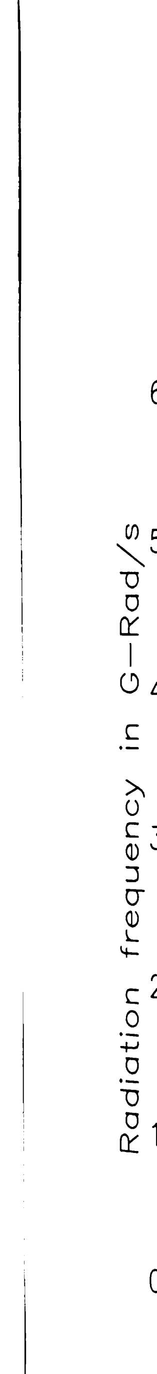

Figure

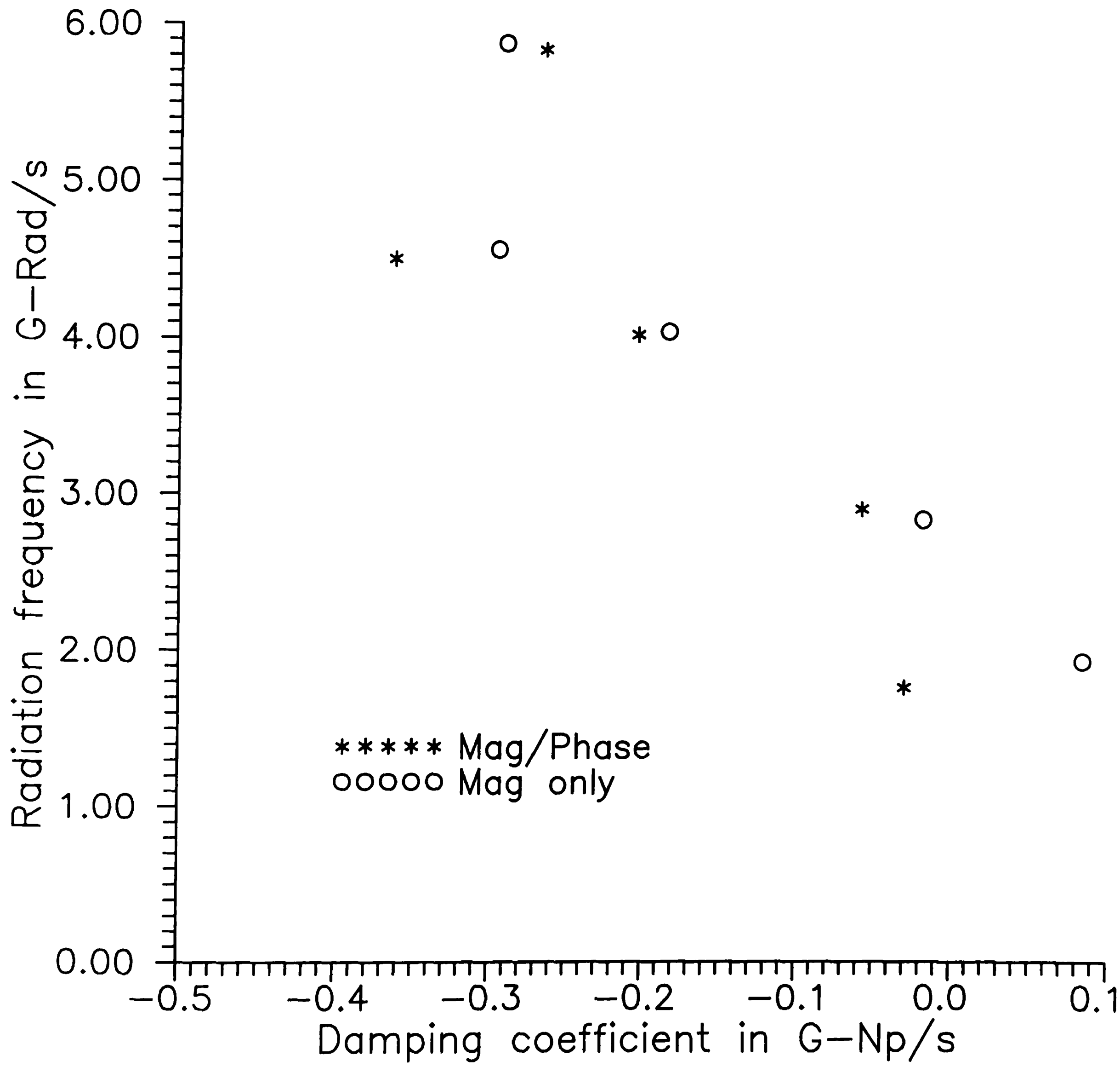

Figure 6.21 Complex frequency locations of late-time response for F-14.

Figure

Radiation frequency in G—Rad/s

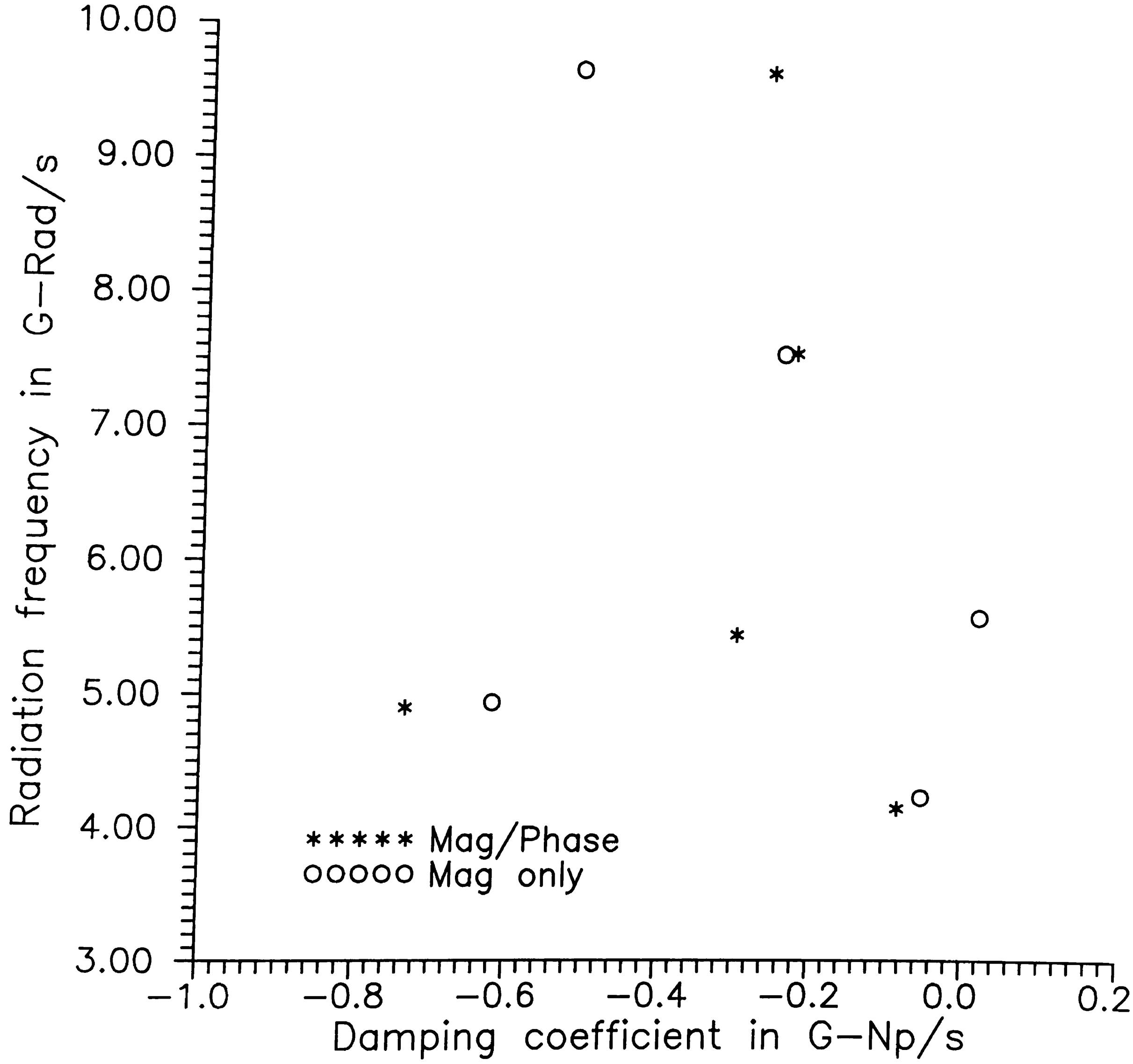

Figure 6.22 Complex frequency location for late-time response using F-18.

Figure

Radiation frequency in G—Rad/s

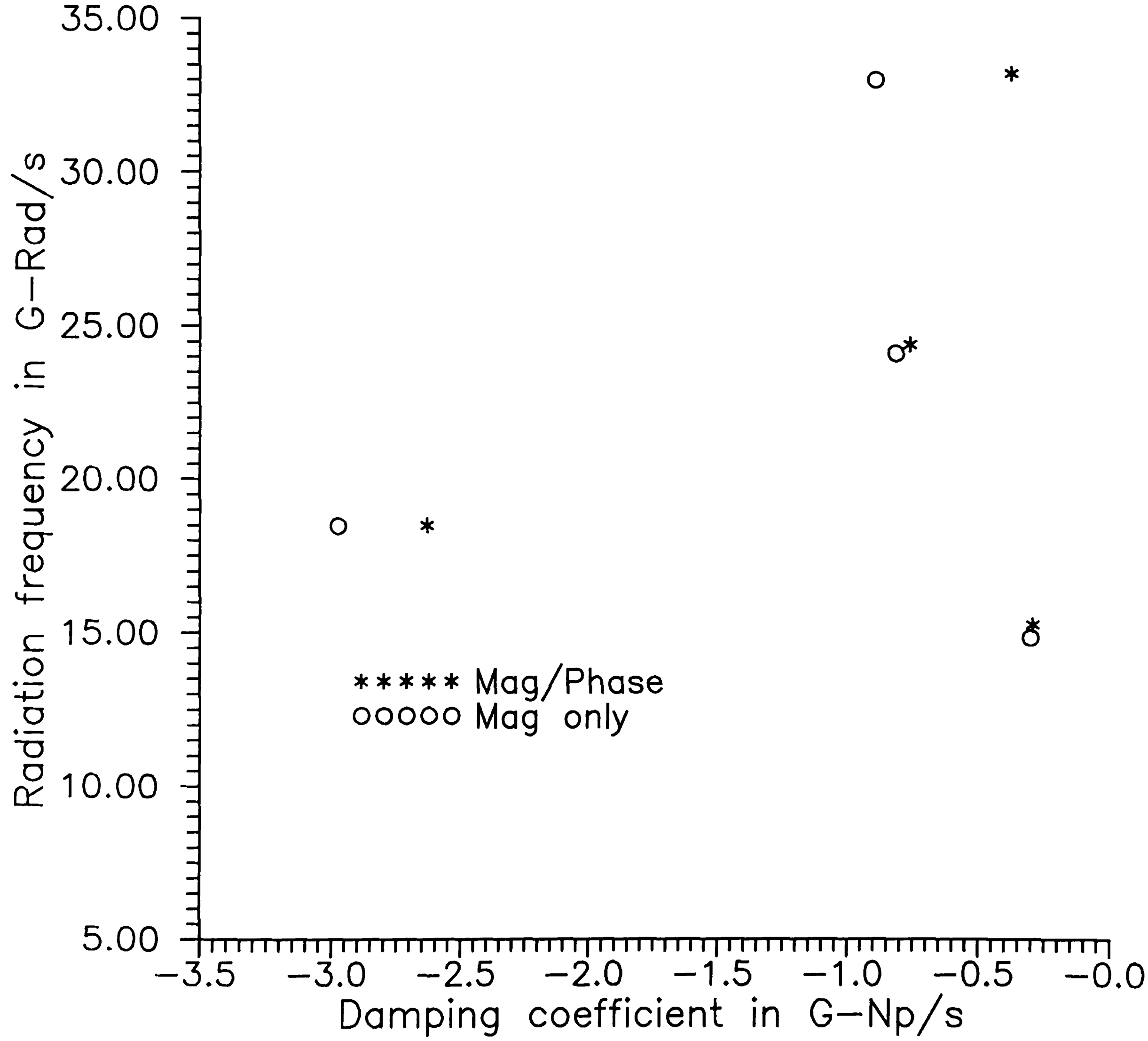

Figure 6.23 Complex frequency for late-time response of missile #1.

Radiation frequency in G—Rad/s

Figure

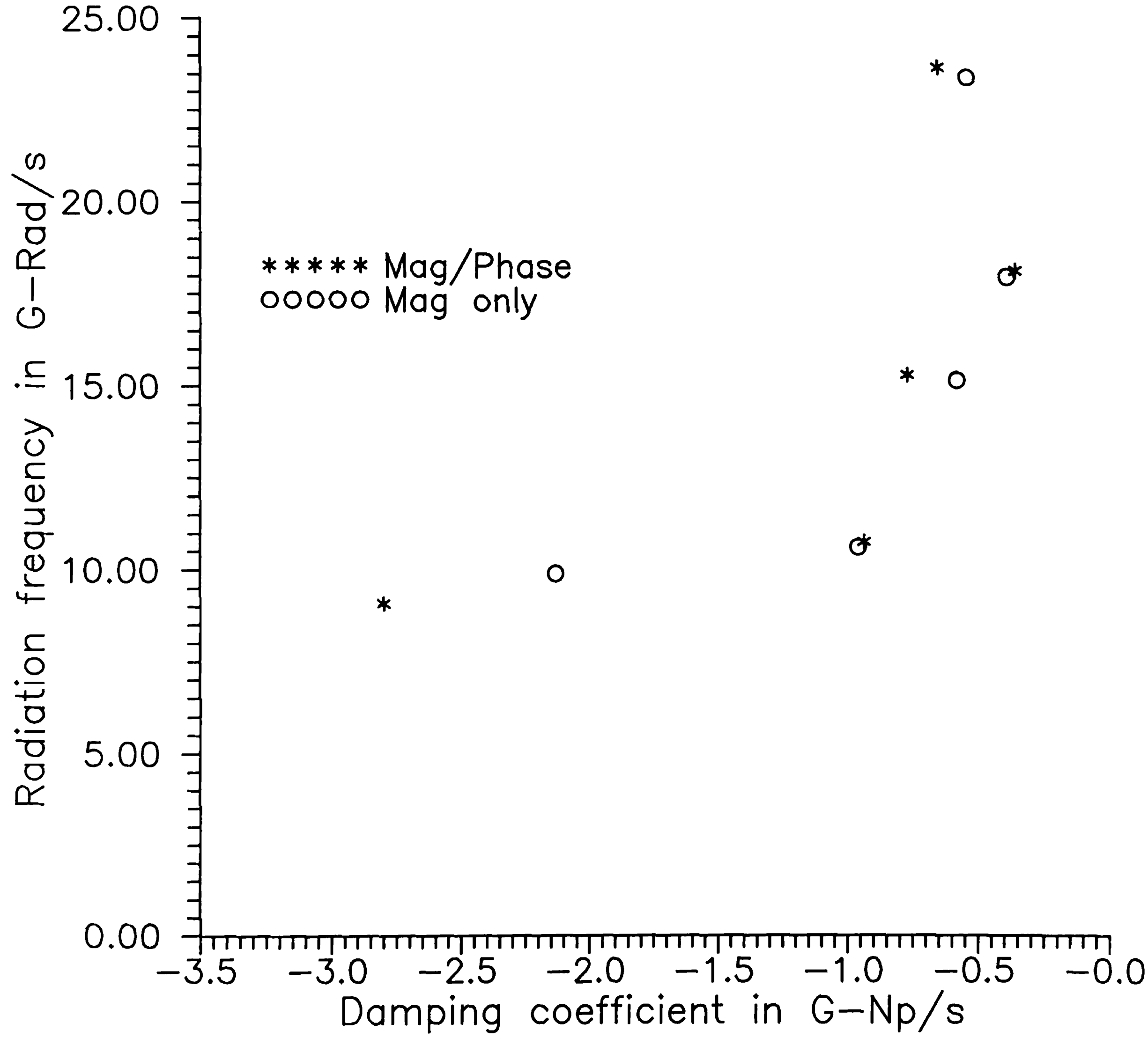

Figure 6.24 Complex frequency locations for late-time response of missile #2.

7.1

wideba

detecti

detecti

skimm

introdu

implen

E-puls

transie

Lab at

to the

target'

detecti

like su

an infi

requiri

2, a ne

Chapter 7

Conclusions

7.1 Summary

This thesis has presented a number of topics related to the application of ultra-wideband (UWB) radar to the detection and discrimination of radar targets. Both the detection and discrimination algorithms are based on the E-pulse method. A new detection technique has been introduced which can be used to detect the presence of sea-skimming missiles in a sea-clutter environment. The new detection technique has been introduced in order to overcome some of the difficulties associated with previous implementations of the E-pulse detection method. A discrimination scheme, based on the E-pulse method, has been developed which uses the late-time portion of a target's transient signal. This scheme differs from previous work done by researchers in the EM Lab at MSU by using the methods of cepstral analysis to construct a close approximation to the late-time portion of a target's transient response using only the modulus of a target's spectral return. One problem often encountered in the theoretical study of detection techniques is the generation of theoretically calculated radar returns for a sea-like surface. Therefore, a new numerical method to compute the scattered return from an infinite, perfectly-conducting, periodic surface has been developed.

Scattering from most types of sea-like surfaces is very computationally expensive, requiring large amounts of computer memory and fast processing capabilities. In Chapter 2, a new numerical-scattering method has been developed and tested. This new method

calcul
of inf
dimen
crests
been
numer
Using
in ord
by rec
approx
genera
The in
use wi

made
can be
compu
the me
is sign
period
in mer
times

calculates the scattered field in the far zone from a perfectly-conducting, periodic surface of infinite extent. The periodic surface, characterized by surface roughness in one dimension, is illuminated by a plane wave whose electric field is parallel to the surface crests (TE excitation). Due to the periodicity of the surface, a periodic current model has been used to develop an electric field integral equation. The integral equation was numerically solved using the method of moments with rectangular-pulse basis functions. Using several test cases, this new algorithm was compared to several established methods in order to validate the new technique. The performance of the new method was tested by recording the combined array fill and solve time as a function of the number of approximation terms used in the algorithm. Finally, the new technique was used to generate the scattered field from a sinusoidal surface having a wavelength of 1 meter. The importance of this new algorithm is that it can be used to generate scattering data for use with different target detection schemes.

Several important conclusions in regard to computational considerations can be made for the new scattering algorithm. First, the scattering from a finite-length surface can be approximated by the periodic current method. The new method decreases the computation tim by a factor of 10 to 20 as compared to the non-periodic solution using the method of moments for the EFIE. Second, the amount of computer memory required is significantly reduced due to the periodic nature of the solution and the use of a single period of the scattering surface. Due to the increase in computational speed and reduction in memory this new method can be applied to a surface having a dimension nearly ten times larger than used in the past. For research in the lab at MSU most surface have been r

1 to 2

freque

surface

possib

about

for a s

be the

is an e

have t

target

using

3 was

finite-

since a

length

rectang

also ap

at the

proble

compu

been restricted to approximately 1000 surface segments and an overall surface length of 1 to 2 meters. For a 2 meter surface length consisting of 10000 surface segments the frequency range must also be restricted to a maximum value of about 15 GHz (if 10 surface segments are used per wavelength). Using the new methodology it becomes possible to compute the scattered field from a surface with an individual wavelength of about 1 to 2 meters in the same frequency range and using about 1000 surface segments for a single period. In this case the computational time and memory requirements will be the same as before, however a much larger surface period can be used.

The detection of a sea-skimming missile in a heavily cluttered sea environment is an extremely important problem for the navy. Previous researchers in the EM Lab have tackled the problem using the E-pulse method. Chapter 3 reviewed the E-pulse target detection scheme. The theory for this method was developed and several test cases using non-baseband scattering data were presented. Another topic reviewed in Chapter 3 was the numerical solution to the electric field integral equation for scattering from a finite-length, perfectly-conducting, 2-dimensional surface. This discussion was included since a large number of scattering calculations were performed in this thesis for finite length surfaces. The computation of the electric field uses the method of moments with rectangular pulse basis functions. The use of the spatial decomposition technique was also applied to the basic scattering algorithm. Although this method was not developed at the EM Lab, the implementation allowed the author to solve larger scale scattering problems. Implementation of the spatial decomposition algorithm did not change the computational speed, but the technique was shown to be very useful for problems requiri

the me

require

genera

eradica

target.

One p

target/

to clu

metho

transm

to ma

numer

These

CRTW

discus

the ge

The fi

model

requiring large amounts of computer memory. Several examples were used to illustrate the method and data was presented showing the amount of memory and computer time required to successfully run different size scattering problems.

In the E-pulse detection technique, a finite duration waveform (E-pulse) is generated which, when convolved with a target/clutter response signal, effectively eradicates the clutter component of the signal to allow for detection of the embedded target. A great amount of care and experience is needed to create an effective E-pulse. One problem often encountered is that the convolution of the E-pulse with the combined target/clutter response will attenuate both the clutter and target, resulting in a poor target to clutter ratio. Chapter 4 discussed a new detection algorithm, based on the E-pulse method, that overcomes this problem. The new algorithm generates a clutter reducing transmit waveform (CRTW) which is designed not to eradicate the clutter altogether but to maximize the target to clutter energy ratio.

The theory for this new CRTW technique was presented in Chapter 4. The numerical calculation of an effective CRTW becomes a global maximization problem. These problems are inherently difficult to solve so a genetic algorithm was applied to the CRTW construction problem. A detailed implementation of the genetic algorithm was discussed including computational considerations. The chief problem facing the use of the genetic algorithm is its inherently slow convergence time.

To test the effectiveness of the CRTW algorithm several examples were presented. The first example used the measured clutter return from a perfectly conducting sea-surface model in conjunction with the measured scattered return from a scaled missile model.

A CR

This f

for a s

realist

the sc

CRTV

in whi

techni

the CI

and ar

schem

the CI

variati

chang

CRTV

missil

create

CRTW

and di

target

A CRTW was constructed and applied to a combined sea-surface/target-return signal. This first example was designed to show the effectiveness of this new detection technique for a static situation. A second example considered an evolving sea surface using a more realistic sea-surface model. A time simulation of an evolving sea surface was created and the scattered fields were numerically calculated. Using a measured missile model, a CRTW was calculated for the initial sea-surface state. A simulation was then performed in which a missile traveling over the evolving sea surface was detected using the CRTW technique. Results of that simulation showed the effects of an evolving sea surface on the CRTW technique and the need to update the CRTW.

A CRTW is created from the measured return of a clutter producer (sea surface) and an anticipated target. The effect of return from different target types on the detection scheme was also studied in Chapter 4. Early detection of an antiship missile depends on the CRTW method being tolerant to variations in a missile's scattered return. These variations can be due to roll-stabilized flight-control systems, missile configuration changes, or variation in the incident and scattering angles. To test the tolerance of the CRTW method to different target geometries, the scattered returns from several different missile models were measured in the anechoic chamber at the EM Lab. A CRTW was created from the scattered return of a sea surface and one of the measured targets. The CRTW detection algorithm was then applied to the combined return of the sea surface and different targets. In every test the CRTW detection algorithm was able to detect each target with only slight variations in the calculated convolution energy ratio.

The detection variable known as the convolution energy ratio paramaterizes the effect

a targ

backg

prope

Chapt

threat

the pr

the Cl

value

scatte

the se

return

antici

a simp

the tar

see th

surfac

sinuso

surfac

measu

differe

effectiveness of the CRTW detection algorithm. A large value indicates the presence of a target. For no target this variable has a value of 0 dB (for a non-evolving clutter background). The calculation of the convolution energy depends on the selection of a proper energy window size. The topic of energy window size was also discussed in Chapter 4. The use of a narrow window allows for finer range resolution of the target threat. However, a narrow window can lead to a higher probability of false detection in the presence of an evolving sea surface. Nonetheless, a narrow window can be used if the CRTW is updated at a high rate. A wider energy window will broaden and lower the value for the convolution energy ratio, including the maximal baseline value from the scattering surface.

An important topic for sea-surface scattering is the multipath interaction between the sea surface and the target. The creation of the CRTW involves using the sea-clutter return having no target contribution and a calculated or measured return from an anticipated target. In the detection process, the target/clutter return is not derived from a simple combination of the individual returns. There can be significant coupling between the target and surface, including multipath effects, which effect the measured return. To see the effect on the detection algorithm, the scattered return from several different sea-surface models was measured. These models included the Stoke's surface and the double sinusoid. The response from a small missile model was also measured. With the sea-surface and missile return a CRTW was created. Next, the missile and target were measured together. Several measurements were performed by placing the missile at different locations with respect to the wave crests and at different heights above the sea-surfac

and th

algori

Howe

wavef

able to

known

been

algorit

were

proces

return

techni

at this

amoun

period

this u

detecti

metho

CRTW

surface models. Using these measurements, the CRTW detection algorithm was applied and the convolution energy ratio was calculated. In every test, the CRTW detection algorithm was very effective in finding a target that was located over a wave trough. However, the effect of the interaction was clearly evident in the convolution energy waveforms. For a target located close to a wave crest the detection algorithm was not able to find the target.

A final topic covered in Chapter 4 was the use of a clutter suppression technique known as coherent processing clutter reduction. This technique, discussed by Iverson, has been used for detecting moving targets on a static clutter background. The basic algorithm was modified for a non-stationary clutter background. Several simulated tests were performed for a missile flying over an evolving sea surface. The coherent processing clutter reduction technique was shown to be very effective if the sea-clutter return could be measured at a high rate. The most appealing characteristic of this technique is the simple nature of the algorithm, making it ideal for real-time applications.

Several important conclusions regarding the new detection algorithm can be made at this point. First, the new CRTW algorithm is extremely robust but suffers from the amount of computer time required to construct the CRTW. Second, the CRTW must be periodically updated for a changing sea surface. Using the Kinsman sea-surface model this update rate must occur approximately once a second. Third, the new CRTW detection scheme is quite tolerant to different target types. This makes the CRTW method very good for target detection but a poor candidate for target discrimination. The CRTW method is also very effective in detecting targets even in the presence of the multip

well f

in tim

this m

algori

freque

or me

to the

metho

the m

necess

of mi

were

respor

time r

late-ti

early

cepstr

respon

of a m

multipath phenomena. Finally, the modified coherent processing technique works quite well for target detection in the presence of a changing background clutter. At this point in time the author has some reservations about the robustness of this method. However, this method can easily be used in a real-time application due to the simplicity of the algorithm.

Construction of the radar transient response can be done using the method of frequency domain synthesis. In this method, the frequency domain response is calculated or measured over some bandwidth. Next, an inverse discrete Fourier transform is applied to the frequency-domain data to generate the transient response. In Chapter 5, the methods of cepstral analysis were used to reconstruct the transient response using only the modulus of the spectral response. The purpose of Chapter 5 was to provide the necessary background for the target discrimination analysis in Chapter 6.

A discussion of cepstral analysis theory was presented in Chapter 5. The topics of minimum-phase conditions and energy relations were discussed, and several examples were presented illustrating the use of minimum-phase reconstruction. The transient response from an UWB radar can be characterized by an early-time response and a late-time response. A discussion of the minimum-phase reconstruction for the early-time and late-time responses was presented. Also, some time was devoted to the separation of the early and late-time transient response using cepstral analysis. For most signals the cepstral reconstruction of the early-time response is unpredictable. The late-time response, although not minimum phase, has an energy-concentration nature similar to that of a minimum-phase signal. Several examples were presented showing the reconstruction of the

the n

uniqu

scatte

late-ti

devel

perfor

the di

and e

worke

be ca

difficu

techni

the co

low.

7.2

This s

presen

of the late-time waveform using only the magnitude of its frequency spectrum. One of the most important properties for target detection using the E-pulse method is the uniqueness of a target's complex frequencies in the late-time portion of the transient scattered signal. Several examples were used to show that a cepstral reconstruction of the late-time response contains a good match to the actual complex frequencies.

A target identification scheme using the E-pulse method and cepstral analysis was developed in Chapter 6. Several numerical examples were presented showing the performance of cepstral analysis in regard to target discrimination. The performance of the discrimination scheme was evaluated using both numerically derived scattering data and experimentally measured results from practical target models. Cepstral analysis worked very well for the numerically generated data since a very accurate E-pulse could be calculated. Construction of a good E-pulse from measured data is a much more difficult task. For the measured data presented in Chapter 6 the cepstral analysis technique worked quite well. In every case the detection algorithm was able to identify the correct target, although in several cases the E-pulse discrimination ratios were quite low.

7.2 Topics For Further Study

There are several topics in this thesis which could be the basis for future work. This section will address several of them.

The new CRTW technique was presented in Chapter 4. Several examples were presented showing the effectiveness of this new method. The use of data from an actual

UWB

algori

certai

data c

comp

few s

comp

realiz

proble

One p

over a

and w

valuab

signals

area.

directl

and ex

resona

recons

UWB radar would be extremely useful for additional testing of the new detection algorithm. Not only would this data present the effects of noise and multipath, but it certainly would provide information about how often to update the CRTW. Also, this data could be used to thoroughly test the coherent processing detection algorithm.

One of the real problems with the CRTW detection algorithm is the amount of computer time required to generate a CRTW. Since the CRTW must be updated every few seconds, the computation of the CRTW must be quite fast. Therefore, a computationally fast algorithm must be designed if this detection technique is to be realized. This problem may be very difficult due to the global minimization nature of the problem.

The effect of multipath and sea-surface/target interaction is a very interesting topic. One possible area of work is designing a scattering algorithm for a 3-dimensional target over a 2-dimensional sea-surface waveform. Once again, this could be a difficult problem and would be computationally slow. However, the generated results will be quite valuable for use with different target-detection algorithms.

Two chapters were devoted to the application of cepstral analysis to UWB radar signals and target identification. There are several possibilities for future work in this area. First, a target identification algorithm could possibly be designed by working directly in the cepstral domain. This project would require a great deal of knowledge and experience with cepstral analysis. Second, more research is needed in regards to the resonant frequencies extracted from the late-time portion of the minimum-phase reconstructed signal. Several examples in this thesis showed that the minimum-phase extrac

Howe

greate

filters

again.

extracted frequencies match the magnitude/phase reconstructed frequencies quite well. However, there is a significant amount of material here if the problem is analyzed in greater detail. A final area of research would be in the design and testing of various filters to separate the early and late-time signal components using cepstral analysis. Once again, this could possibly be done in the cepstral domain.

APPENDIX

A.1

signa

use o

may

Henc

analy

time

frequ

meas

extrac

signal

recon

magn

based

becon

to acc

cepstr

Appendix A

Scattering Measurements

A.1 Introduction

A target identification scheme is based upon a set of target characteristics or signatures. If these signatures have been derived from scattering measurements, then the use of an accurate measurement system is essential. The use of noisy or inaccurate data may be detrimental to the identification process, even making the scheme nearly useless. Hence, it becomes vital to a detection scheme using the E-pulse method or cepstral analysis to collect the best possible data.

An E-pulse discrimination scheme requires an accurate measurement of the late-time portion of the transient response from a scattering target. Extracted resonant frequencies are derived from the late-time portion of the signal. Hence, poor measurements will lead to an inaccurate characterization of the scattering target. The extracted modes become very difficult to calculate from a noisy or inaccurate late-time signal and may lead to wrong or non-physical values for the resonant modes. The reconstruction of the late-time portion of a target response using only the spectral magnitude is also highly susceptible to inaccurate measurements. A discrimination system based upon the extraction of resonant frequencies from the reconstructed waveform will become useless if poor measurements are made. Therefore, it becomes very important to accurately measure complicated scattering structures in order to verify the utility of cepstral analysis in conjunction with an E-pulse detection scheme.

perfo

discu

at M

order

of w

essen

A.2

durat

wide

of a

time-

then

select

pulse

scatte

of cl

the s

meas

calcu

This appendix will describe the frequency-domain synthesis approach [43],[44] for performing transient measurements. The frequency-domain synthesis method will be discussed as well as the principal components of the measurement system in the EM lab at MSU. A discussion of system deconvolution and calibration will be presented. In order to illustrate some of the concepts an example will be presented. Finally, the topic of windowing or weighting functions will be examined. Discussion of this topic is essential since the concept of frequency windowing is used throughout this thesis.

A.2 Frequency-Domain Synthesis and Scattering Measurements in the EM lab

In a frequency-domain synthesis system, the scattered response due to a short-duration time pulse is synthesized using a frequency-domain measurement made over a wide bandwidth. The basic idea behind this method is to measure the scattering response of a stationary target at a large number of frequencies. Once this has been done, the time-domain response is formed by applying a weighting function to the measure data and then transforming to the time domain by using an IFFT. The measured bandwidth and selected weighting function determine the duration and shape of the equivalent input pulse. Unfortunately, the measured response in a real system does not consist of a scattered return from just the target under investigation. The measured data also consists of clutter, noise, and effects due to the system response. To eliminate any effect due to the system response, a measurement is made of a known scatterer (calibrator). The measured scattering field from the calibrator can then be compared to a theoretically calculated response of the calibrator to determine the system response. From this infor

Figur

12' x

pyrar

place

cham

frequ

meas

Analy

"low-

signa

a 10c

Preci

placi

GHz)

Packa

analy

the

config

port 2

openi

information the system response can be eliminated from the desired target measurement.

The frequency-domain synthesis system used at the EM lab is shown in Figure A.1. This system consists of an anechoic chamber having floor dimensions of 12' x 24' and a ceiling height of 12'. The surfaces of the chamber are covered with pyramidal absorbers having a pyramid depth of 6 inches. Various scattering targets were placed on a pedestal which was located approximately in the middle of the anechoic chamber. This pedestal is made of styrofoam and is nearly transparent to the microwave frequencies normally used in the measurements (.5 - 18.0 GHz). The frequency-domain measurements were performed using a Hewlett-Packard HP8720-B Vector Network Analyzer. Two different configurations were used in the scattering measurements. The "low-band" configuration used a PPL 5812 10dB broadband amplifier to amplify the signal from port 1 of the network analyzer to the transmit antenna. This amplifier has a 10dB gain from .1 to 2 GHz and is powered by an external power source (B&K Precision D.C. Power Supply 1610). A nearly monostatic system was designed by placing two America Electronics Laboratory (AEL) H-1734 TEM Horn antennas (.5 - 6.0 GHz) approximately 24 inches apart. The "high-band" configuration used a Hewlett-Packard HP8349B Microwave Amplifier to amplify the signal from port 1 of the network analyzer to the transmit antenna. A nearly monostatic antenna arrangement consisted of the AEL H-1498 Wideband TEM Horn Antennas (2.0 - 18.0 GHz). In both configurations no external amplifier was used to amplify the receiver signal connected to port 2 of the network analyzer. The transmitting and receiving horns were placed through openings in a wall of the anechoic chamber approximately 24 inches apart and at a height of 60

from

spher

extern

netwo

A.3

the t

meas

The

meas

proce

anech

scatte

transf

calibr

The r

where

$H_a(f$

of 60 inches from the floor. The unknown targets and calibrator were located 12 feet from the horns and at a height of 60 inches from the floor. A 14 inch diameter metallic sphere was used as the system calibrator. The network analyzer is connected to an external IBM PC/AT compatible microcomputer which controls the functions of the network analyzer, the rotating podium, and stores all measurements for later processing.

A.3 Calibration Procedures

The goal of measuring the scattered return from an unknown target is to obtain the target's transfer function. As discussed in the previous section, a scattering measurement also includes transfer functions associated with other system components. The purpose of this section is to review the calibration procedures used for the measurements in this thesis. An example will also be included to illustrate these procedures. A detailed discussion of the calibration procedure can be found in [6].

Figure A.2 shows the system block diagram for the measurement system in the anechoic chamber at MSU. The aim of the calibration procedure is to calculate the target scattering transfer function by using the theoretical response of a known calibration transfer function. Here, f represents the frequency parameter. The first step in the calibration process is to make a measurement without any target in the anechoic chamber. The received signal $R^b(f)$ for the background measurement can be modeled as

$$R^b(f) = S(f)\left\{H_a(f) + H_c(f)\right\} \tag{A.1}$$

where $S(f)$ represents the system transfer function, $N^b(f)$ represents random noise, $H_a(f)$ models the transfer function due to direct coupling between the transmit and recei

cham

funct

anten

where

calibr

thesis

usefu

in the

the s

calibr

where

intera

noise,

target

receive antennas, $H_c(f)$ represents the interaction between the antennas via the anechoic chamber environment, and f represents the frequency parameter. The system transfer function can be written in terms of the transfer functions of the receive and transmit antennas $H_r(f)$ and $H_t(f)$ as

$$S(f) = H_r(f)\, H_t(f)\, E(f) \tag{A.2}$$

where $E(f)$ represents the spectrum of the input signal.

The next step in the calibration procedure is to measure the response from a calibration target whose theoretical response is known. For the measurements done in this thesis a 14 inch diameter metallic sphere was used as the calibrator. The sphere is a very useful calibrator since a closed form solution for the scattered electric field can be found in the Mie series. Also, the scattered electric field from the sphere is not a function of the sphere's orientation with respect to the incident field. The response from the calibration target measurement $R^{c+b}(f)$ can be written as

$$R^{c+b}(f) = S(f)\left\{H_a(f) + H_c(f) + H_s^c(f) + H_{sc}^c\right\} + N^{c+b}(f) \tag{A.3}$$

where $H_s^c(f)$ represents the known calibration transfer function, $H_{sc}^c(f)$ represents the interaction between the calibrator and the anechoic chamber, and $N^{c+b}(f)$ is random noise.

The last step in the measurement process is to measure the response of the desired target $R^{t+b}(f)$. This measurement can be modeled with the following equation

$$R^{t+b}(f) = S(f)\left\{H_a(f) + H_c(f) + H_s^t(f) + H_{sc}^t\right\} + N^{t+b}(f) \tag{A.4}$$

wher

intera

rando

both

where

that

elimi

(A.6)

repres

to tra

delay

user e

If the

calibr

Next,

respo

where $H_s^t(f)$ represents the target scattering transfer function, $H_{sc}^t(f)$ represents the interaction between the target and the anechoic chamber, and $N^{t+b}(f)$ is once again random noise.

Following the measurement process, the background term can be subtracted from both the calibration and target measurements. This subtraction yields

$$R^c(f) = S(f)\left\{H_s^c(f) + H_{sc}^c(f)\right\} + N^{c+b}(f) - N^b(f) \tag{A.5}$$

$$R^t(f) = S(f)\left\{H_s^t(f) + H_{sc}^t(f)\right\} + N^{t+b}(f) - N^b(f) \tag{A.6}$$

where $R^c(f)$ and $R^t(f)$ represent the clutter free calibration and target terms. Notice that the direct and indirect antenna coupling terms $H_a(f)$ and $H_c(f)$ have been eliminated. For a high quality anechoic chamber the random noise terms in (A.5) and (A.6) can be neglected. The interaction terms $H_{sc}^c(f)$ and $H_{sc}^t(f)$ in (A.5) and (A.6) represent unwanted signal in the spectral content of $R^c(f)$ and $R^t(f)$.

One method of eliminating most of the interaction in the calibration spectrum is to transform $R^c(f)$ into the time domain and window out any interaction term that is delayed beyond the end of the calibrator's response. The step requires a great deal of user experience, including knowledge of the target and chamber scattering characteristics. If the inverse Fourier transform of (A.5) is taken, then the time response $r^c(t)$ of the calibration measurement is

$$r^c(t) = \mathscr{F}^{-1}\left\{R^c(f)\right\} \tag{A.7}$$

Next, an appropriate window function w(t) is applied to (A.7), yielding a windowed time response $r^{cw}(t)$ as

If the

and t

For a

is tim

Appl

where

be wr

Next,

A tim

transf

$$r^{cw}(t) = w(t)\, r^{c}(t) \tag{A.8}$$

If the time response $r^{c}(t)$ is written as the sum of a calibrator only time response $r_s^{c}(t)$ and the interaction term $r_{sc}^{c}(t)$, then (A.8) can be written as

$$r^{cw}(t) = w(t)\left\{r_s^{c}(t) + r_{sc}^{c}(t)\right\} \tag{A.9}$$

For a properly chosen window, the interaction term $r_{sc}^{c}(t)$ can be eliminated. If $r_s^{c}(t)$ is time limited and not truncated by the time window, then (A.9) can be written as

$$r^{cw}(t) = r_s^{c}(t) \tag{A.10}$$

Applying a Fourier transform to (A.10) yields

$$R^{cw}(f) = R_s^{c}(f) = S(f)\, H_s^{c}(f) \tag{A.11}$$

where $R^{cw}(f) = \mathscr{F}\{\, r^{cw}(t)\,\}$. With this result, the system transfer function S(f) can be written as

$$S(f) = \frac{R^{cw}(f)}{H_s^{c}(f)} \tag{A.12}$$

Next, (A.6) can be written as

$$H_s^{t}(f) + H_{sc}^{t}(f) = \frac{R^{t}(f)}{S(f)} \tag{A.13}$$

A time-domain representation of (A.13) can be obtained by applying an inverse Fourier transform to the above equation to obtain

$$h_s^{t}(t) + h_{sc}^{t}(t) = \mathscr{F}^{-1}\left\{\frac{R^{t}(f)}{S(f)}\right\} \tag{A.14}$$

To isolate the target scattering response, $H_s^t(f)$, the time-domain response in (A.14) can be time gated as before. $h_s^t(t)$ must be time limited and not truncated by the window function w(t). Also, the interaction term $h_{sc}^t(t)$ must be delayed in time beyond the target response $h_s^t(t)$.

An example will be used to illustrate the features of the calibration process. Figure A.3 shows the measured response of a 14 inch diameter calibration sphere (background subtracted) over the frequency band from 2.0 GHz to 17.0 GHz with a step size of .01 GHz. After time windowing out the interaction terms between the sphere and the chamber, the windowed spectral response of the 14 inch sphere is shown in Figure A.4. Dividing by a theoretically calculated response (see (A.12)) leads to the calibration curve shown in Figure A.5.

As a check on the calibration process, a 3 inch metallic sphere was measured in the anechoic chamber. The background-subtracted spectral return is shown in Figure A.6. A windowed response from the 3 inch sphere is shown in Figure A.7. This spectrum was obtained by time gating out the interaction term in the time domain and then transforming the time response back into the frequency domain. Finally, the response in Figure A.7 was divided by the calibration curve. The resulting response of the 3 inch sphere is shown in Figure A.8 along with the theoretically calculated response. This figure shows quite a good match between the two curves.

A.4 Windowing Functions

The use of different windowing functions has been employed in every phase of this thesis. Therefore, some time will be devoted to this topic. Due to the broad scope of this topic, only features pertinent to this thesis will be discussed. This section will present a brief overview of windowing functions and their use. The most common window functions used in this thesis will be discussed and several examples will be presented in order to illustrate some of the most import window characteristics.

A window function can be used in a number of ways to modify a time or frequency signal. For signal processing applications involving the transformation of data from one domain to the other, the use of proper windowing becomes a necessity. For any broadband signal which is frequency truncated, a transformation from one domain to the other usually introduces unwanted oscillations in the transformed domain. If the signal to be transformed is multiplied by an appropriate window function, then the number of oscillations in the transformed domain may be reduced. To see this, consider a frequency-domain signal $F(\omega)$ which is multiplied by a windowing function $W(\omega)$ to yield the frequency-domain response $R(\omega)$. This is given by

$$R(\omega) = W(\omega)\ F(\omega) \tag{A.15}$$

A transformation to the time domain yields the following convolution

$$r(t) = w(t) * f(t) \tag{A.16}$$

where r(t), w(t), and f(t) are the time-domain representations of R(ω), W(ω), and F(ω),

respectively. Consider the case where the windowing function is a simple rectangular window of unit height. The time domain representation of a rectangular window will be a sinc function. With this function, the convolution in (A.16) may yield a highly oscillatory response. To overcome this problem, a proper choice for the window function must be selected. The selection of a "good" window function is highly dependent on the characteristics of the signal. The type of signals derived from measurements or theoretical calculations in this thesis are usually band-limited with discontinuities at the endpoints. These discontinuities always cause problems after applying a forward or reverse Fourier transform. The effects of the discontinuities can be reduced by smoothing the data at the endpoints by using a carefully chosen window.

The ideas in the preceding paragraph can also be used in a slightly different manner. Take, for example, the use of an ultra-wideband (UWB) radar. A short pulse signal is transmitted in order to detect or identify a potential threat. The transient response of the target can be represented as the convolution of the time-domain input signal and the target's impulse response. In the frequency domain, the target frequency response is formed by multiplying the target's transfer function with the Fourier transform of the input signal. In this case, the input signal (in the frequency domain) acts as a window on the target's transfer function. Therefore, a window function applied to a calculated or measured transfer function represents the Fourier transform of a short pulse that an UWB radar would be transmitting.

Two different window functions have been used in this thesis. They are the cosine taper and the Gaussian modulated cosine (GMC). These functions were chosen to reduce

the effects of the oscillation phenomena and to represent the Fourier transforms of the short pulses for studies in UWB radar phenomena.

The cosine taper function (also known as the Tukey function) can be represented in the frequency domain as

$$W(f) = \begin{cases} \sin^2\left(\frac{\tau}{2}\pi\frac{f-F_L}{\Delta F}\right) & \dots \quad f > \frac{\tau-1}{\tau}F_H \;\; or \;\; f < \frac{F_L}{\tau} \\ 1 & \dots \quad f < \frac{\tau-1}{\tau}F_H \;\; and \;\; f > \frac{F_L}{\tau} \end{cases} \qquad \textbf{(A.17)}$$

where F_H and F_L represent the highest and lowest frequencies in the band-limited spectrum, Δ is F_H - F_L, and τ is a shape factor which must be an even integer. The standard notation for the cosine taper is $1/\tau$ cosine taper. Notice that large values of τ result in a window that is nearly rectangular.

The GMC window can be represented in the frequency domain as

$$W_{GMC}(f) = \mathrm{T}\left\{ e^{-\pi[(f-f_c)\mathrm{T}]^2} + e^{-\pi[(f+f_c)\mathrm{T}]^2} \right\} \qquad \textbf{(A.18)}$$

where f_c is the center of the window and T controls the width of the window. The time-domain representation of this function can be written as

$$w_{GMC}(t) = \cos(\pi f_c t)\, e^{-\pi(t/\mathrm{T})^2} \qquad \textbf{(A.19)}$$

With the variables f_c and T, the shape and position of this window can easily be changed. This window is ideal for baseband spectral data (data down to DC). For this case, f_c can be set to 0 and the value of T varied to slowly taper off the higher frequency data.

The best way to illustrate the characteristics of the cosine taper and GMC windows is through several examples. These examples will be reflective of the type of windows used in this thesis. Figure A.9 shows the cosine taper function applied to the frequency band 1.0 GHz to 5.0 GHz for several different values of τ. As can be seen, large values of τ form a window that is more rectangular in shape. Small values of τ flatten out the window leading to a bell shaped curve. The time-domain representation of the curves in Figure A.9 are shown in Figure A.10. Notice that the curve associated with a large value of τ is highly oscillatory. On the other hand, using a small value of τ will lead to a less oscillatory function, but there will be a loss of spectral information and energy. For a larger bandwidth signal, the transformed cosine taper window will have an associated pulse that is narrower. However, the parameter τ will control the number of oscillations in the pulse. Figure A.11 shows several cosine taper functions for the frequency band from 2.0 GHz to 17.0 GHz. Figure A.12 shows the time-domain representations associated with the transforms of the cosine taper windows. In this figure, the peaks are much narrower than in Figure A.10, but the oscillations are very similar.

The GMC window is a function of the parameters f_c and T. In this thesis, the selected value of f_c depended on whether the frequency band was baseband or non-baseband. For a baseband signal, the value of f_c was set to 0. For the non-baseband signal, f_c was set centered between the high and low frequency endpoints. The characteristics of this window can be compared to the cosine taper window using the frequency band 1.0 to 5.0 GHz. Figure A.13 shows several different GMC windows as a function of the window shape parameter T. More information in the frequency spectrum is used when using smaller values of T. The corresponding time-domain representations of the curves in Figure A.13 are shown in Figure A.13. Here, small values of T are associated with narrow pulses. As compared to the cosine taper window, the generated pulses can still be oscillatory, and spectral information will be lost for a window that is too narrow.

For a baseband signal, the GMC window parameter f_c is set to zero. This window was used extensively in the cepstral analysis section (Chapter 5 and 6). A good example of this window is shown in Figure A.15 for different values of the shape parameter T. Here, the baseband ranges from 0 GHz to 5 GHz. All of these windows keep the low-frequency spectral information but attenuate the higher components. The associated time-domain pulses for the windows shown in Figure A.15 are shown in Figure A.16. A nice feature of these pulses is that all are Gaussian in shape and have no oscillations. The fact that there are no oscillations makes this window very attractive for baseband signal processing.

The above examples are very typical of the window functions used in this thesis, and the frequency bands used in the examples are representative of those used in the preceding chapters. Parameters associated with each window are explained in the main body of the thesis.

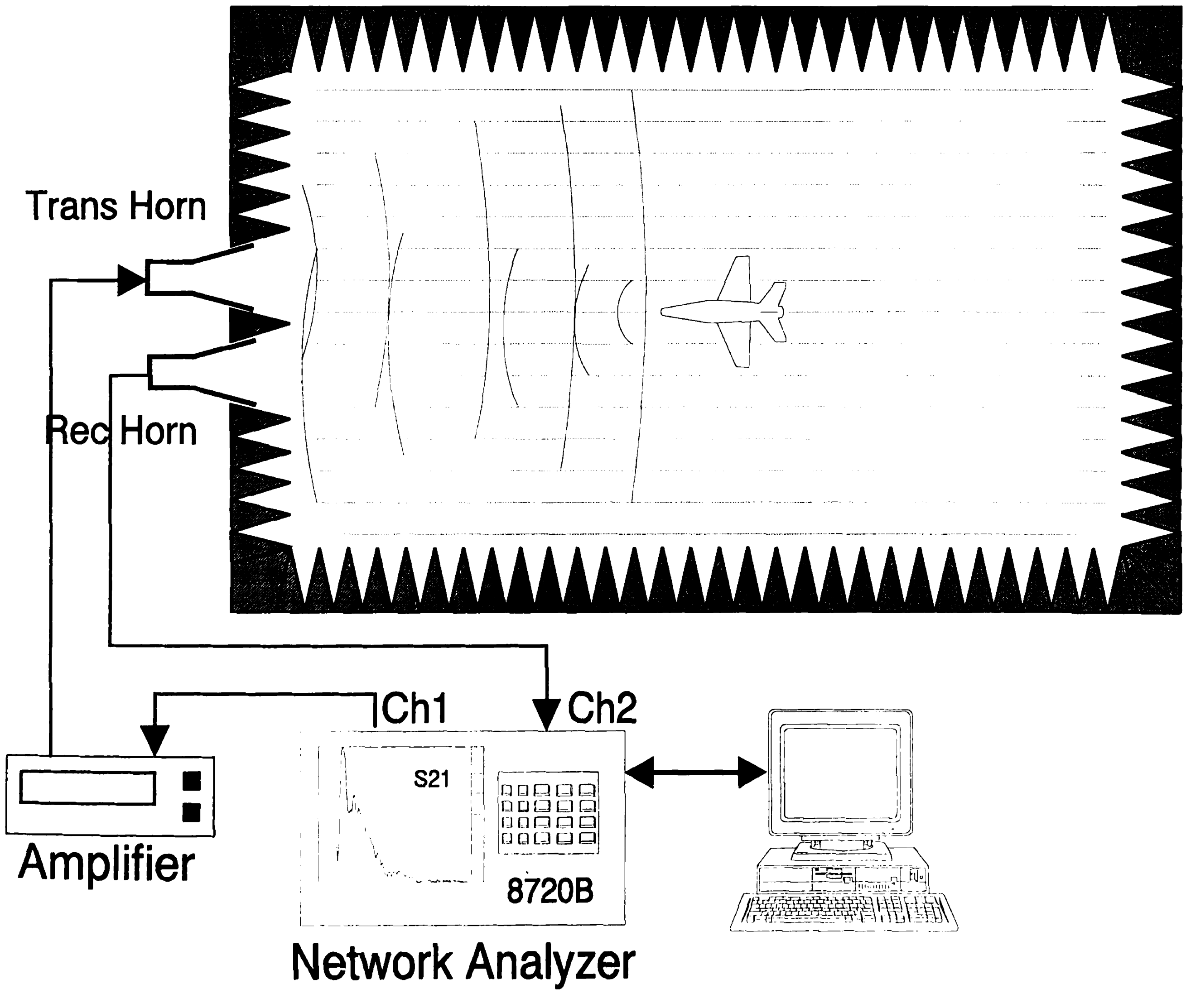

Figure A.1 Anechoic chamber using a frequency-domain measurement system at Michigan State University.

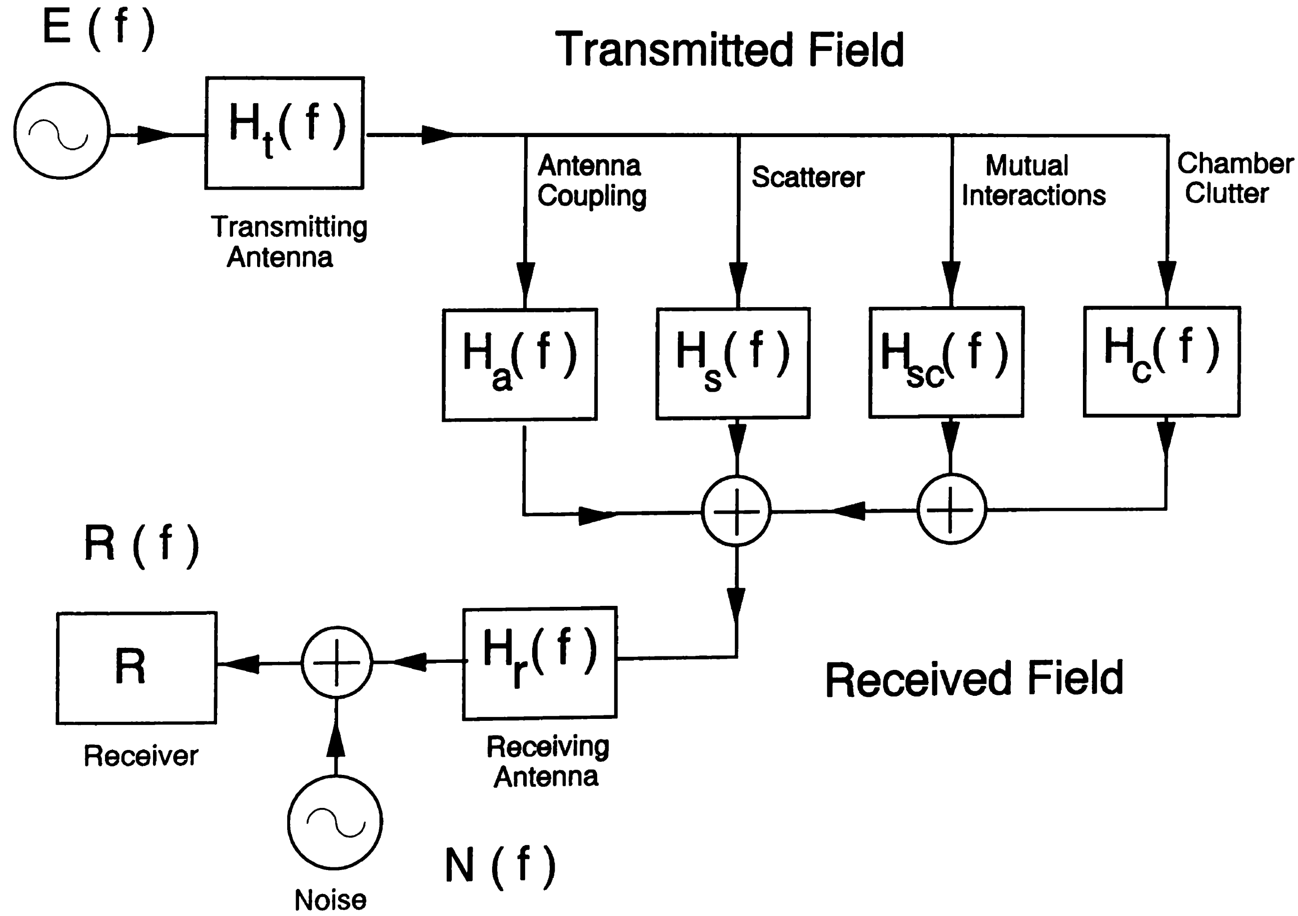

Figure A.2 Measurement system block diagram for scattering measurement analysis. Taken from Ross, [6].

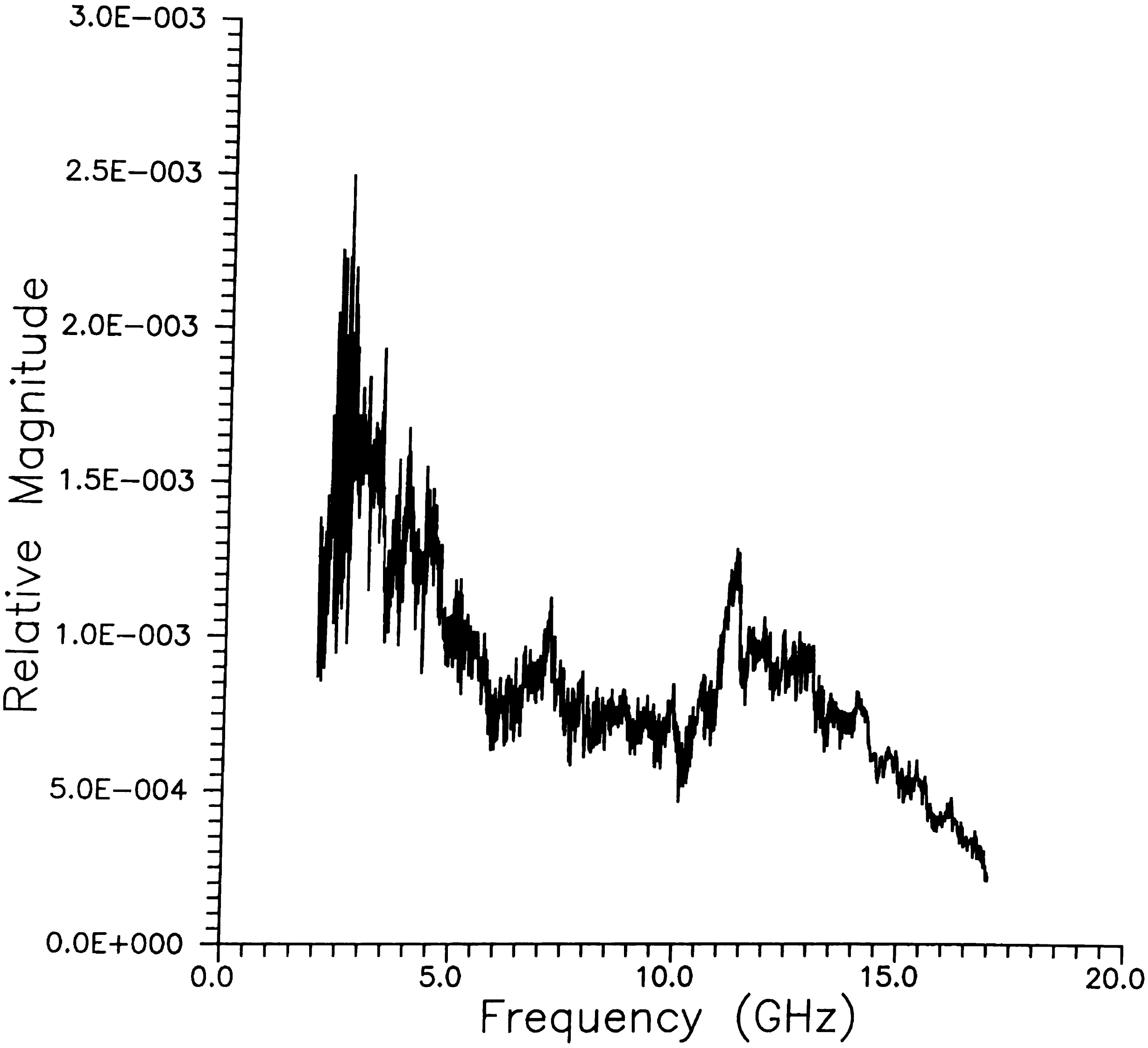

Figure A.3 Measured frequency response of 14 inch diameter metal calibration sphere.

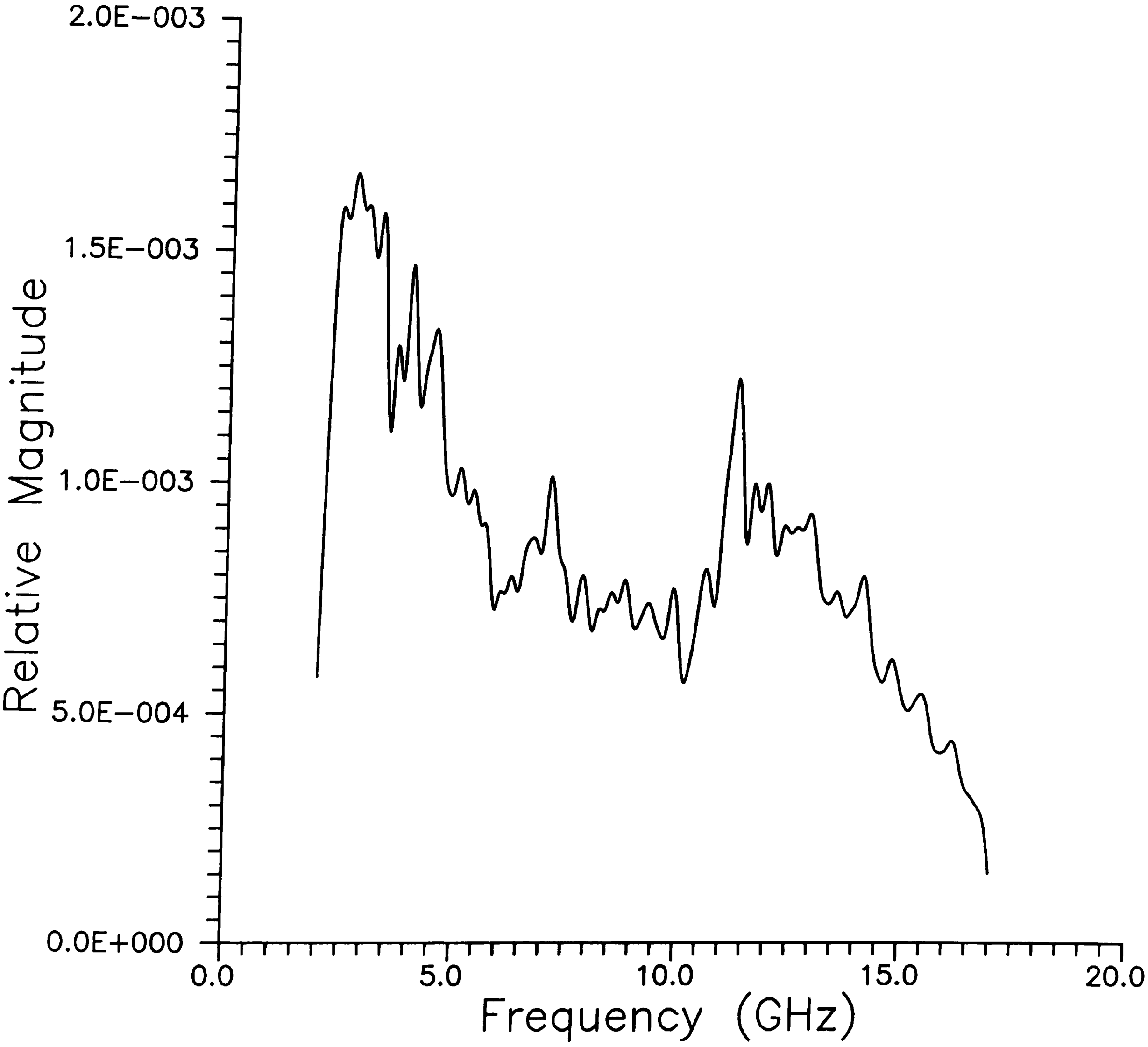

Figure A.4 Spectral response of 14 inch diameter calibration sphere after time domain gating of chamber wall reflections.

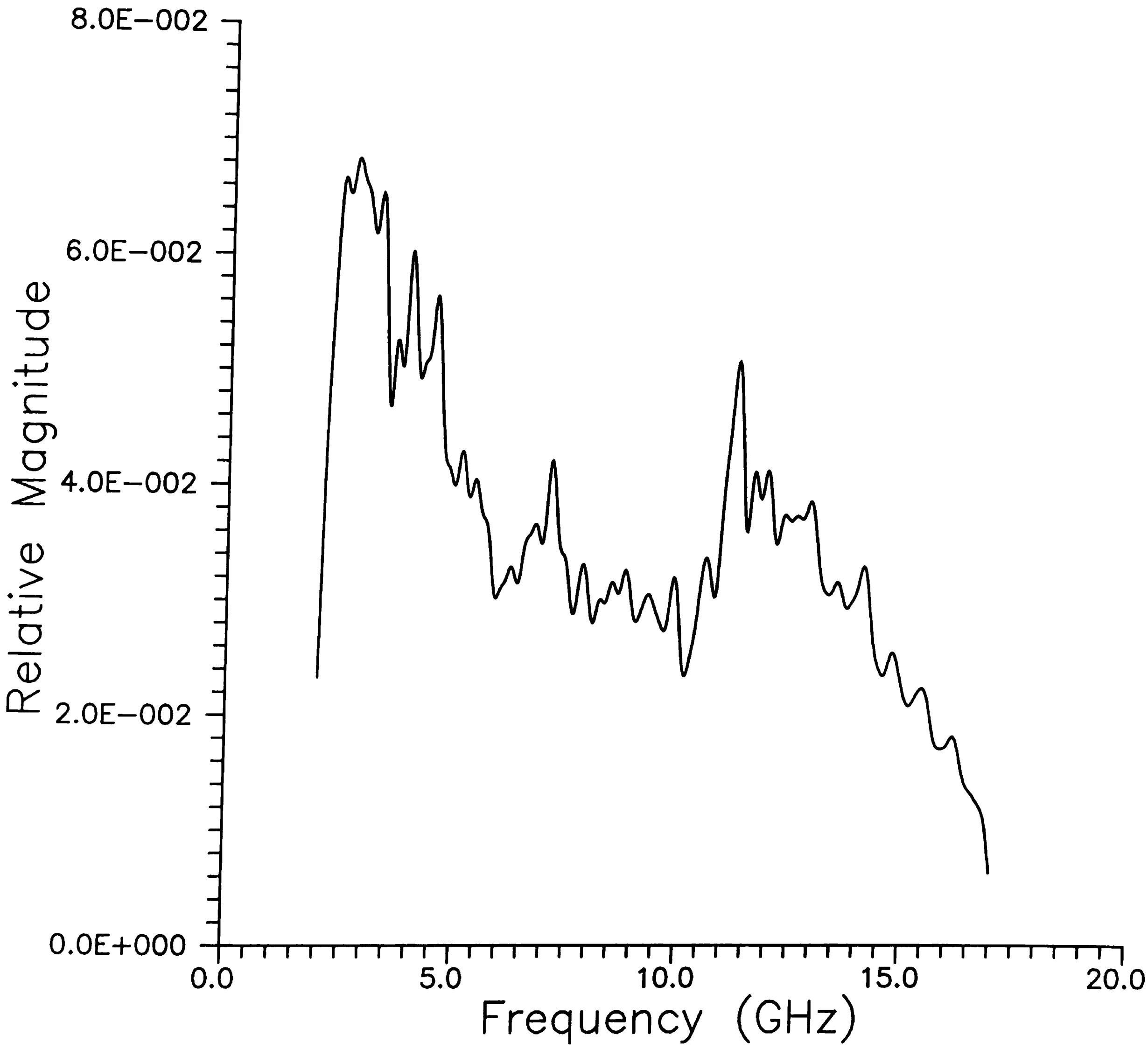

Figure A.5 Transfer function for the frequency-domain system using the 14 inch diameter sphere as a system calibrator.

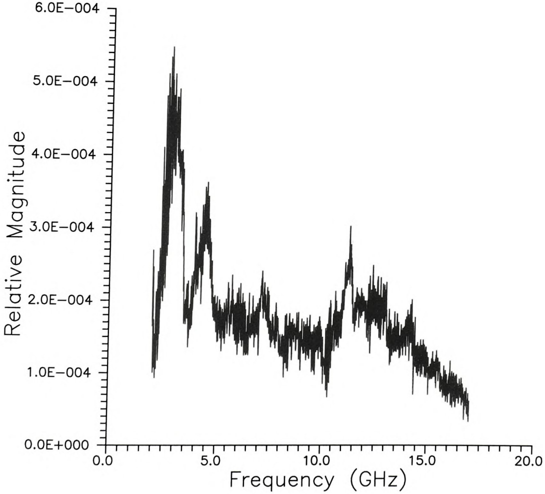

Figure A.6 Measured frequency response of a 3 inch diameter metallic sphere.

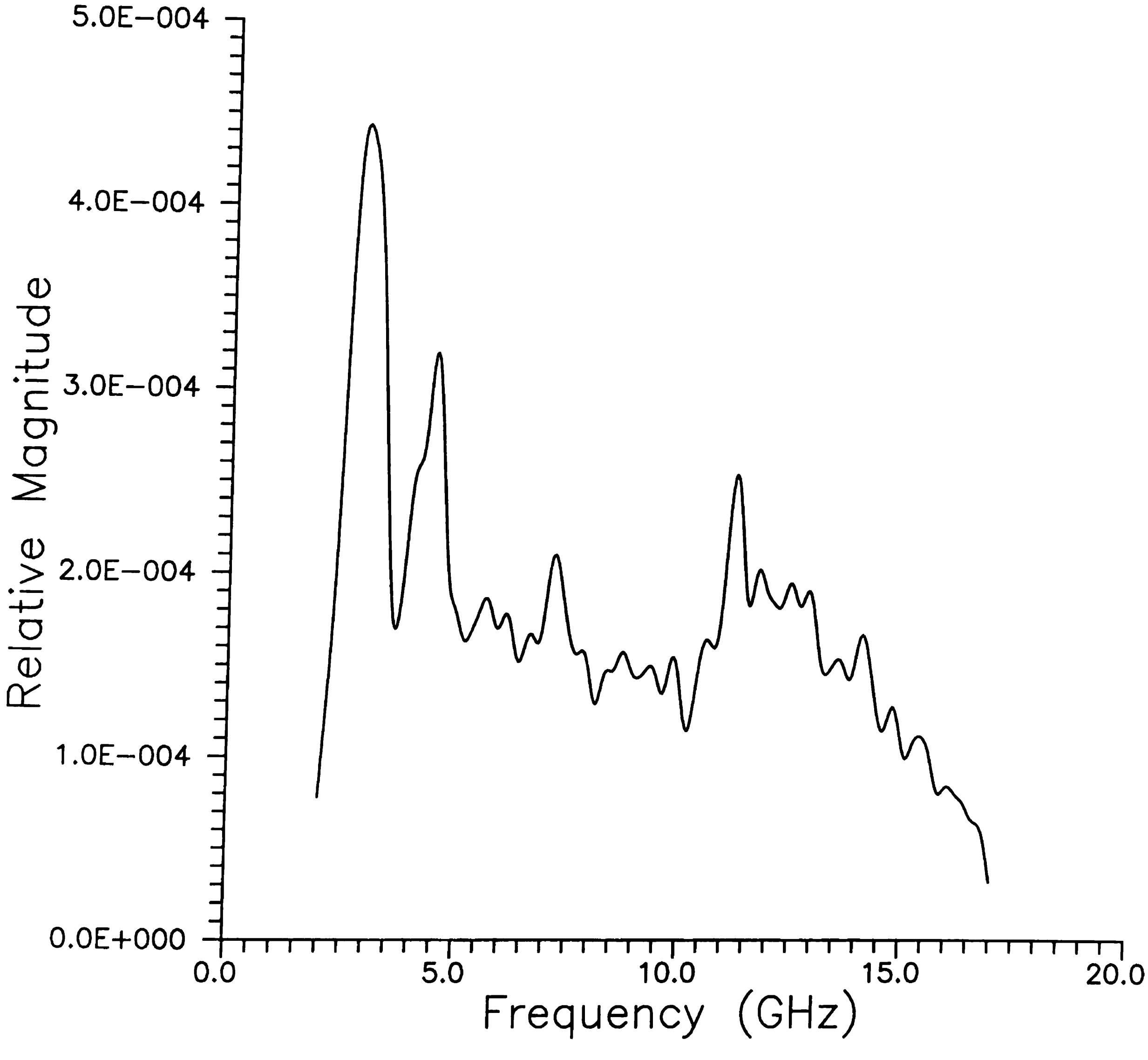

Figure A.7 Spectral response of a 3 inch diameter sphere after time-domain gating of the chamber wall reflections.

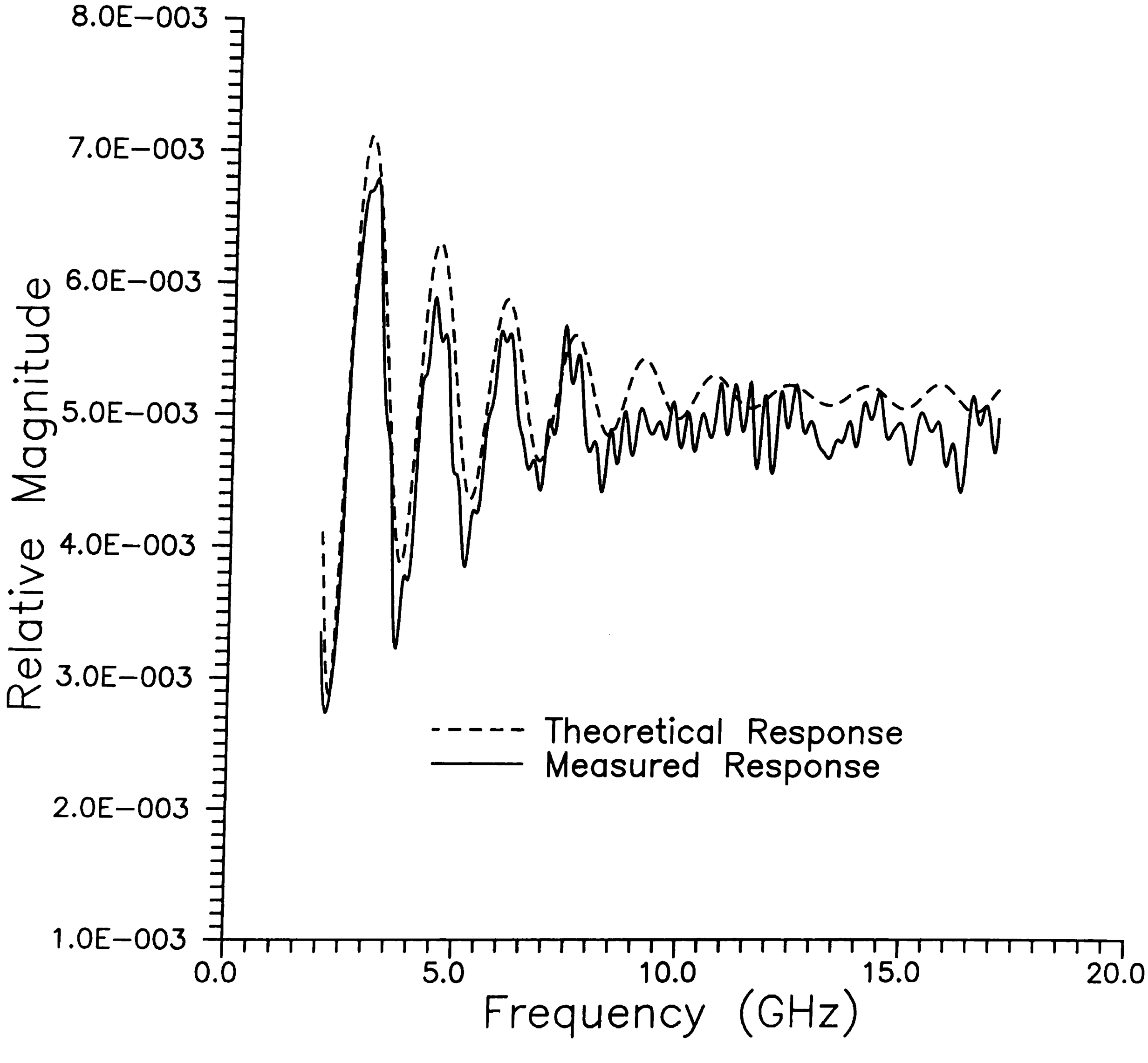

Figure A.8 Comparison between theory and experiment for a 3 inch diameter metallic sphere. The measured data has had the system transfer function removed.

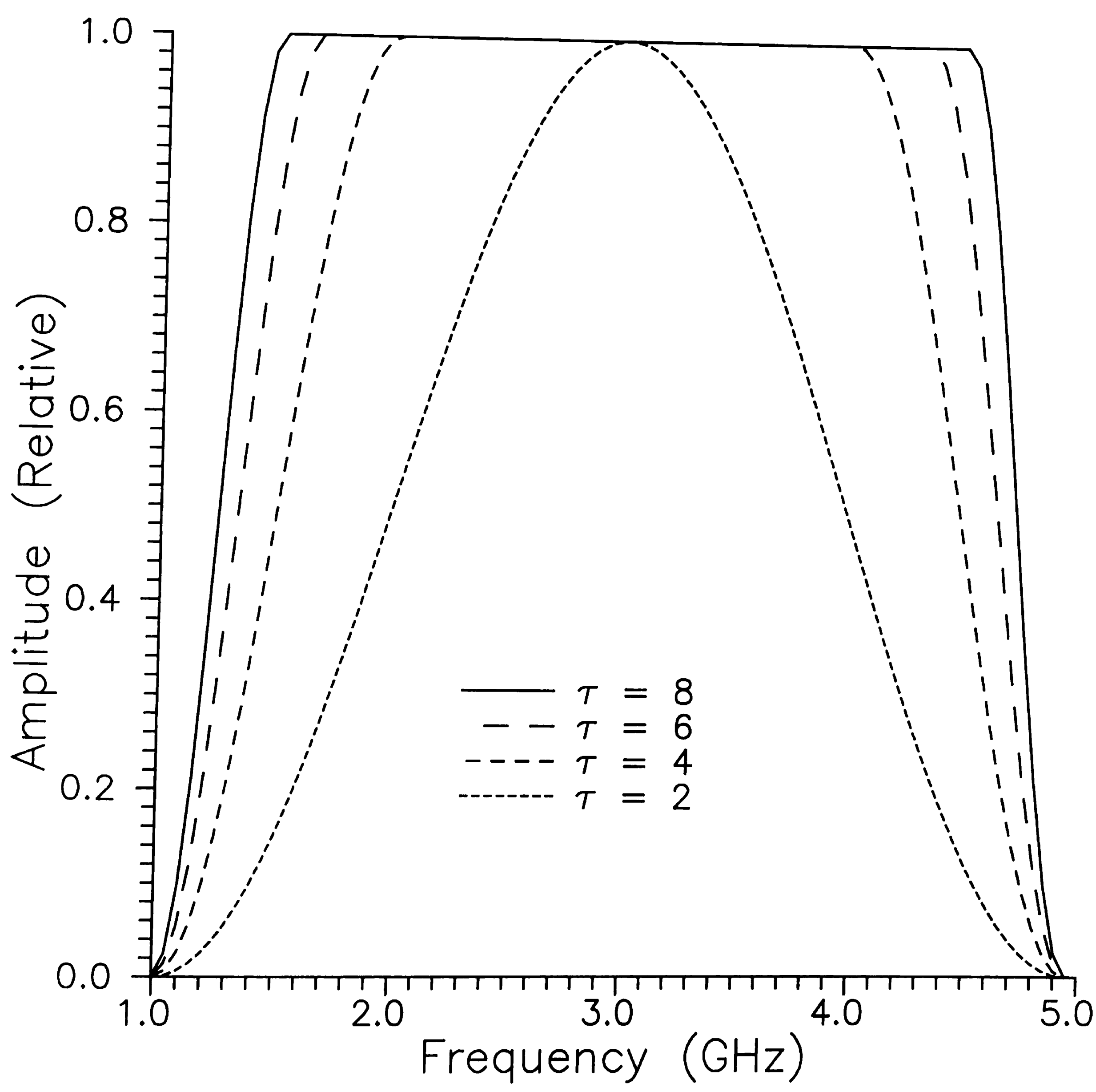

Figure A.9 Cosine taper weighting curves as a function of the window shape parameter τ.

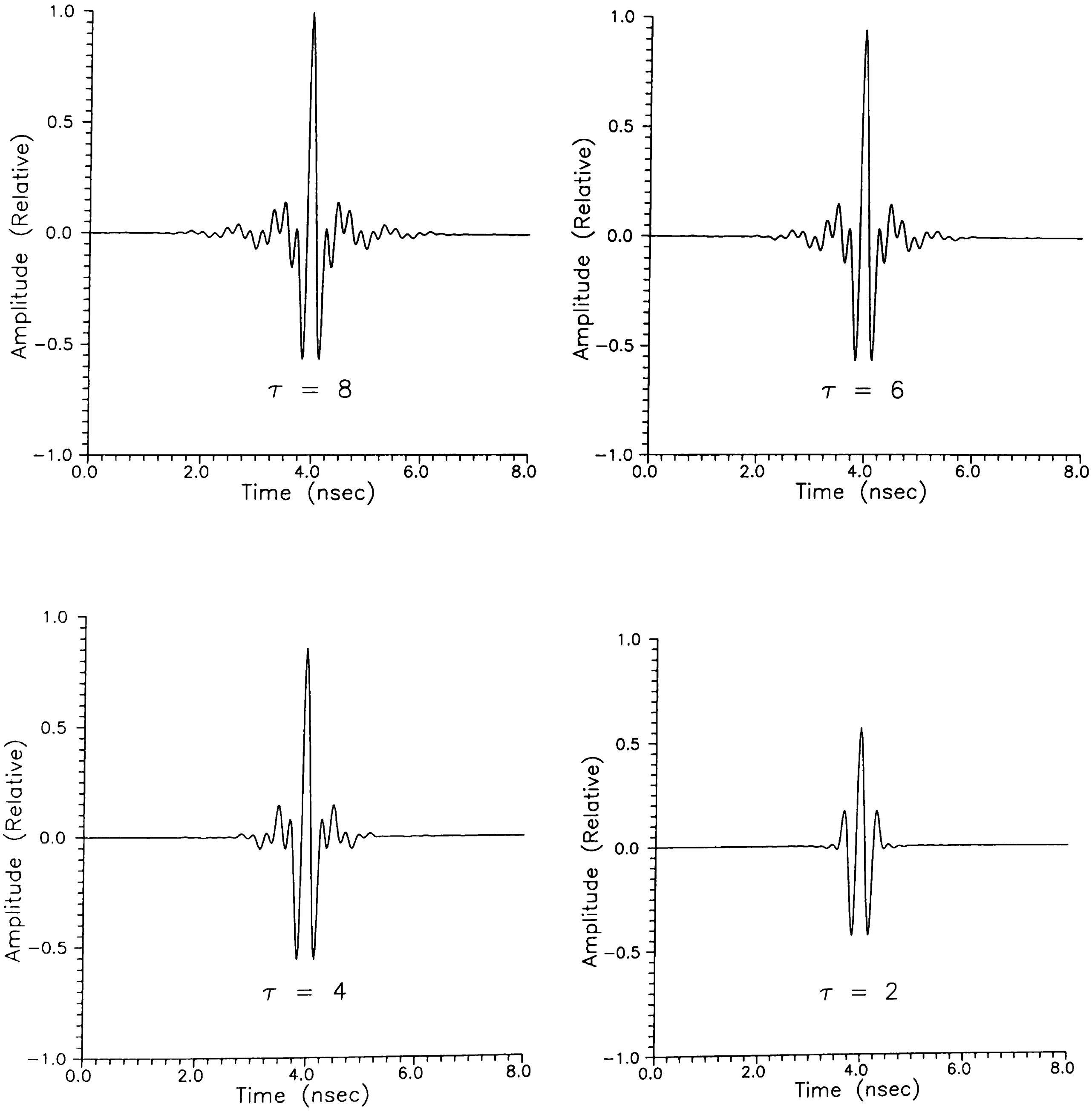

Figure A.10 Cosine taper weighting functions transformed to the time domain. Original window bandwidth from 1.0 to 5.0 GHz.

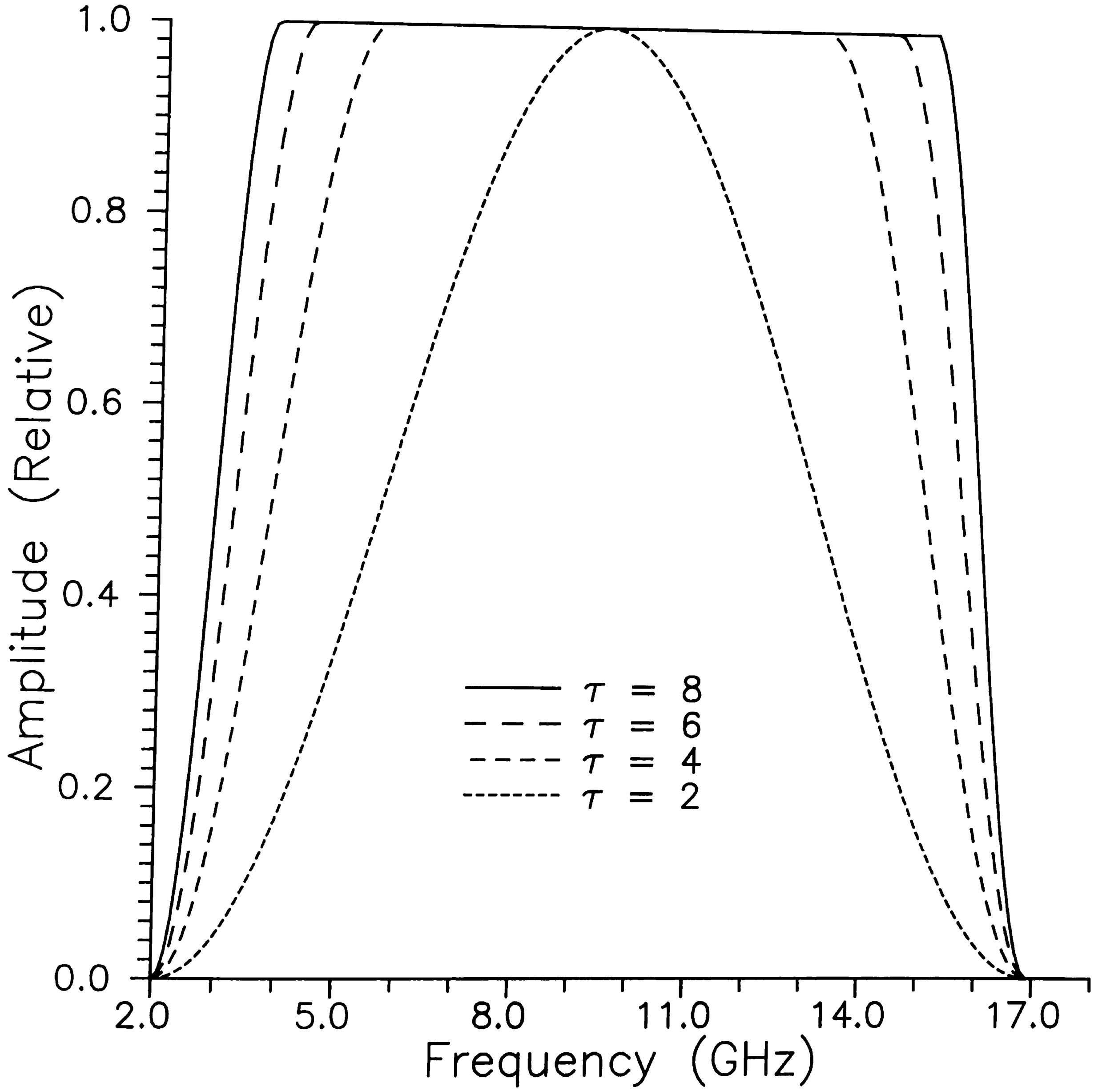

Figure A.11 Cosine taper weighting curves as a function of the window shape parameter τ.

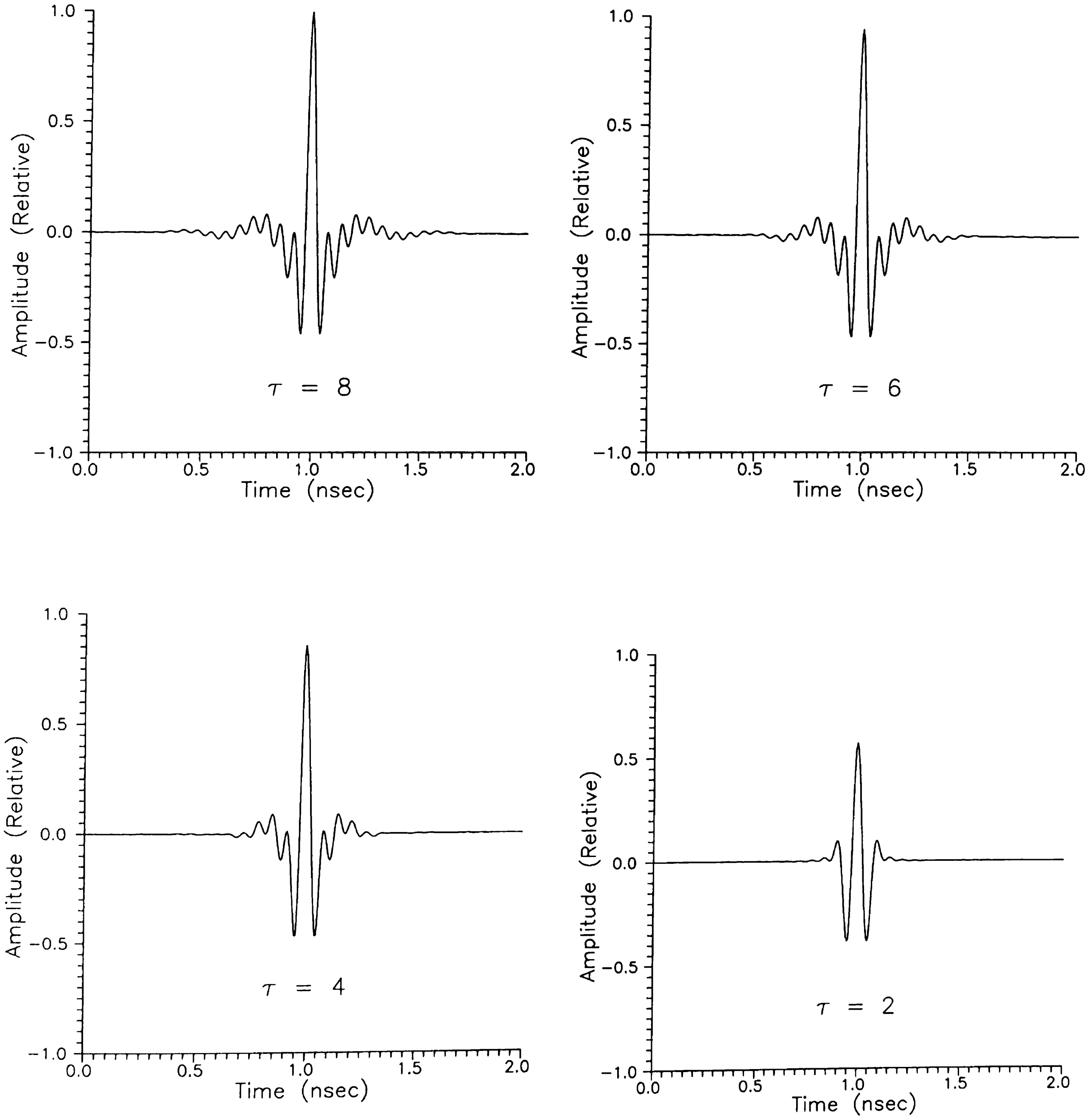

Figure A.12 Cosine taper weighting functions transformed to the time domain. Original window bandwidth from 2.0 to 17.0 GHz.

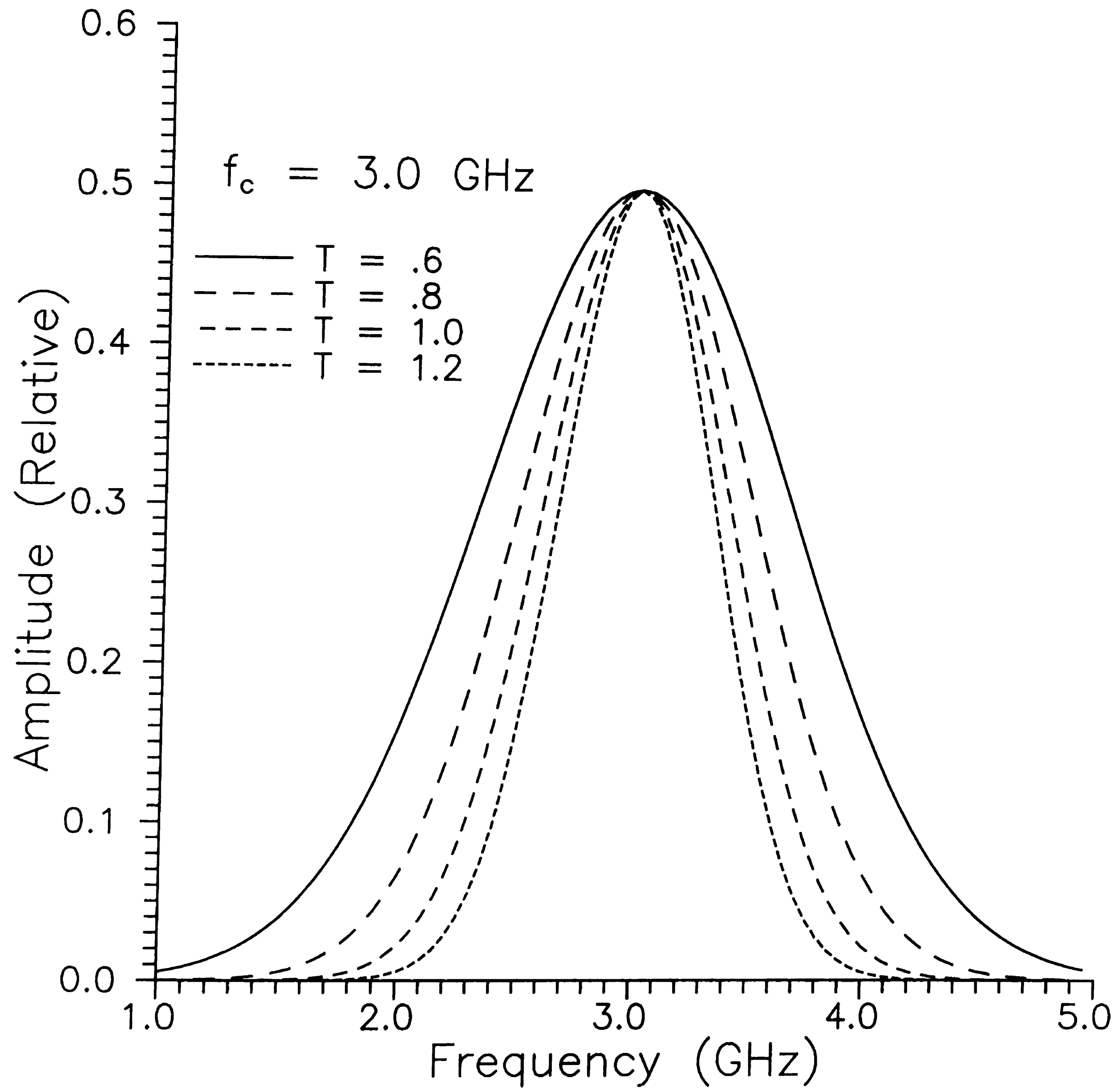

Figure A.13 Gaussian modulated cosine weighting curves as a function of the window shape parameter T. Center frequency f_c = 3.0 GHz.

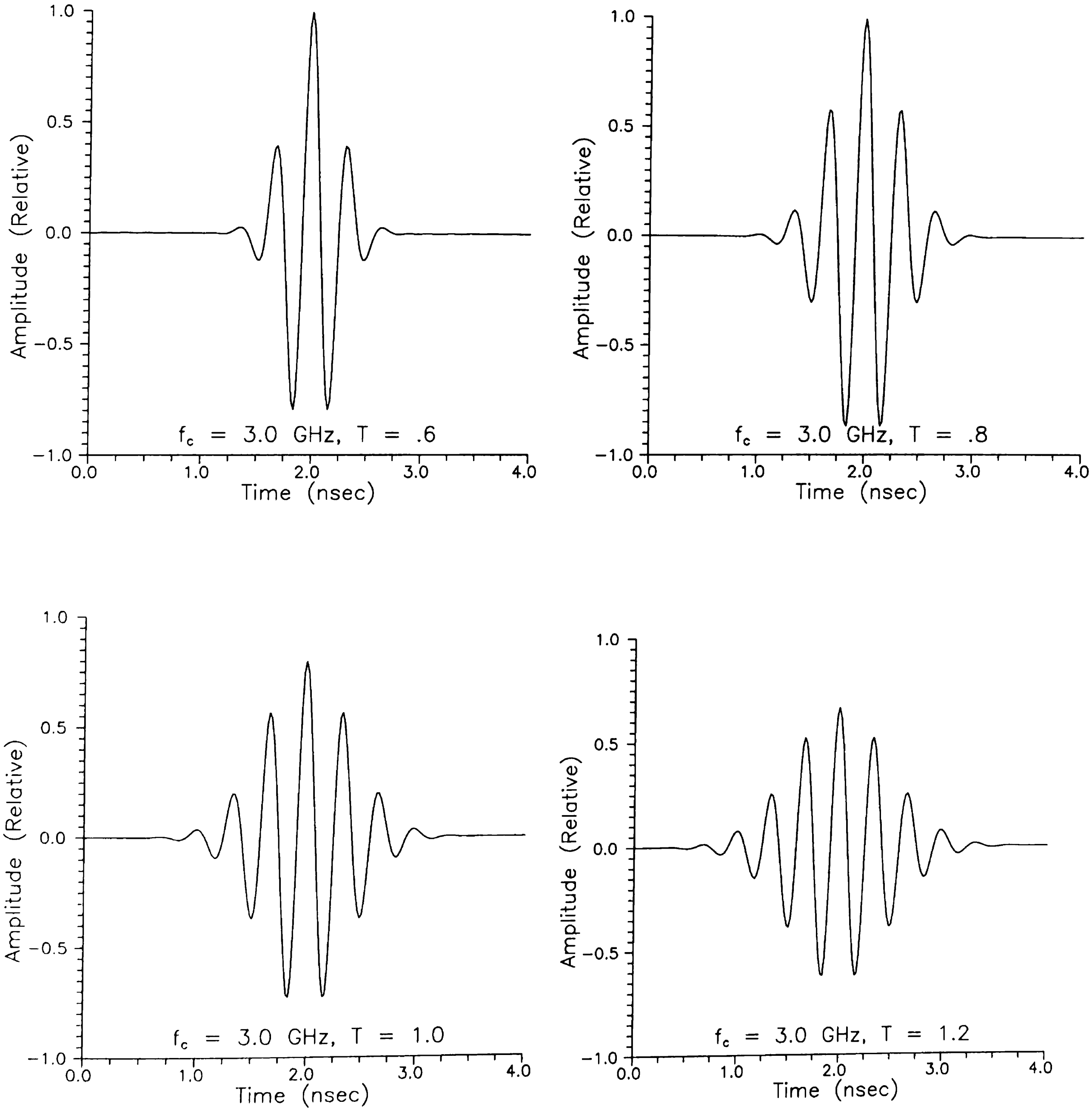

Figure A.14 Gaussian modulated cosine weighting functions transformed to the time domain. Original window centered at f_c = 3.0 GHz.

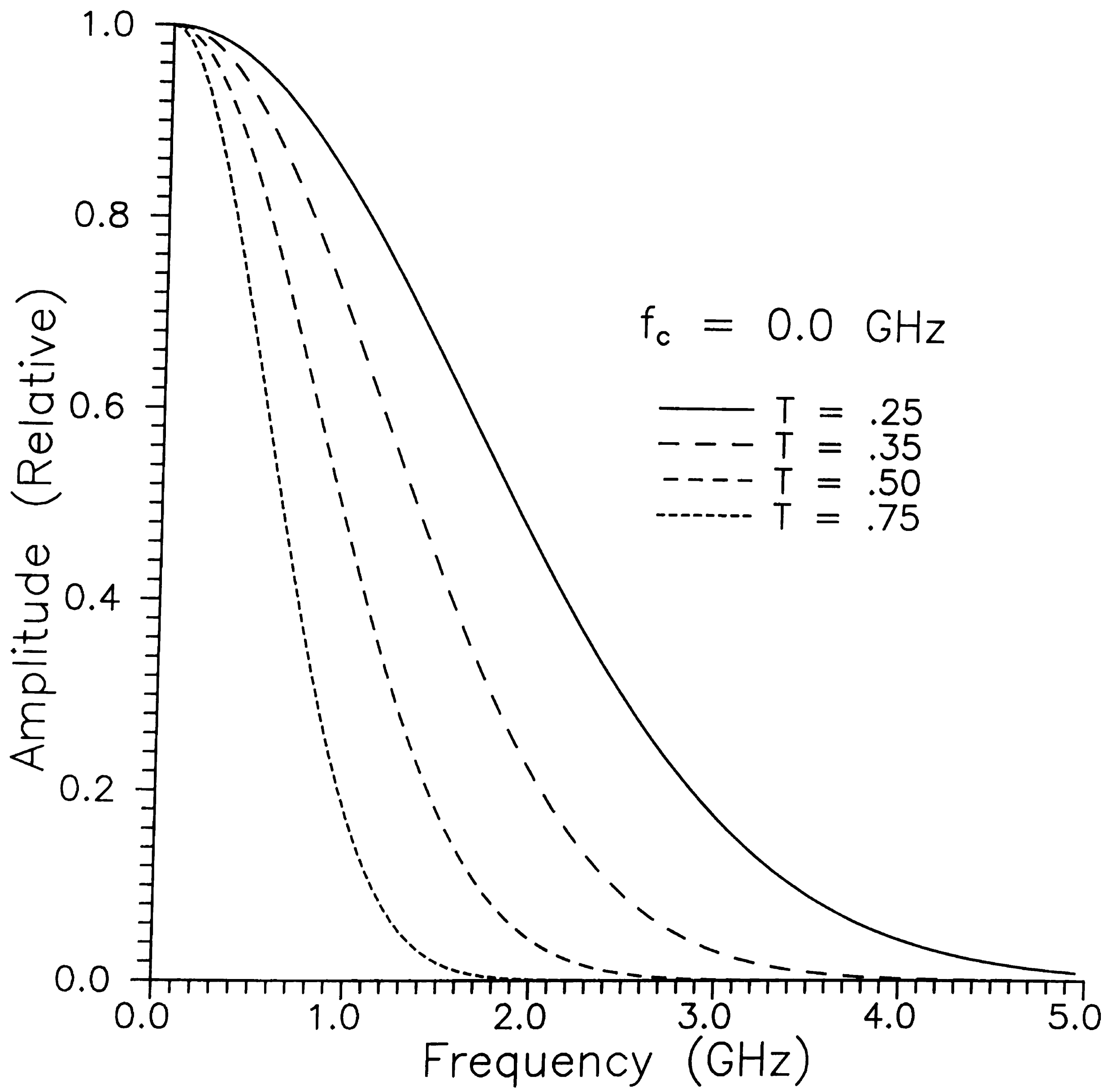

Figure A.15 Gaussian modulated cosine weighting as a function of window shape parameter T. Center frequency f_c = 0.0 GHz.

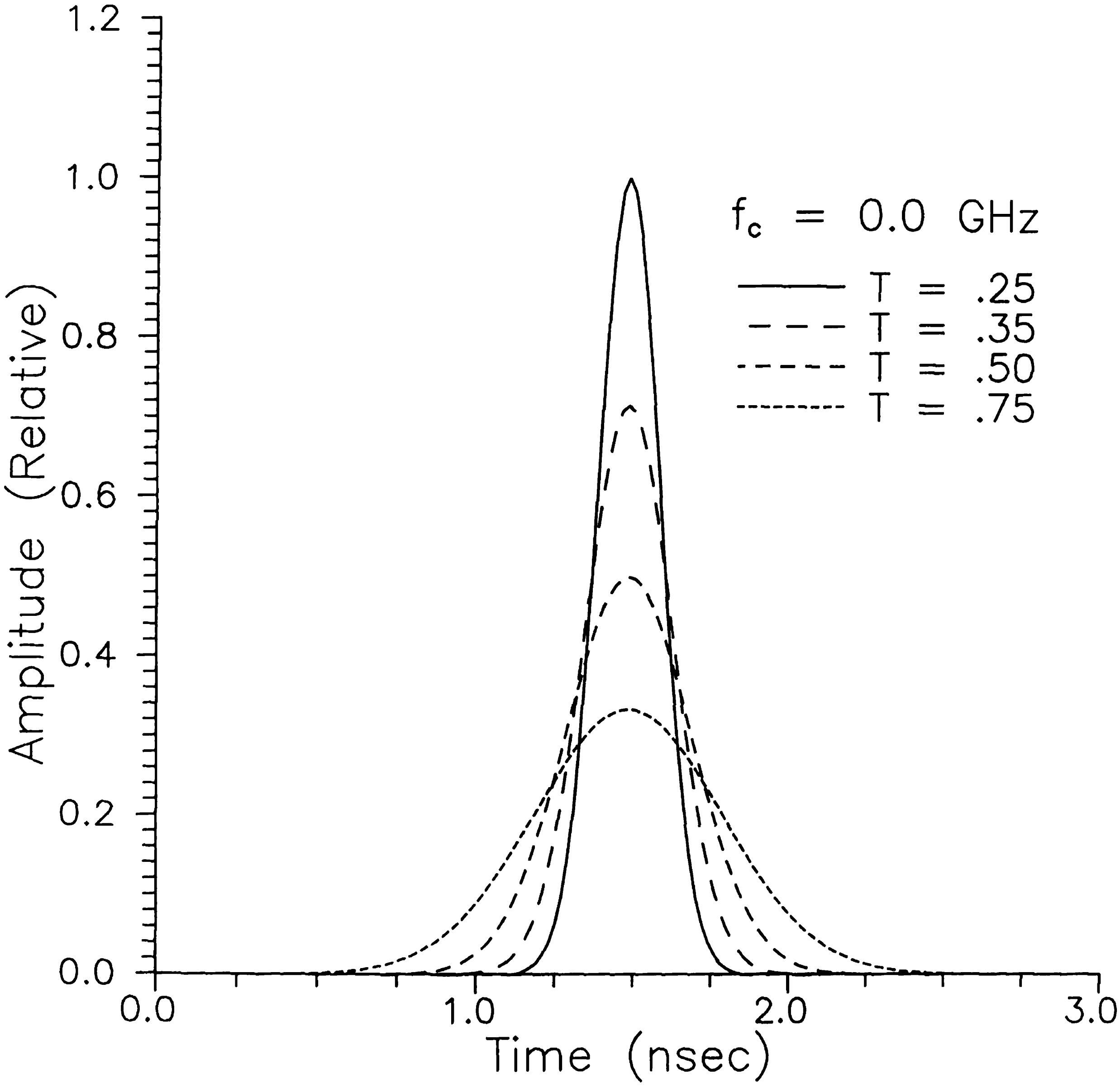

Figure A.16 Gaussian modulated cosine weighting functions transformed to the time domain. Original windows centered at f_c = 0.0 GHz.

LIST OF REFERENCES

LIST OF REFERENCES

[1] C.Phillips, P. Johnson, K. Garner, G. Smith, A. Shek, R.C. Chou, and S. Leong, "Ultra-high-resolution radar development and test," in: *Ultra-Wideband, Short-Pulse Electromagnetics 2*, Lawrence Carin and Leopold B. Felsen, ed., Plenum Press, New York, 1999.

[2] M.P. Fargues, and W.A. Brooks, "Comparative study of time-frequency and time-scale transforms for ultra-wideband radar transient signal detection," *IEE Proc.-Radar,Sonar Navig.*, Vol. 142, No.5, pp.236-242, October 1995.

[3] E.J. Rothwell, K.M. Chen, D.P. Nyquist, A. Norman, G. Wallinga, and Y. Dai, "Target detection and identification using a stepped-frequency ultra-wideband radar," *SPIE*, vol 2845, pp. 26-37, Denver, Colorado, Aug. 5-6, 1996.

[4] C. Baum, E.J. Rothwell, K.M. Chen, and D.P. Nyquist, "The singularity expansion method and its application to target identification," *IEEE Proc.*, vol. 79, no. 10, p. 1481-1492, Oct. 1991.

[5] E.J. Rothwell, "Radar Target Discrimination Using the Extinction-Pulse Technique," Ph.D. Thesis, Department of Electrical Engineering, Michigan State University, 1985.

[6] J.E. Ross, III, "Application of Transient Electromagnetic Fields to Radar Target Discrimination," Ph.D. Thesis, Department of Electrical Engineering, Michigan State University, 1992.

[7] P. Ilavarasn, "Automated Radar Target Discrimination Using E-pulse and S-pulse Techniques", Ph.D. Thesis, Department of Electrical Engineering, Michigan State University, 1992.

[8] Q. Li, "Radar Target Discrimination Using Early-Time Responses", Ph. D. Thesis, Department of Electrical Engineering, Michigan State University, 1995.

[9] P. Ilavarasan, J.E. Ross, E.J. Rothwell, K.M. Chen, and D.P. Nyquist, "Performance of an automated radar target discrimination scheme using E pulse and S pulses," *IEEE Antennas Propagat.*, vol 41, no. 5, pp. 582-588, May 1993.

[10] R.R. Lentz, "A numerical study of electromagnetic scattering from ocean-like surfaces," *Radio Science*, vol. 9, no. 12, pp. 1139-1146, Dec. 1974.

[11] C.L. Rino, T.L. Crystal, A.K. Koide, H.D. Ngo, H. Guthart, "Numerical simulation of backscatter from linear and nonlinear ocean surface realizations," *Radio Science*, Vol. 26, no. 1, pp. 51-71, Feb. 1991.

[12] A. Norman, "Transient Scattering of Electromagnetic Waves in an Ocean Environment," Ph.D. Thesis, Dept. of Electrical Engineering, Michigan State University, 1996.

[13] R. Chen and J.C. West, "Analysis of Scattering from Rough Surfaces at Large Incidence Angles Using a Periodic-Surface Moment Method," *IEEE Trans. Geoscience and Remote Sensing*, Vol. 33, No. 5, pp. 1206-1213, Sept. 1995.

[14] R.F. Harrington, Time-Harmonic Electromagnetic Fields, McGraw-Hill, New York, 1961

[15] S. Singh, W.F. Richards, J.R. Zinecker, D.R. Wilton, "Accelerating the convergence of series representing the free space periodic green's function," *IEEE Trans. Antennas Prop.*, vol. 38, no 12, pp. 1958-1962, Dec. 1990.

[16] I.S. Gradshteyn, and I.M. Ryzhik, Table of Integral, Series and Products, New York, Academic Press, 1980.

[17] M. Abramowitz, and I.A. Stegun editors, Handbook of Mathematical Functions, Dover Publications Inc., New York, 1965.

[18] C.A. Balanis, Advanced Engineering Electromagnetics, John Wiley & Sons, Inc., 1989.

[19] Blair Kinsman, Wind Waves; Their Generation and Propagation on the Ocean Surface, Chap. 8, Prentice-Hall, Englewood Cliffs, N.J. 1965.

[20] E. Rothwell, D.P. Nyquist, K.M. Chen, and B. Drachman, "Radar target discrimination using the extinction-pulse technique," *IEEE Trans. Antennas Propagat.*, vol. AP-33, no. 9, pp. 929-936, Sept. 1985.

[21] K.M. Chen, D.P. Nyquist, E.J. Rothwell, L.L. Webb, and B. Drachman, "Radar target discrimination by convolution of radar return with extinction-pulses and single-mode extraction signals," *IEEE Trans. Antennas Propagat.*, vol. AP-34, no. 7, pp. 896-904, July 1986.

[22] K.M. Chen, E. Rothwell, D.P. Nyquist, J. Ross, P. Ilavarasan, R. Bebermeyer, Q.

Li, C.Y. Tsai, and A. Norman, "Radar identification and detection using ultra-wideband/short-pulse radars," *Ultra-Wideband, Short-Pulse Electromagnetics 2*, Edited by L. Carin and L.B. Felsen, Plenum Press, New York pp.535-542, 1995.

[23] E.J. Rothwell, K.M. Chen, D.P. Nyquist, A. Norman, G. Wallinga, and Y. Dai, "Target detection and imaging using a stepped-frequency ultra-wideband radar," *Short-Pulse Electromagnetics 3*. Albuquerque, NM, May 27-31, 1996.

[24] E.Rothwell, K.M.Chen, D.P. Nyquist, P. Ilavarasan, J.E. Ross, R. Bebermeyer, and Q. Li, "A general E-pulse scheme arising from the dual early-time/late-time behavior of radar scatterers," *IEEE Trans. Antennas Prop.*, vol. 42, no.9, pp. 1336-1341, Sept. 1994.

[25] K.R. Umashankar, S. Nimmagadda, and A. Taflove, "Numerical analysis of electromanetic scattering by electrically large objects using spatial decomposition technique," IEEE Trans. Antennas Prop., Vol. 40, No. 8, pp.867-877, August 1992.

[26] D.E. Iverson, "Coherent processing of ultra-wideband radar signals," *IEE Proc.-Radar, Sonar Navig.*, vol. 141, no. 3, pp. 171-179, June 1994.

[27] D.E. Goldbert, Genetic Algorithms, New York: Addison-Wesley, 1989.

[28] F.M. Tesche, "On the use of the Hilbert transform for processing measured CW data", *IEEE Trans. Electromagnetic Compatibility*, vol. 34, no. 3, pp. 259-266, Aug. 1992.

[29] A.V. Oppenheim, and R.W. Schafer, Digital Signal Processing. New York: Prentice-Hall, 1975.

[30] T. Ulrych, "Application of homomorphic deconvolution to seismology," *Geophysics*, vol. 36, no. 4, pp. 650-660, Aug. 1971.

[31] W.D. Blair, J.E. Conte, and T.R. Rice, "An Instructive Example of Homomorphic Signal Processing," *IEEE Trans. Educ.* , Vol. 38, No. 3, pp. 211-218, Aug. 1995.

[32] D.G. Childers, D.P. Skinner, and R.C. Kemerait, "Cepstrum: A Guide to Processing," *Proceedings of the IEEE*, Vol. 65, No. 10, pp. 1428-1443, Oct. 1977.

[33] A.J. Berkhout, "On the Minimum Phase Criterion of Sampled Signals," *IEEE Trans. Geosci. Elect.*, Vol. GE-11, No. 4, pp. 186-198, Oct. 1973.

[34] P. Henrici, Applied and Computational Complex Analysis, Vol. 1, John Wiley & Sons, Inc. 1974.

[35] T.F. Quatieri, and J.M. Tribolet, "Computation of the real cepstrum and minimum phase," in *Programs for Digital Signal Processing.* New York: IEEE Press, 1979.

[36] J. Wilkinson, The Algebraic Eigenvalue Problem, Oxford University Press, Oxford, England, 1965.

[37] K.E. Atkinson, An Introduction to Numerical Analysis, John Wiley & Sons, Inc., 1978.

[38] E.J. Rothwell, K.M. Chen, D.P. Nyquist, and W. Sun, "Frequency domain E-pulse synthesis and target discrimination," *IEEE Trans. Antennas Propagat.*, vol. AP-35, no. 4, pp. 426-434, Apr. 1987.

[39] E.J. Rothwell, and K.M. Chen, "A hybrid E-pulse/least squares technique for natural resonance extraction," *IEEE Proc.*, vol. 76, no. 3, pp. 296-298, March 1988.

[40] P. Ilavarasan, E.J. Rothwell, R. Bebermeyer, K.M. Chen, and D.P. Nyquist, "Natural Resonance Extraction from Multiple Data Sets Using a Genetic Algorithm," *1994 International Symposium Digest Antennas and Propagation*, Vol. 1, pp. 576-579.

[41] P. Ilavarasan, E.J. Rothwell, K.M. Chen, and D.P. Nyquist, "Natural resonance extraction from multiple data sets using physical constraints," *Radio Science*, vol. 29, no. 1, pp. 1-7, Jan.-Feb. 1994.

[42] Q. Li, E.J. Rothwell, K.M. Chen, and D.P. Nyquist, "Scattering center analysis of radar targets using fitting scheme and genetic algorithm," *IEEE Trans. Antennas and Propagation*, Vol. 44, No. 2, pp. 198-206, Feb. 1996.

[43] M.A. Morgan and N.J. Walsh, "Ultra-wide-band transient electromagnetic scattering laboratory," *IEEE AP-S*, Vol. AP-39, No. 8, pp.1230-1234, August 1991.

[44] M.A. Morgan, "Ultra-wideband impulse scattering measurements," *IEEE AP-S*, Vol. 42, No. 6, pp.840-846, June 1994.